Development of a computationally efficient model for the control of Ziegler-Natta catalysed industrial production of high density polyethylene

John Themba McCoy

A thesis presented for the
Degree of Doctor of Philosophy
in the Department of Chemical Engineering
Faculty of Engineering and the Built Environment
University of Cape Town

February 2016

Supervisor
Professor Randhir Rawatlal
Co-supervisor
Professor Joao BP Soares

DECLARATION

I, **JOHN THEMBA MCCOY**, hereby declare that the work on which this thesis is based is my original work (except where acknowledgements indicate otherwise) and that neither the whole work nor any part of it has been, is being, or is to be submitted for another degree in this or any other university. I authorise the University to reproduce for the purpose of research either the whole or any portion of the contents in any manner whatsoever.

Signature:……. Date: 6 February 2016

SYNOPSIS

High density polyethylene (HDPE) is commonly produced by the slurry phase co-polymerisation of ethylene and other alkenes, using heterogeneous titanium-based Ziegler-Natta catalysts.

During grade transitions, the conditions in the reactor are deliberately manipulated in order to change the properties of the polymer product. During the grade transition, a period of unsteady-state operation occurs in which significant quantities of off-specification material are produced. Implementing a model predictive controller may allow for minimising the loss of product and raw material which occurs during unsteady-state operation. In order to implement such a controller, an unsteady model of the reactor system is required.

Such a reactor model must account for the influence of, and interactions between, polymerisation reaction kinetics, particle size distributions (PSD), reactor mixing patterns, and operating conditions at steady and unsteady-state, on the production rate and polymer properties.

Current reactor models are based on the Population Balance Model (PBM), but are associated with heavy computational loads to the point that they are unsuitable for real time control applications. The Segregation Approach is proposed here as an alternative with computational costs that are lower by orders of magnitude. It may be that such a model would be suitable for fundamental model-based control to the point where optimal control in applications such as grade transition could be rigorously developed.

Most kinetic models of Ziegler-Natta catalysts are based on the multi-site interpretation, in which the catalyst is assumed to consist of a number of distinct polymerising sites. Each of these sites possesses different polymerisation and termination reaction rates, essentially making each site a different catalyst, in order to explain the wide distribution of chain lengths produced. The recently-developed pseudo-sites model is used in this study as a more fundamental kinetic explanation of polymer property distributions, without resorting to empirically-determined multiple sites.

In the experimental part of this thesis, a laboratory study of an industrial catalyst was performed with the specific goal of extracting meaningful kinetic parameters for a kinetic scheme based on the pseudo-sites model, which has never been experimentally tested. A generalised regression procedure was developed for the determination of meaningful fundamental kinetic parameters from this experimental study, and which is applicable to similar laboratory studies. The kinetic model was able to reproduce the laboratory results, including polymerisation activity profiles, co-polymerisation rate constants, and polymer chain length distributions.

The next part of the thesis led up to the development of the model of an industrial reactor, by considering the impacts of particle size, non-ideal mixing patterns, and the mathematical basis of the model.

The Multi Grain Model of polymer particle growth was used to investigate the effect of mass transfer in the layers of polymer around the catalyst sites. The analysis showed that, for the conditions in the laboratory and industrial reactors, mass transfer had a negligible impact on the polymerisation reactions. Thus the impact of particle size, and evolving particle size distributions, was removed from the reactor model.

A rigorous comparison of the PBM and the Segregation Approach, in the context of polymer particle size distribution modelling, was performed. The comparison showed the equivalence of the two models' predictions. More importantly, it was also demonstrated that even under conditions most heavily favouring the PBM, the Segregation Approach is more efficient and more accurate. This result confirmed the choice of the Segregation Approach as a suitable mathematical basis for a dynamic reactor model.

Non-ideal reactor mixing was investigated for the industrial reactor, which consists of a well-mixed tank with external cooling loops. This combination suggested a Continuously-Stirred Tank Reactor (CSTR) with a Plug Flow Reactor (PFR) recycle. The Residence Time Distribution (RTD) function for this interesting system was developed from first principles. Although it was shown through case studies that the impact of the cooling loops on overall RTD and polymerisation activity is negligible for the industrial reactor to be

considered in this thesis, the RTD formulation of this system is still proposed as a useful tool for researchers studying other such systems.

Finally, the kinetic scheme was extended to the unsteady-state situation, and the dynamic reactor model was developed, based on the Segregation Approach. The model integrates the kinetic scheme and parameters from the laboratory study with time-varying fluid phase properties, flow rates, catalyst activities, and vapour-liquid equilibria in order to simulate the performance of an industrial polymerisation reactor.

Industrial data for steady- and unsteady-state operation was described and analysed. A number of points of comparison between the industrial data and the reactor model were identified; these included Outputs, such as the polymer properties, monomer conversion and catalyst efficiency, and Internal Checks, such as the ratio of hydrogen to ethylene in the reactor cap-gas and the concentration of co-catalyst in the liquid phase of the reactor.

The reactor model predictions were compared with the steady-state industrial data for four different sets of conditions. Initially, the reactor model could not successfully reproduce the industrial results, due to an under-prediction of monomer conversion. This discrepancy led to the re-evaluation of some of the assumptions underlying the reactor model. When accounting for the presence of catalyst and co-catalyst poisons in the laboratory study, and modifying the role of the co-catalyst in the kinetic scheme, the reactor model was shown to successfully simulate the steady-state industrial data, and to reconcile the industrial data with the laboratory-scale data.

The reactor model was then applied to unsteady-state operation, and successfully compared with data for three industrial grade transitions. In particular, the model was able to reproduce the changes to the polymer properties during the transition periods. The transition times of between 30 and 40 hours were simulated in 15 to 25 seconds of computational time, demonstrating the efficiency of the reactor model, and applicability to real-time process control situations.

A sensitivity study of the reactor model was conducted to develop optimal control strategies, by determining the sensitivity of the reactor operation to the feed rates of the various reactants. The polymer product properties (the most important controlled variable when attempting to optimise a grade transition) were found to be most sensitive to the feed rates of the catalyst, monomer and solvent, with the feed rate of hydrogen the next most important manipulated variable. For reactor stability reasons, hydrogen was proposed as the most suitable variable to manipulate in order to optimise the trajectory of a grade transition.

The results of the sensitivity study were used to propose some improved grade transition trajectories. These trajectories were compared with the trajectories from the typical industrial grade transitions. The model-based trajectories were shown to reduce both the quantity of off-specification produced and the time for each transition, by between 20 and 45%, and to require minimal increases in reactant consumption during the grade transition period.

The reactor model which has been proposed is based on a fundamental kinetic scheme, which can explain phenomena such as catalyst activity profiles and wide molecular weight distributions in polymer products. The parameters in the kinetic scheme were fitted to data from a laboratory study. Once the kinetic parameters were built into a dynamic model of the reaction system, the laboratory data and a set of steady-state industrial data were consolidated, and the reactor model then validated with unsteady-state industrial operating data. Because of the computational efficiency of the reactor model, it could be used in a real-time process control application. This would likely allow for even greater improvements to the operation of an industrial polymerisation reactor, particularly during grade transitions.

ACKNOWLEDGEMENTS

Firstly, thanks are due to my supervisor, Prof Randhir Rawatlal. His interest, skill and delight in approaching almost any problem from a modelling point of view is what first attracted me to the field of reactor modelling, and my interactions with him during my undergraduate studies led to the current project, which has alternately excited and exasperated me over the last seven years.

Thanks also to Prof Joao Soares, for hosting me at the University of Waterloo for six months, and for his input during the project. Also at the University of Waterloo, special thanks to Abolfazl, Anthony, Odilia and Ahmad.

The South African (and worldwide) Ultimate community has been a constant source of friendship and support. Although I probably would have graduated years ago if I hadn't spent all of that time chasing a piece of plastic, I am thankful for the people who came into my life through the sport.

To those who have supported me through the last seven years, with encouragement, friendship, sympathy and occasionally a talking-to: thank you. I won't try to name all of you, but special mentions to my parents, Jackie, Davor, the esteemed Junction Fantastic, and all members of The Clique.

And, finally, thank you to Joy, who has written up her own thesis, kept me going on mine, and always been there, through everything.

The financial assistance of Safripol (Pty) Ltd towards this research is gratefully acknowledged. In addition to financial assistance, Safripol (Pty) Ltd also provided valuable assistance in the form expertise, advice and information about industrial polymer production. In particular, the assistance of Mike Gradwell, the former Research & Development Director at Safripol, must be acknowledged, especially for arranging catalyst samples for the laboratory study portion of this work. The assistance of Gert Claasen, the current Research & Development Director at Safripol, particularly during the final stages of the project write-up, is also gratefully acknowledged. Opinions expressed and conclusions arrived at are those of the author and are not necessarily to be attributed to Safripol (Pty) Ltd.

The financial assistance of the National Research Foundation (NRF) towards this research is hereby acknowledged. Opinions expressed and conclusions arrived at, are those of the author and are not necessarily to be attributed to the NRF.

TABLE OF CONTENTS

TABLE OF FIGURES

TABLE OF TABLES

PART A. BACKGROUND

CHAPTER 1. INTRODUCTION

Polyolefins are one of the highest-volume bulk commodity chemicals produced. High density polyethylene (HDPE) is a major polyolefin, with global production of over 30 millions tons every year. As a non-toxic, lightweight and recyclable plastic with good physical properties, HDPE has particular applications in the packaging market, as well as major use as piping for water, natural gases or electrical conduits (Gerdeen et al., 2006).

HDPE is commonly produced on an industrial scale in continuous flow slurry phase reactors. The mechanical properties of the polymer are highly dependent on a variety of factors, including reactor operating conditions like temperature and pressure, reactant concentrations and ratios, catalyst activity and reactor mixing characteristics.

This thesis details the development of an unsteady-state reactor model capable of simulating the operation of a Ziegler-Natta catalysed, slurry-phase reactor producing HDPE.

1.1 Basics of polymerisation chemistry

Polymers are formed by the chemical linking of individual monomer units to build a stable chain, which can be anywhere from hundreds to hundreds of thousands of monomer units in length.

Polyolefin chain growth on Ziegler-Natta catalysts occurs when monomer units are inserted between the active polymerising site of the catalyst and the polymer chain (Kim & Somorjai, 2000a, Kissin et al., 1993), as illustrated in Figure 1.1 (a). A single monomer unit (denoted "M" in the figure) diffuses from the reaction phase to the surface of the catalyst. The catalyst's active site (labelled "Ti^{3+}") facilitates addition of the monomer unit into the polymer chain.

Chain transfer or termination occurs when a terminating agent (such as hydrogen) is added between the catalyst site and the polymer chain, separating the chain from the catalyst site, as in Figure 1.1 (b). The relative rates of the chain propagation and termination reactions determine the average length of the polymer chains produced.

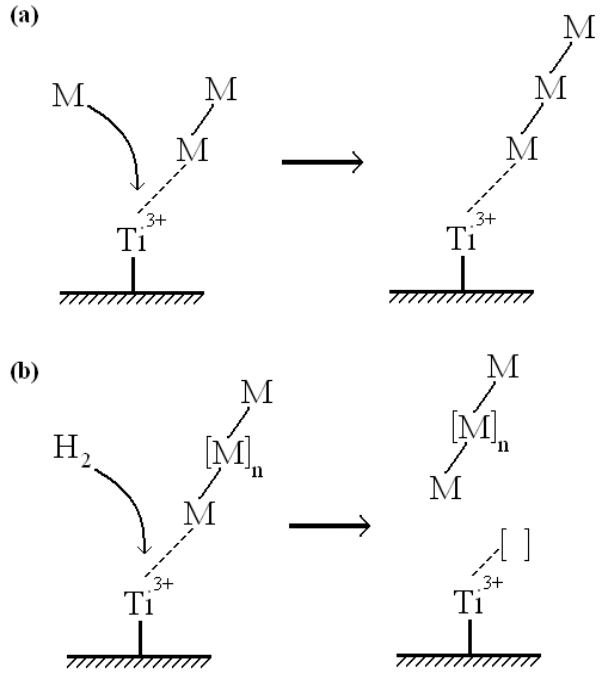

Figure 1.1: (a) Polymer chain growth. (b) Polymer chain termination

The most common monomers are ethylene and propylene, with higher α-olefins such as 1-butene or 1-hexene being used as comonomers. Polymer chain length is generally controlled through the addition of a chain transfer agent, most commonly hydrogen.

1.2 Ziegler-Natta catalysts

Since their discovery in the 1950s by Karl Ziegler and Giulio Natta, Ziegler-Natta catalysts have been the principle industrial promoters of olefin polymerisation, including HDPE. Modern heterogeneous Ziegler-Natta catalysts consist of $TiCl_4$ supported on $MgCl_2$ and/or silica, and are activated by aluminium alkyl co-catalysts. These catalysts exhibit extremely high activities, on the order of 200 kg HDPE/g-Ti/h (Kim et al., 1990, Han-Adebekun et al., 1997b).

This activity is not constant, however: Ziegler-Natta catalysts typically display an activity profile characterised by an initial rapid increase in activity and a more gradual decline from the peak. An example of an activity profile is shown in Figure 1.2.

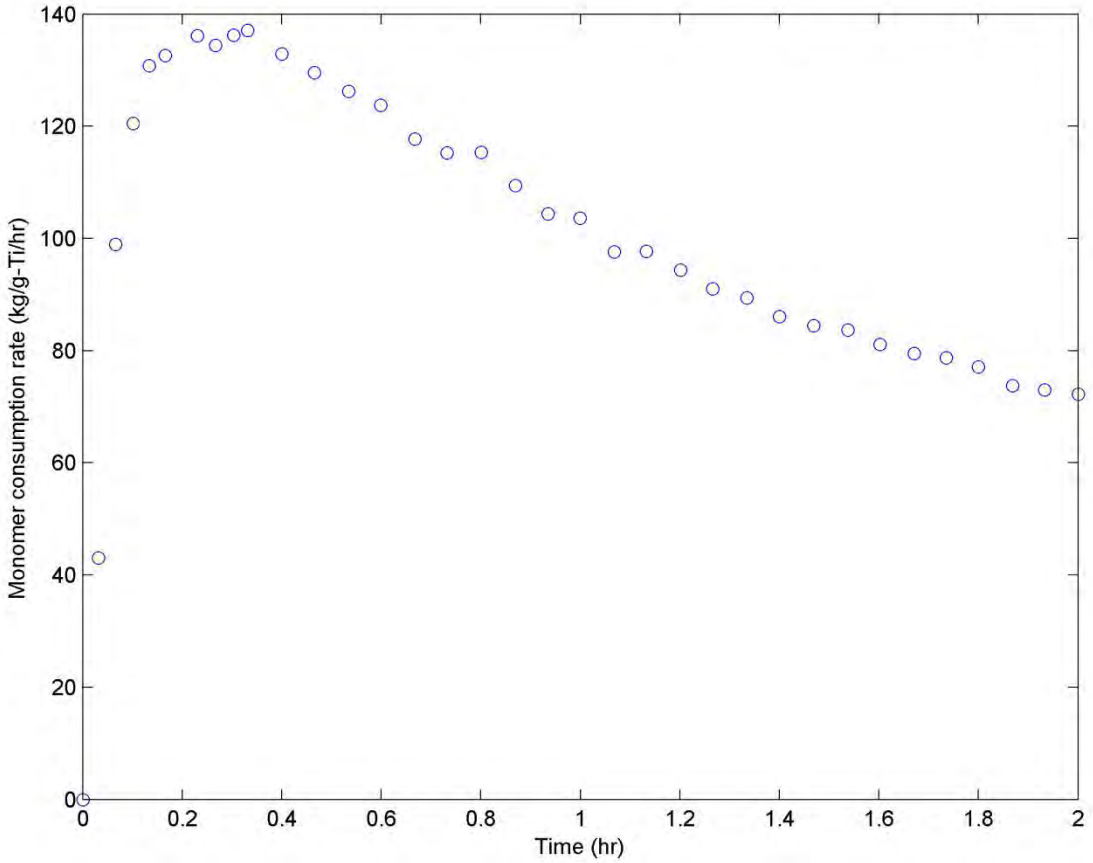

Figure 1.2: Activity profile for typical Ziegler-Natta catalyst (data from Kim et al, 1990)

Another feature of Ziegler-Natta catalysts is their heterogeneous nature: the catalyst sites are not in solution with the reactants, but are on the surface of solid catalyst particles. Polymer chains form a growing layer of solid polymer around the catalyst particle, creating a barrier to diffusion for the reactants. This diffusion resistance may have an effect on the activity of the catalyst and the properties of the polymer.

The solid particles in a slurry phase reactor can grow in size from a few microns to several hundred microns. Particle size can affect the handling of the polymer product, especially at the blending stage.

1.3 Polymer properties

Polymer grade type, which influences the potential end-use of the product, is determined by the physical properties of the polymer. These physical properties include hardness, crystallinity, melting temperature range, flow properties and chemical resistance.

The physical properties of a polymer are determined by the properties of the polymer chains, including average chain length, chain length distribution, degree of branching and relative incorporation of monomer and comonomer.

HDPE, when produced using Ziegler-Natta catalysts, is a linear polymer with short chain branches, due to the presence of the comonomer (Huang et al., 1997, Anantawaraskul et al., 2003, Philipsen, 2004). The most important properties of the polymer chains are thus the chain length and the degree of comonomer incorporation. Chain length, or molecular weight, primarily influences properties like melting temperature and hardness. Comonomer content has the biggest effect on crystallinity, but also influences the melting temperature, flow properties and hardness (Gabriel & Lilge, 2001, Assumption et al., 2006, Fazeli et al., 2006).

The chain length distribution of a polymer, such as that shown in Figure 1.3, from data presented in (Pontes et al., 2008), can be complex to represent mathematically, and so polymers are frequently characterised using the number- and weight-average molecular weights (M_n and M_w, respectively) and polydispersity index (PDI), which indicates the width of the distribution.

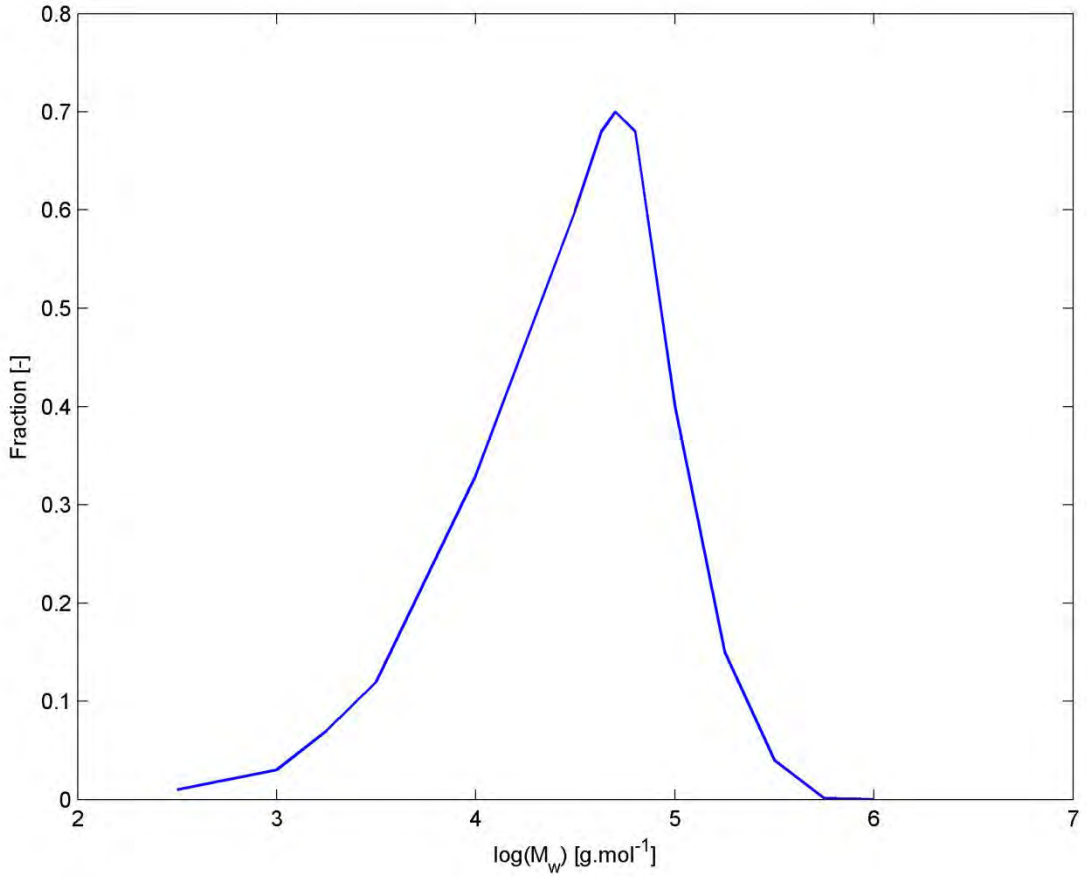

Figure 1.3: Molecular weight distribution of a typical polyolefin (data from Pontes et al, 2008)

The molecular weight averages can be defined in terms of the moments of the chain length distribution. If the concentration of polymer chains of length *n* is denoted P_n, then the *k*-th moment of the distribution of chain lengths is defined in equation 1.1.

$$\lambda_k = \sum_{n=0}^{\infty} n^k P_n \qquad 1.1$$

The moments can then be used with the molecular weight of the monomer, $MW_{monomer}$, to define the molecular weight averages and PDI, as shown in equations 1.2, 1.3 and 1.4.

$$M_n = MW_{monomer} \frac{\lambda_1}{\lambda_0} \qquad 1.2$$

$$M_w = MW_{monomer} \frac{\lambda_2}{\lambda_1} \qquad 1.3$$

$$PDI = \frac{\lambda_0 \lambda_2}{(\lambda_1)^2} \qquad 1.4$$

Experimental analysis of polymers, particularly by size exclusion chromatography (SEC), will frequently report these averages to define a given polymer sample. SEC is an expensive and time- and labour-intensive method, however.

A simpler and more common experimental and industrial indicator of polymer grade is the Melt Flow Index, or MFI (van Krevelen, 1994), which is a measure of the mass of polymer that can be extruded through a die under standard weight, temperature and time conditions (ASTM:D1238, 2010).

It has been suggested by a number of authors (Bremner et al., 1990, McAuley et al., 1990, Huang et al., 1997, Seavey et al., 2003, Alizadeh et al., 2004) that the MFI and weight-average molecular weight of linear polyolefins can be related using an equation of the form shown in equation 1.5.

$$M_w^k = A \frac{1}{MFI} \qquad 1.5$$

In equation 1.5, A and k are constants which can be obtained by fitting data to the equation. Based on the literature, k is expected to have a value of between 3.4 and 4.6, depending on the polydispersity of the polymer samples.

1.4 Industrial production

Polyolefins are produced industrially in a wide range of reactor types and configurations, including batch and continuous reactors with gas-, liquid- and slurry-phases present.

High density polyethylene (HDPE) is commonly produced on an industrial scale in continuous flow slurry phase reactors. A typical slurry phase process is shown in Figure 1.4.

The solvent, typically an alkane such as n-hexane, forms the reaction medium, allowing for more efficient heat and mass transfer between the reactants and the catalyst.

The gaseous reactants (ethylene, the comonomer and hydrogen) are sparged through the reactor, to promote contact with the solvent, the dissolved co-catalyst and the suspended catalyst particles.

Due to the highly exothermic nature of the polymerisation reaction, significant cooling is required. Cooling jackets and loops remove much of the heat of reaction. Gaseous reactants may also be fed at cryogenic temperatures as liquids; the phase changes as they enter the reactor can further help to keep reactor temperature under control.

Polymer particles are removed from the reactor as a slurry, and separated from the solvent, which can be recycled. The polymer powder can then be sent on to further processing, such as blending and extrusion.

This thesis focuses on an industrial polymer production facility which produces various grades of HDPE, amongst other polymers, through the continuous slurry-phase Ziegler-Natta-catalysed co-polymerisation of ethylene and 1-butene, using a reaction system similar to that shown in Figure 1.4. Hydrogen is used as a chain transfer agent, and n-nonane acts as a solvent.

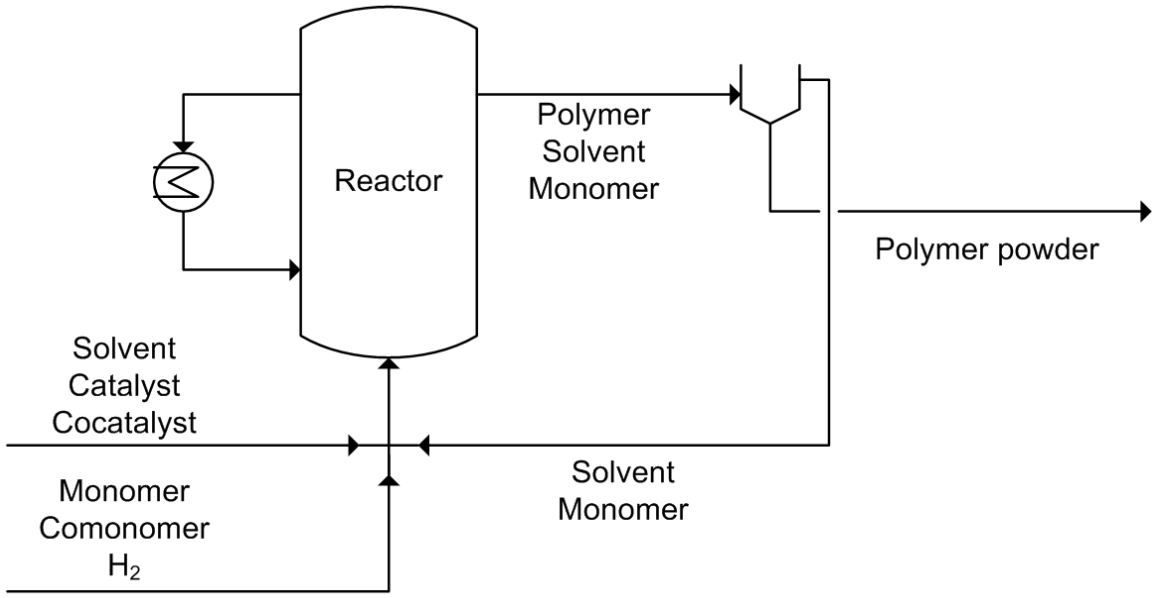

Figure 1.4: Schematic diagram of typical slurry phase olefin polymerisation system

1.5 Grade transitions

The greatest challenge in the operation of continuous flow polymerisation reactors occurs during grade transitions, which involve a controlled change in reaction conditions so as to change the grade of polymer being produced. Grade transitions are inherently periods of unsteady-state operation, and the polymer produced during this time is off-specification material of lower value.

Operators make use of empirical “recipes” in order to determine the reactor conditions for each grade, and experience-based “rules of thumb” or strategies in order to minimise the waste produced during grade transitions. To improve the operation of the ethylene polymerisation reactors by the implementation of model-based control, accurate unsteady-state plant simulators are required.

Unfortunately, there is a dearth of such models in the literature. Current models are based on steady-state residence time distributions, computationally inefficient Population Balance Models and empirically determined catalyst kinetics. Steady-state models are obviously not applicable to the unsteady-state modes of operation experienced during grade transitions. Computational inefficiency becomes problematic when attempting real time control of a real process; Population Balance approaches in particular are too

computationally intensive for application in the control environment. Empirical kinetic models can only be applied to the situation for which they were derived; they can not be extended to different catalysts or operating conditions.

1.6 Thesis outline

This thesis is divided into four main parts, each of which consists of a number of chapters.

Part A provides the background to the thesis, beginning with **Chapter 1**, the introduction to some of the basic concepts of polymerisation chemistry and the ideas that will be addressed in the thesis.

Chapter 2 is a review of the literature, describing the state of the art in the polymer reaction engineering field. Developments in polymerisation kinetics, particle morphology and reactor simulation are discussed, and some gaps in current knowledge identified. These gaps primarily relate to the lack of simulations of polymerisation processes that are based on fundamental kinetic schemes, and are also computationally efficient enough to be used in a real-time control application.

In **Chapter 3**, the objectives of this thesis are developed. The overall objective is to develop a computationally efficient model of industrial-scale polymer production; intermediate objectives include the extraction of kinetic parameters from laboratory data, the mathematical formulation of a reactor simulation, and validation of the model with industrial data.

Part B describes the experimental part of the thesis, focussed on polymerisation reaction kinetics. **Chapter 4** develops a set of regression procedures that can be used to extract kinetic parameters from experimental data, with a focus on fitting parameters to meaningful regions of data.

The actual experimental work is described in **Chapter 5**. A set of laboratory-scale polymerisation reactions were conducted, over a range of industrially-relevant conditions, in order to generate a data set that could be analysed using the methods developed in Chapter 4.

Chapter 6 demonstrates the application of the regression procedure from Chapter 4 to the data from Chapter 5, and the extraction of a set of kinetic parameters that can reproduce the experimental results, including catalyst activity profiles, comonomer incorporation and molecular weight distribution.

Part C describes a number of mathematical developments towards the formulation of an unsteady-state reactor model. The first chapter in this part, **Chapter 7**, analyses the potential for concentration gradients in growing polymer/catalyst particles. The results indicated that mass transfer limitations were not present for the current study, and so the effects of particle size on polymerisation kinetics were neglected.

A rigorous comparison of the prediction of distributions in polymerisation reactors is presented in **Chapter 8**. The computational efficiency of the widely used Population Balance Model was compared to the Segregation Approach, which can predict the moments of distributions without the need to solve multidimensional partial differential equations. The results of the comparison showed that the Segregation Approach is as much as an order of magnitude more efficient, and so the approach was used in the development of the reactor model for this work.

Chapter 9 shows a rigorous solution for the Residence Time Distribution of a typical slurry-phase polymerisation reactor: a well-mixed vessel with external cooling loops. Although this reactor configuration was shown not to have an influence on reaction kinetics for the current study, more general applications of this Residence Time Distribution were discussed.

The final chapter in Part C**, Chapter 10**, details the formulation of the dynamic reactor model which is used to simulate an industrial reactor. The model makes use of the Segregation Approach, for computational efficiency.

Part D concerns the industrial context, starting with **Chapter 11**, which describes the industrial operating data that was used in the project. The available industrial data was analysed and classified into a number of points of comparison between the data and the simulation.

In **Chapter 12**, the experimentally developed kinetics are combined with the dynamic reactor model from Chapter 10, and compared to steady-state industrial operating data. This initial comparison revealed that the simulation was significantly under-predicting the conversion of ethylene in the reactor.

Chapter 13 details the reevaluation of a number of assumptions that were made in the formulation of the reactor model, in order to determine why the monomer conversion is under-predicted. The impact of imperfect reactor mixing patterns, catalyst and co-catalyst poisons and the role of the co-catalyst in the kinetic scheme were investigated. Because of the resulting modifications to the reactor model formulation, the kinetic parameters fitted to the data in Chapter 6 needed to be reevaluated.

In **Chapter 14**, in light of the changes to the model formulation, the kinetic parameters determining polymer chain length were refitted to the laboratory and industrial data simultaneously, in order to reconcile these two data sets.

Chapter 15 describes the unsteady-state industrial operational data that was available, and analyses the trajectories of three industrial grade transitions. The reactor model, fitted to laboratory data and steady-state industrial data, was then compared to the unsteady-state data, and shown to reproduce dynamic reactor behaviour very well.

The validated reactor model was analysed in **Chapter 16**, to determine the sensitivity of the various reactor outputs to the different reactor feeds. A number of methods to improve industrial grade transitions are proposed.

In **Chapter 17**, the proposals for grade transition trajectory optimisation are illustrated, and the potential for improvements to operation demonstrated, along with the computational efficiency of the reactor model, which is shown to be suitable for real-time process control applications.

Part E contains only **Chapter 18**, the conclusions chapter of the thesis, which summarises the results of the work.

Part F shows the list of references that were used in the literature review, and throughout the thesis.

Part G is the Appendix, showing further details of the work that was performed, where including this detail in the main text would have been inappropriate.

CHAPTER 2. LITERATURE REVIEW

In order to successfully predict the behaviour of polymerisation reaction systems, it is necessary to consider three levels of detail: micro, meso and macro (Ray, 1986, Ray, 1988, Dube et al., 1997, McKenna & Soares, 2001). These scales are illustrated in Figure 2.1.

This review of the literature will be organised according to this multiscale understanding of polymerisation systems. A brief description of each scale is given below. The sections that follow will cover each scale of interest in more detail, and analyse the research that has been performed in each area.

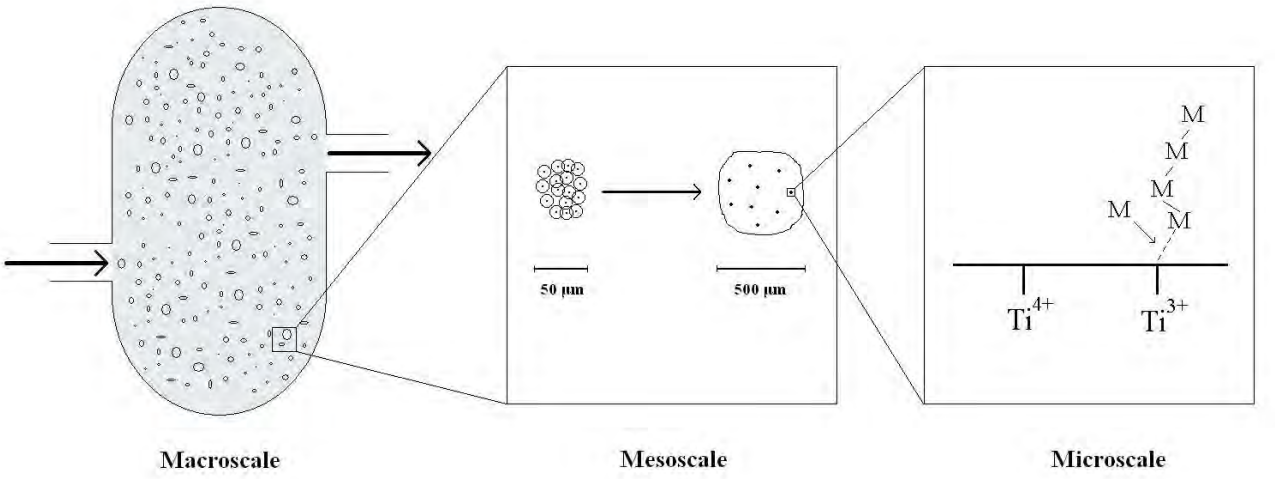

Figure 2.1: The three scales of modelling

Micro scale

The micro scale (more correctly nano scale, but the term has become accepted in the literature) is concerned with the kinetics of the catalysed polymerisation reaction, including catalyst site activation, chain propagation and termination and comonomer incorporation.

Kinetic studies of Ziegler-Natta catalysts have shown that activity profiles exist, and are a complex function of the concentrations of various reactants and operating conditions (Kim & Woo, 1990, Kim et al., 1990, Han-Adebekun et al., 1997a, Wu et al., 1999).

Ziegler-Natta catalysts have also been shown to produce unusually wide chain length distributions during olefin polymerisation (Singh & Merrill, 1971, Soares & Hamielec, 1995a, Chen et al., 2006). The most probable (or Flory) distribution of chain lengths produced at a single catalyst site is expected to have a polydispersity index (PDI) of 2; polymers produced with Ziegler-Natta catalysts frequently have PDI values greater than 10 (Singh & Merrill, 1971).

Some authors have proposed the existence of multiple active site types, which polymerise at different rates, to explain the catalyst activity profiles and polymer property distributions, especially the very high values for PDI (Kissin et al., 1993, Soares & Hamielec, 1995a, Chen & Fan, 2006, Kissin et al., 2008, Kissin, 2012, Xu et al., 2015).

Meso scale

On the meso scale, catalyst particle growth must be modelled. As polymerisation proceeds, catalyst particles become encased in a growing layer of polymer, affecting the transfer of heat and mass and the particle

morphology (Floyd et al., 1986a, Kittilsen et al., 2001, Kittilsen & McKenna, 2001). The final polymer particles are considered to be highly porous agglomerations of catalyst fragments surrounded by polymer. Figure 2.2 shows such a particle.

Mean particle size, particle morphology and particle size distribution (PSD) can affect the rate of polymerisation and product handling in post-reaction steps such as transport, storage and blending (Choi et al., 1994, Zacca & Debling, 2001). In order to predict these effects, particle growth models are required which can determine the changes in PSD within a reactor, and the influence of particle size on the reaction kinetics, including mass and heat transfer limitations (Browning et al., 2012, Rashedi & Sharif, 2015).

Macro scale

On the macro scale, reactor hydrodynamics and vapour liquid equilibria must be quantified. There are published attempts at modelling the transfer of monomer from gas to liquid phase, and the effects of reactor mixing type, residence time and agitation rate (Floyd et al., 1986b, Bhagwat et al., 1994, Soares & Hamielec, 1995b, Zacca et al., 1996, Zacca et al., 1997). More recent publications have applied Computational Fluid Dynamics (CFD) to the problem of simulating complex flow patterns in industrial reactors (Yan et al., 2012, Khan et al., 2014, Schneiderbauer et al., 2015).

In order to be considered successful, a model must integrate all the above-mentioned concepts in a single coherent formulation, and be able to predict not just the rate of polymer production, but also the properties of the polymer, particularly the PDI and M_n described above.

Extensive research has been conducted over the decades on all three scales of interest. Some works focussed on extending knowledge on just one scale at a time, such as particle morphology (Floyd et al., 1986a, Kittilsen et al., 2001, Martin & McKenna, 2002) or reactor staging and residence time distribution (Soares & Hamielec, 1995b, Zacca et al., 1996, Meng et al., 2013). More recent works (Dompazis et al., 2008, Soni & Bhagwat, 2008, Rawatlal, 2009, Shamiri et al., 2012, Krallis et al., 2015) have investigated integrating all three scales in order to predict system performance.

Macro-scale models have also been applied in the process control field, to optimise grade transitions. Earlier works focussed on using rigorous models of the polymerisation process (Chatzidoukas et al., 2003) but more recent publications have made use of empirical correlations (Wei et al., 2014) or even proposed novel mathematical techniques such as neural networks and fuzzy functions to analyse plant operating data and develop predictive control models (Xu & Liu, 2014). These empirical methods were proposed to avoid the computational cost of solving the rigorous models of polymerisation processes.

2.1 Micro scale

As mentioned above, the micro scale actually refers to the nano scale: the realm of catalyst sites, polymer chains and chemical reactions. However, in the literature, the term micro scale has become generally accepted, and so it is adopted here.

2.1.1 Traditional multi-site kinetic model

It is generally assumed in the literature that Ziegler-Natta catalysts are "multi-site" catalysts; in other words there are several distinct types of active sites, each of which produces polymer with different average properties at different rates, and may also be activated and deactivated at different rates (Hutchinson et al., 1992).

The kinetic scheme proposed by Hutchinson et al. is summarised in Table 2.1.

Table 2.1: Traditional kinetic scheme

	Reaction	**Rate constant**
Site activation		
Spontaneous	$C_p \rightarrow P_0^q$	$k_{a,sp}^q$
Aluminium Alkyl (A)	$C_p + \alpha_A A \rightarrow P_0^q$	$k_{a,A}^q$
Electron Donor (E)	$C_p + \alpha_E E \rightarrow P_0^q$	$k_{a,E}^q$
Hydrogen (H_2)	$C_p + \alpha_{H_2} H_2 \rightarrow P_0^q$	k_{a,H_2}^q
Monomer (M_i)	$C_p + \alpha_{M_i} M_i \rightarrow P_0^q$	k_{a,M_i}^q
Site deactivation		
Spontaneous	$P_n^q \rightarrow C_d + D_n^q$	$k_{d,sp}^q$
Poison (Z)	$P_n^q + \alpha_Z Z \rightarrow C_d + D_n^q$	$k_{d,Z}^q$
Aluminium Alkyl (A)	$P_n^q + \alpha_A A \rightarrow C_d + D_n^q$	$k_{d,A}^q$
Electron Donor (E)	$P_n^q + \alpha_E E \rightarrow C_d + D_n^q$	$k_{d,E}^q$
Hydrogen (H_2)	$P_n^q + \alpha_{H_2} H_2 \rightarrow C_d + D_n^q$	k_{d,H_2}^q
Monomer (M_i)	$P_n^q + \alpha_{M_i} M_i \rightarrow C_d + D_n^q$	k_{d,M_i}^q
Site transformation		
Spontaneous	$P_*^q \rightarrow P_0^r + D_n^q$	$k_{st,sp}^{q,r}$
Poison (Z)	$P_*^q + \alpha_Z Z \rightarrow P_0^r + D_n^q$	$k_{st,Z}^{q,r}$
Aluminium Alkyl (A)	$P_*^q + \alpha_A A \rightarrow P_0^r + D_n^q$	$k_{st,A}^{q,r}$
Electron Donor (E)	$P_*^q + \alpha_E E \rightarrow P_0^r + D_n^q$	$k_{st,E}^{q,r}$
Hydrogen (H_2)	$P_*^q + \alpha_{H_2} H_2 \rightarrow P_0^r + D_n^q$	$k_{st,H_2}^{q,r}$
Chain transfer		
Spontaneous	$P_{n,i}^q \rightarrow P_0^q + D_{n,i}^q$	$k_{t,sp}^q$
Aluminium Alkyl (A)	$P_{n,i}^q + A \rightarrow P_0^q + D_{n,i}^q$	$k_{t,A}^q$

Electron Donor (E)	$P_{n,i}^{q} + E \rightarrow P_{0}^{q} + D_{n,i}^{q}$	$k_{t,E}^{q}$
Hydrogen (H_2)	$P_{n,i}^{q} + H_{2} \rightarrow P_{0}^{q} + D_{n,i}^{q}$	k_{t,H_2}^{q}
Monomer (M_i)	$P_{n,i}^{q} + M_{i} \rightarrow P_{1,i}^{q} + D_{n,i}^{q}$	k_{t,M_i}^{q}
Propagation		
Initiation	$P_{0}^{q} + M_{i} \rightarrow P_{1,i}^{q}$	$k_{0,i}^{q}$
Propagation	$P_{n,i}^{q} + M_{j} \rightarrow P_{n+1,j}^{q}$	$k_{p,ij}^{q}$

Table 2.2: Key to kinetic scheme in Table 2.1

α_X	Stoichiometric coefficient for reactant X
C_p	Potential, un-activated catalyst site
C_d	Deactivated catalyst site
$D_{n,i}^{q}$	Dead polymer chain of length *n*, at site *q*, with monomer *i* last added
P_{*}^{q}	Active site of type *q*, vacant or occupied
P_{0}^{q}	Active site of type *q*, vacant
$P_{n,i}^{q}$	Active site of type *q*, with growing chain of length *n* and monomer *i* last added

The kinetic scheme in Table 2.1, and its multiple site types, has been proposed to explain the activity profiles of the catalysts in lab reactors (Kissin et al., 1999, Wu et al., 1999), and the wide molecular weight distributions and frequently bimodal chemical composition distributions of the polymer produced by Zeigler-Natta catalysts (Soares & Hamielec, 1995a, Huang et al., 1997, Chen et al., 2006, Zakharov et al., 2007, Matsko et al., 2009).

Kinetic studies of Ziegler-Natta catalysts have generally been conducted to obtain an understanding of the mechanisms involved, rather than to extract parameters for process simulation (Kim & Woo, 1990, Kim et al., 1990, Soares & Hamielec, 1996a, Soares & Hamielec, 1996b, Han-Adebekun & Ray, 1997, Han-Adebekun et al., 1997a, Kim & Somorjai, 2000a, Garoff et al., 2002, Chen & Fan, 2006, Taniike et al., 2012).

The parameters used in most simulation studies are assigned representative values in order to present qualitative results of reactor configuration and operation (Zacca et al., 1996, Zacca et al., 1997, Zacca & Debling, 2001, Luo et al., 2008, Shamiri et al., 2010, Meng et al., 2013).

The exception to this is the deconvolution of MWD curves from Gel Permeation Chromatography (GPC) into most probable Flory distributions (Flory, 1953), a method proposed by Soares & Hamielec (Soares & Hamielec, 1995a). Many authors have used this method to analyse polymer samples, and propose models or kinetic schemes to describe polymerisation reactor products.

The results of these analyses have differed quite significantly, with various authors proposing different numbers of sites, and offering different interpretations for site heterogeneity.

Kissin et al (Kissin et al., 1999) analysed ethylene-1-hexene co-polymers, identifying five active sites which differed in activation, deactivation and termination reaction rates. A more recent paper by the same authors (Kissin, 2012) investigated the kinetics of active site formation in a number of different titanium-based Ziegler-Natta catalysts, and identified between three and five types of sites (based on deconvolution into

Flory distributions) which were active at different temperatures, had different activity curves, and polymerised at different rates.

The group of Kiparissides et al has published several papers investigating gas-phase propylene polymerisation, and proposed kinetic models with two sites, differing only in propagation rates (Hatzantonis et al., 1998), differing in initiation and propagation rates (Hatzantonis et al., 2000), differing in termination rates and propagation with respect to comonomer (Chatzidoukas et al., 2003), differing in termination and propagation rates (Dompazis et al., 2005, Dompazis et al., 2006, Dompazis et al., 2008), and four sites which differ in termination rates only (Touloupides et al., 2010).

Khare et al have simulated slurry-phase ethylene polymerisation, using five sites (Khare et al., 2002), and polypropylene polymerisation, using four sites (Khare et al., 2004).

Neto et al used three sites, differing in termination rates, to simulate ethylene-1-butene co-polymerisation (Neto et al., 2005).

Hakim et al have simulated similar systems, using six sites that differed in termination and propagation rates (Hakim & Moballegh, 2006), but in a later study adjusted the number of sites to four (Hakim et al., 2008).

A three-site model was proposed by Matsko and coworkers (Zakharov et al., 2007), suggesting that the sites differed in termination rates; the same authors made use of five sites in a later study (Matsko et al., 2009).

Other authors have also made use of five or six sites based on fractionation results (Chen et al., 2006), and five sites that differ in initiation, termination and propagation rates (Luo et al., 2009). An earlier simulation paper by the same authors proposed two sites which differed in propagation rate only (Luo et al., 2008). Shamiri et al used two sites, also differing in initiation, termination and propagation rates (Shamiri et al., 2010, Shamiri et al., 2012). A continuum of active site types has also been proposed (Ha & Rhee, 2001).

Two more recent studies of polymerisation of ethylene and 1-hexene also used deconvolution to identify four or five sites which differed in monomer and comonomer propagation rates (Xu et al., 2015, Yang et al., 2015), and produced very different molecular weight polymers, depending on co-catalyst and comonomer concentrations.

The large number of different interpretations of site heterogeneity suggests that there is not a cohesive understanding of the nature of the sites which are responsible for the production of polyolefins with wide MWDs. In particular, no physically realistic explanation has yet been offered for the existence of different rates of propagation.

Surface science studies and experiments with model catalysts have shown that there may be different sites for the adsorption of titanium onto $MgCl_2$ supports, based on crystal structures and catalyst manufacturing techniques, including the impact of interactions between adjacent catalyst sites, and the interactions between catalyst sites and catalyst surface electron donors (Lin & Catlow, 1995, Shiga et al., 1995, Kim & Somorjai, 2000b, Boero et al., 2002, Brambilla et al., 2007, Andoni et al., 2008, Stukalov & Zakharov, 2009, Bahri-Laleh et al., 2011).

Differently-structured adsorption sites for active centers may be a physical explanation for the proposed multiple site types, potentially explaining steric effects such as stereoselectivity in polypropylene (Garoff et al., 2003, Lee & Jo, 2007), preferential incorporation of comonomer into selected polymer chains (Chatzidoukas et al., 2003), or preferential termination by different terminating agents. However, these adsorption effects can not explain the fundamental differences in monomer insertion rate that are proposed in most multi-site catalyst models.

2.1.2 New interpretations

Polymer properties

In principle, a kinetic scheme with multiple sites that differ in propagation rates is not the correct approach to modelling wide chain length distributions. As Floyd et al (Floyd et al., 1987) pointed out, in order to produce a wide MWD, a catalyst must have distinct sites each producing the same mass of polymer, but of different chain lengths. Sites with different propagation rates will produce different masses of polymer, limiting the width of distribution that is possible (Rawatlal & Tincul, 2008). Zakharov et al (Zakharov et al., 2007) have also suggested that sites do not differ in propagation but in termination rates.

Earlier work simulating industrial reactors (Neto et al., 2005) proposed three types of sites which had identical propagation rates, but differing termination rates, based on deconvolution of molecular weight distributions. This study ignored the terminating effects of hydrogen and the co-catalyst; each of the three types of sites had differing terminating rates for the monomer and the comonomer.

A more recent simulation study proposed four distinct sites, also differing in termination rates but identical in activity and propagation rate (Touloupides et al., 2010). Termination reactions were due to hydrogen or spontaneous chain termination.

Although the catalysts in these two studies were referred to as "multi-site" catalysts (based on the deconvolution of molecular weight distrubtions) they differed from the usual interpretation of a multi-site catalyst as having distinct activity and propagation rate constants for each site.

While there has been no physical explanation for differing propagation rates at each site, differing termination rates could relate to the presence of different terminating agents: it has been shown that hydrogen, monomers and co-catalysts can all be active for chain termination (Kissin et al., 1993).

Catalyst activity

Studies of the oxidation state of the titanium catalyst sites have shown a very strong correlation between oxidation state and activity, with only one (or at most two) oxidation states being active for polymerisation. This concept was originally established by Soga et al (Soga et al., 1982), and has been supported by a number of experimental and simulation studies (Han-Adebekun & Ray, 1997, Han-Adebekun et al., 1997a, Fregonese et al., 2001, Ostrovskii & Kenig, 2005, Bhaduri et al., 2006).

A number of authors have found evidence of the reduction of Ti^{4+} on catalyst surfaces when exposed to typical alkylaluminium co-catalysts (Kissin et al., 2008, Stukalov & Zakharov, 2009, Kissin, 2012, Groppo et al., 2015). Some authors propose that only Ti^{3+} is active for polymerisation and that Ti^{4+} is sequentially reduced to the active Ti^{3+} and then the inactive Ti^{2+} (Bahri-Laleh et al., 2011), while others have suggested that the surface titanium species are preferentially reduced to Ti^{3+} by the co-catalyst triethylaluminium (Stukalov & Zakharov, 2009).

More recently, direct evidence of a correlation between the fraction of titanium in the Ti^{3+} state and polymerisation activity has been found in Ziegler-Natta catalysts with very low titanium content (Koshevoy et al., 2014). In particular, isolated Ti^{3+} ions were found to correlate directly with polymerisation activity.

The studies above suggest that polymerisation activity can be directly correlated with the oxidation state of the titanium ions on the surface of the catalyst, and that activation and deactivation of the sites could be interpreted in terms of changes to the titanium ions' oxidation states.

2.1.3 New kinetic model

The use of termination (rather than propagation) rates to describe the development of polymer properties was built into a reformulated kinetic scheme (Rawatlal, 2004), which also correlates activity and oxidation state. The differentiation of catalyst sites by the terminating agent acting at that site is known as the pseudo-sites concept.

Each pseudo-site is identical in terms of activity and propagation rate, but polymer chains growing at each pseudo-site are considered to be terminated by only one terminating agent. Thus the pseudo-sites are not necessarily physically distinct catalyst sites, but are identified as being associated with particular termination reactions.

The total number of active sites in a catalyst consists of all the pseudo-sites, and the full range of chain lengths is composed of the fractional contributions of the chains produced at each pseudo-site.

The kinetic scheme proposed (Rawatlal, 2004) is outlined in Table 2.3.

Table 2.3: Kinetic scheme of Rawatlal (2004)

	Reaction	Rate constant
Catalytic reactions		
Site transformation		
Spontaneous	$P_*^q \rightarrow P_0^r + D_n^q$	$k_{st,sp}^{q,r}$
Aluminium Alkyl (A)	$P_*^q + \alpha_A A \rightarrow P_0^r + D_n^q$	$k_{st,A}^{q,r}$
Hydrogen (H_2)	$P_*^q + \alpha_{H_2} H_2 \rightarrow P_0^r + D_n^q$	$k_{st,H_2}^{q,r}$
Polymeric reactions		
Propagation		
Initiation	$P_0^q + M_i \rightarrow P_{1,i}^q$	$k_{0,i}^q$
Propagation	$P_{n,i}^q + M_j \rightarrow P_{n+1,j}^q$	$k_{p,ij}^q$
Termination		
Spontaneous	$P_{n,i}^q \rightarrow P_0^q + D_{n,i}^q$	$k_{t,sp}^q$
Aluminium Alkyl (A)	$P_{n,i}^q + A \rightarrow P_0^q + D_{n,i}^q$	$k_{t,A}^q$
Monomer (M_i)	$P_{n,i}^q + M_i \rightarrow P_{1,i}^q + D_{n,i}^q$	k_{t,M_i}^q
Hydrogen (H_2)	$P_{n,i}^q + H_2 \rightarrow P_0^q + D_{n,i}^q$	k_{t,H_2}^q

The main difference between this kinetic scheme and those based on the original proposal of Hutchinson et al (Hutchinson et al., 1992), shown in Table 2.1, is the separation of reactions into those occurring at the catalyst site (catalytic reactions) and those affecting the growth of polymer chains (polymeric reactions). In both cases, the equations describe the changes to catalyst and polymer in a batch reactor, in the absence of flow.

One of the primary concerns of this study is the effect of site transformations on the activity of the catalyst. As in previous studies (Hutchinson et al., 1992), a lumped kinetic parameter can be introduced to simplify the notation for site transformations (equation 2.1).

$$\beta_{st}^{q,r} = k_{st,sp}^{q,r} + k_{st,A}^{q,r}\left[A\right]^{\alpha_A} + k_{st,H_2}^{q,r}\left[H_2\right]^{\alpha_{H_2}} \qquad 2.1$$

Similarly, a lumped parameter can account for the effects of all terminating agents, as shown in equation 2.2. This parameter is used in traditional, multi-site models.

$$\beta_t = k_{t,sp} + k_{t,A}[A] + \sum_i k_{t,M_i}[M_i] + k_{t,H_2}[H_2] \qquad 2.2$$

Catalyst activity

Taking oxidation state as the basis for site type (and therefore catalyst activity), and assuming that titanium sites enter in the Ti^{4+} oxidation state, a set of differential equations can be derived to describe the rates of change of titanium site oxidation states.

If it is assumed that sites can be reduced or oxidised, then the set of differential equations predicting activity evolution will be as shown in equations 2.3. Previous attempts (Rawatlal, 2004) to fit experimental data using the kinetic scheme presented above showed that the most promising scheme involved irreversible reduction of inactive Ti^{4+} to Ti^{3+}, and reversible reduction of Ti^{3+} to Ti^{2+}. This results in the set of differential equations shown in equations 2.3.

$$\begin{aligned}
\frac{dP_*^{4+}}{dt} &= -\beta_{st}^{4+,3+} P_*^{4+} \\
\frac{dP_*^{3+}}{dt} &= \beta_{st}^{4+,3+} P_*^{4+} - \beta_{st}^{3+,2+} P_*^{3+} + \beta_{st}^{2+,3+} P_*^{2+} \\
\frac{dP_*^{2+}}{dt} &= \beta_{st}^{3+,2+} P_*^{3+} - \beta_{st}^{2+,3+} P_*^{2+} \\
P_*^{4+}(0) &= 1;\ P_*^{3+}(0) = P_*^{2+}(0) = 0
\end{aligned} \qquad 2.3$$

In the equations above, P_*^q represents the fraction of sites of oxidation state q. This set of linear ordinary differential equations can be solved analytically using standard techniques when the $\beta_{st}^{q,r}$ values do not vary with time. Since the lumped parameters depend on reactant concentrations, if the concentration of co-catalyst, monomers and hydrogen does not change with time then the solution is relatively simple. For semi-batch lab-scale experiments, concentrations are maintained as close to constant as possible, and so this approach is ideal for the analysis of lab-scale activity data.

For cases when concentrations vary, the lumped site transformation parameters will be time-varying; in this situation there is no closed solution and numerical methods must be applied (Iserles, 1984).

Polymer properties

The extraction of the MWD and polymer properties from the kinetic scheme is not trivial. The mathematical representation of the chain length distribution for growing polymer populations can contain hundreds of thousands of equations, one for each chain length, and is therefore numerically and computationally intensive.

The moments of a distribution can be used to reduce the quantity of information required, and predict useful indices of the molecular weight distribution; in particular the number-average molecular weight (M_n), the weight-average molecular weight (M_w) and the polydispersity index (PDI). The k-th moment of the distribution of chain lengths is defined in equation 1.1, reproduced below.

$$\lambda_k = \sum_{n=0}^{\infty} n^k P_n \quad 1.1$$

The moments can then be used to define the mean chain length and PDI, as shown in equations 1.2, 1.3 and 1.4, which are reproduced below.

$$M_n = MW_{monomer} \frac{\lambda_1}{\lambda_0} \quad 1.2$$

$$M_w = MW_{monomer} \frac{\lambda_2}{\lambda_1} \quad 1.3$$

$$PDI = \frac{\lambda_0 \lambda_2}{\lambda_1^{\,2}} \quad 1.4$$

Due to the formulation of the pseudo-sites kinetic scheme in this thesis, with a single type of polymerising catalyst site (corresponding to a single oxidation state of the Titanium catalyst sites), it is not possible to reproduce bi- or multi-modal chemical composition distributions, as have been observed by many authors studying polyolefin systems (Huang et al., 1997, Sarzotti et al., 2004, Barabanov et al., 2015).

2.1.4 Kinetic studies

There have been relatively few publications (Hamba et al., 1997, Matos et al., 2001, Kou et al., 2005b, Kou et al., 2005c) describing methods to obtain kinetic parameters to describe the activity of the catalysts and the properties of the polymer products.

The gas-phase polymerisation of propylene was studied with a view to extracting parameters for a kinetic scheme to investigate an industrial reactor (Matos et al., 2001), but ignored the effect of evolving catalyst activity, focussing instead on experimental design with a very simple kinetic scheme.

McAuley and co-workers have conducted a series of studies of the gas-phase polymerisation of ethylene over a metallocene catalyst (Kou et al., 2005a), and detailed their methods for the extraction of kinetic parameters from the data (Kou et al., 2005b, Kou et al., 2005c). The same group has also published methods to determine estimability of kinetic parameters from experimental data (Yao et al., 2003). They obtained good fits for activity profiles and polymer properties, using one- and two-site models for homo- and co-polymerisation experiments, finding that better results were obtained when using a two-site model.

These kinetic studies were performed to analyse experimental data in terms of the kinetic scheme shown in Table 2.1. No work has yet rigorously analysed experimental results in light of the newer kinetic framework of Table 4.1.

2.1.5 Summary

While the multi-site model of Ziegler-Natta catalysts is widely applied in the literature, there is an inconsistency in the applications of this scheme. The number of catalyst sites proposed, and the ways in which they differ, seems to vary from author to author, and in some cases from paper to paper. The lack of a physical interpretation of the different site types further argues against the traditional kinetic scheme of Table 2.1 (Hutchinson et al., 1992).

The kinetic model presented in Table 2.3 is based on a more fundamental understanding of catalyst activity, in terms of catalyst site oxidation state, and on the pseudo-sites concept, which differentiates sites by termination rate. However, this kinetic framework has not yet been applied to experimental data.

2.2 Meso scale

During heterogeneous polymerisation, catalyst particles become encased in a growing layer of polymer, affecting particle morphology and the transfer of heat and mass (Floyd et al., 1986a, Kittilsen et al., 2001, Kittilsen & McKenna, 2001). The meso scale addresses phenomena such as these.

A magnified image of a typical polymer particle is shown in Figure 2.2. The particle in this image is from the experimental work described in Chapter 5, specifically experimental Run #8. Reaction conditions can be found in Table 5.1.

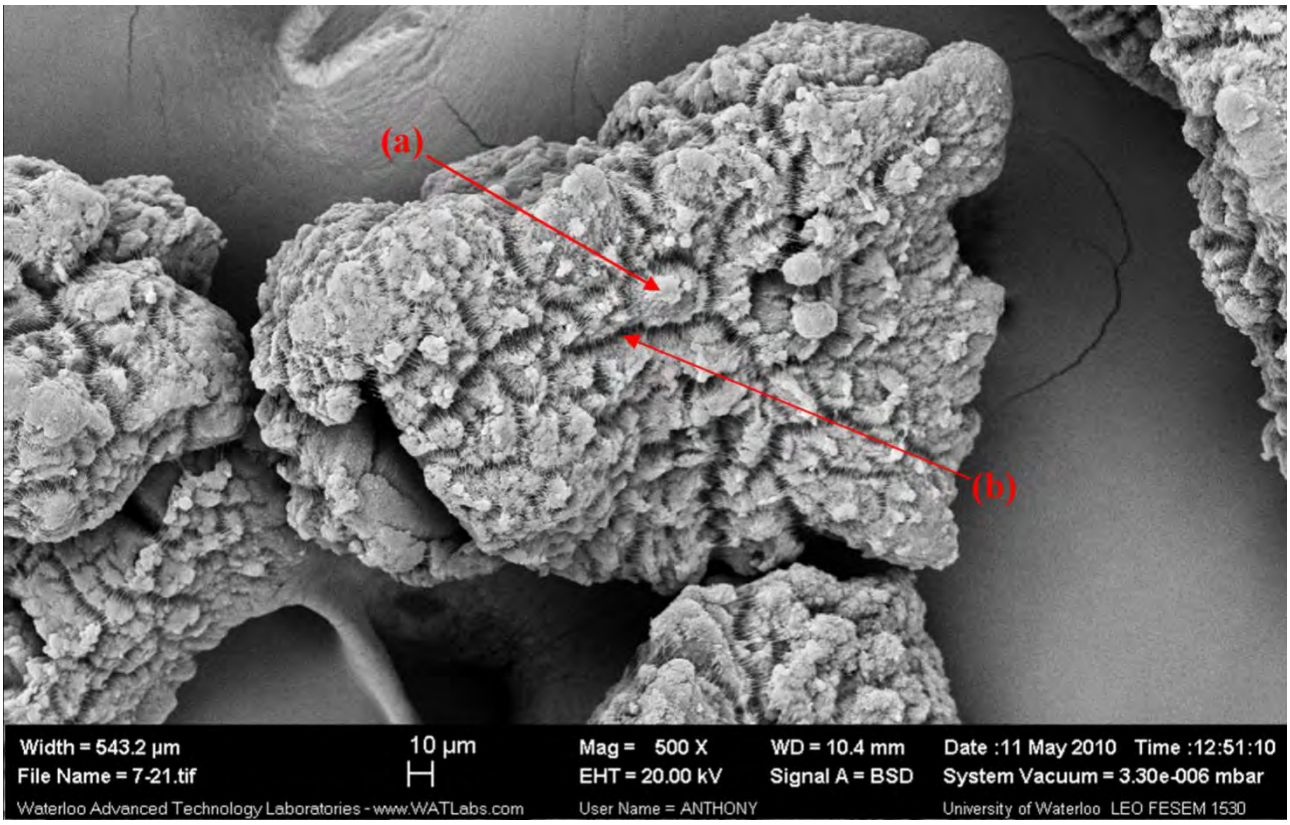

Figure 2.2: SEM image of a polymer particle from slurry-phase polymerisation. (a) Catalyst fragment encased in growing polymer layer. (b) Pore.

The most commonly-used model to account for the development of concentration gradients within growing polymer particles is the Multigrain Model (Yermakov et al., 1970, Floyd et al., 1986a, Floyd et al., 1987), as illustrated in Figure 2.3.

Development of the Multigrain Model involves reaction-diffusion balances on a number of scales for the diffusion of monomer from the bulk phase in the reactor to the active site on the surface of a catalyst particle. These resistances are the external film around the macroparticle, diffusion through the pores of the macroparticle, transfer to the surface of the microparticle, and diffusion through the polymer coating the microparticle.

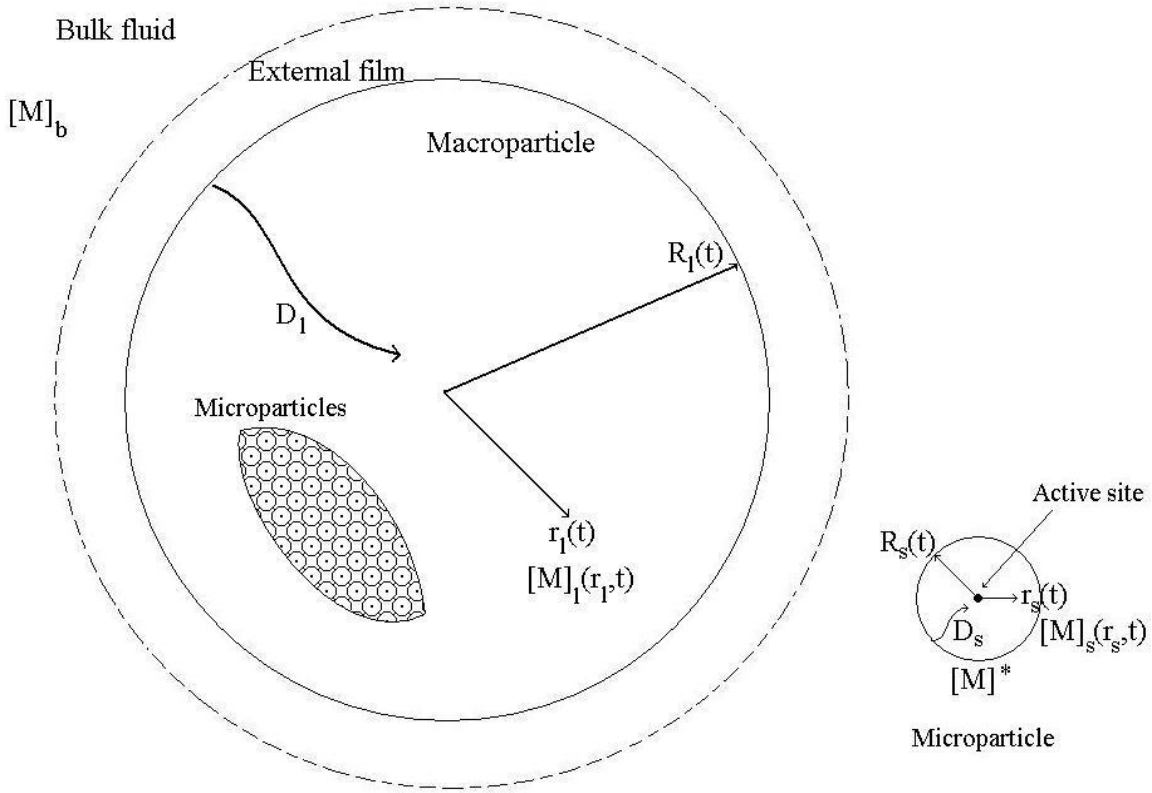

Figure 2.3: The Multigrain Model (based on figures in (Floyd et al., 1986a))

There is still doubt in the literature whether significant concentration gradients (indicating that mass transfer effects limit the reaction rate) exist in the catalyst particles. It has been suggested by many authors (Nagel et al., 1980, Floyd et al., 1986a, Soares, 2001) that these intraparticle gradients, if they exist, could be responsible for the observed activity profiles and chain length distributions.

Early attempts at modelling the particles and mass transfer around and through the particles suggested that external mass transfer was negligible for gas phase polymerisation, and could be neglected in certain situations for slurry phase polymerisation (Floyd et al., 1986a).

Early kinetic studies (Kim et al., 1990, Kim & Woo, 1990) clearly showed that the rate of decay of polymerisation was not dependent on degree of polymerisation, even at very high rates of polymerisation (up to 230 kg/g-Ti.hr), when one would expect the formation of large gradients within the particles due to rapid build-up of polymer.

A more recent kinetic study (Lim & Choung, 1997) investigated the decay of activity in gas phase polymerisation. Their conclusions were that both chemical deactivation (such as changes in site activity) and mass transfer resistance were responsible for the observed deactivation.

These conclusions were refuted (McKenna et al., 1999) when it was shown that particles could have very large pores in which bulk movement of monomer may exist, reducing the scale over which concentration gradients could occur within the particles. This was particularly true for gas phase polymerisation, but the authors felt that, depending on particle morphology, mass transfer effects may also be negligible for slurry phase polymerisation, based on earlier experimental and modelling work by the same group (McKenna et al., 1996, McKenna et al., 1997). This was supported in more recent studies into mass transfer in slurry phase polymerisation (Wu et al., 1999, Fisch et al., 2008), which concluded that concentration gradients were negligible within particles.

An investigation into the interaction between particle morphology and mass transfer effects (Kittilsen et al., 2001) assumed that concentration gradients would affect activity to the extent that differing polymerisation rates within particles could cause the particles to rupture. This was done in order to investigate how the morphology caused by ruptures could affect mass transfer, given that the prevailing theories of the time seemed to over-predict the importance of mass transfer effects on activity.

A review of literature on modelling single catalyst particles (McKenna & Soares, 2001) concluded that more research was required into the effect of mass transfer on catalyst activity, particularly taking into account the particle morphology.

More recently it has been suggested that the effects of gradients in polypropylene particles in gas phase polymerisation were negligible, but only when polymerisation has not occurred to a great extent (Martin & McKenna, 2002). This means that, at greater extents of polymerisation, gradients could form due to the build-up of polymer around the active sites.

These experimental results were directly contradicted by a reactor simulation study, in which it was demonstrated that mass transfer limitations have a negligible effect for long residence times, but can have an impact at short residence times, in gas phase fluidised bed reactors (Fernandes & Lona, 2002). A study of the initial development of particle morphology in gas phase polymerisation found that temperature gradients can occur, even in small, well-mixed reactors, supporting the idea that mass and heat transfer may be most important early in the polymerisation reaction (Browning et al., 2012). Decreases in polymerisation rate were ascribed to mass transfer limitations in the initial stages of liquid phase propylene polymerisation, although the authors stated they were unable to clearly distinguish between chemical effects (such as site activation) and physical effects (such as mass transfer limitation).

Particle simulation studies have shown, through the use of the Polymeric Flow Model (Yiagopoulous et al., 2001) and Random Pore Polymeric Flow Model (Kanellopoulos et al., 2004), that particle overheating can occur in the initial stages of propylene polymerisation due to heat and mass transfer limitations. This further supports the idea that gradients may be significant in the early stages of polymerisation.

Studies focussed on modelling industrial polyethylene and polypropylene reactors generally make the assumption that gradients within particles are negligible (Rawatlal, 2004, Hakim & Moballegh, 2006, Hakim et al., 2008, Luo et al., 2008). These studies succeeded in predicting industrial experimental results.

2.2.1 Summary

The most recent works quoted above reflect the current view in the field of research: mass transfer limitations may exist within growing polymer particles, and could have an influence on reaction rates. However, mass and heat transfer limitations are generally not seen as responsible for observed activity profiles or wide chain length distributions; these phenomena are described through kinetic models, generally using the “multi-site” approach discussed previously.

2.3 Macro scale

Macro scale modelling of industrial polyolefin reactors is primarily concerned with predicting the distributions of various properties within the reaction vessel. Distributions of interest include particle size distribution, chain length distribution, activity profiles and residence time distributions.

Other parameters of interest are vapour liquid equilibria and gas-liquid mass transfer rates (Floyd et al., 1986b, Bhagwat et al., 1994), and the mixing patterns and hydrodynamics of reaction vessels in various configurations (Soares & Hamielec, 1995b, Zacca et al., 1996, Zacca et al., 1997, Zacca & Debling, 2001, Alizadeh et al., 2004, Shamiri et al., 2010).

The modelling and simulation of polyolefin reactors has (understandably) received significant attention in the literature.

In particular, the group of Kiparissides has published many papers on the simulation of polymer properties and particle size distributions in gas-phase polypropylene reactors (Alexopoulos & Kiparissides, 2005, Alexopoulos et al., 2004, Alexopoulos et al., 2009, Dompazis et al., 2005, Dompazis et al., 2008, Hatzantonis & Kiparissides, 1998, Hatzantonis et al., 1998, Hatzantonis et al., 2000, Kanellopoulos et al., 2004, Kotoulas & Kiparissides, 2006, Meimaroglou et al., 2006, Roussos et al., 2005, Touloupides et al., 2010, Yiannoulakis et al., 2000, Yiannoulakis et al., 2001).

The effects of gas velocity on the ratio of bubble- and emulsion-phases in a fluidised bed have also been studied by other authors (Kiashemshaki et al., 2006, Shamiri et al., 2010).

Khare and coworkers have developed steady-state and dynamic models of both gas-phase polypropylene and slurry-phase polyethylene production, using commercial simulators and the multi-site model of polymerisation (Khare et al., 2002, Khare et al., 2004). These models were used to investigate commercial processes, including some strategies for grade transitions.

Liquid phase propylene polymerisations have been studied with Monte Carlo methods, in order to compare single- and multiple-site catalysts, and the effect of hydrogen on catalyst activity and polymer properties (Luo et al., 2008). The results of this simulation were compared with earlier works (Zacca et al., 1996, Zacca et al., 1997).

The production of polyethylene in slurry phase reactors has also been extensively studied, from models based on the Multi-Grain Model and a multi-site catalyst kinetic scheme (Ha et al., 2001, Ghafelebashi Zarand & Mortazavi, 2005) to studies of multi-reactor setups (Hakim & Moballegh, 2006, Soni & Bhagwat, 2008, Meng et al., 2013).

More recently, Computational Fluid Dynamics (CFD) methods have been applied to simulations of reactors, in order to account for complex mixing patterns or reactor geometries and the influence of temperature and velocity distributions (Yan et al., 2012, Zhu et al., 2014, Khan et al., 2014, Che et al., 2015, Schneiderbauer et al., 2015).

2.3.1 Population Balance Model

The most commonly used mathematical tool for investigating distributions of properties is the population balance equation. The general, unsteady-state, multiple-property population balance equation (PBE) is given by equation 2.4 (Hulburt & Katz, 1964).

$$\frac{\delta \Psi}{\delta t} + \sum_i \frac{\delta}{\delta \alpha_i}\left(\frac{\delta \alpha_i}{\delta t}\Psi\right) = B - D \qquad 2.4$$

In equation 2.4, Ψ is the time-varying number-density of a population (of particles or fluid elements, for example) which is distributed in the properties α_i, each of which can also vary with time. The number density is defined such that $\Psi(t, \alpha_1, \alpha_2, ...)\Delta\alpha_1\Delta\alpha_2, ...$ is the number fraction of particles or fluid elements having properties in the ranges $[\alpha_1, \alpha_1 + \Delta\alpha_1]$, $[\alpha_2, \alpha_2 + \Delta\alpha_2]$… at time *t*. Size is a typical property of interest; others could be age, temperature or catalytic activity. If size were the property of interest, then the number density function, Ψ, would represent the number-based particle size distribution (PSD).

The functions *B* and *D* represent the distribution of the rates of birth and death of the members of the population. The birth and death functions are generally related to the flow of material in and out of a reactor, but can also refer to processes such as nucleation (birth) or fragmentation (death).

In order to find the distribution of n properties within a population, one must solve an (*n*+1)-dimensional Partial Differential Equation (PDE): one dimension for each property, plus one for time.

Population Balances in reactor models

Application of Population Balance Modelling (PBM) in predicting steady-state PSD in polymerisation processes is well-developed in fluidised-bed gas-phase reactors (Choi et al., 1994, Khang & Lee, 1996, Hatzantonis & Kiparissides, 1998, Hatzantonis et al., 1998) and emulsion polymerisation reactors (Vale & McKenna, 2005).

Some more general models, based on Population Balance methods, have been developed to investigate the influence of residence time on steady-state reactor performance (Soares & Hamielec, 1995b, Zacca et al., 1996, Zacca et al., 1997, Zacca & Debling, 2001). These models consisted of *n*-dimensional PDEs, since the time dimension was not investigated in these steady-state systems.

The effects of velocity and temperature on the steady-state PSD in a fluidised bed reactor were investigated by discretising the reactor into a series of ideal reactors (Continuously Stirred Tank Reactors and Plug Flow Reactors) and using a Population Balance approach to determine the PSD in each section (Ashrafi et al., 2012).

There is growing interest in developing dynamic reactor models for the eventual goal of model-based control (McCoy & Madras, 2003, Alexopoulos et al., 2004, Harshe et al., 2004, Alexopoulos & Kiparissides, 2005, Roussos et al., 2005, Neto et al., 2005, Meimaroglou et al., 2006). The major focus of much of this work is on finding the most efficient numerical method for the solution of the PDEs that naturally result when developing PBMs.

Discretisation and Finite Element- or Volume-based methods (Alexopoulos et al., 2004, Alexopoulos & Kiparissides, 2005, Roussos et al., 2005, Dorao & Jakobsen, 2006, Chakraborty & Kumar, 2007, Kumar et al., 2008, Pinto et al., 2008, Qamar et al., 2009, Alexopoulos et al., 2009) have been proposed to predict an approximation of the distribution of properties in a reactor.

The method of moments, and extensions of the method of moments (McCoy, 2002, Ahmadzadeh et al., 2008, Attarakih et al., 2009) are designed to predict the moments of the solution of the sets of PDEs, rather than the distribution itself.

PBM methods have been coupled to CFD simulations to investigate the impacts of velocity and temperature on industrial reactor operation, in some cases with very simple kinetic schemes (Yan et al., 2012), but more recently with more sophisticated models of the interactions between flow patterns, PSD and kinetics (Zhu et al., 2014) and even including breakage and agglomeration in the PSD models (Che et al., 2015).

Computational efficiency

Many models based on the Population Balance can very accurately predict the distributions of properties such as polymer molecular weight, particle size or residence time in polymerisation reactors. Unfortunately, the computational expense of solving the models (whether discretised, finite element or method of moments) is still very high: solution of the most efficient methods can still require hundreds or thousands of seconds (Ahmadzadeh et al., 2008, Alexopoulos et al., 2009, Attarakih et al., 2009). When coupled with CFD models, high-performance computing resources are required. This makes these models unsuitable for use in real-time process control.

Parallel processing has been proposed as a way to speed up the solution of models predicting the MWD for multi-site catalysts (Weng et al., 2015), but would be difficult to apply to more coupled models such as the Population Balance Model.

While the PBM can predict the full distributions of multiple variables, in engineering applications it can be sufficient to determine only the mean (and possibly the variance) of a property, rather than the entire distribution. For example, in the polymer field, it is not always necessary to know the chain length distribution: a polymer can be characterised by the number-average chain length (M_n), weight-average chain length (M_w), and/or chain length variance (PDI) (Rawatlal, 2004).

In most applications of the Population Balance Model, in order to find the mean of the *i*-th property, α_i, the full distribution, Ψ, must be determined from the solution of the PDEs. Once this distribution is known, the mean can be found as the first moment of the distribution (equation 2.5).

$$\overline{\alpha_i} = \int_{\underline{\alpha}} \alpha_i \underline{\underline{\Psi}}(\underline{\alpha}) d\underline{\alpha} \qquad 2.5$$

Even if only the moments of a distribution are required, the partial differential equations of the Population Balance Model (equation 2.4) must be solved before the moments can be found.

2.3.2 Segregation Approach

The Segregation Approach has been proposed as a computationally efficient alternative to the PBM (Rawatlal, 2004), and successfully applied in the field of polymer reaction engineering, to predict polymer properties (Rawatlal, 2009), and in the field of bioprocess engineering, predicting the performance of tank bioleach reactors (Kotsiopoulos et al., 2008).

The Segregation Approach is a method of predicting the mean (and other moments) of a distribution without having to determine the whole distribution first. Again considering the *i*-th property, α_i, of a distribution, the current value of the property can in general be expressed in terms of the initial value of the property, $\alpha_{i,0}$, and age, θ. For example, particle size can be found in terms of initial particle size and particle age, related through expressions for the dynamics of particle growth.

If the initial distribution in the *i*-th property, $\Psi_0(\alpha_{i,0})$, and the internal residence time distribution, $I(\theta)$, of the reaction vessel of interest, are also known, then the mean value of the *i*-th property can be found through application of equation 2.6.

$$\overline{\alpha_i} = \iint \alpha_i(\alpha_{i,0},\theta)\Psi_0(\alpha_{i,0})I(\theta)d\alpha_{i,0}d\theta \qquad 2.6$$

It is clear that equations 2.5 and 2.6 are equivalent: they are the first moments of density functions. The difference between equation 2.5 (which would be applied to the solution of the PBM) and equation 2.6 (the Segregation Approach) is in the steps before the evaluation of the integral.

In order to evaluate equation 2.5, the function Ψ is required, and hence the PBM (and the associated multidimensional PDEs) must be solved. The solution of these PDEs is difficult and computationally expensive, as has been discussed above. This is the approach taken by most researchers.

By comparison, evaluation of equation 2.6 is far simpler, requiring knowledge only of the inlet distribution and residence time distribution (both of which can be physically measured on a chemical plant), and the integration of these known functions.

Computational efficiency

The reduced computational expense associated with the Segregation model is its primary benefit over the traditional PBM approach, a benefit which is significant given that it makes model-based control feasible.

The Segregation Approach can function more efficiently and using less information than the PBM because the models differ in terms of frame of reference. The PBM uses an Eulerian reference frame, considering a single position within the fluid (the reactor contents) and the variation of properties that result from the movement of fluid elements through that position.

The Segregation Approach uses a Lagrangian frame of reference, considering fluid elements (the catalyst/polymer particles) and the variation of properties within those elements.

Because of the differing frames of reference for the models, information about the systems of interest is incorporated in different ways. For example, flow in and out of the reactor is specified in the birth and death functions and boundary conditions of the PDEs in the PBM, and must be defined for each fluid element; the same flows can be specified in the Segregation Approach by using residence time distributions, which do not consider individual elements but a continuum.

Residence time distributions

A second benefit of the Segregation Approach over PBM is the ease with which complex or arbitrary mixing patterns can be incorporated using the Segregation Approach. The complexity of simulating non-ideal mixing with the PBM significantly adds to the difficulty of applying the technique.

In the Segregation Approach, all the hydrodynamics can be included explicitly in the form of the residence time distribution (RTD) function (Danckwerts, 1953). There are standard methods for dealing with non-ideal or imperfect mixing using RTD functions, including compartmentalisation or direct measurement by tracer experiments (Levenspiel, 1999, Fogler, 2005). The simulation of air flow patterns in complex air-scrubbing systems has received particular attention in the nuclear industry (Laquerbe et al., 2001a, Laquerbe et al., 2001b, Hocine et al., 2008). These papers constructed non-trivial networks of fundamental models (PFR, CSTR, bypass and recycle) and used various computer-aided design methods (including genetic algorithms and mixed-integer non-linear programming) to fit the parameters describing the networks to experimental RTD data.

The discretisation of real reactors into ideal reactors has also been applied in the polymerisation field, with PBM-based approaches to investigate PSD and product properties (Ashrafi et al., 2012, Krallis et al., 2015). The model formulations in these studies could be simplified by making use of the Segregation Approach.

In addition, the Segregation Approach formulation allows for easy incorporation of the recently developed unsteady-state RTD, allowing simulations of unsteady particle flows or sudden changes in residence time (Rawatlal & Starzak, 2003). In the PBM, unsteady flows can only be incorporated by introducing real time as an additional dimension in the system of multidimensional PDEs. This suggests that the Segregation Approach can be readily applied to the modelling of unsteady-state reactor operation.

2.3.3 Summary

Most of the simulation work available in the literature is based on the Population Balance Model, which suffers from computational inefficiency and difficulty of application to non-ideal mixing patterns. The Segregation Approach shows promise as a computationally efficient method for predicting the moments of distributions, and will be employed in this thesis.

2.4 Grade transitions

Regardless of the particular model(s) used to simulate polymerisation kinetics, particle-scale effects, property distributions and reactor mixing patterns, optimising a grade transition remains difficult: there are interactions between multiple manipulated and controlled variables (Takeda & Ray, 1999, Chatzidoukas et al., 2003), outputs with slow sampling rates, such as determining polymer properties (Embirucu & Fontes, 2006), and reaction dynamics that are very sensitive to the reaction conditions.

In addition to these control engineering challenges, the question of process economics arises: for example, an optimum grade transition may be one which minimises the duration of the transition, or one which minimises the production of waste material (McAuley & MacGregor, 1992); similarly, the relative costs of reactants may determine whether increasing consumption to speed up a transition is economically justifiable. These questions typically have different answers depending on the particular operation and various macroeconomic factors, and will not be directly addressed in this work.

The goal of this thesis is to develop a reactor model that is suitable for application to reactor control and optimisation; the development of a reactor control scheme is beyond the scope of the current project. However, the literature pertaining to attempts to control polymerisation reactors, and specifically to optimise grade transitions, must be interrogated to understand the challenges that exist.

Early work on optimising grade transitions identified certain characteristics of an "optimal grade transition trajectory", including achieving the transition quickly and producing as little waste as possible and remaining within certain limits (such as temperature and pressure) for safety reasons (McAuley & MacGregor, 1992). These basic requirements have not changed, but the methods to achieve an "optimal" grade transition strategy differ.

Many authors approach the problem of optimising grade transitions from a polymer reaction engineering perspective, by seeking to understand the process and propose heuristics to improve unsteady-state operation.

Other authors use a background in control engineering to approach the problem, and focus on the challenges of controlling and optimising complex processes.

2.4.1 Heuristic approach

Strategies for optimising grade transitions in gas-phase production of polyethylene were investigated by McAuley and MacGregor (1992), based on a dynamic, multi-site kinetic model of the reactor. This work proposed a few strategies, including reducing catalyst feed and bed height to reduce the production of waste material, and using large overshoots for the hydrogen feed rate, because of the slow dynamics of hydrogen in the gas phase reactor.

A dynamic polymerisation process simulator coupled to a nonlinear optimisation routine was used to investigate two-stage slurry-phase reactors (Takeda & Ray, 1999), by comparing simple step-change trajectories to optimised trajectories, including over- and undershoot strategies. The authors were able to achieve a 30-40% improvement in simulated grade changes when applying more complex trajectories, but did not apply the results to industrial or laboratory data.

Industrial operating data was used to determine a set of kinetic parameters (including propagation rate, mass transfer rates and vapour-liquid equilibrium constants); this reactor model was then applied to the grade transition problem (Moudgalya & Jaguste, 2001). Because of the complexity of the calculations, up to 2 hours of computation time were required to propose optimum trajectories, making this model unsuitable for

real-time control; however the authors were able to propose the use of catalyst feed rate to effect large changes in operating conditions, with pressure control used for finer control of reactor conditions.

Neto and coworkers investigated slurry-phase co-polymerisation of ethylene and 1-butene (Neto et al., 2005) by fitting kinetic parameters for a multi-site model to both laboratory and industrial data. They found that the feed rate of ethylene had the greatest impact on reactor performance, and was the most effective manipulated variable for improving grade transitions.

Grade transitions in gas-phase reactors with metallocene catalysts were investigated using a commercial dynamic simulator and kinetics based on laboratory data (Lo & Ray, 2005, Lo & Ray, 2006). Although the authors were not attempting to optimise a specific process, they suggested strategies such as venting a portion of the gas phase to more rapidly adjust gas composition, or overshooting certain properties to achieve more rapid grade transitions. They also pointed out the complexity of a grade transition in which multiple factors change, as opposed to one in which only the ratio of hydrogen to monomer is adjusted.

A simplified model of polymerisation, assuming that the polymer MWD depends only on the ratio of hydrogen to monomer, was used by Ali & Ali (2010, 2011) to investigate a gas-phase reactor. Based on their investigations, the authors proposed a number of approaches to optimising transitions, including manipulating the hydrogen feed rate or feeding different types of catalyst (Ali & Ali, 2010), and manipulating both hydrogen and monomer feed rates simultaneously (Ali & Ali, 2011).

2.4.2 Control engineering approach

The alternative approach to polymer reaction engineering and grade transition optimisation makes some simplifying assumptions about the polymerisation kinetics or reactor in order to focus on control engineering methods.

A typical approach is to use simplified empirical models of polymerisation, such as simplified linearised models of a polyethylene reactor (Embirucu & Fontes, 2006), or relating certain reactant ratios to instantaneous MFI, and using an empirical model to relate the instantaneous MFI to the cumulative product properties in a slurry-phase polyethylene reactor (Lee et al., 2008, Kim & Yeo, 2010). A similar approach was applied to gas-phase reactors (Wei et al., 2014), in which the process was discretised into three steps: fresh feed modifies the gas-phase reactant concentrations, an empirical model relates these concentrations to instantaneous polymer properties, and finally the instantaneous properties are used to determine the accumulation of properties into the final product distributions. All of these studies were able to demonstrate improved process control of the simulated reactors, but the simplifications make the results difficult to apply to actual polymerisation reactors.

An extension of the simplified approach is to ignore the detail behind the polymerisation process altogether, and view it as a “black box” which can be controlled by adaptive controllers, including differential evolution algorithms (Lee et al., 1999), or neural networks (Xu & Liu, 2014).

In light of the complexity of polymerisation systems, conventional proportional-integral controllers and standard controller tuning methods may not be the best solution; Mjalli and coworkers have studied gas-phase polymerisation, using multi-site models, and concluded that although more advanced control methods (such as the proposed Adaptive Predictive Model-Based Control) require greater computational loads, the benefits to operation justify the additional effort (Ho et al., 2012, Shamiri et al., 2013).

Work by the group of Kiparissides proposed that not only must the grade transition itself be optimised, but that selection of the closed-loop controllers as part of the optimisation problem could significantly improve

the controllability and economics of the process (Chatzidoukas et al., 2003). A problem of this nature can be solved by commercial mixed-integer nonlinear programming optimisation software.

Weng and coauthors recently proposed that grade transitions should be optimised using the full molecular weight distribution (MWD), rather than just the moments or averages of the MWD; solution of this problem requires discretisation of the dynamic process into time steps short enough to apply a Quasi-Steady State Assumption and calculate the MWD using steady-state moment methods combined with a multi-site model (for numerical efficiency). This approach was shown to succesfully improve some transitions of industrial interest, but the actual computational load was not specified (Weng et al., 2014).

2.4.3 Summary

Current approaches to optimisation of grade transitions are based on the multi-site model of polymerisation (or even more empirical approaches), and many make use of the Population Balance Model, resulting in computationally expensive models that can not be applied to real-time control.

The control engineering perspective on this problem frequently treats the polymerisation reactor as a “black box”, or makes significant simplifying assumptions, because rigorous models of polymerisation are too computationally expensive.

There is thus a lack of fundamental models of polymerisation, which can be built into a reactor simulation that is computationally efficient enough for real-time process control applications.

CHAPTER 3. THESIS OBJECTIVES

Based on the review of the literature, it is clear that although there are models capable of simulating the behaviour of industrial reactors none of these are numerically efficient enough to be used for real-time process control and optimisation. It has been shown that an approach based on the Segregation Model can yield results which may be detailed enough for process control (Rawatlal, 2009). In addition, many models are based on empirical correlations, rather than a fundamental understanding of polymerisation reactions.

There are three hypotheses for this project:

- First, that a Segregation-based model will provide sufficient information for achieving real-time control of an industrial olefin polymerisation reactor.
- Second, that the pseudo-sites concept can be used to validate a kinetic model based on the concept (as outlined in Table 2.3) against laboratory experimental data.
- Third, that the experimentally-derived kinetic data can be applied to the simulation of an industrial reactor, and successfully reproduce industrial data.

Three main questions arise:

1. Can the proposed kinetic scheme (see Table 2.3) be successfully used to unify experimentally observed phenomena, including polymer properties (PDI, M_n, M_w, and comonomer content) and catalyst activity?
2. To what degree is the Segregation Approach more numerically efficient than the Population Balance Model?
3. Does the Segregation Approach provide sufficient data that a reactor model based on it successfully
    a. Predicts the behaviour of an industrial olefin polymerisation reactor, and
    b. Is useful for real-time reactor control?

In order to answer these questions, we can identify several objectives, which are detailed below.

The first goal is to obtain kinetic parameters for the proposed kinetic system from experimental data. Once these constants are known, they can be used within a reactor model.

The second goal is the formulation and application of a dynamic model of the polymerisation reaction system. This model will utilise the kinetic parameters obtained by experiments, and make use of the Segregation Approach to track the leading moments of distributions in the reactor. The model will predict polymer properties, product PSD, rate of polymerisation and reactor conditions not only for steady-state operation but most importantly for unsteady-state operation, as occurs during grade transitions.

The third goal is the validation of the model by comparison with data from the operation of the industrial reactors of interest. This may require the fitting of some parameters on the macroscale, such as the parameters to define possible compartmentalisation of the reactor in order to represent non-ideal mixing. The use of the Segregation Approach simplifies the application of residence time distributions in fitting possible non-ideal mixing patterns. The validation of the model with industrial data will promote an industrially applicable and robust model for reactor control.

Once the model has been validated, the model will be used in a number of case studies applicable to the real-time control of a polymerisation reaction process. These case studies will demonstrate the suitability of the Segregation-based model to applications in reactor control.

PART B. KINETIC STUDY

CHAPTER 4. KINETIC MODEL DEVELOPMENT

In a reaction system such as a polymerisation reactor, the kinetics are of fundamental importance: the kinetics determine not only reaction rates, but also the properties of the polymer product. Accurately describing micro scale phenomena (such as catalyst activation and deactivation, and polymer chain growth and termination reactions) is the basis for a successful model of a polymerisation reactor, which can predict reaction rates, polymer properties, particle growth rates, and even reactor operation itself (Dube et al., 1997, McKenna et al., 2005).

To be used in such a model of polymerisation, a kinetic scheme requires that three sets of kinetic model parameters be obtained from experimental or industrial data (Yao et al., 2003):

- Parameters defining polymerisation rate and catalyst activity;
- Parameters defining the rate of comonomer incorporation, and
- Parameters defining the distribution of chain lengths produced.

In addition, parameters relating the molecular weight distribution (MWD) to Melt Flow Index data will be required; a kinetic model will typically predict the MWD, but polymer properties are typically (and most easily) measured by empirical tests that determine Melt Flow characteristics (Bremner et al., 1990, Seavey et al., 2003, Fazeli et al., 2006).

This thesis makes use of the kinetic scheme proposed by Rawatlal (2004), which separates reactions into those affecting the catalyst sites (relating to catalyst activity) and those affecting polymer growth and termination (determining polymer properties). The idea of multiple types of active sites (which is common in the literature) is replaced with the concept of pseudo-sites: polymerising sites which do not differ in terms of polymerisation rate or activity profile, but in terms of which terminating agent is active. Thus, the production of polymers with wide distributions of chain lengths is physically explained by the existence of different termination rates, rather than the more frequently-applied multi-site proposal, which is based on deconvolution of molecular weight distributions (Soares & Hamielec, 1995a) and a range of physical interpretations (Lin & Catlow, 1995, Kim & Somorjai, 2000b, Boero et al., 2002, Stukalov & Zakharov, 2009, Bahri-Laleh et al., 2011).

As discussed in the Literature Review, the formulation of the pseudo-sites scheme used in this thesis does not allow for the reproduction of chemical composition distributions: the single polymerising site that is simulated produces polymer chains with a constant comonomer fraction. While the chemical composition distribution can have a significant impact on polymer properties (Philipsen, 2004), this thesis focuses on the prediction of catalyst activity profiles and molecular weight distributions.

While some fitting of kinetic parameters to experimental data was demonstrated by Rawatlal (2004) to illustrate some properties of the pseudo-sites based kinetic scheme, a rigorous regression procedure was not described. In addition, the data sets (obtained from the literature) were relatively small, and the regressions performed were applied to selected portions of the data. In particular, the method for extracting a common propagation rate relied on selecting a maximum value from a small section of data; the pages below detail a more rigorous method to determine the propagation rate, using the full data set.

A second difference relates to the determination of the copolymerisation propagation rates, which in Rawatlal (2004) were fitted to rate curves; in this thesis, the copolymerisation rate constants are determined from the results of polymer product analysis, which indicates actual comonomer incorporation, and is considered more accurate and reliable.

Part B. Kinetic study

The sets of parameters described above will be incorporated into the kinetic scheme reproduced in Table 4.1 below. The kinetic parameters can be reclassified in terms of the nomenclature of the kinetic scheme:

- Parameters defining polymerisation rate and catalyst activity:
    - Site transformation rate constants, $k_{st,X}^{q,r}$
    - Polymer chain propagation rate constants, $k_{p,ij}^{q}$
- Parameters defining the rate of comonomer incorporation:
    - Relative rates of propagation rate constants, $k_{p,11}^{q} : k_{p,12}^{q}$
- Parameters defining the distribution of chain lengths produced:
    - Termination rate constants for each pseudo-site, $k_{t,X}^{q}$

Table 4.1: Kinetic scheme

	Reaction	Rate constant
Catalytic reactions		
Site transformation		
Spontaneous	$P_*^q \rightarrow P_0^r + D_n^q$	$k_{st,sp}^{q,r}$
Aluminium Alkyl (A)	$P_*^q + \alpha_A A \rightarrow P_0^r + D_n^q$	$k_{st,A}^{q,r}$
Hydrogen (H_2)	$P_*^q + \alpha_{H_2} H_2 \rightarrow P_0^r + D_n^q$	$k_{st,H_2}^{q,r}$
Polymeric reactions		
Propagation		
Initiation	$P_0^q + M_i \rightarrow P_{1,i}^q$	$k_{0,i}^q$
Propagation	$P_{n,i}^q + M_j \rightarrow P_{n+1,j}^q$	$k_{p,ij}^q$
Termination		
Spontaneous	$P_{n,i}^q \rightarrow P_0^q + D_{n,i}^q$	$k_{t,sp}^q$
Aluminium Alkyl (A)	$P_{n,i}^q + A \rightarrow P_0^q + D_{n,i}^q$	$k_{t,A}^q$
Monomer (M_i)	$P_{n,i}^q + M_i \rightarrow P_{1,i}^q + D_{n,i}^q$	k_{t,M_i}^q
Hydrogen (H_2)	$P_{n,i}^q + H_2 \rightarrow P_0^q + D_{n,i}^q$	k_{t,H_2}^q

The following sections will outline development of methods to determine values for the various kinetic parameters from experimental data.

4.1 Polymerisation and site transformation rate constants

A strong correlation between polymerisation activity and catalyst site oxidation state was described in the Literature Review, based on work by various authors (Soga et al., 1982, Han-Adebekun & Ray, 1997, Han-Adebekun et al., 1997a, Fregonese et al., 2001, Ostrovskii & Kenig, 2005, Bhaduri et al., 2006). From the literature, there seems to be general agreement that titanium catalysts are active for ethylene polymerisation when in the Ti^{3+} oxidation state, and that the Ti^{4+} and Ti^{2+} forms are inactive (Bahri-Laleh et al., 2011, Koshevoy et al., 2014)

The kinetic scheme proposed by Rawatlal (2004) distinguishes between catalytic reactions and polymeric reactions. Catalytic reactions are classed as "site transformations", in line with the nomenclature of previous kinetic schemes (Hutchinson et al., 1992), but more explicitly could be called "redox reactions", as they describe the changes in catalyst site oxidation state.

This section describes a method to extract meaningful kinetic parameters for the kinetic scheme from activity profile data. Note that nomenclature is tabulated in Chapter 19 in the Appendix.

4.1.1 Model development

As discussed in the Literature Review, one of the primary concerns in this project is the effect of site transformations on the activation of the catalyst. As in previous studies (Hutchinson et al., 1992), a lumped kinetic parameter can be introduced to simplify the notation for site transformations (equation 2.1, reproduced below).

$$\beta_{st}^{q,r} = k_{st,sp}^{q,r} + k_{st,A}^{q,r}\left[A\right]^{\alpha_A} + k_{st,H_2}^{q,r}\left[H_2\right]^{\alpha_{H_2}} \qquad 2.1$$

Once again taking oxidation state as the basis for site type, and assuming that titanium sites enter in the Ti^{4+} oxidation state (Ostrovskii & Kenig, 2005, Bahri-Laleh et al., 2011), the set of differential equations predicting site evolution will be as shown in equations 2.3, reproduced below. Previous attempts (Rawatlal, 2004) to fit experimental data using the kinetic scheme presented above showed that the most promising scheme involved reduction of inactive Ti^{4+} to the active Ti^{3+}, reduction of Ti^{3+} to Ti^{2+}, and oxidation of Ti^{2+} to Ti^{3+}; this scheme will be used here.

$$\begin{aligned}
\frac{dP_*^{4+}}{dt} &= -\beta_{st}^{4+,3+} P_*^{4+} \\
\frac{dP_*^{3+}}{dt} &= \beta_{st}^{4+,3+} P_*^{4+} - \beta_{st}^{3+,2+} P_*^{3+} + \beta_{st}^{2+,3+} P_*^{2+} \\
\frac{dP_*^{2+}}{dt} &= \beta_{st}^{3+,2+} P_*^{3+} - \beta_{st}^{2+,3+} P_*^{2+} \\
P_*^{4+}(0) = 1;\ & P_*^{3+}(0) = P_*^{2+}(0) = 0
\end{aligned} \qquad 2.3$$

As before, P_*^q represents the fraction of sites of oxidation state q. When the lumped transformation parameters, $\beta_{st}^{q,r}$, do not vary significantly with time, the ordinary differential equations can be solved analytically. This approach can be applied to semi-batch laboratory data, where reactant conditions (on which the lumped parameters depend) are kept close to constant.

Assuming that the active site is the Ti^{3+} oxidation state, the polymerisation rate can be expressed in equation 4.1.

$$r_p(t) = P_*^{3+}(t)\sum_i\sum_j k_{p,ij}\xi_i[M_j] \qquad 4.1$$

The active site fraction ($P_*^{3+}(t)$) can be found from the analytical solution of the set of differential equations (equations 2.3), as shown in equation 4.2.

$$P_*^{3+}(t) = \alpha + \gamma\exp\left(-\beta_{st}^{4+,3+}t\right) + \delta\exp\left(-\left(\beta_{st}^{3+,2+} + \beta_{st}^{2+,3+}\right)t\right) \qquad 4.2$$

Where:

$$\alpha = \frac{\beta_{st}^{2+,3+}}{\beta_{st}^{3+,2+} + \beta_{st}^{2+,3+}}$$

$$\gamma = \frac{\beta_{st}^{2+,3+} - \beta_{st}^{4+,3+}}{\beta_{st}^{4+,3+} - \beta_{st}^{3+,2+} - \beta_{st}^{2+,3+}}$$

$$\delta = \frac{\beta_{st}^{4+,3+}\beta_{st}^{3+,2+}}{\beta_{st}^{4+,3+}\beta_{st}^{3+,2+} + \beta_{st}^{4+,3+}\beta_{st}^{2+,3+} - 2\beta_{st}^{2+,3+}\beta_{st}^{3+,2+} - \left(\beta_{st}^{3+,2+}\right)^2 - \left(\beta_{st}^{2+,3+}\right)^2}$$

The consumption rate of ethylene (r_{M_1}) is the experimentally-measured indicator of catalyst activity (equation 4.3).

$$r_{M_1}(t) = \sum_i k_{p,i1}\xi_i[M_1]P_*^{3+}(t) \qquad 4.3$$

In co-polymerisation, the incorporation of comonomer is frequently very low (at most a few percent), and so the fraction of chains ending in comonomer (ξ_2) will be very close to zero. For this study, the comonomer content (shown in Table 5.8 on page 72) for each sample is a fraction of one percent. The expression for the consumption rate of ethylene can therefore be simplified to the form shown in equation 4.4.

$$r_{M_1}(t) = k_{p,11}[M_1]P_*^{3+}(t) \qquad 4.4$$

This simplified relation is the basis for the fitting of kinetic parameters to experimental data.

4.1.2 Regression approach

Using the simplified expression for polymerisation rate, shown in equation 4.4, as a proxy for catalyst activity, it is possible to find values for the unknown kinetic parameters, based on experimental data such as that described above. There are a total of 10 parameters required in this model to describe catalyst activity: the propagation rate, $k_{p,11}$ (for brevity referred to as k_p in the discussion below), and three site transformation rate constants for each of the three active site oxidation states (Ti^{4+}, Ti^{3+} and Ti^{2+}). The site transformation rate constants will initially be combined into lumped site transformation parameters, as shown in equation 2.1.

This section describes a method to extract physically meaningful values for the kinetic model, from obtaining initial guesses for the parameters through to a single set of values for a scheme that describes all of the experimental data.

Initial guesses

To fit the model to each experimental rate curve, values for four parameters must be found: the three lumped site transformation parameters ($\beta_{st}^{4+,3+}, \beta_{st}^{3+,2+}, \beta_{st}^{2+,3+}$) and the propagation rate (k_p). Given the number of parameters involved, and in order to avoid "fitting an elephant" (Dyson, 2004), it is vital that realistic initial guesses are obtained for the regression procedure.

In addition, certain components of the model are more sensitive to the data in particular regions. This fact can be exploited to reduce the number of parameters that are to be estimated in at any given time. With this in mind, the first step will be determining values for these initial guesses from an analysis of the data.

An order of magnitude guess for the polymerisation rate, k_p, can be obtained from the experimental yield of polymer, $m_{polymer}$, mass of catalyst, m_{cat}, monomer concentration, $[M_1]$, and reaction time, τ_{rxn}, for each experimental run, *e* (equation 4.5).

$$k_{p,e} = \frac{m_{polymer,e}}{MM_{ethylene}[M_1]_e m_{cat,e} \tau_{rxn,e}} \qquad 4.5$$

Three features of the experimental polymerisation rate curves (shown in Figure 4.1, which includes data from experimental Run #16; reaction conditions are described in Table 5.1) can be used to extract initial guesses for the three lumped site transformation parameters by decoupling the effects of the different variables. These features are:

- The initial slope
- The time at which the maximum polymerisation rate occurs, t^{peak}, and
- The maximum rate, $r_{M_1}\left(t^{peak}\right)$

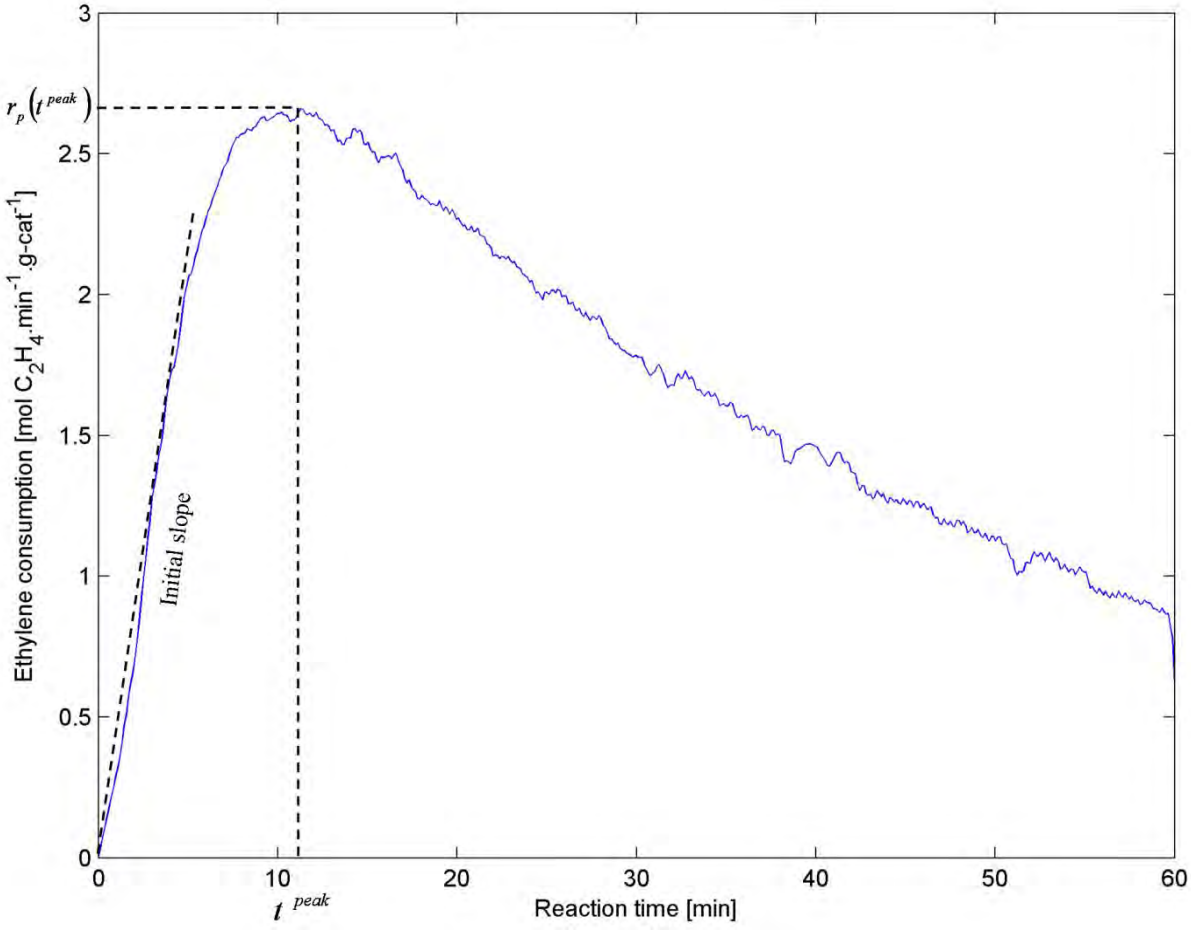

Figure 4.1: Experimental activity curve, including the three important features

By combining equations 2.3 and 4.4, we obtain equation 4.6. The left-hand side of the equation represents the initial slope of the polymerisation rate curve; the right-hand side makes use of the assumption that at t=0 all sites are in the Ti^{4+} oxidation state.

$$\left.\frac{d}{dt}\left(\frac{r_{M_1}}{k_p[M_1]}\right)\right|_{t=0} = \left.\frac{dP_*^{3+}(t)}{dt}\right|_{t=0} = \left(\beta_{st}^{4+,3+}P_*^{4+} - \beta_{st}^{3+,2+}P_*^{3+} + \beta_{st}^{2+,3+}P_*^{2+}\right)_{t=0} = \beta_{st}^{4+,3+} \qquad 4.6$$

It is therefore possible to determine (in equation 4.7) the lumped site transformation parameter $\beta_{st}^{4+,3+}$ from the initial slope of the experimental rate curve and the propagation rate from equation 4.5.

$$\beta_{st}^{4+,3+} = \left.\frac{d}{dt}\left(\frac{r_{M_1}}{k_p[M_1]}\right)\right|_{t=0} \qquad 4.7$$

Values for $\beta_{st}^{4+,3+}$ obtained in equation 4.7, for each experimental run, will be used as initial guesses in the regression steps that follow.

The time at which the peak polymerisation rate occurs, t^{peak}, and the rate at this time, $r_p\left(t^{peak}\right)$, can be used to determine values for the other two site transformation parameters. The peak will occur when the first derivative of equation 4.2 is equal to zero, as shown in equation 4.8. Equation 4.9 is simply equation 4.4, evaluated at $t = t^{peak}$.

$$\frac{d}{dt}\left(P_*^{3+}\left(t^{peak}\right)\right) = -\beta_{st}^{4+,3+}\gamma\exp\left(-\beta_{st}^{4+,3+}t^{peak}\right) - \left(\beta_{st}^{3+,2+} + \beta_{st}^{2+,3+}\right)\delta\exp\left(-\left(\beta_{st}^{3+,2+} + \beta_{st}^{2+,3+}\right)t^{peak}\right) = 0 \quad 4.8$$

$$r_{M_1}\left(t^{peak}\right) = k_p\left[M_1\right]P_*^{3+}\left(t^{peak}\right) \quad 4.9$$

Values for k_p (from equation 4.5), $\beta_{st}^{4+,3+}$ (from equation 4.7) and $\beta_{st}^{3+,2+}$ and $\beta_{st}^{2+,3+}$ (satisfying equations 4.8 and 4.9) will be used as initial guesses for the non-linear least-squares regression steps that are applied to each experimental run's data, as outlined below.

Non-linear least-squares regression – lumped parameters to rate curves

The values from the analysis of the data described above can be used as initial guesses for non-linear least-squares fitting of the experimental data. The objective function which must be minimised by a non-linear solver for each experimental activity profile is given in equation 4.10. In this equation, and the equations that follow, the index *e* refers to experiment number, and the index *te* refers to experimental time within a given experiment.

$$Obj_e = \sum_{te}\left\{r_{M_1,e}\left(t_{te}\right) - k_{p,e}\left[M_1\right]P_*^{3+}\left(t_{te}, \beta_{st,e}^{4+,3+}, \beta_{st,e}^{3+,2+}, \beta_{st,e}^{2+,3+}\right)\right\}^2 \quad 4.10$$

The four parameters are logarithm transformed to ensure that positive (and therefore physically meaningful) values are obtained in the regression; an alternative approach would be to use a non-linear solver which accepts parameter bounds. Note also that it may be advisable to use a weighting function to ensure that the data points at the peak do not have an excessive influence on the objective function; possible weighting functions could include the absolute value of the experimental data point, standard deviation estimates from replicate experiments, or the average of the data point and the predicted value. Weighting has not been applied in this work, since the polymerisation rate curves do not typically span across multiple orders of magnitude.

In addition, in order to obtain physically meaningful parameter values, regions of sensitivity are identified in which each of the parameters can be fitted, as illustrated in Figure 4.2.

At different times, different site transformation reactions become more or less important; the model will therefore become more or less sensitive to the parameters relating to these reactions. These two regions of sensitivity are described below.

During the initial rise in polymerisation rate (region one), the reduction of sites from the inactive Ti^{4+} to the active Ti^{3+} oxidation state predominates. The model is therefore most sensitive to the parameter $\beta_{st}^{4+,3+}$ in region one. Using the initial guesses obtained in the previous step, model predictions as described by equation 4.4 are fitted to the first part of the rate curve by varying the four parameters.

After the peak rate has been achieved, the dominant reactions will be the reduction of sites from the active Ti^{3+} to the inactive Ti^{2+} oxidation state, and the oxidation reaction transforming Ti^{2+} into Ti^{3+}. The lumped parameters describing these reactions, $\beta_{st}^{3+,2+}$ and $\beta_{st}^{2+,3+}$, have the greatest influence on the model in this region. Again using the initial guess from the previous step, the model is fitted to region two of the activity curve.

The values for $\beta_{st}^{4+,3+}$, fitted from region one, and $\beta_{st}^{3+,2+}$ and $\beta_{st}^{2+,3+}$, fitted from region two, are then used as initial guesses to fit the model to the entire rate curve. The initial guess for the polymerisation rate, k_p, is the average of the fits for k_p from regions one and two.

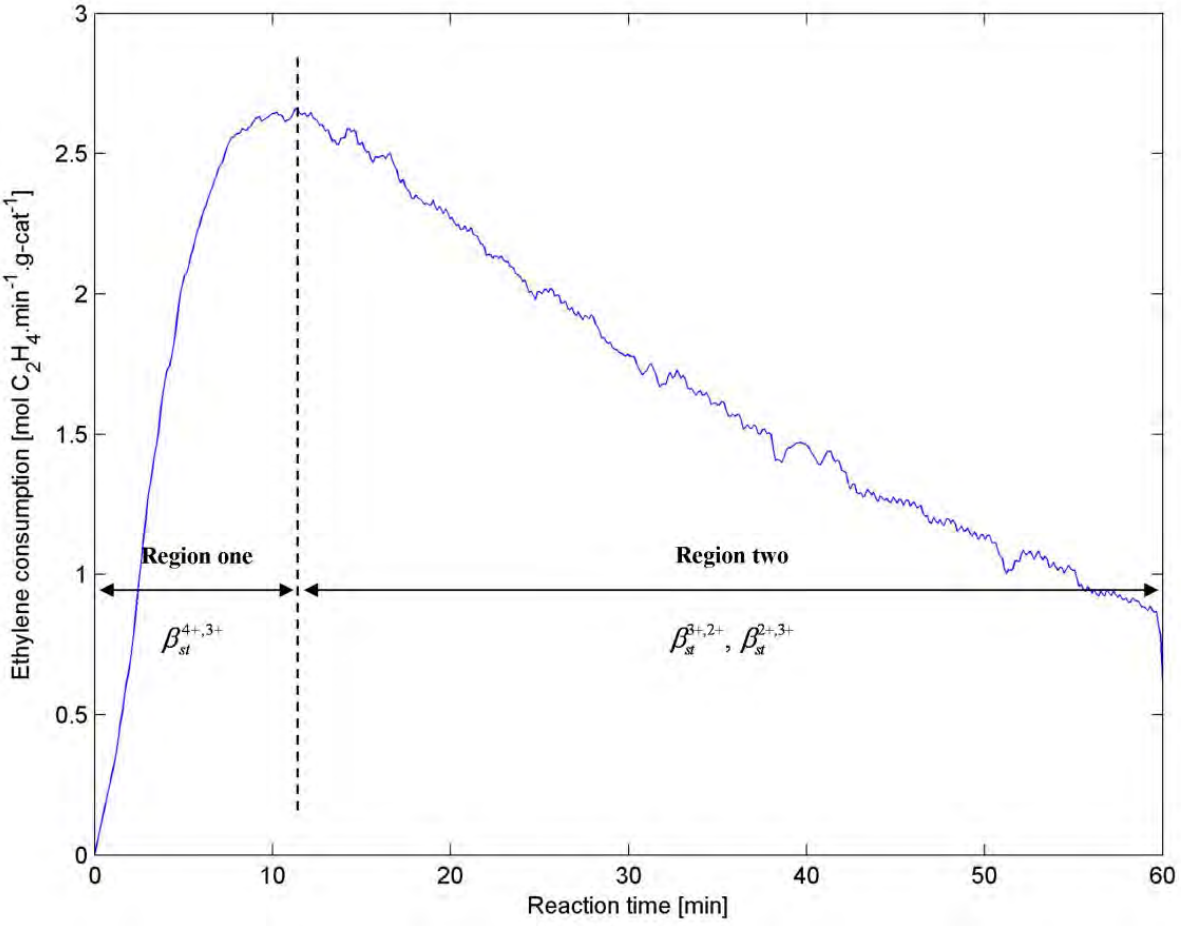

Figure 4.2: Regions of sensitivity to lumped parameters

Non-linear least-squares regression – consolidating propagation rates

The set of values for $k_{p,e}$ and $\beta_{st,e}^{q,r}$ for each experimental run must now be compared. Since the lumped site transformation parameters are dependent on reactant concentrations (see equation 2.1), they will generally differ from experiment to experiment. The values for k_p, however, should depend only on temperature and catalyst properties; for a single catalyst at uniform temperatures, these values should not vary between experiments.

The next step is thus to choose a single value for k_p for all runs which are at the same temperature. The first and most obvious guess for this single value is the average of the $k_{p,e}$ values regressed for each of the runs. With this constant value for the polymerisation rate, the site transformation constants can be re-evaluated using the methods described above, fitting values in the two regions of sensitivity.

The constant value for k_p can now be evaluated again, by finding the value which minimises the objective function given in equation 4.11.

$$Obj = \sum_{e}\sum_{te}\left\{r_{M_1,e}\left(t_{te,e}\right) - k_p\left[M_{1,e}\right]P_*^{3+}\left(t_{te,e},\beta_{st,e}^{4+,3+},\beta_{st,e}^{3+,2+},\beta_{st,e}^{2+,3+}\right)\right\}^2 \qquad 4.11$$

This procedure, of evaluating k_p from the $\beta_{st,e}^{q,r}$ values, and then $\beta_{st,e}^{q,r}$ with the new k_p value, must be repeated until the value for k_p converges. This results in a set of $\beta_{st,e}^{q,r}$ and k_p values which are consistent and can be used in the next step.

Multi-linear regression – rate constants to lumped parameters

As shown in equation 2.1, each lumped site transformation parameter $\beta_{st,e}^{q,r}$ is a function of the liquid phase reactant concentrations and the site transformation rate constants, $k_{st,i}^{q,r}$. If the relationship is linear (as it is in equation 2.1), the set of values for each parameter from the previous regression steps can be expressed using matrix algebra (equation 4.12).

$$\underline{\beta_{st}^{q,r}} = \underline{\underline{C}} \cdot \underline{k_{st}^{q,r}} \qquad 4.12$$

The vectors and matrix in equation 4.12, for *e* sets of values of $\beta_{st}^{q,r}$, are given in equations 4.13.

$$\underline{\beta_{st}^{q,r}} = \left[\beta_{st,1}^{q,r},\beta_{st,2}^{q,r},\ldots,\beta_{st,e}^{q,r}\right]$$

$$\underline{\underline{C}} = \begin{bmatrix} 1 & \left[A_1\right] & \left[H_{2,1}\right] \\ 1 & \left[A_2\right] & \left[H_{2,2}\right] \\ & \ldots & \\ 1 & \left[A_e\right] & \left[H_{2,e}\right] \end{bmatrix} \qquad 4.13$$

$$\underline{k_{st}^{q,r}} = \left[k_{st,sp}^{q,r} \quad k_{st,A}^{q,r} \quad k_{st,H_2}^{q,r}\right]^T$$

The subscript *e* refers to the experiment number in the matrix expansions above.

The best fit value for $\underline{k_{st}^{q,r}}$ can be found using multilinear regression by solving equation 4.14.

$$\underline{k_{st}^{q,r}} = \left(\underline{\underline{C}}^T\,\underline{\underline{C}}\right)^{-1}\underline{\underline{C}}^T\,\underline{\beta_{st}^{q,r}} \qquad 4.14$$

Multilinear regression will provide the best fit of the nine site transformation rate constants to the lumped parameters; the solution of equation 4.14 will be unique, and the global optimum, because of the linear nature of the relationship between the reactant concentrations and the lumped site transformation rate constants. It is important to take advantage of this linear relationship, because of the unique and relatively simple solution; extraction of kinetic parameters generally requires much more complex nonlinear regression procedures.

The drawback to this multilinear regression is that the solution does not impose any constraints on the values assigned to the rate constants. Physically, rate constants must be positive, and so to make use of the results of the multilinear regression, any negative values resulting from regression will be assigned values of zero and refitted in a non-linear regression scheme.

The values for the site transformation rate constants obtained from multilinear regression can then be used as initial guesses for the final step of regression: least squares regression.

Non-linear least-squares regression – rate constants to rate curves

The final step in the regression of kinetic parameters is to fit the model, based on the site transformation rate constants and propagation rate as shown in equation 4.4, to the experimentally-measured rate curves, such as the profile in Figure 4.2. The objective function is shown in equation 4.15. The function can be minimised using a suitable non-linear solver.

$$Obj = \sum_{e}\sum_{te}\left\{ r_{M_1,e}\left(t_{te,e}\right) - k_p\left[M_1\right]_e P_*^{3+}\left(t_{te,e}, \sum_{q}\sum_{r}\underline{k_{st}^{q,r}} \right)\right\}^2 \qquad 4.15$$

The values of $\underline{k_{st}^{q,r}}$ which minimise the objective function are the final values for the site transformation rate constants, which can be used to describe the activity of Ziegler-Natta catalysts such as those used for polymer production.

4.1.3 Summary

A rigorous regression approach to extract meaningful kinetic constants from experimental rate data in Ziegler-Natta catalysed olefin polymerisation has been presented. The approach makes use of a fundamental kinetic scheme that describes polymerisation activity in terms of titanium oxidation state, avoiding the need for physically unrealistic multiple active site types. The principles on which the regression scheme was developed included reducing the number of parameters to be fitted simultaneously, and fitting parameters in regions of greatest sensitivity to obtain meaningful parameter values.

Using the kinetic model and regression methods proposed, lab-scale polymerisation rate data can be used to obtain parameters to describe the activity of industrial catalysts. These parameters, and the kinetic scheme, can be used to perform computer simulation studies of the behaviour of industrial-scale olefin polymerisation reactors, including process scale-up, optimisation and control.

Fitting values to the kinetic constants requires rate profiles for a range of experimental conditions, such as temperature, reactant concentration and reaction time.

4.2 Co-polymerisation rate constants

Once the parameters describing catalyst activity are known, the parameters describing the incorporation of comonomer in the polymer must be determined.

The comonomer content of the polymer can be used to obtain values for the co-polymerisation rate constants. These constants are:

- The rate of addition of 1-butene to chains ending in ethylene, $k_{p,12}$;
- The rate of addition of ethylene to chains ending in 1-butene, $k_{p,21}$;
- The rate of addition of 1-butene to chains ending in 1-butene, $k_{p,22}$.

In principle, 1-butene homopolymerisation experiments could be performed to determine a value for $k_{p,22}$, just as a value for $k_{p,11}$ was determined in Section 4.1. However, polymerisation of olefin monomers other than ethylene and propylene is very uncommon; the higher carbon-number olefins (such as 1-butene) are added to the two primary monomers in small quantities, to modify the crystalline properties of the product. Because of the significantly higher value of 1-butene (when compared to ethylene), performing a 1-butene homopolymerisation experiment is prohibitively expensive; thus the regression method must be accomplished without this separate experiment.

Since the polymer of interest frequently has a very low rate of comonomer incorporation, it is assumed that the rate of addition of 1-butene to chains ending in 1-butene ($k_{p,22}$) is negligible, and so $k_{p,22} = 0$. This assumption will be re-examined during the analysis of experimental data.

4.2.1 Regression approach

If it is assumed that the fraction of a polymer which was monomer *k* (f_{M_k}) can be inferred by the ratio of that monomer's propagation rate to the total propagation rate, then equation 4.16 will hold. This assumption is particularly valid under steady-state conditions, when the relative rates of monomer propagation will not vary with time; thus at any time the instantaneous rate of addition of a monomer, relative to the total propagation rate, will be equivalent to the fractional incorporation of that monomer in the polymer.

$$f_{M_k} = \frac{r_{p,M_k}}{r_p} \qquad 4.16$$

Recalling the definition for the rate of propagation (equation 4.1), the propagation rates can be expressed as shown in equation 4.17.

$$f_{M_k} = \frac{\sum_i k_{p,ik} \xi_i [M_k]}{\sum_i \sum_j k_{p,ij} \xi_i [M_j]} \qquad 4.17$$

Equation 4.17 holds for any number of monomers; however, polymerisation of more than two monomers is extremely rare, and so equation 4.17 can be evaluated for $i, j = \{1,2\}$. If we also accept the assumption of

negligible addition of 1-butene to chains with 1-butene most recently added (in other words, $k_{p,22} = 0$), then equation 4.17 can be expanded as shown in equation 4.18.

$$f_{C_4H_8} = \frac{k_{p,12}\xi_1[M_2]}{k_{p,11}\xi_1[M_1] + k_{p,12}\xi_1[M_2] + k_{p,21}\xi_2[M_1]} \quad 4.18$$

Since a growing chain must either have ethylene or 1-butene most recently added, equation 4.19 applies.

$$\xi_1 + \xi_2 = 1 \quad 4.19$$

Under steady-state conditions, as stated above, the instantaneous rate of addition of a monomer, relative to the total propagation rate, will be equivalent to the fractional incorporation of that monomer in the polymer. Similarly, the number of live chains with 1-butene most recently added (ξ_2) will be equivalent to the instantaneous rate of addition of 1-butene, relative to the total propagation rate.

Thus, assuming that the number of live chains with 1-butene most recently added (ξ_2) is the same as the mole fraction comonomer content of the polymer ($f_{C_4H_8}$), and substituting for ξ_1 using equation 4.19, results in equation 4.20.

$$\xi_2 = \frac{k_{p,12}(1-\xi_2)[M_2]}{k_{p,11}(1-\xi_2)[M_1] + k_{p,12}(1-\xi_2)[M_2] + k_{p,21}\xi_2[M_1]} \quad 4.20$$

Rearranging equation 4.20 gives the quadratic form in equation 4.21, which can be solved for ξ_2 (the comonomer fraction) using standard methods.

$$\xi_2^2\left(k_{p,21}[M_1] - k_{p,11}[M_1] - k_{p,12}[M_2]\right) + \xi_2\left(k_{p,11}[M_1] + 2k_{p,12}[M_2]\right) - k_{p,12}[M_2] = 0 \quad 4.21$$

When fitting the model parameters ($k_{p,12}$ and $k_{p,21}$) to data, the comonomer content, concentrations of the monomers, and ethylene propagation rate ($k_{p,11}$) are known. The solution to equation 4.21 is the model-predicted comonomer content, as a function of the two co-polymerisation rate constants.

The objective function to be minimised by a suitable nonlinear solver is given in equation 4.22.

$$Obj = \sum_e \left\{ f_{C_4H_8,e} - \xi_2\left([\underline{M}]_e, k_{p,12}, k_{p,21}\right) \right\}^2 \quad 4.22$$

The values for $k_{p,12}$ and $k_{p,21}$ which minimise the objective function in equation 4.22 are the final values for the co-polymerisation rate constants.

4.2.2 Summary

A method of extracting values for the co-polymerisation rate constants from experimental data has been proposed. Comonomer content data is required for a range of experimental conditions, particularly comonomer concentration.

4.3 Termination rate constants

The termination rate constants (in tandem with the propagation rate constants) determine the length of polymer chains produced. As discussed in the Literature Review, the question of site heterogeneity has not been answered conclusively, with various authors proposing a range of numbers of active sites to match chain length distributions and observed polymer properties.

The pseudo-sites concept (Rawatlal, 2004) is used in this project to interpret the chain length data.

The following section describes the development of a mathematical model to determine the moments of the MWD, and thereby predict the properties of the polymer. The moments of a distribution are found using equation 1.1, reproduced below.

$$\lambda_k = \sum_{n=0}^{\infty} n^k P_n \qquad 1.1$$

4.3.1 Model development

Most of the model development shown below has been published previously (Rawatlal, 2004), but is included here for clarity and the reader's convenience.

Molecular weight distribution

In order to extract the live moments, balances on chains of length one at pseudo-site m (equation 4.23), and on chains of length n at pseudo-site m (equation 4.24) are required. The concentration of polymer chains of length *n*, growing at pseudo-site *m* and with monomer *i* most recently added to the chain is denoted by the symbol $P_{n,i}^m$ (Hutchinson et al., 1992, Rawatlal, 2004).

The superscript *m* in the following derivations refers to the pseudo-site at which terminating agent *m* is active. For brevity, the phrase "at pseudo-site *m*" is not used throughout the derivation, except where clarity requires it.

$$\frac{d}{dt}P_{1,i}^m = -\beta_{st}^{3+,2+}P_{1,i}^m + k_{0,i}P_0^m[M_i] - \sum_j k_{p,ij}P_{1,i}^m[M_j] - k_{t,i}^m P_{1,i}^m C_m \qquad 4.23$$

$$\frac{d}{dt}P_{n,i}^m = -\beta_{st}^{3+,2+}P_{n,i}^m + \sum_j k_{p,ji}P_{n-1,j}^m[M_i] - \sum_j k_{p,ij}P_{n,i}^m[M_j] - k_{t,i}^m P_{n,i}^m C_m \qquad 4.24$$

The first term in each of these equations is the rate at which site transformations reduce the number of growing chains, due to their being terminated during the transformation reaction. The second term indicates the formation of sites of interest, either by the initiation of vacant sites (equation 4.23), or by addition of monomer to a shorter growing chain (equation 4.24). The third terms are the rate at which sites are polymerised into longer chains. The final term is the rate at which growing chains are terminated by a particular terminating agent m.

The concentration of vacant sites is the difference between all available sites and those sites which have polymer chains growing on them (equation 4.25).

$$P_0^m = P_*^m - \sum_j \sum_n P_{n,j}^m = P_*^m - \sum_j \lambda_{0,j}^m \qquad 4.25$$

The zeroth moments for polymer chains ending in monomer *i* are obtained by adding equations 4.23 and 4.24 for all values of *n*, as shown in equation 4.26.

$$\frac{d}{dt}\lambda_{0,i}^{m} = -\beta_{st}^{3+,2+}\lambda_{0,i}^{m} + k_{0,i}\left[M_i\right]\left(P_*^m - \sum_j \lambda_{0,j}^{m}\right) + \sum_j k_{p,ji}\lambda_{0,j}^{m}\left[M_i\right] - \sum_j k_{p,ij}\lambda_{0,i}^{m}\left[M_j\right] - k_{t,i}^{m}\lambda_{0,i}^{m}C_m \qquad 4.26$$

In polymer growth kinetics, it is generally accepted that chain lifespans are very short (Hutchinson et al., 1992), and so the Quasi-Steady State Assumption (QSSA) can be applied to equation 4.26. Evaluating this equation for all monomer types *i*, and making use of matrix algebra, results in the concentrations of chains ending in each monomer type, $\lambda_{0,i}^{m}$. In practice, almost all systems contain just two monomers; the concentration of growing chains ending in each of two monomer types is shown in equations 4.27 and 4.28.

$$\lambda_{0,1}^{m} = \frac{c - \frac{bf}{e}}{a - \frac{bd}{e}} P_*^m = \xi_1^m P_*^m \qquad 4.27$$

$$\lambda_{0,2}^{m} = \frac{f - \frac{cd}{a}}{e - \frac{bd}{a}} P_*^m = \xi_2^m P_*^m \qquad 4.28$$

Where:

$$a = \beta_{st}^{3+,2+} + k_{0,1}\left[M_1\right] + k_{p,12}\left[M_2\right] + k_{t,1}^{m}C_m$$
$$b = k_{0,1}\left[M_1\right] - k_{p,21}\left[M_1\right]$$
$$c = k_{0,1}\left[M_1\right]$$
$$d = k_{0,2}\left[M_2\right] - k_{p,12}\left[M_2\right]$$
$$e = \beta_{st}^{3+,2+} + k_{0,2}\left[M_2\right] + k_{p,21}\left[M_1\right] + k_{t,2}^{m}C_m$$
$$f = k_{0,2}\left[M_2\right]$$

The fraction of catalyst sites which are occupied by chains ending in monomer *i* is given by ξ_i^m in equations 4.27 and 4.28. This parameter indicates the comonomer content of the polymer.

From equations 4.27 and 4.28, and assuming that the concentration of vacant sites is negligible compared to the concentration of occupied sites, the composition of the polymer is approximated by equation 4.29.

$$\xi_i^m = \frac{\lambda_{0,i}^{m}}{P_*^m} = \frac{\lambda_{0,i}^{m}}{P_0^m + \sum_j \lambda_{0,j}^{m}} \approx \frac{\lambda_{0,i}^{m}}{\lambda_0^m} \qquad 4.29$$

Assuming that the overall composition of the polymer is identical to the instantaneous composition of each chain length gives equation 4.30, relating the concentration of all chains of length *n* and the concentration of those chains which end in monomer *i*.

$$\xi_i^m = \frac{P_{n,i}^m}{P_n^m} \qquad 4.30$$

Substituting equation 4.30 into equation 4.23 and applying the QSSA results in the balance on all chains of length 1 (equation 4.31).

$$0 = -\beta_{st}^{3+,2+}\xi_i^m P_1^m + \sum_i k_{0,i}[M_i]P_0^m - \sum_i\sum_j k_{p,ij}\xi_i^m[M_j]P_1^m - \sum_i k_{t,i}^m\xi_i^m C_m P_1^m \qquad 4.31$$

Similar treatment of equation 4.24 gives the balance on all chains of length *n*.

$$0 = -\beta_{st}^{3+,2+}\xi_i^m P_n^m + \sum_i\sum_j k_{p,ji}\xi_j^m[M_i]P_{n-1}^m - \sum_i\sum_j k_{p,ij}\xi_i^m[M_j]P_n^m - \sum_i k_{t,i}^m\xi_i^m C_m P_n^m \qquad 4.32$$

Equations 4.33 and 4.34 result from rearranging equations 4.31 and 4.32.

$$P_1^m = \frac{\sum_i k_{0,i}[M_i]P_0^m}{\sum_i\left(\xi_i^m\left(\beta_{st}^{3+,2+} + k_{t,i}^m C_m\right) + \sum_j k_{p,ij}\xi_i^m[M_j]\right)} \qquad 4.33$$

$$P_n^m = \frac{\sum_i\sum_j k_{p,ji}\xi_j^m[M_i]P_{n-1}^m}{\sum_i\left(\xi_i^m\left(\beta_{st}^{3+,2+} + k_{t,i}^m C_m\right) + \sum_j k_{p,ij}\xi_i^m[M_j]\right)} \qquad 4.34$$

Through recursion, the concentration of chains of length *n* can be determined, as shown in equation 4.35.

$$P_n^m = P_0^m\varphi^m\left(\gamma^m\right)^{n-1} \qquad 4.35$$

Where

$$\varphi^m = \left(\frac{\sum_i k_{0,i}[M_i]}{\sum_i\left(\xi_i^m\left(\beta_{st}^{3+,2+} + k_{t,i}^m C_m\right) + \sum_j k_{p,ij}\xi_i^m[M_j]\right)}\right)$$

$$\gamma^m = \left(\frac{\sum_i\sum_j k_{p,ji}\xi_j^m[M_i]}{\sum_i\left(\xi_i^m\left(\beta_{st}^{3+,2+} + k_{t,i}^m C_m\right) + \sum_j k_{p,ij}\xi_i^m[M_j]\right)}\right) \qquad 4.36$$

The parameter γ^m is the ratio of the propagation reaction to all reactions (site transformation, chain termination and propagation) occurring at pseudo-site m. Since the relative rates of chain propagation to chain termination (and site transformation) will define the length of polymer chains, the parameter γ^m has been called the Chain Length Characteristic Parameter, or CLCP (Rawatlal, 2004).

Since the propagation rate is significantly larger than the transformation or termination rates, and all terms in equation 4.36 are positive, γ^m will be a value close to, but smaller than, 1. As the propagation rate increases, the CLCP approaches 1; similarly, as the termination rate at a particular pseudo-site increases, the CLCP for that site decreases.

The zero-th moment can be obtained from the convergent infinite series, since γ^m is smaller than 1.

$$\lambda_0^m = \sum_n P_n^m = \sum_n P_0^m \varphi^m \left(\gamma^m\right)^{n-1} = P_0^m \varphi^m \frac{1}{1-\gamma^m} \qquad 4.37$$

The fraction of chains of length n can then be found in terms of the parameter γ^m, as shown in equation 4.38.

$$\nu_n^m = \frac{P_n^m}{\lambda_0^m} = \left(\gamma^m\right)^{n-1}\left(1-\gamma^m\right) \qquad 4.38$$

An alternative expression for the concentration of chains of length n is given by equation 4.39. Evaluation of this equation for all values of *n* will produce the polymer MWD.

$$P_n^m = \nu_n^m \lambda_0^m = P_*^m \left(\gamma^m\right)^{n-1}\left(1-\gamma^m\right)\sum_i \xi_i^m \qquad 4.39$$

Live polymer moments

Using the definition of the moments of a distribution of chain length (equation 1.1) and the definition for P_n^m (equation 4.39) gives the definition of the first three moments for polymer chains growing at each pseudo-site.

$$\begin{aligned}
\lambda_0^m &= P_*^m \sum_i \xi_i^m \\
\lambda_1^m &= P_*^m \sum_i \xi_i^m \frac{1}{1-\gamma^m} \\
\lambda_2^m &= P_*^m \sum_i \xi_i^m \frac{1+\gamma^m}{\left(1-\gamma^m\right)^2}
\end{aligned} \qquad 4.40$$

In order to find the moments of the chain length distribution across all pseudo-sites, the total concentration of sites must be related to the concentration of each of the pseudo-sites. It is proposed that the fractional parameter f^m can be used for this purpose (equation 4.41).

$$P_*^m = f^m P_* \qquad 4.41$$

The pseudo-site fraction can be defined by the ratio of termination rate at pseudo-site *m* to the sum of all termination rates at all pseudo-sites (equation 4.42). This definition is proposed because of the statistical view of termination: stronger terminating agents will terminate more chains. The fraction of the total number of active sites which are considered to be pseudo-sites corresponding to that agent will be higher.

$$f^m = \frac{\sum_i k_{t,i}^m \xi_i^m C_m}{\sum_m \sum_i k_{t,i}^m \xi_i^m C_m} \qquad 4.42$$

The overall live moments can be found by using the definition of the pseudo-site fraction, f^m, to add the moments at each pseudo-site. The average properties of the polymer (such as number-and weight-average molecular weight) can then be predicted using these moments.

$$\lambda_0 = P_* \sum_m f^m \sum_i \xi_i^m$$

$$\lambda_1 = P_* \sum_m f^m \sum_i \xi_i^m \frac{1}{1-\gamma^m} \qquad 4.43$$

$$\lambda_2 = P_* \sum_m f^m \sum_i \xi_i^m \frac{1+\gamma^m}{\left(1-\gamma^m\right)^2}$$

The number- and weight-average molecular weights (M_n and M_w) and polydispersity index (*PDI*) for each pseudo-site can be found from the live moments in equation 4.43, as was shown in equations 1.2, 1.3 and 1.4, reproduced below.

$$M_n = MW_{monomer} \frac{\lambda_1}{\lambda_0} \qquad 1.2$$

$$M_w = MW_{monomer} \frac{\lambda_2}{\lambda_1} \qquad 1.3$$

$$PDI = \frac{\lambda_0 \lambda_2}{\left(\lambda_1\right)^2} \qquad 1.4$$

4.3.2 Regression approach

In order to fit the termination parameters to the chain length data from the experiments, one very important assumption is required: that the rate of termination at a particular pseudo-site is independent of the monomer most recently added to the growing chain. This is expressed in equation 4.44.

$$k_{t,1}^m = k_{t,2}^m = k_t^m \qquad 4.44$$

This reduces the number of terminating rate constants from 10 to 5: one for each reactant species (co-catalyst, monomer, comonomer, hydrogen) and one for spontaneous termination.

The termination rate constants can then be fitted to the chain length data by non-linear least-squares regression. The moments of the chain length distribution are predicted by equation 4.43, and used to calculate the number- and weight-average molecular weights for each experimental run, *e*.

The objective function to be minimised is given in equation 4.45.

$$Obj = \sum_e \left\{ M_{n,e} - m_{mon} \frac{\lambda_1}{\lambda_0}\left(\underline{C}_e, \underline{k_t}\right) \right\}^2 + \sum_e \left\{ M_{w,e} - m_{mon} \frac{\lambda_2}{\lambda_1}\left(\underline{C}_e, \underline{k_t}\right) \right\}^2 \qquad 4.45$$

The values for $\underline{k_t}$ which minimise the objective function are the final termination rate constants for the kinetic model.

4.3.3 Summary

A method has been developed to predict the number- and weight-average molecular weights of a polymer, based on the pseudo-sites concept and a set of termination rate constants. In order to extract values for the termination rate constants from experiments, chain length distribution data is required for a range of experimental conditions, particularly the concentration of monomers, co-catalyst and hydrogen.

CHAPTER 5. LABORATORY-SCALE KINETIC STUDY

This section describes the experiments carried out to provide experimental data for the regression methods presented in the previous chapter. The experimental materials and methods, and analytical methods described, followed by the presentation of the experimental results.

5.1 Experimental materials and methods

An industrial heterogeneous Ziegler-Natta catalyst ("Catalyst A", manufactured by Grace), activated by triethyl aluminium, was used to produce ethylene-1-butene co-polymer in an n-hexane slurry reaction system. Hydrogen was used as a chain-transfer agent. The experiments were performed with the reactor operating in isothermal, isobaric fed-batch mode; this allows the extraction of activity profiles from the experimental data, and keeps the conditions in the reactor stable, making the regression procedure simpler.

Polymerisation experiments were conducted in a 1L stainless steel vessel manufactured by Parr Instrument Company, equipped with a thermocouple, external electric heating jacket and internal cooling coil for temperature control (by PI controller). A diagram of the reactor is shown in Figure 5.1, and a photograph of the experimental apparatus in Figure 5.2.

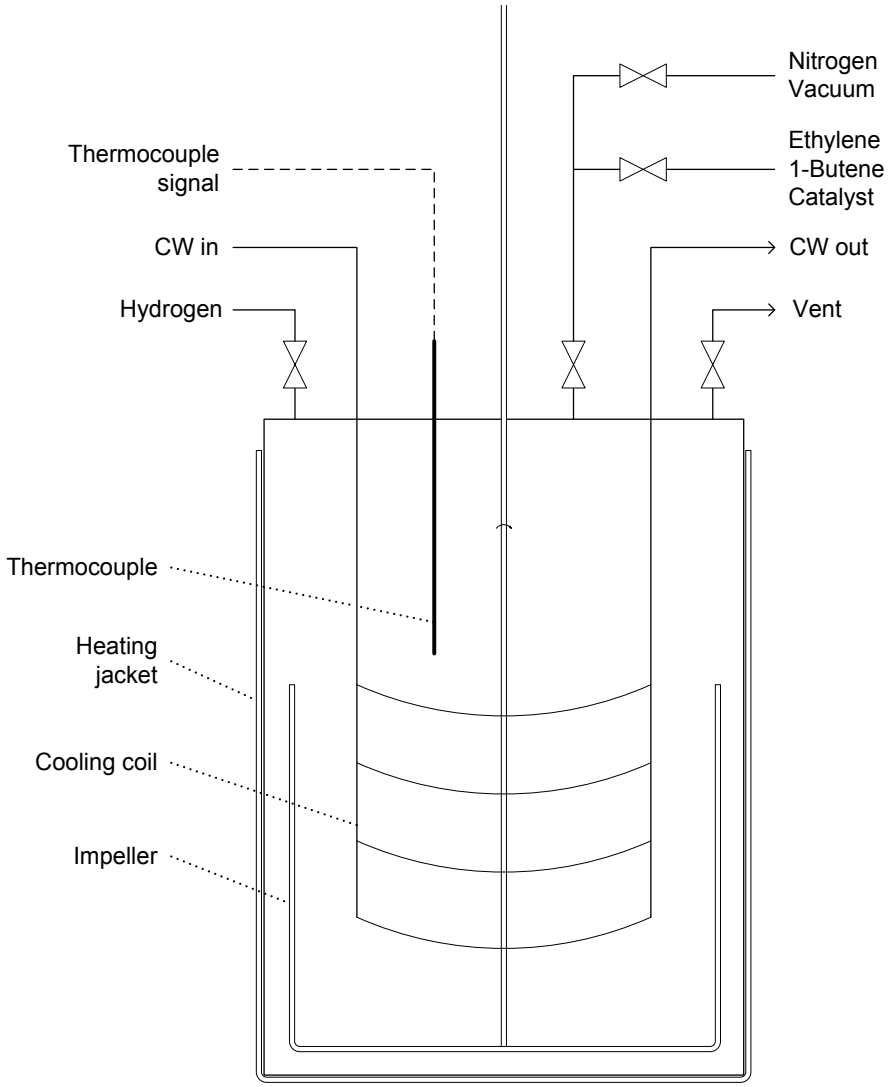

Figure 5.1: Schematic of lab-scale slurry-phase polymerisation reactor

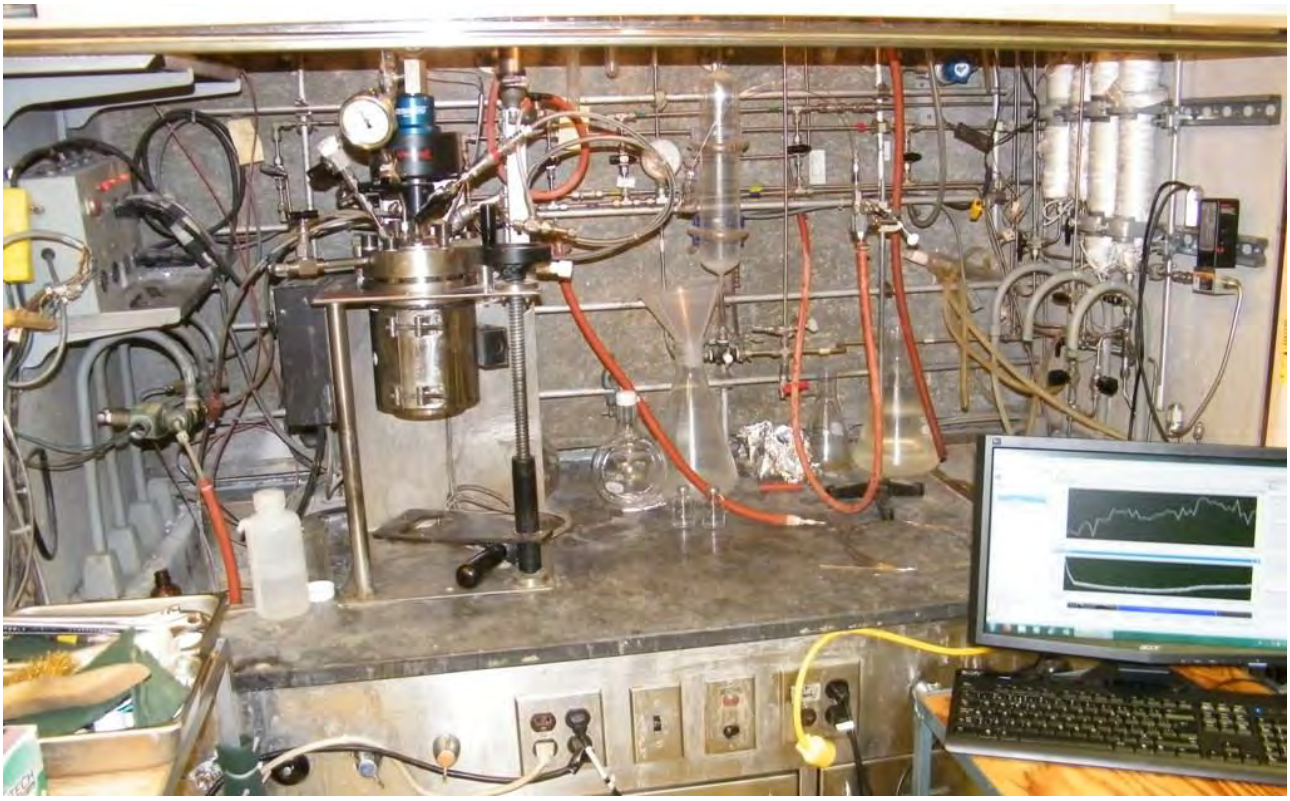

Figure 5.2: Experimental apparatus at the University of Waterloo

The reaction vessel was stored in an oven at 150°C for at least two hours (generally overnight) to remove oxy-compounds such as oxygen, water or ethanol, as these would poison the catalyst and co-catalyst. In preparation for an experimental run, the reactor was attached to the rig and heated under vacuum until the thermocouple indicated a temperature of 150°C, followed by five cycles of flushing with nitrogen and purging with vacuum for a minute each time, using Schlenk lines. The reactor was then cooled under positive nitrogen pressure until the thermocouple reading was below 60°C, well below the normal boiling point of n-hexane (69°C). At this point the reactor was ready for a polymerisation run.

In a glovebox, catalyst powder and co-catalyst (triethylaluminium at 1M in hexanes, from Aldrich) were weighed and sealed in separate vials. Vials were kept free of contaminants by cleaning in an acid bath, rinsing with de-ionised water, and drying at 150°C overnight.

500mL of n-hexane (purified in an MBraun Solvent Purification System and stored under nitrogen with 4A molecular sieves) at room temperature was transferred by cannula from storage bottles to the reactor, using standard Schlenk line techniques. Agitation was started, and reactor temperature stabilised at 60°C by the controller. Once the temperature was stable, agitation was stopped and the TEA was transferred by cannula from the sample vial to the reactor. TEA acted primarily as co-catalyst, but also served as an oxy-compound scavenger to remove any contaminants which may be present in the solvent or reactor. TEA was added in excess (when compared with industrial quantities of co-catalyst, relative to catalyst; see Chapter 11: Industrial operational data, on page 155) in order to ensure catalyst activity. Agitation was restarted and the temperature stabilised at 60°C.

After the temperature had stabilised again, agitation was stopped and the reactor vented to reduce the presence of inert nitrogen (supplied at ~2.5barg). The reactor pressure was reduced to between 1 and 1.5 barg, stopping when solvent condensed in the purge line, indicating that the solvent was evaporating.

Hydrogen gas (ultrahigh purity from Praxair) was added until the reactor pressure reached the desired level of hydrogen pressure. Agitation was then restarted, and the temperature controller set point adjusted to the desired reaction temperature (between 85 and 90^{o}C).

While the reactor heated, the required mass of 1-butene was placed in a bomb. The bomb was placed inline with the ethylene feed to the reactor, and added to the reactor with ethylene (polymer grade from Praxair) which was supplied at ~650 kPag when reactor temperature had stabilised. This step was performed to saturate the reactor with monomer and comonomer, so that when the catalyst was added the measured flow rate of ethylene represented consumption rather than addition of monomer to saturate the reactor.

The catalyst powder was transferred by cannula, using nitrogen pressure and 15-20 ml fresh n-hexane, from the sample vial into a specially-constructed bomb (shown in Figure 5.3) which allowed the addition of catalyst to the reactor in a single shot. The bomb apparatus included a bypass so that once the catalyst had been added the flow of ethylene could continue but the bomb remained sealed from the reactor. This prevented the polymerisation reaction from proceeding with any of the catalyst which may have remained in the bomb.

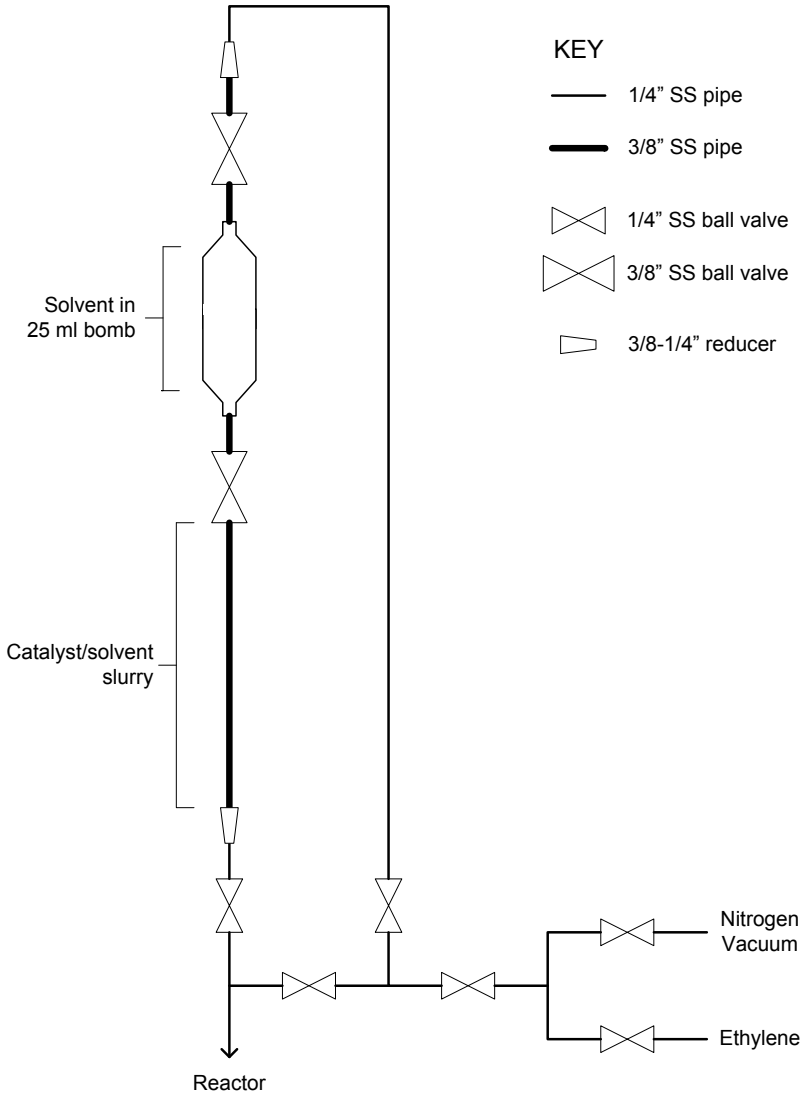

Figure 5.3: Schematic of catalyst-addition apparatus

The ethylene supply pressure was increased to 700 kPag (the desired reaction pressure), in order to provide a pressure gradient to drive the shot of solvent and suspended catalyst powder into the reactor.

While polymerisation proceeded, the flow rate of ethylene into the reactor and the temperature of the reaction mixture were logged. The flow rate of ethylene is taken as an indicator of the activity of the catalyst, and was measured using a Brooks 5860i Mass Flow Meter.

Once the desired reaction time had passed, the flow of ethylene to the reactor was stopped and the vent opened to reduce pressure and remove the reactant. The temperature set point was adjusted to 25^{o}C and the heating jacket removed in order to cool the mixture as rapidly as possible, and slow the polymerisation reaction. As soon as the pressure reached 1bar, the vessel was opened and ethanol injected to finally deactivate the catalyst.

Solvent and polymer powder were removed from the vessel. Approximately 100ml of ethanol with 2% 1M HCl was added to the mixture, which was left in a glass beaker on a magnetic stirrer for at least two hours, to ensure that all remaining catalyst had been deactivated.

5.2 Experimental conditions

With the experimental apparatus decribed above, it is possible to produce polymer at a range of conditions (pressure and temperature) and with different ratios of reactants (catalyst, co-catalyst, monomer, comonomer and hydrogen).

While temperature and pressure are monitored continuously, and the catalyst activity can be inferred from the consumption of ethylene, the properties of the polymer (including MWD, comonomer content, particle size distribution and morphology) can only be measured offline, once the reaction is completed. For this reason, when the experimental campaign was planned, it was necessary to include some experimental runs at identical conditions but different reaction times.

To allow the fitting of kinetic parameters using the methods described in Chapter 4, and for the kinetic parameters to be useful in a reactor model that can simulate an industrial reactor, sets of data at a range of conditions, including industrial conditions, are required. The conditions in the industrial reactor of interest are described later in the thesis (see Table 11.1 on page 159).

The conditions in the runs were chosen to simulate industrial conditions in the lab-scale reactor, in terms of liquid phase concentration (for 1-butene) and gas phase ratios (for hydrogen). As mentioned above, the co-catalyst was added in excess to scrub the reactor and equipment of any remaining poisons, to ensure catalyst activity.

In principle, for kinetic parameter identification, a sophisticated experimental design is required (de Camargo Forte et al., 2003, Yao et al., 2003, Thompson et al., 2010). However, given the time constraints for the experimental section of this work, and the regression procedure developed in Chapter 4, a more concise experimental campaign was planned.

The conditions for each experimental run are given in Table 5.1. A larger set of experiments was planned, including replicate runs, but could not be completed, again because of time constraints.

Part B. Kinetic study

Table 5.1: Conditions for experimental runs

Run #	Date code	Catalyst (mg)	TEA (mmol)	Temp (^{o}C)	Reaction time (min)	1-Butene (g)	Hydrogen (bar a)
1	0505b	12	1.508	88	60	0.98	3.5
2	0605a	12.1	1.503	88	35	0.6	3.5
3	0605b	12.1	1.508	88	60	1.63	3.5
4	0705	12.5	1.507	88	60	0.99	2.5
5	0805a	12.1	1.507	90	60	0.95	3.5
6	0805b	12.8	1.505	88	60	1.02	3.5
7	0805c	12.8	1.837	88	60	0.99	3.5
8	0905a	12.5	1.513	85	60	0.99	3.5
9	0905b	12.2	1.500	85	15	1	3.5
10	0905c	12.5	1.502	88	30	1.01	2.5
11	1205	12.3	1.503	85	45	0.99	3.5
12	1305a	12.8	1.508	88	15	1.01	3.5
13	1305b	12.3	1.508	88	45	1.02	2.5
14	1405a	12.7	1.507	88	60	1.02	4.5
15	1405b	12.9	1.507	88	45	0.96	4.5
16	1905a	12	1.507	85	60	1.02	2.5
17	2005	12.3	1.505	88	45	0.58	3.5
18	2105a	12.2	2.003	90	60	1.03	3.5
19	2105b	12.5	1.503	88	30	1.59	3.5
20	2205a	12.6	1.500	88	30	0.62	3.5

5.3 Analytical methods

5.3.1 Catalyst activity

As mentioned above, the consumption rate of ethylene in the reactor (taken as a proxy for catalyst activity) was measured using a Brooks 5860i Mass Flow Meter. The average activity was also determined by measuring the total yield of polymer for each experimental run.

5.3.2 Melt flow index (MFI)

The melt flow index for the polymer samples was determined using a DYNISCO Melt Flow Indexer, and following the procedures described in ASTM D1238. Where possible, samples were extruded using 2.16kg and 5kg weights, both at 190^{o}C.

5.3.3 Gel Permeation Chromatography (GPC)

The molecular weight distribution (MWD) of the polymer samples was determined at the University of Waterloo using a PolyChar GPC instrument. Samples of 10-15 mg polymer powder were dissolved in 9 ml 1,2,4-trichlorobenzene and one drop n-heptane. Measurements were performed at 160^{o}C and a flow rate of 1 ml/min.

The polymer samples were also analysed at the University of Stellenbosch, using a Polymer Laboratories GPC 220 high temperature chromatograph instrument, with three 300 × 7.5 mm PLgel Olexis columns and a 50 × 7.5 mm PLgel Olexis guard column (all from Polymer Laboratories). Measurements were performed at 150^{o}C and a flow rate of 1 ml/min, using 1,2,4-trichlorobenzene stabilised with 0.0125% 2,6-di-*tert*-butyl-4-methylphenol (BHT) as a solvent.

5.3.4 Nuclear Magnetic Resonance Spectroscopy (NMR)

NMR spectroscopy data was obtained to determine the short chain branching (SCB) of the polymer; this represents the incorporation of comonomer. Polymer powder was melted into thin sheets in a press, cut into strips and dissolved in 1,2,4-trichlorobenzene in NMR sample tubes in a heating block at 150^{o}C for at least four hours. The samples were analysed with a Bruker Avance 500, and the spectra analysed using methods in the literature (de Pooter et al., 1991).

5.3.5 Crystallisation elution fractionation (CEF)

CEF data was determined using a PolyChar CEF instrument. All samples (of approximately 10 mg) were dissolved in 9 ml 1,2,4-trichlorobenzene and one drop n-heptane before being added to the autosampler. The operating parameters for the instrument are detailed in Table 5.2.

Table 5.2: CEF operating conditions

Crystallization Temperature (ºC)	35
Crystallization Rate (ºC / min)	3.00
Crystallization Pump Flow (mL / min)	0.04
Elution Temperature (ºC)	140
Elution Rate (ºC / min)	3.00
Elution Pump Flow (mL / min)	1.00

5.3.6 Particle size distribution (PSD)

The PSD of the polymer particles was measured using a Malvern Mastersizer 2000, with a Hydro G sample dispersion unit. Approximately 0.5g of polymer powder was added to the unit, followed by 10 drops of 1% ammonium citrate solution and approximately 10ml of ethanol, then agitated for 4 minutes before analysing for size distribution. This method was found to give very good reproducibility.

The evolution of the PSD was also qualitatively inspected by the use of Scanning Electron Microscopy (SEM) for selected polymer samples.

5.4 Experimental results

5.4.1 Catalyst activity

The consumption rate of ethylene (measured by a flow meter) was taken as an indicator of the activity of the catalyst. The activity profiles are shown in full in Section 20.1 in the Appendix. A typical activity profile (in this case, from Run #1) from the experimental runs is shown in Figure 5.4. It demonstrates the typical rapid initial increase in activity, and gradual decay from the maximum.

Table 5.3 shows the comparison of the mass of polymer recovered from the reactor following each experiment, and the mass of polymer obtained by integrating the consumption of ethylene (measured by the flow meter) over the reaction period.

As mentioned previously, replicate experimental runs were planned, but not completed due to time constraints. However, several of the experimental runs were under similar conditions, but different reaction times, and the reproducibility of the activity profiles can be examined by comparing these results. The activity profiles are compared for Runs #8, #9 and #11 (see Figure 5.5), Runs #10 and #13 (see Figure 5.6) and Runs #14 and #15 (see Figure 5.7). As these figures show, the activity profiles show good reproducibility between experimental runs under similar conditions

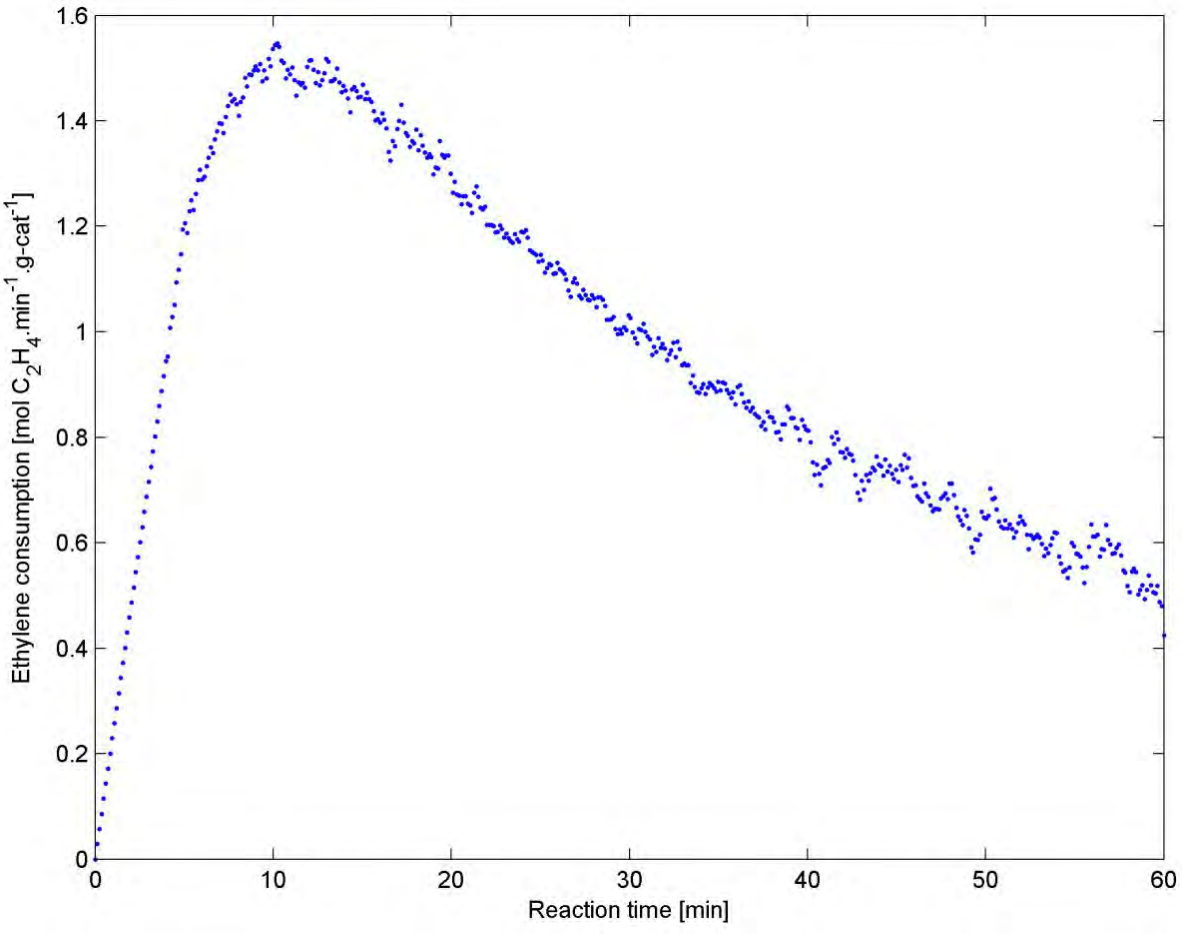

Figure 5.4: Typical experimental activity profile

Part B. Kinetic study

Table 5.3: Comparison of recovered polymer and measured ethylene consumption

Run #	Polymer mass (g)	
	Recovered	Integrated
1	18.19	19.34
2	5.48	7.06
3	18.93	14.91
4	28.61	22.96
5	16.06	19.19
6	24.94	26.33
7	19.49	20.37
8	21.17	22.26
9	5.12	4.53
10	22.57	22.35
11	17.46	18.09
12	6.76	6.10
13	33.1	34.16
14	8.58	10.47
15	7.09	8.14
16	38.17	39.90
17	12.48	13.48
18	14.32	15.77
19	19.71	16.28
20	13.84	14.20

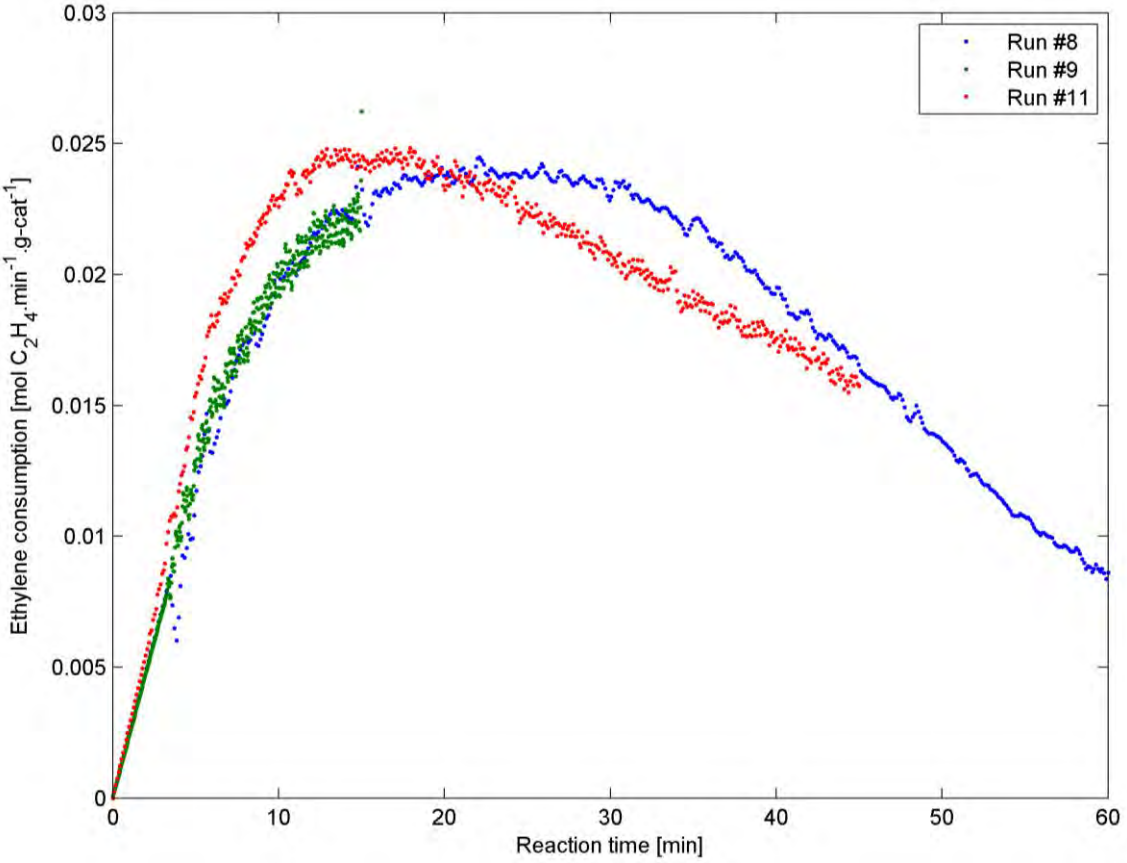

Figure 5.5: Comparison of activity profiles for Runs #8, #9 and #11

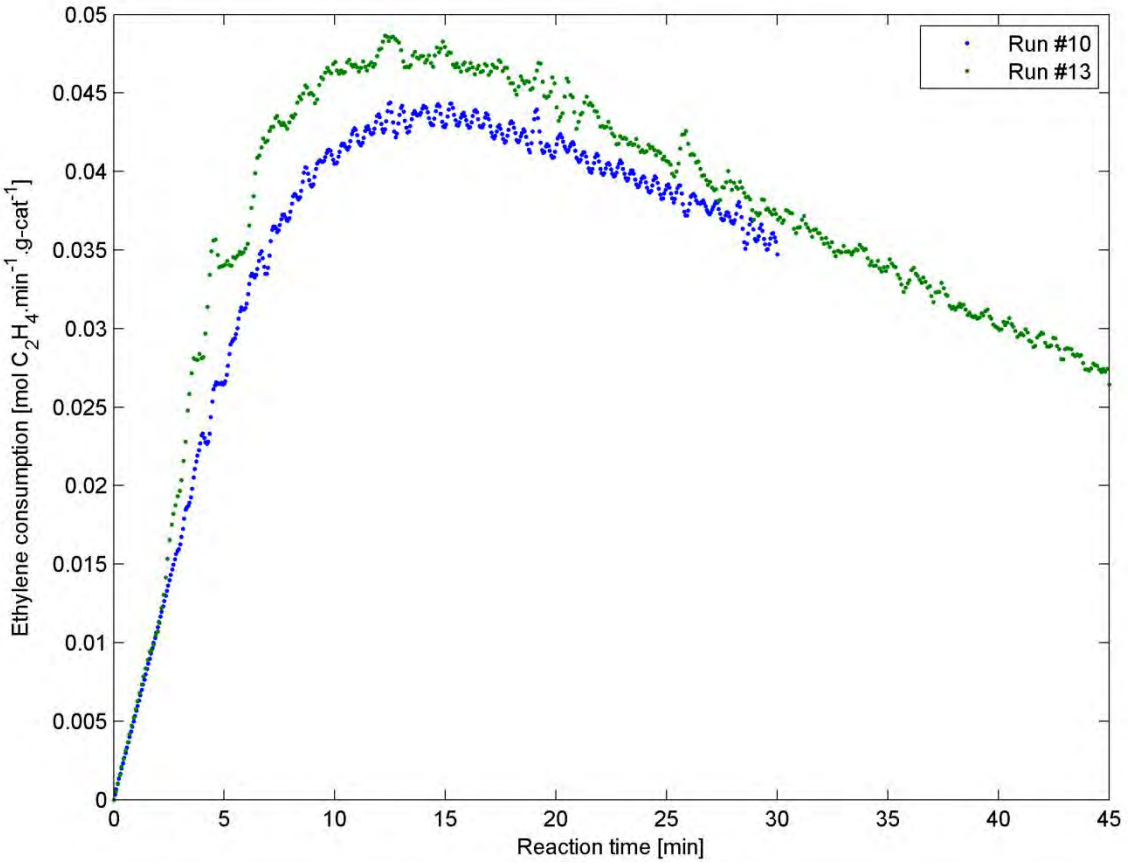

Figure 5.6: Comparison of activity profiles for Runs #10 and #13

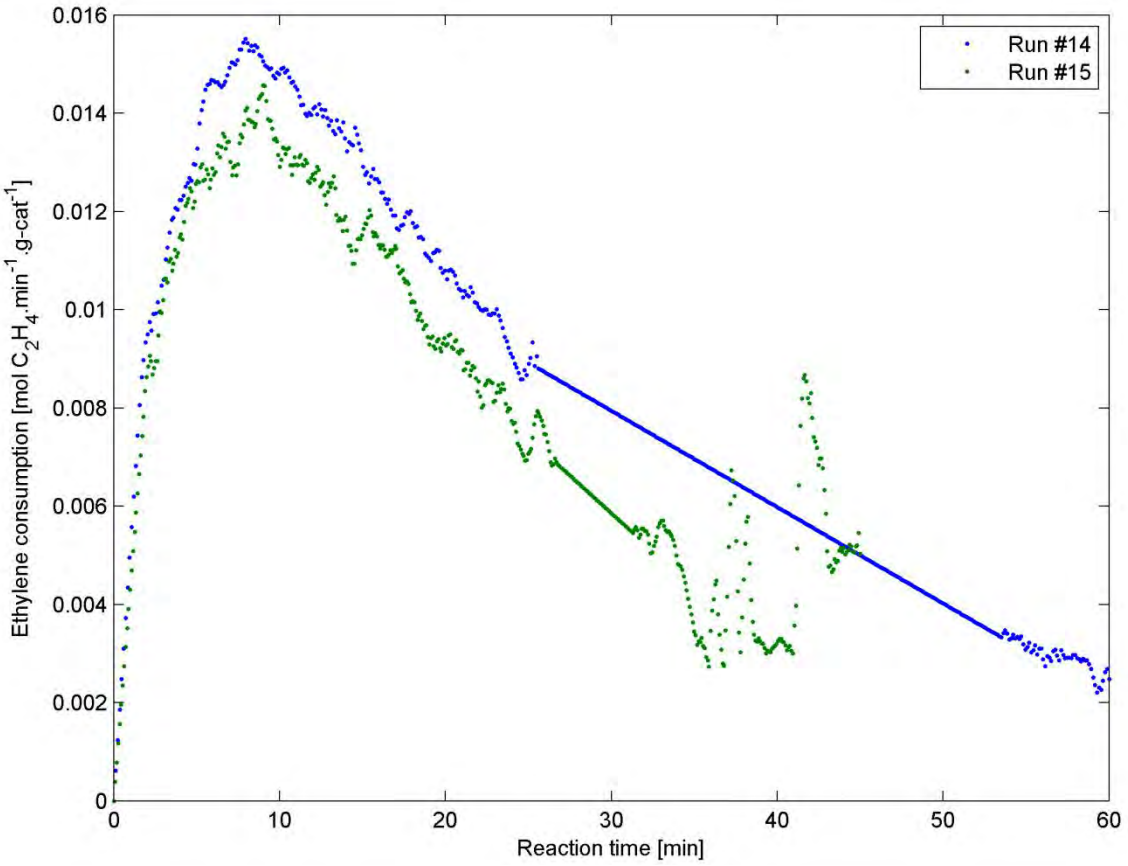

Figure 5.7: Comparison of activity profiles for Runs #14 and #15

5.4.2 Liquid phase concentrations

The initial molar hold-up of the reactor, for each component and each experimental run, was determined using an isothermal flash calculation, based on the Peng-Robinson equation of state (Peng & Robinson, 1976). The details of the calculation steps are given in Chapter 21 in the Appendix. The results of these calculations are shown in Table 5.4.

Table 5.4: Initial molar hold-up of laboratory reactor

Run #	TEA (mmol)	C_2H_4 (mol)	C_4H_8 (mol)	H_2 (mol)	C_6H_{14} (mol)	N_2 (mol)
1	1.508	0.174	0.0175	0.0441	3.78	0.0174
2	1.503	0.175	0.0107	0.0441	3.78	0.0174
3	1.508	0.172	0.0291	0.0441	3.78	0.0174
4	1.507	0.233	0.0177	0.0221	3.78	0.0174
5	1.507	0.166	0.0170	0.0441	3.78	0.0174
6	1.505	0.174	0.0182	0.0441	3.78	0.0174
7	1.837	0.174	0.0177	0.0441	3.78	0.0174
8	1.513	0.187	0.0177	0.0441	3.78	0.0174
9	1.500	0.186	0.0179	0.0441	3.78	0.0174
10	1.502	0.233	0.0180	0.0221	3.78	0.0174
11	1.503	0.187	0.0177	0.0441	3.78	0.0174
12	1.508	0.174	0.0180	0.0441	3.78	0.0174
13	1.508	0.233	0.0182	0.0221	3.78	0.0174
14	1.507	0.116	0.0182	0.0661	3.78	0.0174
15	1.507	0.116	0.0171	0.0661	3.78	0.0174
16	1.507	0.247	0.0182	0.0221	3.78	0.0174
17	1.505	0.175	0.0104	0.0441	3.78	0.0174
18	2.003	0.166	0.0184	0.0441	3.78	0.0174
19	1.503	0.173	0.0284	0.0441	3.78	0.0174
20	1.500	0.175	0.0111	0.0441	3.78	0.0174

The equilibrium concentrations of the various reactants in the liquid phase of the reactor (where the reaction occurs) were also determined using the isothermal flash calculation, based on the initial molar hold-up of each of the components in the table above.

The impact of mass transfer limitation on the transfer of the monomer from the gas phase to the liquid phase was accounted for using methods proposed in the literature (Floyd et al., 1986b). Based on the calculations, the average liquid side diffusion coefficient has a value of 2.16×10^{-2} s^{-1}. The average ratio of the concentrations, accounting for mass transfer limitation, to the equilibrium concentrations is 0.91. The impact of mass transfer limitation is therefore small, but not negligible.

The concentrations of the reactants in the liquid phase of the reactor are shown below, in Table 5.5.

Since the experiments were performed in a batch reactor, it is possible that there will be some drift in the concentration of reactants such as 1-butene, the comonomer, or hydrogen, the chain transfer agent, from the initial concentrations shown in Table 5.5. However, maintain the simplicity and speed of the regression procedure described in Chapter 4 (in particular, to avoid the solution of the mass balance differential

equations during the regression calculations), it has been assumed that this concentration drift will be negligible.

Table 5.5: Liquid phase equilibrium concentrations

Run #	Concentration (mol/l)				
	C_2H_4 (eq)	C_2H_4	C_4H_8	H_2	TEA
1	0.2242	0.2075	0.0298	0.0313	$3.01x10^{-3}$
2	0.2255	0.2169	0.0182	0.0313	$3.01x10^{-3}$
3	0.222	0.2046	0.0494	0.0314	$3.01x10^{-3}$
4	0.2996	0.2733	0.0299	0.0202	$3.67x10^{-3}$
5	0.2128	0.1980	0.0287	0.0316	$3.03x10^{-3}$
6	0.2241	0.2012	0.031	0.0313	$3.00x10^{-3}$
7	0.2242	0.2063	0.0301	0.0313	$3.00x10^{-3}$
8	0.2417	0.2222	0.0302	0.0309	$3.01x10^{-3}$
9	0.2416	0.2228	0.0305	0.0309	$3.02x10^{-3}$
10	0.2995	0.2580	0.0305	0.0202	$3.02x10^{-3}$
11	0.2417	0.2203	0.0302	0.0309	$3.01x10^{-3}$
12	0.2241	0.1992	0.0307	0.0313	$3.01x10^{-3}$
13	0.2995	0.2589	0.0308	0.0202	$3.01x10^{-3}$
14	0.1494	0.1415	0.0311	0.0423	$3.01x10^{-3}$
15	0.1497	0.1410	0.0293	0.0423	$4.01x10^{-3}$
16	0.3185	0.2834	0.031	0.0199	$3.01x10^{-3}$
17	0.2256	0.2103	0.0176	0.0313	$3.00x10^{-3}$
18	0.2125	0.1993	0.0311	0.0316	$3.01x10^{-3}$
19	0.2221	0.1859	0.0482	0.0314	$3.01x10^{-3}$
20	0.2255	0.2000	0.0188	0.0313	$3.01x10^{-3}$

5.4.3 Chain length distributions: MFI and GPC

The polymer samples were analysed by size exclusion chromatography (at both the University of Waterloo, and the University of Stellenbosch), to get full chain length distributions, and by melt flow index (ASTM:D1238, 2010), which is used industrially to indicate polymer grade. The data from these analyses is shown in Table 5.6.

Table 5.6: Chain length distribution data

Run #	MFI (g polymer/10 min)		University of Waterloo (g/mol)		University of Stellenbosch (g/mol)	
	2.16kg	5kg	M_n	M_w	M_n	M_w
1	1.17	3.90	-	-	37678	269028
2	-	-	-	-	74205	441827
3	1.38	4.39	-	-	38809	265864
4	-	-	-	-	87169	684598
5	1.21	4.08	17132	85603	39800	263470
6	1.34	4.45	18225	101570	48287	273247
7	1.54	4.80	16514	99065	37988	234585
8	1.02	3.41	18284	111737	40937	264781
9	1.08	-	14364	105813	38429	258205
10	0.06	-	-	-	77359	575528
11	0.83	2.94	17349	106120	36486	316732
12	-	7.07	14809	89548	35957	252557
13	0.20	0.70	23058	153517	66929	415465
14	14.08	46.03	11137	55120	11191	93231
15	-	54.73	10835	47997	22358	122168
16	-	0.08	-	-	94617	620421
17	0.48	1.82	-	-	44454	352882
18	1.81	5.55	-	-	38088	246439
19	1.78	5.74	-	-	38012	252381
20	1.22	4.13	-	-	41675	306330

It has been suggested by a number of authors (Bremner et al., 1990, McAuley et al., 1990) that the MFI and weight-average molecular weight of linear polyolefins can be related using an equation of the form shown in equation 5.1.

$$M_w^k = A\frac{1}{MFI} \qquad 5.1$$

In equation 5.1, A is a constant which can be obtained by fitting data to the equation, and k is expected to have a value of between 3.4 and 4.6 (Bremner et al., 1990, McAuley et al., 1990, Huang et al., 1997, Seavey et al., 2003, Alizadeh et al., 2004).

Figure 5.8 and Figure 5.9 show plots of the average molecular weights against the inverse of the MFI (on a logarithmic scale). The results of GPC analyses from the University of Waterloo (UW) and the University of Stellenbosch (US) are compared with the data from the article by Bremner et al. (1990).

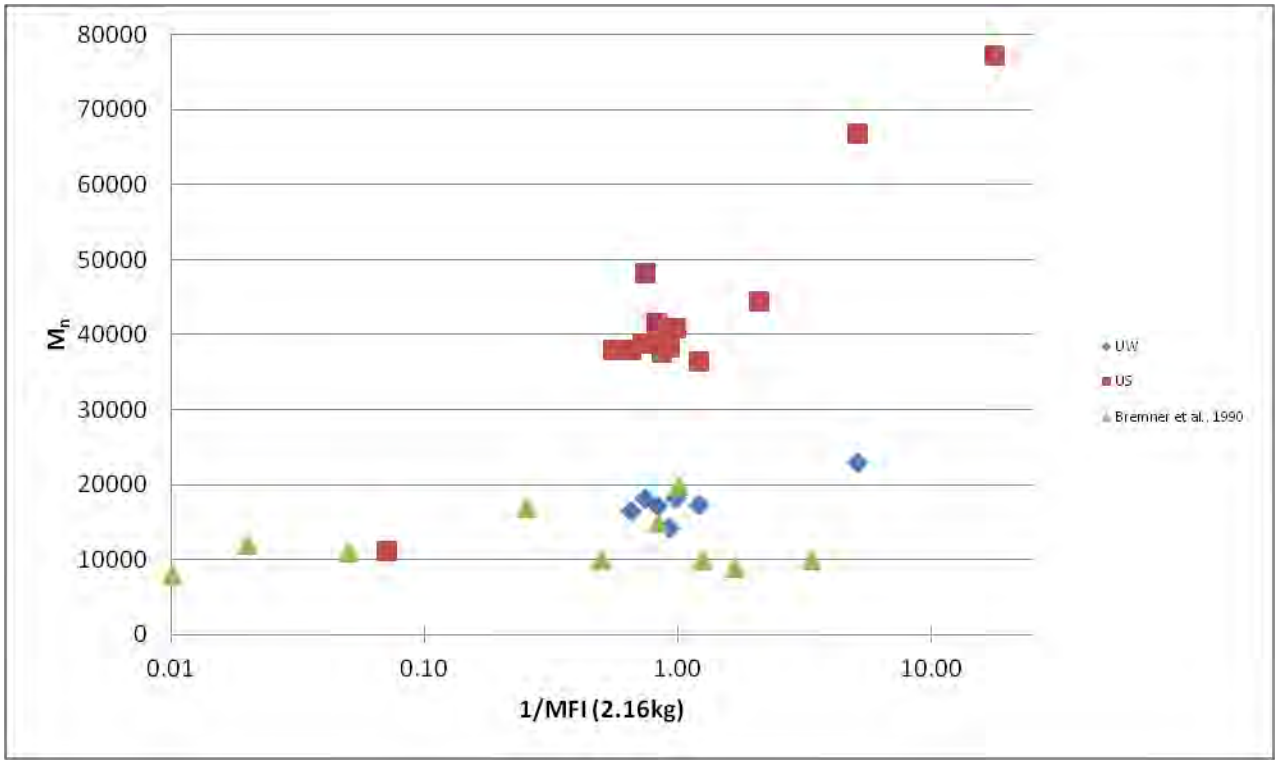

Figure 5.8: Plot of number-average molecular weight against Melt Flow Index

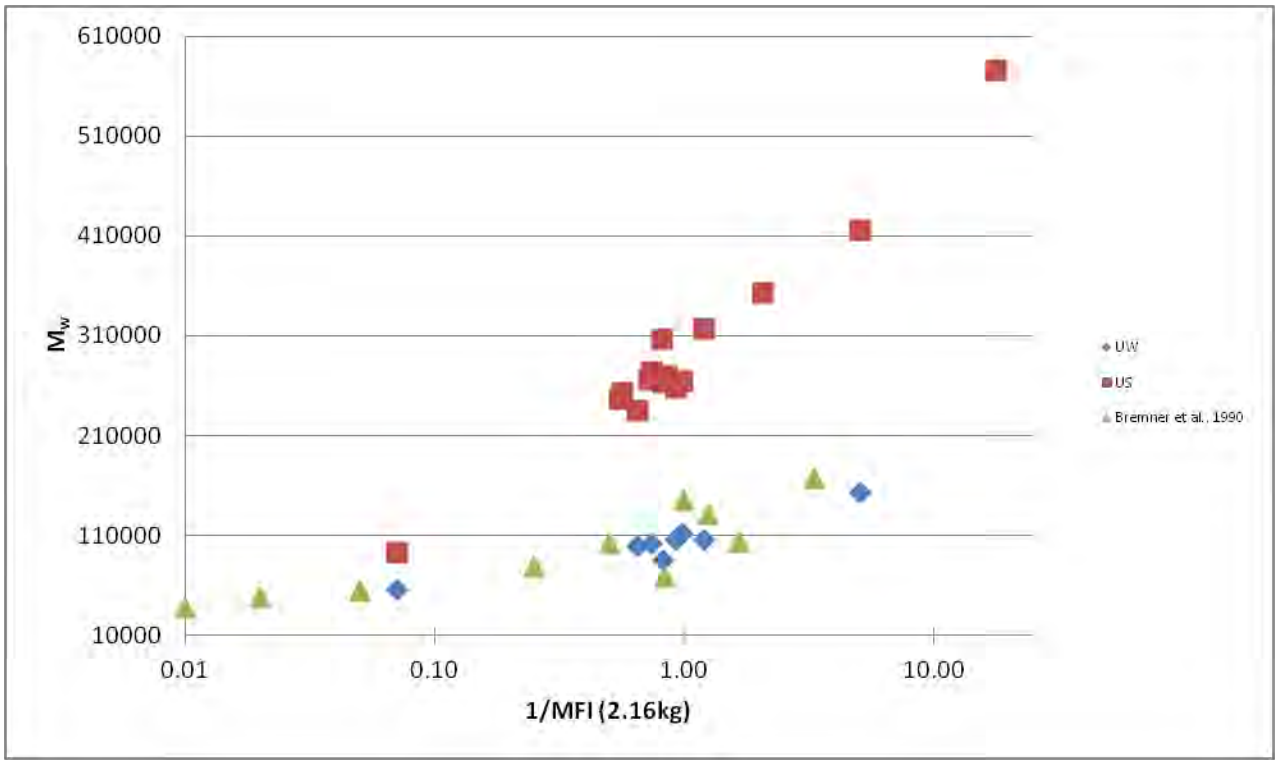

Figure 5.9: Plot of weight-average molecular weight against Melt Flow Index

The GPC results from Waterloo and Stellenbosch differ significantly, with the mean chain lengths determined in the analysis at the University of Stellenbosch being between 2 and 3 times larger than the values from the University of Waterloo. The trend of increasing M_w and M_n with increasing inverse MFI is clear, but to different extents for each data set.

Round-robin studies performed by various groups have shown that the results of GPC analysis (and other liquid chromatography methods) can differ significantly from institution to institution and operator to operator, because of differences in preparation methods, calibration standards and equipment (D'Agnillo et al., 2002, Podzimek, 2004).

Since there is relatively good agreement between the data from Waterloo and the data from Bremner et al. (1990), it was decided to assume that the Waterloo data could be used as reference data, to which the Stellenbosch data could be "fitted". The trends are similar, but the values are different between the two data sets, suggesting that the discrepancy is due to calibration or sample preparation, rather than a fundamental difference in the results.

The mean chain lengths from the Stellenbosch data were modified using a linear multiplier, in order to bring them into greater agreement with the Waterloo data. It was found that the best fit of the two data sets was found when multiplying the Stellenbosch weight-average molecular weight by a factor of 0.376, and the number-average molecular weight by a factor of 0.404. The results of these fits are shown in Figure 5.10 and Figure 5.11, and Table 5.7.

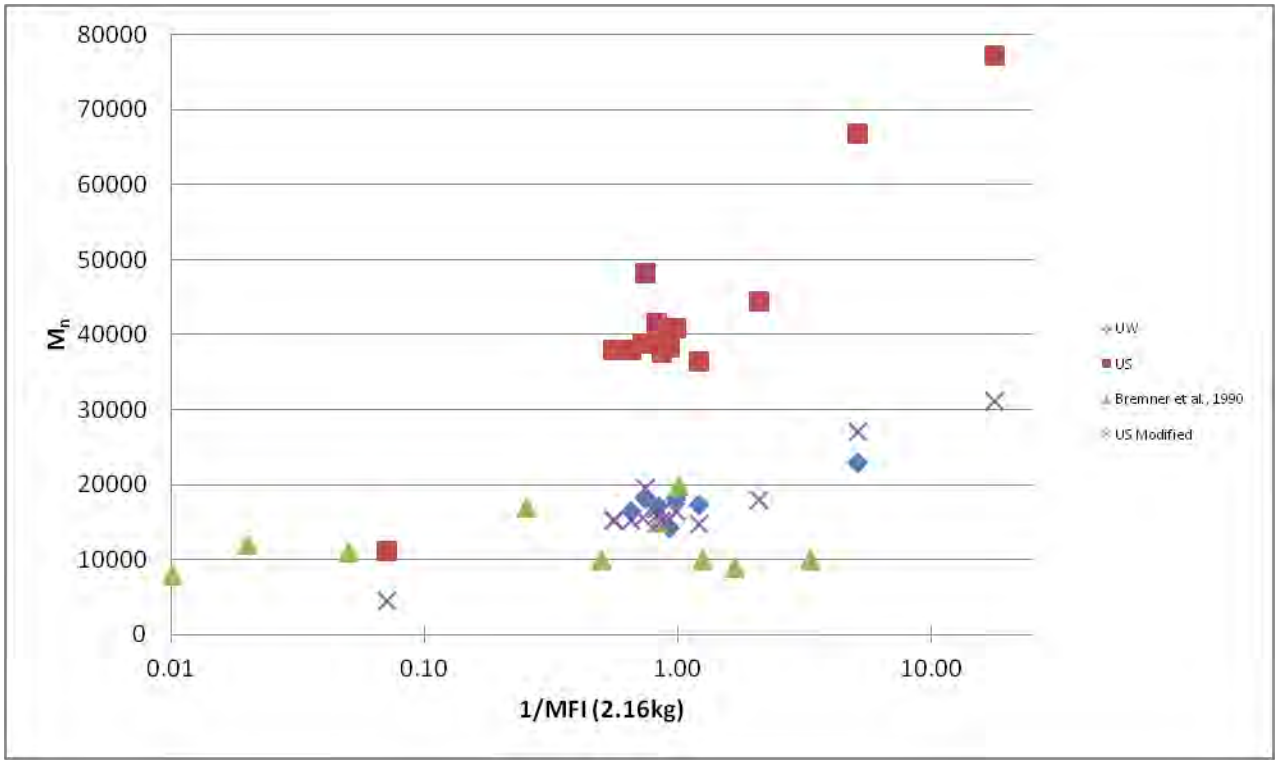

Figure 5.10: Plot of number average molecular weight against Melt Flow Index

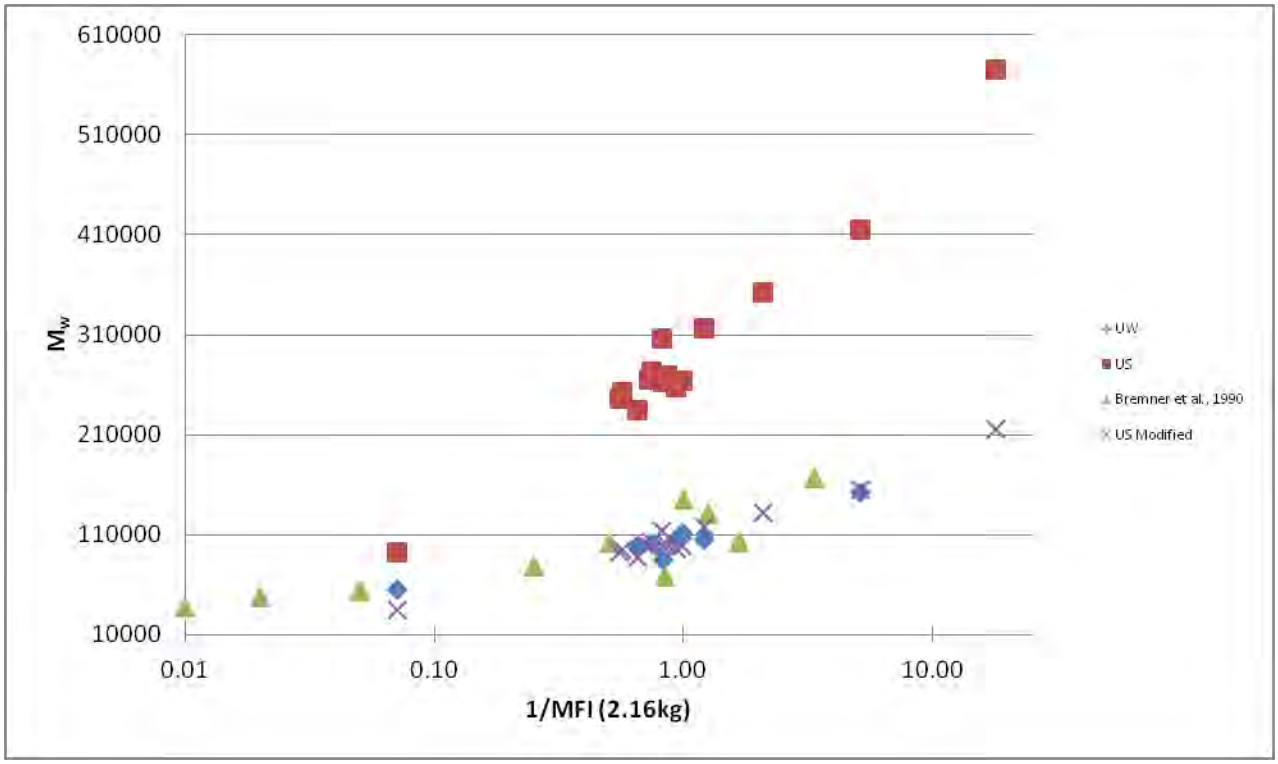

Figure 5.11: Plot of weight average molecular weight against Melt Flow Index

The modified University of Stellenbosch data is shown in Table 5.7.

Table 5.7: Summary of modified University of Stellenboch chain length data

Run #	University of Stellenbosch (g/mol)		Modified University of Stellenbosch (g/mol)	
	M_n	M_w	M_n	M_w
1	37678	269028	15232	101033
2	74205	441827	29998	165928
3	38809	265864	15689	99845
4	87169	684598	35239	257100
5	39800	263470	16090	98946
6	48287	273247	19521	102618
7	37988	234585	15357	88098
8	40937	264781	16549	99438
9	38429	258205	15536	96969
10	77359	575528	31274	216139
11	36486	316732	14750	118948
12	35957	252557	14536	94847
13	66929	415465	27057	156027
14	11191	93231	4524	35013
15	22358	122168	9039	45880
16	94617	620421	38250	232998
17	44454	352882	17971	132524
18	38088	246439	15398	92550
19	38012	252381	15367	94781
20	41675	306330	16848	115042

5.4.4 Comonomer content

Nuclear Magnetic Resonance

The methods of de Pooter et al. (1991) were used for the analysis of NMR spectra to determine the comonomer content of the polymer. The full spectra are shown in Section 20.2 in the Appendix; Table 5.8 shows the integrated values of the peaks for the ranges used in the analysis, and the molar percentage of 1-butene incorporated in the polyethylene chain.

Table 5.8: Integrated NMR peak values for comonomer content analysis

	Region (ppm)						C_4H_8
Run #	**41.5-38.5**	**39.4**	**37.8-36.8**	**36-33.2**	**33.2-25.5**	**25.2-24.0**	**(mol%)**
6	0.191	0	0	0.355	98.815	0	0.371
7	0.178	0	0	0.355	99.441	0	0.356
10	0.165	0	0	0.319	99.416	0	0.326
12	0.235	0	0	0.464	98.927	0	0.470
13	0.173	0	0	0.330	99.087	0	0.340
14	0.435	0	0	0.597	90.036	0	0.808
15	0.284	0	0	0.547	96.356	0.152	0.574
17	0.179	0	0	0.251	98.968	0	0.307
19	0.300	0	0	0.623	97.813	0	0.622

Apart from the average 1-butene content of the co-polymer, the NMR data also indicates the presence or absence of "blocks" of comonomer within the polymer backbone. Blocking is indicated by peaks in the NMR spectrum at ~39.4 and ~37.2 ppm (de Pooter et al., 1991).

Neither of these peaks is present in the data, and so it is concluded that only isolated 1-butene is found within the ethylene backbone. This confirms the assumption (made in the development of the co-polymerisation rate constant regression method) that the rate of addition of 1-butene to chain ending in 1-butene ($k_{p,22}$) is negligible.

Crystallisation Elution Fractionation analysis

The results of the analysis of the polymer samples by CEF are shown in Section 20.3 in the Appendix. The mean crystallisation temperature for each sample is shown in Table 5.9.

Table 5.9: Mean crystallisation temperature data from CEF analysis

	CEF
Run #	**$T_{crys,mean}$ (deg C)**
1	93.41
2	95.73
3	92.31
4	96.36
5	92.77
6	93.74
7	93.89
8	93.66
9	92.91
10	-
11	93.72
12	92.49
13	95.39
14	89.30
15	89.85
16	96.60
17	95.25
18	93.53
19	91.80
20	94.47

Since the full CEF profile indicates the distribution of comonomer content in a polymer sample, the mean crystallisation temperature can be related to the average comonomer content. A comparison of the results of the NMR analysis with the mean crystallisation temperatures reveals an inverse linear relationship (Figure 5.12). Equation 5.2 represents this correlation.

$$\text{mol\% } C_4H_8 = 7.003 - 0.0703\, T_{crys,mean} \qquad 5.2$$

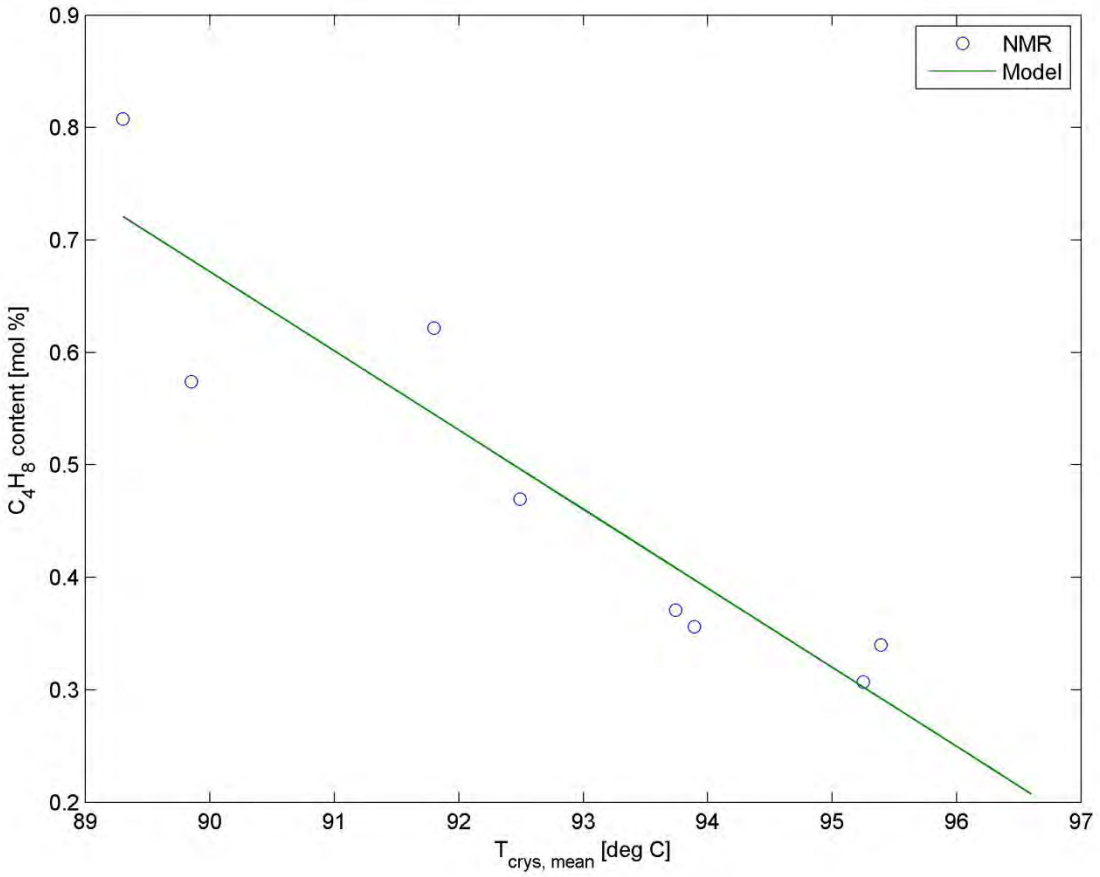

Figure 5.12: Comparison of mean crystallisation temperature with comonomer content (R^2 = 0.853)

5.4.5 Particle size distribution (PSD)

While the full PSD of the catalyst cannot be published for intellectual property reasons, more than 90% of the catalyst particles are smaller than 30µm, which allows for comparison with the final polymer particle sizes that are described below.

Malvern PSD analysis

The full particle size distribution curves for the polymer produced in the laboratory reactor can be found in Section 20.4 in the Appendix. The mean particle diameters of the polymer produced in the experiments are shown in Table 5.10.

Table 5.10: Mean particle size

Run #	D_{mean} [µm]
1	300.23
2	226.71
3	311.83
4	352.39
5	287.75
6	302.26
7	291.60
8	302.38
9	208.25
10	303.01
11	295.52
12	242.97
13	353.47
14	240.49
15	219.16
16	376.81
17	273.01
18	286.24
19	288.03
20	297.16

Scanning Electron Microscopy (SEM) analysis

Two polymer samples were inspected by SEM: run #8, to represent polymer after a long period in the reactor, and run #9 to represent polymer that has undergone a lesser degree of polymerisation. These two runs were performed at the same reaction conditions (see Table 5.1) so that direct comparison could be made. Further images of these polymer particle samples are shown in Section 20.5 in the Appendix.

Comparison of Figure 5.13 and Figure 5.14 (15 minutes of polymerisation) and Figure 5.15 and Figure 5.16 (60 minutes of polymerisation) reveals that even early on in the polymerisation process, there are large pores and spaces between the active sites, which would allow almost unhindered diffusion of reactants within the growing particles, as has been described in the literature (McKenna et al., 1999, Wu et al., 1999, Fisch et al., 2008).

Figure 5.14 shows some features of the formation of the pores as the particle expands; the lower left of the image shows a portion of the surface of the particle with no pores. However, this is a very small fraction of the total surface area of the particle, and is unlikely to cause significant mass transfer limitations, even at an early stage of polymerisation.

In addition, the significant growth of particles during polymerisation can be seen by comparing Figure 5.13 and Figure 5.15, which are at the same magnification; this observation is supported by the PSD analysis in Table 5.10, which shows the mean particle size increases from ~200µm in Run #9 to ~300µm in Run #8.

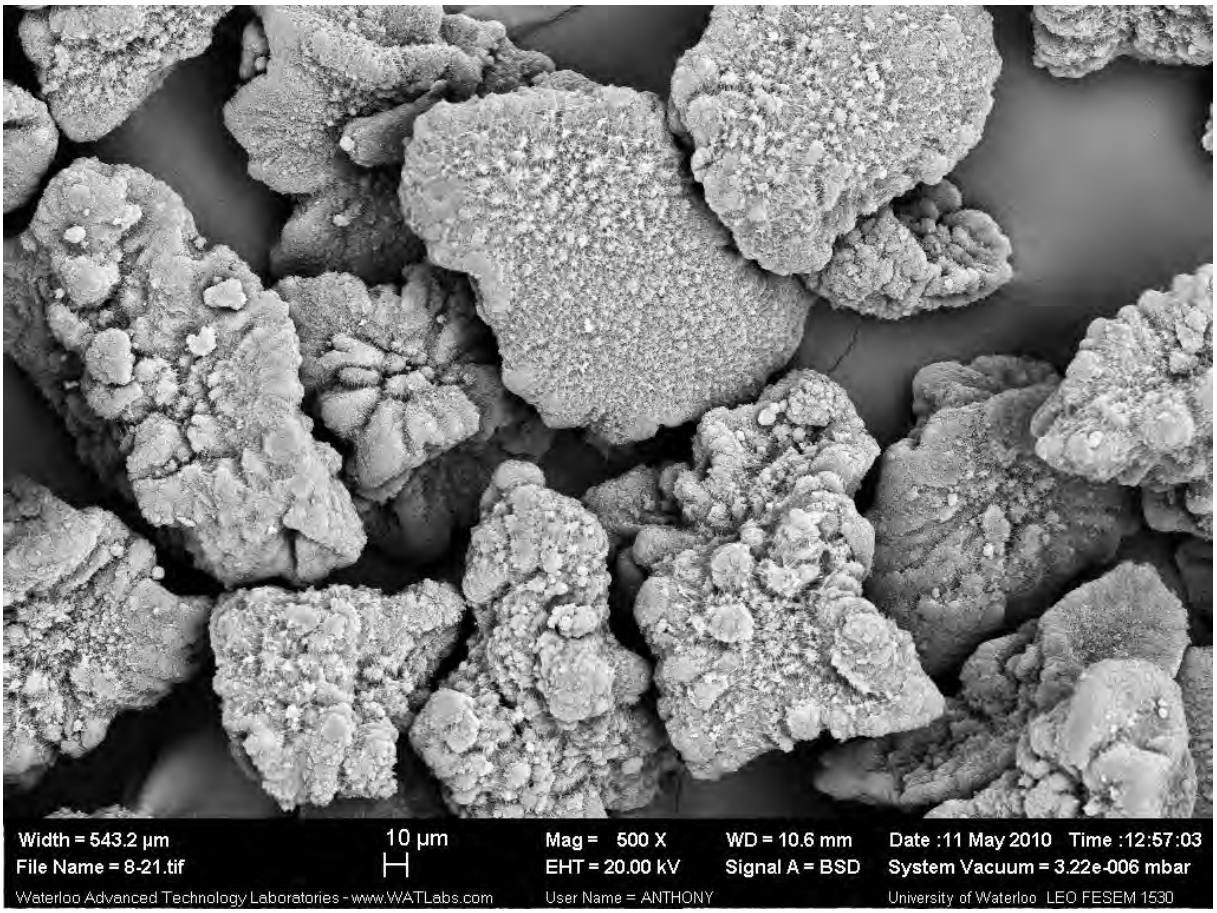

Figure 5.13: SEM of polymer from run #9 (15 min reaction time)

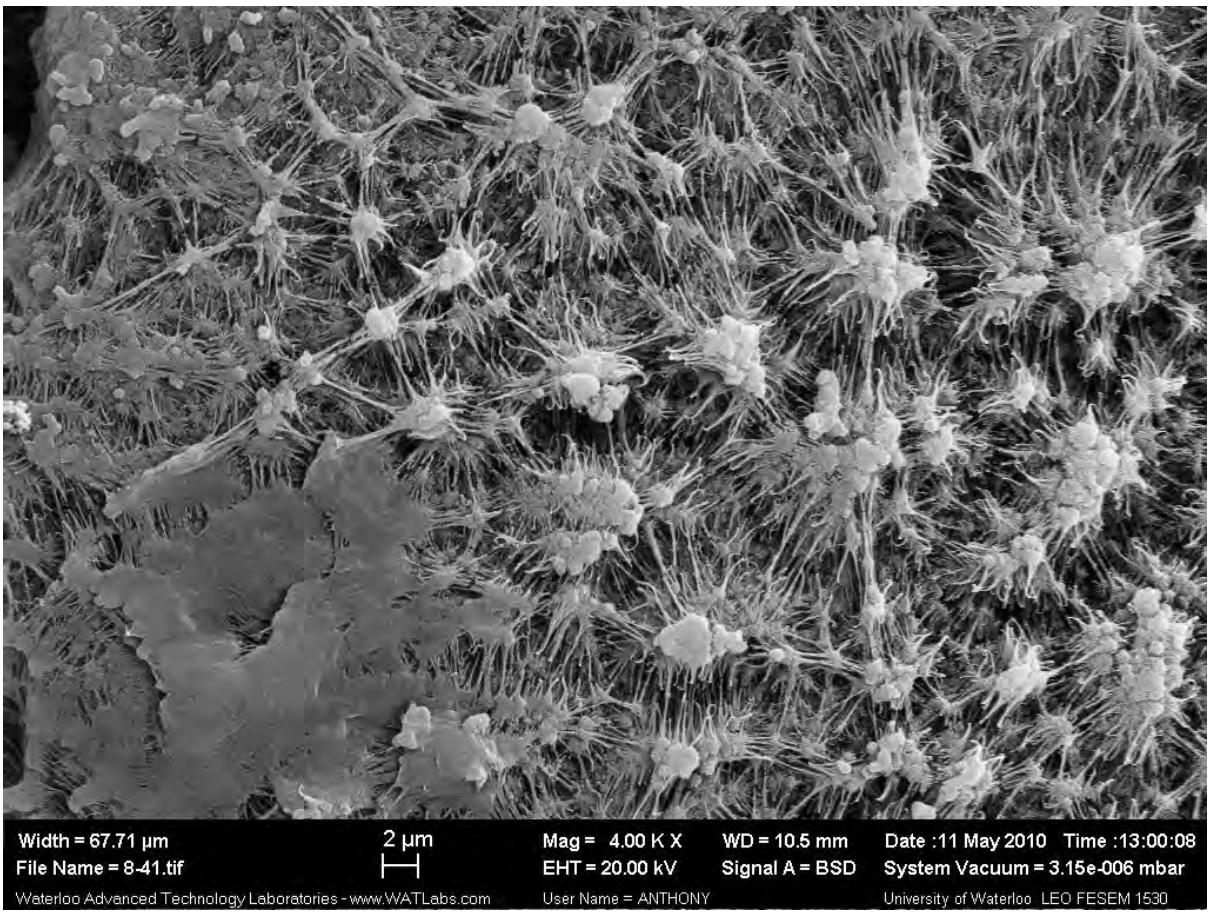

Figure 5.14: SEM of polymer from run #9 (15 min reaction time), close-up

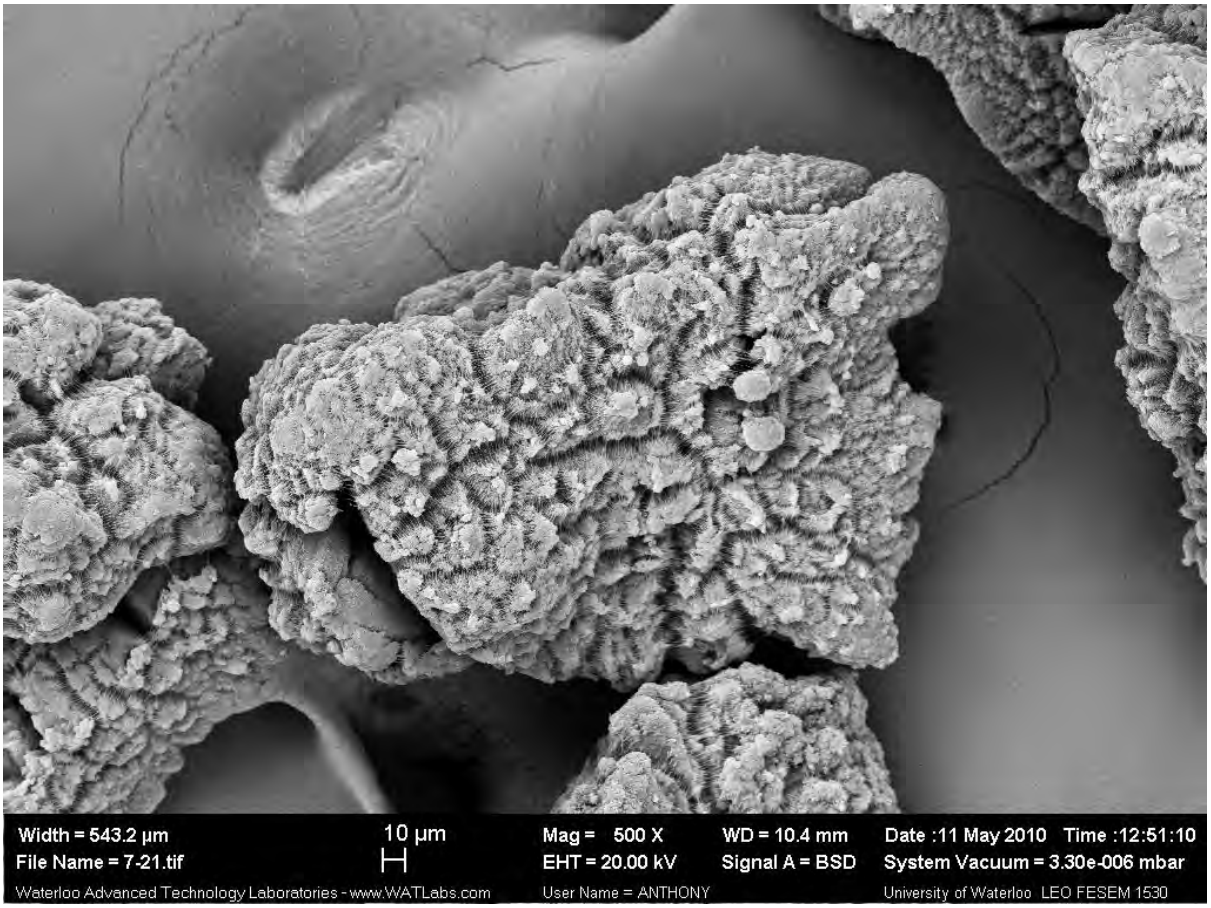

Figure 5.15: SEM of polymer from run #8 (60 min reaction time)

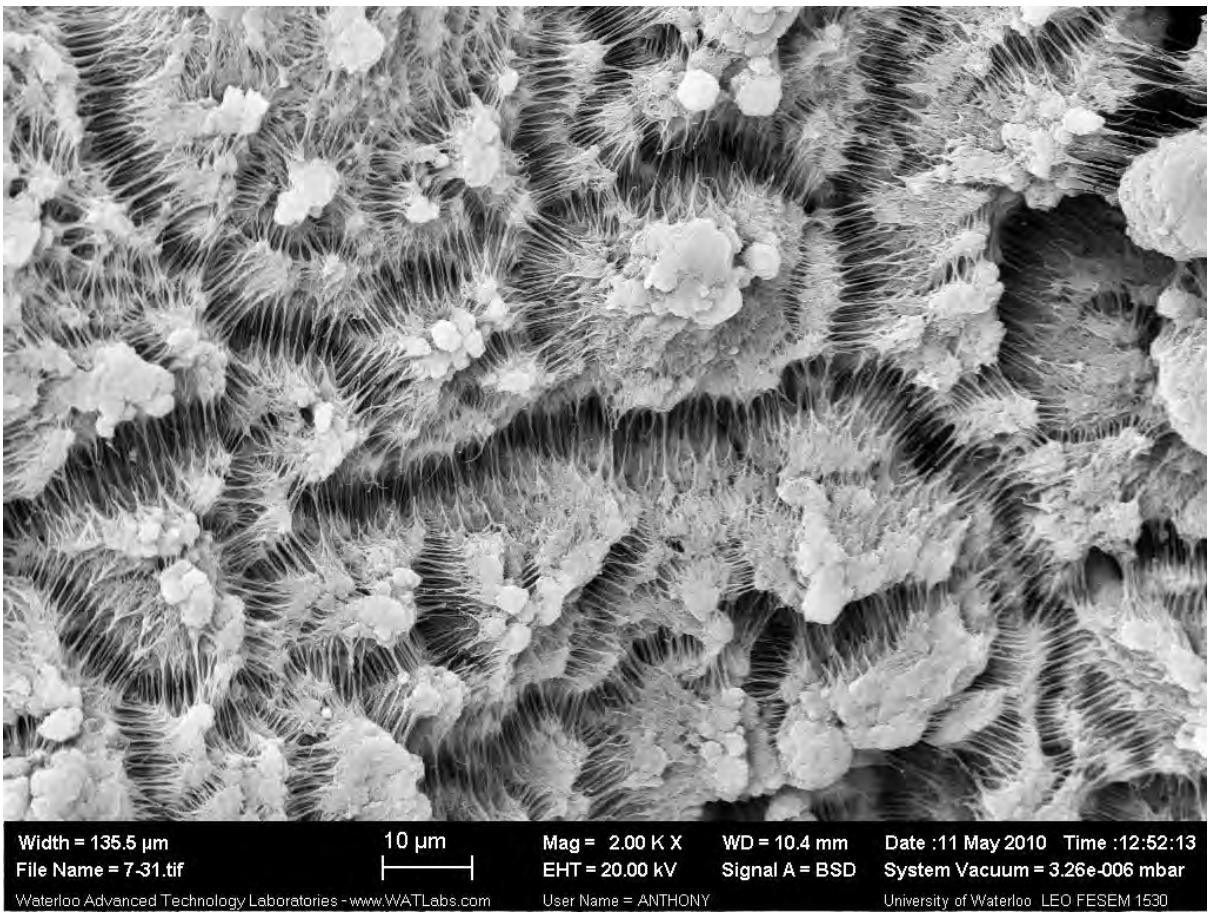

Figure 5.16: SEM of polymer from run #8 (60 min reaction time), close-up

CHAPTER 6. ANALYSIS OF EXPERIMENTAL DATA

The extraction of kinetic rate constants from experimental data is not a simple task, given the number of parameters and the nonlinearity of the relationships between parameters and data.

The regression procedure developed in Chapter 4 provides generalised steps for the extraction of these parameters from a set of experimental data, including polymerisation rate curves, comonomer fractions, and molecular weight distributions.

The regression procedure was specifically formulated to generate meaningful initial guesses for each non-linear regression step, to take advantage of linearity where it is present, and to fit parameters to portions of data where the most sensitivity is present.

The data required to perform the regression procedure is described in Chapter 5; the following pages describe the extraction of the following sets of parameters from the data presented above:

- Parameters defining polymerisation rate and catalyst activity;
- Parameters defining the rate of comonomer incorporation;
- Parameters defining the rate of chain termination;
- Parameters relating molecular weight data to Melt Flow Index data.

The pages below describe the first rigorous application of the pseudo-sites concept and kinetic scheme proposed by Rawatlal (2004) to a comprehensive set of kinetic data, and is the first test of the kinetic scheme.

Minimisation of the various objective functions was achieved with the “fminsearch” multidimensional unconstrained nonlinear minimisation scheme, based on the Nelder-Mead method (Nelder & Mead, 1965), using Matlab R2011b, running on an Intel® Core™2 Quad CPU Q9300 @2.5GHz, with 4GB of RAM.

Note that nomenclature is tabulated in Chapter 19 in the Appendix.

6.1 Polymerisation rate and activity constants

The activity of the Ziegler-Natta catalyst has been modelled for a range of experimental conditions, using the kinetic scheme presented in Table 4.1. The experimental conditions reflect the conditions in an industrial slurry phase polymerisation reactor, and are shown in Table 5.1. The liquid phase concentrations are in Table 5.5. The activity profiles are shown in Chapter 20 in the Appendix, on page 294.

The regression scheme makes use of ten independent parameters: nine site transformation rate constants, which determine the rates at which each site type is formed and decays, and one polymerisation rate constant, describing the intrinsic rate at which polymerisation occurs. The site transformation rate constants are collected into lumped site transformation rate parameters.

The first step of the regression process is to find initial guesses for the three lumped site transformation rate parameters and the polymerisation rate constant.

6.1.1 Initial guesses

Initial guess values for $k_{p,e}$ (from equation 4.5), $\beta_{st,e}^{4+,3+}$ (from equation 4.7) and $\beta_{st,e}^{3+,2+}$ and $\beta_{st,e}^{2+,3+}$ (satisfying equations 4.8 and 4.9) are determined from the equations reproduced below, as described in Chapter 4.

$$k_{p,e} = \frac{m_{polymer,e}}{MM_{ethylene}[M_1]_e m_{cat,e} \tau_{rxn,e}} \qquad 4.5$$

$$\beta_{st}^{4+,3+} = \frac{d}{dt}\left(\frac{r_{M_1}}{k_p[M_1]} \right)\Bigg|_{t=0} \qquad 4.7$$

$$\frac{d}{dt}\left(P_*^{3+}\left(t^{peak}\right)\right) = -\beta_{st}^{4+,3+}\gamma \exp\left(-\beta_{st}^{4+,3+} t^{peak}\right) - \left(\beta_{st}^{3+,2+} + \beta_{st}^{2+,3+}\right)\delta \exp\left(-\left(\beta_{st}^{3+,2+} + \beta_{st}^{2+,3+}\right) t^{peak}\right) = 0 \qquad 4.8$$

$$r_{M_1}\left(t^{peak}\right) = k_p[M_1]P_*^{3+}\left(t^{peak}\right) \qquad 4.9$$

The initial guesses for the four parameters for each experimental run are given in Table 6.1.

Table 6.1: Initial guesses for kinetic parameters

Run #	$\beta_{st}^{4+,3+}$	$\beta_{st}^{3+,2+}$	$\beta_{st}^{2+,3+}$	k_p
	[min^{-1}]	[min^{-1}]	[min^{-1}]	[$L.min^{-1}.g\text{-}cat^{-1}$]
1	0.2639	$2.23x10^{-2}$	$7.46x10^{-18}$	4.36
2	0.1807	$1.62x10^{-2}$	$4.81x10^{-19}$	2.13
3	0.3206	$3.41x10^{-2}$	$1.73x10^{-18}$	4.56
4	0.1797	$1.54x10^{-2}$	$7.33x10^{-19}$	4.99
5	0.3190	$1.32x10^{-3}$	$6.93x10^{-18}$	4.00
6	0.2070	$2.05x10^{-2}$	$1.18x10^{-17}$	5.78
7	0.2438	$1.28x10^{-2}$	$5.44x10^{-19}$	4.40
8	0.1437	$6.95x10^{-3}$	$9.41x10^{-20}$	4.54
9	0.1437	$2.39x10^{-2}$	$5.45x10^{-19}$	4.49
10	0.1523	$3.51x10^{-2}$	$6.51x10^{-18}$	8.34
11	0.1526	$1.86x10^{-2}$	$3.24x10^{-17}$	5.12
12	0.1574	$2.01x10^{-2}$	$6.05x10^{-18}$	6.32
13	0.1855	$2.61x10^{-2}$	$1.07x10^{-17}$	8.26
14	0.6935	$2.17x10^{-3}$	$3.06x10^{-17}$	2.85
15	0.5980	$5.08x10^{-3}$	$1.56x10^{-20}$	3.10
16	0.2557	$1.70x10^{-2}$	$2.94x10^{-19}$	6.69
17	0.1740	$1.34x10^{-2}$	$1.16x10^{-18}$	3.84
18	0.5947	$9.24x10^{-3}$	$1.20x10^{-17}$	3.51
19	0.2156	$7.05x10^{-2}$	$2.22x10^{-18}$	10.12
20	0.1385	$1.84x10^{-2}$	$7.16x10^{-18}$	6.55

6.1.2 Non-linear least-squares regression – lumped parameters to rate curves

After obtaining initial guesses for each of the kinetic parameters, the first step in the non-linear regression procedure is to fit all four parameters to each activity curve individually. This is achieved by minimising equation 4.10, reproduced below.

$$Obj_e = \sum_{te} \left\{ r_{M_1,e}(t_{te}) - k_{p,e}[M_1] P_*^{3+}\left(t_{te}, \beta_{st,e}^{4+,3+}, \beta_{st,e}^{3+,2+}, \beta_{st,e}^{2+,3+}\right) \right\}^2 \qquad 4.10$$

As described in Chapter 4 (see Figure 4.2), the lumped parameters are most sensitive in different regions of the activity curves; thus, $\beta_{st}^{4+,3+}$ is fitted to the initial period of each activity curve when activity increases rapidly, and $\beta_{st}^{3+,2+}$ and $\beta_{st}^{2+,3+}$ are fitted to the later period of the activity curves, when activity is decreasing.

The results of this regression are given in Table 6.2. Comparisons between the model predictions and experimental catalyst activity are shown in the Appendix, Chapter 20 on page 350.

Table 6.2: Kinetic parameters from first non-linear regression

Run #	$\beta_{st}^{4+,3+}$	$\beta_{st}^{3+,2+}$	$\beta_{st}^{2+,3+}$	k_p
	[min^{-1}]	[min^{-1}]	[min^{-1}]	[$L.min^{-1}.g\text{-}cat^{-1}$]
1	0.2009	$2.56x10^{-2}$	$5.70x10^{-14}$	9.46
2	0.1023	$1.02x10^{-1}$	$6.89x10^{-8}$	7.30
3	0.2047	$6.51x10^{-2}$	$7.14x10^{-3}$	12.27
4	0.0814	$8.14x10^{-2}$	$3.59x10^{-23}$	21.30
5	0.0839	$8.39x10^{-2}$	$1.22x10^{-20}$	26.12
6	0.1450	$2.15x10^{-2}$	$7.71x10^{-10}$	11.66
7	0.1706	$2.23x10^{-2}$	$9.52x10^{-15}$	8.83
8	0.0484	$4.84x10^{-2}$	$2.04x10^{-76}$	17.81
9	0.0491	$4.90x10^{-2}$	$3.88x10^{-32}$	17.49
10	0.0701	$6.38x10^{-2}$	$6.23x10^{-3}$	25.85
11	0.0741	$6.05x10^{-2}$	$1.36x10^{-2}$	15.79
12	0.0525	$5.25x10^{-2}$	$2.13x10^{-46}$	24.30
13	0.1541	$2.40x10^{-2}$	$5.02x10^{-18}$	15.47
14	0.3152	$3.36x10^{-2}$	$5.71x10^{-17}$	8.23
15	0.2186	$6.65x10^{-2}$	$1.15x10^{-2}$	9.79
16	0.1902	$2.64x10^{-2}$	$3.53x10^{-15}$	14.59
17	0.0745	$7.45x10^{-2}$	$5.18x10^{-10}$	16.92
18	0.3342	$3.43x10^{-2}$	$4.11x10^{-3}$	8.69
19	0.2298	$5.18x10^{-2}$	$5.64x10^{-15}$	17.95
20	0.0548	$5.48x10^{-2}$	$1.46x10^{-8}$	22.75

6.1.3 Non-linear least-squares regression – consolidating propagation rates

The second step in the non-linear regression is to fit a single value for the polymerisation rate k_p, using equation 4.11 (reproduced below), and then re-evaluate the values for the lumped site transformation parameters and polymerisation rate until they converge, as described in Chapter 4.

$$Obj = \sum_{e}\sum_{te}\left\{r_{M_1,e}\left(t_{te,e}\right) - k_p\left[M_{1,e}\right]P_*^{3+}\left(t_{te,e}, \beta_{st,e}^{4+,3+}, \beta_{st,e}^{3+,2+}, \beta_{st,e}^{2+,3+}\right)\right\}^2 \qquad 4.11$$

The parameter values from this step are shown in Table 6.3. Comparisons between the model predictions and experimental catalyst activity are shown in the Appendix, Chapter 20 on page 363.

Table 6.3: Kinetic parameters from non-linear regression; single k_p value

k_p	16.93	[L.min^{-1}.g-cat^{-1}]	
Run #	$\beta_{st}^{4+,3+}$	$\beta_{st}^{3+,2+}$	$\beta_{st}^{2+,3+}$
	[min^{-1}]	[min^{-1}]	[min^{-1}]
1	0.0985	7.94x10^{-2}	1.37x10^{-2}
2	0.0433	1.95x10^{-1}	0
3	0.1374	1.03x10^{-1}	1.01x10^{-2}
4	0.0919	6.30x10^{-2}	0
5	0.1217	5.24x10^{-2}	0
6	0.0911	4.98x10^{-2}	1.11x10^{-2}
7	0.0791	7.65x10^{-2}	1.34x10^{-2}
8	0.0440	4.44x10^{-2}	0
9	0.0502	4.76x10^{-2}	0
10	0.1063	3.32x10^{-2}	0
11	0.0685	6.62x10^{-2}	1.34x10^{-2}
12	0.0746	3.24x10^{-2}	0
13	0.1308	2.89x10^{-2}	1.83x10^{-26}
14	0.1137	1.12x10^{-1}	1.16x10^{-2}
15	0.1179	1.40x10^{-1}	1.57x10^{-2}
16	0.1537	3.98x10^{-2}	7.18x10^{-3}
17	0.0649	7.20x10^{-2}	0
18	0.1262	1.10x10^{-1}	1.61x10^{-2}
19	0.2438	4.41x10^{-2}	0
20	0.0697	3.81x10^{-2}	0

6.1.4 Multi-linear regression – rate constants to lumped parameters

Table 6.4 contains the values for $k_{st,i}^{q,r}$ fitted to the lumped parameters using multilinear regression. These values are the best fit of the site transformation rate constants to the lumped site transformation parameters, $\beta_{st}^{q,r}$.

Table 6.4: Values for $k_{st,i}^{q,r}$ fitted to lumped parameters using multilinear regression

	sp	**A**	**H_2**
	[min^{-1}]	[min^{-1}.{mol-TEA.L^{-1}}$^{-1}$]	[min^{-1}.{mol-H_2.L^{-1}}$^{-0.5}$]
$k_{st,i}^{4+,3+}$	$1.09x10^{-1}$	16.8	**$-3.69x10^{-1}$**
$k_{st,i}^{3+,2+}$	**-0.221**	32.4	1.08
$k_{st,i}^{2+,3+}$	**$-5.32x10^{-2}$**	10.4	0.157

Some of the values obtained from multilinear regression were negative (values shown in bold). It is not physically reasonable to have negative values for these kinetic constants, and so they were set to zero for use as initial guesses in the nonlinear fitting of the site transformation rate constants.

6.1.5 Non-linear least-squares regression – rate constants to rate curves

The final step in the regression is to fit the site transformation rate constants to the full set of polymerisation activity curves, using the values from the multilinear regression as initial guesses. The value for propagation rate, $k_{p,11}$, is the same as that determined in the second step of the regression, when the fits of the propagation rate and lumped site transformation parameters were converged to a set of consistent values.

The complete set of kinetic parameters used to describe the experimental activity data is given in Table 6.5. These values are the final propagation rate constant (fitted with the lumped parameters to the activity curves) and the site transformation rate constants (fitted to the activity curves). The comparisons between experimental and modelled activities are shown in Figure 6.1.

Table 6.5: Final kinetic parameters

$k_{p,11}$	16.93		[L.min^{-1}.g-cat^{-1}]
***i* =**	**sp**	**A**	**H_2**
	[min^{-1}]	[min^{-1}.{mol-TEA.L^{-1}}$^{-1}$]	[min^{-1}.{mol-H_2.L^{-1}}$^{-0.5}$]
$k_{st,i}^{4+,3+}$	0	**31.7**	0
$k_{st,i}^{3+,2+}$	0	0	**0.325**
$k_{st,i}^{2+,3+}$	0	**0.924**	0

The values in Table 6.5 show that there are only three site transformation rate constants which have an effect on the activity of the catalyst. During the regression process, it was found that for this catalyst the other six values are either identically zero, or so small that they will not have any effect on the model, and can be neglected. The important parameters are shown in bold text in the table.

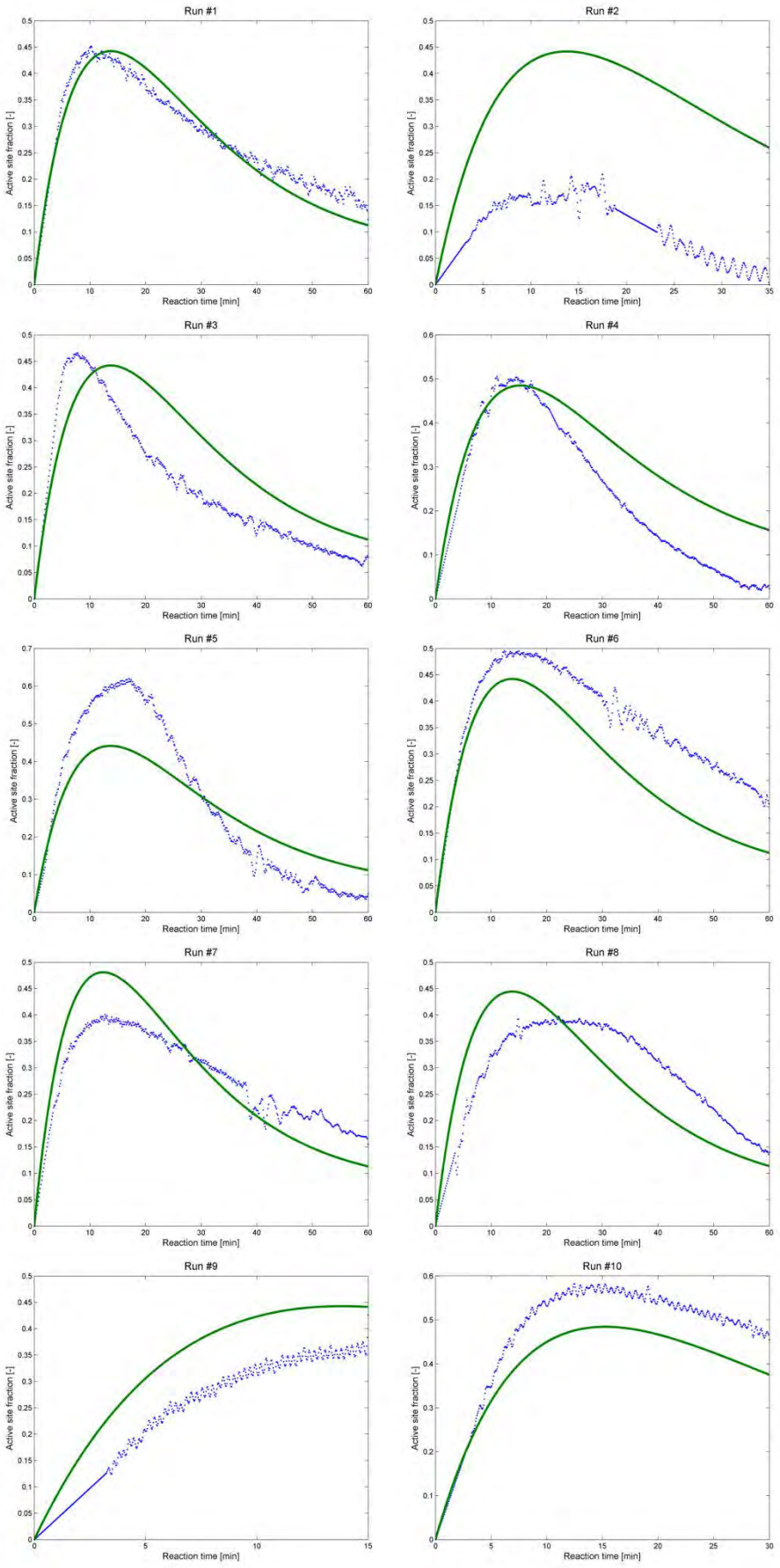

Figure 6.1: Final model fits to experimental curves (mean R^2 = 0.37)

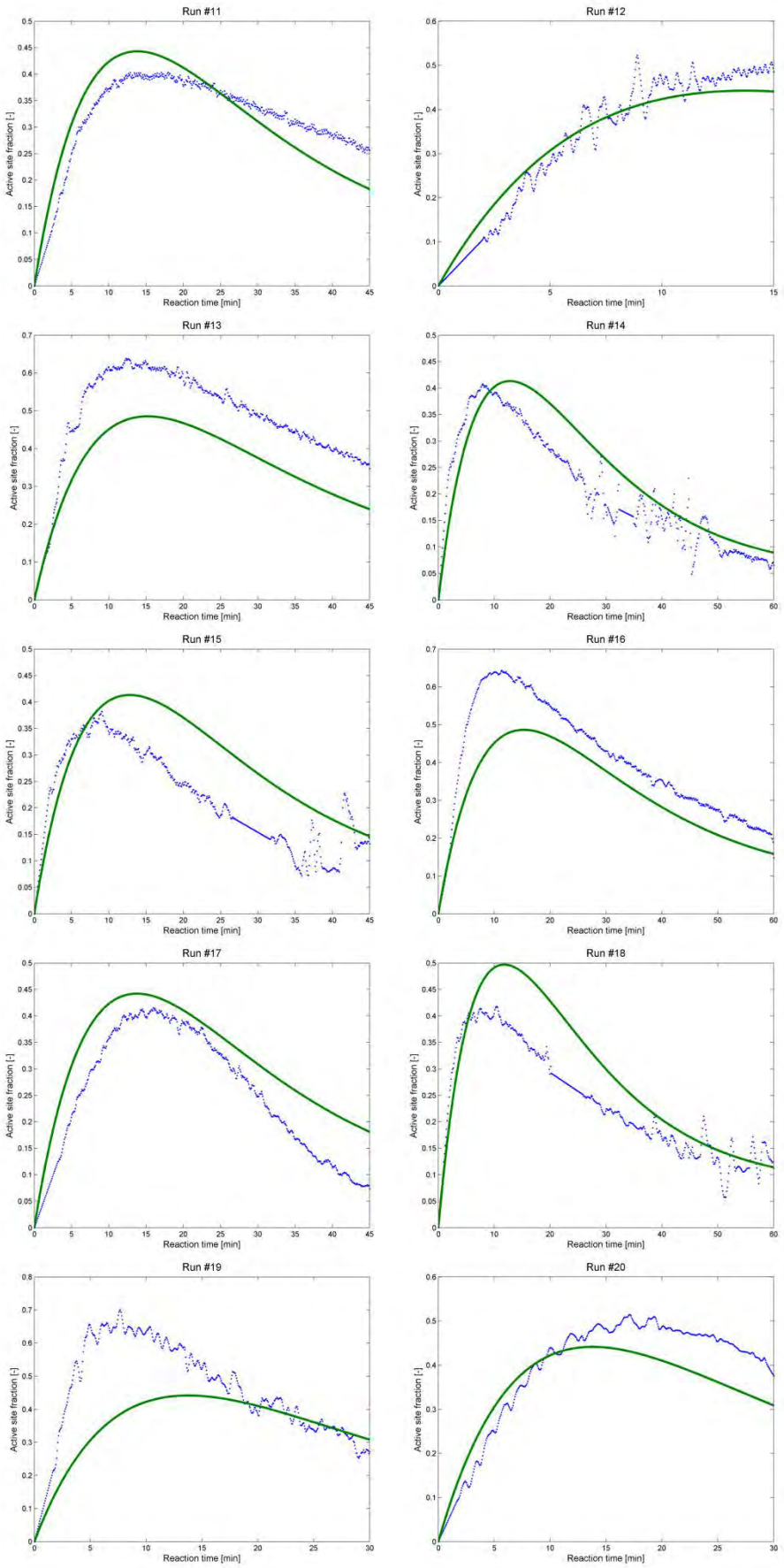

Figure 6.1 continued

Activation of the catalyst, physically the reduction of the titanium site from the 4+ to 3+ oxidation state, is sensitive only to the concentration of co-catalyst, triethyl aluminium. The co-catalyst is generally understood to be responsible for the activation of the catalyst, and so this result makes sense.

The deactivation of the catalyst is most sensitive to the concentration of hydrogen. The role of hydrogen in polymerisation is not only that of a chain transfer agent; various authors have described the effects of hydrogen on the activity of Ziegler-Natta catalysts, generally decreasing activity (Kissin et al., 1999, Czaja & Bialek, 2001, Garoff et al., 2002). In the current study, the deactivating effect of hydrogen was significant, and so the dependence of the model on the concentration of hydrogen was expected, and in line with the findings of other authors.

The reactivation of the catalyst sites, achieved by oxidation of sites from Ti^{2+} to Ti^{3+}, is only sensitive to the concentration of co-catalyst. The relatively small value for the rate of oxidation indicates that this "reactivation" reaction does not contribute significantly to the activity profile of the catalyst. It has not been removed from the scheme and regression procedure for the sake of generality; the reactivation may be more significant for other catalyst systems or reaction conditions.

The activity of the catalyst can therefore be described by four parameters: the propagation rate and three site transformation rate constants, which relate to the concentrations of co-catalyst and hydrogen.

Apart from the studies of gas-phase polymerisation of ethylene and 1-hexene with a metallocene catalyst by Kou et al (Kou et al., 2005b, Kou et al., 2005c, Kou et al., 2005a), the authors have not found any other work presenting a comprehensive model of catalyst activity and a method for the extraction of meaningful kinetic constants from the data.

While the fits to the experimental curves shown in Figure 6.1 are not perfect (mean $R^2 = 0.37$), they generally follow the trends of the data in response to reactant changes and residence time. In particular, the location in time of the peak polymerisation rate is closely matched in run numbers 1, 4-7, 10, 11, 13, 16 and 17. The rapid increase and more gradual decay in the rate of polymerisation are well-predicted for most of the experimental runs.

The fit of the model to run number 2 is significantly worse than the others; it is thought that a poison may have been present during this experimental run, as activity is much lower than in comparable experiments. This curve was excluded from the objective function when fitting the final kinetic parameters, but the comparison of the model and data is included for completeness.

In experimental runs 3, 5, 16 and 19, the experimental peak is significantly sharper and larger than the proposed model predictions. It is possible that there is a factor involved in the evolution of the site oxidation states that was not distinguished due to a lack of data in this study. A kinetic study of polymerisation rate with a wider range of conditions may reveal the influence of site transformation rate parameters that were deemed negligible in the current work. It is for this reason that the above regression methods have been proposed: to provide a generalized framework that can be applied to polymerisation rate data by other researchers in the field.

The model predictions show similar qualitative accuracy to the fits obtained by other authors, who also found difficulties in fitting the peaks when rapid changes in the initial polymerisation rate occurred (Kou et al., 2005a, Kou et al., 2005b, Kou et al., 2005c). The fits in those papers made use of two types of active site, proposed to reproduce the distributions in chain length produced by the "multi-site" catalyst.

In contrast, the current model postulates only one active site by making use of the correlation between activity and titanium oxidation state for Ziegler-Natta catalysts (Soga et al., 1982, Han-Adebekun & Ray, 1997, Han-Adebekun et al., 1997a, Fregonese et al., 2001, Ostrovskii & Kenig, 2005).

While the fit of the model to each experimental rate curve can be improved by varying parameters independently, by following the regression scheme presented above a set of meaningful values can be obtained to describe the polymerisation rate profile of a Ziegler-Natta catalyst for the production of a polyolefin.

6.1.6 Summary

The regression approach was applied to experimental data for the polymerisation rate of the catalyst in slurry phase co-polymerisation of ethylene and 1-butene on a laboratory scale, and shown to provide good fits to the data. In order to fit the model to the data, a total of four parameters were required: three site transformation rate constants, and one polymerisation rate constant.

The final site transformation kinetic parameters reveal a model for catalyst activity that is determined by co-catalyst and hydrogen concentration. The co-catalyst is responsible for the activation of the catalyst, and for the small reactivation reaction. Hydrogen was shown to be responsible for the deactivation of the catalyst.

The next step in the analysis of the experimental data is to find values for the co-polymerisation rate constants.

6.2 Co-polymerisation rate constants

The comonomer content of the polymer can be simulated for a range of experimental conditions. These simulations, and the fitting of co-polymerisation rate constants, is based on the data from NMR spectroscopy (summarised in Table 5.8, with full spectra on page 305 in the Appendix) and the liquid-phase reactant concentrations in Table 5.5.

The model predictions are also compared with the results of CEF analysis, as summarised in Table 5.9.

6.2.1 Results

Based on the NMR data in Table 5.8, which indicated a lack of blocks of 1-butene in the ethylene backbone, the assumption of a negligible rate of addition of 1-butene to chains ending in 1-butene ($k_{p,22}$) was indeed justified.

Thus, the fitting of the other two propagation rates ($k_{p,12}$ and $k_{p,21}$) could be accomplished according to the developments in Section 4.2; specifically, the minimisation of the objective function in equation 4.22, reproduced below, which compares the experimental comonomer content for a given experiment e ($f_{C_4H_8,e}$) with the model predictions.

$$Obj = \sum_e \left\{ f_{C_4H_8,e} - \xi_2\left(\underline{[M]}_e, k_{p,12}, k_{p,21}\right)\right\}^2 \qquad 4.22$$

Using the data in Table 5.8, the value for $k_{p,11}$ in Table 6.5, and equation 4.22, values for the parameters $k_{p,12}$ and $k_{p,21}$ can be fitted. The fitted values are shown in Table 6.6, and the comparison with the data in Figure 6.2.

Table 6.6: Co-polymerisation propagation rates

$k_{p,ij}$ [L.min^{-1}.g-cat^{-1}]		
	j=1	**j=2**
i=1	16.93	0.524
i=2	265.5	0

The relatively small value of the rate constant for the addition of 1-butene onto a chain ending in ethylene ($k_{p,12}$) is indicative of the low comonomer content of the polymer.

The very large value for the rate constant for the addition of ethylene to a chain with 1-butene most recently added ($k_{p,21}$) agrees with the results of NMR analysis, in which no evidence of blocks of 1-butene was seen. 1-Butene exists in the polyethylene chain only as isolated short chain branches because the addition of ethylene is much more rapid (and therefore, statistically more likely) than the addition of another 1-butene monomer unit.

This result is also consistent with the findings of other authors, who have reported an increase in polymerisation activity in the presence of a comonomer (Han-Adebekun et al., 1997a, Wester & Ystenes,

1997, Soares, 2001, Xu et al., 2015); the rate of addition of ethylene to chains ending in 1-butene is even higher than the rate of addition of ethylene to chains ending in ethylene.

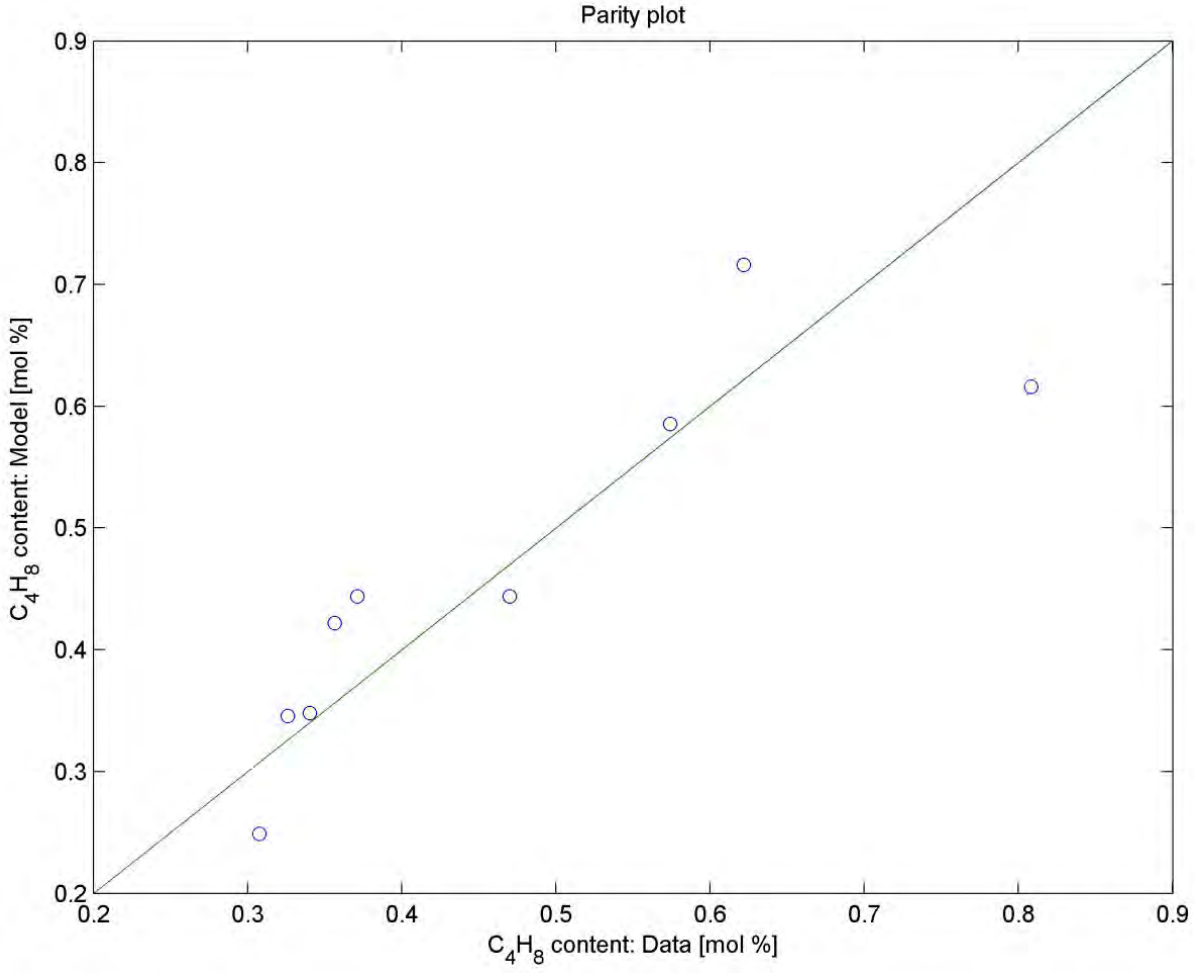

Figure 6.2: Parity plot of model fit for co-polymerisation constants (R^2 = 0.747)

The model can also be compared with the comonomer content data obtained by fitting the mean crystallisation temperature in Crystallisation Elution Fractionation (Table 5.9) to equation 5.2, reproduced below.

$$\text{mol\% } C_4H_8 = 7.003 - 0.0703 T_{crys,mean} \qquad 5.2$$

This comparison (Figure 6.3) confirms the fitted values of the co-polymerisation constants by displaying a relatively good fit to a wider range of data.

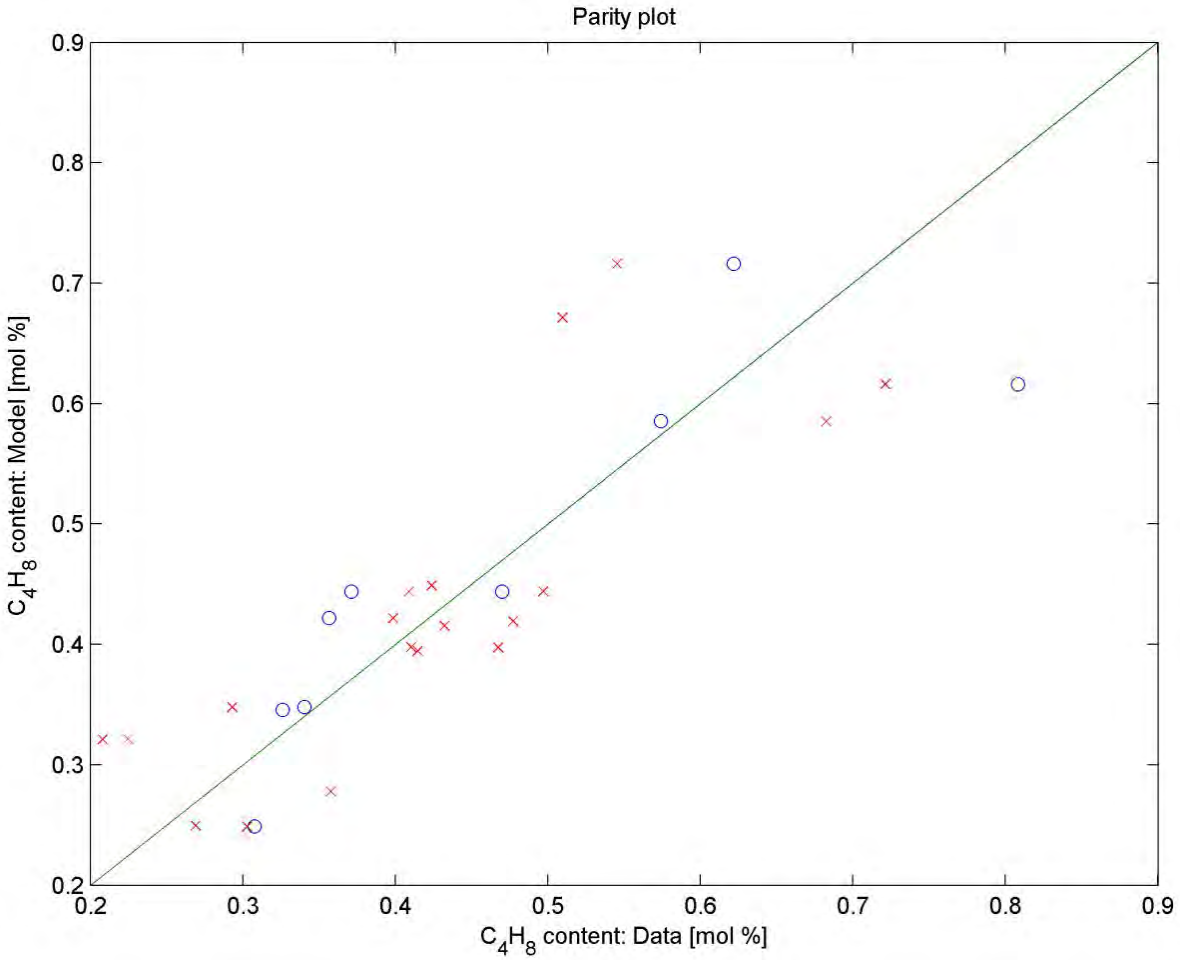

Figure 6.3: Comparison of model to co-polymerisation data. Key: o - NMR data. x - CEF data

6.2.2 Summary

Values for the co-polymerisation rate constants have been obtained from the experimental data for comonomer content in the polymer. With the parameters in Table 6.5 and Table 6.6, the catalyst activity and polymer propagation rate can be fully described for the given catalyst.

The final step in obtaining values for parameters in the kinetic scheme is to fit the termination parameters, which determine chain length.

6.3 Termination rate constants

The chain length distribution data from GPC analysis, summarised in Table 5.6 and Table 5.7, can be simulated by finding appropriate values for the termination rate constants, and minimising the objective function in equation 4.45. The liquid phase concentrations are summarised in Table 5.5.

$$Obj = \sum_e \left\{ M_{n,e} - m_{mon} \frac{\lambda_1}{\lambda_0}\left(\underline{C}_e, \underline{k}_t\right)\right\}^2 + \sum_e \left\{ M_{w,e} - m_{mon} \frac{\lambda_2}{\lambda_1}\left(\underline{C}_e, \underline{k}_t\right)\right\}^2 \qquad 4.45$$

In order to use the propagation rate constants in Table 6.6 in the chain length distribution model developed in Section 4.3, the units of these rate constants must be adjusted from their current form of [L.min^{-1}.g-cat^{-1}] to [L.min^{-1}.mol^{-1}]. This conversion is achieved by making use of the titanium content of the catalyst.

Since the propagation and termination reactions are all first order reactions with respect to monomers, terminating agents and catalyst sites, for rate constants the unit [mol-X] is equivalent to [mol-Ti], where X is a reactant.

Dividing the propagation rate constants in Table 6.6 by the titanium content of the catalyst results in the values in Table 6.7.

Table 6.7: Polymerisation propagation rate constants (adjusted units)

$k_{p,ij} * 10^{-5}$ [L.min^{-1}.mol^{-1}]		
	j=1	**j=2**
i=1	0.6232	0.0193
i=2	9.775	0

6.3.1 Results

The five termination rate constants (one for each of the four reactants, and one for spontaneous termination) were fitted to the GPC data. The results are summarised in Table 6.8 and Figure 6.4.

The termination rate constants were fitted to the average chain lengths, M_n and M_w. As Figure 6.4 shows, the fits of the model are good for the average chain lengths (for M_n, $R^2 = 0.79$; for M_w, $R^2 = 0.84$). The fit for PDI is not good ($R^2 = -0.29$), but is included for completeness. PDI was excluded from the objective function that was fitted for a number of reasons:

- PDI is determined by the mean chain lengths, and the least important parameter to describe polymer properties in this project;
- Attempting to fit PDI data drastically reduced the goodness of the fits for the mean chain lengths ($R^2 < 0.6$) without achieving a good fit for PDI ($R^2 < 0.2$);
- The model predicts PDI values in the right range without fitting the PDI data, because the fits to the mean chain lengths are good;
- Since the PDI is the ratio of the M_n and M_w, small errors in the fitting of either of these parameters can lead to compounded errors in the fitting of the ratio, and so the relatively poor fit of PDI in Figure 6.4 may be due more to numerical issues than an inability of the model to accurately predict widely distributed chain lengths.

Table 6.8: Termination rate constants

m	sp	TEA	C_2H_4	C_4H_8	H_2
k_t^m [L.mol^{-1}.min^{-1}]	7.04x10^{-4}	3701.2	51.74	353.8	2311.4

The relative values of the chain termination rate constants suggest that the most active terminating agents are the co-catalyst and hydrogen. However, the influence of a terminating agent on chain length (as defined in equation 4.36, shown below) is dependent not just on the rate constant, but on the product of the rate constant AND the concentration in the liquid phase of the terminating agent: $k_t^m C_m$.

$$\gamma^m = \left(\frac{\sum_i \sum_j k_{p,ji} \xi_j^m [M_i]}{\sum_i \left(\xi_i^m \left(\beta_{st}^{3+,2+} + k_{t,i}^m C_m \right) + \sum_j k_{p,ij} \xi_i^m [M_j] \right)} \right) \qquad 4.36$$

The average values of this concentration-weighted termination rate for the experimental data are shown in Table 6.9. The termination rate constants are from Table 6.8, and the concentrations used were the averages of the values in Table 5.5.

Table 6.9: Concentration-weighted termination rates

m	sp	TEA	C_2H_4	C_4H_8	H_2
$k_t^m C_m$ [min^{-1}]	7.04x10^{-4}	11.45	10.996	10.74	69.68

Since the pseudo-sites model for polymer chain growth (Rawatlal, 2004) is based on differences in termination rates at each pseudo-site, the values in Table 6.9 provide qualitative information about the number of chains and the chain lengths of polymer produced at each theoretical pseudo-site. Pseudo-sites with large termination rates will produce a large number of relatively short polymer chains, and smaller termination rates will correspondingly produce a smaller number of longer polymer molecules.

The most active terminating agent, based on the concentration-weighted termination rates in Table 6.9, is hydrogen. On average, the hydrogen-terminating pseudo-sites were responsible for producing the shortest polymer chains in the experimental campaign. Changes in the concentration of hydrogen affect the shorter end of the chain length distribution significantly, because of the relatively large number of chains produced at hydrogen pseudo-sites. The number-average molecular weight is particularly sensitive to the lower end of the chain length distribution, and thus to the concentration of hydrogen.

On the other end of the scale, pseudo-sites that terminate spontaneously are responsible for the production of a very small number of very high-weight chains.

Since the concentration of co-catalyst in the reactor is orders of magnitude lower than the other reactants (see Table 5.5), it does not have as large an influence on chain length as the magnitude of its termination rate constant (Table 6.8) would suggest. However, the magnitude of the termination rate constant in Table 6.8, when compared with the site transformation rate constants for TEA (see Table 6.5), does indicate that the co-catalyst, added to the reactor primarily as a catalyst activator (interpreted in this work through site transformation reactions) and oxy-compound scavenger, is mostly consumed in chain termination reactions. In the absence of any evidence to refute this surprising result, it must stand.

Returning to Table 6.9, we see that in fact, the termination rates of the co-catalyst, ethylene and 1-butene are all very similar, approximately a seventh of the termination rate of hydrogen. Pseudo-sites associated with TEA and the two monomers each produce a relatively low number of relatively high molecular weight polymer. Changes in the liquid phase concentrations of these reactants will influence the heavier end of the chain length distribution, where the weight-average molecular weight is most sensitive.

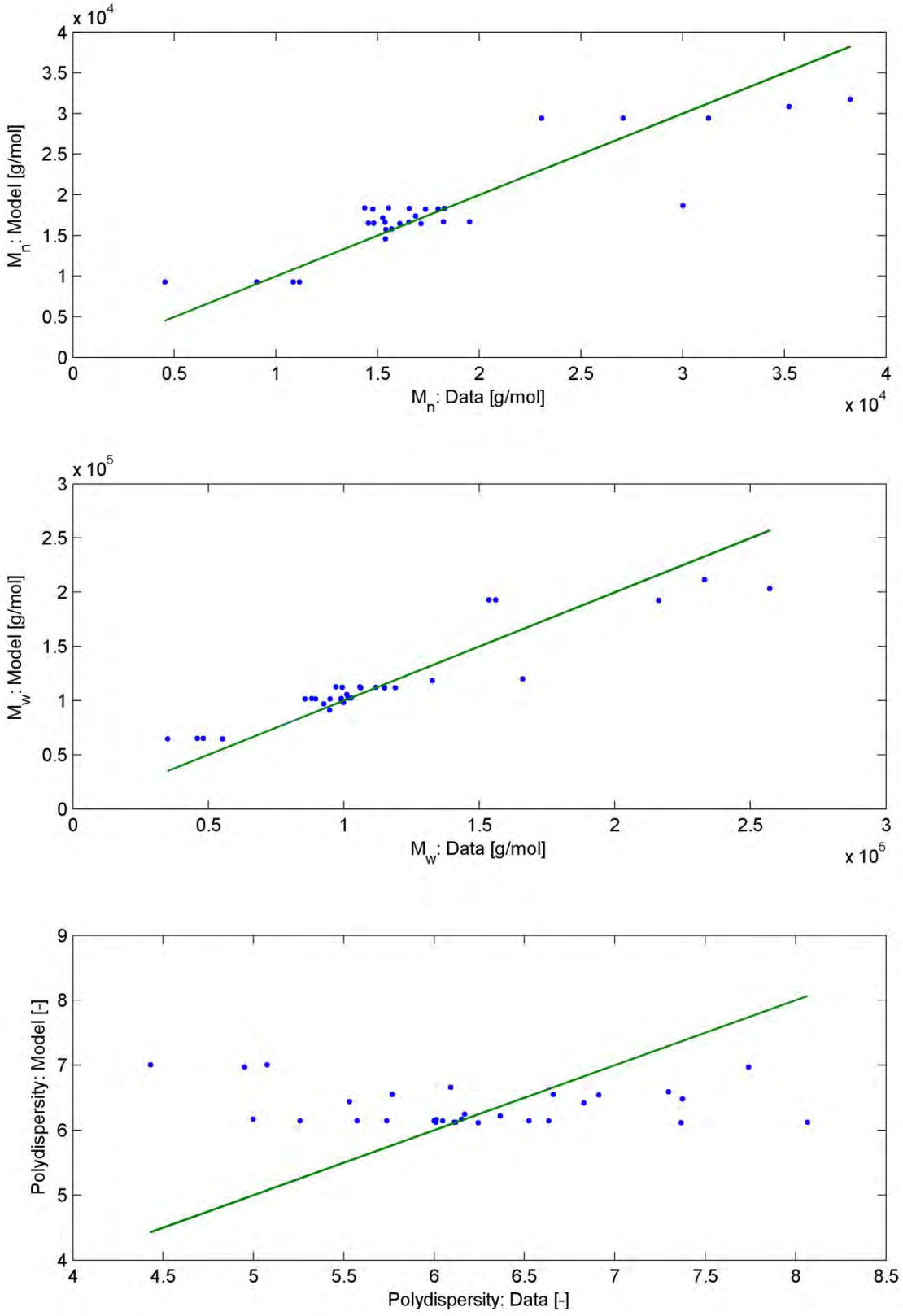

Figure 6.4: Results of termination rate constant regression

6.3.2 Correlation between Melt Flow Index and GPC data

The final step in the analysis of the data is a correlation between the MFI and the GPC data. As discussed earlier, the form of this relationship is given in equation 5.1, reproduced below.

$$M_w^k = A\frac{1}{MFI} \qquad 5.1$$

The best fit (found through non-linear parameter fitting) to this model was:

$$M_w^{3.882} = 1.012 * 10^{20}\frac{1}{MFI} \qquad 6.1$$

The results of this data fitting are shown in Figure 6.5. The model was fitted to the University of Waterloo data, but also shows a good fit to the modified Stellenbosch data, which is available for a greater range of values.

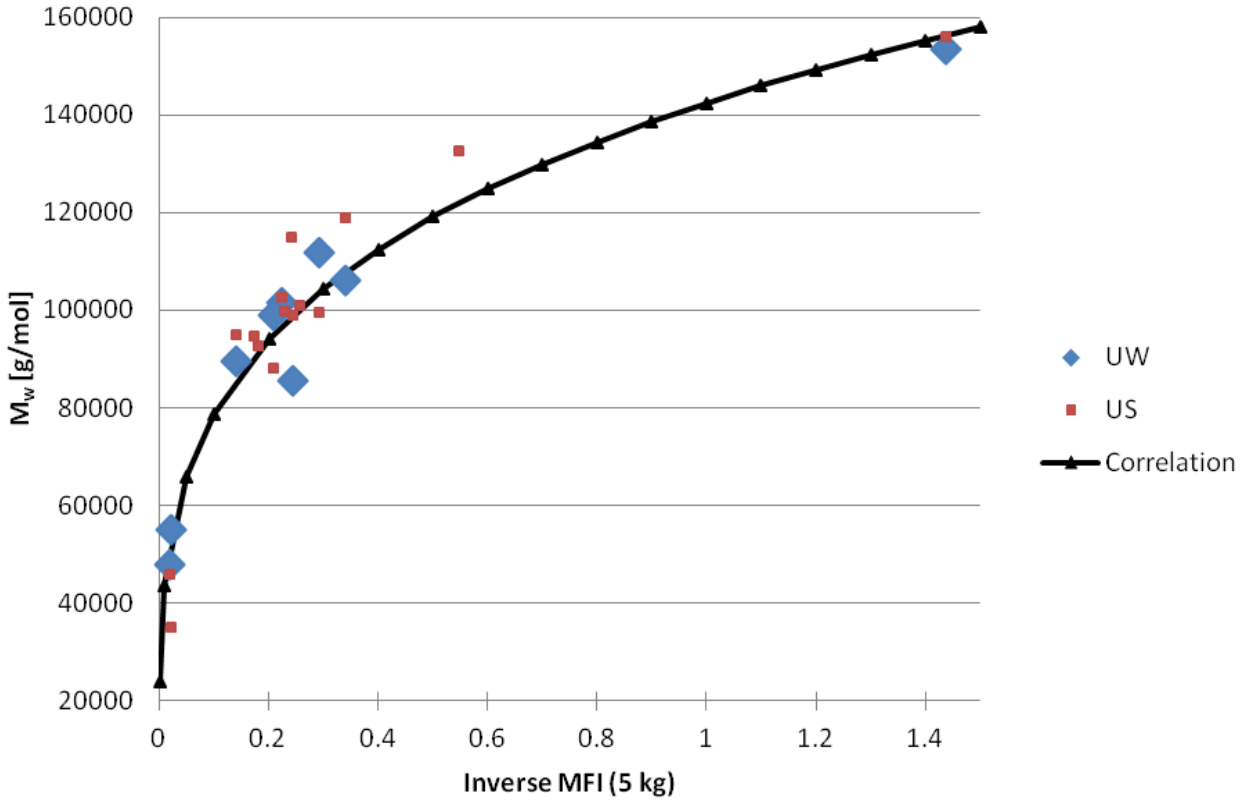

Figure 6.5: Correlation between MFI and M_w

6.3.3 Summary

A set of termination rate constants has been found that fits the chain length data available from experiments. These rate constants are based on the pseudo-sites concept, which proposes a single propagation rate with different termination rates for a number of terminating agents (Rawatlal, 2004).

The difference between the rates of termination at each of the pseudo-sites is the cause of the production of polymer with a wide range of chain lengths. Based on the termination rates, pseudo-sites terminated by hydrogen will produce a relatively large quantity of relatively short-chained polymer, pseudo-sites terminated by TEA, ethylene or 1-butene will each produce a small quantity of longer-chained polymer, and pseudo-sites that terminate spontaneously will produce a very small number of much longer-chained polymer chains. The combination of all of these contributions results in the polydisperse polymer that is observed.

The correlation between the Melt Flow Index and weight-average molecular weight allows for the comparison between model predictions and industrial data.

6.4 Summary

Chapter 4 detailed the development of rigorous methods to extract kinetic parameters from experimental data. These kinetic parameters describe the behaviour of a Ziegler-Natta catalyst producing high-density polyethylene.

The kinetic scheme (presented in Table 4.1) is based on the pseudo-sites concept, which proposes that catalyst sites differ in terms of the rate of action of various terminating agents, rather than differing intrinsic activities. The result of this proposal is a kinetic scheme which aims to simulate the behaviour of a catalyst in a physically meaningful manner, in contrast with the many multi-site catalyst models in the literature.

A set of laboratory experiments was described in Chapter 5, providing the data required to find values for the parameters in the kinetic scheme. This data included activity profiles and polymer product properties, for a range of experimental conditions.

The final set of kinetic parameters fitted to the experimental data, summarised in Table 6.10, is able to reproduce the activity profiles, comonomer incorporation and number- and weight-average molecular weights that were measured during the experimental campaign. The confidence intervals for the parameters are shown in Table 6.11, Table 6.12 and Table 6.13; confidence intervals would be improved by having a larger experimental data set, but are included for completeness.

Table 6.10: Summary of parameters in kinetic model

$k_{p,ij}$			j=C_2H_4	j=C_4H_8	
		i=C_2H_4	16.93	0.524	[L.min^{-1}.g-cat^{-1}]
		i=C_4H_8	265.5	0	
	sp	**TEA**	**C_2H_4**	**C_4H_8**	**H_2**
	[min^{-1}]	[L.mol^{-1}.min^{-1}]	-	-	[min^{-1}.{mol-H_2.L^{-1}}$^{-0.5}$]
$k_{st,i}^{4+,3+}$	-	31.7	-	-	-
$k_{st,i}^{3+,2+}$	-	-	-	-	0.325
$k_{st,i}^{2+,3+}$	-	0.924	-	-	-
	[min^{-1}]	[L.mol^{-1}.min^{-1}]	[L.mol^{-1}.min^{-1}]	[L.mol^{-1}.min^{-1}]	[L.mol^{-1}.min^{-1}]
k_t^m	7.04x10^{-4}	3701.2	51.74	353.8	2311.4

Table 6.11: 95% confidence intervals for propagation rate constants

$k_{p,ij}$		j=C_2H_4		j=C_4H_8		
	i=C_2H_4	16.90	16.96	0.339	0.81	[L.min^{-1}.g-cat^{-1}]
	i=C_4H_8	34.5	2043	-		

Table 6.12: 95% confidence intervals for site transformation rate constants

	TEA		**H_2**	
	[L.mol^{-1}.min^{-1}]		[min^{-1}.{mol-H_2.L^{-1}}$^{-0.5}$]	
$k_{st,i}^{4+,3+}$	31.23	32.17	-	
$k_{st,i}^{3+,2+}$	-		0.319	0.331
$k_{st,i}^{2+,3+}$	0.720	1.186	-	

Table 6.13: 75% confidence intervals for termination rate constants

	sp		**TEA**		**C_2H_4**		**C_4H_8**		**H_2**	
	[min^{-1}]		[L.mol^{-1}.min^{-1}]		[L.mol^{-1}.min^{-1}]		[L.mol^{-1}.min^{-1}]		[L.mol^{-1}.min^{-1}]	
k_t^m	5.27x10^{-4}	9.41x10^{-4}	74.0	185000	5.05	529	244	512	302	17700

PART C. MODEL DEVELOPMENT

The previous chapter detailed an experimental kinetic study of the slurry-phase co-polymerisation of ethylene and 1-butene by a Ziegler-Natta catalyst, and the extraction of parameter values within a kinetic scheme to describe the behaviour of that catalyst. The catalyst activity, comonomer incorporation, and molecular weight distribution were described by the kinetic model, for the results of the laboratory experiments.

In order to translate a fundamental set of kinetics to the industrial reactor system scale, the following model developments are required.

After molecular-scale kinetics are developed, the next scale involves the particle. The presence of mass transfer limitations in the growing polymer particles, and particularly the development of concentration gradients within the particles, must be accounted for in obtaining more accurate reaction rate estimates. The kinetic scheme of the previous section was developed with the assumption that all catalyst sites experienced the same reactant concentrations, regardless of radial position within a particle. If this assumption is disproved, then the results must be re-evaluated. Thus the need for study of the dynamics of mass transfer within the polymer particles, at both laboratory and industrial conditions.

Second, before the kinetic scheme is built into a Segregation Approach-based reactor-modelling scheme, the efficiency and accuracy of the Segregation Approach must be investigated. As described in the Literature Review, the principle benefit of the Segregation Approach is its numerical and computational superiority over the more traditional Population Balance Model. To our knowledge, no study has rigorously tested the performance of the two models, particularly with regard to computational expense and model accuracy.

Third, if the Segregation Approach indeed displays the desired computational efficiency, a second benefit of the model can be exploited: the explicit inclusion of the residence time distribution function (RTD) in the Approach's formulation. This allows for the relatively simple simulation of complex mixing patterns. This strength is relevant to the modelling of large industrial reactors, which are unlikely to exhibit hydrodynamics that can be described by simple ideal RTD models. Some possibilities for RTD models that may describe the industrial situations must be proposed and investigated.

When integrating the particle and RTD models, an unsteady-state model of a reactor results. This industrial model is based on the data of the kinetic study outlined in the previous chapter, and the various preliminary developments which will be described in the current chapter. The models used to describe the laboratory-scale reactor for the purposes of parameter regression must be extended to an unsteady-state form, and integrated within the Segregation Approach-based reactor model. The use of unsteady-state RTD functions will also be described, within the context of the industrial reactor model.

CHAPTER 7. ANALYSIS OF MASS TRANSFER WITHIN GROWING POLYMER PARTICLES

Mass transfer limitations can cause the formation of concentration gradients within growing polymer particles. As described in the Literature Review, these gradients were proposed, particularly in the earlier works in the field, as an explanation for activity profiles and the wide range of chain lengths produced by Ziegler-Natta catalysts.

More recent research suggests that these gradients may be negligible in certain cases. It is generally assumed that mass transfer limitations are not responsible for activity profiles or molecular weight distributions; kinetic effects are used to explain these phenomena.

Nonetheless, gradients within the particles may exist, and can not be ignored in any particular case without some analysis. It is also possible that external mass transfer limitations exist: that rather than resulting in gradients within particles, mass transfer limitations give rise to a uniform reduction in reactant concentration through the particle (compared to the bulk fluid), and a lowering of the overall reaction rate.

The following section comprises a brief investigation of mass transfer within growing polymer/catalyst particles, using values for physical parameters from the literature and from the experimental work described in Chapter 5. The Multi-Grain Model (Yermakov et al., 1970, Floyd et al., 1986a, Floyd et al., 1987) provides the mathematical basis for the analysis, in order to determine whether gradients exist within the particles, and the potential for mass transfer limitation of the reactions.

7.1 Multi-Grain Model

The principal equations describing the Multi-Grain Model (MGM) are outlined below, based on the original model and more recent applications of the model (Yermakov et al., 1970, Floyd et al., 1986a, Floyd et al., 1987, Rawatlal, 2004). Figure 2.3 shows a schematic representation of the basis of the model, as was presented in the Literature Review, and is reproduced below for convenience.

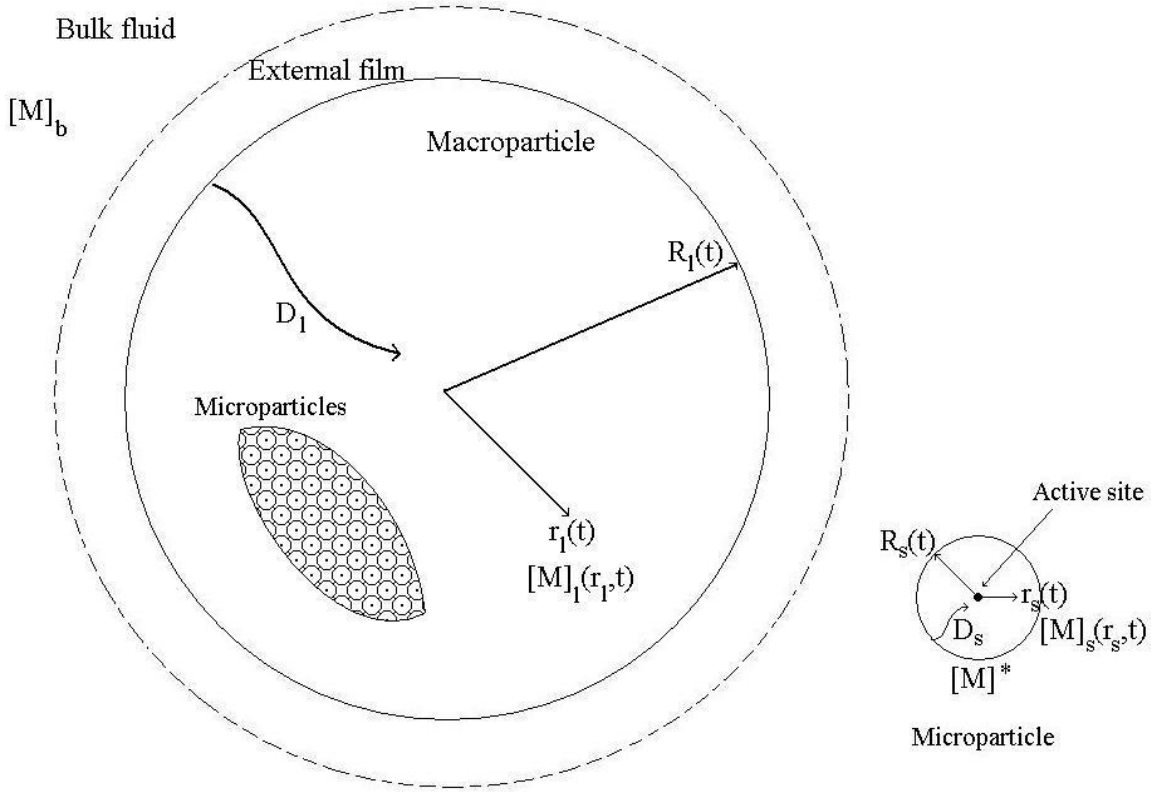

Figure 7.1: The Multigrain Model (based on figures in (Floyd et al., 1986a))

The partial differential equation describing the variation of the monomer concentration through the macro-particle is shown in equation 7.1. This equation can be discretised using standard methods into ordinary differential equations.

$$\frac{\partial M_l}{\partial t} = \frac{1}{r_l^2}\frac{\partial}{\partial r_l}\left(D_l r_l^2 \frac{\partial M_l}{\partial r_l} \right) - R_v \qquad 7.1$$

The concentration gradients within the micro-particle can be found more simply, by applying the Quasi-State Assumption to the analogous PDE, as has been described previously (Floyd et al., 1986a, Rawatlal, 2004). This results in the definition of a micro-particle growth factor, as shown in equation 7.2, and the calculation of the concentration at the catalyst crystallite surface, as shown in equation 7.3.

$$\frac{d\phi(r_l)}{dt} = \frac{R_p(r_l)}{\phi(r_l)^2}\frac{m_{mon}}{\rho_s} \qquad 7.2$$

$$M_{crys} = \frac{\eta_{crys} M_l}{1 + \frac{r_{crys}^2}{3D_s} k_p P_*(t)\left(1 - \frac{1}{\phi}\right)} \qquad 7.3$$

The ratio of the concentration of monomer at the catalyst site to the concentration of monomer in the bulk phase is thus defined as the effectiveness factor, shown in equation 7.4.

$$eff = \frac{M_{crys}}{M_b} \qquad 7.4$$

The following sections describe the analysis of mass transfer resistance within a growing particle, using the MGM and the effectiveness factor described above.

7.2 Base case

The values for the physical and kinetic parameters to be used in the base case of this study are given in Table 7.1.

Table 7.1: Base case parameters for mass transfer calculations

Parameter	Description	Value	units
T	Temperature	361	K
M_0	Initial concentration in particle	0	mol/m^3
M_b	Bulk monomer concentration	212	mol/m^3
D_{part}	Particle initial size	20	μm
D_{crys}	Catalyst fragment initial size	0.1	μm
ρ	Polymer density	950	kg/m^3
ρ_{cat}	Catalyst density	2300	kg/m^3
k_s	Mass transfer coefficient for particle bulk film[a]	$7.50x10^{-4}$	m/s
η_{crys}	Absorption onto micro-molecule[b]	0.507573	-
D_l	Macromolecule diffusion coefficient[c]	$1.50x10^{-8}$	m^2/s
D_s	Micro-molecule diffusion coefficient[c]	$1.60x10^{-10}$	m^2/s
k_p	Propagation rate	16.9	L/min/g-cat
$\beta^{4+,3+}$	Site transformation rate constant	$1.88x10^{-3}$	s^{-1}
$\beta^{3+,d}$	Site transformation rate constant	$1.06x10^{-3}$	s^{-1}
$\beta^{d,3+}$	Site transformation rate constant	$8.63x10^{-5}$	s^{-1}

Notes:

[a]From the original paper describing the MGM (Hutchinson et al., 1992), a conservative estimate of the mass transfer coefficient can be found from equation 7.5.

$$Sh = \frac{k_s d_p}{D_b} = 2 \qquad 7.5$$

[b]From the same paper (Hutchinson et al., 1992), the absorption onto the micro-molecule can be found from equation 7.6.

$$\eta_{crys} = 1 + 3.6329 - 2.3547 * 10^3 \left(1/T\right) + 3.1243 * 10^5 \left(1/T\right)^2 \qquad 7.6$$

[c]From parameters in a paper by the same authors (Floyd et al., 1986a)

The effectiveness factor (as defined by equation 7.4) as a function of normalised radial position and time is shown in Figure 7.2.

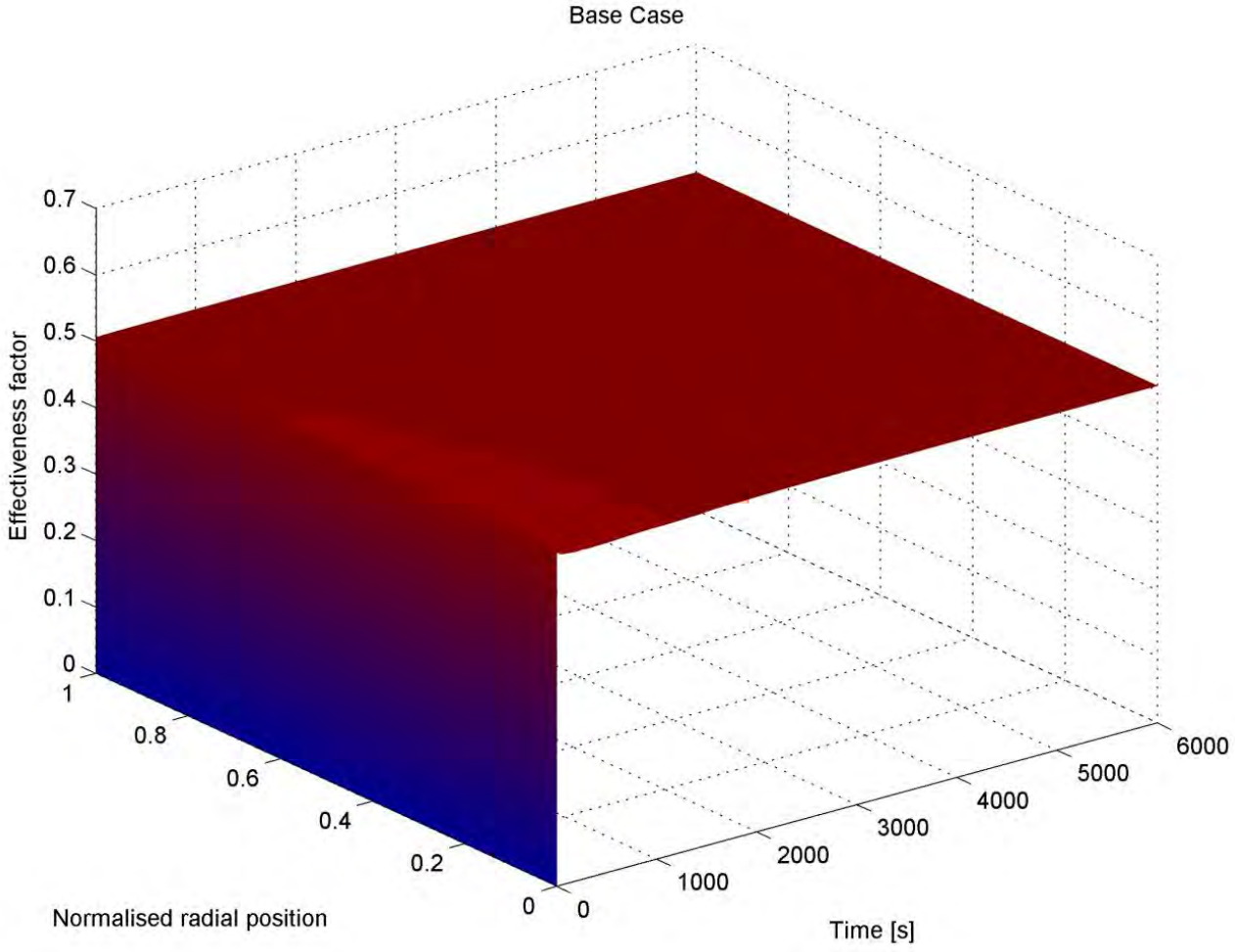

Figure 7.2: Effectiveness factor for base case

It is clear from Figure 7.2 that the concentration of monomer at the active site is approximately half that of the bulk fluid, resulting from the specific value assigned to the factor for adsorption onto micromolecules. This external mass transfer resistance would result in a reduction of the overall polymerisation rate at the conditions inside the particle, when compared to the polymerisation rate calculated at the conditions of the bulk fluid (as determined in Chapter 5).

However, it is also clear from Figure 7.2 that there are no significant concentration gradients inside the particle; the dominant resistance to mass transfer is in the movement from the macro-particle pores to the micro-particle surface, rather than diffusion.

A small deviation from the average value is visible towards the centre of the particle (radial position < 0.2) in the early stages of polymerisation (t < 1000s), but this is considered negligible.

This base case will now be compared with model predictions for variations in particle size, catalyst fragment size, bulk diffusivity, polymerisation rate and micro-particle sorption factor.

7.3 Initial catalyst particle size

A larger particle will provide greater potential for mass transfer resistance, and so the influence of initial catalyst particle size will be investigated by varying initial particle size from 15 to 60µm, as shown in Figure 7.3. The PSD analysis of the catalyst in Chapter 5 showed that catalyst particles should not exceed 40µm, but a larger size will be investigated for completeness.

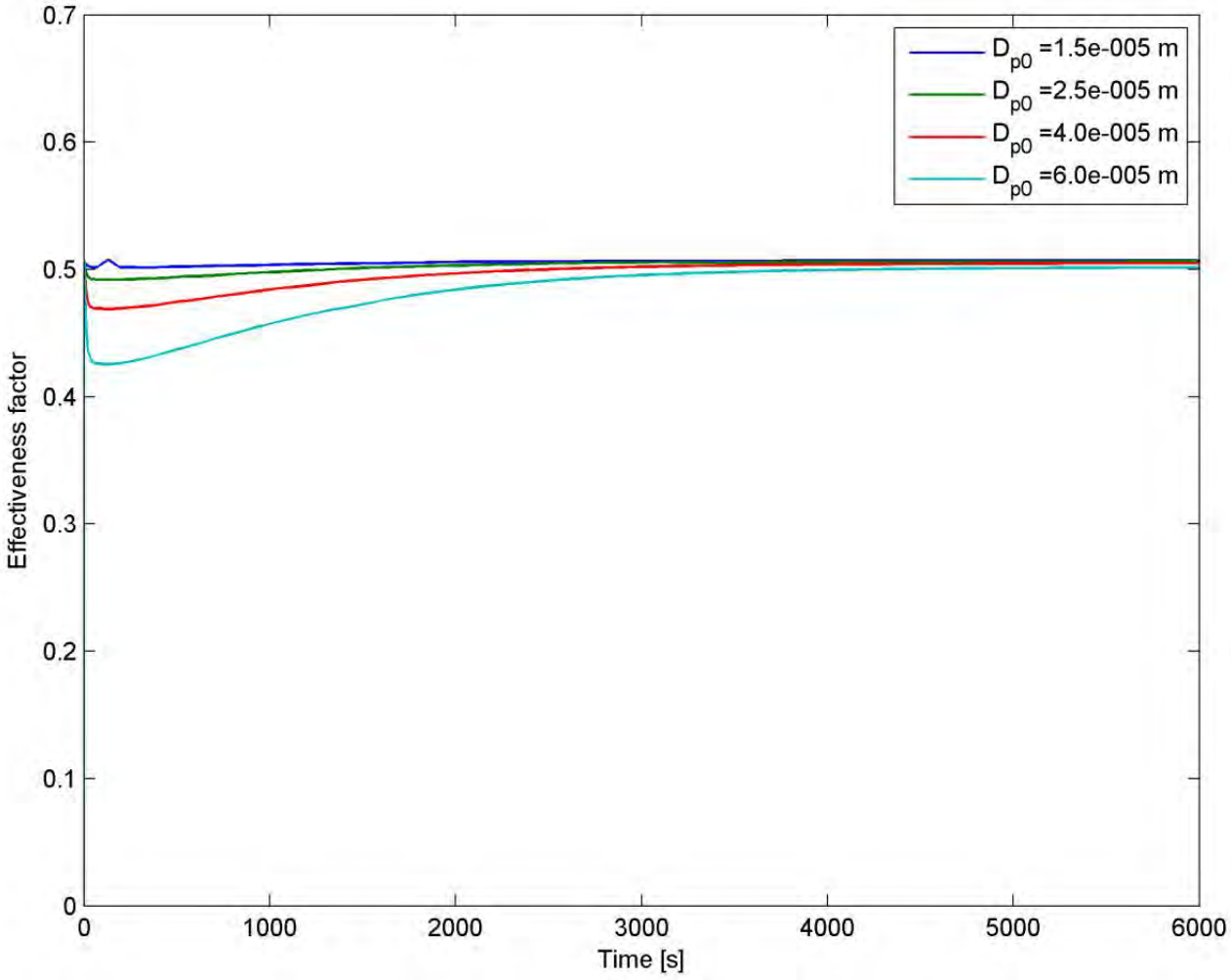

Figure 7.3: Effectiveness factor as a function of catalyst initial particle size

Figure 7.3 shows a summary of the impact of initial catalyst particle size on the effectiveness factor. It is clear that there is no significant change to effectiveness factor, but that for much larger particles (40µm and, in particular, 60µm) there is more variation in the initial stages of particle growth.

Figure 7.4 and Figure 7.5 show the effectiveness factor across the normalised particle radius, revealing that there are some concentration gradients that develop towards the middle of the particle, especially in the early stage when the catalyst sites are most active, as would be expected. These gradients are negligible for smaller particles, and only become significant when the macro-particles are initially very large.

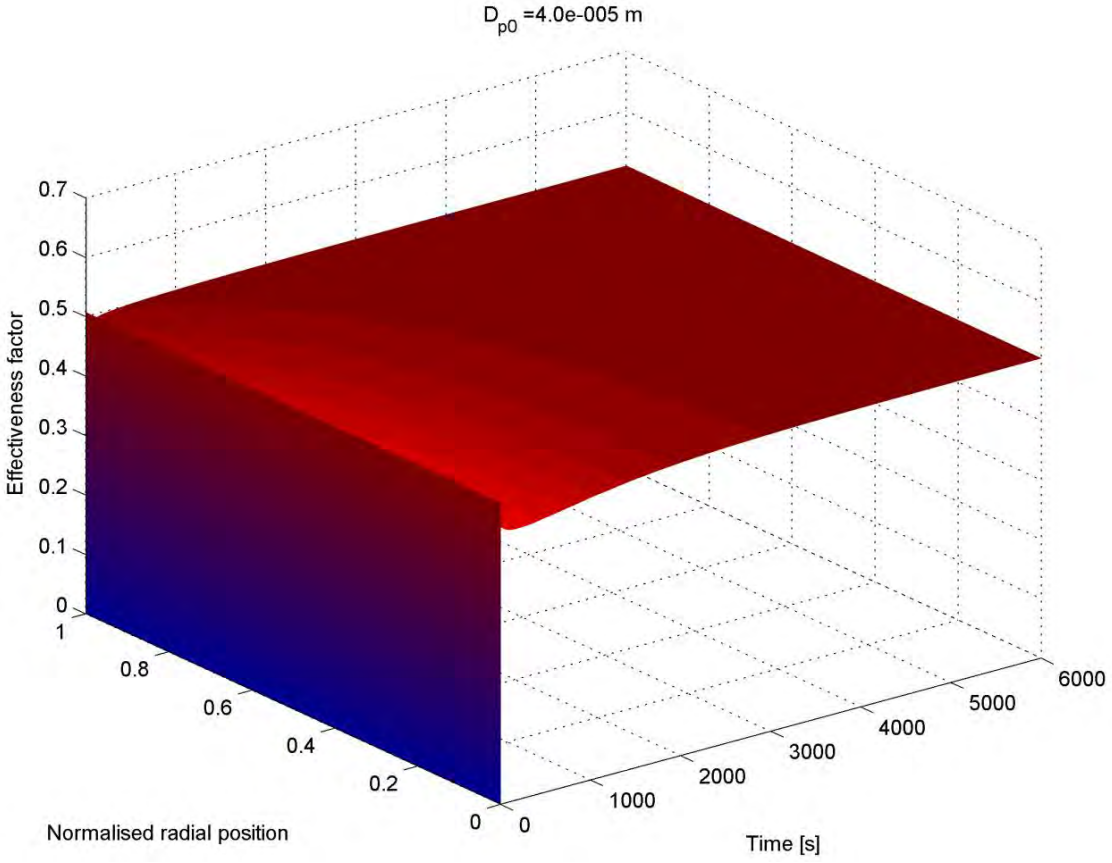

Figure 7.4: Effectiveness factor for initial particle size 40µm

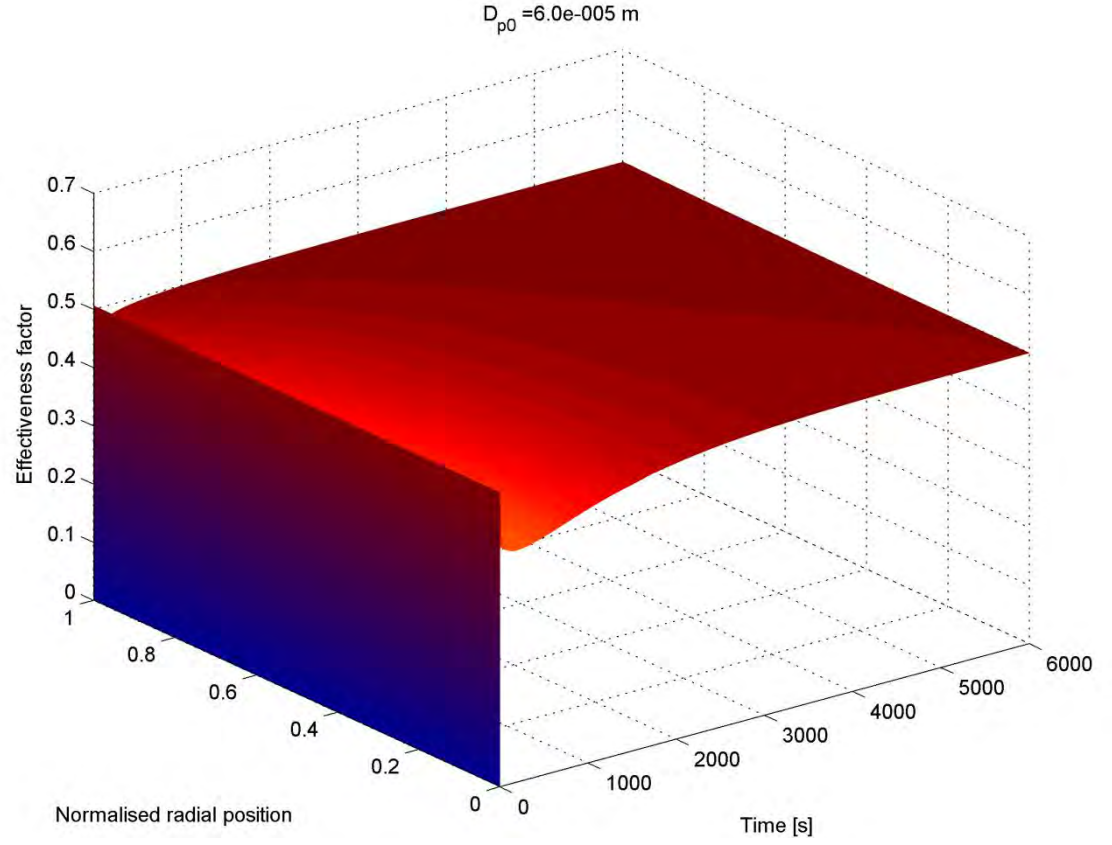

Figure 7.5: Effectiveness factor for initial particle size 60µm

7.4 Catalyst fragment size

The catalyst fragments, which compose the micro-particles in the MGM, are generally considered to be between 0.01 and 0.1µm (Floyd et al., 1986a, Hutchinson et al., 1992). The size of the crystallite fragments will be varied between 0.01 and 1µm to investigate its influence on the effectiveness factor. This is shown in Figure 7.6.

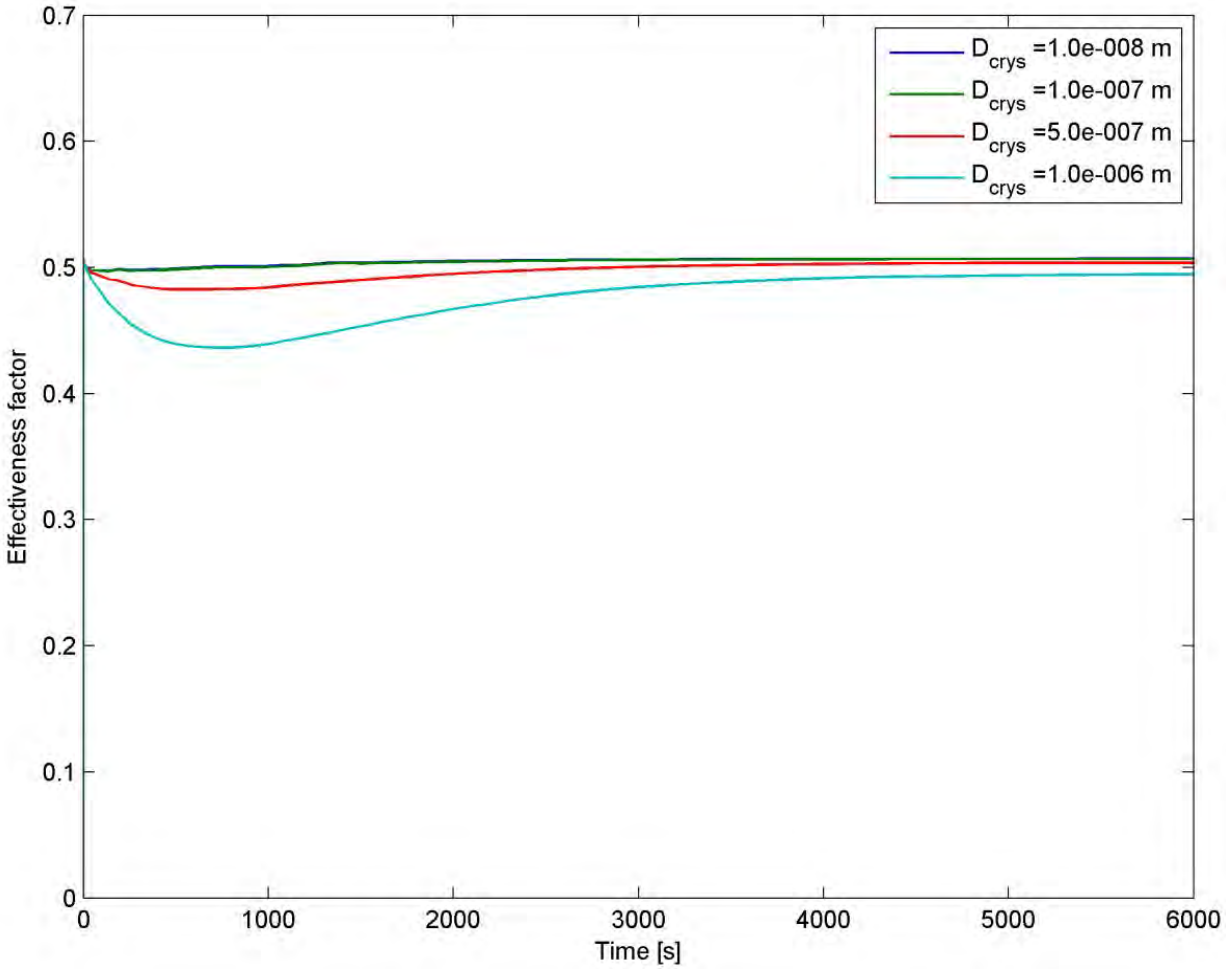

Figure 7.6: Effectiveness factor as a function of catalyst fragment size

Figure 7.6 reveals that below 0.1µm there is no impact on effectiveness factor, but that larger fragments can reduce the effectiveness factor.

Figure 7.7 displays the effectiveness factor across the macro-particle for catalyst fragment size 1µm, and shows that the limitation of monomer concentration is right across the macro-particle in the initial stages, rather than there being gradients towards the centre, as was observed for large macro-particles (Figure 7.5). This effect is because larger micro-particles will limit the diffusion of monomer to the active sites regardless of position in the macro-particle; the dominant mass transfer resistance occurs in the micro-particle, not the macro-particle.

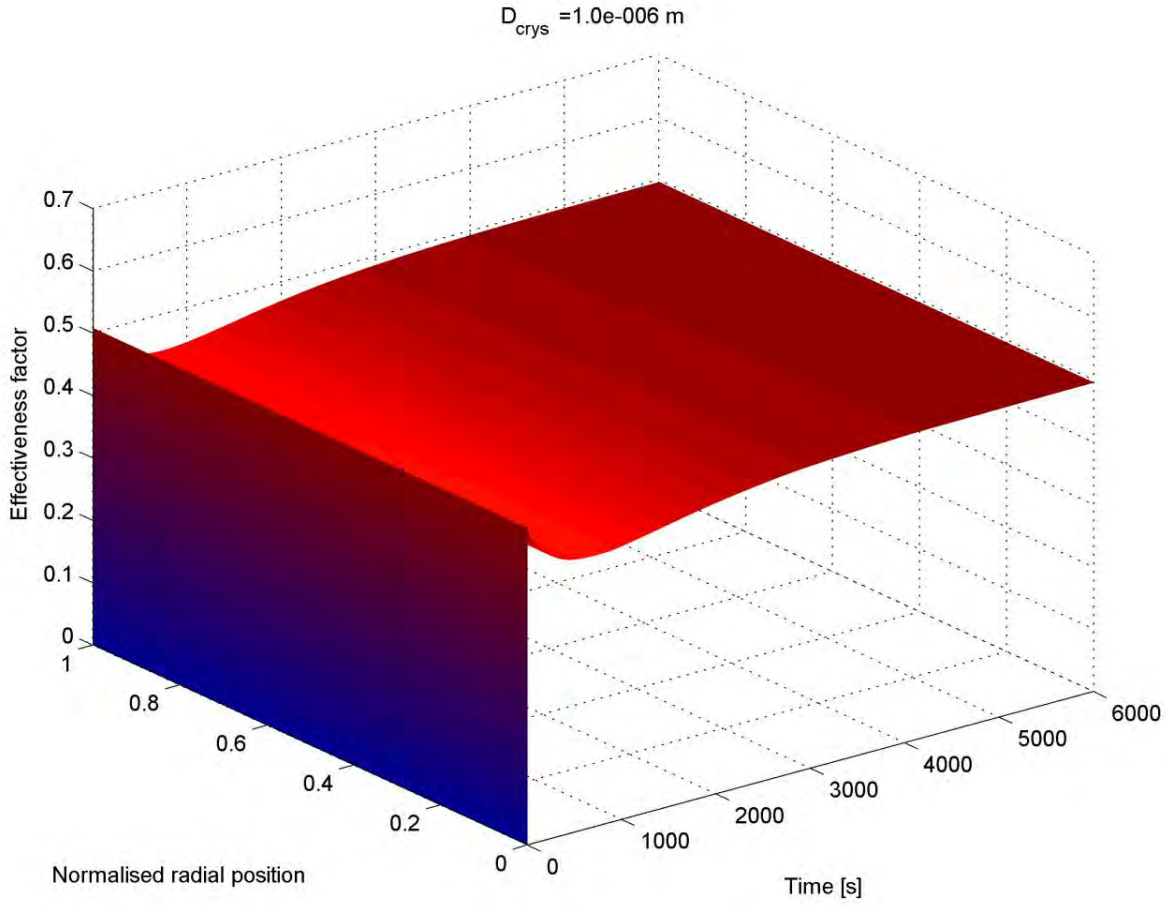

Figure 7.7: Effectiveness factor for catalyst fragment size 1µm

7.5 Bulk and macro-particle diffusivity

Bulk diffusivity of ethylene in typical solvents (such as n-hexane, as was used in the kinetic study) is ~1.5x10^{-8} m^2/s (Hutchinson et al., 1992). The diffusivity within the particle itself can be affected by the porosity and tortuosity of the growing particle, which could reduce the diffusivity within the macro-particle by as much as two orders of magnitude.

This effect has been investigated by varying the bulk diffusion coefficient between 1.5x10^{-8} and 1.5x10^{-10} m^2/s, and assigning this value to the macro-particle diffusion coefficient, as shown in Figure 7.8. The effectiveness factor gradients within a particle are shown in detail for the lowest diffusivity value in Figure 7.9.

It is clear from Figure 7.8 and Figure 7.9 that the magnitude of the diffusivity coefficient can have a significant impact on the effectiveness factor: not only is the concentration of monomer at the active sites as much as 80% less than that predicted for the base case, but there are also significant gradients that develop within the growing particle when the diffusivity is at the lowest simulated value, as shown in Figure 7.9.

When diffusivity is very low, the dominant mass transfer resistance is the diffusion of reactants through the macro-particle, rather than the external resistance of sorption onto the micro-particles.

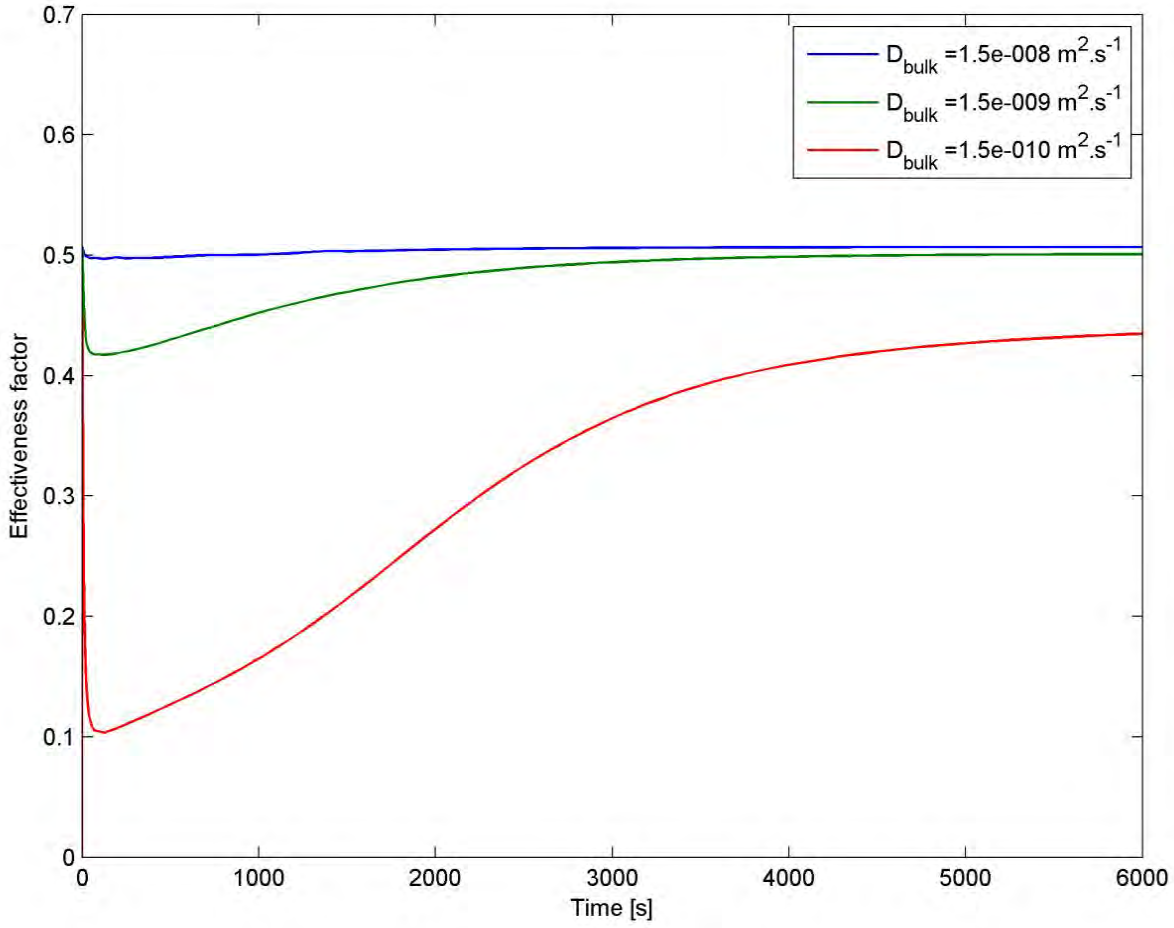

Figure 7.8: Effectiveness factor as a function of bulk diffusivity

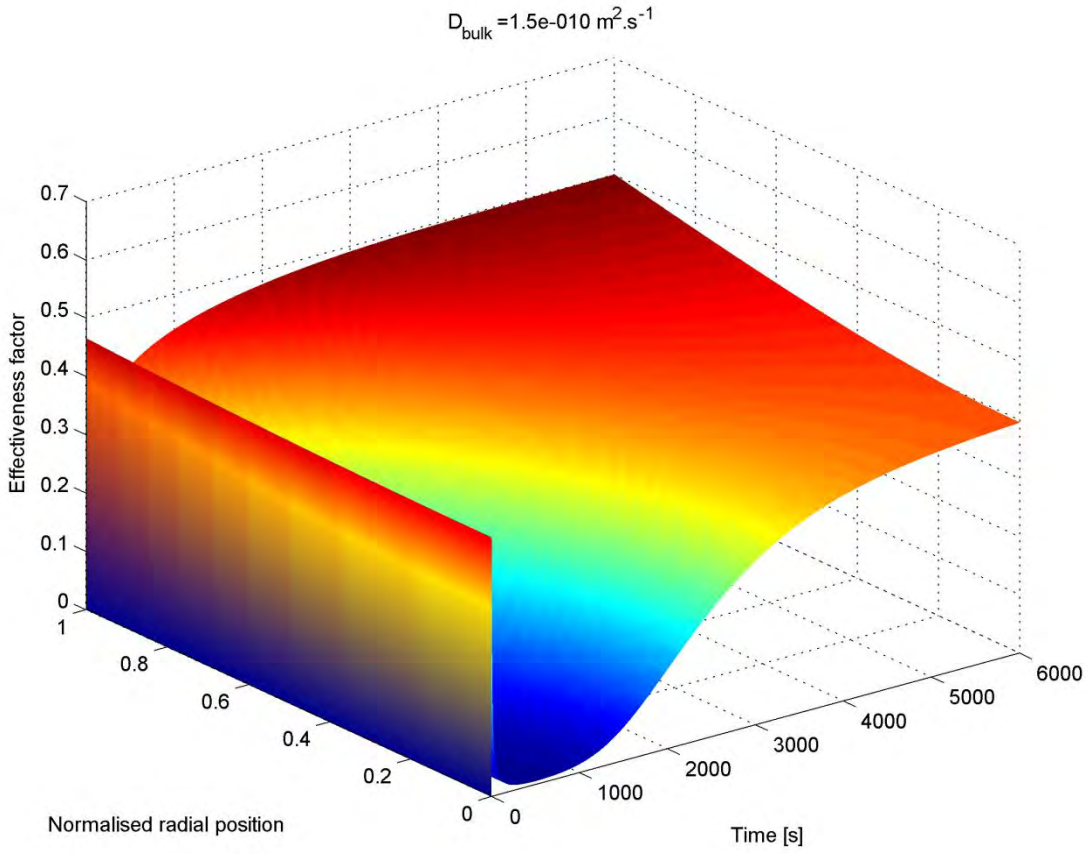

Figure 7.9: Effectiveness factor for macroparticle diffusivity 1.5×10^{-10} m^2/s

7.6 Polymerisation rate

In each case shown above, the most significant limitation of the effectiveness factor has been when the catalyst is most active; since this is when monomer is consumed most rapidly, this result is expected. To investigate the impact of the polymerisation rate on the effectiveness factor, and determine whether the polymerisation reaction is hindered by diffusion limitations, the polymerisation rate has been set at a range of values, as shown in Figure 7.10.

Figure 7.10 shows that for most values of polymerisation rate, including when the value is increased by a factor of 3 or 6 over the rate observed in the laboratory experiments, there is a very small impact on the effectiveness factor. Only at vastly unrealistic values of polymerisation rate, such as shown in Figure 7.11, do concentration gradients develop within the particle.

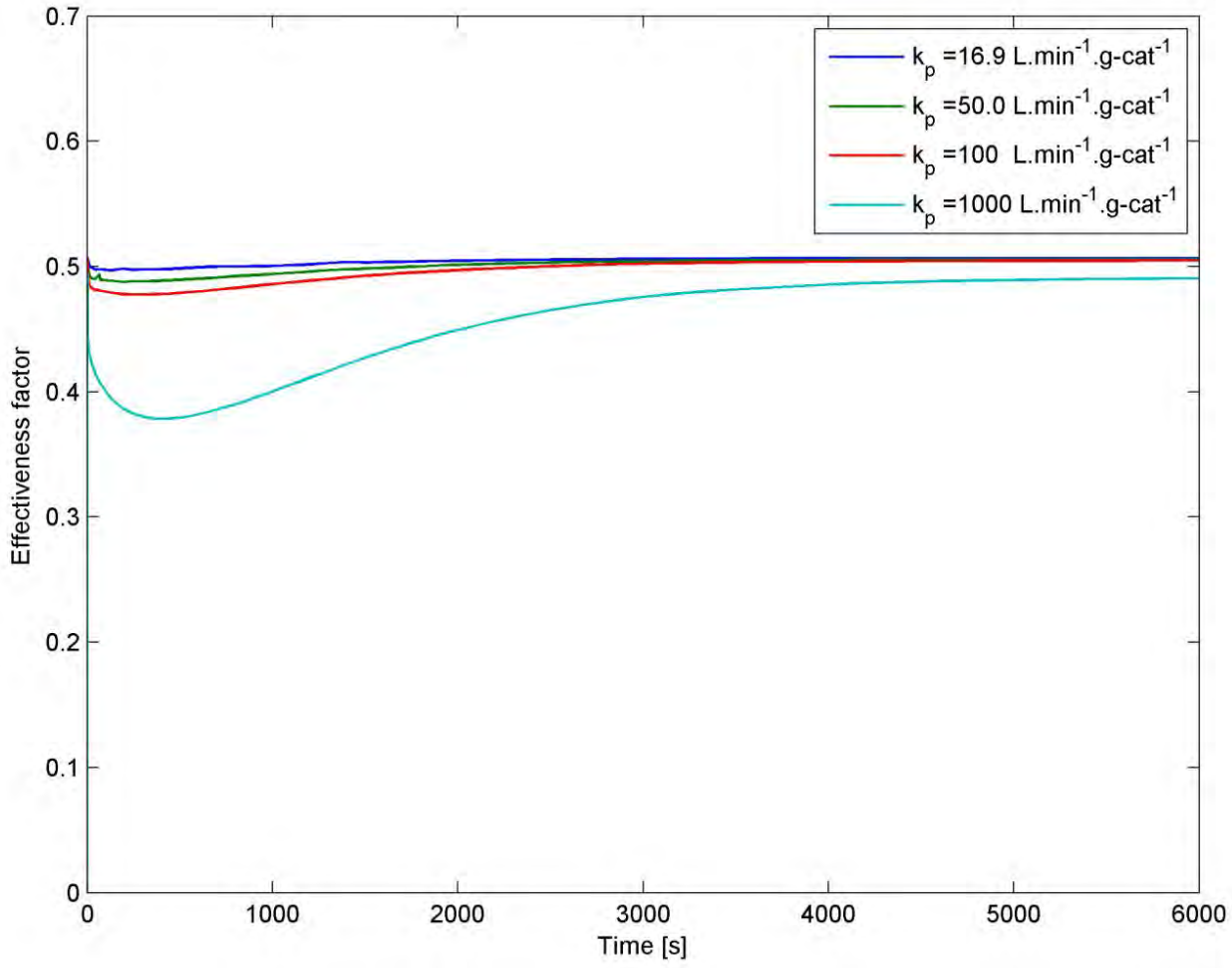

Figure 7.10: Effectiveness factor as a function of polymerisation rate

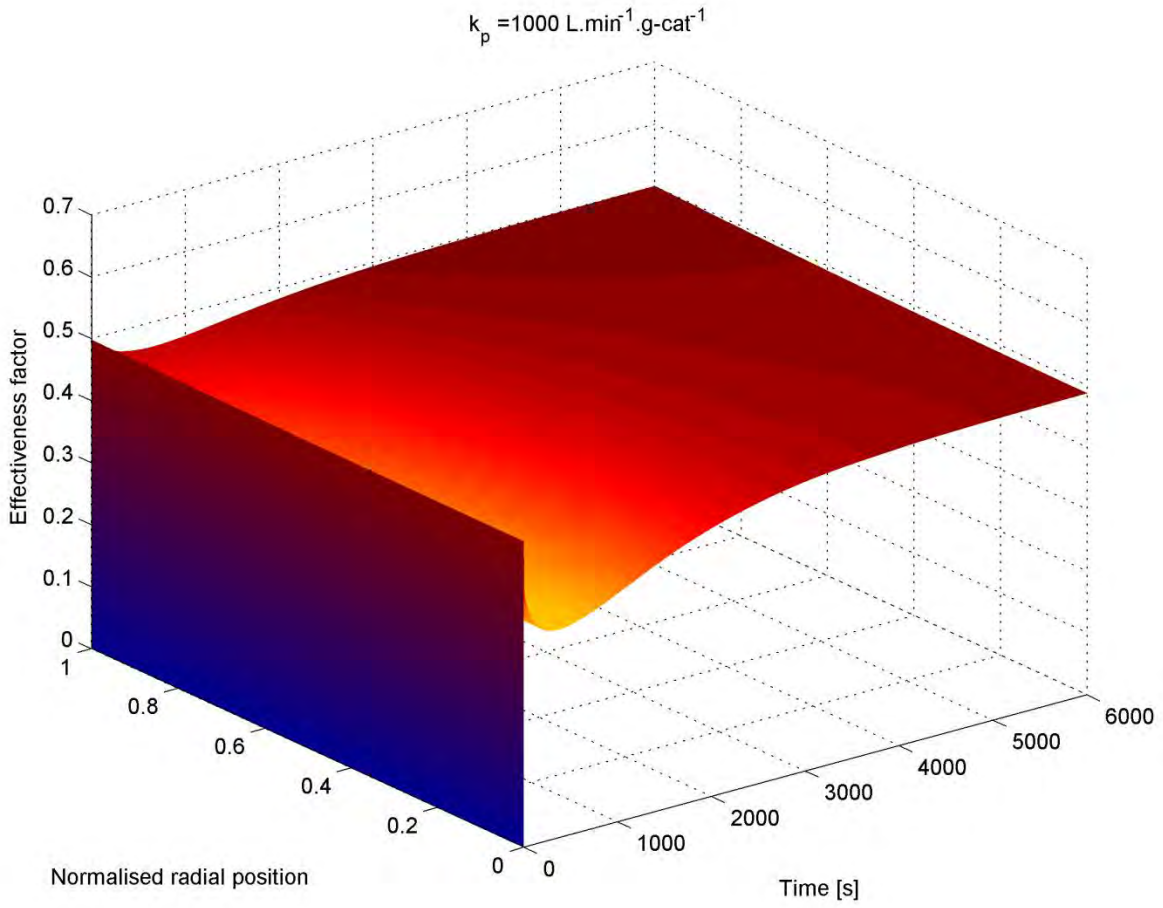

Figure 7.11: Effectiveness factor for polymerisation rate 1000 L.min^{-1}.g-cat^{-1}

7.7 Micro-particle sorption factor

The sorption of the monomer from the pores of the macro-particle onto the micro-particles is a function of temperature, as described in equation 7.6. The impact of the sorption factor on the effectiveness factor is shown in Figure 7.12.

It is clear that the effectiveness factor varies almost directly with the sorption factor, with only slight deviations in the early stages of polymerisation. The effectiveness factor does not vary within the particle, i.e., there are no concentration gradients, regardless of the value of the sorption factor, as shown in Figure 7.13, for a sorption factor of 1.

This result confirms that the dominant resitance to mass transfer is in the sorption of monomer onto the micro-particle surface, rather than due to diffusion resistance.

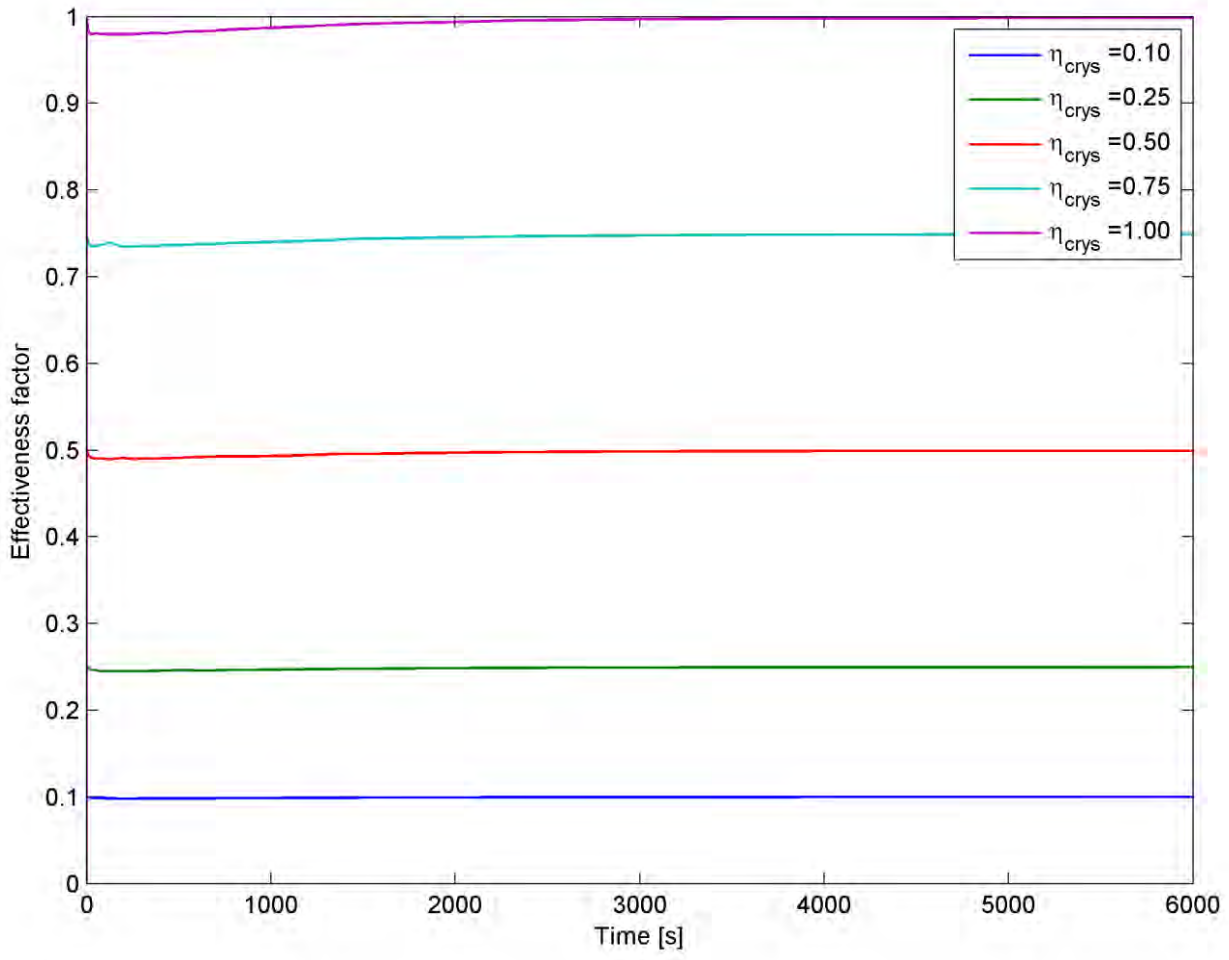

Figure 7.12: Effectiveness factor as a function of micro-particle sorption

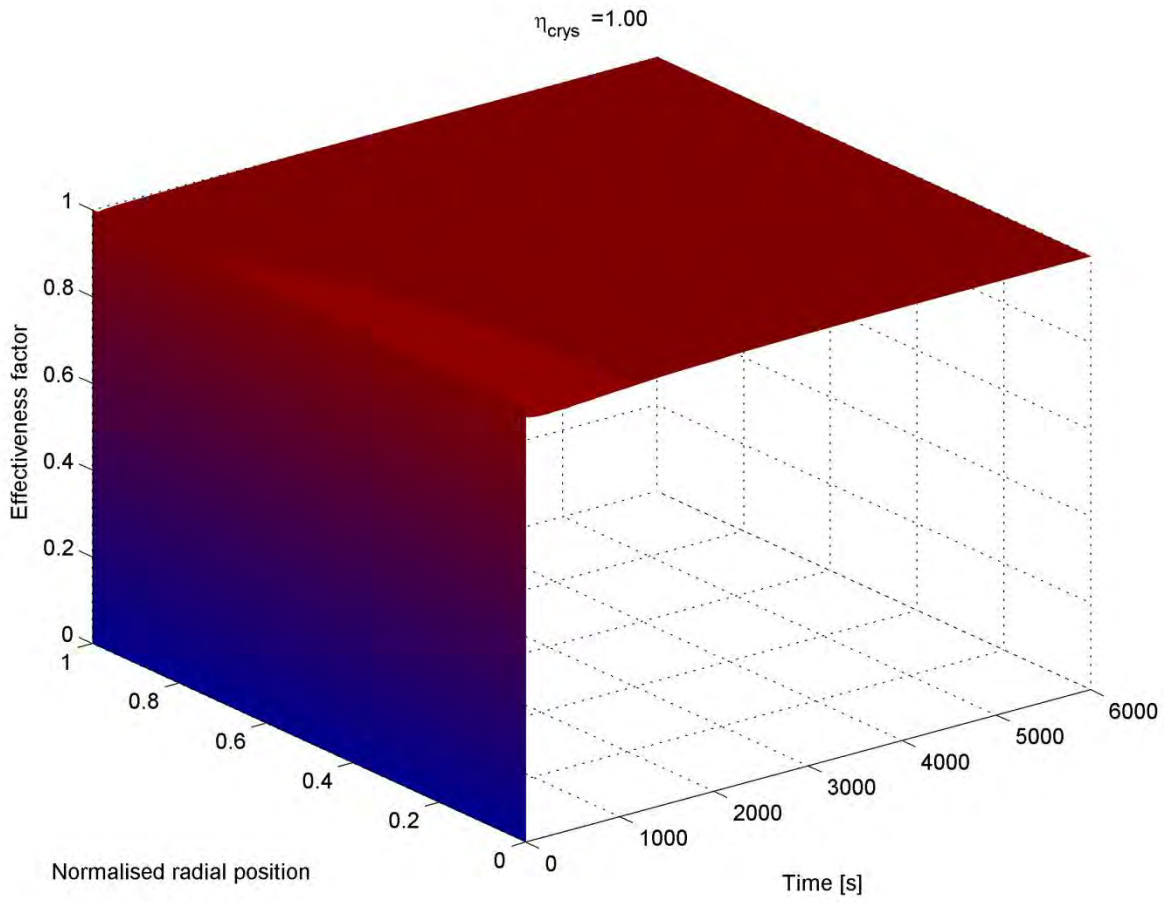

Figure 7.13: Effectiveness factor for micro-particle sorption factor = 1

7.8 Worst case scenario

The worst case for mass transfer limitation of the polymerisation reaction would be:

- A large macro-particle, limiting diffusion towards the centre of the particle;
- Large catalyst fragments, limiting diffusion to the active sites;
- Low bulk diffusivity and
- High polymerisation rate, increasing the possibility of a diffusion-limited reaction.

The values for the parameters which represent this worst case are presented in Table 7.2; parameters not specified in this table retain the same values as in Table 7.1.

Table 7.2: Worst case parameters for mass transfer calculations

Parameter	Description	Value	units
D_{part}	Particle initial size	40	μm
D_{crys}	Catalyst fragment initial size	0.2	μm
D_l	Macromolecule diffusion coefficient	$8x10^{-9}$	m^2/s
k_p	Propagation rate	50	L/min/g-cat

Figure 7.14 clearly shows the development of concentration gradients within the growing particle, particularly during the early period when the catalyst is most active for polymerisation, as expected. A comparison between base and worst case of the average effectiveness factor across the particle is shown in Figure 7.15, further emphasising the deviation from the base case values in the early stages of polymerisation.

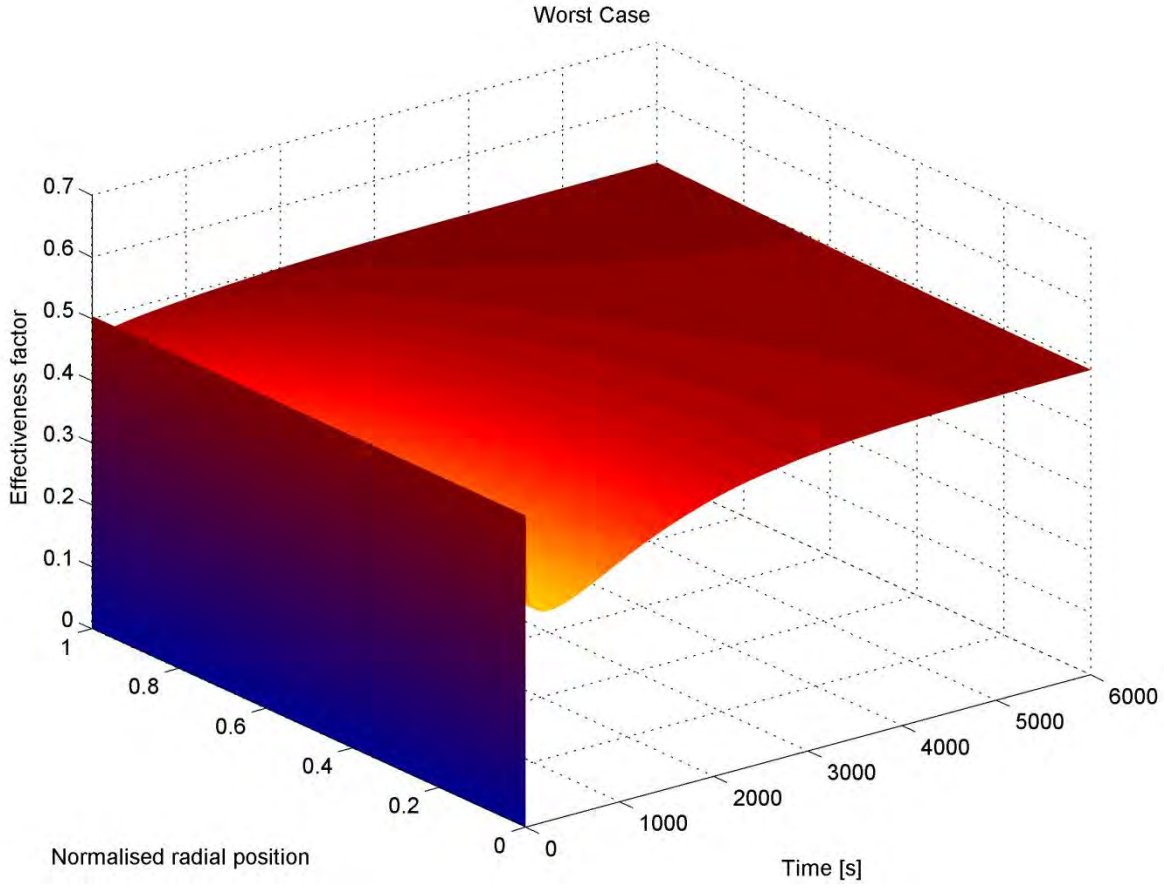

Figure 7.14: Effectiveness factor for worst case

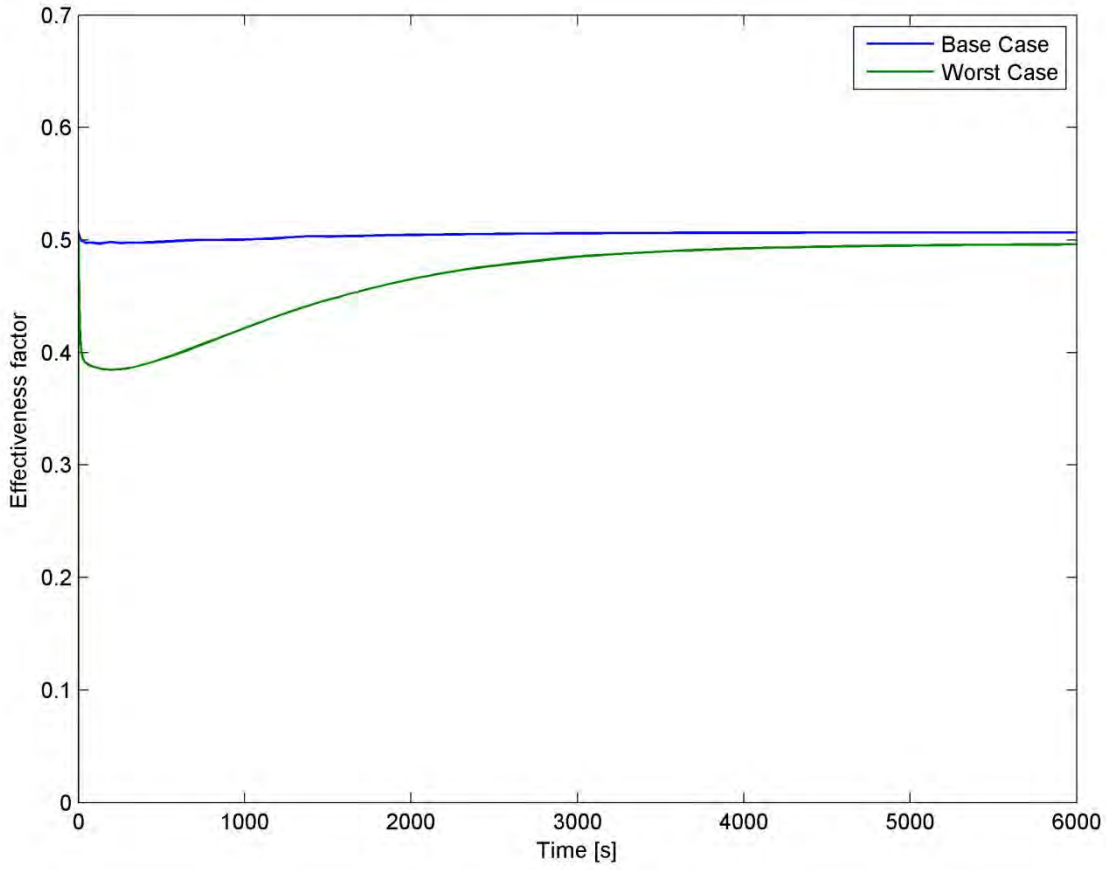

Figure 7.15: Comparison of effectiveness factor for best and worst cases

7.9 Summary

Although some of the results in the preceding sections seem to suggest that mass transfer limitations can not be ignored in growing particles, particular attention must be paid to the results of the worst case scenario. There are a number of arguments for making the assumption that mass transfer limitations will be negligible, even though Figure 7.14, the result of the worst case simulation, shows the development of significant gradients within the particle.

The macro-particle that has been simulated is significantly larger than the catalyst particles of interest, and (based on PSD data, see section 5.4.5) beyond the expected range of particle sizes for the catalyst.

In addition, the catalyst fragments are twice as large as the expected size. Data from the literature, and analysis of the SEM images of polymer particles (such as Figure 5.14 on page 77, which shows catalyst fragments well below 1μm, when already encased in polymer layers), suggests that most catalyst fragments will be significantly smaller than the 0.2μm simulated in the worst case study.

The value for macro-molecular diffusivity used in the worst case study is much smaller than typical values that would be expected, particularly given the presence of large pores and open spaces within the growing polymer particles. These pores dramatically increase the ease with which diffusion can occur within the particle, as described in the literature (McKenna et al., 1999, Wu et al., 1999, Fisch et al., 2008). The pores are also clearly visible in the SEM images of polymer particles from the kinetic study, both at the early stages of polymerisation, and later in the reaction time.

Finally, the rate of polymerisation used in the worst case study is three times higher than the rate observed in the kinetic study.

Given that the parameters used in the worst case scenario are extraordinary, it seems reasonable to assume that the overwhelming majority of growing polymer particles will experience significantly less resistance to mass transfer than the results displayed in Figure 7.14. The presence of concentration gradients within growing particles will be ignored.

The only other factor of importance is the sorption of monomer from the macro-particle onto the surface of the micro-particle. As shown in section 7.7 above, if all other parameters are at base case values, then the effectiveness factor is almost exactly equal to the sorption factor, and there are no gradients within the particles.

The effect of sorption is an indication of external mass transfer resistance; the results above suggest that this external resistance dominates, and that diffusion within the growing polymer particles is sufficiently rapid to prevent the formation of concentration gradients.

It is also expected that, under industrial conditions, the resistance to mass transfer will also be primarily in the sorption onto the surface of the microparticle. There is no reason to expect the morphology of the polymer particles to differ between the laboratory and industrial reactors.

It is therefore proposed that the kinetic parameters regressed from experimental data can be used to describe the behaviour of the Ziegler-Natta catalyst in the industrial scale model with no adjustments for mass transfer. The effects of particle size will therefore be neglected.

CHAPTER 8. COMPARISON OF POPULATION BALANCE MODEL AND SEGREGATION APPROACH

As discussed in the Literature Review, the most common method for tracking changes in distributions of properties in chemical reactors is the Population Balance Model (PBM), equation 2.4, which is reproduced below (Hulburt & Katz, 1964).

$$\frac{\partial \Psi}{\delta t} + \sum_i \frac{\delta}{\delta \alpha_i}\left(\frac{\delta \alpha_i}{\delta t}\Psi\right) = B - D \qquad 2.4$$

In equation 2.4, Ψ is the time-varying number-density of a population (of particles or fluid elements, for example) which is distributed in the properties α_i, each of which can also vary with time. The number density is defined such that $\Psi(t,\alpha_1,\alpha_2,...)\Delta\alpha_1\Delta\alpha_2,...$ is the number fraction of particles or fluid elements having properties in the ranges $[\alpha_1,\alpha_1+\Delta\alpha_1]$, $[\alpha_2,\alpha_2+\Delta\alpha_2]$… at time *t*. Size is a typical property of interest; others could be age, temperature or catalytic activity. If size were the property of interest, then the number density function, Ψ, would represent the number-based particle size distribution (PSD).

The functions *B* and *D* represent the distribution of the rates of birth and death of the members of the population. The birth and death functions are generally related to the flow of material in and out of a reactor, but can also refer to processes such as nucleation (birth) or fragmentation (death).

In order to find the distribution of n properties within a population, one must solve an $(n+1)$-dimensional Partial Differential Equation (PDE): one dimension for each property, plus one for time.

The largest drawback to applications of the PBM is the computational expense of solving the sets of partial differential equations (Ahmadzadeh et al., 2008, Alexopoulos et al., 2009). PBM-based models are unsuitable for real-time control due to this large solution time.

The proposed alternative to the PBM is the Segregation Approach (Rawatlal, 2004, Rawatlal, 2009). The Segregation Approach predicts the leading moments of a distribution, based on initial distribution and residence time distribution, as shown in equation 2.6.

$$\overline{\alpha_i} = \iint \alpha_i(\alpha_{i,0},\theta)\Psi_0(\alpha_{i,0})I(\theta)d\alpha_{i,0}d\theta \qquad 2.6$$

The Segregation Approach is numerically more efficient than the PBM, and has been applied to a range of industrial processes (Kotsiopoulos et al., 2008, Rawatlal, 2009).

However, the performance (in terms of accuracy and efficiency) of these two models has never been directly compared. This chapter describes the comparison of the Population Balance Model and the Segregation Approach, in the context of predicting the particle size distribution in an olefin polymerisation reactor.

8.1 Model development

The models developed here will predict the particle size distribution (PSD) for an olefin polymerisation reactor. The starting point is the prediction of the rate of propagation of the polymerisation reaction at the active sites, which is considered to be a microscale property. The propagation rate will be incorporated within a model for a single particle's size, which is a mesoscale level of detail. These mesoscale particle models will then be used in macroscale models which predict the PSD of the reactor contents.

8.1.1 Polymerisation propagation rate

The polymerisation propagation rate, r_p, [mol.s^{-1}], can be expressed in terms of k_p, the polymerisation rate constant [m^{3}s^{-1}mol^{-1}], $P_*(t)$, the number of moles of polymerising sites at time t [mol], and [M], monomer concentration [mol.m^{-3}], as given in equation 8.1.

$$r_p = k_p P_*(t)[M] \tag{8.1}$$

The number of active sites can be rewritten as a product of $C_{Ti,0}$, the initial concentration of sites in the particle [mol.kg^{-1}], the particle's initial mass, $m_{p,0}$, voidage, ε, density, ρ, and the fraction of sites which are active at a given time, $a(t)$, as shown in equation 8.2.

$$P_*(t) = C_{Ti,0}\frac{m_{p,0}}{\rho\varepsilon}a(t) \tag{8.2}$$

8.1.2 Single particle growth model

A single particle's mass increases as polymer is formed through the propagation reaction. Particle mass can also be affected by fragmentation and agglomeration; these effects will be ignored here as they are less significant in slurry phase reactors. The mass balance, defining the rate at which particle mass changes in a single growing catalyst/polymer particle, is expressed in equation 8.3.

$$\frac{dm_p}{dt} = k_p P_*(t)[M]MM_{mon} \tag{8.3}$$

Here, m_p is the particle mass [kg], t is particle time (or particle age in the context of a reactor) [s], and MM_{mon} is monomer molar mass [kg.mol^{-1}]. Combining equations 8.2 and 8.3, the expression for particle mass as a function of time can be simplified to equation 8.4.

$$\frac{dm_p}{dt} = Gm_p;\quad m_p(0) = m_{p,0} \tag{8.4}$$

where $m_{p,0}$ is the mass of a particle at the inlet to the reactor, before any growth has occurred, and G is the growth factor, defined as $G = \frac{k_p C_{Ti,0}}{\rho\varepsilon}[M]a(t)MM_{mon}$. This growth factor is introduced to simplify the notation.

If it is assumed that the rate constant, k_p, concentration of Ti sites, $C_{Ti,0}$, monomer concentration, [M], and active sites fraction, $a(t)$, are all constant with time, then the mass of the particle can be found in terms of the growth function, G, and the time of polymerisation, t, by solving equation 8.4 to yield equation 8.5.

$$m_p(t) = m_{p,0}(1+Gt) \tag{8.5}$$

It should be noted that the activity of the Ziegler-Natta catalyst is generally understood to vary with time, and is correlated with the oxidation state of the titanium active sites on the particle (Soga et al., 1982, Han-Adebekun et al., 1997a). In this chapter, this effect will be ignored in order to focus on particle size effects and allow for simpler comparison of the solution of the two models of interest.

By assuming perfectly spherical particles, particle size and particle mass can be related through equation 8.6.

$$m = \frac{\pi}{6} l^3 \rho \varepsilon \qquad 8.6$$

Using the relation between mass and size, and the expression for time-dependent mass (equation 8.5), the particle diameter after polymerisation time *t* can be found by equation 8.7.

$$l(l_0, t) = l_0 \sqrt[3]{1 + Gt} \qquad 8.7$$

It is important to note that l_0 is the initial size of a particle, or the size of a particle as it enters the reactor, and that equation 8.7 can be used to predict the final size of a particle for which the inlet size and polymerisation time are known.

The next step is to use this expression for a single particle's size to determine the evolution of the PSD of a population of particles which are distributed in initial size and reaction time.

8.1.3 Segregation model

The product PSD of a polymerisation reactor could be represented by the mean particle size, which can be found by using the Segregation Approach, as shown in equation 8.8.

$$\bar{l} = \iint l(l_0, \theta) f_{m,0}(l_0) I(\theta) dl_0 d\theta \qquad 8.8$$

Equation 8.8 is used to determine the mean particle size, $\bar{l}$, in terms of the mass-based initial size distribution, $f_{m,0}(l_0)$, RTD function, $I(\theta)$, and the relationship between initial size, age and current size, as developed in equation 8.7. The important factor is this alternative formulation allows for predicting the mean size without needing to find the internal particle size distribution, $f_m(l)$, as opposed to the requirements when applying the traditional PBM framework.

In the present work the equivalence of the Population Balance and Segregation models will be rigorously demonstrated. For this reason alone, the entire mass-based particle size distribution, $f_m(l)$, rather than only the mean size, will be determined. Thus a modified version of the Segregation model which will predict this full distribution is required.

This modified model will represent a worst-case scenario of the performance of the Segregation model since far more data is generated than is usually required. However, the modified model also shows the flexibility of the Segregation Approach; it can be extended to predict the same information as the PBM, but primarily lends itself to averaged properties at extremely high computational efficiencies (such as in equation 8.8).

The exit size distribution function, $f_m(l)$, and the inlet size distribution function, $f_{m,0}(l_0)$, are defined such that $f_m(l)\Delta l$ is the mass fraction of particles in the reactor in the size range $[l, l + \Delta l]$, and $f_{m,0}(l_0)\Delta l_0$ is the mass fraction of particles in the feed in the initial size range $[l_0, l_0 + \Delta l_0]$. By multiplying the fraction in that size range by the mass feed rate, $\dot{m}_{in}$, and then dividing by the mass of each of these particles, $\frac{\pi}{6} l_0^3 \rho \varepsilon$, the number of particles in the feed that are in the initial size range $[l_0, l_0 + \Delta l_0]$ can be found: $\frac{f_{m,0}(l_0)\Delta l_0 \dot{m}_{in}}{\frac{\pi}{6} l_0^3 \rho \varepsilon}$.

The fraction of particles currently in the reactor in the age range $[\theta,\theta+\Delta\theta]$ can be found in terms of the internal reactor residence time distribution $I(\theta)$, as $I(\theta)\Delta\theta$. The mass of particles that entered the reactor during this time is given by $\dot{m}_{in}\Delta\theta$. The number of particles currently in the reactor in the age range $[\theta,\theta+\Delta\theta]$ that were in the feed size range $[l_0,l_0+\Delta l_0]$ is then $\frac{f_{m,0}(l_0)\Delta l_0\dot{m}_{in}\Delta\theta}{\frac{\pi}{6}l_0^3\rho\varepsilon}I(\theta)\Delta\theta$.

The mass of each of these particles can be written in terms of the relation between current size and initial size, developed in the previous section (equation 8.7), as given in equation 8.9.

$$m_p=\frac{\pi}{6}l^3\rho\varepsilon=\frac{\pi}{6}l_o^3(1+G\theta)\rho\varepsilon \qquad 8.9$$

Multiplying the mass of each particle by the number of such particles gives the mass of all particles in the reactor, $M_{l_0,\theta}$, which, while in the feed, were in the feed size range $[l_0,l_0+\Delta l_0]$ and are currently in the age range $[\theta,\theta+\Delta\theta]$. This is given by equation 8.10.

$$M_{l_0,\theta}=(1+G\theta)f_{m,0}(l_0)\Delta l_0\dot{m}_{in}\Delta\theta I(\theta)\Delta\theta \qquad 8.10$$

Dividing by the total mass of particles then returns the mass fraction of particles of interest, $m_{l_0,\theta}$, as given in equation 8.11.

$$m_{l_0,\theta}=(1+G\theta)f_{m,0}(l_0)\Delta l_0 I(\theta)\Delta\theta \qquad 8.11$$

This function can be interrogated to determine the mass fraction of particles of size l or smaller in the reactor; this will be a cumulative distribution function. This function, which will be used to determine the exit PSD, will be referred to as the kernel for the model.

Figure 8.1 shows a typical feed size distribution, residence time distribution and kernel for this model. The feed size (a) is a normal distribution with a mean of 50μm and a variance of 8μm. Any curve whose domain runs parallel to the l_0 axis through the surface of the kernel shown in (c) displays a similar "bell-curve" shape. The residence time distribution (b) is for a CSTR with a mean residence time of 4000s. Any curve whose domain runs parallel to the θ axis through the surface of the kernel displays the form of an initial rise and then decay from the maximum. This is caused by the interaction of the linearly increasing growth term, $(1+G\theta)$, and the exponential decay of the RTD function.

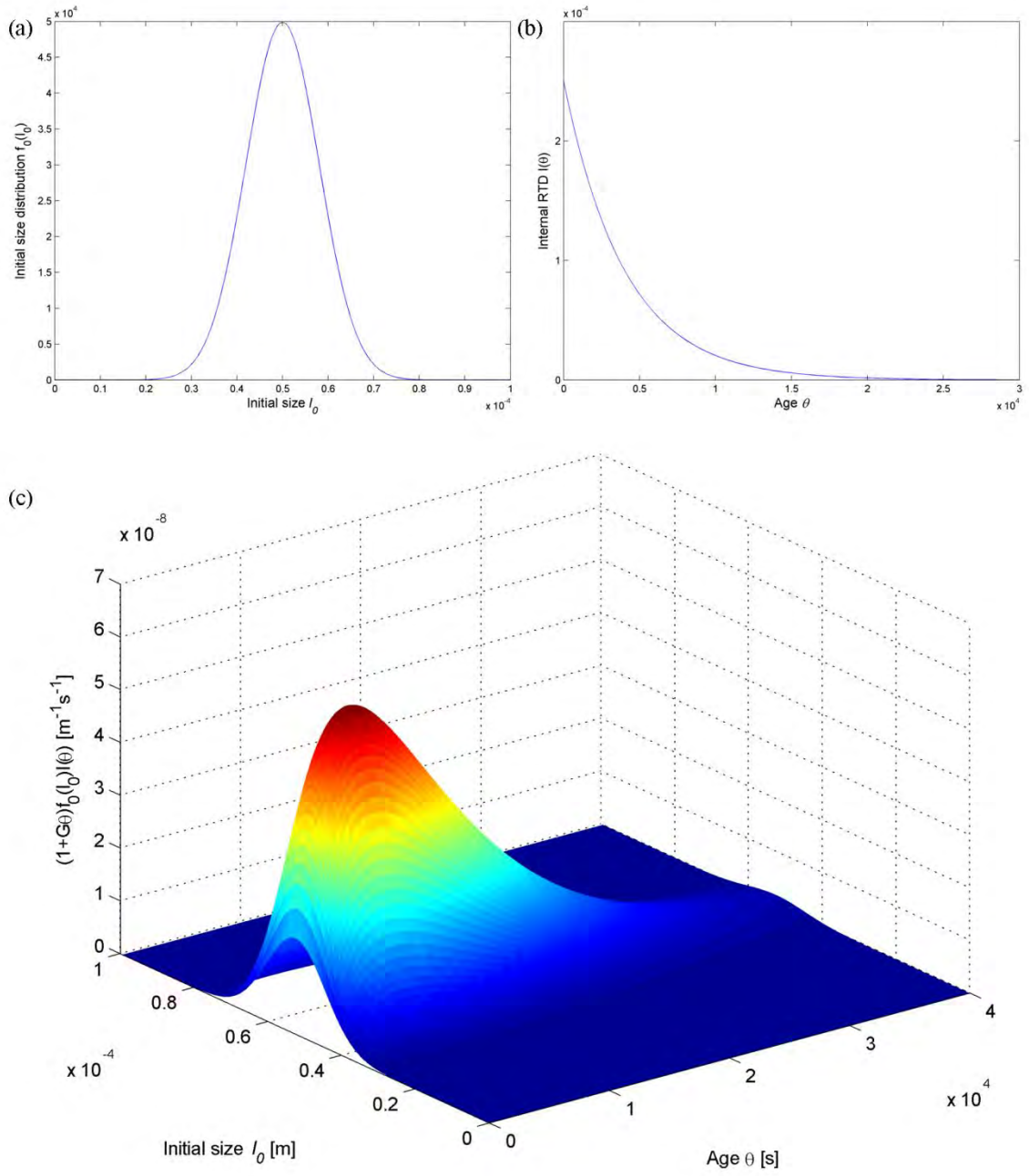

Figure 8.1: Typical inputs to the Segregation model: (a) Feed size dsitribution; (b) Residence time distribution; (c) Kernel. See text for a description of the features of these graphs.

It is therefore clear that the kernel to be integrated is of the form that should be expected from a physical understanding of the processes that it represents. The ranges of initial sizes and ages that will contribute to size l are now sought. In the absence of fragmentation, only particles which were initially smaller than size l can contribute to the mass of particles of interest. Thus only particles with initial sizes that satisfy the following inequality are of interest: $l_0 \leq l$.

Particle age is slightly more complex, due to the relationship between initial size, current size and age developed in equation 8.7. Rearranging equation 8.7 allows the age range of interest to be defined as $\theta \leq \dfrac{l^3 / l_0^3 - 1}{G}$.

By integrating across all relevant initial sizes and ages, the cumulative mass fraction, $M(l)$, can be found, as shown in equation 8.12.

$$M(l) = \int_{l_0=0}^{l_0=l} \int_{\theta=0}^{\theta=\frac{l^3/l_0^3-1}{G}} (1+G\theta) f_{m,0}(l_0) I(\theta) d\theta dl_0 \qquad 8.12$$

Differentiating the cumulative mass distribution with respect to l gives the particle size distribution, $f_m(l)$, as shown in equation 8.13.

$$f_m(l) = \frac{d}{dl} M(l) = \frac{d}{dl} \int_{l_0=0}^{l_0=l} \int_{\theta=0}^{\theta=\frac{l^3/l_0^3-1}{G}} (1+G\theta) f_{m,0}(l_0) I(\theta) d\theta dl_0 \qquad 8.13$$

Successive applications of Leibniz's Rule result in the simpler equation 8.14.

$$f_m(l) = \frac{3l^5}{G} \int_{l_0=0}^{l_0=l} f_{m,0}(l_0) I\left(\theta = \frac{l^3/l_0^3-1}{G}\right) dl_0 \qquad 8.14$$

As mentioned earlier, the explicit inclusion of the residence time distribution function, $I(\theta)$, allows the Segregation Approach to model imperfect reactor mixing or unsteady-state operation with relative ease. It is also important to note that this form of the Segregation model represents worst-case performance: rather than just predicting the mean of the distribution, as could be done using equation 8.8, the full distribution has been extracted.

An analogous expression for the Population Balance Model will now be derived.

8.1.4 Population Balance Model

The general, unsteady-state, multiple-property population balance equation (PBE) is given by equation 2.4. There are two properties of interest: size, l, and age, θ, at steady-state, so the PBE assumes the specific form shown in equation 8.15.

$$\frac{\delta}{\delta l}\left(\frac{\delta l}{\delta t}\Psi(l,\theta)\right) + \frac{\delta}{\delta \theta}\left(\frac{\delta \theta}{\delta t}\Psi(l,\theta)\right) = B(l,\theta) - D(l,\theta) \qquad 8.15$$

In the absence of nucleation, aggregation or fragmentation, the rate of birth of particles is only due to the flow of particles into the reactor in the feed stream. Similarly, particle death is due only to the flow of particles out of the reactor in the product stream.

For a perfectly mixed reactor the distribution of the rate of particle birth is simply the distribution in the feed stream, Ψ_0, divided by the mean residence time, τ. Similarly, the exit stream is assumed to have the same properties as the reactor contents and so the distribution of the rate of particle death is the distribution function, Ψ, divided by the mean residence time. The birth and death functions can then be expressed in equation 8.16.

$$B = \frac{\Psi_0}{\tau} = \frac{\delta(\theta) f_{n,0}(l_0)}{\tau}; \qquad D = \frac{\Psi}{\tau} \qquad 8.16$$

The feed distribution, Ψ_0, can be expressed as the product of the Dirac-δ function, $\delta(\theta)$, since all entering particles are assumed to be of age zero, and the number-based feed size distribution, $f_{n,0}(l_0)$. Note that the feed size distribution is number-based, since this is the basis for the PBM, in contrast with the Segregation Approach, which used a mass basis.

The dependence of particle size on age given by equation 8.7 can be differentiated with respect to age to determine the $\frac{\delta l}{\delta t}$ term in equation 8.15. The $\frac{\delta \theta}{\delta t}$ term is simply unity, as age increases at the same rate as time.

The final PBE for a steady-state perfectly mixed reactor with time-constant concentrations and activities can then be expressed as equation 8.17.

$$\frac{l_0 G}{3(1+G\theta)^{2/3}}\frac{\delta \Psi}{\delta l}+\frac{\delta \Psi}{\delta \theta}=\frac{\delta(\theta) f_{n,0}(l_0)-\Psi}{\tau} \qquad 8.17$$

This relatively simple PDE can be reduced, using the method of characteristics, to a set of ordinary differential equations.

$$\frac{d\Psi'(l_0,s)}{ds}=-\frac{\Psi'(l_0,s)}{\tau} \quad \text{for } s>0; \quad \Psi'(l_0,s=0)=\frac{f_{n,0}(l_0)}{\tau} \qquad 8.18$$

The applied parameterisation in the variable s gives $\theta = s$ and $l = l_0\sqrt[3]{1+Gs}$. The solution of equation 8.18 is the full distribution of particles within the reactor, in terms of initial size and current age. The cumulative number fraction, $N(l)$, is found from the age and initial size distribution, $\Psi'(l_0,s)$, using the same integration limits as for the Segregation model (equation 8.12). The current size distribution, $f_n(l)$, can be found by differentiating the cumulative number fraction, $N(l)$, with respect to l, as shown in equation 8.19.

$$f_n(l)=\frac{d}{dl}N(l)=\frac{d}{dl}\int_{l_0=0}^{l_0=l}\int_{s=0}^{s=\frac{l^3/l_0^3-1}{G}}\Psi'(l_0,s)\,ds\,dl_0 \qquad 8.19$$

Application of the Leibniz Rule results in the number-based PSD (equation 8.20).

$$f_n(l)=\frac{3l^2}{G}\int_{l_0=0}^{l_0=l}\frac{\Psi'\left(l_0,s=\frac{l^3/l_0^3-1}{G}\right)}{l_0^3}dl_0 \qquad 8.20$$

A comparison of equation 8.20 (PBM) and equation 8.14 (Segregation model, reproduced below) reveals the difference between the two methods: while the PBM requires the solution of a two dimensional PDE, the Segregation model only requires integration over known functions: the inlet conditions and reactor mixing characteristics.

$$f_m(l)=\frac{3l^5}{G}\int_{l_0=0}^{l_0=l}f_{m,0}(l_0)I\left(\theta=\frac{l^3/l_0^3-1}{G}\right)dl_0 \qquad 8.14$$

The Segregation model can also account for more complex kinetic systems (such as deactivating catalysts) through a simple modification of the growth function *G*. To include such properties in the PBM would require reformulation and the inclusion of additional dimensions to the PDE shown in equation 8.17, unnecessarily complicating the present efforts to compare the performance of the two models. It should be noted that incorporating this influence would cause the PBM to become an even more inefficient simulator due to the additional computational expense associated with the extra property dimension (activity). The present approach is therefore a very conservative investigation into the effectiveness of the Segregation Approach over the Population Balance.

It should also be noted that the PBM predicts the number-based PSD, and the Segregation model predicts the mass-based PSD. A method for conversion between the number- and mass-based size distributions is detailed in the Appendix (see Chapter 23 in the Appendix).

Having developed expressions for the PSD of the product of a polymerisation reactor, the Segregation and Population Balance Models can be compared through simulation.

8.2 Results and Discussion

8.2.1 Model equivalence

Before comparing computational efficiencies, it must first be established that the two methods predict the same results. Rigorously, this requires the proof that, for all possible combinations of parameter values, equation 8.20 (the PBM) and equation 8.14 (the Segregation model) predict exactly the same result.

However, for the purposes of this work, a more qualitative approach is taken: a continuous stirred tank reactor will be simulated. The simulated reactor has a mean residence time of 4000s; the feed is catalyst particles with a normal distribution of mean size 50μm and variance 8μm. The growth function, G, has a value of $3.136\times10^{-3}s^{-1}$. The values for these parameters were selected based on typical values from the experimental campaign.

The results of this simulation are shown in Figure 8.2. The dotted line represents the feed PSD described above. The solid line and points represent product stream PSD predictions of the Segregation model and PBM, respectively. Particles leaving the reactor are clearly larger than those entering the reactor, as expected. The distribution has also widened considerably, and displays a slight skew, with a long tail; this is due to the distribution of residence times used in the simulation.

It is clear that the product PSD predicted by the new Segregation model is identical to that predicted by the more established PBM ($R^2 = 1$). This equivalence has been tested by the author for various combinations of residence time and feed PSD.

It must also be confirmed that the predicted PSDs reflect reality, at least qualitatively. Figure 8.3 shows the influence of residence time on the product PSD, as predicted by the models. It is clear that a longer residence time corresponds to an increase in average particle size, as expected. A quantitative validation of the PSD model is beyond the scope of this chapter; however, it is clear that the models do qualitatively reflect the physical situation of interest.

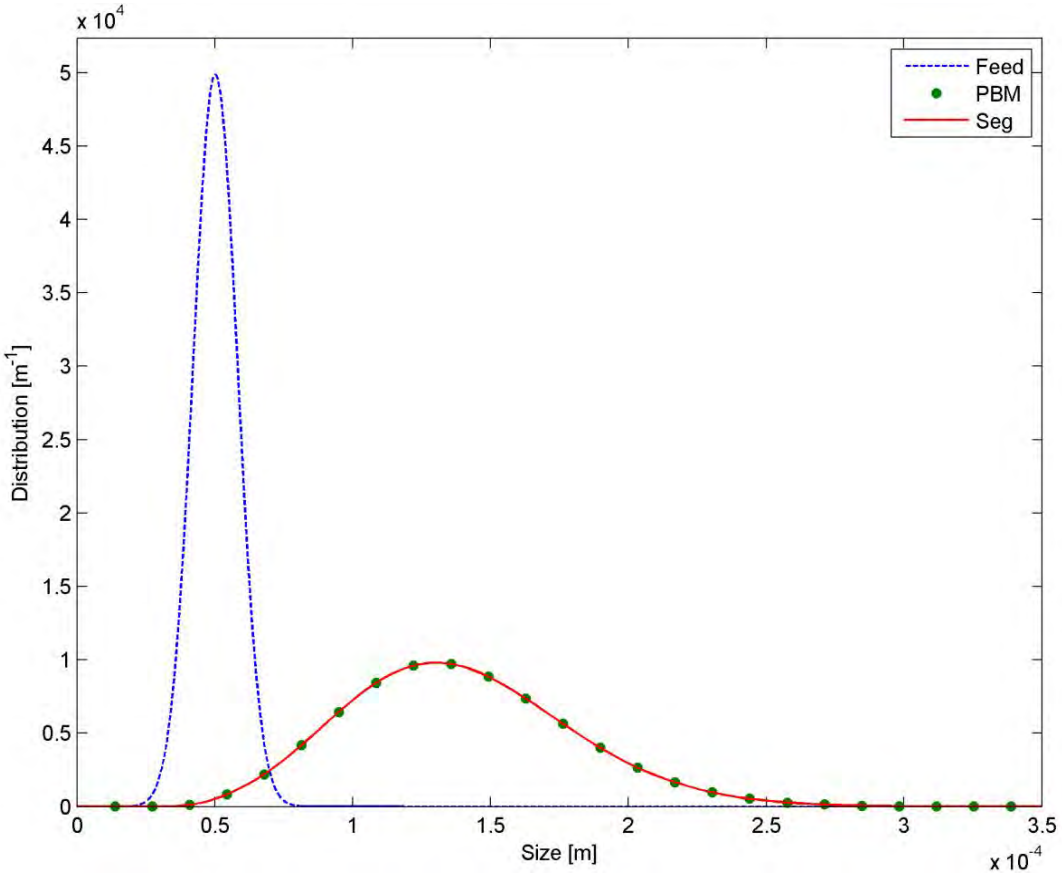

Figure 8.2: Comparison of output of Population Balance and Segregation Models

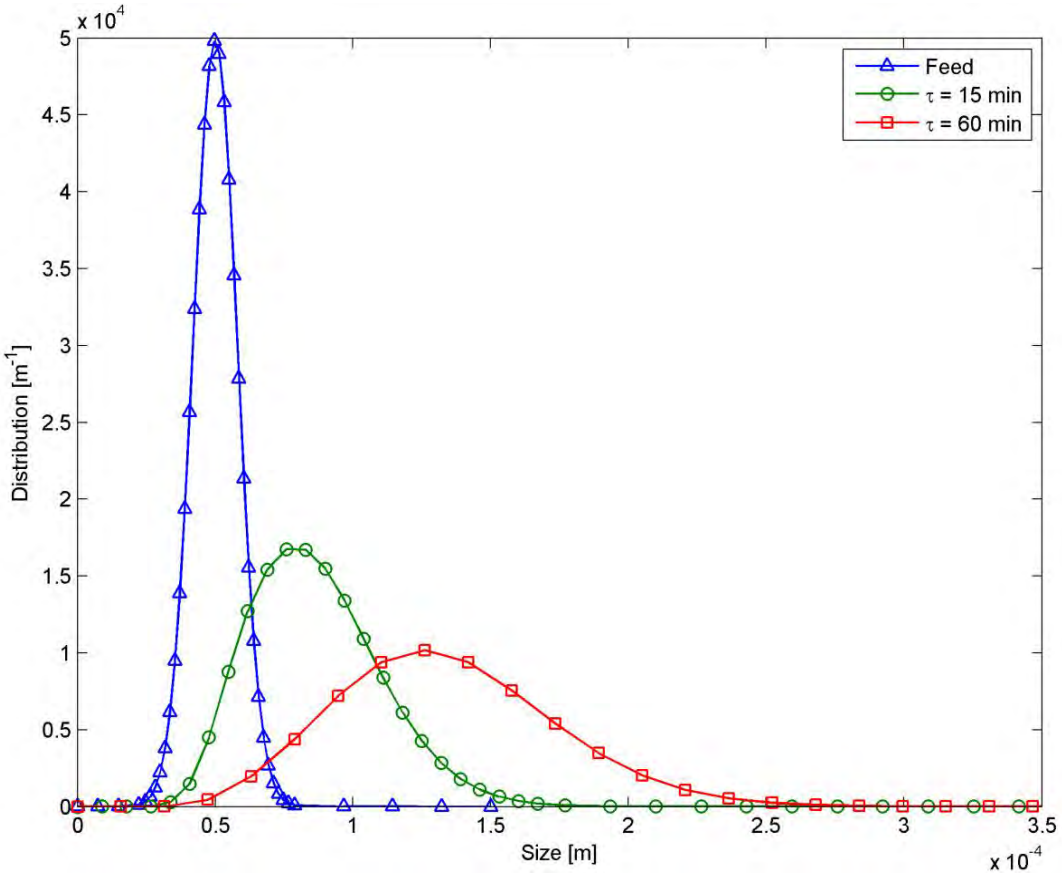

Figure 8.3: Effect of mean residence time on PSD

8.2.2 Model efficiency

Having shown (qualitative) equivalence of the results generated by the two formulations, it must be determined which model yields the more efficient simulation in terms of an eventual application in the control environment. As such, the time taken to predict the PSD must be as low as possible.

The review of the literature has already highlighted the research that has been conducted in order to find the most efficient solution to the PDEs which result from application of the PBM.

The run-times for the PBM and Segregation models are dependent on the resolution required in each of three variables: the feed PSD, which specifies the initial conditions, the age distribution, and the product PSD, which is the output. A balance must be found between resolution and efficiency: at low resolution, the models run very quickly, but accuracy is lost, while at high resolution accuracy improves, but the models can take significantly greater periods of time to converge.

Run time was determined using Matlab's built-in "tic … toc" function. Average error was quantified by comparing the prediction of each model at each resolution with a reference size distribution, PSD_{ref}, taken as the benchmark.. One reasonable proposal for PSD_{ref} is the average of the predictions of the two models at very high resolution. For a predicted distribution, *PSD*, at a resolution of an intermediate number of n points, the average error is found in terms of the reference distribution, as shown in equation 8.21.

$$\overline{error} = \frac{\sqrt{\sum_{i=1}^{n}\left(PSD(i) - PSD_{ref}(i)\right)^2}}{n} \qquad 8.21$$

Accuracy was found to be practically insensitive to resolution in the feed PSD and resolution in age distribution, and so the resolutions for the functions $f_0(l_0)$ and $I(\theta)$ were set at 250 points. The resolution in product PSD was varied between 100 and 2000 points. The benchmark, PSD_{ref}, was determined at product PSD resolution of 4000 points, and feed PSD and age distribution resolutions of 800 points. The run time and accuracy of each model were then compared (Figure 8.4).

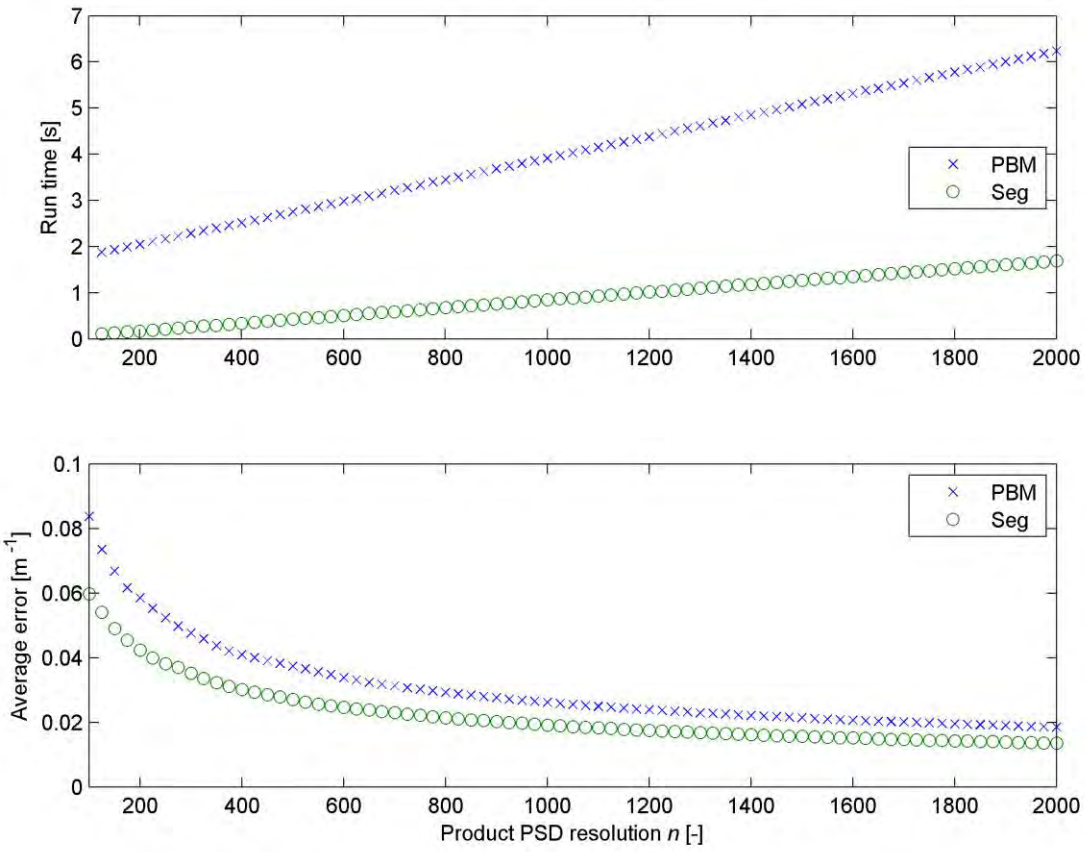

Figure 8.4: Comparison of run time and average error for Segregation and Population Balance Models

These results make clear the practical benefits of the Segregation model over the Population Balance model. Not only does the Segregation model run an order of magnitude faster, it also has a lower average error when the models are run at the same resolution.

The order of magnitude decrease in run time becomes particularly significant when considering the ultimate application of the PSD model. The Segregation model can give good accuracy even in a control environment, which requires per-second model solution times.

More importantly, the PSD is only one of several important state variable distributions that are needed to fully describe a reactor's operation, which requires all three scales of detail (micro, meso and macro). Within this larger model, particularly in order to predict unsteady-state operation, the PSD sub-module may be evaluated hundreds or thousands of times.

Industrially, polyolefins are commonly produced in multiple reactors in series. Although the results of the comparison of the PBM and Segregation Approach to multiple reactors will not be shown here, a brief discussion will show that the Segregation Approach remains more efficient.

There are two methods that could be used to apply the PBM to multiple reactors. The first option is to include additional time dimensions in the formulation of the PBM partial differential equations (equation 1). The other option is to use the PBM in series multiple times, once for each additional reactor, with different values for the parameters relating to hold up. Both of these options will severely increase the solution time of the PBM.

The Segregation Approach will require the use of a joint RTD function in order to simulate multiple reactors. This will impact on the calculations performed to set up the kernel for integration, but will not have an impact on the integration steps. There is thus a minimal effect on the computational cost of the Segregation approach.

8.3 Case study: Varying model parameters

Having demonstrated the equivalence of the Population Balance and Segregation Models, and that the Segregation model is more efficient than the PBM, model efficiency will now be investigated more rigorously. In order to optimise the code, the algorithms which offer the biggest delays must be identified. This is done by separating the calculation steps for each model into three categories:

- Numerical solution of the ordinary differential equations of equation 8.18 in the PBM (the Segregation Approach avoids the need for ODE solution),
- Interpolation and integration steps for the solution of equations 8.14 and 8.20, and
- Sundry calculation steps, such as vector initialization and distribution basis conversion.

Performing ODE solution and interpolation and integration steps requires significantly more computing power than the sundry steps; the former are measured in seconds, but the latter in milliseconds. For this reason, the investigation is limited to the impact of resolution on ODE solution and interpolation and integration processes. The results of this investigation are shown in Figure 8.5, Figure 8.6 and Figure 8.7.

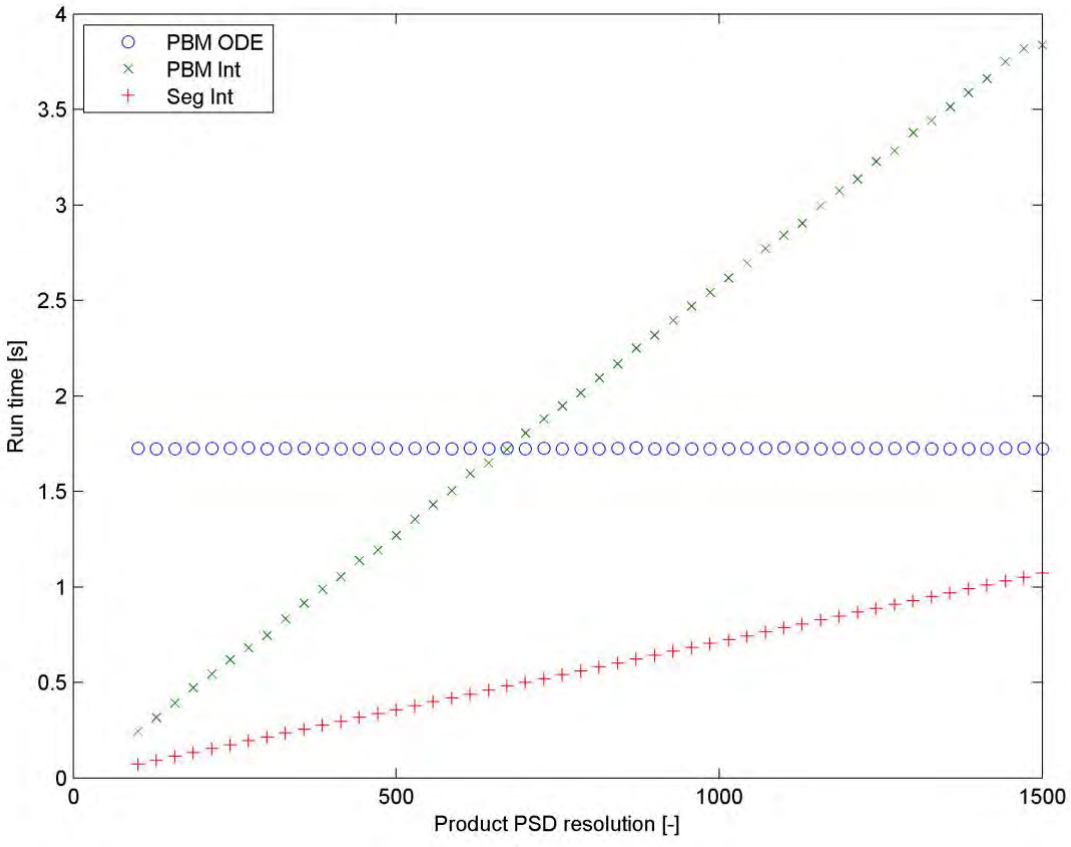

Figure 8.5: Effect of product PSD resolution on model solution

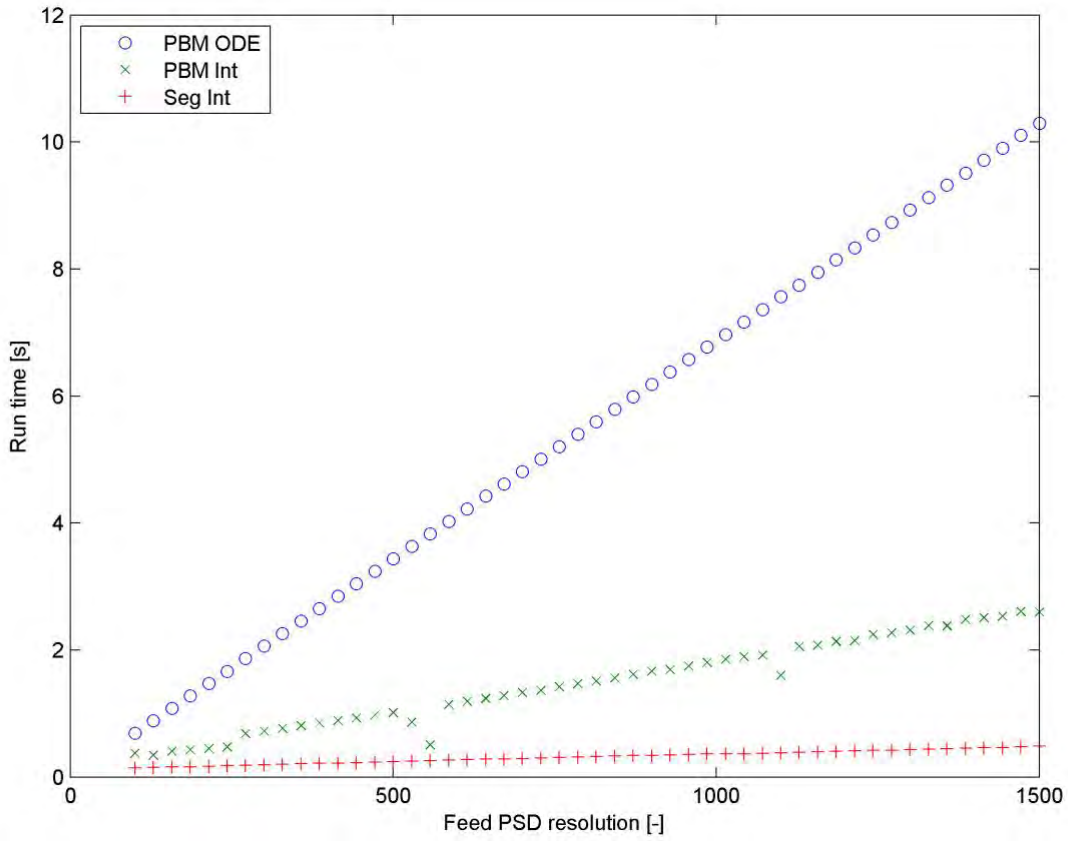

Figure 8.6: Effect of feed PSD resolution on model solution

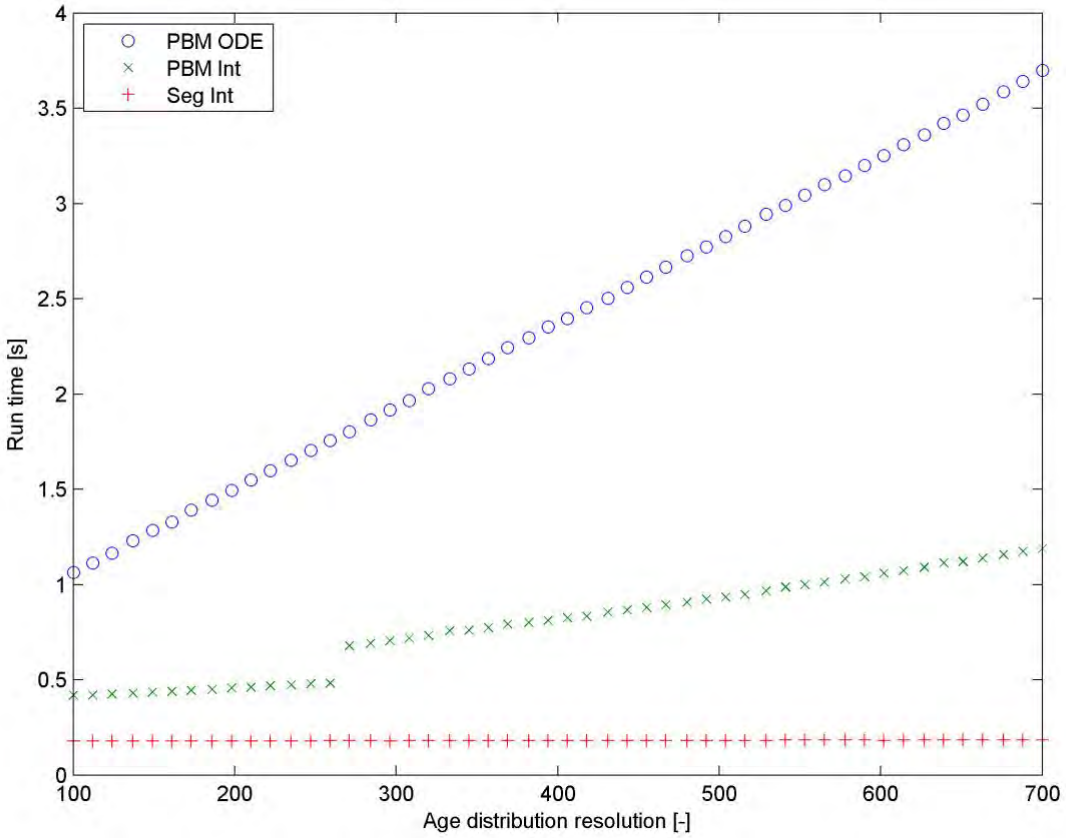

Figure 8.7: Effect of age distribution resolution on model solution

Figure 8.5 shows the effect of product PSD resolution on the solution times for the calculation steps. The clearest result from this plot is that ODE solution is independent of product PSD resolution. This is to be expected, as the solution of the ODEs in the PBM (equation 8.18) involves only the feed distribution and age variables.

The second result from Figure 8.5 is that the integration and interpolation steps for the solution of equation 8.20 (the PBM) are more sensitive to product PSD resolution than the solution of equation 8.14 (the Segregation model). This is because the interpolation for the PBM is over a two-dimensional matrix (in initial size and age), but the Segregation model requires interpolation in only one dimension (initial size).

Figure 8.6 shows how feed PSD resolution affects solution times. It is clear that the ODE solution is very sensitive to feed resolution. This is because the number of discrete ODEs in equation 8.18 is directly determined by the resolution in feed PSD.

The influence of feed resolution on interpolation and integration is slightly less than the impact of product resolution, as can be seen by comparing Figure 8.5 and Figure 8.6; however, PBM interpolation is still more sensitive than Segregation interpolation, as it is still in two dimensions.

The deviations from linearity of the results for integration and interpolation in Figure 8.6 (and Figure 8.7) are completely reproducible, and believed to be caused by interventions by switching functions in Matlab's built-in interpolation routines.

Figure 8.7 reveals the impact of resolution in age, which determines the resolution in the ODEs in equation 8.18 for the PBM, and the resolution in age distribution in equation 8.14 for the Segregation model. The ODE solution time is, as expected, sensitive to resolution in age. Interpolation in the PBM is still sensitive to age resolution, since this is one of the dimensions in the matrix over which interpolation occurs; however, interpolation in the Segregation model is independent of age resolution, since the interpolation is only in the initial size dimension.

What is clear from all three figures is that the time required for the solution of the ODEs in the PBM is always a significant contributor to the total solution time for the model. Even if the differences between the integration and interpolation steps for the two models could be eliminated, the PBM would still be significantly less efficient. By avoiding the solution of ODEs, the Segregation model gains a large computational advantage over the traditional PBM.

It should also be noted that as more complex systems are simulated, the benefits of the Segregation Approach over the Population Balance Model increase. Two typical additions to these models would be to simulate a catalyst which displays activity decay and to simulate particles which undergo fragmentation and agglomeration.

Terms relating to particle breakup and coalescence and catalyst activity profiles can be included by extending the single particle growth model. This would lead to a modified version of the expression describing particle size as a function of initial size and age (equation 8.7). Modification of the particle growth function to include activity decay is developed in the Appendix (see Chapter 24).

This extended particle size function would be evaluated only once for the Segregation model (in order to generate the kernel for numerical integration), having a minor effect on the computational requirements for this approach.

The impact on the computational cost of the PBM will be much greater, however. At best, the formulation of the PBM will not change significantly; computational cost will still increase, because this more complex function must be evaluated at each step of the numerical solution of the differential equations. At worst, the extension of the particle size function will lead to non-linear effects in the PBM equations, making their solution significantly more computationally demanding.

Since this work attempts to present a conservative comparison between the two approaches, such complexities have not been considered.

8.4 Summary

The Segregation Approach has been extended to the prediction of the particle size distribution of the population of growing polymer particles in an olefin polymerisation reactor. The Segregation model avoids the need to solve multidimensional partial differential equations, the major drawback to the currently-used Population Balance Modelling approach.

The Segregation model and PBM were applied to the same situation of a perfectly mixed reactor with a size-distributed feed and time-constant reactor conditions and catalyst properties. The two models were compared through simulation, and it was demonstrated that the Segregation model predicts the same results as the PBM. It was also shown, through comparison of run time and accuracy, that the Segregation model solves more quickly and more accurately at the same distribution resolutions.

Through further analysis of the solution steps in each model, it was shown that the PBM is less efficient than the Segregation model not only because of the required solution of a set of ODEs (avoided by the Segregation model), but also because interpolation steps are performed over two-dimensional matrices in the PBM, and only one-dimensional matrices for the Segregation model.

The Segregation Approach has been demonstrated to be considerably more computationally efficient than the Population Balance Approach due to differences in formulation.

The obvious benefits of the Segregation Approach over the Population Balance Model answer one of the key questions of this thesis. The Segregation Approach will therefore be used as the mathematical basis for the further development of an unsteady-state reactor model.

CHAPTER 9. NON-IDEAL REACTOR MIXING

In the previous chapter, the computational efficiency of the Segregation Approach and Population Balance Model (PBM) were compared, and the superiority of the Segregation Approach demonstrated in a comparison that favoured the PBM.

It was also mentioned in the Literature Review that the Segregation Approach is significantly more flexible and easy to implement, again due to differences in formulation. This applies particularly to the simulation of complex reactor mixing patterns through the explicit inclusion of the residence time distribution (RTD) in the Segregation Approach, as shown in equation 2.6 (reproduced below).

$$\overline{\alpha_i} = \iint \alpha_i\left(\alpha_{i,0},\theta\right)\Psi_0\left(\alpha_{i,0}\right)I\left(\theta\right)d\alpha_{i,0}d\theta \qquad 2.6$$

The first two functions under the double integral in equation 2.6 depend on reaction kinetics, particle properties and initial conditions, and have been discussed and analysed in detail in the preceding sections. The third function under the integral is the Residence Time Distribution (RTD) function, which depends only on macro-scale phenomena feed and product flow rates and reactor mixing patterns. This chapter focuses on the RTD function and its role in the Segregation Approach and reactor simulation.

In order to apply the lab-scale, batch reactor data to the industrial reactor, hydrodynamic models will be required, based on an understanding of the physical structure of the reactor itself. Since the industrial reactor is a continuous, stirred tank reactor (CSTR), the first approach will be to use the RTD for an ideal CSTR. It is likely, however, that the mixing within the reactor will not perfectly match the ideal CSTR model, and so other approaches will be required.

As described in the Literature Review, there are standard methods for using RTD functions to describe non-ideal reactor mixing patterns (Danckwerts, 1953, Levenspiel, 1999, Fogler, 2005), including the use of compartmentalisation models, which simulate a real reactor as some combination of ideal reactors, recycles and bypasses in a network.

This compartmentalisation approach has been applied to the nuclear industry, where particularly complex, computer-generated RTD models are developed to fit the experimental residence time distributions determined from tracer studies of air-flow networks (Laquerbe et al., 2001a, Laquerbe et al., 2001b, Hocine et al., 2008). The computer-generated RTD models are empirical, rather than fundamental, relying on non-linear integer-based minimisation techniques.

The discretisation of real reactors into ideal reactors has also been applied in the polymerisation field, with PBM-based approaches to investigate PSD and product properties (Ashrafi et al., 2012, Krallis et al., 2015).

In this chapter, we seek to develop a fundamental RTD model that will describe the industrial reactor setup. This model development is described in the following section.

9.1 RTD function for CSTR with PFR recycle

The reactor of interest is an 80m^3 stirred tank, with jacketing and an external cooling loop to remove heat from the reactor. Because of this external loop, the mixing characteristics of the industrial reactor will resemble those of a CSTR with a PFR recycle stream. This may cause significant deviations from the RTD of an ideal CSTR.

The mathematical development of the RTD function to describe a CSTR with a PFR recycle is shown in the Appendix (see Chapter 25 on page 376). The result of this development, the external RTD function for the system of interest, is given in equation 9.1.

$$E(t) = \frac{\sum_{X=0}^{n} \frac{1}{X!}\left(\frac{1}{\tau_C}\frac{\nu_P}{\nu_C}\right)^X (t - X\tau_P)^X \exp\left(-\frac{t - X\tau_P}{\tau_C}\right)}{\tau_C \frac{\nu_C}{\nu_C - \nu_P}} \qquad 9.1$$

$$n = \left\lfloor t/\tau_P \right\rfloor$$

The mean residence time of the RTD function described by equation 9.1 is shown in equation 9.2.

$$\tau = \frac{V_C + V_P}{\nu_F} \qquad 9.2$$

9.1.1 Normalised residence time distribution function

A more useful form of the RTD function is the normalised RTD, which is defined in terms of normalised age, Θ. The formal relationship between the RTD ($E(t)$) and normalised RTD functions ($E(\Theta)$) is given in equation 9.3.

$$\Theta = t/\tau$$
$$E(\Theta) = \tau E(t) \qquad 9.3$$

To further allow for comparisons between this new RTD model and other RTD functions, we will also define two other terms: the flow fraction, f_f, defining the recycle ratio, and the volume fraction, f_v, defining the fraction of total volume accounted for by the PFR, as shown in equation 9.4. These fractions succinctly specify the flow rates and volumes in the system, removing the need for the terms ν_P, ν_C, V_P, V_C, τ_P and τ_C.

$$f_f = \frac{\nu_P}{\nu_C}$$
$$f_v = \frac{V_P}{V_C + V_P} \qquad 9.4$$

The normalised RTD function can then be expressed by equation 9.5, in terms of normalised age, Θ, and the two fractions defined above.

$$E(\Theta) = \frac{\sum_{X=0}^{n} \frac{1}{X!}\left(\frac{f_f}{(1-f_v)(1-f_f)}\right)^X \left(\Theta - X\frac{f_v(1-f_f)}{f_f}\right)^X \exp\left(-\frac{\Theta - X\frac{f_v(1-f_f)}{f_f}}{(1-f_v)(1-f_f)}\right)}{(1-f_v)} \qquad 9.5$$

$$n = \left\lfloor \Theta \Big/ \frac{f_v(1-f_f)}{f_f} \right\rfloor$$

A comparison of the standard RTD for an ideal CSTR with a typical RTD for a CSTR with a PFR recycle is shown in Figure 9.1, for $f_f = 0.25$ and $f_v = 0.5$.

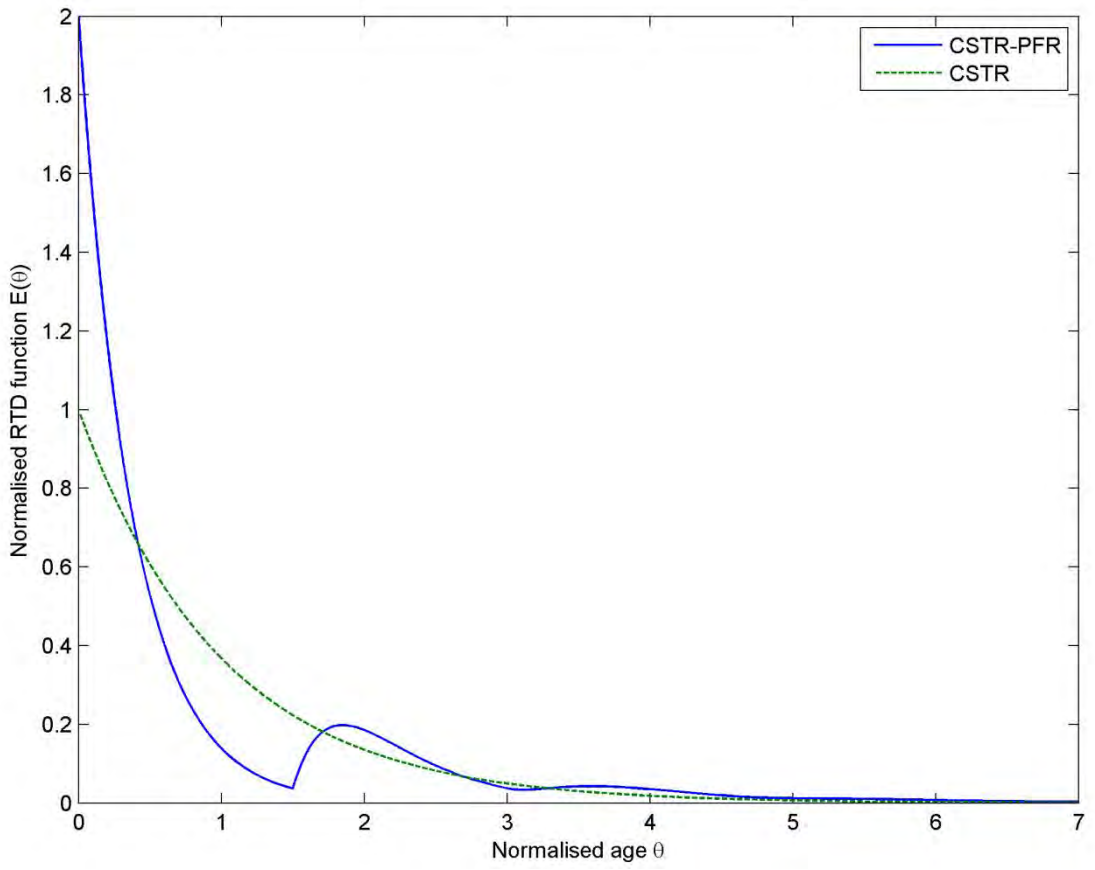

Figure 9.1: Comparison of standard CSTR RTD with new RTD model

The RTD for the CSTR with PFR recycle displays a periodic nature, as the delayed output from the recycle stream once again enters the CSTR section of the reactor. The fluctuations occur every 1.5 age units, since the period of the fluctuations is determined by the relative residence time of the PFR. The mean residence time of the PFR depends on both f_f and f_v, as shown in equation 9.6.

$$\tau_P = \tau \frac{f_v\left(1-f_f\right)}{f_f} \qquad 9.6$$

The intercept with the y-axis for the CSTR-PFR model is determined only by the relative volumes of the PFR and CSTR, summarised by the factor f_v, shown in equation 9.7. In Figure 9.1, the intercept is at 2; as the relative volume of the PFR increases, a greater fraction of the fluid is considered to spend zero time in the CSTR segment of the system before exiting the system, thereby increasing the value of the intercept on the y-axis.

$$E(0) = \frac{1}{\left(1-f_v\right)} \qquad 9.7$$

There are three major applications for a fundamental equation for the RTD of a CSTR with a PFR recycle:

- As a tool to investigate the impact of different recycle ratios on a CSTR with an external loop, such as the reactor being investigated in this thesis;
- As a tool to investigate the influence of the addition of a PFR recycle stream on the RTD of an existing CSTR; and
- As a discrete addition to computer-generated networks of ideal reactor models, such as those used in the nuclear industry, to reduce the number of parameters to be fitted in the non-linear integer minimisation problems.

The performance of the normalised RTD model in equation 9.5 will be briefly investigated in two case studies.

9.1.2 Case Study 1: Behaviour of CSTR with external loop

The first application for the new RTD model will be to the industrial reactor of interest. The stirred tank reactor has a volume of 80m^3, and a feed flow rate of approximately 0.01m^3/s. Exact data for the cooling loops is not available, but estimates from plant visits put the diameter of the cooling tubes at between 15 and 20 cm, and the total length between 50 and 75m. This puts the volume of the PFR section at between 0.88 and 2.36m^3.

In terms of the nomenclature of equation 9.5, the volume fraction in the PFR is therefore between 0.01 and 0.03.

Aside from the potential changes to the RTD functions for the reactor, the effect of the PFR recycle on the average catalyst activity will be investigated. The lumped site transformation rate constants, to define the active fraction of the catalyst, will have the same values as in the mass transfer study previously described; these values are reproduced below in Table 9.1. The activity profile associated with these parameters is shown in Figure 9.2.

The average catalyst activity can be calculated using the Segregation Approach, as shown in equation 9.8.

$$\bar{a} = \int a(\Theta)E(\Theta)d\Theta \qquad 9.8$$

Table 9.1: Site transformation rate constant values for RTD study

Parameter	Value	units
$\beta^{4+,3+}$	1.88×10^{-3}	s^{-1}
$\beta^{3+,d}$	1.06×10^{-3}	s^{-1}
$\beta^{d,3+}$	8.63×10^{-5}	s^{-1}

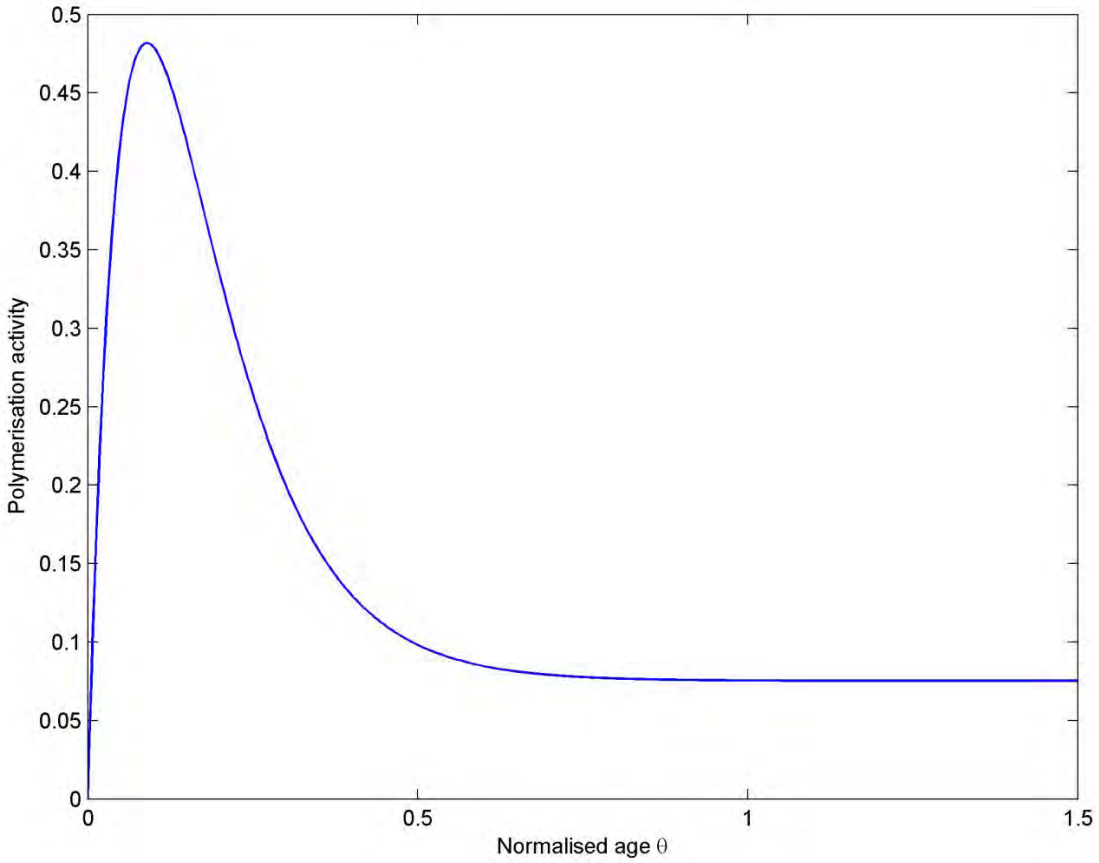

Figure 9.2: Catalyst activity profile for RTD study

The normalised RTD functions for a CSTR with a PFR recycle, for a range of recycle ratio (f_f) values, are shown in Figure 9.3 and Figure 9.4, for the two values of f_v. The average activities for all values of f_f and f_v are shown in Figure 9.5.

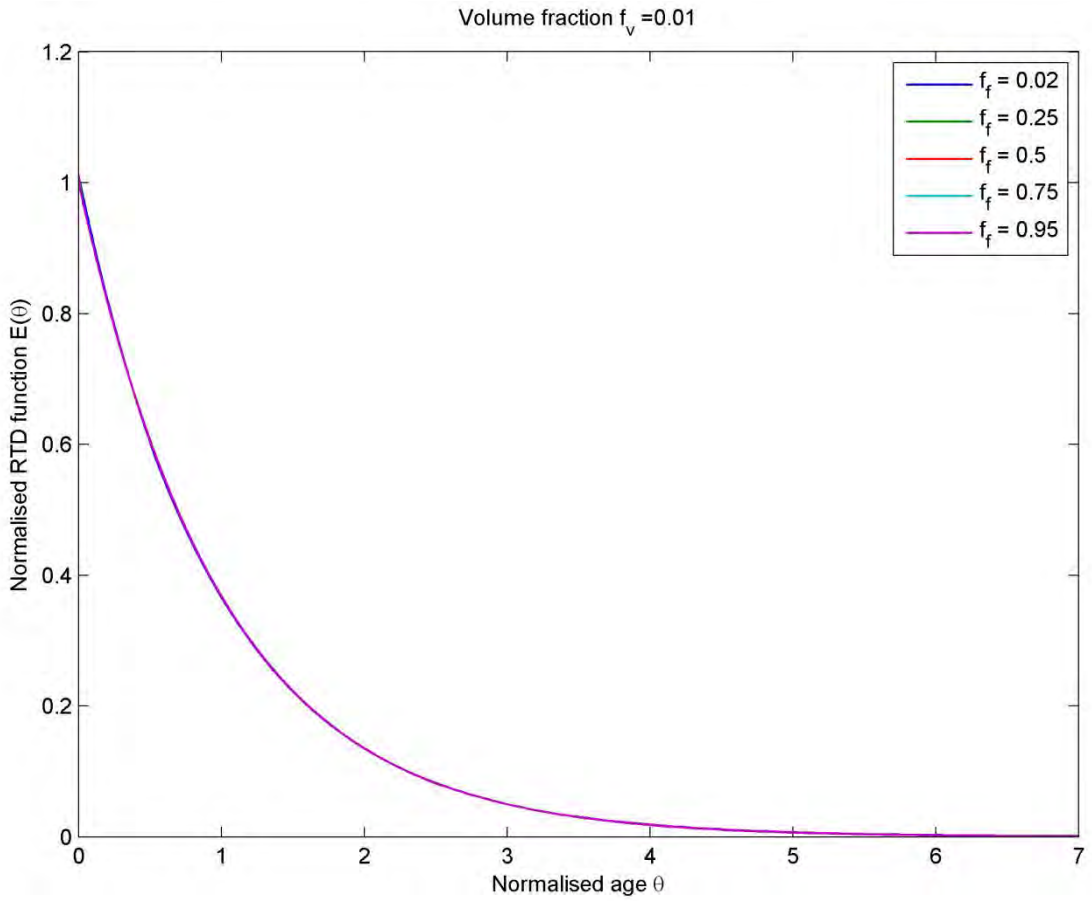

Figure 9.3: Normalised RTD function for f_v = 0.01

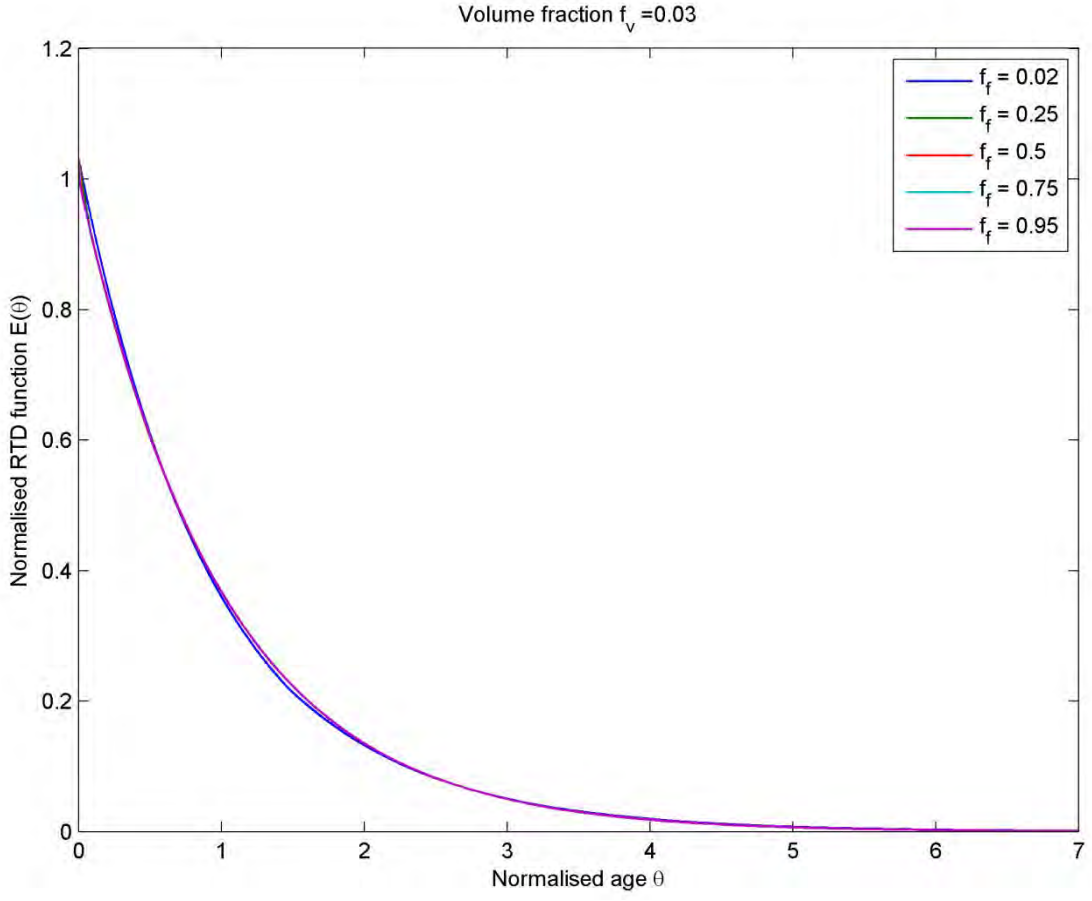

Figure 9.4: Normalised RTD function for f_v = 0.03

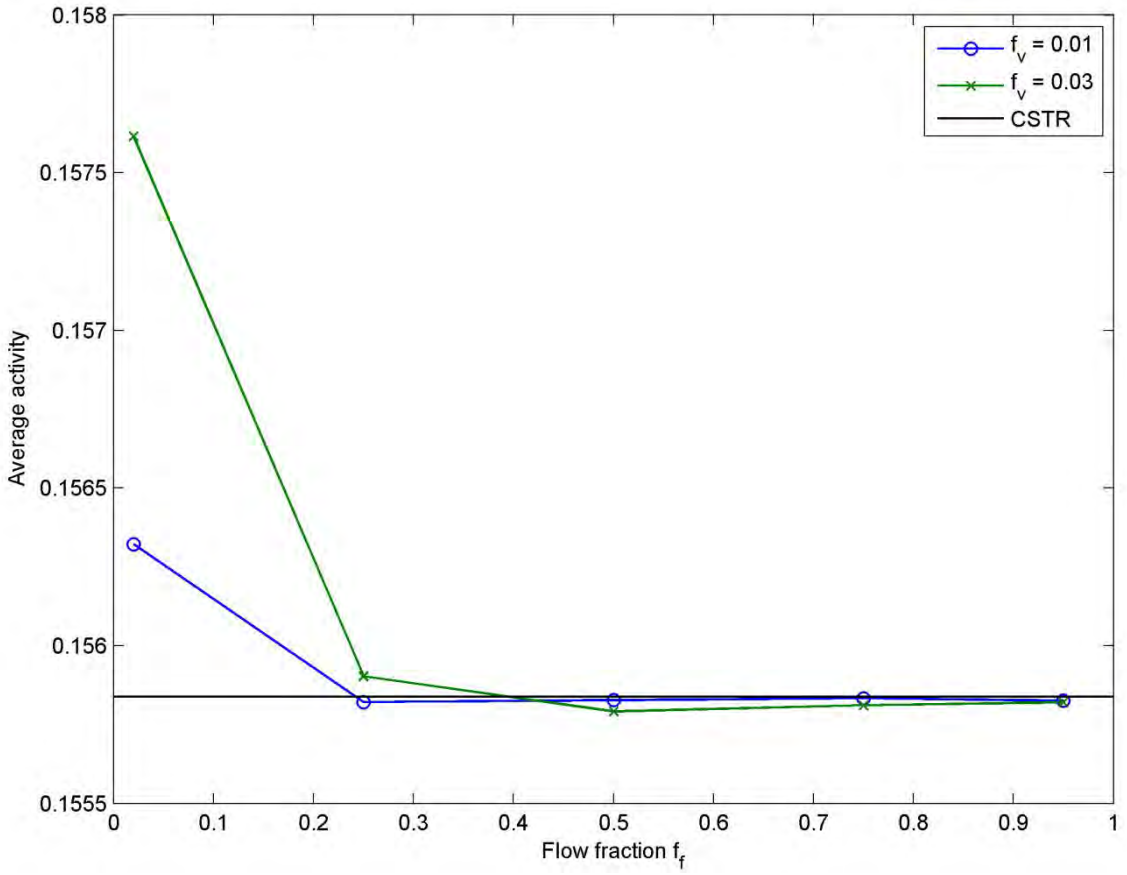

Figure 9.5: Average catalyst activity for low values of f_v

Inspection of Figure 9.3 and Figure 9.4 suggests that the PFR recycle, regardless of the actual dimensions of the cooling loop (within the bounds of the best-guesses defined above), and irrespective of the flow rate diverted through the cooling loop, has no significant impact on the RTD function of the reactor system: the RTD curves shown in those figures are almost identical to the RTD for an ideal CSTR, such as that shown in Figure 9.1. If the residence time distribution were the only factor of interest, then it would appear that the addition of a relatively small PFR recycle to a relatively large CSTR (such as simulated here) has no effect.

However, the catalyst used in such a reactor has a complex and time-varying activity profile, as described in the previous chapters, and so the impact of small changes in the RTD on the average activity must be investigated. The result of this investigation is shown in Figure 9.5, in which the average activity of the catalyst for various values of f_f and f_v is compared to the average activity that would occur in an ideal CSTR, with no recycle stream.

The average activities are slightly higher for the simulations with very low recycle ratios ($f_f = 0.02$), but for the larger values of recycle ratio ($f_f > 0.25$) there is almost no effect. For the small values of the PFR volume ($f_v = 0.01$ and $f_v = 0.03$), it is only at very small recycle ratios that the residence time of the PFR is sizeable and has an effect on the residence time distribution of the reactor system.

Larger values of the recycle ratio mean that the PFR has such a low residence time that fluid elements passing through it have almost no additional age when compared to fluid elements that do not pass through the PFR. This effect is illustrated in Figure 9.6, in which it can be seen that the RTD functions for high f_f values very rapidly converge with the RTD function for an ideal CSTR.

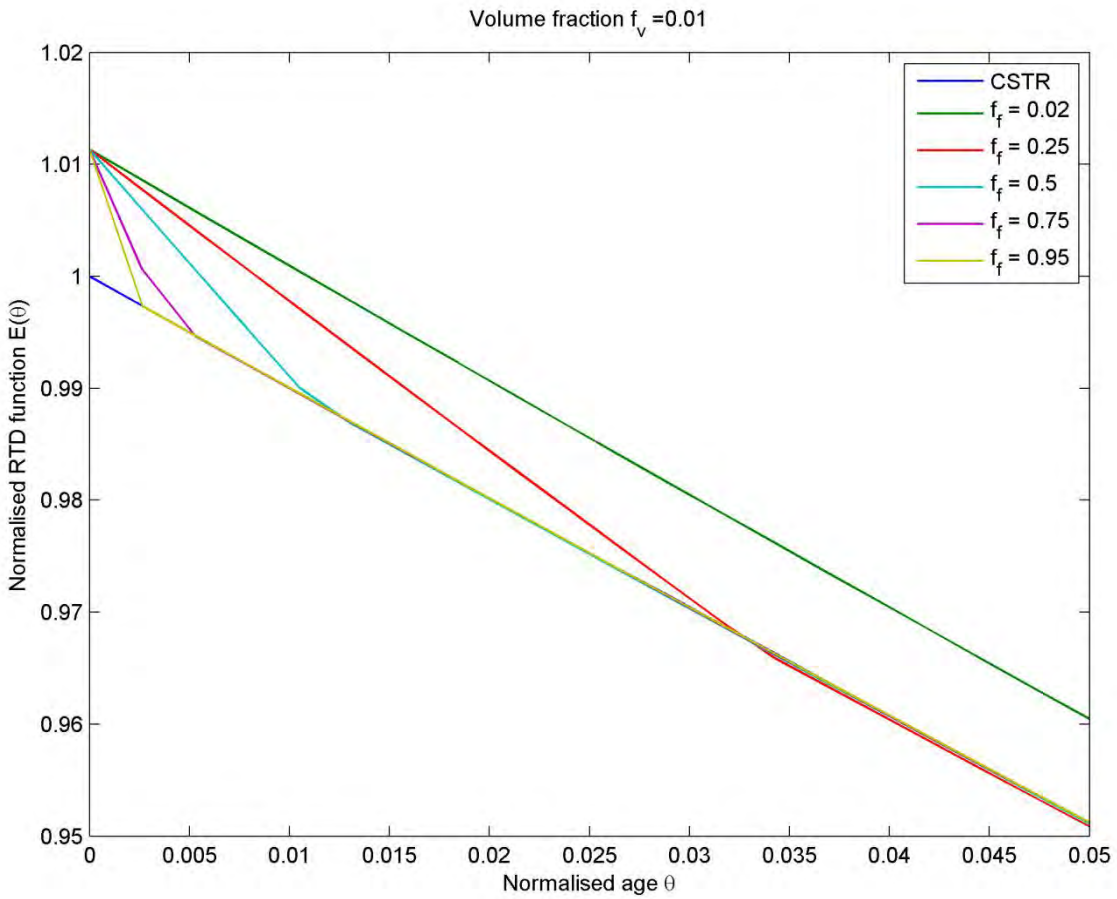

Figure 9.6: Zoomed comparison of RTD values

Depending on how quickly the RTD function for a CSTR-PFR system converges with that of an ideal CSTR, there can be an impact on the average activity, since the largest fraction of active catalyst particles occur at a normalised age of $\Theta < 0.25$, as shown in Figure 9.2. When the effect of a PFR recycle is to increase the fraction of fluid elements with a normalised age of $\Theta < 0.25$, then the average activity will increase. This occurs only for very low recycle ratios in the current case study, since the volume fraction of the PFR is very low.

For the reaction system of interest, it seems unlikely that the recycle ratios in the cooling loops would be as low as those required by the simulations to have an impact on the average activity. We must thus conclude that, for the industrial reactor of interest, there is a negligible impact on either the residence time distribution or the average activity of the catalyst. The RTD model developed in this chapter is therefore of no further direct use in attempting to develop a model of the industrial reactor.

Despite this, the impact of a PFR on a CSTR remains a topic of more general interest, and will be investigated for a wider range of values in the second case study below.

9.1.3 Case Study 2: Impact of addition of PFR recycle to existing CSTR

In this case study, the results of the previous study will be extended to include a wider range of values of f_v, in order to simulate the impact of the addition of a PFR recycle to a CSTR. An upper limit for of $f_v = 0.5$ has been imposed, since a recycle PFR with a volume greater than the volume of the CSTR it is associated with seems nonsensical. The same range of f_f values as in the previous case study will be investigated.

The normalised RTD functions for f_v values of 0.2, 0.35 and 0.5 have been computed, and compared with the RTD of an ideal CSTR, in Figure 9.7, Figure 9.8 and Figure 9.9.

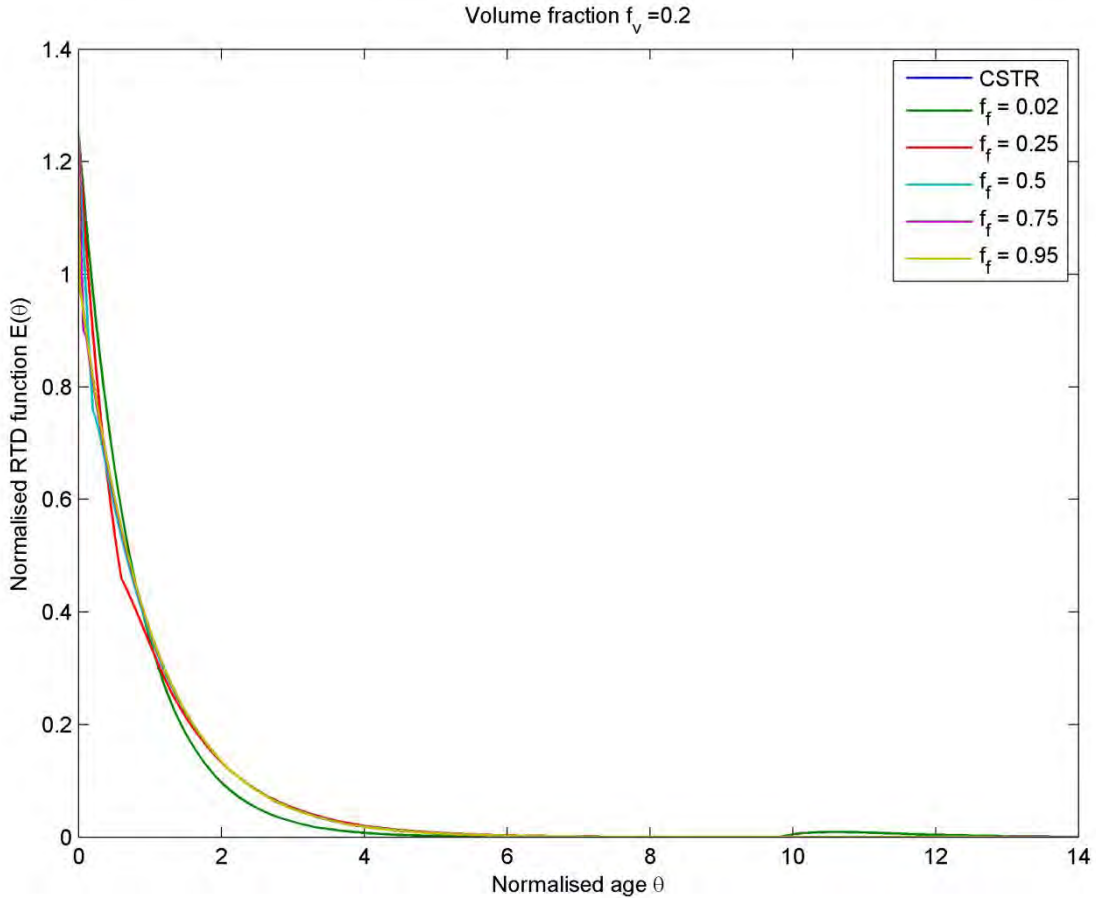

Figure 9.7: Normalised RTD for $f_v = 0.2$

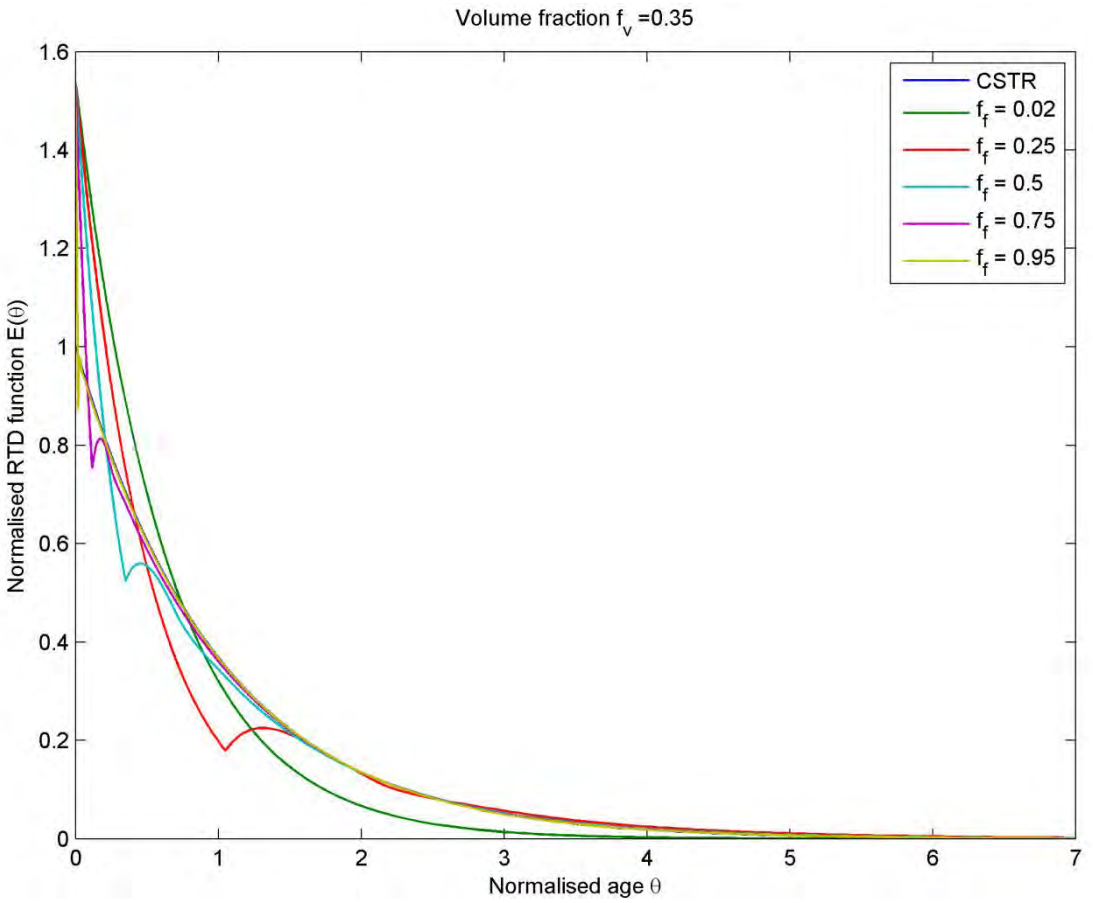

Figure 9.8: Normalised RTD for f_v = 0.35

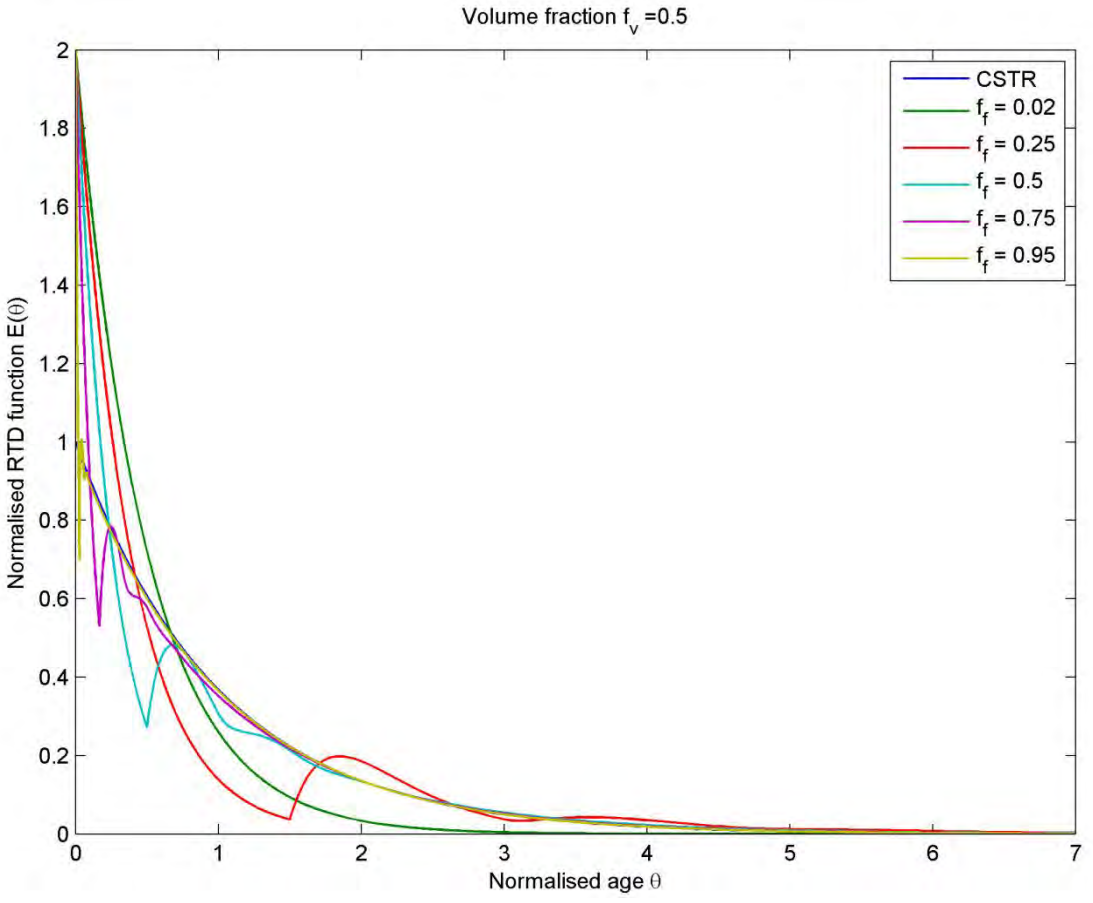

Figure 9.9: Normalised RTD for f_v = 0.5

The RTD functions in Figure 9.7, Figure 9.8 and Figure 9.9 show a range of periodicities as a result of the delay effect of the PFR recycle. The periods of these fluctuations is defined by equation 9.6.

The upper extreme is a period of $\Theta = 9.8$ for the case of $f_f = 0.02$ and $f_v = 0.2$, where a small peak is visible on the extreme right of Figure 9.7. The other two cases where $f_f = 0.02$ ($f_v = 0.35$ and $f_v = 0.5$) have periods of $\Theta = 17.15$ and $\Theta = 24.5$, respectively, by which time the RTD function has long died away to zero.

The lower visible extreme is a period of $\Theta = 0.0184$, visible in the initial rapid oscillation of the case for $f_f = 0.95$ and $f_v = 0.35$ in Figure 9.8.

This range of different oscillations interacts with the activity profile of the catalyst (from the previous case study, see Figure 9.2) to produce different average activities, depending on whether the peaks in the RTD curves intersect with the areas of highest activity for the catalyst. The average activities resulting from the RTD functions and the activity profile are shown in Figure 9.10, and compared with the average activity of an ideal CSTR.

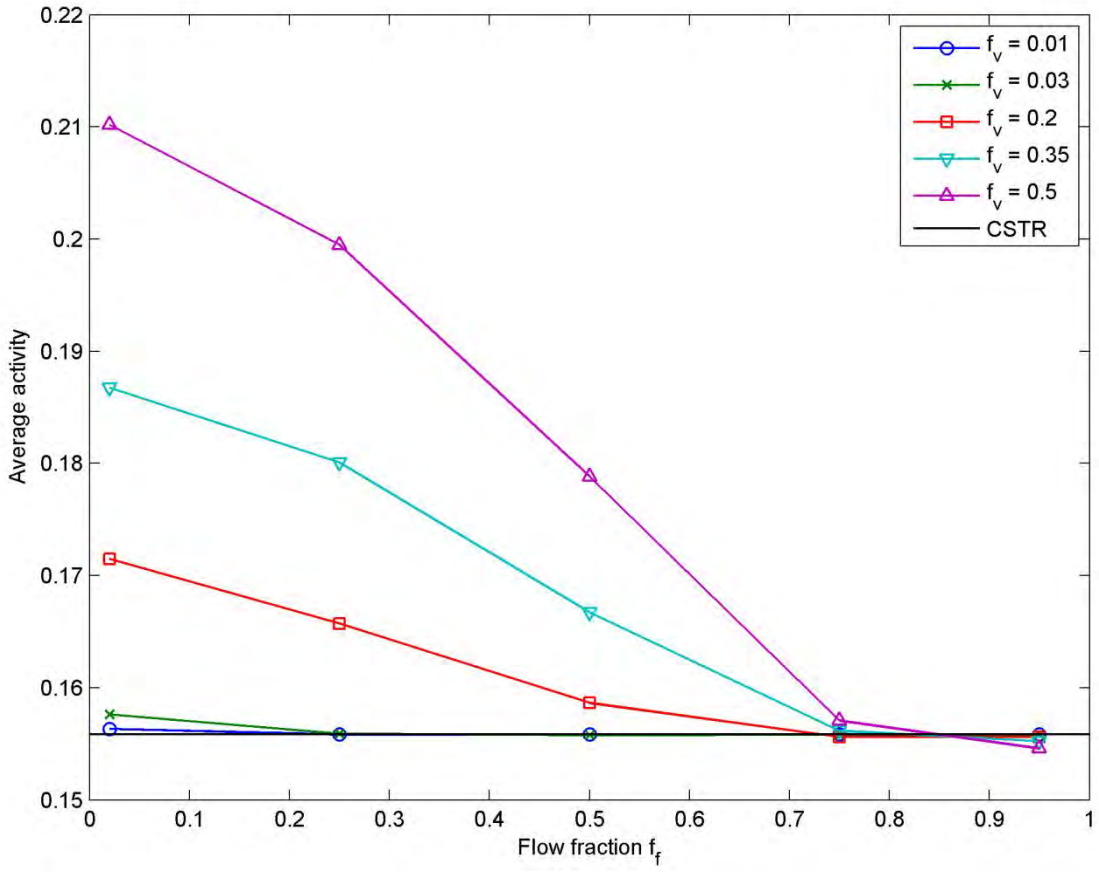

Figure 9.10: Average catalyst values for all values of f_v

Just as in the previous case study, the average activity for each volume fraction decreases with increasing recycle ratio, until at very high values for f_f the average activity is almost identical to the activity expected in an ideal CSTR reactor. The same reasoning applied in the previous section to explain this phenomenon is applicable here: a low recycle ratio causes an increase in the fraction of fluid particles that have ages in the range $\Theta < 0.25$, which is when the catalyst is most active.

The clear difference visible in Figure 9.10 (when compared to Figure 9.5) is that the impact on average activity can be quite significant, with increases of up to 35% in the extreme case. This effect is significant, and could be important if a new polymerisation reactor with sizeable recycle cooling loops were being designed, or when the flow rate in cooling loops is very low.

9.2 Summary

A new model of the residence time distribution of a continuous stirred-tank reactor with a plug flow reactor recycle has been developed, and the impact of this PFR recycle on the RTD of the original reactor analysed in two case studies.

The first case study showed that the RTD model developed has no direct applications to the current project, since the PFR recycle is too small to have any significant impact on the RTD or average activity of the reactor of interest.

The second case study clearly demonstrated that the presence of a PFR recycle with a volume that is a significant fraction of the associated CSTR can have a significant effect not only on the RTD of the reactor system, but can also have significant and interesting interactions with the reactions themselves. In this case, the activity of a Ziegler-Natta catalyst was shown to be susceptible to the configuration of the reactor system, and this effect must be taken into account when reactors are being designed, particularly when the cooling loops have a large volume and/or low flow rate.

CHAPTER 10. DYNAMIC REACTOR MODELLING

In the previous sections, it has been shown that the kinetic parameters from the experimental study can be applied to industrial conditions, and that the Segregation Approach provides the most efficient mathematical basis for simulating the evolution of distributions in a reactor. The next step is the extension of the previous developments to be suitable for dynamic reactor modelling.

In particular, the modelling approaches in the kinetic study were designed to predict the activity of the catalyst and formation of chain length distributions for a steady-state situation. The activity model and polymer property prediction must be extended to the unsteady-state case.

A brief summary of the RTD function for a perfectly mixed reactor must be given, since this formulation will provide the primary method of investigating the dynamic operation of the industrial reactor.

Finally, an algorithm of the reactor model will be presented, integrating the various models that have been developed in the preceding chapters.

10.1 Catalyst activity

In the kinetic study, a set of differential equations was proposed to describe the changes in catalyst site oxidation state as a function of the lumped site transformation rate constants, $\beta_{st}^{q,r}$, as shown in equations 2.3, reproduced below.

$$\begin{aligned}
\frac{dP_*^{4+}}{dt} &= -\beta_{st}^{4+,3+} P_*^{4+} \\
\frac{dP_*^{3+}}{dt} &= \beta_{st}^{4+,3+} P_*^{4+} - \beta_{st}^{3+,2+} P_*^{3+} + \beta_{st}^{2+,3+} P_*^{2+} \\
\frac{dP_*^{2+}}{dt} &= \beta_{st}^{3+,2+} P_*^{3+} - \beta_{st}^{2+,3+} P_*^{2+} \\
P_*^{4+}(0) &= 1;\ P_*^{3+}(0) = P_*^{2+}(0) = 0
\end{aligned} \qquad 2.3$$

For steady-state conditions, there was a relatively simple solution to the differential equations. The fraction of catalyst sites in a state of potential polymerising activity can be predicted as a function of age, $P_*^{3+}(\theta)$, using equation 4.2, reproduced here from the previous chapter.

$$P_*^{3+}(\theta) = \alpha + \gamma \exp\left(-\beta_{st}^{4+,3+}\theta\right) + \delta \exp\left(-\left(\beta_{st}^{3+,2+} + \beta_{st}^{2+,3+}\right)\theta\right) \qquad 4.2$$

Where:

$$\alpha = \frac{\beta_{st}^{2+,3+}}{\beta_{st}^{3+,2+} + \beta_{st}^{2+,3+}}$$

$$\gamma = \frac{\beta_{st}^{2+,3+} - \beta_{st}^{4+,3+}}{\beta_{st}^{4+,3+} - \beta_{st}^{3+,2+} - \beta_{st}^{2+,3+}}$$

$$\delta = \frac{\beta_{st}^{4+,3+}\beta_{st}^{3+,2+}}{\beta_{st}^{4+,3+}\beta_{st}^{3+,2+} + \beta_{st}^{4+,3+}\beta_{st}^{2+,3+} - 2\beta_{st}^{2+,3+}\beta_{st}^{3+,2+} - \left(\beta_{st}^{3+,2+}\right)^2 - \left(\beta_{st}^{2+,3+}\right)^2}$$

In an industrial reactor that is not operating at steady-state, the active fraction of catalyst sites depends not only on age, but also on time. The differential equations must therefore be extended to reflect this more

complex relationship. The Population Balance Equation provides the framework for this extension: for each site oxidation state *q*, an equation of the form of equation 10.1 can be written.

$$\frac{\partial P_*^q}{\partial t} + \frac{\partial}{\partial \theta}\left(\frac{\partial \theta}{\partial t} P_*^q\right) = B^q - D^q \qquad 10.1$$

The right hand sides of equations 2.3 correspond to the respective birth and death functions in equation 10.1. Substitution for these functions results in the set of partial differential equation shown in equation 10.2.

$$\begin{aligned}
&\frac{\partial P_*^{4+}}{\partial t} + \frac{\partial P_*^{4+}}{\partial \theta} = -\beta_{st}^{4+,3+} P_*^{4+} \\
&\frac{\partial P_*^{3+}}{\partial t} + \frac{\partial P_*^{3+}}{\partial \theta} = P_*^{4+}\left(\beta_{st}^{4+,3+} - \beta_{st}^{2+,3+}\right) - P_*^{3+}\left(\beta_{st}^{3+,2+} + \beta_{st}^{2+,3+}\right) + \beta_{st}^{2+,3+} \qquad 10.2 \\
&P_*^{2+} = 1 - P_*^{4+} - P_*^{3+} \\
&P_*^{4+}(t,0) = 1;\ P_*^{3+}(t,0) = 0
\end{aligned}$$

In the reactor model, this set of PDEs will be discretised in age, θ, and transformed into a set of ordinary differential equations by the method of lines (Schiesser, 1991, Schiesser & Griffiths, 2009). When steady-state conditions are simulated, the active fraction is determined by equation 2.3, rather than the PDEs of equation 10.2, for computational efficiency.

The changes in the activity of the catalyst in response to changing conditions in the reactor can therefore be predicted, by the solution of equation 10.2.

10.2 Polymer properties

In the kinetic study, the molecular weight distribution was represented by the live polymer moments, as shown in equation 4.43.

$$\begin{aligned}
\lambda_0 &= P_* \sum_m f^m \sum_i \xi_i^m \\
\lambda_1 &= P_* \sum_m f^m \sum_i \xi_i^m \frac{1}{1-\gamma^m} \qquad 4.43 \\
\lambda_2 &= P_* \sum_m f^m \sum_i \xi_i^m \frac{1+\gamma^m}{\left(1-\gamma^m\right)^2}
\end{aligned}$$

This formulation to describe the polymer properties is only accurate when conditions in the reactor are constant with time. Because of the application of the Quasi-Steady State Assumption, the live polymer moments react instantly to changes in reaction conditions, and do not track the history of conditions in the reactor and their effect on polymer properties. For this we require the bulk polymer moments, which can be calculated from equation 10.3, as developed by Rawatlal (2004).

$$\begin{aligned}
&\frac{d\mu_k}{dt} = \left(\beta_{st}^{3+,2+} + \beta_t\right)\lambda_k \qquad 10.3 \\
&\mu_k(0) = 0
\end{aligned}$$

The rate of change of the bulk chain moments reflects the live chain moment at each instant, and the contribution to the total by those chains that are terminated in site transformation or chain termination reactions. By integrating these equations, in parallel with the equations describing activity, the properties of polymer being produced in the reactor can be predicted.

10.3 Unsteady-state RTD

The unsteady-state residence time distribution has been developed for a perfectly mixed reactor (Rawatlal & Starzak, 2003). For a single tank, the age distribution can be expressed in terms of the time-varying inlet and outlet flow rates, $h_{in}(t)$ and $h_{out}(t)$, and holdup, $H(t)$, as shown in equations 10.4 and 10.5.

$$I(t,\theta)=\frac{h_{in}(t-\theta)}{H(t)}\exp\left[\alpha(t)-\alpha(t-\theta)\right] \qquad 10.4$$

where:

$$\alpha(t)=-\int_0^t \frac{h_{out}(t')}{H(t')}dt' \qquad 10.5$$

This formulation of unsteady-state RTD allows the extension of the reactor model to truly dynamic simulations, including start up, shut down and grade transitions.

10.4 Reactor model formulation

The dynamic reactor model is based on the solution of sets of differential equations that describe the flows in and out of the reactor, the rate of reactions that occur, and the resulting effects on polymer properties. These equations will be outlined below.

The most fundamental equation is the balance on components that flow through, and react in, the reaction vessel, as shown in equation 10.6. The accumulation of component *N* in the reactor is determined by the molar flows in and out of the tank (the first two terms on the right hand side of equation 10.6), and the molar reaction rate, in which *N* is consumed in polymerisation and related reactions. The total hold up in the reactor is denoted *N*, and the concentration of the components in the liquid reaction phase is denoted $\underline{C}$; this is determined using the isothermal flash calculations outlined in Chapter 21 in the Appendix.

$$\frac{dN}{dt}=F_{0,N}-\frac{N}{\tau_{out}}-n_{Ti}m_{cat}(t)\overline{r_N}\left(t,\underline{C},\underline{P_*}\right) \qquad 10.6$$

The rate of reaction is expressed in terms of the hold up of the catalyst in the reactor, $m_{cat}(t)$, and the consumption rate averaged over the age distribution in the reactor at that time, $\overline{r_N}\left(t,\underline{C},\underline{P_*}\right)$. The factor n_{Ti} converts the mass of catalyst into available moles of titanium sites, based on the chemistry of the catalyst, as described in the Kinetic Study, Chapter 5.

The averaging of the reaction rate across the age distribution is achieved through application of the Segregation Approach, as shown in equation 10.7. The reaction rate for component *N* for each age, $r_N\left(\underline{C},\underline{P_*}(\theta)\right)$, is combined using the unsteady-state RTD function described in equation 10.4.

$$\overline{r_N}\left(t,\underline{C},\underline{P_*}\right)=\int_0^\infty r_N\left(\underline{C},\underline{P_*}(\theta)\right)I(t,\theta)d\theta \qquad 10.7$$

The reaction rate for each age class has a slightly different formulation for the monomers and other components. Equation 10.8 shows the consumption rate of monomers (either ethylene or 1-butene in this project) as a function of propagation and termination reactions, since the monomers are not involved in site transformation reactions.

$$r_{M_i}\left(\underline{C},\underline{P_*}(\theta)\right)=\frac{dM_i}{dt}=[M_i]\left(\sum_j \lambda_{0,j}\left(k_{p,ji}+k_{t,j}^{M_i}f^{M_i}\right)\right) \quad 10.8$$

Equation 10.9 details the consumption rates of either co-catalyst or hydrogen, which do not play a part in propagation reactions, but are consumed in termination and site transformation reactions.

$$r_X\left(\underline{C},\underline{P_*}(\theta)\right)=\frac{dX}{dt}=[X]\left(\sum_i \lambda_{0,i}k_{t,i}^{X}f^{X}+\sum_q \alpha^{q,r}k_{st,X}^{q,r}P_*^{q}\right) \quad 10.9$$

The equations above describe the accumulation of reactive components in the reactor. The hold up of the catalyst is described simply by the flow of catalyst into the reactor at the feed, F_{cat}, and the exit from the reactor, denoted $\frac{m_{cat}}{\tau_{out}}$ in the case of a perfectly mixed reactor. This is shown in equation 10.10.

$$\frac{dm_{cat}}{dt}=F_{cat}-\frac{m_{cat}}{\tau_{out}} \quad 10.10$$

The accumulation of polymer chains in the reactor also requires the application of the Segregation Approach. The rate of change in the bulk chain moments can be found by averaging the contributions from each age (which are determined by equation 10.3) with the unsteady-state RTD, as shown in equation 10.11.

$$\overline{\frac{d\mu_k}{dt}}\left(t,\underline{C},\underline{P_*}\right)=\int_0^\infty \frac{d\mu_k}{dt}I(t,\theta)d\theta \quad 10.11$$

The balance on the bulk moments in the reactor can then be performed, as shown in equation 10.12. This equation predicts the evolution of the polymer properties with time.

$$\frac{d\mu_k}{dt}=\overline{\frac{d\mu_k}{dt}}\left(t,\underline{C},\underline{P_*}\right)-\frac{\mu_k}{\tau_{out}} \quad 10.12$$

Finally, the balance on the polymer in the reactor must be formulated. Unlike the other components, this balance is expressed in terms of mass. Because of the polymer's distribution of molar masses, a molar balance is not a useful measure, and so the mass balance in equation 10.13 expresses the changes in mass of polymer in the reactor.

$$\frac{dm_{pol}}{dt}=r_{pol}-\frac{m_{pol}}{\tau_{out}} \quad 10.13$$

The mass-based rate of polymer formation, r_{pol}, is equal to the total rate of consumption of the monomer, comonomer, co-catalyst and hydrogen in propagation, termination and site transformation reactions, which is shown in equation 10.14.

$$r_{pol}(t)=n_{Ti}m_{cat}(t)\sum_i \overline{r_{N,i}}\left(t,\underline{C},\underline{P_*}\right)m_{mass,i} \quad 10.14$$

The molar mass of each component, $m_{mass,i}$, converts the molar rate of consumption of each component, $\overline{r_{N,i}}\left(t,\underline{C},\underline{P_*}\right)$, as defined in equation 10.7, into a mass-based rate of consumption.

10.5 Summary

Given the feed flow rates of each of the components, the pressure and temperature of a reactor, the size of the reactor (or the mean residence time), and a set of kinetic constants, the behaviour of the reactor can therefore be completely specified by the solution of the following differential equations:

- Equation 10.6, the balance on reactant hold up in the reactor;
- Equation 10.10, the balance on catalyst hold up in the reactor;
- Equation 10.2, specifying the activity of the catalyst sites;
- Equation 10.12, the balance on the bulk moments of the polymer formed in the reactor and
- Equation 10.13, the balance on the mass of polymer in the reactor.

The interaction of these equations is shown as an algorithm in Figure 10.1 below.

This formulation of the reactor model is based on the Segregation Approach, lending it flexibility and computational efficiency, and on the kinetic scheme developed in the previous chapters.

The kinetic parameters have been extracted from laboratory data (see Chapter 6), and so all that remains is to specify the feed rates and reactor size and conditions. Industrial operational data can provide this information.

The following chapters will detail the extraction of relevant data from industrial operational data, and the comparison of the reactor model with the industrial data. Finally, the model will be applied to various industrially-relevant case studies, including grade transitions and other unsteady modes of operation.

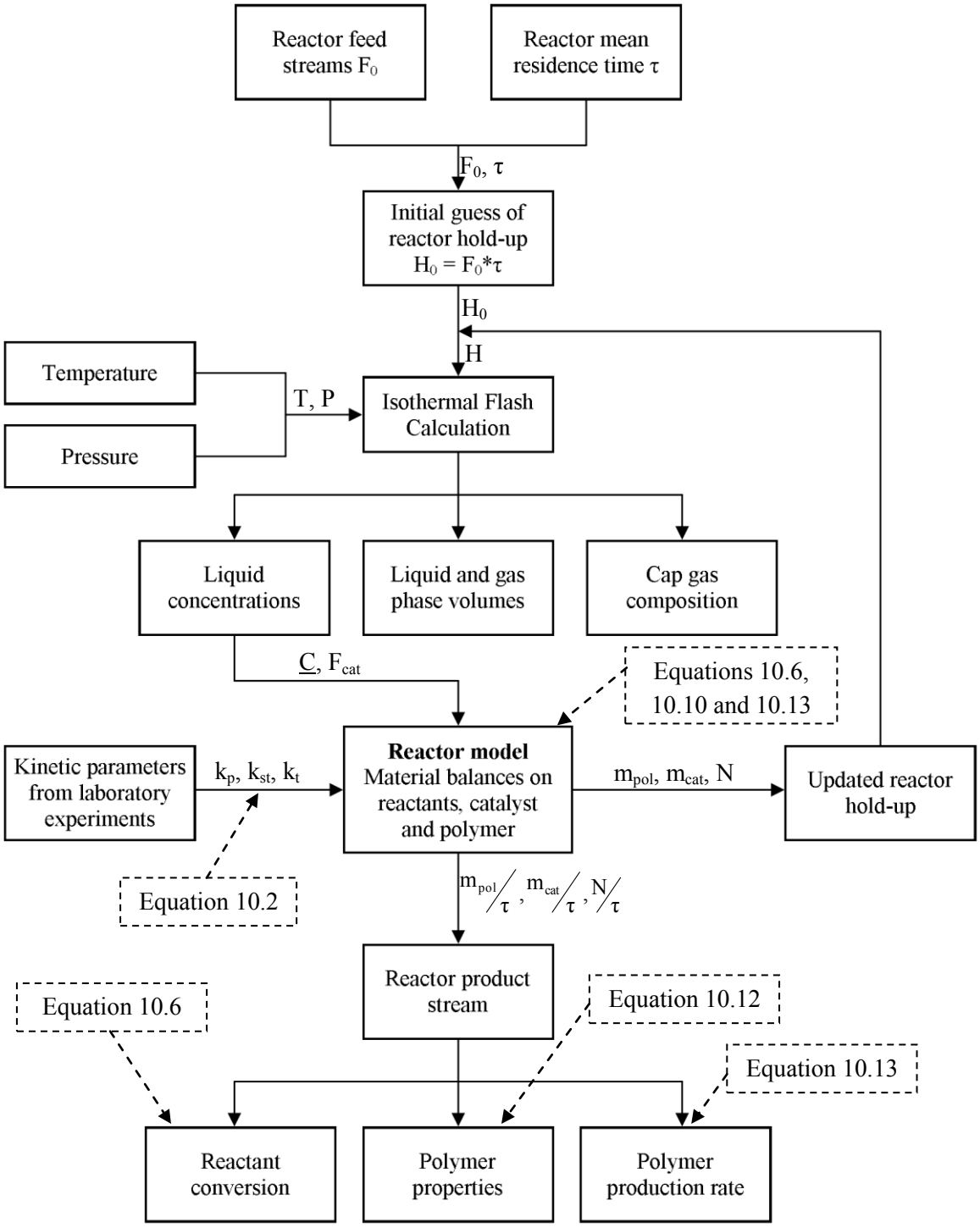

Figure 10.1: Algorithm of reactor model

PART D. APPLICATION TO INDUSTRIAL CONTEXT

CHAPTER 11. INDUSTRIAL OPERATIONAL DATA

The reactor model formulation developed in Chapter 10 and the kinetic parameters extracted from the laboratory experiments in Chapter 5 can be combined to form the basis of a simulation of an industrial polymerisation reactor. This simulation can be used in various ways: to investigate new operating strategies; to optimise unsteady-state operational conditions, especially grade transitions; and, ultimately, to control the reactor in real time during operation.

Before any of these goals can be achieved, however, the model must be validated against real industrial data, both for steady and unsteady-state operation. Validation would require that, for a given set of inputs (physically, the feed rates, reactor temperature and pressure, and reactor volume) the simulation provides the same outputs (such as polymer properties and production rate) as the industrial data.

To this end, steady and unsteady-state data for the production of four polymer grades in the reactor of interest has been supplied.

Unfortunately, industrial data typically includes data that does not directly connect with a fundamentally-based reactor model. Frequently, not all of the desired variables are measured, and it is not always simple to relate the measured variables to model parameters.

This section therefore begins with a description of the available industrial data, and an analysis of how this data can be used to test the reactor model and reaction kinetics developed previously.

The goal of this chapter is to describe the industrial process and the available data, and then to develop the relationship between the available industrial data and the reactor model.

11.1 Process description

The process of interest produces various grades of HDPE in three separate reactor systems: two batch reactor systems and one continuous stirred-tank reactor (CSTR) system. A schematic diagram of the continuous system is shown in Figure 11.1. This flow diagram provides an overview of the process, and simplifies the process of describing the data.

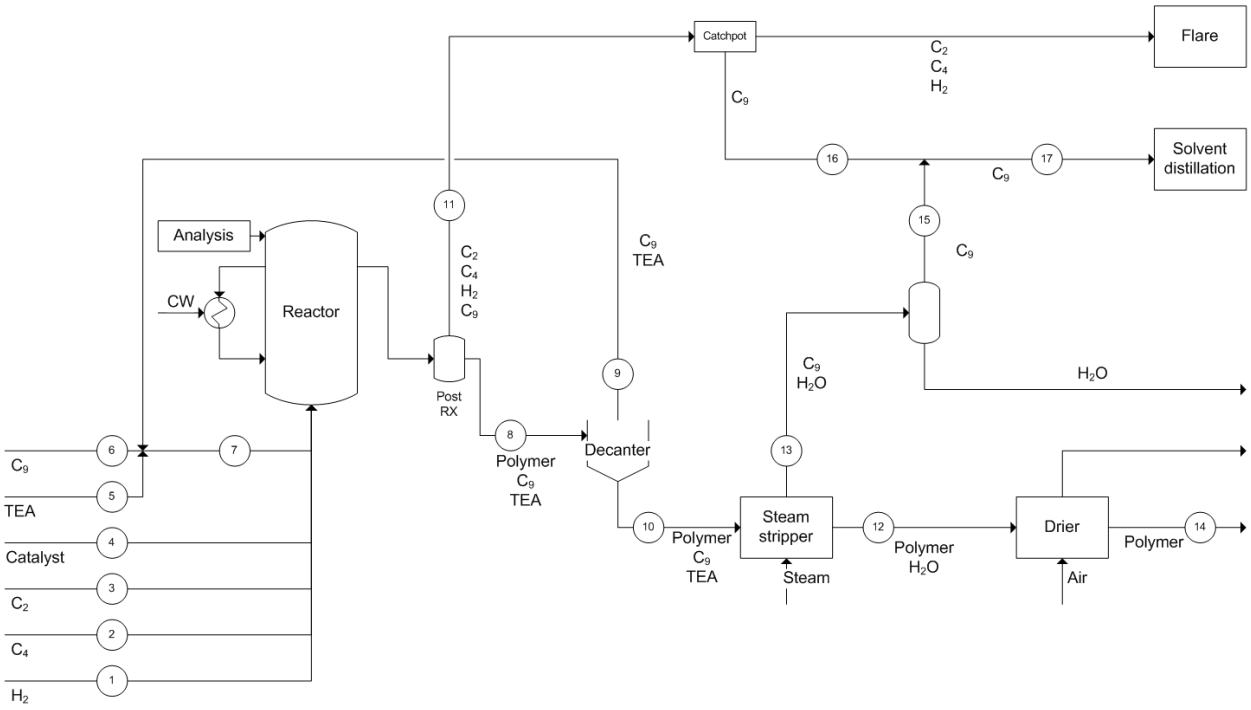

Figure 11.1: Schematic diagram of slurry-phase HDPE production

A C_9-alkane is used as the solvent for the process and the suspension medium for the solid catalyst and polymer particles, and also improves the mass and heat transfer rates in the reactor. Freshly-distilled solvent is combined with recycled solvent (stream 9) before being fed to the reactor.

Ethylene, 1-butene and hydrogen are fed (streams 1-3) at high pressure in gaseous form through a sparger, ensuring good contact between gas, liquid and solid phases. The cooling of the gases as they are reduced to reaction pressure helps to counteract the extremely exothermic nature of the polymerisation reaction.

The Ziegler-Natta catalyst is fed in a suspension of a small amount of solvent (stream 4). The co-catalyst (tri-ethyl aluminium, or TEA, stream 5) is fed as a liquid to the solvent stream.

The reactor operates at ~7 barg and ~88^{o}C. Heat is removed from the reactor by a cooling jacket and the circulation of slurry through external heat exchangers. Both jacket and external exchangers use cooling water to reduce the temperature from 88 to 78^{o}C. Because of the continuous circulation of fluid within the reactor, sparging of gases at the feed, and mechanical agitation, the vessel is very well mixed.

The reaction process was designed to operate at 99.5% conversion of monomer and comonomer to polymer, to avoid the need for post-reactor separation and monomer recycles. Such a high conversion in a CSTR generally results in a relatively low reactant concentration, and thus relatively low reaction rates which require a relatively large reaction volume (compared with, for example, a Plug Flow Reactor). In this case, however, the extremely high activity catalyst keeps the reaction rate in an acceptable range. The high activity also means that there is a large mass of polymer produced per mass of catalyst, which remains embedded in the polymer particles and can not be reused.

The reactor vessel volume is 80m^3, with vessel level being a controlled variable. Although the exact volume occupied by the gas is not measured, process engineers assume that the vessel is almost completely filled with liquid. The gas phase of the reaction vessel ("cap gases") are analysed continuously to infer the concentration of monomer and hydrogen in the liquid phase. The ratio of hydrogen to ethylene is the manipulated variable which influences the Melt Index of the reactor product.

Slurry is removed from the reactor and sent to the post-reactor vessel and suspension receivers, where it is cooled and off-gas is removed. Off-gas (stream 11) consists of un-reacted ethylene, 1-butene, hydrogen and solvent. Solvent is recovered in catchpots and recycled to the solvent distillation process (stream 16). The remaining off-gas is flared.

Cooled slurry from the post-reactor (stream 8) is sent to the decanters, which separate the polymer powder and solvent (referred to as the "mother liquor"). The mother liquor (with some co-catalyst, for which analysis is performed) is recycled to the reactor (stream 9).

The thickened solids (stream 10, approximately 25% liquid) go to a steam stripper, which removes all remaining solvent. Solvent and steam (stream 13) are separated in a fractionating column, and the distillate solvent (stream 15) is recycled to solvent distillation, where impurities are removed.

The powder is dried using hot air blowers, separated with cyclones, and then classified on shake-tables before being sent to the silos for blending and extrusion (stream 14).

11.2 Summary of industrial operational data

Ideally, industrial process measurements would be sufficient to specify all of the streams in Figure 11.1, making the comparison of the model and the industrial data relatively simple. Unfortunately, since this data is from an industrial operation, not all of the desired data is available; what is available is described below. This available data must be analysed for ways in which we can use the existing data to "fill in the blanks". Once we have sufficient data to run the reactor model, we can compare the performance of the simulation with the data itself.

Plant data was recorded at 3 hour intervals for the production of each of the four grades, and includes:

- Feed flow rates of the reactants, catalyst, co-catalyst and solvent;
- Analysis of the reactor cap-gas and recycled mother liquor;
- Reactor temperature and pressure;
- Melt Index of polymer product

For intellectual property reasons, the full plant data has not been included in this thesis; however, a summary of the data, based on the average values for the various measurements for each grade, is shown in Table 11.1.

A mass balance analysis of the industrial process (see Figure 11.1) and the available data (in Table 11.1) is given in Chapter 26 in the Appendix. As shown in the mass balance analysis, direct comparisons between the industrial data and the reactor model predictions is not possible without further measurement of process variables, which is not available; thus the following section describes further analysis of the industrial data, and the identification of points of comparison for model validation.

Table 11.1: Summary of industrial data

Grade		**1**	**2**	**3**	**4**
C_2H_4 feed	ton/hr	5.198	5.007	4.874	5.056
C_4H_8 feed	kg/ton C_2H_4	6.044	16.933	14.719	12.035
H_2 feed	Nm^3/ton C_2H_4[a]	4.257	3.22	4.138	2.062
Solvent	m^3/ton C_2H_4	3.166	3.2	3.201	3.2
	Mother liquor m^3/batch[b]	6.658	6.857	7	6.967
	Distillate m^3/batch[b]	1.342	1.137	1	1.033
Catalyst	g-cat/ton C_2H_4	357.334	157.953	266.101	115.192
	g-cat/L[c]	30	30	30	30
	Efficiency [ton C_2H_4/kg-cat]	2.82	6.42	3.79	8.80
Co-catalyst	L/mol TEA[d]	1.3	1.3	1.3	1.3
	L/batch[e]	2.332	2.167	2.453	2.083
Analysis	mmol TEA/L[f]	0.695	0.709	0.665	0.802
Cap gas	H_2 mol%	43.973	34.216	43.381	23.446
	C_2H_4 mol%	27.136	39.309	29.254	50.548
	Ratio H_2:C_2H_4	1.622	0.893	1.498	0.465
Pressure	barg	7.059	6.93	7.042	6.905
Temperature	°C	87.99	87.928	87.97	87.976
MFI	5kg/190°C	21.814	10.488	28.879	1.593
M_w	g/mol[g]	6.439×10^4	7.774×10^4	5.989×10^4	1.263×10^5

Notes:

[a] Nm^3 defined as the volume of an ideal gas at 273.15K and 101.325kPa.

[b] Solvent is mixed in $8m^3$ batches before being fed to the reactor. Mother liquor is recycled solvent, which contains some co-catalyst. Distillate is pure solvent, distilled from the steam stripping process described above.

[c] Concentration of catalyst suspended in solvent. This slurry is fed to the reactor.

[d] Concentration of co-catalyst solution.

[e] Litres of co-catalyst solution added to each $8m^3$ batch of solvent.

[f] Concentration of co-catalyst in mother liquor.

[g] Weight-average molecular weight, estimated from equation 5.1 on page 68

11.3 Analysis of industrial data

As stated above, the relationship between industrial data and a fundamental model is not always simple. Returning to the algorithm of the reactor model (Figure 10.1 on page 153) allows us to determine the relationship between the data in Table 11.1 and the model. Three types of information which relate the industrial data to the reactor model can be identified; these are illustrated in Figure 11.2 and described below.

The first type of information is an Input to the model, supplied directly by the industrial data. This information is required to specify certain conditions within the model. In this case, the Inputs consist of:

- The flow rates of the feed streams (streams 1-7 in Figure 11.1)
- The temperature and pressure in the reactor
- The volume of the reactor and the volumetric flow through the reactor

With these Inputs, the reactor model is fully specified and can be used to simulate production of a particular polymer grade. The inputs from the data, and how they interact with the model, are shown towards the top of Figure 11.2 as the “Feed streams”, “Reactor volume”, “Temperature” and “Pressure”.

The second type of data that we consider here is the Outputs; this information can be used to directly verify the results of the reactor model with the industrial data. The three Outputs are:

- The design conversion (99.5%) of the monomer in the reactor, which can be compared to the predicted monomer conversion. Although the model predicts the conversion of all reactants, this other information is not available in the data.
- The Melt Flow Index of the polymer products, which can be related to the weight-average molecular weight of the simulated polymer through the relationships developed in the Kinetic Study.
- The catalyst efficiency measured on the plant, which can be compared with the predicted catalyst efficiency.

The Outputs are shown at the bottom of Figure 11.2 as the “Monomer design conversion”, “Melt Flow Index” and “Catalyst efficiency”.

The final type of information that is used to relate the data and the model is referred to as the Internal Checks. The two Internal Checks can be used as further verification of the simulation, and are:

- The “mother liquor” analysis for co-catalyst content. This analysis of the recycled solvent stream allows us to deduce (from the well-mixed reactor assumption) the concentration of the co-catalyst in the liquid phase of the reactor itself, and compare this figure with the simulated value. The model also supplies information on the liquid phase concentrations of the other components, but no data is available for comparison.
- The ratio of hydrogen and ethylene in the cap-gas. Although the model predicts the full composition of the cap-gas, only the fractions of hydrogen and ethylene are measured on the plant and can be compared with the model predictions.

The Internal Checks are shown in the centre of Figure 11.2 as the “Mother liquor analysis” and “Cap-gas ratio”.

Now that the interactions between the available industrial data and the reactor model have been described, the information in Table 11.1 can be analysed and manipulated to extract the information required to run and validate the reactor model.

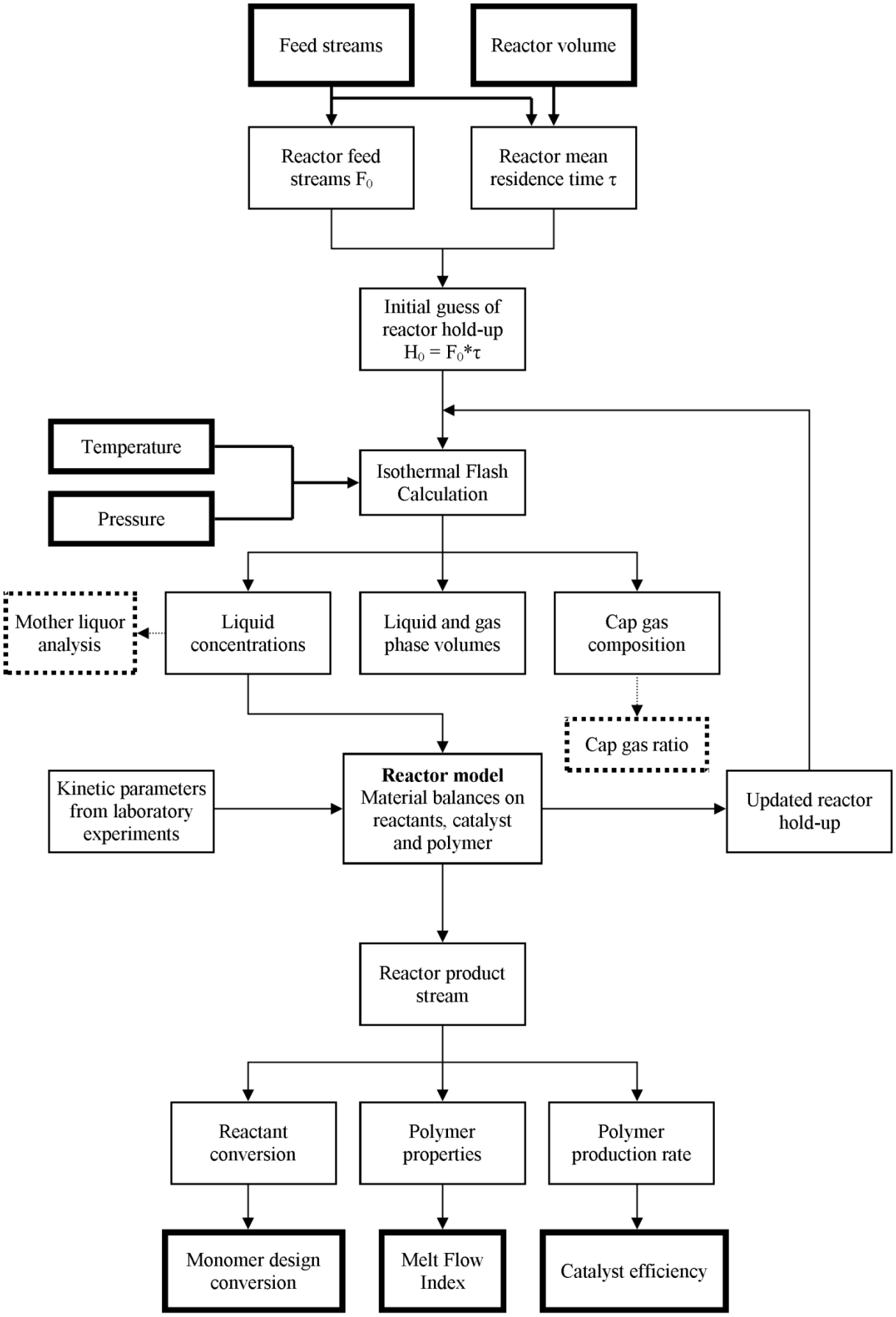

Figure 11.2: Interaction between industrial data and reactor model algorithm

11.3.1 Feed streams

The first Input required for the reactor model is the feed stream specifications. The feed rates of the various components are given in Table 11.1 as functions of the ethylene feed rate. Simple calculations provide the molar flow rates of each of the components, shown in Table 11.2.

Table 11.2: Molar flow rates of feed streams

Grade		**1**	**2**	**3**	**4**
C_2H_4	mol/s	51.6	49.7	48.4	50.2
C_4H_8	mol/s	0.156	0.421	0.356	0.302
H_2	mol/s	0.274	0.200	0.250	0.129
Co-catalyst	mol/s	0.0037	0.0036	0.0035	0.004
Solvent	mol/s	25.9	25.0	24.3	25.2

It is clear from the data in Table 11.2 that the overwhelming majority of the material fed to the reactor is made up of monomer (ethylene) and the solvent (n-nonane). Together with the temperatures and pressures in Table 11.1, the feed rates to the reactor provide most of the information required to simulate the industrial reactor with the reactor model developed previously. The only remaining Input required is the mean residence time of the reactor.

11.3.2 Reactor residence time

The mean residence time of the reactor (the final Input) can be found from the volume of the reactor (which is 80m^3) and the volumetric flow rate of the product stream.

If the molar flow rate of the product stream is known, then the volume of the gases and liquids in the product stream can be found by using the isothermal flash calculations described in section 21.1 of the Appendix. The volume of solid polymer leaving the reactor is determined by the conversion of the reactants and the density of the polymer, (approximately 950 kg/m^3 for HDPE). Thus the conversion of all components is required in order to specify the volumetric flow rate of the product stream.

Unfortunately, the only data available for the conversion of the reactants is the design conversion of the monomer and comonomer of 99.5%. In the absence of any other data, the consumption of the other components will be assumed to be negligibly small in comparison with their supply rates for the calculation of the mean residence time.

Equation 11.1 relates the product stream molar flow rates to the feed molar flow rates in Table 11.2, through the conversion of each component.

$$F_A = F_{A,0}\left(1 - X_A\right) \qquad 11.1$$

The volumetric flow of polymer is calculated from the conversion of monomer and comonomer, as shown in equation 11.2. The contributions of the other reactants to polymer mass are neglected here, since there is no data available; however the contribution of the catalyst, co-catalyst and hydrogen to the mass of polymer will be very small compared to the mass of the monomers.

$$\dot{V}_{pol} = \frac{X_{C_2H_4}\dot{n}_{C_2H_4}m_{mass,C_2H_4} + X_{C_4H_8}\dot{n}_{C_4H_8}m_{mass,C_4H_8}}{\rho_{HDPE}} \qquad 11.2$$

The molar flow rates of the product stream for the design monomer and comonomer conversions, as calculated by equation 11.1, are shown in Table 11.3, together with the volumetric flows of the gaseous and liquid components.

The volumetric flow of polymer in the product stream, calculated with equation 11.2, is also shown in Table 11.3, together with the residence time of the reactor for each grade, based on the reactor volume and the total product stream volume flow.

Table 11.3: Product stream flow rates (assumed conversion of 99.5%)

Grade		**1**	**2**	**3**	**4**
C_2H_4	mol/s	0.258	0.249	0.242	0.251
C_4H_8	mol/s	0.780×10^{-3}	2.11×10^{-3}	1.78×10^{-3}	1.51×10^{-3}
H_2	mol/s	0.274	0.200	0.250	0.129
Co-catalyst	mol/s	0.0037	0.0036	0.0035	0.004
Solvent	mol/s	25.9	25.0	24.3	25.2
Gas volume	m^3/s	2.83×10^{-4}	0.0526×10^{-4}	2.26×10^{-4}	0.0535×10^{-4}
Liquid volume	m^3/s	5.17×10^{-3}	5.03×10^{-3}	4.90×10^{-3}	5.08×10^{-3}
Polymer volume	m^3/s	1.52×10^{-3}	1.48×10^{-3}	1.44×10^{-3}	1.49×10^{-3}
Residence time	min	191.2	204.5	203.1	202.9

Based on the design conversion of the monomer and comonomer of 99.5%, the mean residence time of the reactor is just over three hours for all four grades. In principle, all of the inputs required for the model are available.

However, inspection of the industrial data reveals that more information can be used to further improve the estimation of the mean residence time values in Table 11.3; this is the “Internal Check” of the cap-gas ratio of hydrogen to ethylene. The refinement of this estimation is shown below.

11.3.3 Cap-gas analysis, monomer conversion and residence time

Table 11.1 displays the results of online composition analysis of the cap-gas of the polymerisation reactor for each of the grades. The ratio of hydrogen to ethylene in the cap-gas is an important parameter in predicting and monitoring the molecular weight of the polymer product, because the ratio in the gas phase is indicative of the ratio in the liquid phase. As will be discussed later, the ratio of hydrogen to ethylene in the liquid phase (where the reaction occurs) is the most important factor in determining the ratio of termination to propagation reaction rates, and thus the chain length distribution of the polymer product.

The cap-gas ratio is also very sensitive to the conversion of monomer in the reactor, and can be used to more closely examine the assumed conversion of monomer and comonomer of 99.5%, as well as the associated mean residence times.

Just as in the previous section, the molar flow rate of the product stream can be specified from the conversion of the monomer and comonomer. Because of the Perfect Mixing assumption applied to the reactor, the composition of the product stream exactly matches the reactor contents; thus the ratio of hydrogen to ethylene in the product gas stream, according to the isothermal flash calculation, is equal to the ratio of hydrogen to ethylene in the cap-gas.

The cap-gas ratio in the reactor can therefore be determined for a given conversion of monomer and comonomer.

By varying the conversion of monomer and comonomer, the ratio of hydrogen to ethylene in the product stream can be matched to the industrially-measured cap-gas ratios. In the absence of more direct data, such as the chemical analysis of the reactor product stream, this use of the cap-gas data is the most accurate estimation that can be made for the conversion of the monomers in the reactor.

The sensitivity of the cap-gas ratio, liquid phase concentrations, product stream flow rates and reactor residence time to monomer conversion (for one of the grades of polymer) are shown in Figure 11.3. Similar figures can be plotted for the other three grades, but the trends will remain the same, and so only one is shown here to illustrate the influence of monomer conversion on various aspects of the reactor simulation.

As monomer conversion approaches 99%, the cap-gas ratio rapidly increases. The liquid-phase concentrations of ethylene and hydrogen are also shown to change rapidly in response to monomer conversion in Figure 11.3. The changes in the liquid phase are in proportion to the changes in the gas phase, and so the cap-gas ratio can be seen to be a good indicator of the liquid phase ratio, as mentioned previously.

The volumetric flow rate of the gas phase of the product stream decreases rapidly as monomer conversion increases, because the monomer makes up the bulk of the gas phase. As more monomer is converted to polymer, the gas phase decreases in volume, and the polymer volume increases slightly. The residence time of the reactor increases with increasing monomer conversion, because of the smaller product volumetric flow rate.

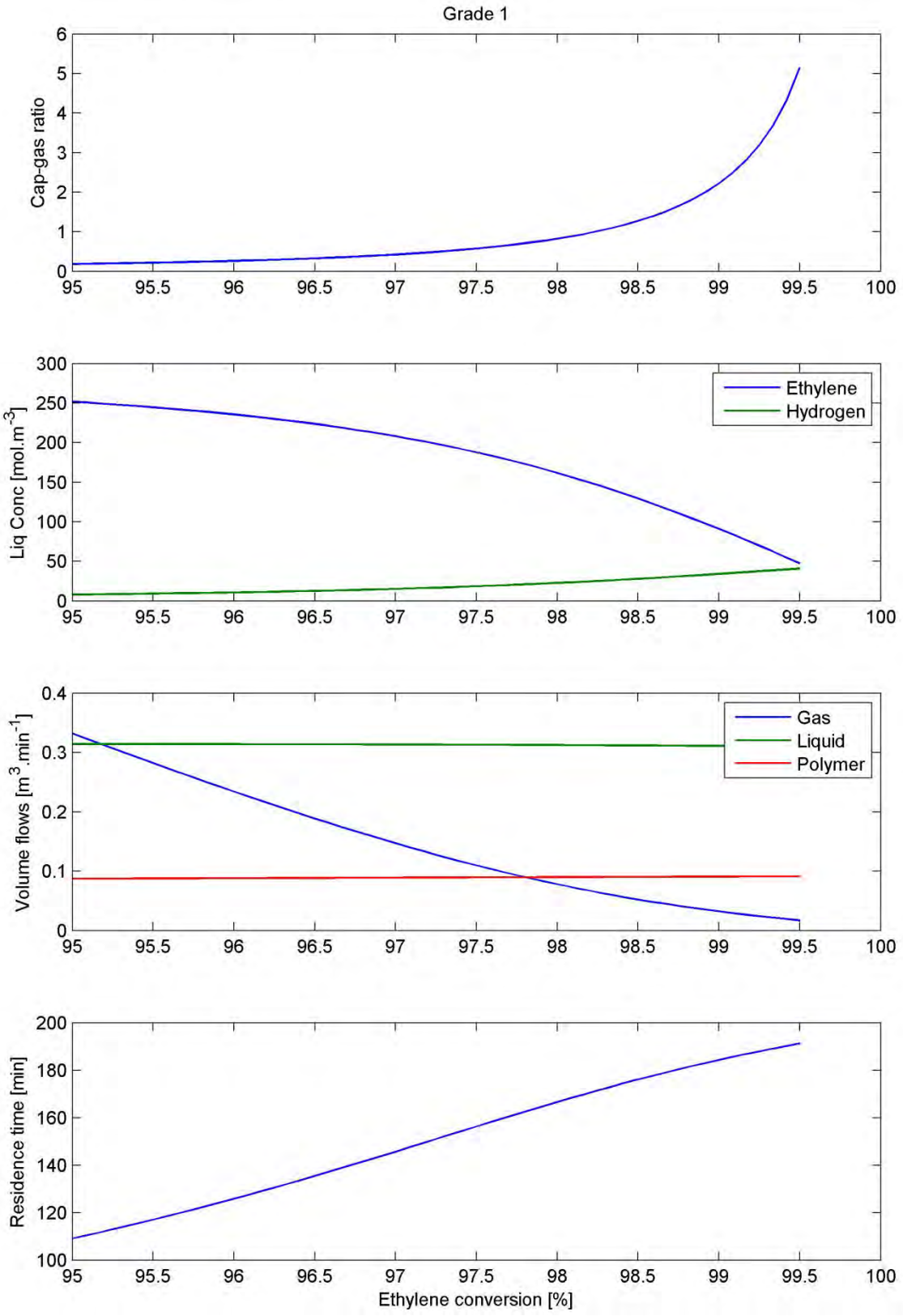

Figure 11.3: Reactor simulation sensitivity to monomer conversion

The values for monomer conversion which provide the best fits for the cap-gas ratios for each grade are used to determine the volume of polymer in the product stream (using equation 11.2), and the total volumes of the gas and liquid phases (from the flash calculation) and the polymer product are used to determine the mean residence time of the reactor.

The conversions of co-catalyst and hydrogen were again assumed to be zero in these calculations, since no other data is available. Starting from an initial guess of 99.5% conversion of ethylene and 1-butene, the isothermal flash calculations were performed and the ratio of hydrogen to ethylene in the gas phase determined. Matlab's non-linear minimisation function "fminsearch" was used to find the values for the conversion which most closely matched the cap-gas data in Table 11.1. The results of this analysis are shown in Table 11.4.

Table 11.4: Monomer conversion determined by cap-gas data

Grade		**1**	**2**	**3**	**4**
$X_{C_2H_4}$		0.987	0.983	0.987	0.978
$X_{C_4H_8}$		0.996	0.996	0.996	0.996
Gas volume	m^3/s	$7.27x10^{-4}$	$6.28x10^{-4}$	$6.30x10^{-4}$	$5.43x10^{-4}$
Liquid volume	m^3/s	$5.19x10^{-3}$	$5.07x10^{-3}$	$4.92x10^{-3}$	$5.13x10^{-3}$
Polymer volume	m^3/s	$1.51x10^{-3}$	$1.46x10^{-3}$	$1.43x10^{-3}$	$1.46x10^{-3}$
Residence time	min	179.5	186.2	191.0	186.7

The conversion of monomer required to match the gas-phase ratio of hydrogen to ethylene is between 97.8 and 98.7% for each of the four grades. These values are relatively close to the 99.5% conversion assumed by operators of the industrial reactor, and so they (and the associated residence times, also shown in Table 11.4) will be assumed to be correct for the purposes of comparing the performance of the reactor model with the industrial data. The Internal Check of the cap-gas ratio has provided a more accurate estimate of the original Output of the Monomer design conversion.

The conversion of the comonomer, 1-butene, is shown to be 99.6% in Table 11.4, very close to the assumed 99.5% conversion. However, the matching of the hydrogen to ethylene ratio was found to be almost entirely independent of the 1-butene conversion. The 1-butene conversion specified by the non-linear solver was dependent on (and proportional to) the initial guess only. Unless more information about the consumption of comonomer can be found, direct comparisons between the reactor model predictions and the industrial data for 1-butene conversion are not possible.

11.4 Summary

The industrial data has been classified into three types in order to relate the various sources of information that have been provided with the functioning of the reactor model itself. Although the discussion above was specific to the current project, the classification of data and the relationships between the data and models are more general, and could provide direction to other researchers facing disparate sources of data that need to be incorporated into a single computational model.

The industrial data can supply the Input data that is required to run a reactor model: the feed stream flow rates, and reactor temperature, pressure and volume. The Outputs (monomer conversion, MFI and catalyst efficiency) and the Internal Checks (mother liquor analysis and cap-gas ratio) can also be extracted from the data, and used to validate the predictions of the model. The Inputs, Outputs and Internal Checks described above are summarised in Table 11.5.

Table 11.5: Data extracted from analysis of industrial data

	Grade		**1**	**2**	**3**	**4**
Inputs	**Feed streams**					
	C_2H_4	mol/s	51.6	49.7	48.4	50.2
	C_4H_8	mol/s	0.156	0.421	0.356	0.302
	H_2	mol/s	0.274	0.200	0.250	0.129
	Co-catalyst	mol/s	0.0037	0.0036	0.0035	0.004
	Solvent	mol/s	25.9	25.0	24.3	25.2
	Reactor conditions					
	Pressure	barg	7.059	6.93	7.042	6.905
	Temperature	°C	87.99	87.928	87.97	87.976
	Reactor volume	m^3	80	80	80	80
	Residence time	min	179.5	186.2	191.0	186.7
Internal Checks	**Mother Liquor Analysis**	mmol TEA/L	0.695	0.709	0.665	0.802
	Cap-gas ratio H_2:C_2H_4		1.622	0.893	1.498	0.465
Outputs	**Monomer conversion**	%	0.987	0.983	0.987	0.978
	MFI	5kg/190°C	21.814	10.488	28.879	1.593
	Catalyst efficiency	ton C_2H_4/kg-cat	2.82	6.42	3.79	8.80

The industrial data directly specifies all of the feeds to the reactor, the temperature and pressure in the reactor, the ratio of hydrogen to ethylene in the cap-gas, the co-catalyst content of the mother liquor, the melt flow index of the polymer product, and the efficiency of the catalyst.

The temperature and pressure, and the feed stream specifications, are not sufficient data to simulate the reactor model developed in the previous chapters, and other relationships had to be established for sufficiency of input data. The mean residence time of the reactor is also needed; this quantity (for each of the four grades) was found by determining the monomer and comonomer conversions that most closely matched the cap-gas ratios, and using these conversions to determine the volumetric flow rate of the product stream.

With all required data specified for the reactor simulation, the predictions of the reactor model can be checked for accuracy by comparison with the industrial data's Internal Checks and Outputs: the monomer conversion, polymer properties, catalyst efficiency, cap-gas analysis and mother liquor TEA analysis.

CHAPTER 12. REACTOR MODEL VALIDATION

The reactor model developed in Chapter 10 and the kinetic parameters obtained from Chapter 5 can be used to simulate the behaviour of the industrial reactor, by using the data in Table 11.5 to specify the feed streams, temperature and pressure and reactor residence time (the model Inputs).

The reactor model can then be compared with the Outputs and Internal Checks from the industrial data, in order to validate the simulation against the data for the industrial production of polyethylene.

12.1 Summary of simulation results

The outputs of the reactor model for each of the four operating schemes specified in the data are shown in Table 12.1. The model outputs will be analysed in detail and compared with the industrial data in the pages that follow.

Table 12.1: Output from reactor model

Grade		**1**	**2**	**3**	**4**
Residence time [min]		179.5	186.2	191.0	186.7
Conversion [%]	TEA	14.0	12.1	12.5	13.8
	C_2H_4	95.7	88.3	94.0	85.2
	C_4H_8	53.2	43.8	50.2	40.5
	H_2	12.6	0.9	5.1	0.4
Catalyst efficiency	ton HDPE/kg-cat	2.69	5.62	3.57	7.44
Polymer properties	MFI (5 kg / 190^{o}C)	4.32×10^{-2}	7.75×10^{-4}	1.86×10^{-2}	7.43×10^{-5}
	M_n [g/mol]	4.270×10^{4}	5.800×10^{-4}	4.537×10^{4}	7.126×10^{-4}
	M_w [g/mol]	3.199×10^{5}	9.013×10^{5}	3.974×10^{5}	1.649×10^{6}
	mol% C_4H_8	0.0525	0.126	0.120	0.0866
Cap-gas ratio	H_2:C_2H_4	0.2117	0.04306	0.13010	0.02082
Liquid concentration [mol/m^3]	TEA	0.601	0.624	0.622	0.675
	C_2H_4	245.3	280.8	262.1	286.9
	C_4H_8	13.0	35.8	31.8	25.2
	H_2	8.96	2.10	5.90	1.037
Hold-up [m^3]	Liquid	56.5	57.2	57.1	57.8
	Gas	44.3	192.3	77.5	256.7
	Polymer	15.7	14.6	15.5	14.2
Chain length characteristic parameter $\left(1-\gamma^m\right)$	sp	2.05×10^{-6}	8.83×10^{-7}	1.56×10^{-6}	6.21×10^{-7}
	TEA	1.47×10^{-4}	1.32×10^{-4}	1.41×10^{-4}	1.40×10^{-4}
	C_2H_4	8.28×10^{-4}	8.23×10^{-4}	8.24×10^{-4}	8.25×10^{-4}
	C_4H_8	3.03×10^{-4}	7.19×10^{-4}	6.85×10^{-4}	4.95×10^{-4}
	H_2	1.35×10^{-3}	2.75×10^{-4}	8.29×10^{-4}	1.34×10^{-4}
Pseudo-sites fraction $\left(f^m\right)$	sp	1.75×10^{-5}	2.05×10^{-5}	1.73×10^{-5}	2.46×10^{-5}
	TEA	0.055	0.067	0.056	0.087
	C_2H_4	0.315	0.423	0.333	0.518
	C_4H_8	0.115	0.369	0.276	0.311
	H_2	0.515	0.141	0.335	0.084

12.2 Monomer conversion

As mentioned above, the industrial reactor is designed for 99.5% of the ethylene to be converted into polymer. Based on the composition analysis of the cap-gas, this assumption was investigated, and shown to be a relatively good approximation: as shown in Table 11.4, the conversion of ethylene must be between 98 and 99% to produce the correct cap-gas ratio of hydrogen to ethylene. The simulation of the reactor must be able to reproduce the monomer conversion and the ratio of hydrogen to ethylene in the cap-gas in order to be considered successful.

The simulation predictions from Table 12.1 relating to monomer conversion are directly compared with the industrial data for monomer conversion (from Table 11.4), and catalyst efficiency and cap-gas ratio (from Table 11.1).

Table 12.2 shows the comparison between the simulated and industrial monomer conversion. The conversion of monomer predicted by the simulation varies between ~85 and ~96%, in contrast to the conversion of monomer in the data, which is ~98% for all four grades. The relative error in the model outputs is between 3 and 13%.

Table 12.2: Monomer conversion for data and model

Grade		**1**	**2**	**3**	**4**
Monomer conversion [%]	**Data**	98.7	98.3	98.7	97.8
	Model	95.7	88.3	94.0	85.2
Relative error [%]		3.04	10.2	4.76	12.9

As discussed previously, a high conversion in a CSTR is commonly associated with inefficient use of reactor volume; even the simulated conversions of between 85 and 95% would be considered high for a CSTR. The reaction system of interest is designed for maximum catalyst efficiency, given the expense of titanium catalysts, and to avoid post-reactor separations and reactant recycles, thus justifying the very high conversions.

12.2.1 Catalyst efficiency

The catalyst efficiency in the simulation (an Output) is compared to the industrial data in Table 12.3 and Figure 12.1. The predicted catalyst efficiency in the simulation is slightly lower than the industrial values for all four simulated grades.

Table 12.3: Catalyst efficiency for data and model

Grade		**1**	**2**	**3**	**4**
Catalyst efficiency [ton C_2H_4/kg-cat]	**Data**	2.82	6.42	3.79	8.8
	Model	2.69	5.62	3.57	7.44
Relative error [%]		4.61	12.5	5.80	15.5

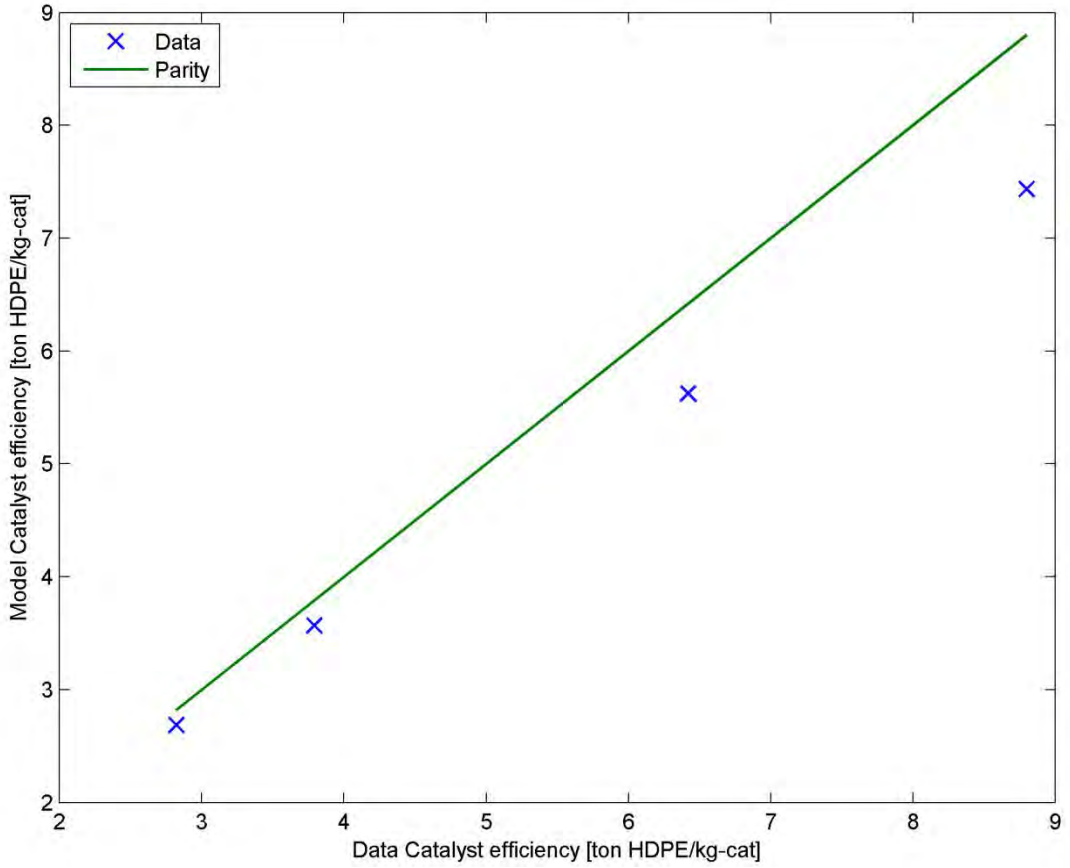

Figure 12.1: Parity plot comparison of industrial and simulated catalyst efficiency

Although the conversion of monomer is very high, and the catalyst efficiency appears to closely match the industrial data (Table 12.3), the reactor operation is very sensitive to exactly these factors. Because of the very large quantities of monomer (and relatively small quantities of hydrogen) fed to the reactor, relatively small changes in the conversion of the monomer can result in large changes in the ratio of hydrogen to ethylene.

12.2.2 Cap-gas ratio

Table 12.4 shows the comparison of the cap-gas ratio for the simulated reactor and the industrial data. The simulated cap-gas ratios are all much lower than the industrial ratios.

Table 12.4: Cap-gas ratio for data and model

Grade		**1**	**2**	**3**	**4**
H_2:C_2H_4 in cap gas	**Data**	1.622	0.893	1.498	0.465
	Model	0.212	0.0431	0.130	0.0208
Relative error [%]		86.9	95.2	91.3	95.5

This sensitivity of the simulated reaction system to monomer conversion is illustrated clearly in the comparison of the data and model predictions of hydrogen to ethylene ratio in the cap-gas. A change of approximately 8% in the monomer conversion (from ~90% in the simulation to ~98% in the data) is responsible for a change in the cap-gas ratio by a factor of between 10 and 20, a full order of magnitude.

The chain length distribution of the polymer product is strongly dependent on the ratio of hydrogen to ethylene in the reactor (indicated by the cap-gas ratio), which is in turn highly dependent on the conversion of monomer.

The impact of the under-prediction of the monomer conversion on the prediction of polymer properties is shown in the following section.

12.3 Polymer properties

The properties of the polymer are strongly dependent on the conditions in the reactor. In particular, the chain length distribution (CLD) is sensitive to the ratio of propagation to termination reaction rates at the catalyst sites.

The CLD is represented by the Melt Flow Index (MFI), and in the simulation by the number-average molecular weight (M_n) and weight-average molecular weight (M_w). The weight-average molecular weight can be related to the MFI through the correlation developed in Chapter 6.

The propagation rate, or rate at which monomer units are added to the growing chain, is dependent only on the concentration of monomer and comonomer at each polymerising site. The termination rate, in contrast, is dependent on the concentrations of a variety of terminating agents at the polymerising site. The most active of these terminating agents is hydrogen (see Table 6.9 in Chapter 6).

Industrially, the ratio of hydrogen to monomer in the cap-gas is used as a proxy for the relative concentrations of ethylene and hydrogen in the liquid phase (see Figure 11.3), and thus the CLD of the polymer product. As was shown in Table 12.4, the reactor model did not correctly predict the cap-gas ratio, suggesting a relative over-abundance of monomer in the simulated reactor.

In the reactor model, the concentration of the monomers and terminating agents are quantified for all phases, making it relatively simple to investigate the impact of these concentrations on the evolution of the polymer chain length distribution.

The simulated CLDs (represented by MFI and M_w) are compared with the industrial data in Table 12.5 and Table 12.6, summarising the industrial data in Table 11.1 and the simulation predictions in Table 12.1.

Table 12.5: Melt Flow Index for data and model

Grade		**1**	**2**	**3**	**4**
MFI [5kg / 190°C]	**Data**	21.81	10.49	28.88	1.59
	Model	$4.32\text{x}10^{-2}$	$7.75\text{x}10^{-4}$	$1.86\text{x}10^{-2}$	$7.43\text{x}10^{-5}$

Table 12.6: Weight-average molecular weight for data and model

Grade		**1**	**2**	**3**	**4**
M_w [g/mol]	**Data**	$6.44\text{x}10^{4}$	$7.77\text{x}10^{4}$	$5.99\text{x}10^{4}$	$1.26\text{x}10^{5}$
	Model	$3.20\text{x}10^{5}$	$9.01\text{x}10^{5}$	$3.97\text{x}10^{5}$	$1.65\text{x}10^{6}$

It is clear from the comparison of weight-average molecular weight that the predicted chain lengths of the polymer are approximately an order of magnitude larger than those in the industrial data. This discrepancy in the molecular weight translates to a difference of between two and four orders of magnitude in the Melt Flow Index predictions when compared to the industrial MFI values. Because of the order of magnitude discrepancy, the relative error has been excluded from Table 12.5 and Table 12.6.

The disagreement between predicted and measured molecular weights can be traced back to the monomer conversion discrepancy identified previously. As a result of the low monomer conversion predicted by the reactor model, the ratio of hydrogen to monomer in the simulated reactor is significantly lower than it should be (see Table 12.4 for the cap-gas ratios). Due to the relative over-abundance of monomer (particularly ethylene), the propagation rate is much higher than it should be, relative to the termination rate.

It appears from these results that the discrepancy in chain length distribution can at least partially be attributed to the simulated excess of monomer, caused by the under-prediction of monomer conversion.

12.4 Simulated co-catalyst concentration

The final point of comparison between the simulation and the data is the Internal Check of the co-catalyst concentration in the liquid phase. The industrial simulation predicts TEA concentrations of ~0.6 to 0.67mol/m^3 (in Table 12.1), compared to ~3mol/m^3 in the laboratory reactor (see Table 5.5 in Chapter 5). A lower concentration of TEA will result in a more gradual reduction from the inactive Ti^{4+} to the active Ti^{3+}, and thus a more gradual activation of the catalyst.

The predicted concentration of TEA for the simulated reactor is also slightly lower than expected from the industrial data: the exit stream concentration should be between ~0.65 and 0.8 mol-TEA/m^3, based on the mother liquor analysis in Table 11.1. The concentrations of TEA in the industrial data and the model predictions are directly compared in Table 12.7. The results in Table 12.7 are shown graphically in Figure 12.2.

The low concentration of co-catalyst in the simulated reactor, when compared to the industrial data, implies that the model is over-predicting the conversion of co-catalyst. This over-prediction may also have an impact on the predicted catalyst activity, and thus the discrepancy between the predicted and observed polymer properties.

Table 12.7: Co-catalyst concentration for data and model

Grade		**1**	**2**	**3**	**4**
TEA concentration [mol/m^3]	**Data**	0.695	0.709	0.665	0.802
	Model	0.601	0.624	0.622	0.675

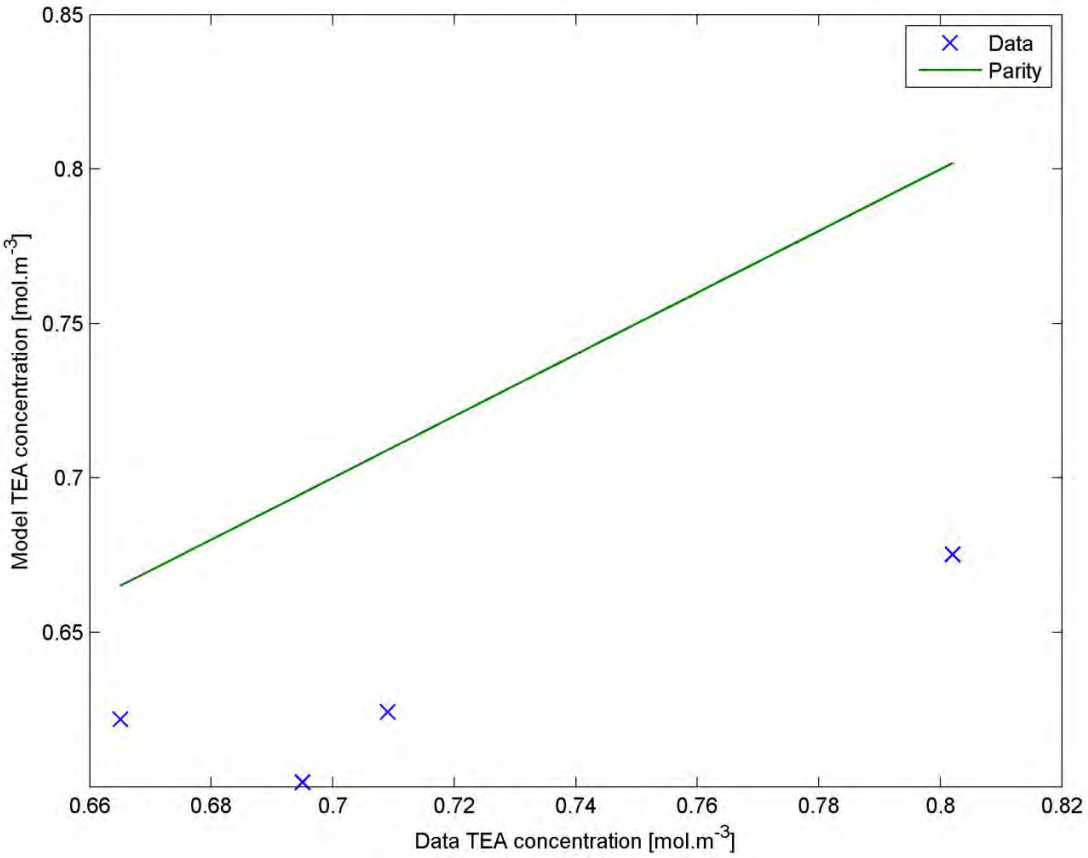

Figure 12.2: Parity plot comparison of industrial and simulated TEA liquid phase concentration

12.5 Summary

The predictions of the reactor model have been compared with the industrial data for a range of reactor conditions and parameters. The predictions of interest included catalyst efficiency, reactant conversion, cap-gas ratios, co-catalyst concentration and polymer properties.

A significant discrepancy between the model and the data has been identified, relating to the prediction of the polymer chain length distribution. The predicted Melt Flow Index (MFI) values (see Table 12.5) are several orders of magnitude smaller than the values in the industrial data. This issue can be primarily traced back to the model's under-prediction of monomer conversion.

The conversion of monomer is under-predicted by the model by between 3 and 12%, depending on the specific conditions of a simulation. Although this appears to be a relatively minor issue by itself, it has a major impact on the behaviour of the simulated reactor.

A falsely-predicted excess of monomer in the reactor results in an incorrect prediction of the ratio of hydrogen to ethylene; this ratio has been shown to be very sensitive to the conversion of ethylene (see Figure 11.3). When the concentration of hydrogen is very low, and the monomer very high, the ratio between propagation and termination reactions for the simulated growing polymer chains is skewed.

The very high propagation rate and relatively low termination rates result in the prediction of extremely long polymer chains, approximately an order of magnitude longer than those produced in the industrial reactor.

A discrepancy of this magnitude suggests that the assumptions made in formulating the reactor model may be incorrect, or may have overlooked some important factor. Since the monomer conversion appears to be the root cause of the erroneous simulation predictions, the assumptions in the model that relate to monomer conversion require investigation.

The simulation of the industrial reactor as a perfectly mixed vessel is one model assumption which may not be correct, given the size of the reaction vessel and the presence of a solid catalyst in a liquid slurry of dissolved gaseous reactants.

Another factor which may have been overlooked is the presence of poisons in the laboratory study, which could reduce the efficacy of the Ziegler-Natta catalyst and the triethyl aluminium co-catalyst.

Reactor mixing patterns and the effects of poisons will be investigated in the following sections.

CHAPTER 13. REACTOR MODEL ASSUMPTIONS

The analysis of the industrial data, and comparison of the reactor model predictions with the industrial data, revealed that the simulation under-predicts the conversion of ethylene by between 3 and 12%. Several model outputs are sensitive to the conversion of monomer, causing small errors in conversion to result in large deviations in other outputs. The most significant of these problems is that the polymer chain lengths predicted by the simulation are approximately an order of magnitude too large.

This discrepancy suggests that there is a problem with the assumptions that underlie the reactor model. Two of these assumptions will be investigated here, to determine what has not been accounted for by the model.

Firstly, the reactor model that was compared to the industrial data was based on the assumption of a perfectly-mixed vessel, represented by the Residence Time Distribution (RTD) of a Continuous Stirred-Tank Reactor (CSTR). This assumption will be evaluated by investigating the impact of reactor mixing patterns on the reactor model predictions.

Secondly, the fitting of the kinetic factors to the laboratory data ignored the potential presence of poisons in the reaction system; a poison would reduce the efficacy of the catalyst and co-catalyst. If not accounted for, this could lead to a reactor model based on a set of kinetic parameters that significantly underestimates catalyst activity. The impact of accounting for catalyst poisons will be studied by refitting the kinetic parameters for a range of assumed poisoning extents.

It is important to note at this point that there are very few published studies that have attempted to directly compare laboratory and industrial data, as in this thesis. When this comparison is made, the laboratory data is typically used to determine parameters describing polymer properties (in the kinetic structure of the multi-sites approach) and the actual production rates and other such “macro” parameters are fitted to the industrial data of interest, entirely empirically (McAuley et al., 1990, Khare et al., 2002, Khare et al., 2004, Neto et al., 2005, Hakim & Moballegh, 2006, Meng et al., 2013). Thus, the underprediction of monomer consumption rates, as observed in this work, is a challenge which has not been encountered or addressed previously to the authors’ knowledge.

13.1 Reactor mixing patterns

The mixing characteristics of the reactor could have a particular impact on the average activity of the catalyst bed in the reactor, due to the catalyst’s activity profile. The interaction of the residence time distribution and the activity profile of the catalyst is significant: for example, if the peak of the activity profile coincides with the mean residence time, then a maximum of polymerising activity will be realised.

On the other hand, if the mean residence time lies in a region of the activity curve that is distant from the peak (for example for very short or very long residence times) then the overall polymerisation activity will be very low.

This influence of mixing pattern on average catalyst activity was investigated in Chapter 9 for the case of a CSTR with a PFR recycle; it was shown that there was only a significant effect on activity when the PFR recycle was a large fraction (ie more than 35%) of the total reactor system volume, and that the impact of this mixing pattern would be negligible for the industrial reactor system considered here, in which the PFR recycle is a very small fraction of the total reactor volume.

The impact of reactor mixing pattern on the catalyst activity and reactant conversion will be further investigated here. If this case study shows that mixing patterns have a significant impact on reactant conversion, then it is possible that the reactor model was based on the wrong mixing pattern, and that correcting this may improve the performance of the model.

13.1.1 Tanks-in-series model

One of the simplest models used to account for non-ideal residence time distributions is the Tanks-in-Series (TIS) model (Danckwerts, 1953, Levenspiel, 1999, Fogler, 2005), which has the added benefit of having been extended to the unsteady-state case (Rawatlal & Starzak, 2003, Rawatlal, 2004).

The TIS model describes the RTD function of a set of CSTRs of equal volume, which can replicate the RTD function of a real reactor which exhibits non-ideal mixing characteristics. The TIS model is particularly useful here because it can represent the mixing patterns of CSTRs, PFRs, and a range of patterns between the two extremes. Because of the model's mathematical simplicity, it can be used to investigate the impact of a wide range of mixing patterns with a relatively small computational effort.

Since we are considering the steady-state industrial reactor, we will make use of the steady-state TIS model, which is shown in equation 13.1 for the case where each of n hypothetical cascaded tanks has the same volume.

$$E_{TIS}(\theta) = \frac{\theta^{n-1}}{(n-1)!\left(\tau/n\right)^{n}} \exp\left(\frac{-\theta}{\tau/n}\right) \qquad 13.1$$

For n=1 hypothetical tanks, the RTD function is identical to a CSTR: an exponential decay. As n approaches infinity, the RTD function for the TIS model approaches that of a PFR: a spike at the mean residence time. The RTD function for this model for several values of n is shown in Figure 13.1.

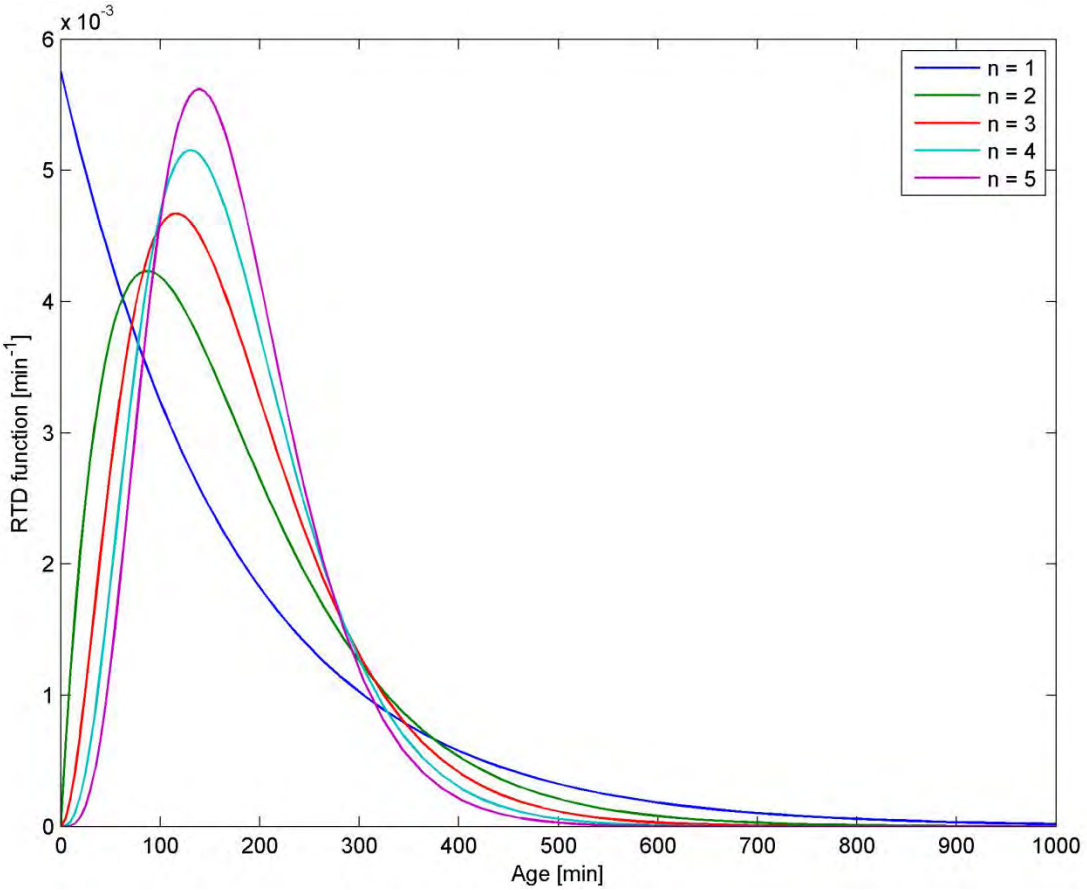

Figure 13.1: Residence time distribution for the equal-volume tanks-in-series model

It is also possible to formulate the TIS model for non-equal volumes in each tank. For two tanks, with mean residence times τ_1 and τ_2 respectively, it can be shown that the residence time function is given by equation 13.2.

$$E_{TIS2}(\theta) = \frac{1}{\tau_1 - \tau_2}\left(\exp\left(\frac{-\theta}{\tau_1}\right) - \exp\left(\frac{-\theta}{\tau_2}\right)\right) \qquad 13.2$$

Graphically, the TIS model for two tanks with uneven volumes, $E_{TIS2}(\theta)$, will lie between the equal-volume TIS model cases for $n = 1$ and for $n = 2$. Defining f as the fraction of the total residence time accounted for by the first tank results in Figure 13.2, which shows how all of the RTD curves determined by the factor f lie in between the curves of equation 13.1.

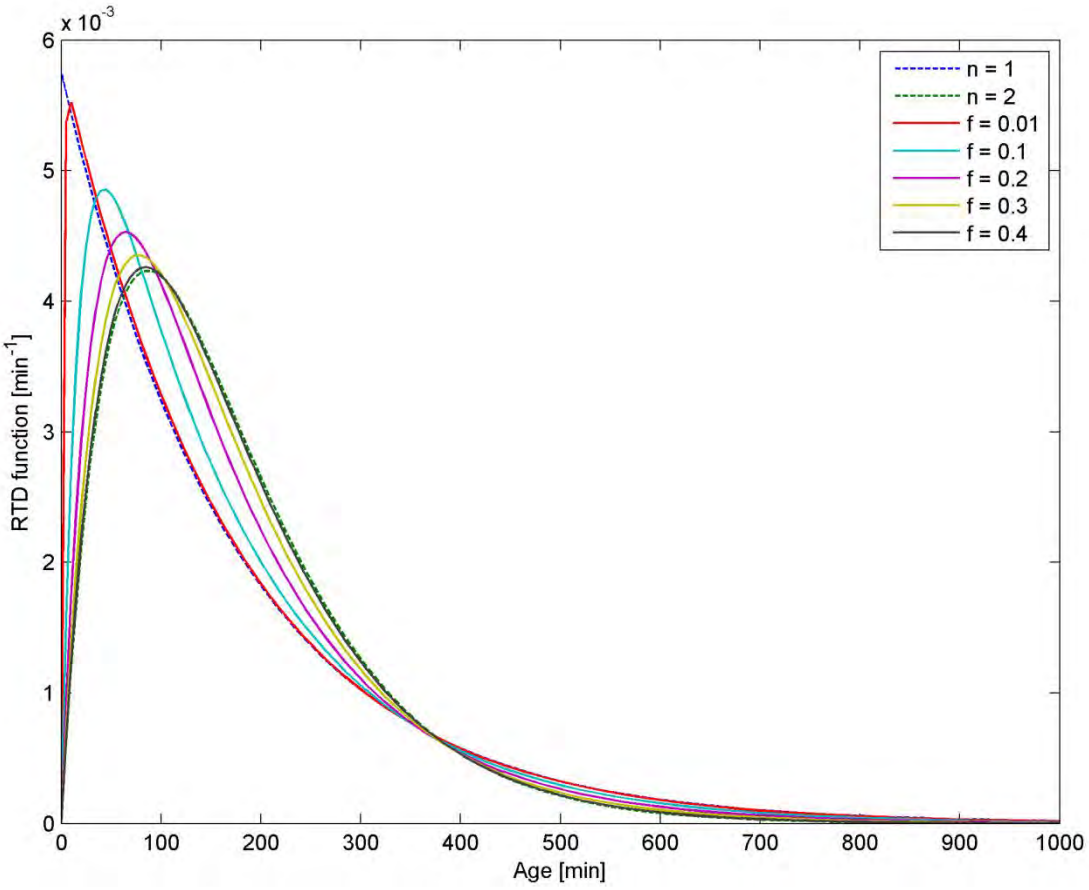

Figure 13.2: Residence time distribution for two tanks-in-series, unequal volume

The RTD function for two tanks, $E_{TIS2}(\theta)$, is symmetrical about $f = 0.5$, at which point it is identical to $E_{TIS}(\theta)$ for $n = 2$. At $f = 0$ and $f = 1$, $E_{TIS2}(\theta)$ is identical to $E_{TIS}(\theta)$ for $n = 1$. For the purposes of comparing the impact of the two versions of the TIS model on the reactor model itself, the parameters *n* and *f* will be related by equation 13.3.

$$n = 1 + 2f \qquad 0 \le f \le 0.5 \qquad 13.3$$

The reactor model will be simulated with the RTD function for a single CSTR replaced by the tanks-in-series model, for a range of values of n and f.

13.1.2 Results

The impact of the number of hypothetical tanks in the tanks-in-series model on the reactor simulation is shown for monomer conversion (Figure 13.3), polymer properties (Figure 13.4), cap-gas ratio (Figure 13.5) and co-catalyst concentration (Figure 13.6). The number of hypothetical tanks was varied between 1 and 4, using equation 13.1, and non-integer values of *n* between 1 and 2 were predicted with equation 13.2, for $f = \{0.01; 0.1; 0.2; 0.3; 0.4\}$. The mean residence time was kept constant, but the distribution of ages about this mean changes with the factor *n*.

In all cases (all four grades and two parameters of interest), the changes in the model predictions as a result of differing mixing patterns were very small. At most, the conversion of monomer increased by ~1.2%.

The MFI only increased by a small fraction as a result of these changes; the MFI predicted by the model is still orders of magnitude smaller than desired.

Despite the low sensitivity, the trends of the changes in the simulation predictions can offer some insight into the behaviour of the model system.

For all four simulated grades, the conversion of ethylene (Figure 13.3) goes through a maximum between $f = 0.1$ and $f = 0.2$, indicating that the maximum overlap of the residence time distribution and activity profile occurs in this region. A greater fraction of catalyst particles are present in the reactor during more active age ranges for these simulated age distributions, resulting in a higher average catalyst activity. The higher average catalyst activity means an increase in the conversion of ethylene.

As a result of the slightly increased conversion of monomer, the MFI predicted by the reactor model (Figure 13.4) goes through a maximum for all four grades, corresponding to the increased activity. The MFI increases as monomer concentration decreases: the termination rates remain unaffected, but the propagation rate will drop, lowering the ratio of propagation to termination rates. This produces shorter polymer chains, which in turn have a higher MFI value.

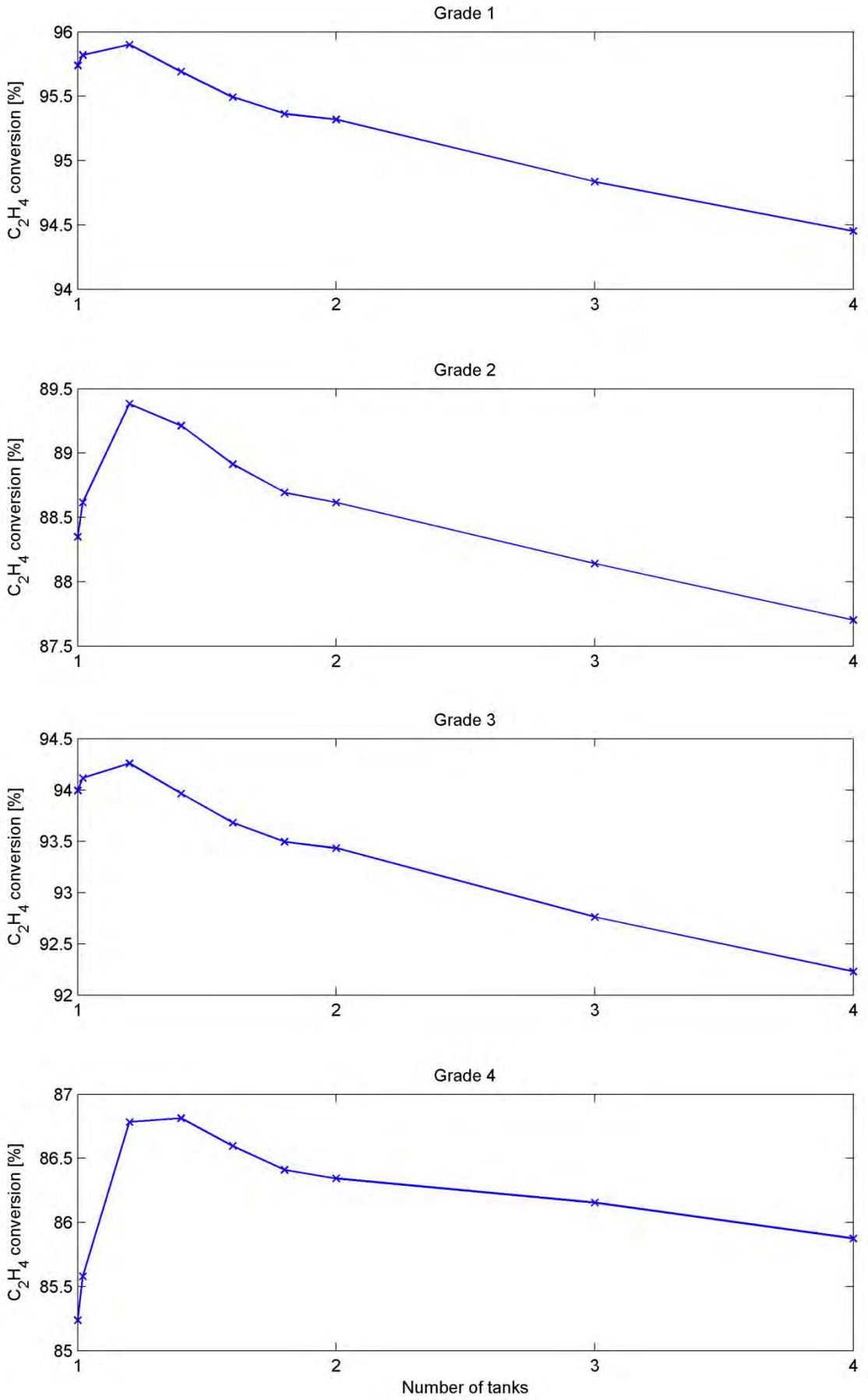

Figure 13.3: Effect of TIS model on monomer conversion

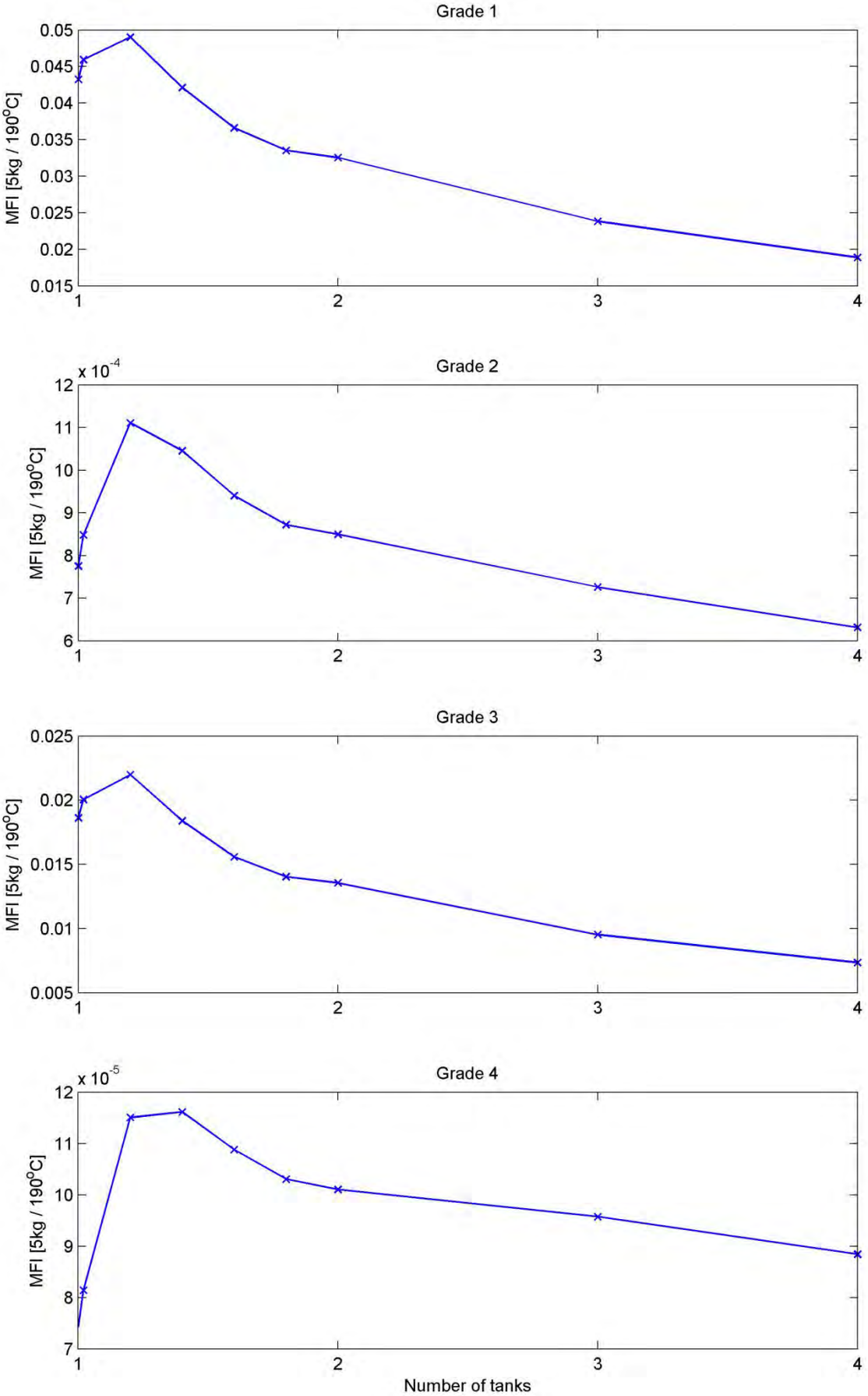

Figure 13.4: Effect of TIS model on Melt Flow Index

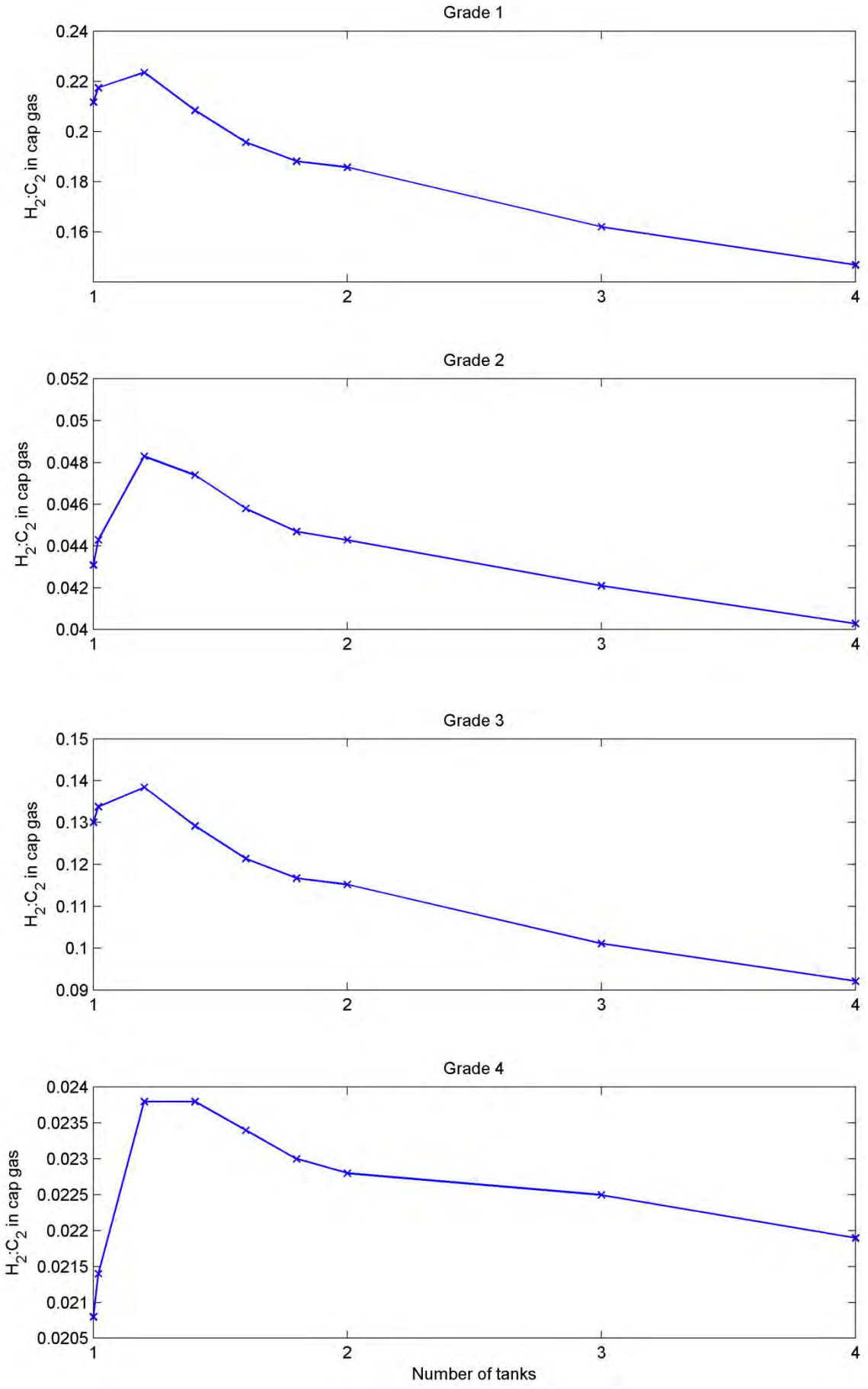

Figure 13.5: Effect of TIS model on cap-gas ratio

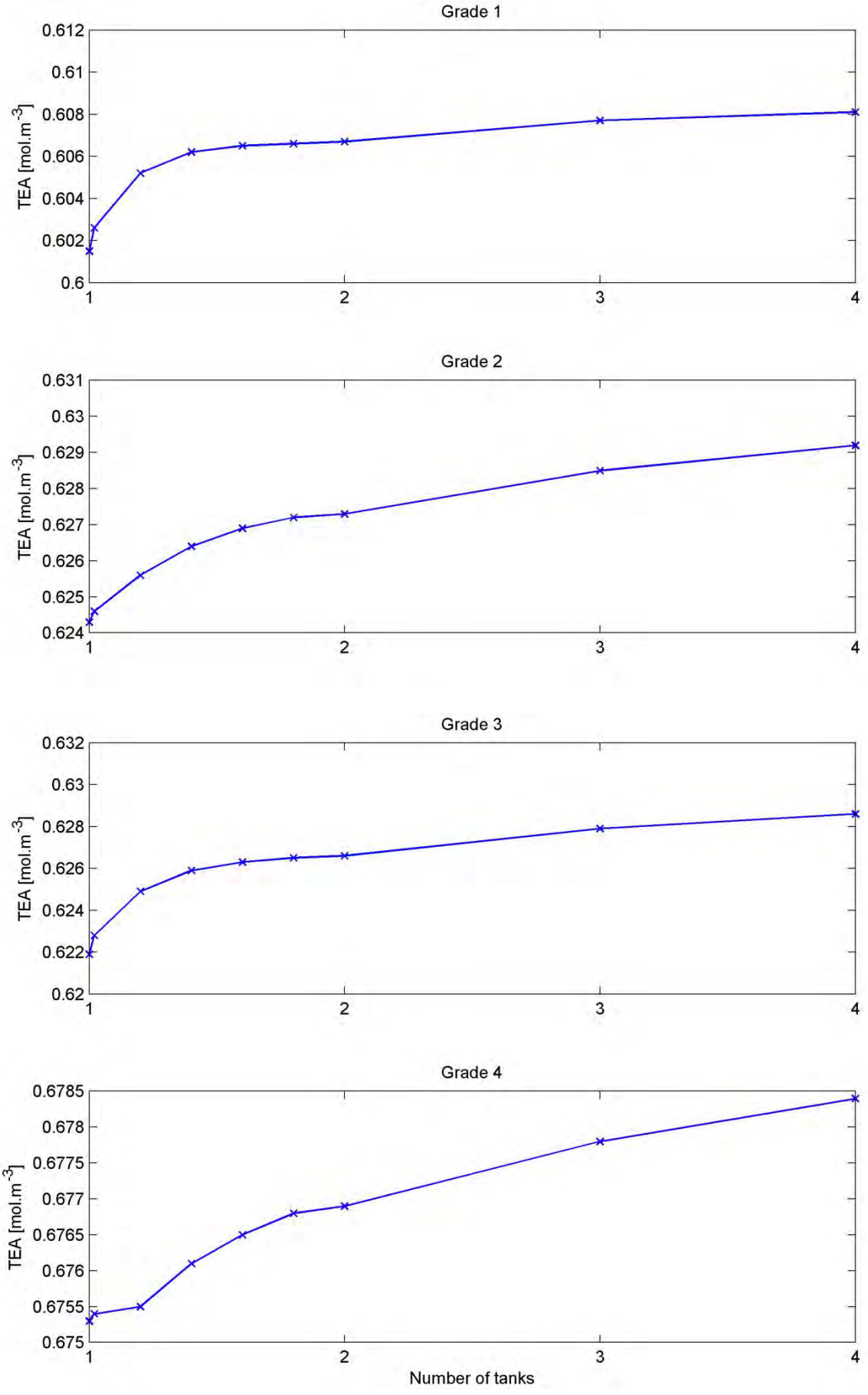

Figure 13.6: Effect of TIS model on TEA concentration

13.1.3 Summary

The tanks-in-series (TIS) model of residence time distribution was used as a case study to investigate the influence of mixing patterns on the polymerisation reactor simulation. The TIS RTD was generated for between one and four tanks of equal volume, and for two tanks with unequal volumes.

The case study showed that the conversion of monomer in the simulated reactor is only slightly sensitive to the effects of mixing patterns. Similarly, other model outputs of interest, such as polymer properties (represented by the MFI), are relatively insensitive to simulated changes in reactor hydrodynamics.

Thus it must be concluded that the original assumption of a perfectly mixed reactor can not have caused the discrepancy between the industrial data and the reactor model.

Instead, we turn to the second potential source of error: the catalyst poisons which may have been present during the kinetic study, which were not accounted for in the reactor model.

13.2 Catalyst poisons

Both the Ziegler-Natta catalyst and the triethyl aluminium (TEA) co-catalyst are very sensitive to the presence of oxidising agents in the reaction medium. The presence of oxygen (or oxygen-containing compounds such as water, carbon monoxide or alcohols) during the experimental study would deactivate the catalyst and co-catalyst.

The co-catalyst, TEA, is added to the reactor not only as a catalyst activator, but also as an oxy-compound scavenger, which reacts with any possible poisons and maintains the polymerisation potential of the catalyst.

If a poison were present during the laboratory experiments (such as in the glovebox where catalyst and co-catalyst samples were prepared, in any of the feed streams, or as impurities on the reaction vessel and internals after washing) then the catalyst and/or co-catalyst would react with the poison. This would reduce the total quantity of catalyst and/or co-catalyst available for reaction. Since the original kinetic parameters (fitted in Chapter 6) are based on the quantities of the various reactants added to the laboratory reactor, any change to the amount of a reactant available for reaction will change the outputs from the regression procedure.

The regression procedure will be extended to account for the situation where a poison was present. The effect of reduced co-catalyst and/or catalyst concentrations in the kinetic study on the results of the industrial reactor model (specifically, the Outputs and the Internal Checks) will be analysed below, to determine whether there is any evidence for the presence of catalyst and co-catalyst poisons. Note that the model equations for the industrial reactor (presented in Chapter 10) have not been modified to include the effect of poisoning; the effects of poisoning are accounted for in the refitted kinetic parameters, as described below.

13.2.1 Effect on co-catalyst

Since the co-catalyst is added to the laboratory reactor as a "poison scavenger" (as well as being a catalyst activator), it seems the most likely candidate when investigating the effects of poisons.

If the hypothetical impurity in the experimental study was present in the reaction vessel or in the reagents, then the co-catalyst would react with that poison. As a result, some fraction of the co-catalyst would be unavailable for site transformation or chain termination reactions.

The regression procedure can be extended to account for this reduced quantity of co-catalyst by replacing the molar concentration of co-catalyst in experimental run *i*, $[TEA_i]$ (specified in Table 5.5 in Chapter 5), with the available molar concentration, $[TEA_i]_{avail}$. These two quantities are related by the introduction of a "co-catalyst poison factor", f_{co-cat}, as shown in equation 13.4.

$$[TEA_i]_{avail} = f_{co-cat}[TEA_i] \qquad 13.4$$

The co-catalyst poison factor defines the extent of poisoning of the co-catalyst in the laboratory reactor, and thus the quantity of TEA available for site transformation and chain termination reactions. The factor can vary between 0 and 1, with a value of 0 indicating that all of the co-catalyst was consumed in reactions with poisons, and 1 indicating that all of the co-catalyst is available for catalytic or polymeric reactions.

The regression procedure was repeated for several values of the co-catalyst poison factor, to determine the effect of a reduced quantity of co-catalyst on the kinetic parameters. These adjusted kinetic parameters were then used in the model of the industrial reactor, and the results of the model compared with the Outputs and

Internal Checks from the industrial data, to determine whether accounting for co-catalyst poisoning can account for the observed differences between the industrial model and data.

Results

Refitting the kinetic parameters with different concentrations of the co-catalyst (as defined by equation 13.4) revealed that only the parameters for site transformation or chain termination reactions associated with the co-catalyst were affected. These parameters vary with the inverse of the quantity of co-catalyst available for reaction, represented by the co-catalyst poison factor, as shown in Table 13.1. All other kinetic parameters remained unchanged from the values determined by the original regression procedure.

Table 13.1: Summary of parameters in kinetic model (co-catalyst poison factor)

$k_{p,ij}$			***j*=C_2H_4**	***j*=C_4H_8**	
		***i*=C_2H_4**	16.93	0.524	[L.min^{-1}.g-cat^{-1}]
		***i*=C_4H_8**	265.5	0	
	sp	**TEA**	**C_2H_4**	**C_4H_8**	**H_2**
	[min^{-1}]	[L.mol^{-1}.min^{-1}]	-	-	[min^{-1}.{mol-H_2.L^{-1}}$^{-0.5}$]
$k_{st,i}^{4+,3+}$	-	$31.7 / f_{co-cat}$	-	-	-
$k_{st,i}^{3+,2+}$	-	-	-	-	0.325
$k_{st,i}^{2+,3+}$	-	$0.924 / f_{co-cat}$	-	-	-
	[min^{-1}]	[L.mol^{-1}.min^{-1}]	[L.mol^{-1}.min^{-1}]	[L.mol^{-1}.min^{-1}]	[L.mol^{-1}.min^{-1}]
k_t^m	7.04x10^{-4}	$3701.2 / f_{co-cat}$	51.74	353.8	2311.4

The results of the reactor simulation (with the adjusted kinetic parameters in Table 13.1) are compared with the Internal Checks and Outputs of the industrial data in the tables and figures below.

Table 13.2 and Figure 13.7 show that the monomer conversion (a model Output) increases slightly with increasing extent of co-catalyst poisoning. The increased model sensitivity to the co-catalyst results in more rapid catalyst activation (through more rapid site transformation reactions). The higher catalyst activity increases the conversion of monomer in the simulation. The ethylene conversion increases by as much as 4% for lower values of the co-catalyst poison factor, but does not match the observed level of ~98% in the industrial data for any of the simulated cases.

Table 13.2: Effect of co-catalyst poison factor on monomer conversion

Co-catalyst poison factor	**Monomer conversion [%]**			
	Grade 1	**Grade 2**	**Grade 3**	**Grade 4**
0.1	96.94	92.33	95.82	90.12
0.25	96.73	91.64	95.49	89.28
0.5	96.39	90.53	94.98	87.91
0.75	96.07	89.44	94.48	86.57
1	95.74	88.35	94.00	85.24

The response of co-catalyst concentration (an Internal Check in the simulated reactor) to the extent of co-catalyst poisoning is shown in Table 13.3 and Figure 13.8. The TEA conversion very rapidly becomes unrealistically high, indicated by the very low concentrations: for a co-catalyst poison factor lower than ~0.75, the predicted concentrations diverge rapidly from the concentrations in the industrial data.

The TEA conversion increases very rapidly because both site transformation and chain termination rate constants for co-catalyst increase with the inverse of the poison factor. The larger fraction of active catalyst sites also increases the rate of termination reactions, further driving up the consumption of TEA.

Table 13.3: Effect of co-catalyst poison factor on TEA concentration

Co-catalyst poison factor	TEA concentration [mol/m^3]			
	Grade 1	Grade 2	Grade 3	Grade 4
0.1	0.166	0.174	0.177	0.174
0.25	0.335	0.348	0.353	0.357
0.5	0.487	0.507	0.509	0.533
0.75	0.562	0.583	0.583	0.624
1	0.601	0.624	0.622	0.675

Table 13.4 and Figure 13.9 show the relatively small changes in predicted cap-gas ratio (a second Internal Check) in response to the co-catalyst activity factor. The change in hydrogen to ethylene ratio is relatively small, because of the correspondingly small increase in monomer conversion (shown in Figure 13.7).

Table 13.4: Effect of co-catalyst poison factor on cap-gas ratio

Co-catalyst poison factor	H_2:C_2H_4 in cap gas			
	Grade 1	Grade 2	Grade 3	Grade 4
0.1	0.342	0.0736	0.218	0.0341
0.25	0.310	0.0657	0.196	0.0308
0.5	0.269	0.0558	0.167	0.0265
0.75	0.237	0.0486	0.146	0.0233
1	0.212	0.0431	0.130	0.0208

The changes in Melt Flow Index (a model Output) as a result of the co-catalyst poison factor are summarised in Table 13.5 and Figure 13.10. Although the MFI for each grade increases by approximately an order of magnitude, the polymer properties are still several orders of magnitude smaller than the industrial measurements.

The simulation still predicts an excess of monomer; the ratio of propagation to termination reactions is too high, and so the predicted chains are too long.

Table 13.5: Effect of co-catalyst poison factor on Melt Flow Index

Co-catalyst poison factor	MFI [5kg / 190^{o}C]			
	Grade 1	**Grade 2**	**Grade 3**	**Grade 4**
0.1	0.306	6.25×10^{-3}	0.164	4.69×10^{-4}
0.25	0.212	4.04×10^{-3}	0.106	3.19×10^{-4}
0.5	0.119	2.15×10^{-3}	0.0551	1.83×10^{-4}
0.75	0.0702	1.25×10^{-3}	0.0311	1.13×10^{-4}
1	0.0432	7.75×10^{-4}	0.0186	7.43×10^{-5}

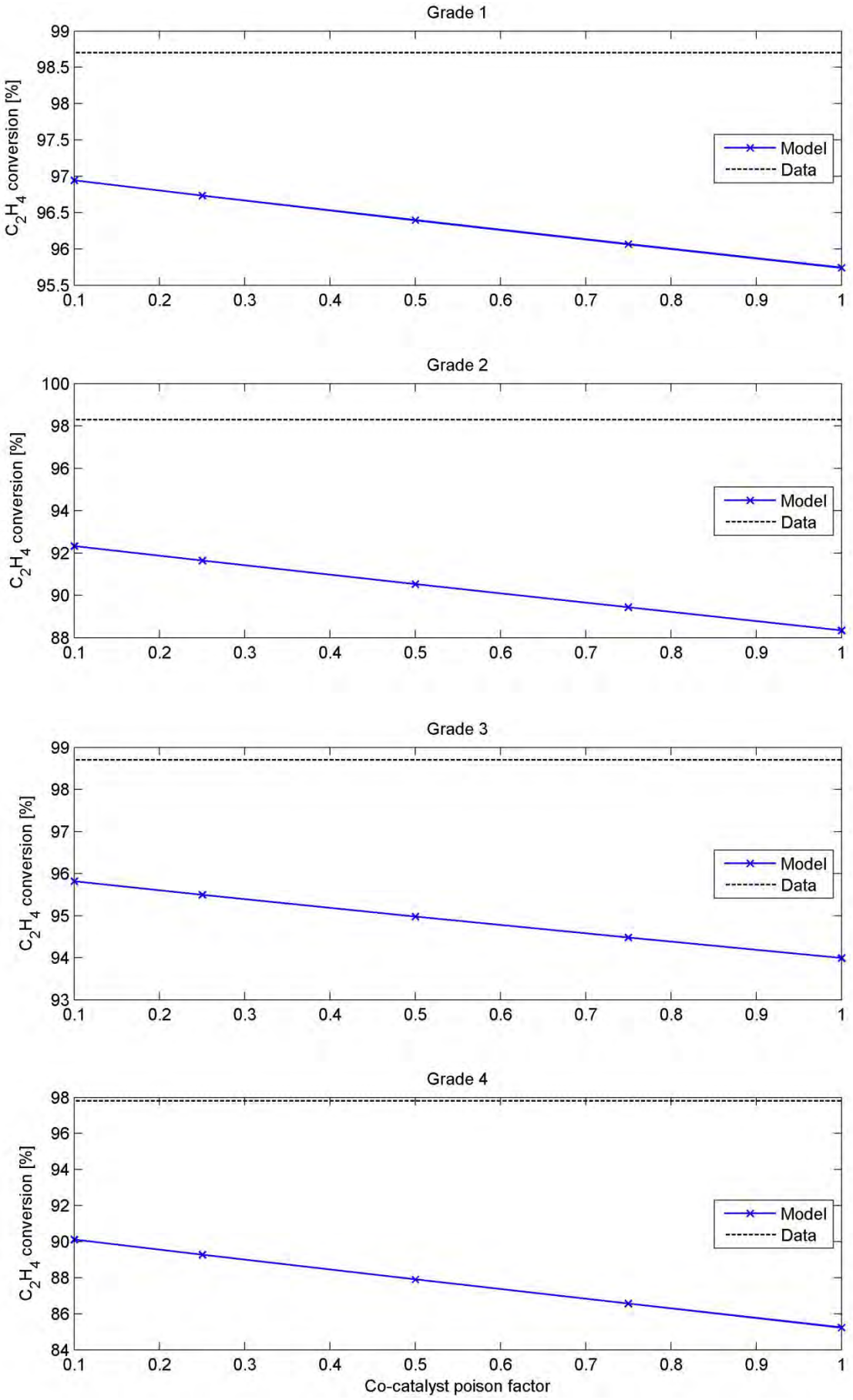

Figure 13.7: Effect of co-catalyst poison factor on monomer conversion

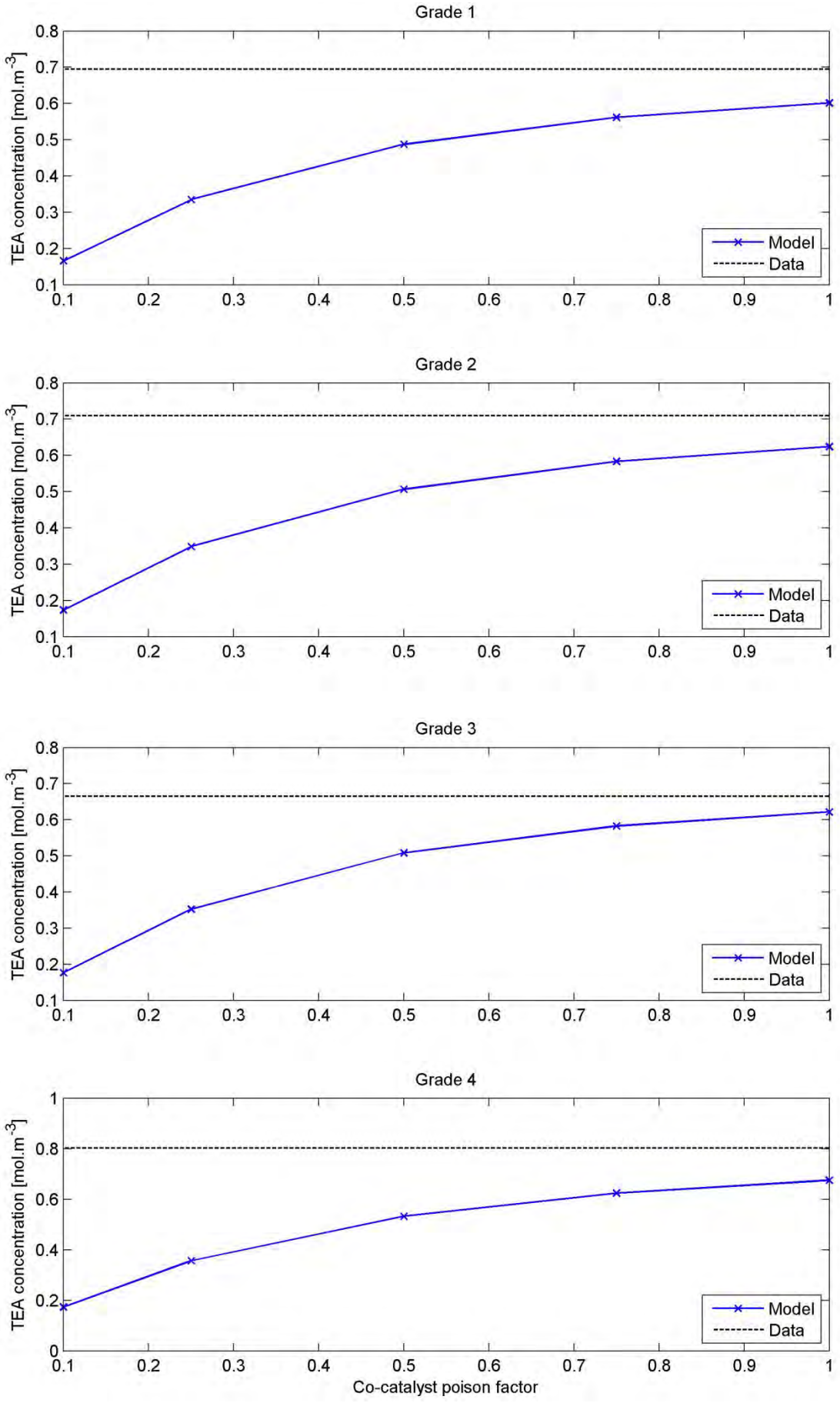

Figure 13.8: Effect of co-catalyst poison factor on co-catalyst concentration

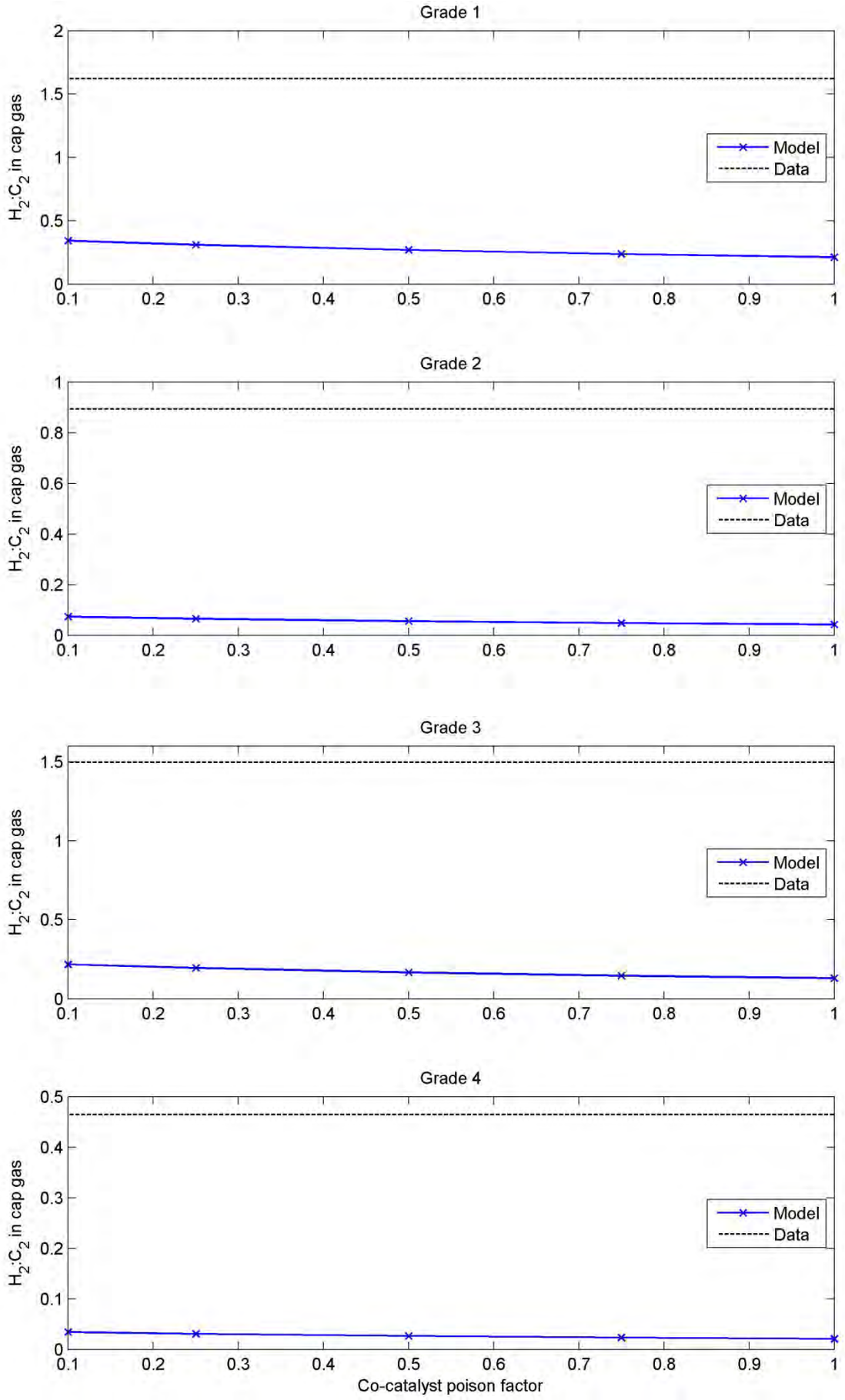

Figure 13.9: Effect of co-catalyst poison factor on cap-gas ratio

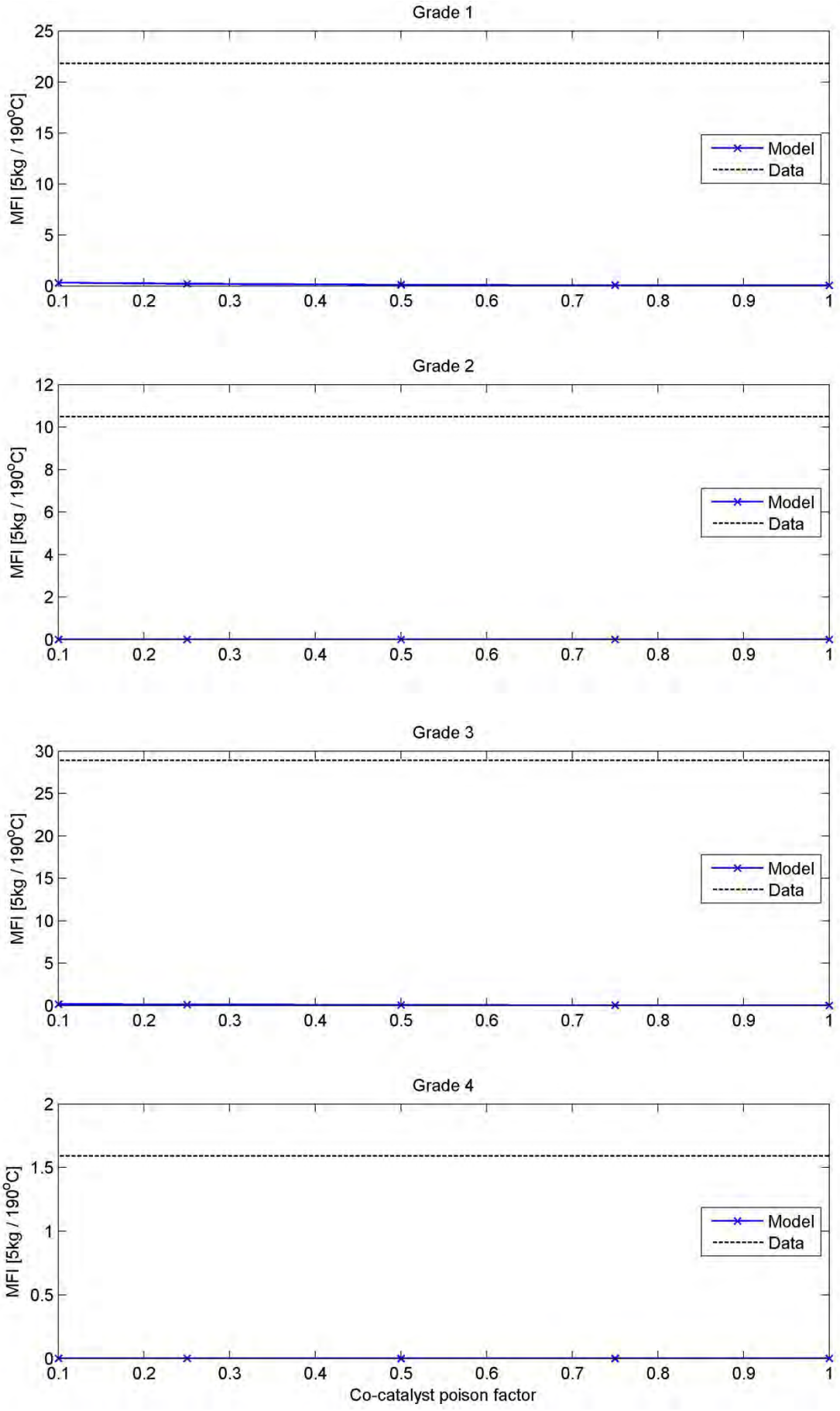

Figure 13.10: Effect of co-catalyst poison factor on Melt Flow Index

Summary

The preceding tables and figures showed the effects of accounting for co-catalyst poisoning in the laboratory reactor on the predictions of the industrial reactor simulation. Simulating the situation where a poison reduced the efficacy of the co-catalyst in the laboratory reactor provided no evidence that such poisoning occurred.

The Internal Check of the co-catalyst concentration was very sensitive to high levels of co-catalyst poisoning, showing a drastic increase in the simulated conversion of TEA. In particular, the consumption of co-catalyst in chain termination reactions increased rapidly, such that even relatively low levels of co-catalyst poisoning resulted in unrealistically low predictions of the liquid-phase TEA concentration. This result in particular suggests that poisoning of the co-catalyst in the laboratory reactor did not occur.

The reactor model Outputs and other Internal Check (monomer conversion, polymer MFI and cap-gas ratio) were shown to be relatively insensitive to changes in the degree of co-catalyst poisoning.

Thus, accounting for the poisoning of the co-catalyst in the laboratory reactor does not show much promise when attempting to account for the discrepancies between the model predictions and the industrial data.

The effects of accounting for catalyst poisons are shown next.

13.2.2 Effect on catalyst

Since including co-catalyst poisoning in the reactor model did not seem to account for the differences between the model's predictions and the industrial data, the focus is turned to poisoning of the catalyst itself.

If a poison or impurity was present in the glovebox or preparation stages of the laboratory experiments and affected the polymerisation potential of the catalyst, then the mass-based propagation rate constants (determined in the Kinetic Study in units of [L.min^{-1}.g-cat^{-1}]) will be incorrect by a quantity relating to the fraction of catalyst that was poisoned.

The regression procedure can be extended to account for a reduced mass of available catalyst by introducing a catalyst poison factor, f_{cat}. The mass of catalyst available for reaction is reduced by the value of the factor, and so, in all equations in the Kinetic Study, the mass of catalyst in experimental run *i*, $m_{cat,i}$, is replaced by a reduced available mass of catalyst, $m_{cat\,avail,i}$, as shown in equation 13.5.

$$m_{cat\,avail,i} = f_{cat} m_{cat,i} \qquad 13.5$$

The factor, f_{cat}, is assumed to be the same for each experiment, since the same methods, materials and equipment were used for each experimental run. This factor can vary between 0 and 1, with 0 indicating that all of the catalyst was poisoned, and 1 indicating no poisoning of the catalyst.

The regression procedure will be repeated for several values of the catalyst poison factor, to account for differing degrees of catalyst poisoning. A new set of kinetic parameters for each value of the factor is produced by the regression procedure. These kinetic parameters are then used in the simulation of the industrial reactor, to determine whether there is any evidence of catalyst poisoning.

Results

The kinetic parameters produced by the regression procedure, associated with each value of the catalyst poison factor, are shown in section 27.1 in the Appendix.

The parameters in the tables in section 27.1 show that the propagation rate constants are inversely proportional to the extent of assumed catalyst poisoning: as less catalyst is available for polymerisation in the laboratory reactor, the rate of polymerisation per mass of catalyst must increase. The site transformation parameters do not change significantly, but the termination rate constants increase in proportion with the propagation rate constants.

The effect of accounting for varying degrees of catalyst poisoning (in the laboratory reactor) on the industrial reactor simulation, and several of the Internal Checks and Outputs from the data, is summarised below.

Table 13.6 and Figure 13.11 show the changes in monomer conversion (an Output in the industrial data) as a function of varying degrees of catalyst poisoning. As expected, the monomer conversion is inversely proportional to the catalyst poison factor: the polymerisation rate per mass of catalyst increases as the factor decreases, increasing the overall simulated catalyst activity. This increased activity results in an increase in monomer conversion in the simulation.

Depending on the grade, the range of monomer conversion observed in the industrial data (~98%) is seen in the simulated reactor for a catalyst poison factor of between 0.15 and 0.4.

Table 13.6: Effect of catalyst poison factor on monomer conversion

Catalyst poison factor	Monomer conversion [%]			
	Grade 1	Grade 2	Grade 3	Grade 4
0.15	99.50	98.75	99.30	98.53
0.2	99.30	98.23	99.00	97.92
0.3	98.82	97.17	98.29	96.78
0.5	97.68	94.68	96.83	93.86
0.6	97.18	93.24	96.12	91.96
0.75	96.25	90.46	94.80	88.41
1	95.74	88.35	94.00	85.24

The changes in the liquid phase concentration of co-catalyst (an Internal Check) in response to changes in the catalyst poisoning is summarised in Table 13.7 and Figure 13.12. The simulated TEA conversion, like monomer conversion, increases with increasing catalyst poisoning. Although the site transformation rate constants associated with TEA do not change significantly, the termination rate constant increases in proportion with the propagation rate constants. The consumption of co-catalyst in termination reactions increases, decreasing the predicted concentration of TEA.

The original reactor model (see Table 12.1) under-predicted the liquid phase concentration of TEA. Unrealistically low concentrations of TEA (based on the TEA concentration in the reactor exit stream in the industrial data in Table 11.1) are predicted for a catalyst poison factor of between 0.15 and 0.3, depending on the grade.

Table 13.7: Effect of catalyst poison factor on TEA concentration

Catalyst poison factor	TEA concentration [mol/m^3]			
	Grade 1	Grade 2	Grade 3	Grade 4
0.15	0.400	0.584	0.492	0.634
0.2	0.469	0.625	0.556	0.681
0.3	0.562	0.631	0.624	0.682
0.5	0.608	0.626	0.627	0.674
0.6	0.606	0.625	0.625	0.673
0.75	0.603	0.624	0.623	0.674
1	0.601	0.624	0.622	0.675

Table 13.8 and Figure 13.13 show the effect of accounting for catalyst poisoning on the ratio of hydrogen to ethylene in the cap-gas (the second Internal Check) of the simulated reactor. The cap-gas ratio increases as the level of poisoning increases. As the conversion of ethylene increases, the fraction of hydrogen in the cap-gas increases, due to the sensitivity of the system to changes in the conversion of the monomer.

Accounting for catalyst poisoning results in much better predictions of cap-gas ratio than when the model included the effect of co-catalyst poisoning (Table 13.3).

Table 13.8: Effect of catalyst poison factor on cap-gas ratio

Catalyst poison factor	H_2:C_2H_4 in cap gas			
	Grade 1	Grade 2	Grade 3	Grade 4
0.15	0.958	0.656	0.932	0.418
0.2	0.902	0.572	0.853	0.359
0.3	0.789	0.316	0.709	0.185
0.5	0.490	0.122	0.322	0.0654
0.6	0.377	0.0872	0.241	0.0448
0.75	0.253	0.0553	0.159	0.0279
1	0.212	0.0431	0.130	0.0208

Changes in the Melt Flow Index of the simulated polymer (a second Output from the data) are shown in Table 13.9 and Figure 13.14. The MFI of the simulated polymers increases as the catalyst poisoning increases, to within an order of magnitude of the industrial MFI values. The MFI increases because the excess of monomer in the simulated reactor decreases with increasing monomer conversion, leading to the prediction of shorter polymer chains.

Table 13.9: Effect of catalyst poison factor on Melt Flow Index

Catalyst poison factor	MFI [5kg / 190^{o}C]			
	Grade 1	Grade 2	Grade 3	Grade 4
0.15	1.74	0.863	2.54	0.288
0.2	1.62	0.592	2.09	0.210
0.3	0.866	0.156	0.866	0.0436
0.5	0.217	0.0134	0.143	0.00218
0.6	0.141	0.00614	0.0835	0.000823
0.75	0.0670	0.00181	0.0332	0.000209
1	0.0432	0.000775	0.0186	0.000074

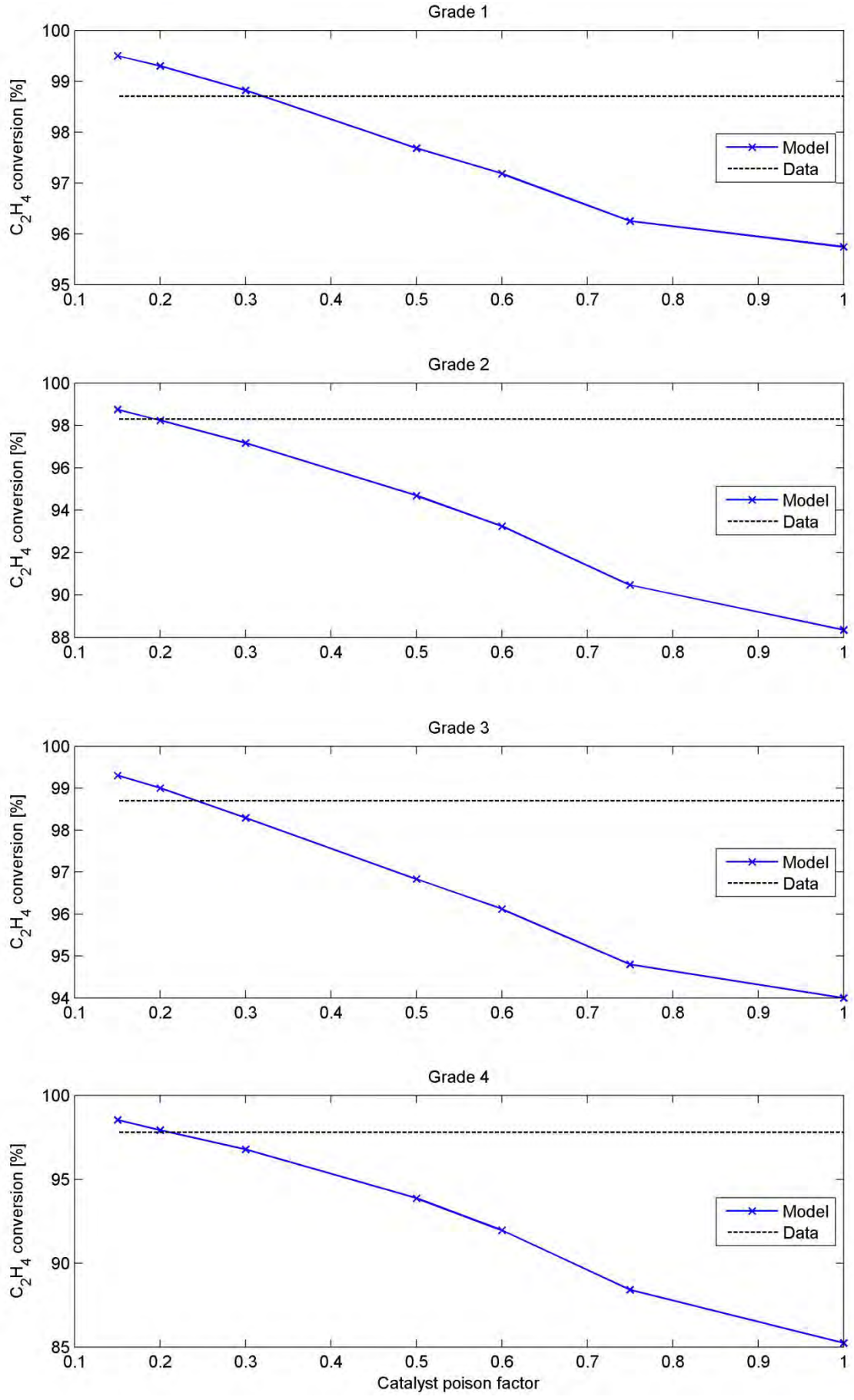

Figure 13.11: Effect of catalyst poison factor on monomer conversion

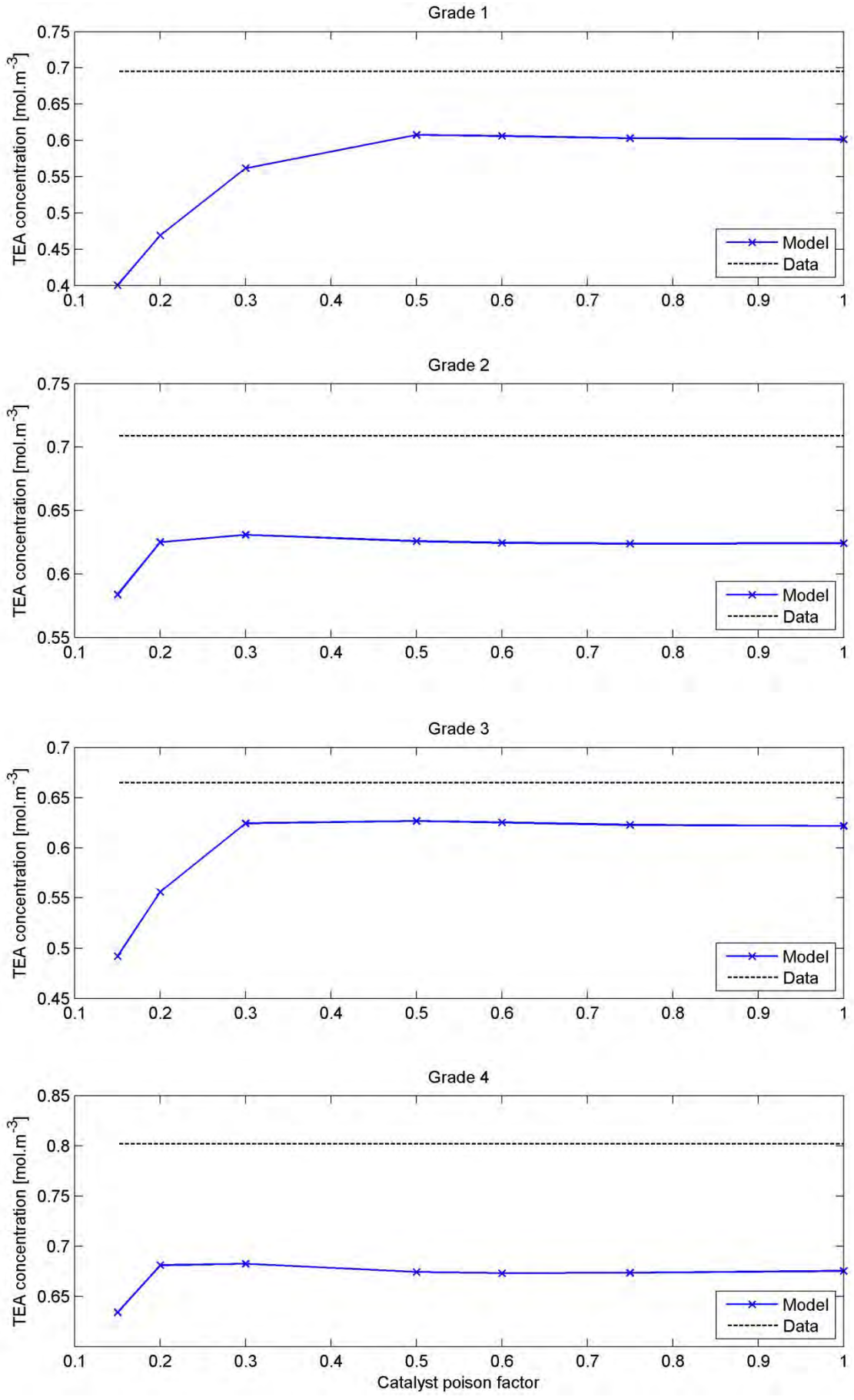

Figure 13.12: Effect of catalyst poison factor on co-catalyst concentration

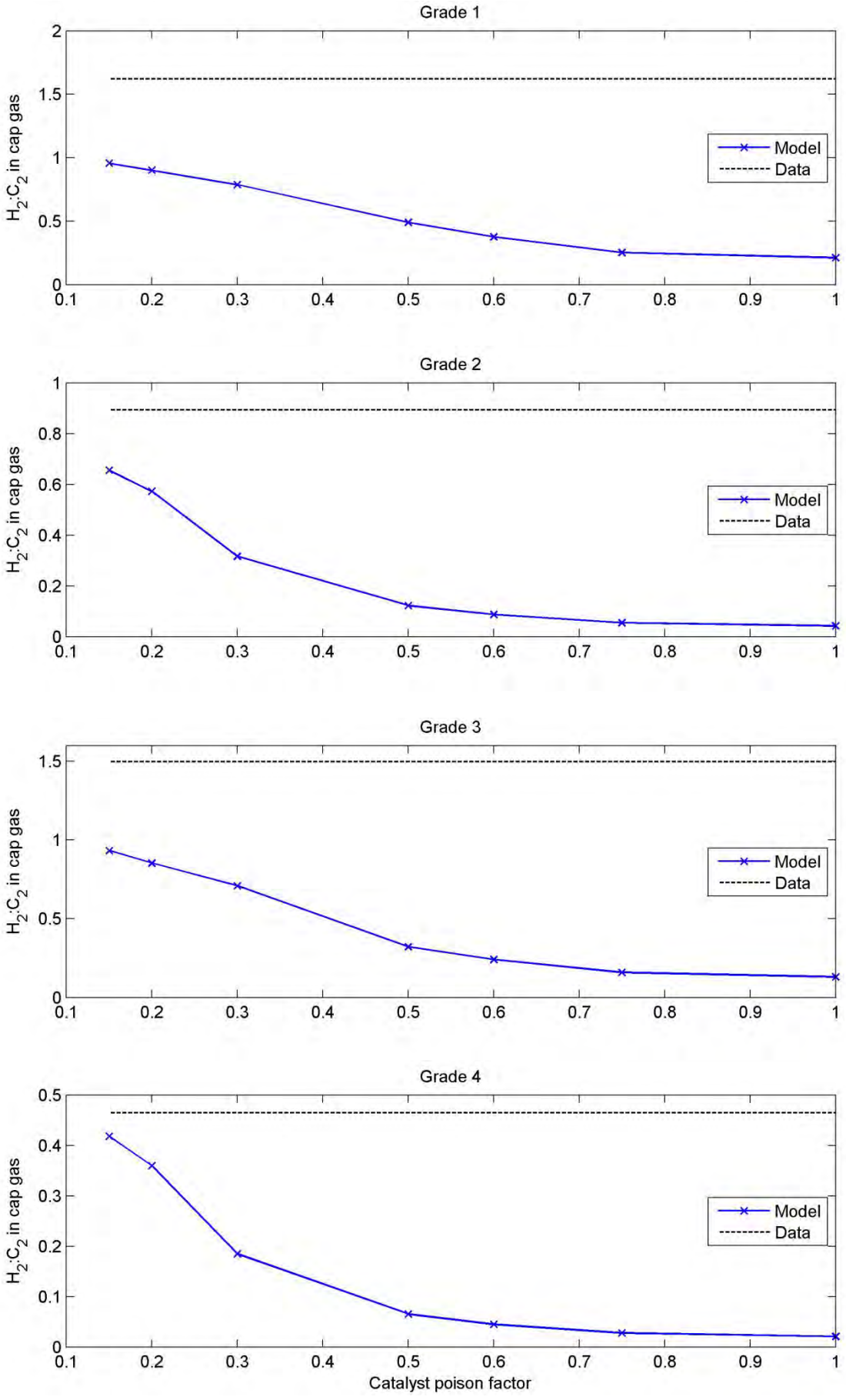

Figure 13.13: Effect of catalyst poison factor on cap-gas ratio

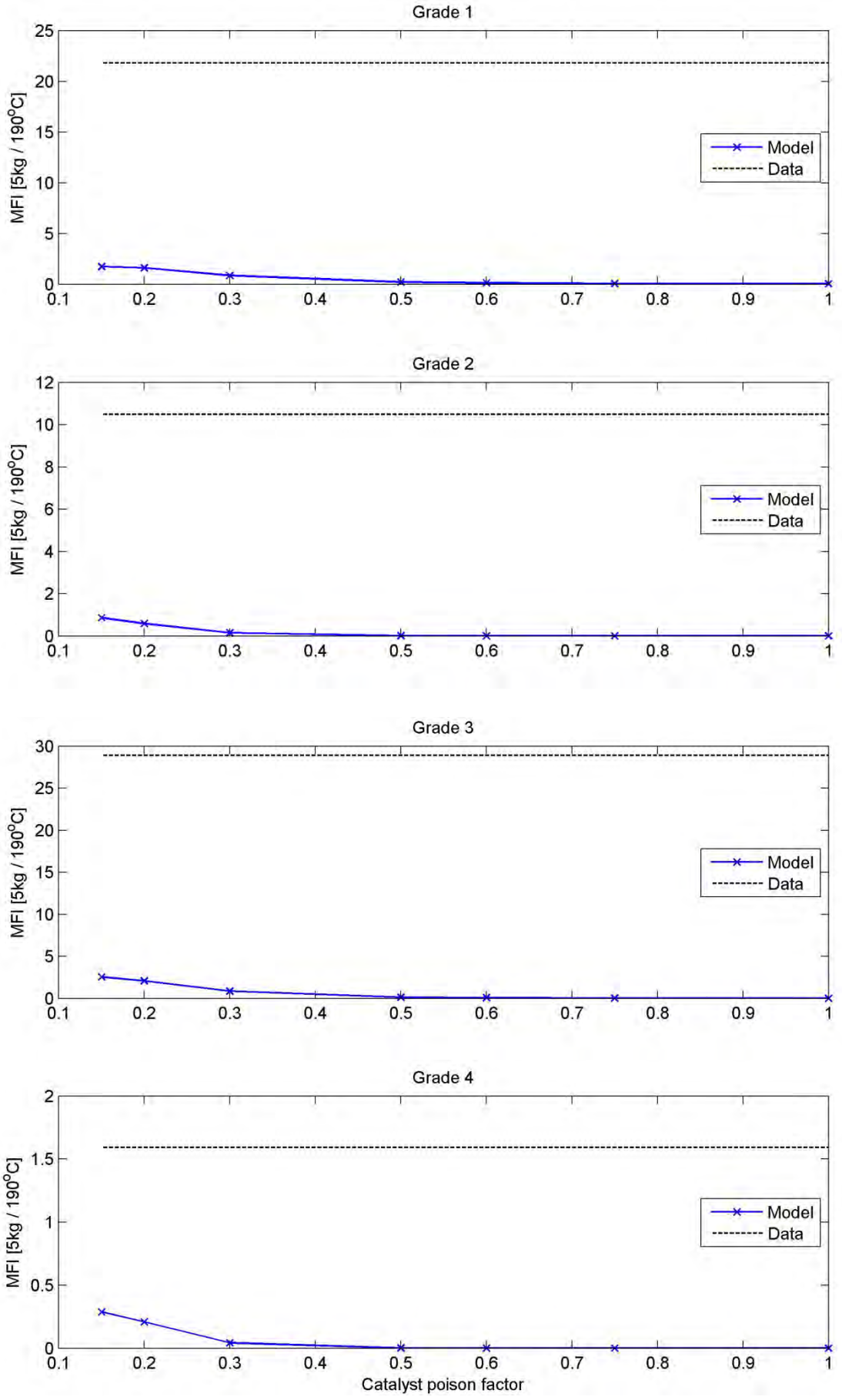

Figure 13.14: Effect of catalyst poison factor on Melt Flow Index

Summary

The preceding tables and figures showed the impact of including catalyst poisoning on the predictions of the industrial reactor model.

When accounting for the presence of a catalyst poison, the model prediction of monomer conversion improved significantly: for low values of the factor (equivalent to a very high proportion of catalyst being poisoned) of between 0.15 and 0.3, the monomer conversion for each grade closely matched the industrial data. This result suggests that some poisoning of the catalyst in the laboratory experiments occurred.

Largely because of the improvements to predicted monomer conversion, the predictions of the cap-gas ratio and the polymer MFI also improved when a catalyst poison was included in the regression procedure. However, even for an unrealistically high degree of catalyst poisoning, the MFI and cap-gas ratio did not match the industrial values.

Just as in the co-catalyst poison study, including the effects of a catalyst poison actually made the model predictions of TEA concentration worse. The conversion of TEA in the reactor increased due to higher rate constants for site transformation and (in particular) chain termination reactions.

Thus, although accounting for a catalyst poison improves the reactor model's predictions of monomer conversion, it does not account for all the discrepancies between the simulation and the industrial data.

It appears that the under-prediction of the monomer conversion, while very important, is not the only factor causing the discrepancy between the polymer properties predicted by the reactor model and the industrial data.

The increased consumption of the co-catalyst in chain termination reactions will have a significant impact on the final simulated chain length distribution, because of the formulation of the pseudo-sites model. This is sufficient reason to re-evaluate the role of the co-catalyst, which in the Kinetic Chapter was identified as being unexpectedly influential in chain termination reactions.

13.3 Role of co-catalyst in polymerisation

Evidence for catalyst poisoning in the lab reactor was presented in the previous section; accounting for this poisoning was shown to correct the model's problems with monomer conversion prediction. However, despite accurately predicting the monomer conversion, the reactor model was not able to accurately reproduce polymer properties.

The discrepancies in monomer conversion prediction masked a second problem in the reactor model, which was identified but not addressed in the Kinetic Study: the co-catalyst is consumed in chain termination reactions at a rate that is surprisingly high, given the traditional understanding of the "catalyst activator" role of the co-catalyst in polymerisation reactions. The secondary role of the co-catalyst as a poison scrubber was also ignored in the Kinetic Study. As shown above, the predicted consumption of co-catalyst increased to unrealistic levels when catalyst (or co-catalyst) poisoning was included in the model.

Given the co-catalyst's significant consumption in termination reactions, the co-catalyst will have a large impact on the final distribution of polymer lengths predicted by the model. The impact of each terminating agent on the final chain length distribution can be explored in more detail by using the pseudo-sites model.

13.3.1 Chain length characteristic parameter

The ratio of propagation to termination rate is specified in the pseudo-sites model by the Chain Length Characteristic Parameter (Rawatlal, 2004), denoted γ^m. The Chain Length Characteristic Parameter (CLCP) is defined as shown in equation 4.36, which is reproduced here from the developments in the Kinetic Chapter.

$$\gamma^m = \left(\frac{\sum_i \sum_j k_{p,ji} \xi_j^m [M_i]}{\sum_i \left(\xi_i^m \left(\beta_{st}^{3+,2+} + k_{t,i}^m C_m \right) + \sum_j k_{p,ij} \xi_i^m \left[M_j \right] \right)} \right) \qquad 4.36$$

The CLCP is a value close to 1, since the propagation rate is significantly higher than the termination or site transformation rates. As the propagation rate increases, the CLCP approaches 1; similarly, as the termination rate at a particular pseudo-site increases, the CLCP for that site decreases.

13.3.2 Pseudo-site chain length distributions

The number- and weight-average molecular weights produced at each pseudo-site, associated with terminating agent *m*, can be found by using the definition of the live polymer moments at each pseudo-site (equation 4.40 in Chapter 4), reproduced below.

$$\lambda_0^m = P_*^m \sum_i \xi_i^m$$

$$\lambda_1^m = P_*^m \sum_i \xi_i^m \frac{1}{1-\gamma^m} \qquad 4.40$$

$$\lambda_2^m = P_*^m \sum_i \xi_i^m \frac{1+\gamma^m}{\left(1-\gamma^m\right)^2}$$

The live number- and weight-average molecular weights, M_n^m and M_w^m, are determined from the ratios of the live moments, as shown in equation 13.6.

$$M_n^m = \frac{1}{1-\gamma^m}$$
$$M_w^m = \frac{1+\gamma^m}{1-\gamma^m} \qquad 13.6$$

The contributions to the total molecular weight distribution for each pseudo-site, as determined by equation 13.6, are shown for three cases: the laboratory data, the industrial simulation, and the industrial simulation when accounting for catalyst poisoning.

Laboratory data

The polymer chain lengths produced at each pseudo-site in the laboratory study, based on the original kinetic parameter fits, are shown in Table 13.10 and Table 13.11. Figure 13.15 summarises the data in the tables.

Table 13.10: Pseudo-site number-average molecular weights for laboratory data

Terminating agent	Spontaneous	Co-catalyst	Ethylene	1-Butene	Hydrogen
Experiment #	Number-average molecular weight [g.mol^{-1}]				
1	$7.344x10^{6}$	$3.254x10^{4}$	$3.392x10^{4}$	$3.449x10^{4}$	$6.969x10^{3}$
2	$7.637x10^{6}$	$3.393x10^{4}$	$3.380x10^{4}$	$5.830x10^{4}$	$7.249x10^{3}$
3	$7.278x10^{6}$	$3.227x10^{4}$	$3.411x10^{4}$	$2.065x10^{4}$	$6.899x10^{3}$
4	$1.352x10^{7}$	$4.286x10^{4}$	$3.392x10^{4}$	$4.522x10^{4}$	$1.810x10^{4}$
5	$6.976x10^{6}$	$3.107x10^{4}$	$3.391x10^{4}$	$3.408x10^{4}$	$6.590x10^{3}$
6	$7.124x10^{6}$	$3.162x10^{4}$	$3.393x10^{4}$	$3.216x10^{4}$	$6.759x10^{3}$
7	$7.302x10^{6}$	$2.658x10^{4}$	$3.392x10^{4}$	$3.395x10^{4}$	$6.928x10^{3}$
8	$7.919x10^{6}$	$3.473x10^{4}$	$3.391x10^{4}$	$3.635x10^{4}$	$7.565x10^{3}$
9	$7.941x10^{6}$	$3.512x10^{4}$	$3.391x10^{4}$	$3.609x10^{4}$	$7.586x10^{3}$
10	$1.277x10^{7}$	$4.062x10^{4}$	$3.393x10^{4}$	$4.187x10^{4}$	$1.710x10^{4}$
11	$7.851x10^{6}$	$3.465x10^{4}$	$3.391x10^{4}$	$3.603x10^{4}$	$7.500x10^{3}$
12	$7.056x10^{6}$	$3.126x10^{4}$	$3.393x10^{4}$	$3.216x10^{4}$	$6.696x10^{3}$
13	$1.281x10^{7}$	$4.060x10^{4}$	$3.393x10^{4}$	$4.161x10^{4}$	$1.716x10^{4}$
14	$4.134x10^{6}$	$2.227x10^{4}$	$3.395x10^{4}$	$2.255x10^{4}$	$3.225x10^{3}$
15	$4.114x10^{6}$	$2.217x10^{4}$	$3.392x10^{4}$	$2.383x10^{4}$	$3.210x10^{3}$
16	$1.412x10^{7}$	$4.447x10^{4}$	$3.392x10^{4}$	$4.527x10^{4}$	$1.904x10^{4}$
17	$7.421x10^{6}$	$3.292x10^{4}$	$3.380x10^{4}$	$5.858x10^{4}$	$7.045x10^{3}$
18	$7.027x10^{6}$	$2.358x10^{4}$	$3.393x10^{4}$	$3.168x10^{4}$	$6.637x10^{3}$
19	$6.618x10^{6}$	$2.944x10^{4}$	$3.413x10^{4}$	$1.925x10^{4}$	$6.277x10^{3}$
20	$7.061x10^{6}$	$3.143x10^{4}$	$3.381x10^{4}$	$5.218x10^{4}$	$6.704x10^{3}$

Table 13.11: Pseudo-site weight-average molecular weights for laboratory data

Terminating agent	Spontaneous	Co-catalyst	Ethylene	1-Butene	Hydrogen
Experiment #	Weight-average molecular weight [g.mol^{-1}]				
1	$1.469x10^{7}$	$6.504x10^{4}$	$6.780x10^{4}$	$6.895x10^{4}$	$1.391x10^{4}$
2	$1.527x10^{7}$	$6.783x10^{4}$	$6.758x10^{4}$	$1.166x10^{5}$	$1.447x10^{4}$
3	$1.456x10^{7}$	$6.451x10^{4}$	$6.820x10^{4}$	$4.128x10^{4}$	$1.377x10^{4}$
4	$2.703x10^{7}$	$8.569x10^{4}$	$6.781x10^{4}$	$9.041x10^{4}$	$3.618x10^{4}$
5	$1.395x10^{7}$	$6.211x10^{4}$	$6.779x10^{4}$	$6.813x10^{4}$	$1.315x10^{4}$
6	$1.425x10^{7}$	$6.322x10^{4}$	$6.784x10^{4}$	$6.428x10^{4}$	$1.349x10^{4}$
7	$1.460x10^{7}$	$5.313x10^{4}$	$6.781x10^{4}$	$6.787x10^{4}$	$1.383x10^{4}$
8	$1.584x10^{7}$	$6.942x10^{4}$	$6.780x10^{4}$	$7.267x10^{4}$	$1.510x10^{4}$
9	$1.588x10^{7}$	$7.022x10^{4}$	$6.780x10^{4}$	$7.215x10^{4}$	$1.514x10^{4}$
10	$2.553x10^{7}$	$8.121x10^{4}$	$6.783x10^{4}$	$8.371x10^{4}$	$3.417x10^{4}$
11	$1.570x10^{7}$	$6.928x10^{4}$	$6.780x10^{4}$	$7.204x10^{4}$	$1.497x10^{4}$
12	$1.411x10^{7}$	$6.250x10^{4}$	$6.783x10^{4}$	$6.430x10^{4}$	$1.336x10^{4}$
13	$2.562x10^{7}$	$8.118x10^{4}$	$6.784x10^{4}$	$8.319x10^{4}$	$3.429x10^{4}$
14	$8.268x10^{6}$	$4.452x10^{4}$	$6.787x10^{4}$	$4.507x10^{4}$	$6.423x10^{3}$
15	$8.229x10^{6}$	$4.430x10^{4}$	$6.782x10^{4}$	$4.763x10^{4}$	$6.392x10^{3}$
16	$2.824x10^{7}$	$8.890x10^{4}$	$6.781x10^{4}$	$9.052x10^{4}$	$3.805x10^{4}$
17	$1.484x10^{7}$	$6.582x10^{4}$	$6.757x10^{4}$	$1.171x10^{5}$	$1.406x10^{4}$
18	$1.405x10^{7}$	$4.713x10^{4}$	$6.784x10^{4}$	$6.334x10^{4}$	$1.325x10^{4}$
19	$1.324x10^{7}$	$5.886x10^{4}$	$6.824x10^{4}$	$3.848x10^{4}$	$1.253x10^{4}$
20	$1.412x10^{7}$	$6.284x10^{4}$	$6.759x10^{4}$	$1.043x10^{5}$	$1.338x10^{4}$

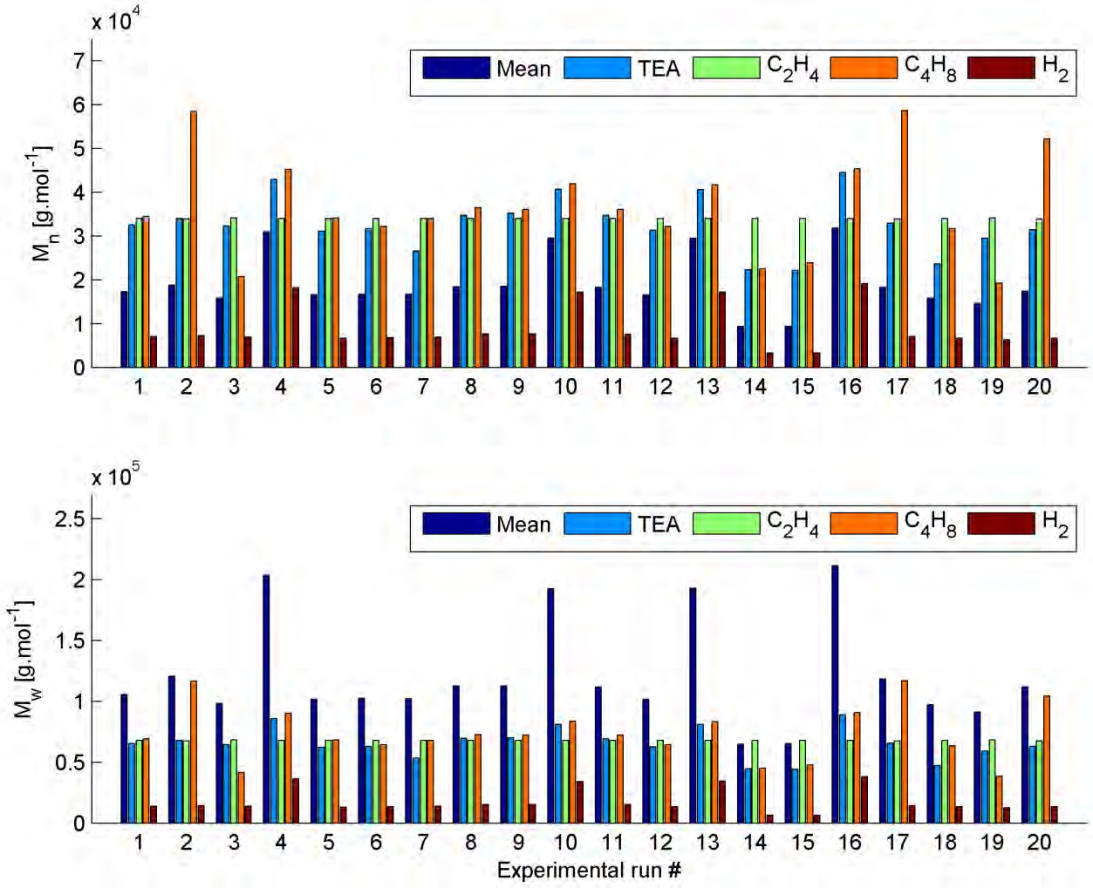

Figure 13.15: Individual pseudo-site contributions for laboratory data (excluding spontaneous termination)

Figure 13.15 shows that, for most of the experimental runs, the pseudo-sites associated with hydrogen produced the shortest chain lengths. Sites associated with the co-catalyst, monomer and comonomer produced polymer chains that were significantly longer than at the hydrogen sites, but still in the same order of magnitude. The values for sites associated with spontaneous termination are not shown in Figure 13.15, since they were as much as four orders of magnitude larger than the other values, and make it difficult to discern differences between the four main terminating agents.

These results, based on the fitted termination rate parameters, can be used as a reference to which the results from the industrial simulation can be compared.

Industrial simulation

The outputs from the simulation of the industrial reactor, with the kinetic parameter values fitted to the laboratory data, are shown in Table 12.1. The values for γ^m in Table 12.1 can be used to determine the molecular weights of the polymer produced at each pseudo-site. The results for each of the simulated polymer grades are shown in Table 13.12 and Table 13.13, and summarised in Figure 13.16.

Table 13.12: Pseudo-site number-average molecular weights for industrial simulation

Terminating agent	**Spontaneous**	**Co-catalyst**	**Ethylene**	**1-Butene**	**Hydrogen**
Experiment #	**Number-average molecular weight [g.mol^{-1}]**				
1	1.367×10^7	1.904×10^5	3.383×10^4	9.251×10^4	2.075×10^4
2	3.173×10^7	2.125×10^5	3.402×10^4	3.896×10^4	1.017×10^5
3	1.798×10^7	1.982×10^5	3.398×10^4	4.088×10^4	3.378×10^4
4	4.512×10^7	2.007×10^5	3.395×10^4	5.651×10^4	2.093×10^5

Table 13.13: Pseudo-site weight-average molecular weights for industrial simulation

Terminating agent	**Spontaneous**	**Co-catalyst**	**Ethylene**	**1-Butene**	**Hydrogen**
Experiment #	**Weight-average molecular weight [g.mol^{-1}]**				
1	2.734×10^7	3.808×10^5	6.762×10^4	1.850×10^5	4.147×10^4
2	6.345×10^7	4.249×10^5	6.802×10^4	7.789×10^4	2.033×10^5
3	3.596×10^7	3.963×10^5	6.794×10^4	8.173×10^4	6.752×10^4
4	9.025×10^7	4.013×10^5	6.788×10^4	1.130×10^5	4.185×10^5

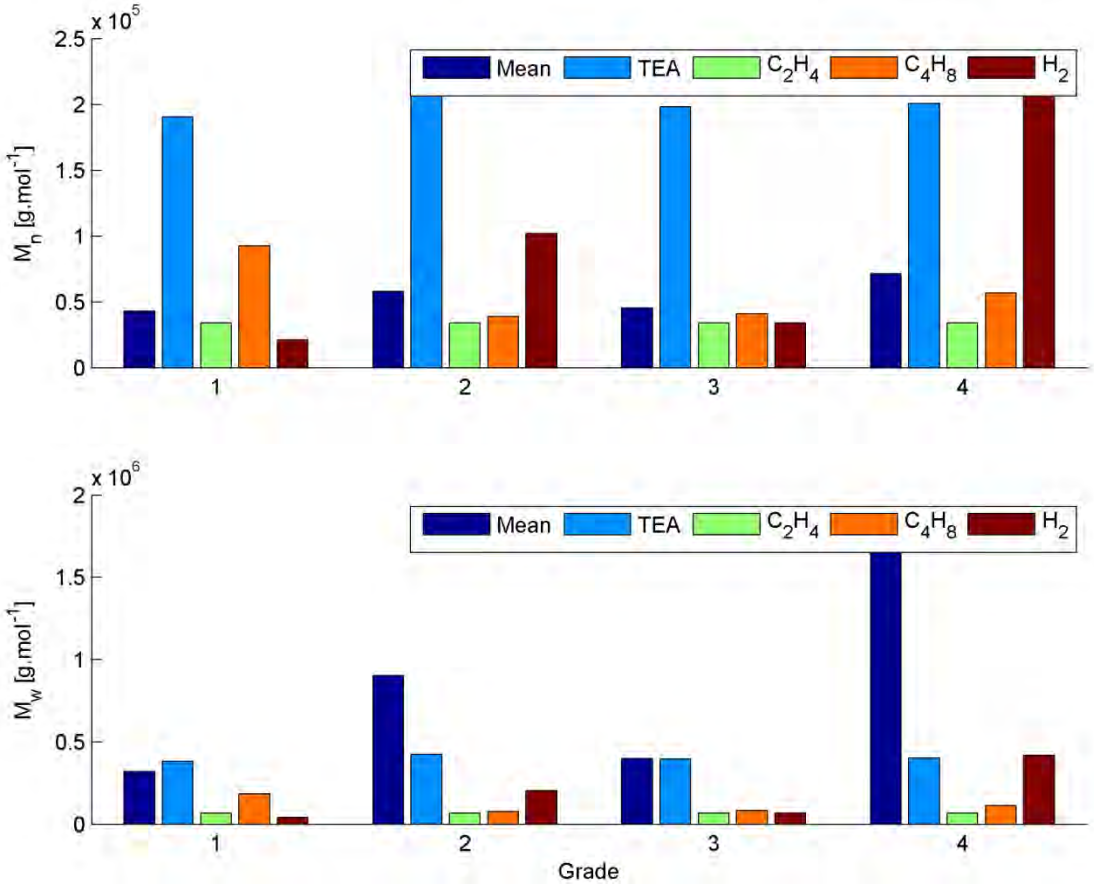

Figure 13.16: Individual pseudo-site contributions for industrial simulation (excluding spontaneous termination)

From the molecular weights shown in Figure 13.16 it is clear that, in the simulation of the industrial reactor, longer polymer chains are formed at pseudo-sites with co-catalyst as the terminating agent, but that the chain lengths produced at the monomer, comonomer and hydrogen pseudo-sites vary from grade to grade.

For grades 2 and 4, the shortest chains are produced by the ethylene and 1-butene pseudo-sites, and relatively long chains are produced at the hydrogen sites.

For grades 1 and 3, the hydrogen pseudo-site produces the shortest chains, followed by the two monomer-associated sites.

The predicted molecular weights in Figure 13.16 contrast with the results of the Kinetic Study in Figure 13.15, where it was shown that the shortest chains were exclusively produced at hydrogen-terminated pseudo-sites, and that the two monomers and co-catalyst all produced longer chains (of roughly the same weight as each other). The molecular weights produced at the pseudo-sites associated with the monomer and comonomer are comparable for the experimental data and the industrial simulation, but the co-catalyst and hydrogen pseudo-sites in the industrial simulation produce significantly longer polymer chains.

The co-catalyst and hydrogen concentrations are lower in the industrial simulation than in the experiments; thus the model predicts lower termination rates at these pseudo-sites, as indicated by the longer chain lengths.

The co-catalyst concentration is higher in the laboratory study because triethyl aluminium (TEA) was added in excess to the reactor as a poison scavenger. Accounting for co-catalyst poisoning may improve the comparison between the laboratory and industrial co-catalyst concentrations.

The lower hydrogen concentration in the simulation is caused by the monomer conversion problems identified previously. Accounting for catalyst poisoning may rectify the hydrogen concentration in the industrial simulation.

Industrial simulation including catalyst poisoning

The outputs from the reactor model, with the kinetic parameters that include the effects of catalyst poisoning (from Table 27.8 in the Appendix), are shown in section 27.2.2 in the Appendix. The values for γ^m in this table were used to determine the polymer lengths produced at each pseudo-site. These polymer chain lengths are shown in Table 13.14 and Table 13.15, and summarised in Figure 13.17.

Table 13.14: Pseudo-site number-average molecular weights for industrial simulation with catalyst poison

Terminating agent	Spontaneous	Co-catalyst	Ethylene	1-Butene	Hydrogen
Experiment #	Number-average molecular weight [g.mol^{-1}]				
1	1.380x10^7	9.844x10^4	3.376x10^4	7.094x10^4	5.717x10^3
2	2.967x10^7	1.656x10^5	3.397x10^4	3.256x10^4	1.400x10^4
3	1.734x10^7	1.263x10^5	3.394x10^4	3.311x10^4	6.313x10^3
4	4.069x10^7	1.701x10^5	3.388x10^4	4.783x10^4	2.379x10^4

Table 13.15: Pseudo-site weight-average molecular weights for industrial simulation with catalyst poison

Terminating agent	Spontaneous	Co-catalyst	Ethylene	1-Butene	Hydrogen
Experiment #	Weight-average molecular weight [g.mol^{-1}]				
1	2.760x10^7	1.968x10^5	6.749x10^4	1.419x10^5	1.141x10^4
2	5.934x10^7	3.311x10^5	6.792x10^4	6.509x10^4	2.796x10^4
3	3.467x10^7	2.526x10^5	6.785x10^4	6.619x10^4	1.260x10^4
4	8.139x10^7	3.402x10^5	6.774x10^4	9.563x10^4	4.755x10^4

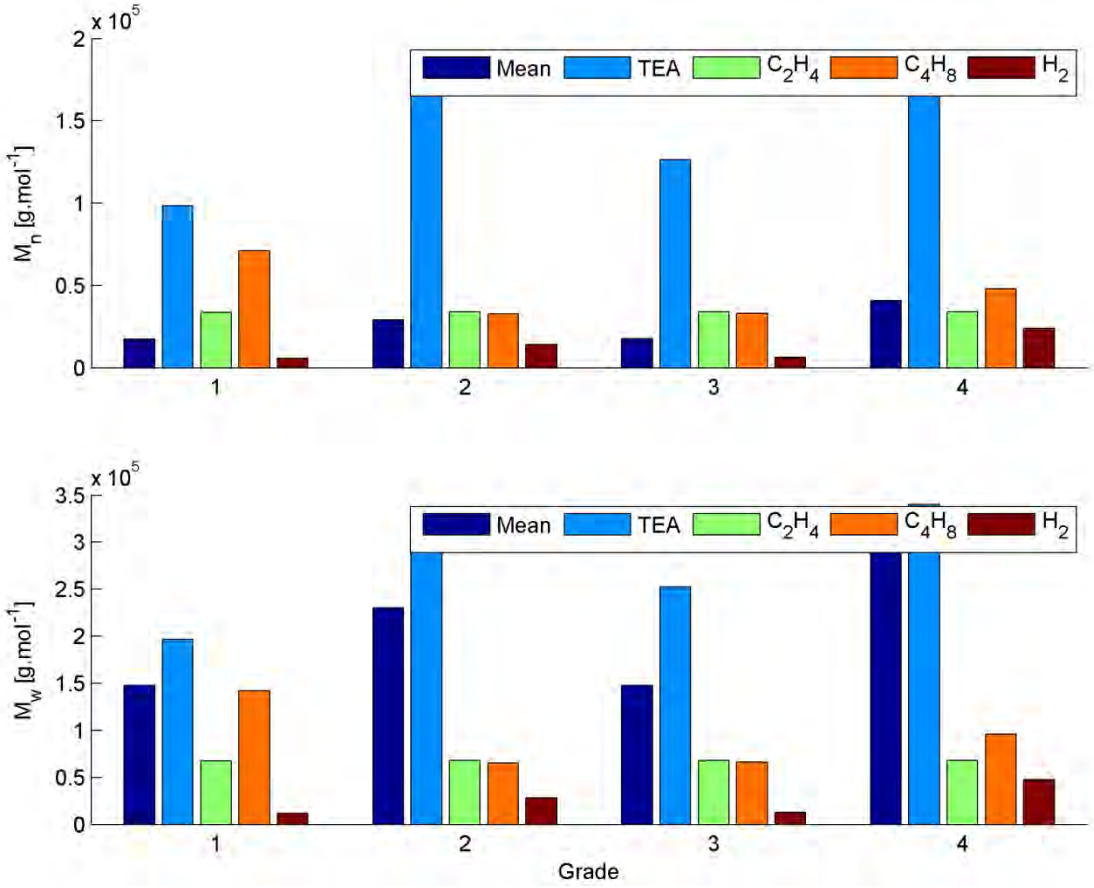

Figure 13.17: Individual pseudo-site contributions for industrial simulation with catalyst poisoning (excluding spontaneous termination)

Figure 13.17 shows the pseudo-site specific chain lengths for the industrial simulation, when accounting for the impact of catalyst poisons. Including the effects of a catalyst poison has improved the predicted ratio of ethylene to hydrogen in the reactor, and so the polymer chains produced at the hydrogen pseudo-sites are now in the same range of lengths as in the laboratory study (see Figure 13.15).

In contrast with the laboratory data, in which the pseudo-sites associated with monomer, comonomer and co-catalyst produced roughly the same weights of polymer, the polymer produced at the pseudo-sites associated with the co-catalyst has a significantly higher molecular weight than at the pseudo-sites associated with the monomer and comonomer in the simulation of the industrial reactor.

The significantly longer polymer chains produced at the co-catalyst pseudo-sites not only contrast with the laboratory data, but are also the reason that the simulated polymer weights still do not agree with the industrial data.

Thus we conclude that the discrepancy between the industrial data and the simulated polymer properties may be due to the co-catalyst-terminated pseudo-sites.

13.4 Summary

Kinetic parameters suggest that consumption of triethyl aluminium (TEA) in termination reactions is much greater than the rate of consumption in site transformation. Including the effects of co-catalyst poisoning (in other words, extending the model to account for the poison-scrubbing role of the co-catalyst) exacerbates this problem, and leads to the prediction of unrealistically high consumption of TEA in the industrial simulation. The kinetic model, in its current formulation, presents the co-catalyst primarily as a chain terminating agent, rather than a catalyst activator or poison scrubber.

In addition, the comparison of pseudo-site chain lengths above suggested that the reason that the chain lengths in the industrial simulation do not agree with the industrial data (or the experimental data) is the contribution from the co-catalyst-terminated sites.

Since the inclusion of chain termination by TEA does not agree with the traditional understanding of the co-catalyst, and causes a discrepancy between the laboratory and industrial data sets, the kinetic model will be modified to exclude the effects of chain termination by the co-catalyst, and to include the poison-scrubbing effect of the co-catalyst in the laboratory reactor.

In addition to the change to the structure of the kinetic scheme, the impact of poisons on the catalyst in the laboratory reactor must be accounted for; the simulations in this chapter have indicated that some poisoning of the catalyst occurred.

CHAPTER 14. VALIDATION OF STEADY-STATE MODEL

In an ideal world, the kinetic scheme and parameters described in Chapter 6 could be combined with the reactor modelling framework in Chapter 10, and be capable of simulating the industrial data presented in Chapter 11 without the need for any modifications of kinetic schemes or reassessing of assumptions.

Unfortunately, the simulation of the industrial reactor with kinetic parameters fitted to the experimental data (in the chapters above), and comparisons with industrial data, revealed the need to account for catalyst and co-catalyst poisons in the laboratory reactor, and to re-evaluate the role of the co-catalyst in termination reactions.

In order to reconcile the sets of data from the laboratory study and the industrial reactor, and produce a useful simulation of the industrial reactor, the regression procedure must be repeated, with three major adaptations:

- The effect of poisons on the catalyst will be included, since the comparison of laboratory and industrial data indicated that significant poisoning of the catalyst had occurred in the laboratory study;
- The effect of poisons on the co-catalyst will be included, since the co-catalyst was added to the laboratory reactor in excess, to act as a poison scrubber; and
- The terminating effect of TEA will be removed from the kinetic scheme, in order to bring the role of TEA in line with the understood role of a co-catalyst.

Further to these changes to the procedures for fitting the kinetic parameters, an adapted form of the reactor model developed in Chapter 10 will be used to more rigorously analyse the lab data by accounting for consumption of all components in the semi-batch reactor, rather than assuming constant concentrations, as in Chapter 4.

The laboratory and industrial models will be run simultaneously to find a set of kinetic parameters that fit all of the available data.

14.1 Fed-batch laboratory reactor model

In addition to the changes to the formulation of the kinetic scheme, a more rigorous model of the fed-batch laboratory reactor has been developed, based on the formulation of the dynamic model of the industrial reactor. This model accounts for the consumption of the reactants, and the potential changes to liquid phase concentrations, during each experimental run.

14.1.1 Mass balances on the laboratory reactor

The balances developed for the industrial reactor (shown in Chapter 10) have been modified for the fed-batch laboratory reactor.

The initial molar hold-up of each of the components in the experimental reactor is given by Table 5.5 in Chapter 5. As before, the concentrations of the reactants in the liquid phase are determined at each time step by the isothermal flash calculations.

The mass balance on the lab reactor for the monomer is shown in equation 14.1. Ethylene is the only component that is fed to the reactor during the experiment, and thus the only component to have a flow term, $F_{C_2H_4}$, in the mass balance. The feed rate of ethylene to the reactor is given by the flowmeter readings.

$$\frac{dC_2H_4}{dt} = F_{C_2H_4} - n_{Ti} m_{cat}(t) r_{C_2H_4}\left(t, \underline{C}, \underline{P_*}\right) \tag{14.1}$$

The mass balances for the other components (which have no flows in or out of the reactor) are given by equation 14.2. Reactants other than ethylene are consumed in various reactions, including propagation, site transformation and chain termination.

$$\frac{dN}{dt} = -n_{Ti} m_{cat}(t) r_N\left(t, \underline{C}, \underline{P_*}\right) \tag{14.2}$$

The monomers (ethylene and 1-butene) are consumed in propagation and termination reactions, as shown in equation 14.3.

$$r_{M_i}\left(t, \underline{C}, \underline{P_*}\right) = [M_i]\left(\sum_j \lambda_{0,j}\left(k_{p,ji} + k_{t,j}^{M_i} f^{M_i}\right)\right) \tag{14.3}$$

Equation 14.4 details the consumption rates of either co-catalyst or hydrogen, which do not play a part in propagation reactions, but are consumed in termination and site transformation reactions.

$$r_X\left(t, \underline{C}, \underline{P_*}\right) = [X]\left(\sum_i \lambda_{0,i} k_{t,i}^X f^X + \sum_q \alpha^{q,r} k_{st,X}^{q,r} P_*^q\right) \tag{14.4}$$

The catalyst activity profiles are given by equation 14.5, just as in Chapter 4.

$$\begin{aligned}
&\frac{dP_*^{4+}}{dt} = -\beta_{st}^{4+,3+} P_*^{4+} \\
&\frac{dP_*^{3+}}{dt} = P_*^{4+}\left(\beta_{st}^{4+,3+} - \beta_{st}^{2+,3+}\right) - P_*^{3+}\left(\beta_{st}^{3+,2+} + \beta_{st}^{2+,3+}\right) + \beta_{st}^{2+,3+} \\
&P_*^{2+} = 1 - P_*^{4+} - P_*^{3+} \\
&P_*^{4+}(t_0) = 1;\ P_*^{3+}(t_0) = 0
\end{aligned} \tag{14.5}$$

The moments of the polymer chain length distribution are determined only by the rate at which growing chains are terminated, since there are no flows of polymer out of the reactor, as shown in equation 14.6.

$$\frac{d\mu_k}{dt} = \left(\beta_{st}^{3+,2+} + \beta_t\right)\lambda_k \qquad 14.6$$
$$\mu_k(0) = 0$$

The balances above describe the changes to the hold up of the reactants, catalyst sites and polymer chains in the laboratory reactor during each experiment.

14.1.2 Outputs from laboratory reactor model

The outputs from the laboratory reactor model must be compared with the relevant laboratory data to determine the accuracy of the simulation.

The ethylene consumption is found from equation 14.7. The rate of ethylene consumption in the polymerisation reaction during each experiment is compared with the rate at which ethylene was fed to the reactor, as measured by the flowmeter.

$$r_{C_2H_4}(t) = k_{p,11}[C_2H_4]P_*^{3+}(t)n_{Ti}m_{cat} \qquad 14.7$$

The comonomer content of the polymer product, which can be compared to the NMR data (see Table 5.8 in Chapter 5) can be determined using equations 14.8 and 14.9.

At each time, the fraction of chains with 1-butene most recently added, ξ_2, which is analogous to the comonomer fraction, can be found by equation 14.8.

$$\xi_2^2\left(k_{p,21}[C_2H_4] - k_{p,11}[C_2H_4] - k_{p,12}[C_4H_8]\right) + \xi_2\left(k_{p,11}[C_2H_4] + 2k_{p,12}[C_4H_8]\right) - k_{p,12}[C_4H_8] = 0 \qquad 14.8$$

The average comonomer content of the final polymer product is the comonomer fraction at each time, weighted by the rate of polymerisation at that time, as shown in equation 14.9.

$$\overline{\xi_2}(t_{end}) = \frac{\int \xi_2(t)P_*^{3+}(t)dt}{\int P_*^{3+}(t)dt} \qquad 14.9$$

The polymer properties (which are compared to the GPC data in Table 5.6 in Chapter 5) are found from equation 14.10 (number-average molecular weight) and equation 14.11 (weight-average molecular weight).

$$M_n = MW_{monomer}\frac{\mu_1(t_{end})}{\mu_0(t_{end})} \qquad 14.10$$

$$M_w = MW_{monomer}\frac{\mu_2(t_{end})}{\mu_1(t_{end})} \qquad 14.11$$

The outputs from the laboratory reactor model will be compared with the experimental data to evaluate the accuracy of the kinetic model.

14.2 Industrial reactor model

The model of the industrial reactor is identical to that used in Chapter 12 above. As before, the points of comparison between the model and the industrial data are classified into two groups: the Outputs (ethylene conversion, catalyst efficiency and polymer properties) and the Internal Checks (cap-gas ratio and “mother liquor” co-catalyst content).

14.3 Regression approach

As has been mentioned before, fitting a large number of parameters simultaneously is a poor approach (Dyson, 2004). With the removal of the chain terminating effect of the co-catalyst, the kinetic scheme now has 10 parameters. These are:

- Three propagation rate constants, $k_{p,ij}$;
- Three site transformation rate constants, $k_{st,i}^{q,r}$ and
- Four termination rate constants, k_t^m.

There is a large set of data to which these ten parameters need to be fitted: the experimental data includes the activity profiles, the comonomer content and the chain length data, for twenty experimental runs; the industrial data includes the three Outputs and two Internal Checks, for each of the four grades of polymer.

Reconciling the laboratory and industrial data requires refitting the kinetic parameters in the context of the changes to the formulation of the model:

- Accounting for catalyst and co-catalyst poisoning, and
- Removing the chain terminating effect of the co-catalyst.

However, accounting for catalyst poisoning will specify the propagation rate constants, as shown in Table 27.8 in the Appendix. Including the effects of co-catalyst poisoning will further determine the site transformation rate constants, as in Table 13.1.

Thus it is only the four termination rate constants which must be refitted to the combined data sets. The objective function for this fitting will consist of the chain properties data:

- The number- and weight-average molecular weights and comonomer content from the laboratory study, and
- The Melt Flow Index from the industrial data.

The objective function is based on the coefficient of correlation for each of the sets of the data described above, as shown in equation 14.12. The advantage of the coefficient of correlation is that it allows the goodness of fit to parameters with very different absolute values (such as number- or weight-average molecular weights, Melt Flow Index and comonomer fraction) to be compared easily. In equation 14.12, the index *e* refers to experiment number (for laboratory data) and the index *ind* refers to the various industrial grades.

$$Obj = \left\{ \sum_{e} \left[\left(1 - R^2_{M_n,e}\right) + \left(1 - R^2_{M_w,e}\right) + \left(1 - R^2_{f_{1-butene},e}\right) \right] + \sum_{ind} \left(1 - R^2_{MFI,ind}\right) \right\}^2 \qquad 14.12$$

The initial guesses of the termination rate constants, and the values of the propagation and site transformation rate constants, are shown in Table 14.1.

Table 14.1: Initial guesses of rate constants for refitting process

$k_{p,ij}$			***j*=C_2H_4**	***j*=C_4H_8**	
		***i*=C_2H_4**	53.43	1.65	[L.min^{-1}.g-cat^{-1}]
		***i*=C_4H_8**	834.7	0	
	sp	**TEA**	**C_2H_4**	**C_4H_8**	**H_2**
	[min^{-1}]	[L.mol^{-1}.min^{-1}]	-	-	[min^{-1}.{mol-H_2.L^{-1}}$^{-0.5}$]
$k_{st,i}^{4+,3+}$	-	$32.6 / f_{co-cat}$	-	-	-
$k_{st,i}^{3+,2+}$	-	-	-	-	0.375
$k_{st,i}^{2+,3+}$	-	$0.889 / f_{co-cat}$	-	-	-
	[min^{-1}]	[L.mol^{-1}.min^{-1}]	[L.mol^{-1}.min^{-1}]	[L.mol^{-1}.min^{-1}]	[L.mol^{-1}.min^{-1}]
k_t^m	3.0x10^{-4}	0	163.7	1095.1	7322.4

The kinetic parameter values that best fit the available data are described below, and compared with the original kinetic parameters that were fitted to the laboratory data.

14.4 Regression results

The kinetic parameters that were fitted to the laboratory data are reproduced in Table 14.2. The set of kinetic parameters that was fitted to the laboratory and industrial data simultaneously is shown in Table 14.3. Confidence intervals are shown in Table 14.4, Table 14.5 and Table 14.6; as before, having a larger experimental data set would improve the confidence intervals, but it is important to note that the inclusion of the industrial data has significantly improved the confidence intervals of the parameters relating to chain termination. The new kinetic parameters are fitted with a catalyst poison factor of 0.3, a co-catalyst poison factor of 0.4, and without the influence of the co-catalyst on chain termination.

As described previously, there are very few published studies which directly compare laboratory and industrial data, and typically polymerisation rate is empirically fitted to the industrial data, rather than making use of experimentally-derived parameters. Thus, the problem of underpredicting monomer conversion has not been encountered before.

It could be suggested that the current approach (of proposing an extent of poisoning, based on the comparison between laboratory and industrial data) is as empirical as the methods used in previous studies (McAuley et al., 1990, Khare et al., 2002, Khare et al., 2004, Neto et al., 2005, Hakim & Moballegh, 2006, Meng et al., 2013). However, the authors believe that it is in fact a significantly more rigorous method of accounting for catalyst kinetics and activity: extensive regression of parameters from laboratory data has been performed, and when these parameters alone have not successfully reproduced industrial data, a physical mechanism (catalyst poisoning in the laboratory) has been proposed and quantified to account for the difference.

Once again, these results point to the difficulties of direct comparisons between industrial and laboratory data, which (as mentioned above) are relatively scarce in the literature.

Table 14.2: Original kinetic parameter fits

$k_{p,ij}$			***j*=C_2H_4**	***j*=C_4H_8**	
		***i*=C_2H_4**	16.93	0.524	[L.min^{-1}.g-cat^{-1}]
		***i*=C_4H_8**	265.5	0	
	sp	**TEA**	**C_2H_4**	**C_4H_8**	**H_2**
	[min^{-1}]	[min^{-1}.{mol-TEA.L^{-1}}$^{-1}$]	-	-	[min^{-1}.{mol-H_2.L^{-1}}$^{-0.5}$]
$k_{st,i}^{4+,3+}$	-	31.7	-	-	-
$k_{st,i}^{3+,2+}$	-	-	-	-	0.325
$k_{st,i}^{2+,3+}$	-	0.924	-	-	-
	[min^{-1}]	[L.mol^{-1}.min^{-1}]	[L.mol^{-1}.min^{-1}]	[L.mol^{-1}.min^{-1}]	[L.mol^{-1}.min^{-1}]
k_t^m	7.04x10^{-4}	3701.2	51.74	353.8	2311.4

Table 14.3: Simultaneously fitted kinetic parameters

$k_{p,ij}$			j=C_2H_4	j=C_4H_8	
		i=C_2H_4	53.43	1.65	[L.min^{-1}.g-cat^{-1}]
		i=C_4H_8	834.65	0	
	sp	**TEA**	**C_2H_4**	**C_4H_8**	**H_2**
	[min^{-1}]	[min^{-1}.{mol-TEA.L^{-1}}$^{-1}$]	-	-	[min^{-1}.{mol-H_2.L^{-1}}$^{-0.5}$]
$k_{st,i}^{4+,3+}$	-	81.46	-	-	-
$k_{st,i}^{3+,2+}$	-	-	-	-	0.372
$k_{st,i}^{2+,3+}$	-	2.23	-	-	-
	[min^{-1}]	[L.mol^{-1}.min^{-1}]	[L.mol^{-1}.min^{-1}]	[L.mol^{-1}.min^{-1}]	[L.mol^{-1}.min^{-1}]
k_t^m	1.53x10^{-4}	-	179.1	2065.6	6457.3

Table 14.4: 95% confidence intervals for propagation rate constants

$k_{p,ij}$		j=C_2H_4		j=C_4H_8		
	i=C_2H_4	53.34	53.52	1.07	2.55	[L.min^{-1}.g-cat^{-1}]
	i=C_4H_8	108	6420	-		

Table 14.5: 95% confidence intervals for site transformation rate constants

	TEA		**H_2**	
	[L.mol^{-1}.min^{-1}]		[min^{-1}.{mol-H_2.L^{-1}}$^{-0.5}$]	
$k_{st,i}^{4+,3+}$	80.3	82.7		
$k_{st,i}^{3+,2+}$			0.366	0.379
$k_{st,i}^{2+,3+}$	1.74	2.86		

Table 14.6: 95% confidence intervals for termination rate constants

	sp		**TEA**		**C_2H_4**		**C_4H_8**		**H_2**	
	[min^{-1}]		[L.mol^{-1}.min^{-1}]		[L.mol^{-1}.min^{-1}]		[L.mol^{-1}.min^{-1}]		[L.mol^{-1}.min^{-1}]	
k_t^m	1.16x10^{-4}	2.01x10^{-4}	-	-	64.0	501	939	4550	3210	13000

14.4.1 Propagation and site transformation rate constants

Most of the differences between the original kinetic fits in Table 14.2 and the values in Table 14.3 are due to the inclusion of the effects of catalyst and co-catalyst poisoning in the kinetic model.

The propagation rate constants are all greater in Table 14.3, because the model now accounts for the effects of catalyst poisoning. A catalyst poison factor of 0.3 implies that 70% of the catalyst used in the laboratory study was not active for polymerisation. Just as in the investigation into the effects of catalyst poisons (section 13.2.2 on page 196), the polymerisation rate constants increase by approximately the inverse of the extent of catalyst poisoning.

The site transformation rate constants associated with the co-catalyst are larger than the original rate constants, because of the effects of co-catalyst poisons. The co-catalyst poison factor of 0.4 implies that 60% of the triethyl aluminium (TEA) added to the laboratory reactor was deactivated, either during preparation in the glovebox, or while "scrubbing" the reactor for catalyst poisons.

Including a co-catalyst poison factor of 0.4 was found to give the best fit of predicted versus measured co-catalyst concentration in the industrial reactor, and of the monomer consumption profiles in the laboratory reactor.

The site transformation rate constant associated with hydrogen has not changed significantly, because the model assumptions relating to hydrogen's influence on catalyst activity have not changed.

14.4.2 Termination rate constants

When compared with the original termination rate constants, the new termination rate constants differ significantly. This is due to the inclusion of catalyst poisoning in the model, and the removal of the terminating effects of the co-catalyst. The termination rate constants for the monomers and hydrogen have increased, and some changes to the relative magnitudes of termination rates have occurred.

As in Chapter 6, the relative magnitudes of termination rates can best be compared when using concentration-weighted termination rates.

In the kinetic model fitted to laboratory data only, the concentration-weighted termination rates (from Table 6.9, reproduced below in Table 14.7) revealed a model of chain termination dominated by hydrogen, which, as the most active terminating agent, produced relatively short chains. The pseudo-sites associated with the co-catalyst, monomer and comonomer all produced polymer chains that were roughly similar to each other, but on average longer than those produced at hydrogen pseudo-sites. The spontaneously-terminated pseudo-sites produced very long polymer chains.

Table 14.7: Concentration-weighted termination rates (fitted to laboratory data)

	m	sp	TEA	C_2H_4	C_4H_8	H_2
$k_t^m C_m$ [min^{-1}]		7.04×10^{-4}	11.45	10.996	10.74	69.68

The concentration-weighted termination rates fitted to the combined data, shown in Table 14.8, show a slightly different picture. Hydrogen is still the most active terminating agent, and spontaneous termination the least, as expected from a fundamental understanding of the reaction system. The removal of the co-catalyst as a terminating agent has had an impact on the relative termination rates of the two monomers.

Whereas in the original fits, ethylene was as active a terminating agent as 1-butene, the comonomer pseudo-sites are now responsible for the production of shorter chains than the monomer pseudo-sites; in other words, the comonomer is a more active terminating agent.

Table 14.8: Concentration-weighted termination rates (fitted to combined data)

m	sp	TEA	C_2H_4	C_4H_8	H_2
$k_t^m C_m$ [min^{-1}]	$1.53x10^{-4}$	-	38.06	62.70	194.7

The reactor model simulations of the laboratory and industrial data, using the kinetic parameter values in Table 14.3, are shown in the following sections.

14.5 Laboratory data fits

The fits of the model and the kinetic parameters in Table 14.3 to the laboratory data are shown below. The simulated liquid-phase concentrations for each laboratory experiment are shown in Section 28.1 on page 399 in the Appendix.

14.5.1 Polymerisation activity profiles

Figure 14.1 to Figure 14.5 show the polymerisation activity profiles, compared with the experimentally measured monomer consumption rates. As shown by the average R^2 value of 0.77, the fits of the activity profiles are significantly better than those shown in Figure 6.1 in Chapter 6, which had an average R^2 value of 0.37. This improvement is due to the more rigorous simulation of the fed-batch laboratory reactor, developed in section 14.1.1.

The kinetic parameters in Table 14.3 result in very good fits of the catalyst activity profiles from the laboratory data.

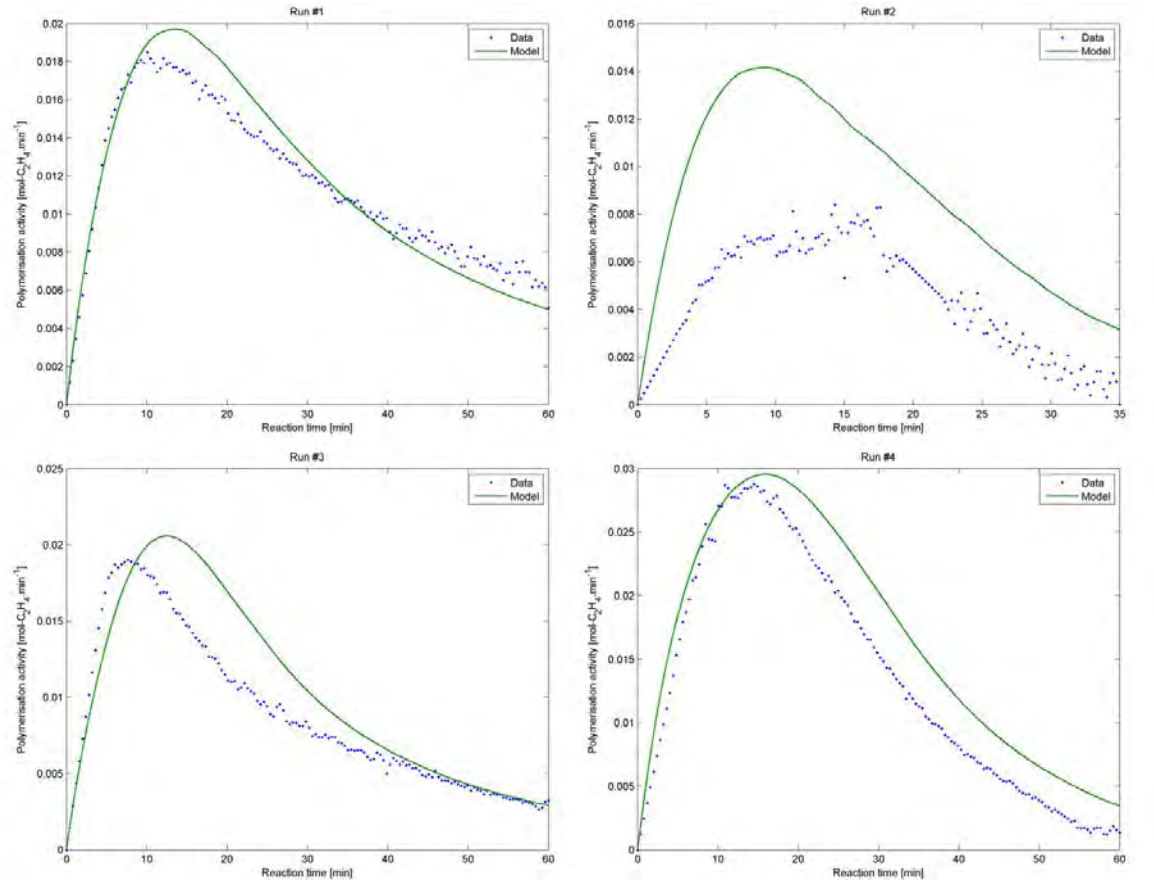

Figure 14.1: Activity profile fits for laboratory data, Runs 1-4

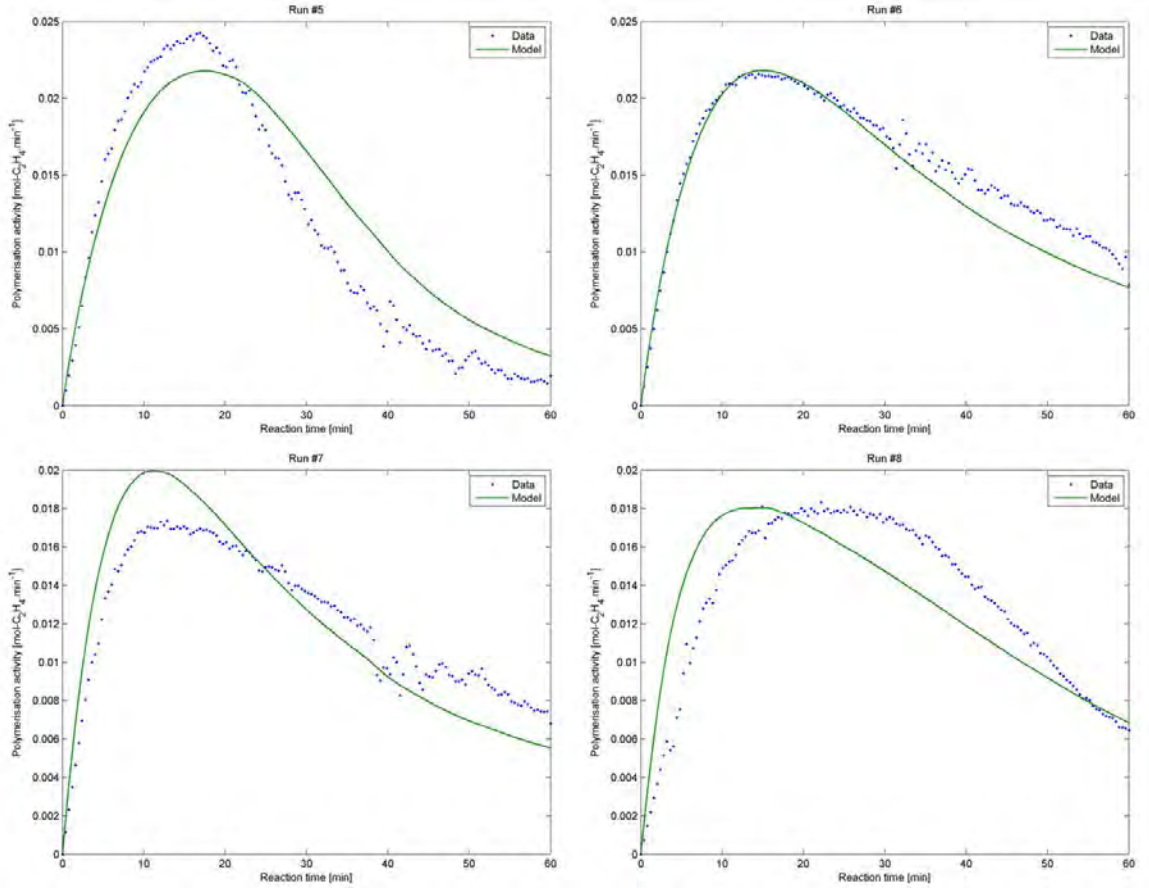

Figure 14.2: Activity profile fits for laboratory data, Runs 5-8

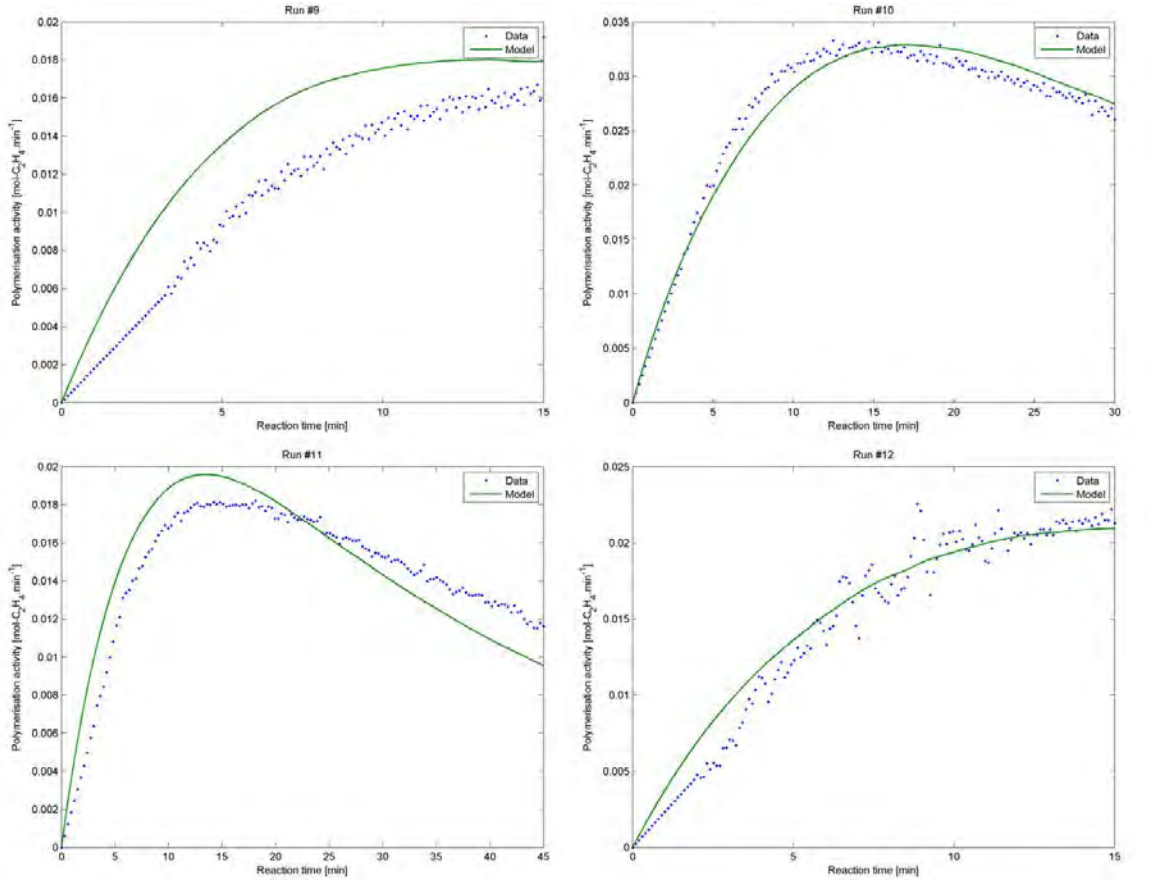

Figure 14.3: Activity profile fits for laboratory data, Runs 9-12

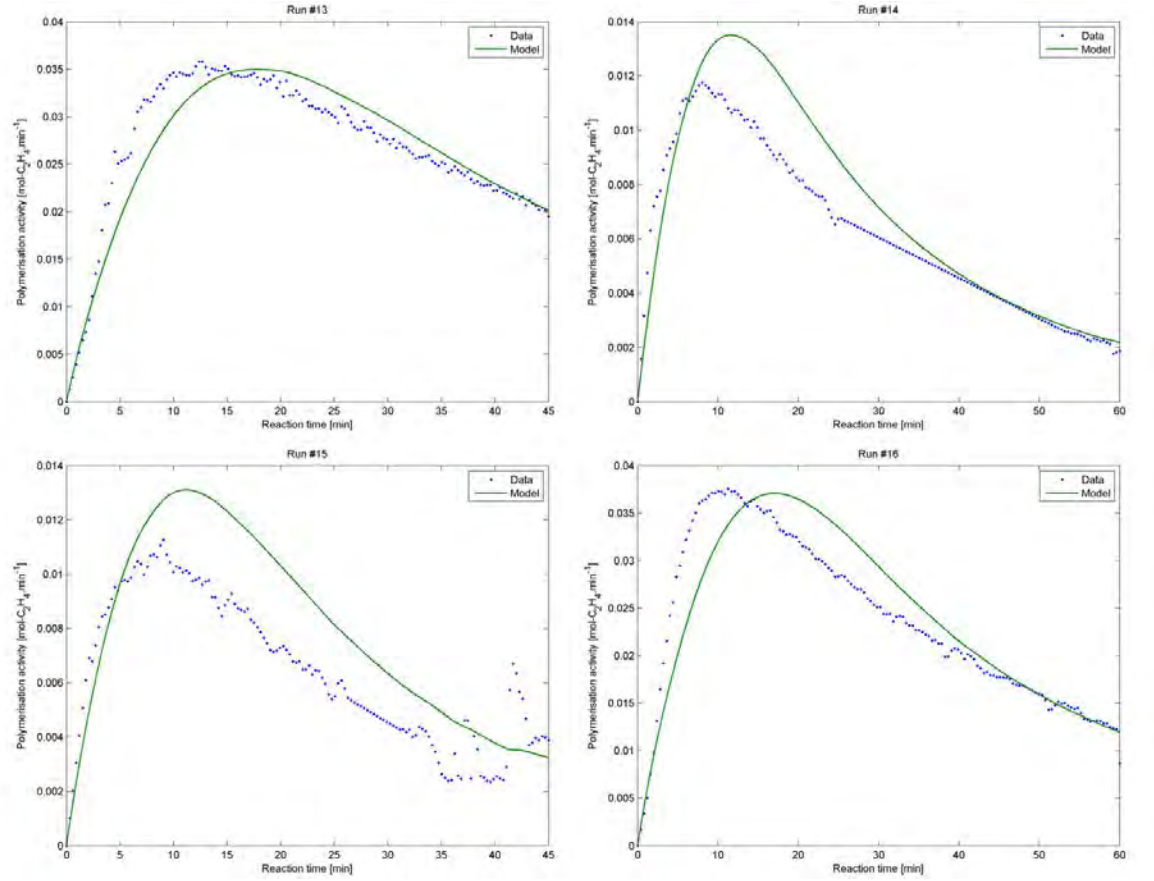

Figure 14.4: Activity profile fits for laboratory data, Runs 13-16

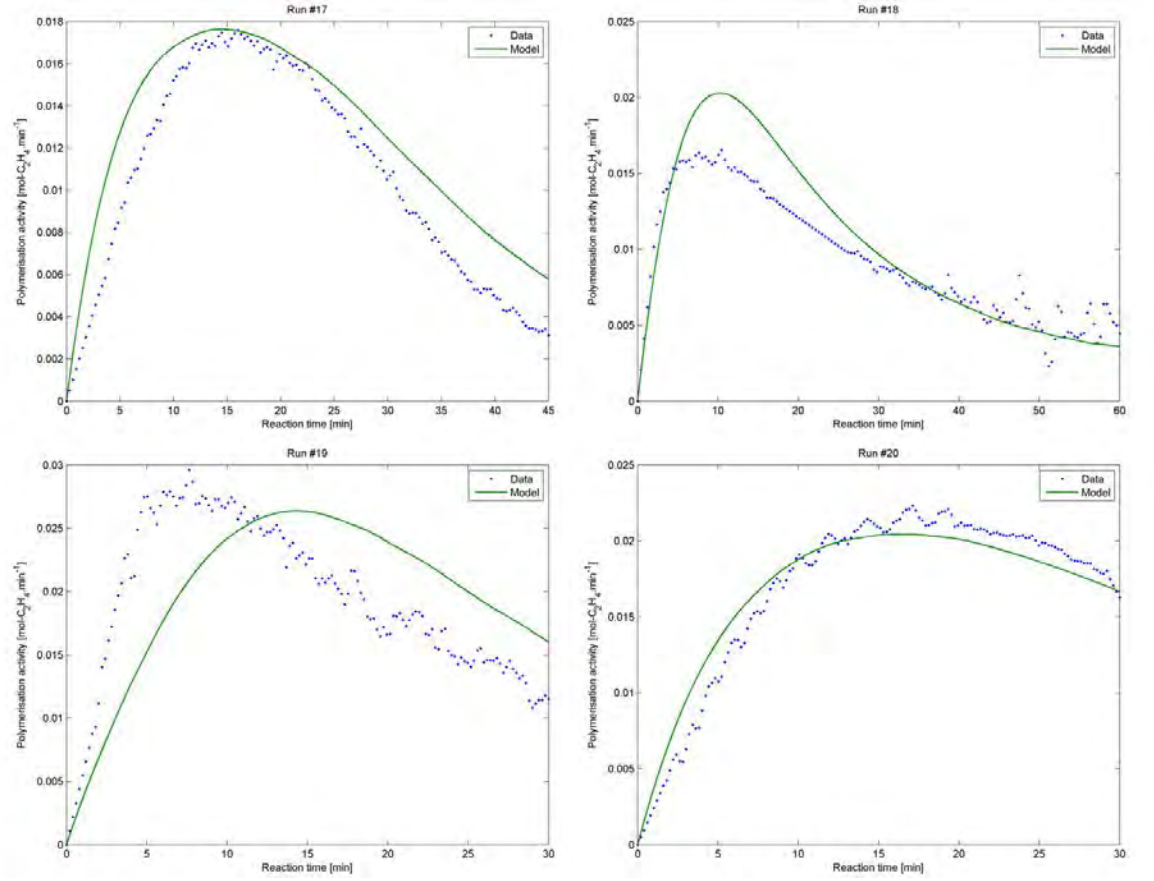

Figure 14.5: Activity profile fits for laboratory data, Runs 17-20

14.5.2 Polymer properties

The properties of the polymer produced in the laboratory reactor, and the model fits, are compared in Figure 14.6 and Figure 14.7.

The comonomer content of the polymer product is compared with the model predictions in Figure 14.6. While the fit of the comonomer incorporation is not as good as when the kinetic model was fitted to the laboratory data only, the model is still able to reproduce the trends from the experiments for the polymer product.

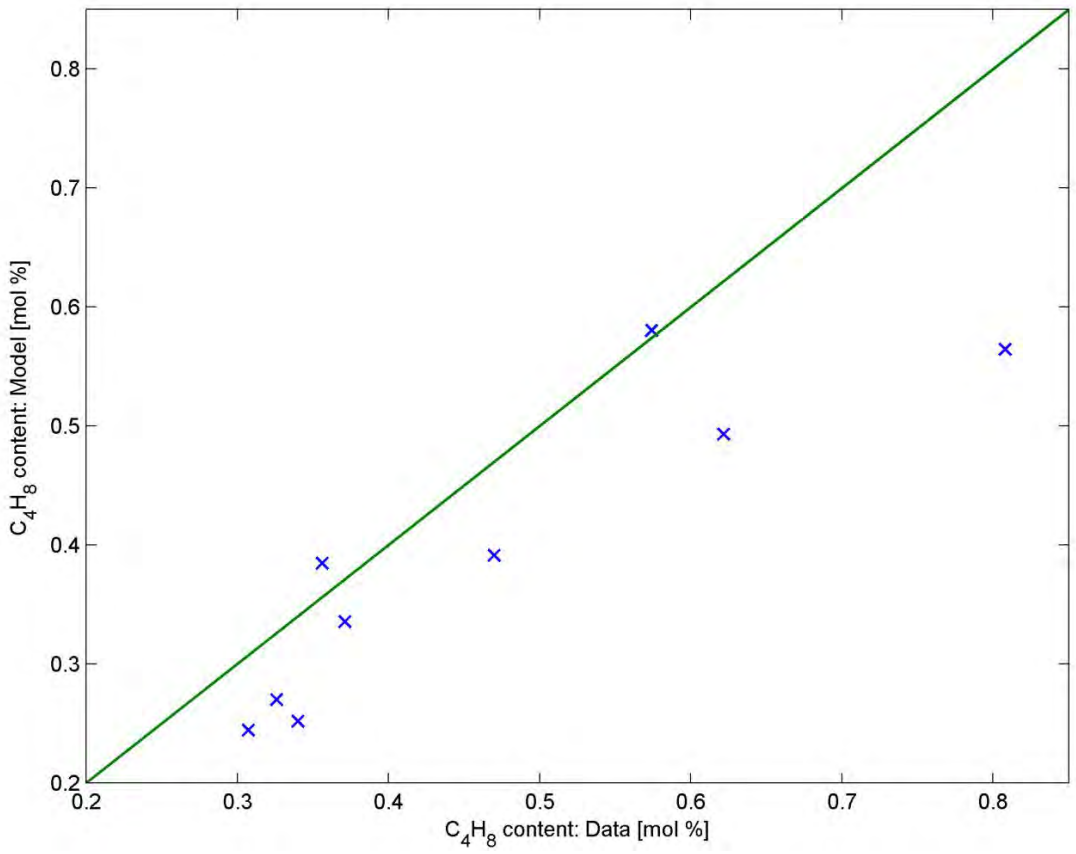

Figure 14.6: Parity plot for comonomer content ($R^2 = 0.57$)

The predicted polymer chain lengths for the new set of kinetic parameters are compared with the laboratory data in Figure 14.7. Once again, the fit for the data is not as good as when the kinetic parameters were fitted to the laboratory data only. Despite including the industrial data in the objective function, the model is still able to reproduce the number- and weight-average molecular weights fairly well.

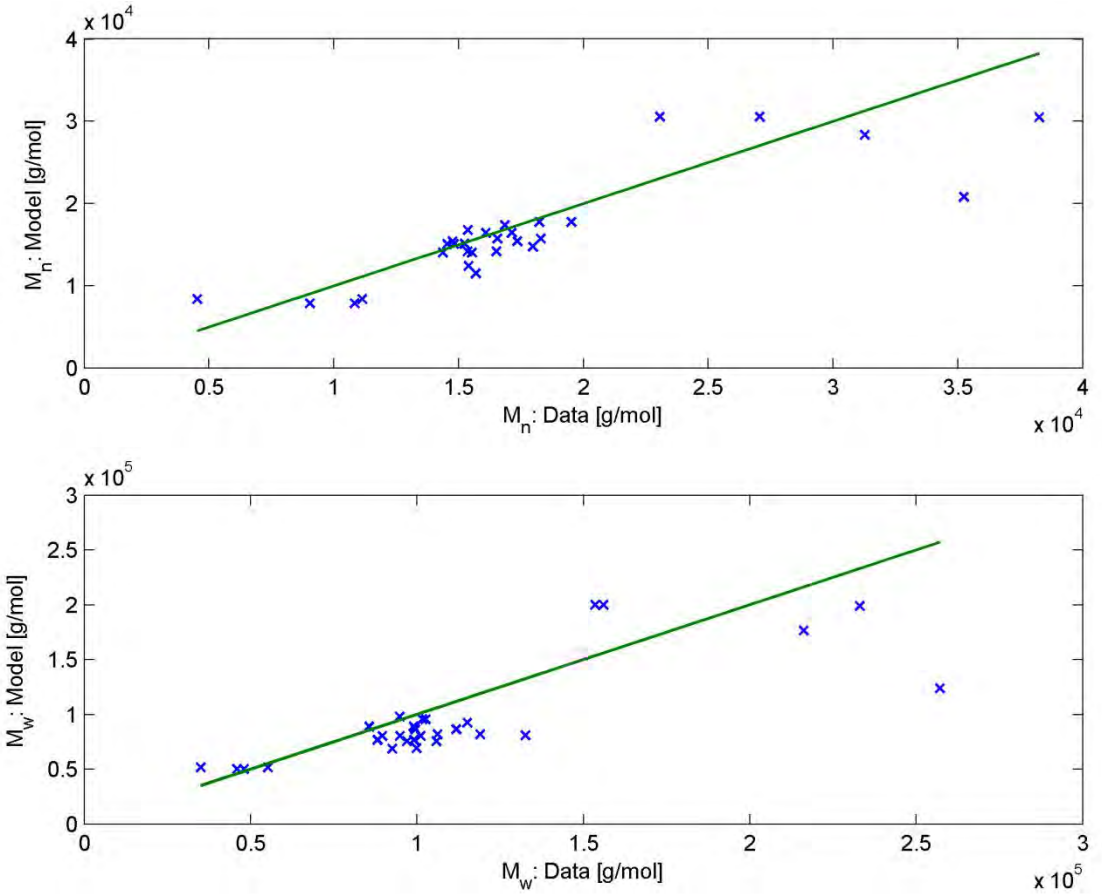

Figure 14.7: Parity plot for chain length distribution ($R^2_{M_n} = 0.40;\ R^2_{M_w} = 0.42$ **)**

14.6 Industrial data fits

The predictions of the reactor model, with the new kinetic parameter values, are compared with the industrial data by means of the Outputs and Internal Checks identified previously. The full set of results from the model is shown in Table 28.1 in the Appendix.

The conversion of the monomer (a model Output) is shown in Table 14.9 and Figure 14.8. The conversion of the monomer has a very large influence on the behaviour of the simulated reactor, particularly the ratio of chain termination to propagation reactions and thus the properties of the polymer product.

Due to the inclusion of the effects of catalyst poisoning in the model, and in contrast to the original comparison between the data and the simulation (see Table 12.2), the predicted conversion now matches the industrial data for all four simulated grades.

Table 14.9: Monomer conversion for data and model

Grade		**1**	**2**	**3**	**4**
Monomer conversion [%]	**Data**	98.7	98.3	98.7	97.8
	Model	99.2	97.8	98.7	97.5

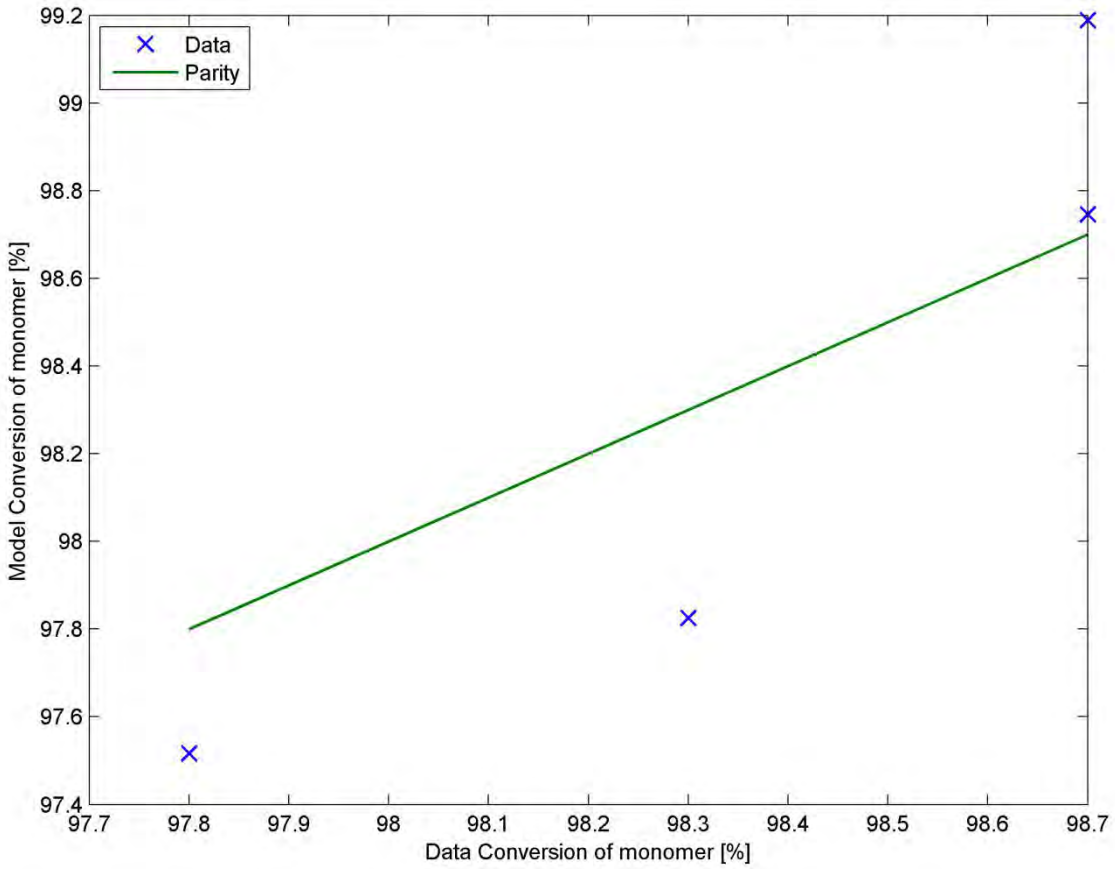

Figure 14.8: Parity plot comparison of industrial and simulated conversion

The catalyst efficiency (the second model Output) is shown in Table 14.10 and Figure 14.9. When catalyst poisons are accounted for in the model, the simulated catalyst efficiency matches the industrially-observed efficiency very closely.

Table 14.10: Catalyst efficiency for data and model

Grade		**1**	**2**	**3**	**4**
Catalyst efficiency [ton C_2H_4/kg-cat]	**Data**	2.82	6.42	3.79	8.8
	Model	2.79	6.24	3.76	8.52

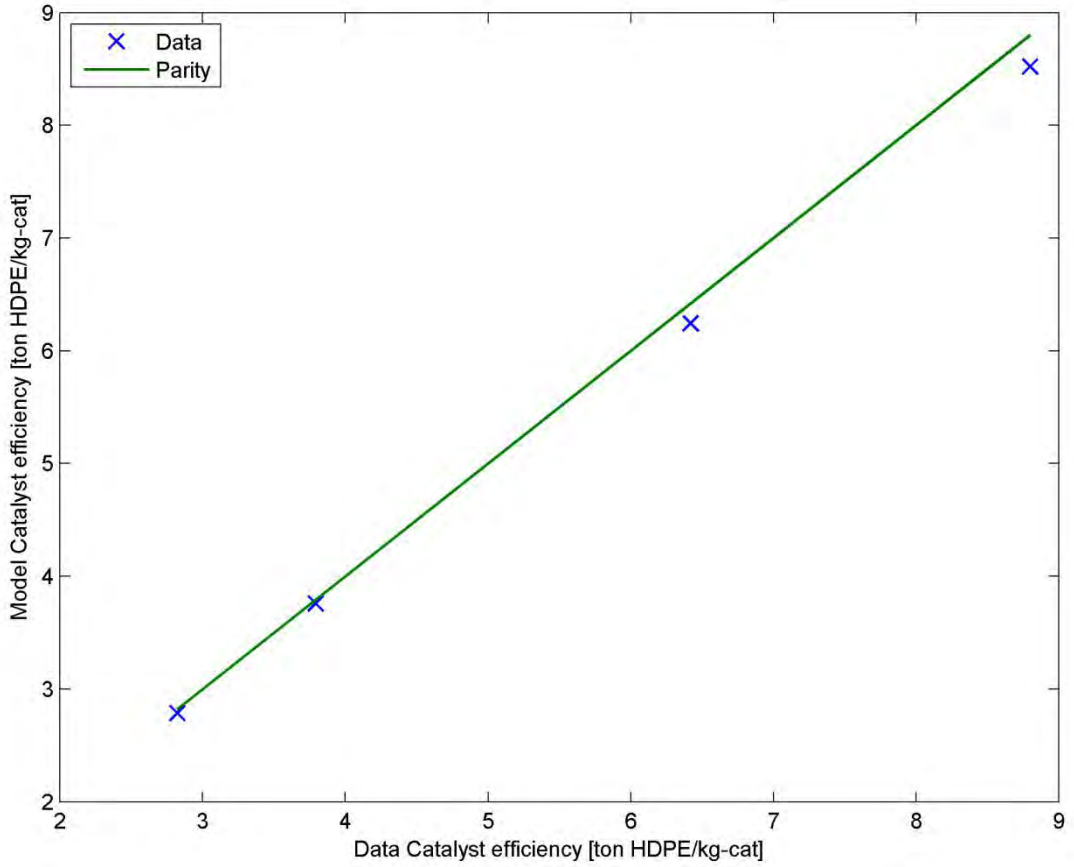

Figure 14.9: Parity plot comparison of industrial and simulated catalyst efficiency

Table 14.11 and Figure 14.10 show a comparison of the cap-gas ratio (an Internal Check) for the simulation and the data.

Table 14.11: Cap-gas ratio for data and model

Grade		**1**	**2**	**3**	**4**
H_2:C_2H_4 in cap gas	**Data**	1.622	0.893	1.498	0.465
	Model	0.971	0.495	0.906	0.305

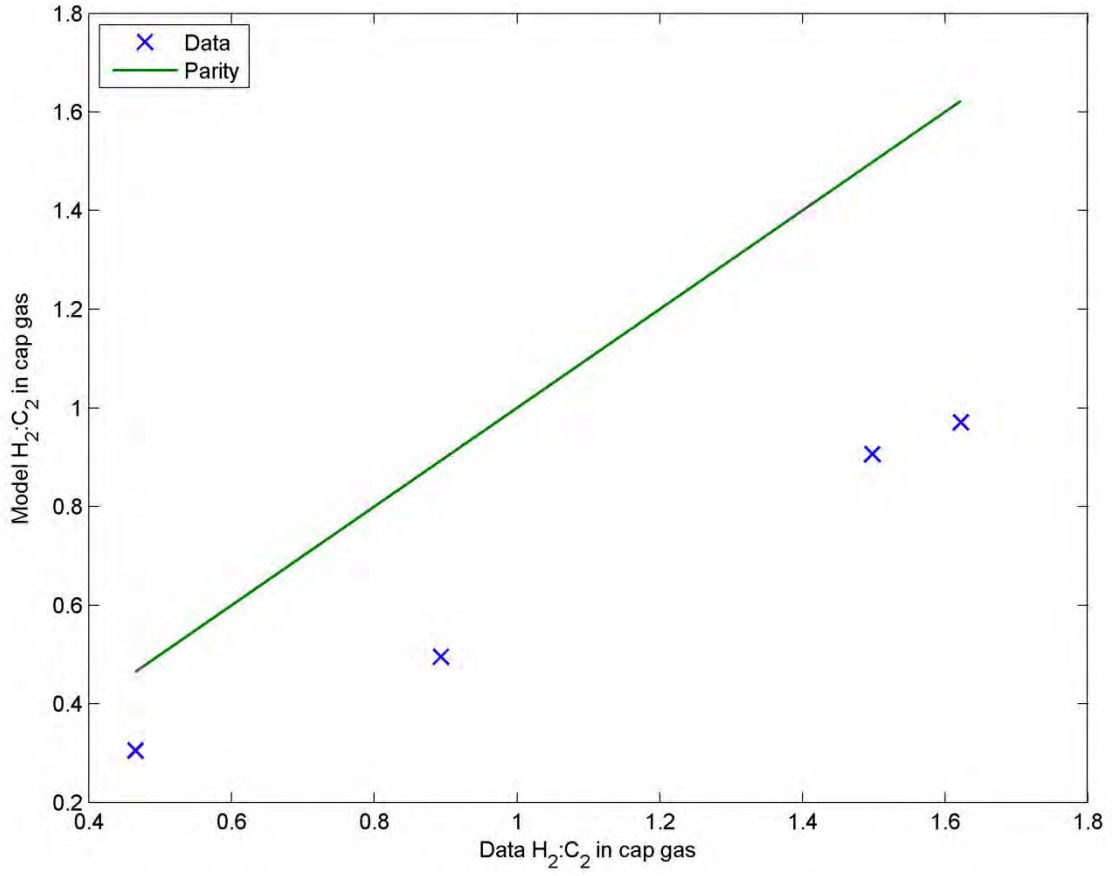

Figure 14.10: Parity plot comparison of industrial and simulated cap-gas ratios

Although the monomer conversion, which has the strongest influence on the cap-gas ratio, is now accurately predicted by the simulation, the cap-gas ratio in Figure 14.10 still does not match the industrial data. While the simulated values follow the same trends as the data, there is an off-set of approximately 40% for each of the simulated grades. Despite every attempt during the parameter fitting process, the fit between the predicted and observed cap-gas ratio could not be improved. The discrepancy may arise from the difficulty of scaling up laboratory data to an industrial-scale application, and represent the challenges faced when attempting to directly compare sets of data from two different sources (laboratory and industrial).

For the purposes of comparisons with the industrial data, the simulation results for cap-gas ratio will be modified by the linear relationship in equation 14.13. This results in the close agreement between industrial and adjusted simulated cap-gas ratio shown in Figure 14.11.

$$[H_2 : C_2]_{adjusted} = 1.663 * [H_2 : C_2]_{model} \qquad 14.13$$

Note that the cap-gas ratio for internal calculations of the simulation (such as isothermal flash calculations or mass balances) is not adjusted by equation 14.13, only the final results.

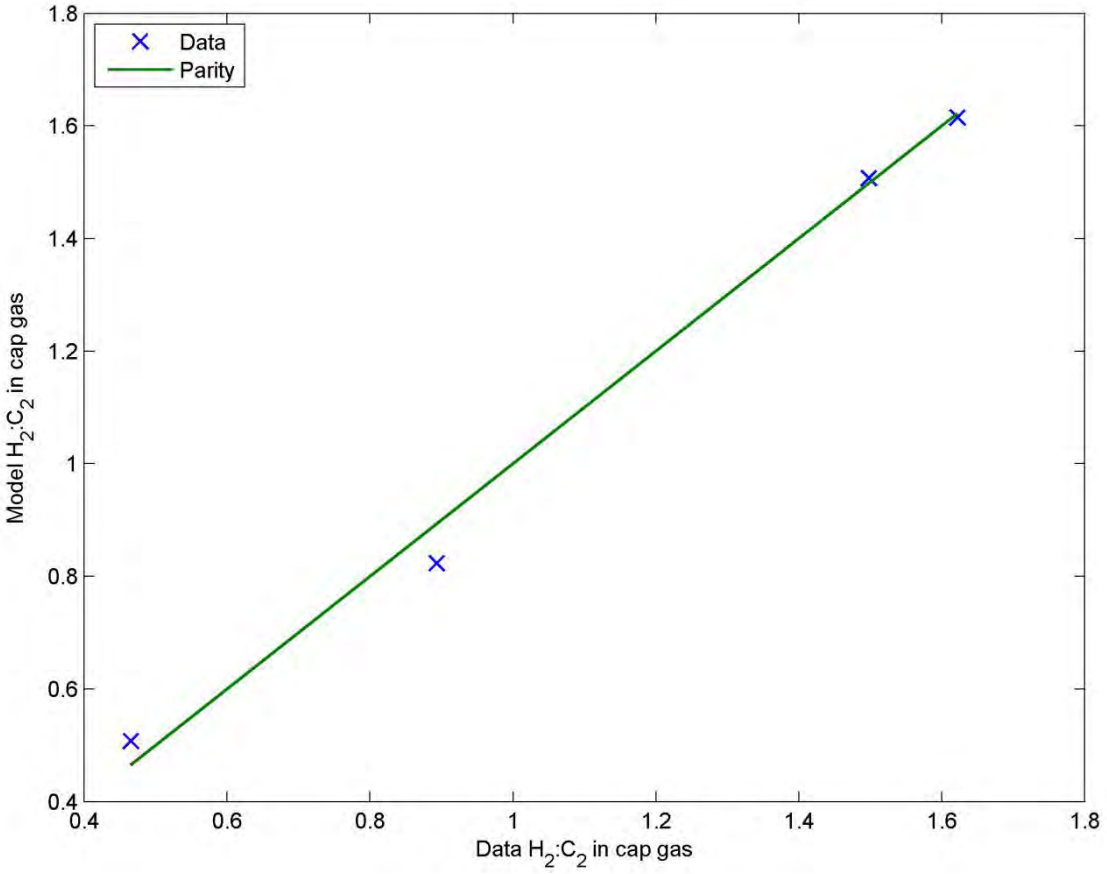

Figure 14.11: Parity plot comparison of industrial and adjusted simulated cap-gas ratios

The predicted properties of the polymer (the final Output) are compared with the industrial data in Table 14.12 and Table 14.13 and Figure 14.12.

Table 14.12: Melt Flow Index for data and model

Grade		**1**	**2**	**3**	**4**
MFI [5kg / 190°C]	**Data**	21.81	10.49	28.88	1.59
	Model	13.95	6.935	25.41	1.655

Table 14.13: Weight-average molecular weight for data and model

Grade		**1**	**2**	**3**	**4**
M_w [g/mol]	**Data**	6.44×10^4	7.77×10^4	5.99×10^4	1.26×10^5
	Model	7.22×10^4	8.65×10^4	6.19×10^4	1.25×10^5

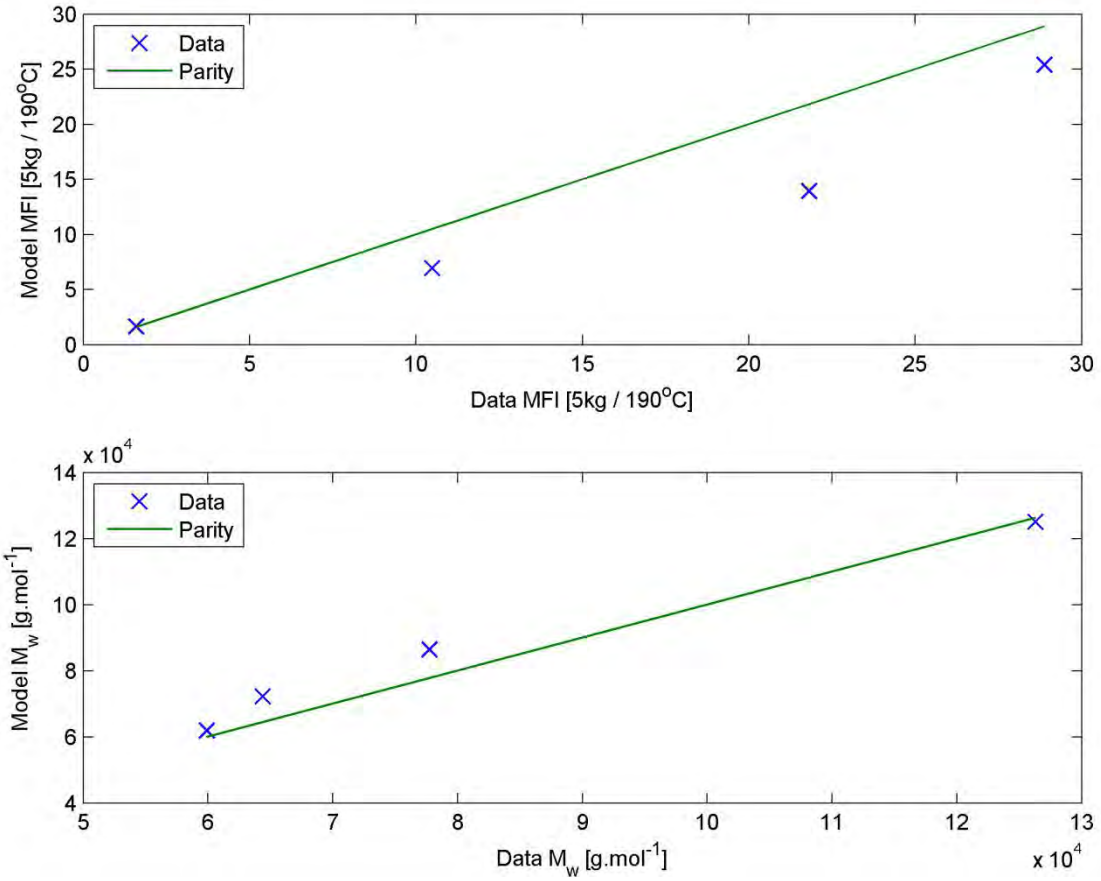

Figure 14.12: Parity plot comparison of industrial and simulated polymer properties

Accounting for catalyst poisoning and removing the terminating effect of the co-catalyst has resulted in improved predictions of polymer properties, and reconciled the industrial and laboratory data sets.

There is still a slight off-set in the model predictions of average molecular weight, despite the improvements. Once again, for comparison with the industrial data, the results of the simulation will be modified. The Melt Flow Index from the simulation will be adjusted according to the relationship in equation 14.14. The parity plot comparison of the adjusted MFI and the industrial data is shown in Figure 14.13.

$$MFI_{adjusted} = -2.07 * 10^{-3} * MFI_{model}^{3} + 0.0415 * MFI_{model}^{2} + 1.45 * MFI_{model} - 0.920 \qquad 14.14$$

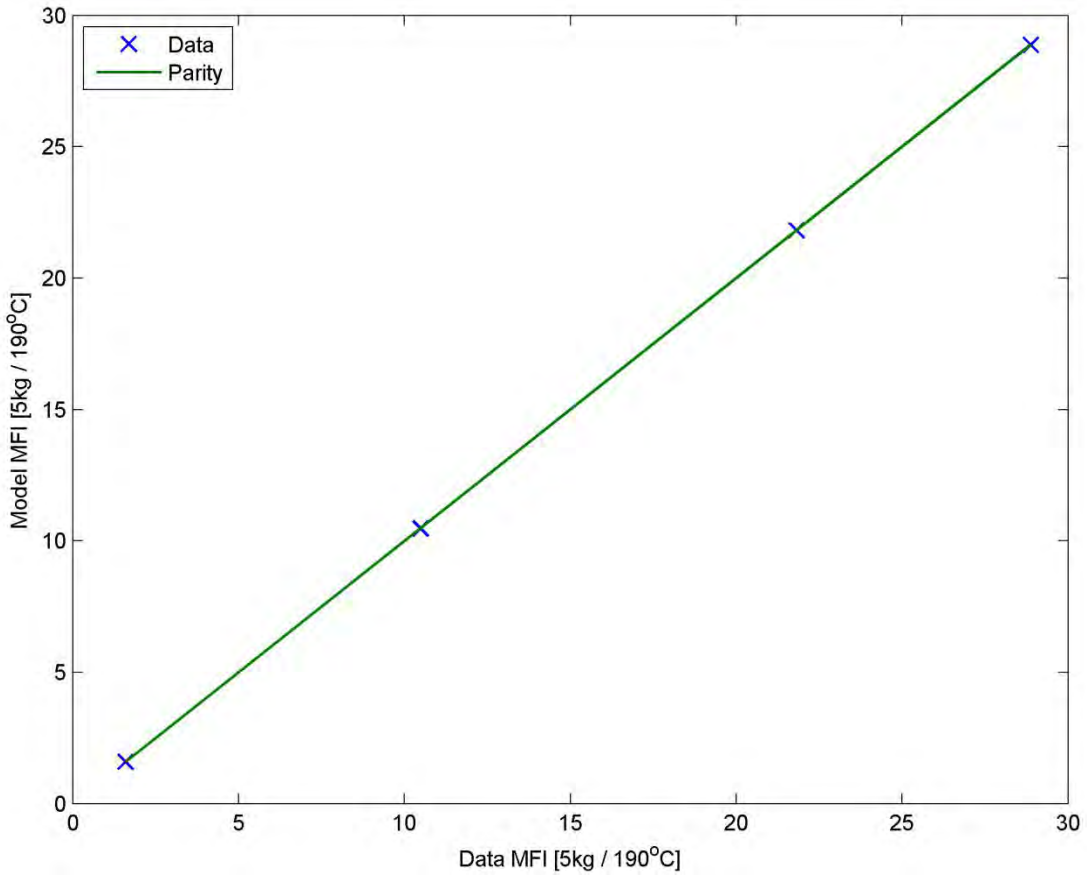

Figure 14.13: Parity plot comparison of industrial and adjusted simulated MFI

Industrially, fluctuations in the MFI of the reactor product of between 10 and 15% in either direction are acceptable, and the final product molecular weight specification can be met by blending together quantities of polymer with slightly differing properties (Nacerodien, 2014). Thus, a polymer product can be said to be within specification for a particular grade, if the MFI falls within a specified range.

Based on industrial data, an allowable range of MFI for each grade can be defined. The minimum and maximum values for product to remain within specification are shown in Table 14.14. Note that the range of MFI values for each grade does not overlap, and so each grade can be distinguished based on its MFI value.

Table 14.14: Minimum and maximum values for MFI to remain within specification

Grade	**1**	**2**	**3**	**4**
MFI	21.81	10.49	28.88	1.59
Min Spec	18	8	25	1.4
Max Spec	23	14	31	1.8

Figure 14.14 and Table 14.15 show the fits of the model to the data for the co-catalyst concentration in the liquid phase of the reactor (an Internal Check). Removing the chain terminating effect of the co-catalyst from the kinetic scheme, and accounting for the effects of co-catalyst poisoning in the laboratory study, has made the model predictions of co-catalyst concentration in the liquid phase significantly better than the original fits (shown previously in Figure 12.2).

Table 14.15: Co-catalyst concentration for data and model

Grade		**1**	**2**	**3**	**4**
TEA concentration [mol/m^3]	**Data**	0.695	0.709	0.665	0.802
	Model	0.678	0.699	0.695	0.773

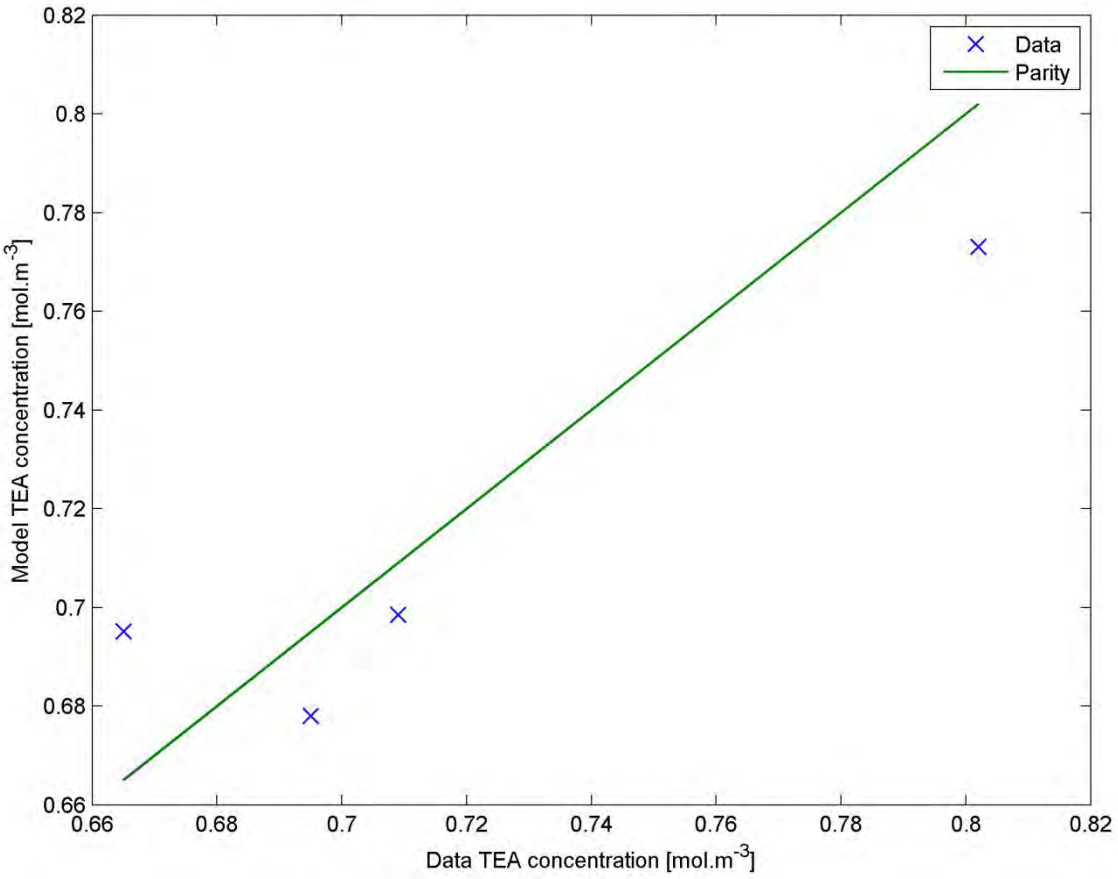

Figure 14.14: Parity plot comparison of industrial and simulated co-catalyst concentration

14.7 Summary

The original formulation of the kinetic model, and resulting fits to the laboratory data, did not account for catalyst or co-catalyst poisoning. Largely due to this lack, the simulation of the industrial reactor did not adequately represent the behaviour of the actual reactor, as shown by the lack of agreement of the points of comparison: the Internal Checks (co-catalyst concentration and cap-gas ratio) and the Outputs (monomer conversion, polymer properties and catalyst efficiency).

A further problem that was identified in the model formulation was the role of the co-catalyst, which was acting primarily as a chain termination agent, rather than a catalyst activator or poison scrubber, further increasing the discrepancy between model and data.

When the reactor model was modified to account for catalyst and co-catalyst poisoning, and the role of the co-catalyst corrected, the model was able to successfully reproduce not only the laboratory data, but the industrial data as well.

In addition, the previously-developed reactor model was used to simulate both sets of data, providing a more rigorous simulation of the laboratory fed-batch reactor than that presented in Chapter 6.

Reconciling these two very different sets of data, through the identification of points of comparison between the laboratory study, the industrial operation and the reactor model itself, is an illustration of not only the effectiveness of the pseudo-sites-based kinetic scheme, but also the power of detailed analysis of such complex processes through the modelling approach.

The reactor model is capable of simulating the steady-state behaviour of an industrial reactor producing four different grades of polyethylene. We now turn our attention to the dynamic behaviour of the reactor, and specifically the process of grade transitions.

CHAPTER 15. VALIDATION OF UNSTEADY-STATE MODEL

As described in the introduction to this thesis, the greatest challenge in the operation of continuous flow polymerisation reactors occurs during grade transitions, which involve a controlled change in reaction conditions so as to change the grade of polymer being produced. Grade transitions are periods of inherently unsteady-state operation.

During a grade transition, polymer is produced which does not yet meet either the specifications of the new target grade, or the grade being produced up to that point. This polymer can be used for low-value applications, at best, and in the worst case is waste material. In most cases, this off-specification material cannot be discarded due to quantity, and must be stored at significant cost.

The minimisation of this waste and the duration of grade transitions is one of the ultimate goals of this project. Before any attempts at optimisation, it must be shown that the proposed reactor model can reproduce the unsteady-state operation of the industrial reactor of interest.

In the industrial reactor, empirical "recipes" are used to determine the reactor conditions in order to produce each grade (corresponding to the data in Table 11.1). Experience-based "rules of thumb" or strategies are typically applied to minimise the waste produced during grade transitions.

The industrial operating data that was provided included data for three grade transitions:

- The change from production of Grade 4 to Grade 1;
- The change from production of Grade 2 to Grade 4 and
- The change from production of Grade 3 to Grade 2.

Given that there are four grades, there are 12 possible grade transitions (from each of the four grades to each of the other three). In the absence of more operational data, the three transitions shown in the available data must represent the strategies employed by reactor operators.

This chapter describes and interprets the available industrial data for grade transitions, and then presents a validation of the predictions of the reactor model with this unsteady-state data. This validation step is of particular importance, given that in Chapter 14 the reactor model was only compared to steady-state industrial data.

15.1 Industrial grade transition operational data

As in Chapter 11, the full industrial operational data cannot be shown for intellectual property reasons; the figures below represent the information that can be shown.

Inspection of the data revealed that the feed rates of ethylene, co-catalyst and solvent are not adjusted during grade transitions, and that the reactor temperature and pressure are also kept steady. In contrast, the feed rates of comonomer, hydrogen and catalyst are varied during the transition from one grade to another; these three feed rates appear to be the manipulated variables that operators use to effect a grade change.

Figure 15.1, Figure 15.3 and Figure 15.5 show the feed rates of comonomer, hydrogen and catalyst for the three grade transitions for which data is available. Since the full set of data cannot be shown, these three figures represent the trajectories between the operating conditions specified in Table 11.1 in Chapter 11.

Figure 15.2, Figure 15.4 and Figure 15.6 show the cap-gas ratio and Melt Flow Index (MFI) measured during the three grade transitions. The MFI represents the result of the changes to the operating conditions in the reactor, and can be used to determine when a transition begins and ends, based on the grade specifications (previously shown in Table 14.14).

The cap-gas ratio is a leading indicator of the properties of the polymer being produced in the reactor, and has been included not only for its industrial importance but also because it is one of the most important points of comparison between the industrial data and the reactor model.

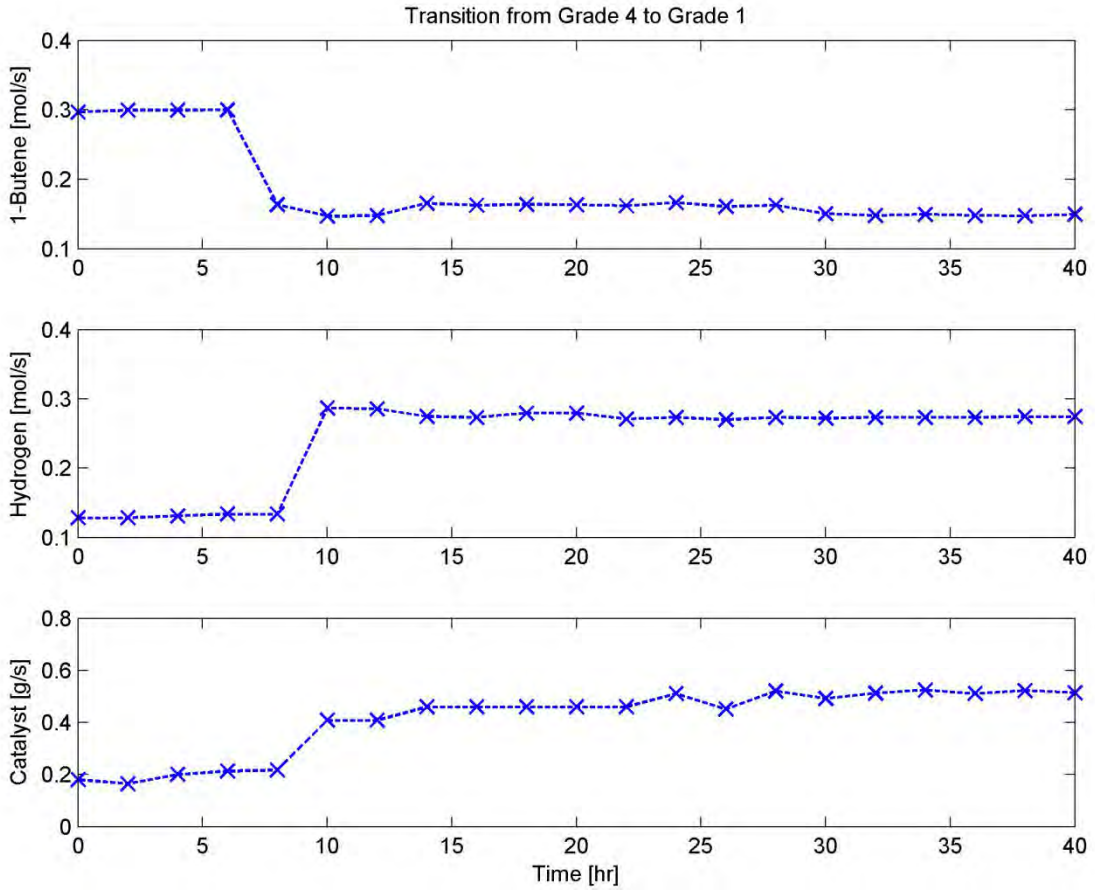

Figure 15.1: Manipulated variables for grade transition from Grade 4 to Grade 1

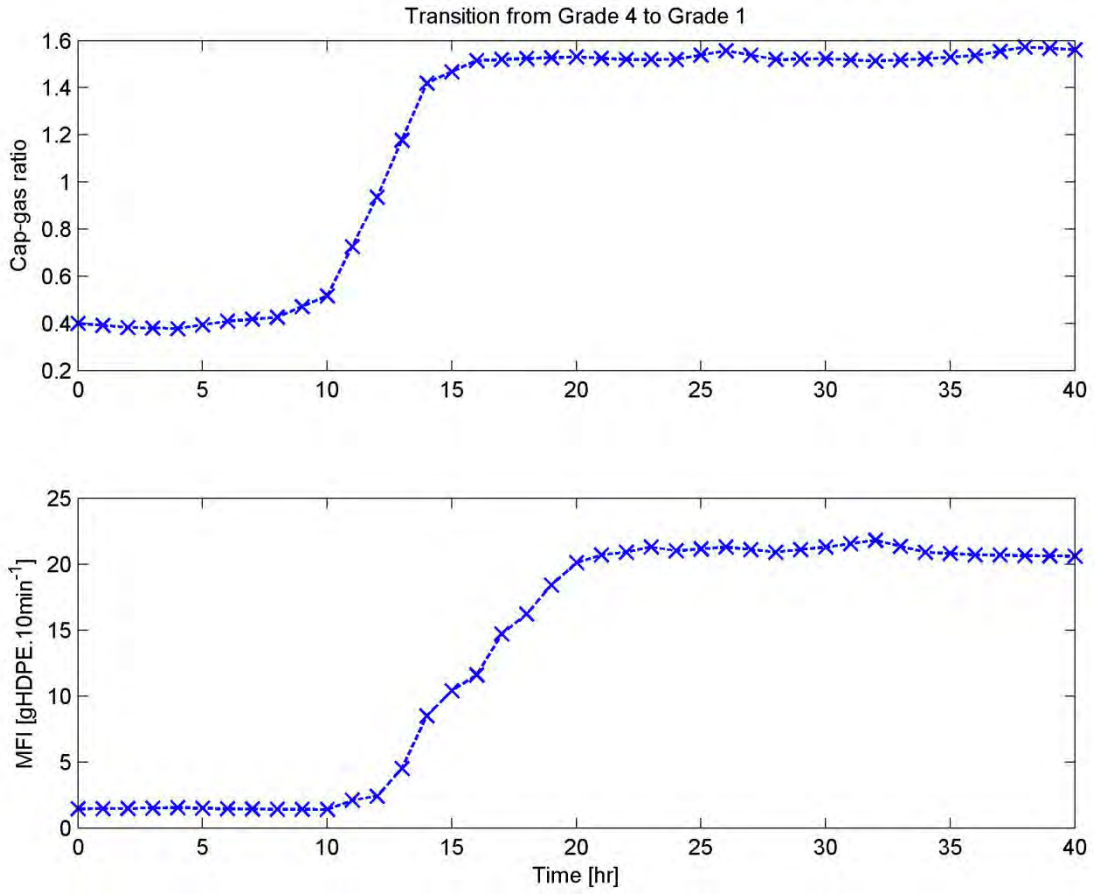

Figure 15.2: Outputs for grade transition from Grade 4 to Grade 1

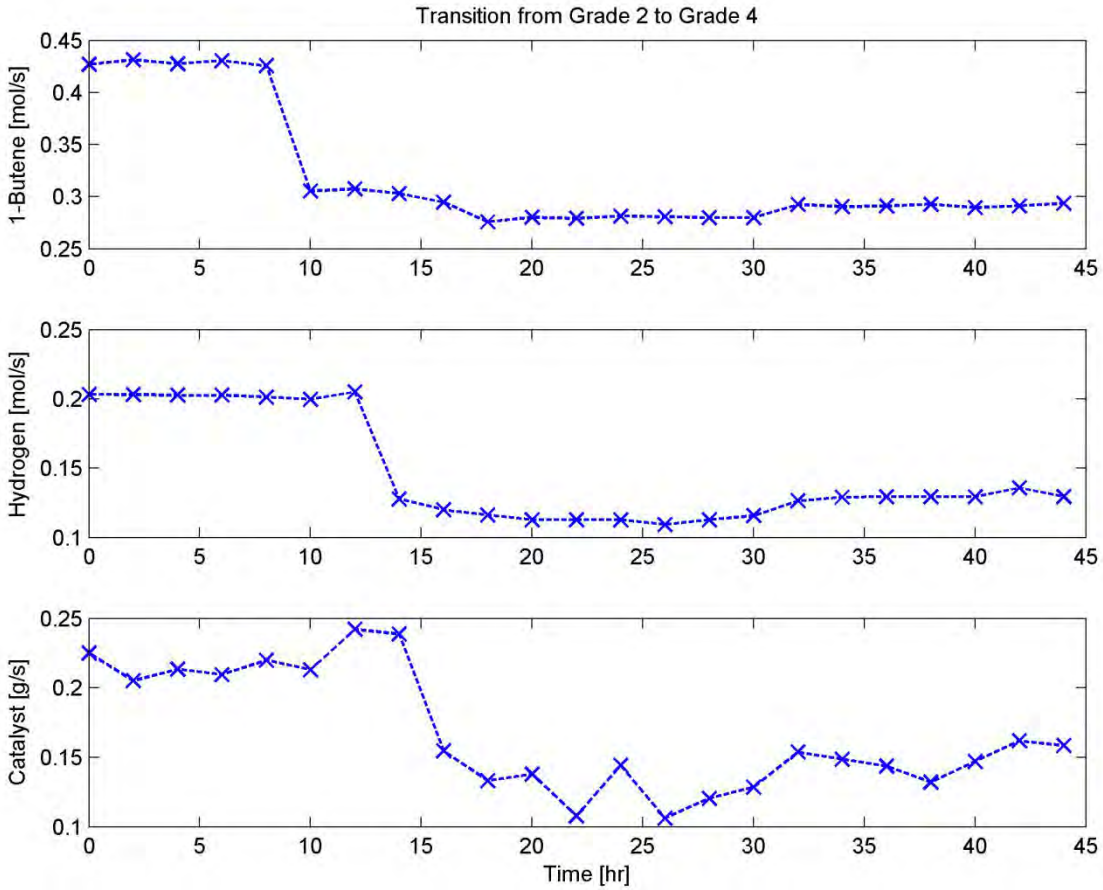

Figure 15.3: Manipulated variables for grade transition from Grade 2 to Grade 4

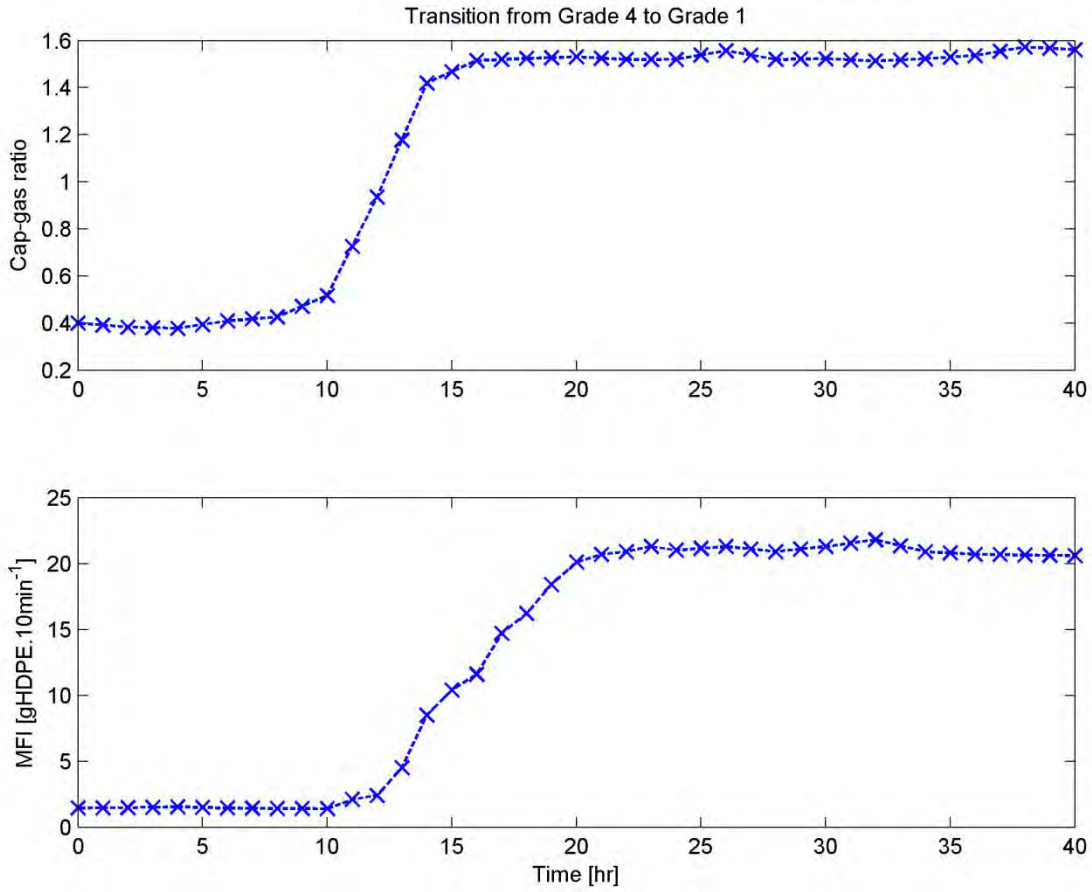

Figure 15.4: Outputs for grade transition from Grade 2 to Grade 4

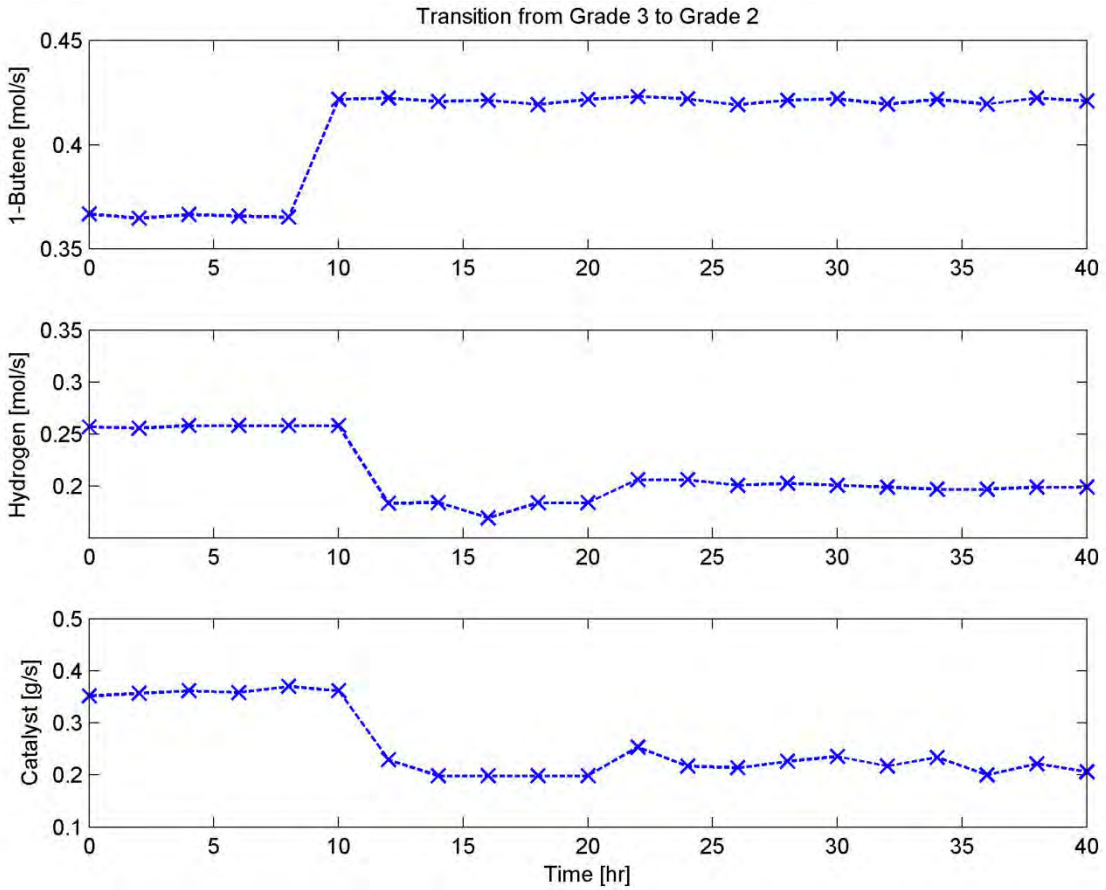

Figure 15.5: Manipulated variables for grade transition from Grade 3 to Grade 2

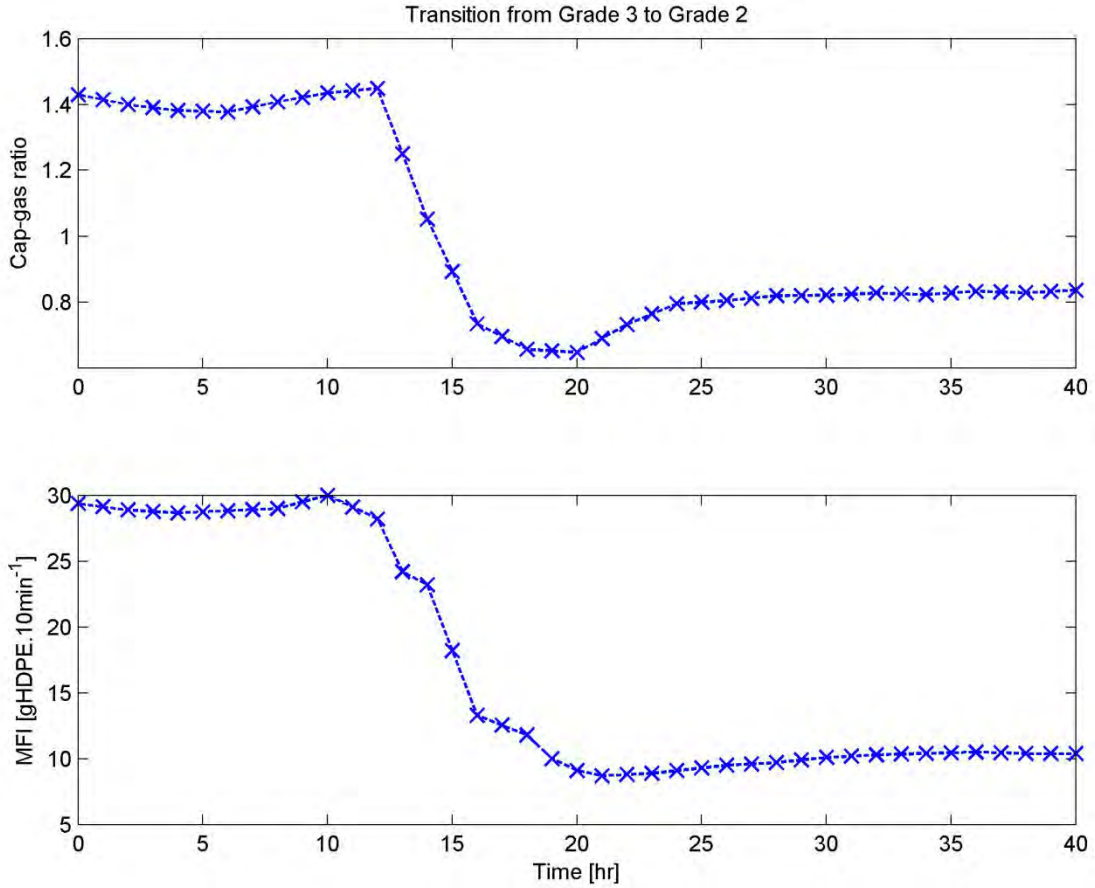

Figure 15.6: Outputs for grade transition from Grade 3 to Grade 2

15.1.1 Interpretation of industrial data

Analysis of the industrial data for grade changes reveals several general characteristics of the grade transition strategies applied to the industrial reactor. As shown in the figures above, the three variables that are manipulated to effect a grade transition are:

- The feed rate of comonomer
- The feed rate of hydrogen
- The feed rate of catalyst

In all cases, the first change to the reactor is the feed rate of 1-butene. The trajectory is a simple step change from the initial flow rate to the target flow rate. Note that in the figures above, due to the resolution of the data, the change appears as a ramp; in reality, the change is almost instantaneous.

Between two and eight hours after the flow rate of comonomer is adjusted, the hydrogen feed rate is changed. Rather than a simple step change, an overshoot trajectory is employed: the feed rate is adjusted to between two and ten per cent beyond the target flow rate, and maintained at that level for between eight and eighteen hours. After that period, the flow rate is set to the final target value.

In industrial operation, hydrogen (more specifically, the cap-gas ratio of hydrogen to ethylene) is the most important factor in determining the chain length of the polymer product. Thus an overshoot strategy in the hydrogen trajectory is likely an attempt to increase the rate at which the grade change occurs.

The changes to the catalyst flow rate are made up to six hours after the 1-butene flow is adjusted. The changes to the 1-butene and hydrogen follow the same strategy for all transitions; in contrast, the adjustments to catalyst flow rate vary from transition to transition.

In one of the transitions (see Figure 15.1) an undershoot trajectory is observed. In the other two transitions (Figure 15.3 and Figure 15.5) an overshoot strategy is employed.

These different strategies may be intended to reduce the total quantity of catalyst consumed during grade transitions, since the feed rate during the transition is always lower than the final set point. It is also possible that the differences in the data that was provided are simply due to decisions made by operating personnel during each transition, based on their experience.

15.1.2 Summary

The data provided for three industrial grade transitions has revealed a general strategy for changing the grade of polymer produced in the reactor:

- The 1-butene flow rate is adjusted first; a simple step-change trajectory is employed.
- The flow rate of hydrogen to the reactor is changed using an overshoot trajectory.
- The feed rate of catalyst is changed by an overshoot strategy in some cases, and an undershoot trajectory in others.

The predictions of the reactor model can now be compared to the three grade transitions from the data provided.

15.2 Model validation with unsteady-state data

In Chapter 14, the reactor model was fitted to a combination of the laboratory data and steady-state industrial operation data. Comparing the model predictions with the unsteady-state operational data described above provides an opportunity to validate the model with data that was not used to fit the kinetic parameters of the model.

The three grade changes described above can be simulated using the reactor model. The following pages show the results of these simulations, including the simulated changes to the manipulated variables, and comparisons between the model predictions and the data for the cap-gas ratios and polymer MFI.

These two variables are selected for comparison because the MFI is the most important controlled variable in a grade transition, and the cap-gas ratio is one of the most important indicators of the relative rates of propagation and termination reactions, and thus of the length of polymer being produced.

The set-points for the feed flow rates of each component (for the production of each grade of polymer) are determined by the values in Table 11.1 and Table 11.2. The trajectories between each set-point are determined by the strategies described in the previous section.

The times at which a grade transition starts and ends are defined by the ranges of MFI values in Table 14.14, reproduced below.

Table 14.14: Minimum and maximum values for MFI to remain within specification

Grade	**1**	**2**	**3**	**4**
MFI	21.81	10.49	28.88	1.59
Min Spec	18	8	25	1.4
Max Spec	23	14	31	1.8

The mass of polymer that is off-specification and the total time required for a grade change can be determined. These are the two most likely candidates for minimisation when using the model to optimise reactor operation, since both can be related to monetary value: the quantity of off-specification material represents waste material, and the total time taken represents time during which more valuable products could be produced.

15.2.1 Transition from Grade 4 to Grade 1

The grade transition from Grade 4 to Grade 1 is a change from a low MFI (high molecular weight) to a high MFI (lower molecular weight). The changes to the manipulated variables are shown in Table 15.1. The changes to the variables are compared with the industrial data in Figure 15.7.

For this grade change, the feed rate of 1-butene is adjusted first. Three hours after that change, the feed rates of hydrogen and catalyst are adjusted. An overshoot trajectory is employed for hydrogen: the feed rate is maintained at a slightly higher value for ten hours before being reduced to the final set point.

The catalyst flow rate is maintained at approximately 90% of its final value for fourteen hours, and then increased to its full flow rate.

Table 15.1: Characteristics of transition from grade 4 to grade 1

Component	t_{Change} [hr]	Over/ undershoot	Over/ undershoot [%]	Over/undershoot duration [hr]
1-Butene	7	-	-	-
Hydrogen	10	Over	2	10
Catalyst	10	Under	10	14

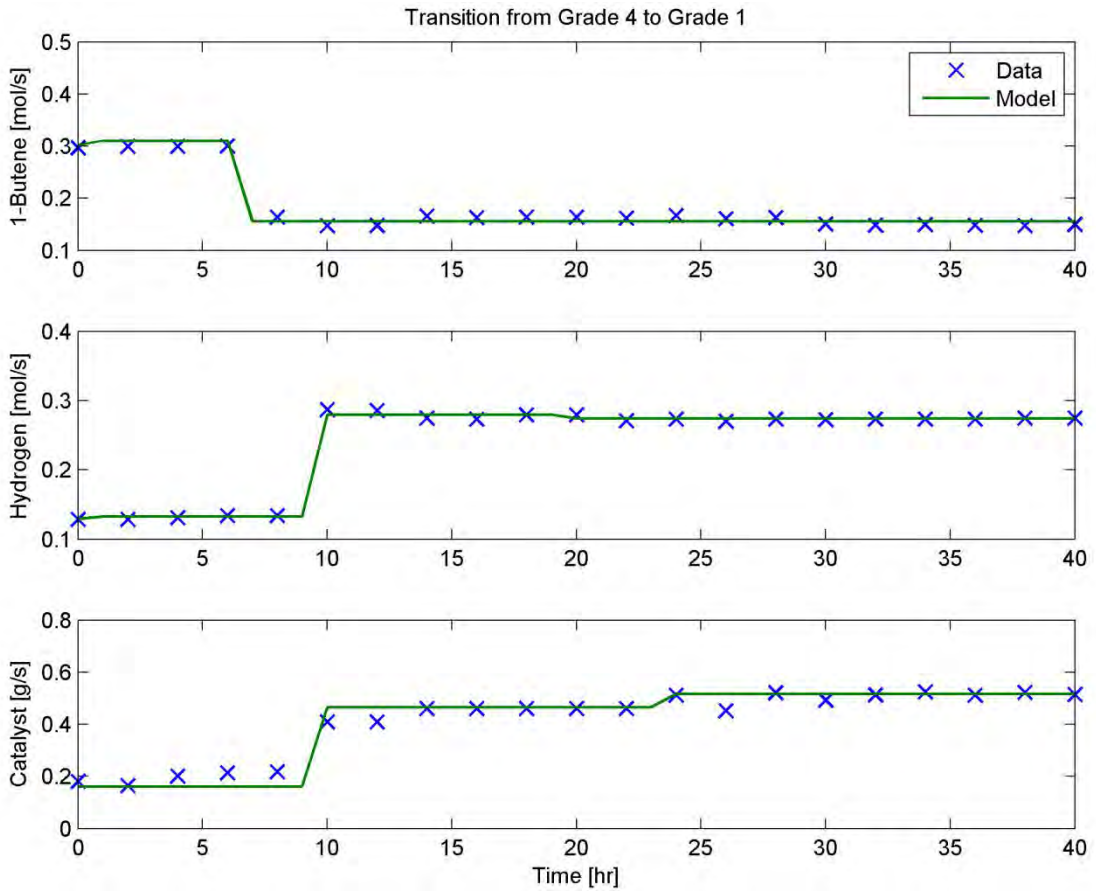

Figure 15.7: Manipulated variables for grade transition from grade 4 to grade 1

The changes to the feed streams in Figure 15.7 affect the ratio of hydrogen and ethylene in the cap-gas. The simulated cap-gas ratios are compared with the industrially measured ratios in Figure 15.8.

Figure 15.8 shows a good agreement between the simulated and measured cap-gas ratios: both begin to increase rapidly after approximately ten hours, and reach a fairly steady value about twelve hours after the first changes to the system were made. Some further fluctuations occur between 15 and 20 hours into the simulated grade change, as the hydrogen and catalyst feed rates settle to the final values.

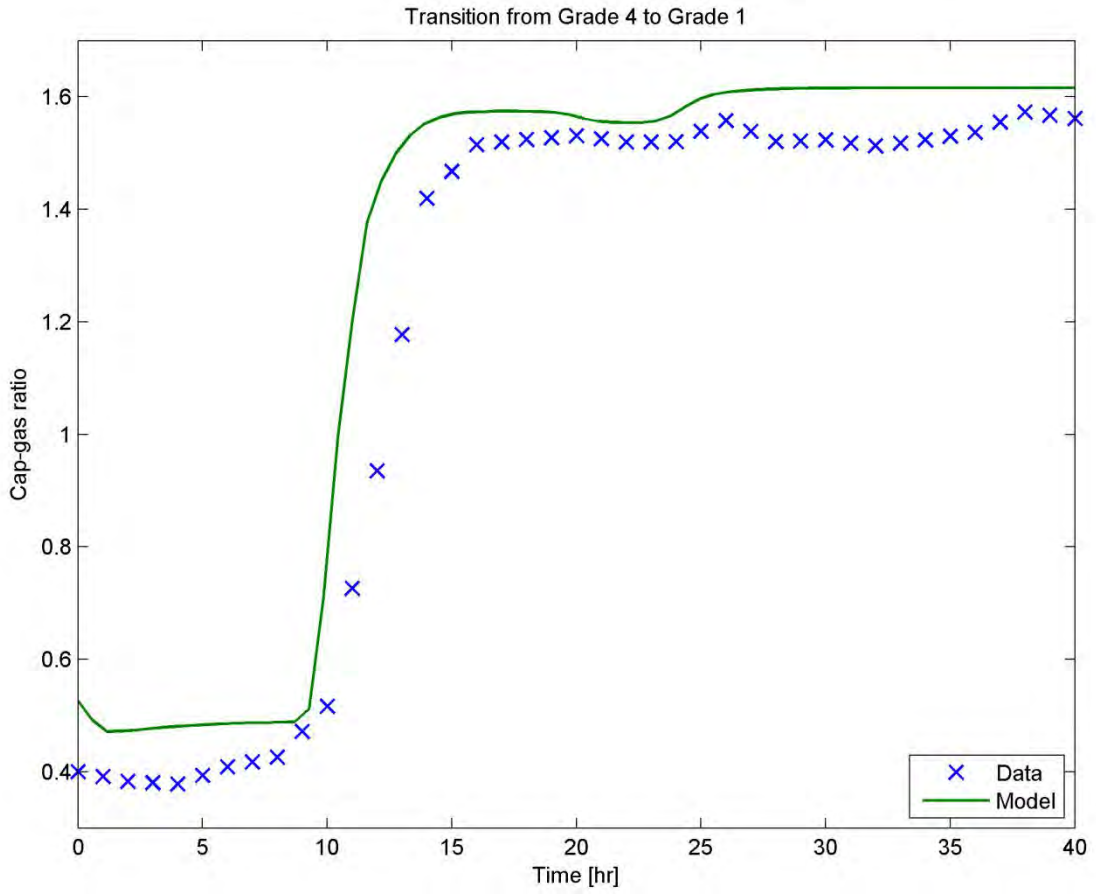

Figure 15.8: Comparison of data and model cap-gas ratios for transition from grade 4 to grade 1

The changes to the Melt Flow Index of the polymer product during the grade transition are shown in Figure 15.9.

Both the measured and the predicted MFI values begin to increase approximately five hours after the first changes to the reactor feeds. The industrial MFI reaches a final steady value 14-15 hours into the transition; by comparison, the simulated value reaches the specification limit for the target MFI after 16-17 hours and reaches a final steady value a few hours after that point. The simulation therefore slightly over-predicts the time the reactor takes to settle to the final MFI value. It is possible that the problem relates to the resolution of the original data; catalyst flow rates are only available at two-hour intervals, which may introduce a slight off-set between the data and the model predictions, or there may be adjustments to the catalyst flow rate (affecting the polymer properties) that are not resolved in the data.

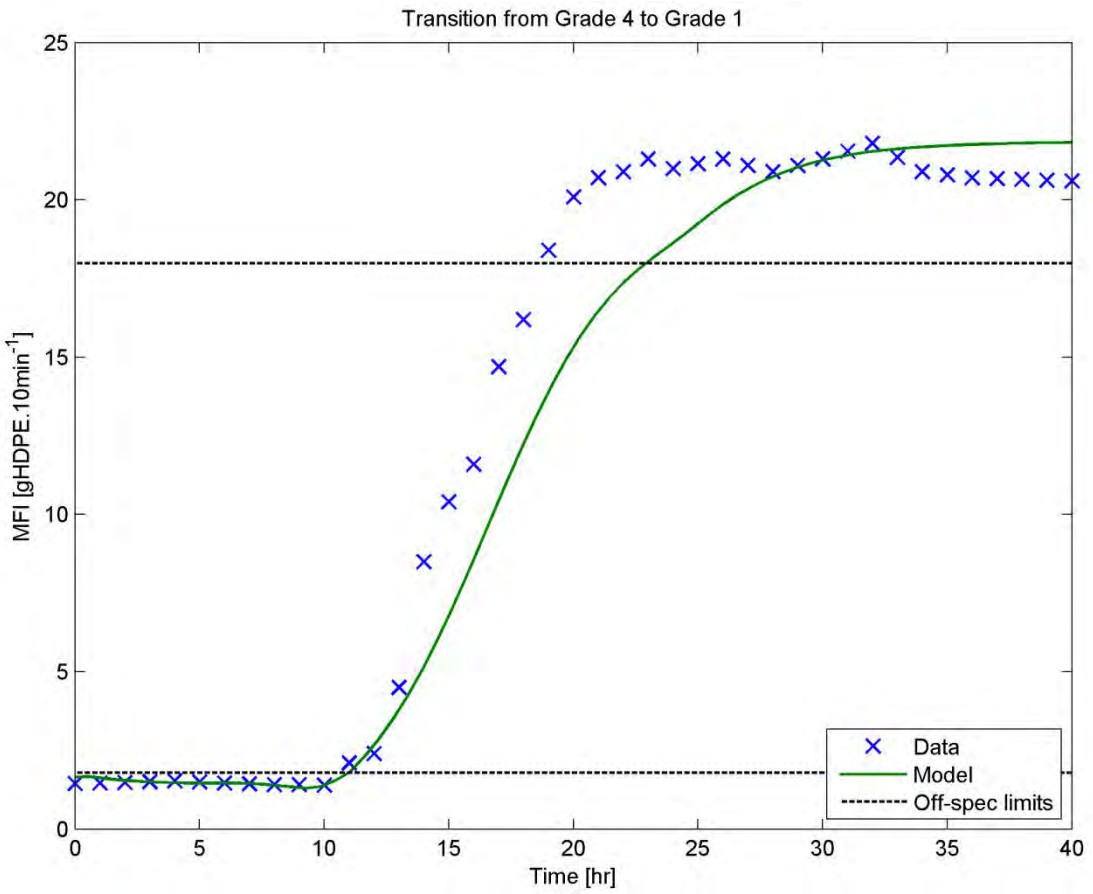

Figure 15.9: Comparison of data and model MFI for transition from grade 4 to grade 1

As shown in Table 15.2, the simulated reactor produces off-specification polymer for almost 12 hours (the period between the "off-spec limits" in Figure 15.9). During this time, more than 62 tons of low-value polymer are produced.

Table 15.2 also shows that the calculation time for this grade transition was just over 25s, for 40 hours of simulated time. These timescales mean that the model is fast enough to be useful in optimisation routines, which could search for the optimum grade transition trajectory, given a particular objective function.

Table 15.2: Grade transition characteristics for transition from grade 4 to grade 1

Off specification time [hr]	11.92
Off specification mass [ton]	62.19
Calculation time [s]	25.53

15.2.2 Transition from Grade 2 to Grade 4

The grade transition between Grade 2 and Grade 4 represents a change between the two polymer grades with lowest MFI. The changes to the manipulated variables, compared with the industrial data, are shown in Figure 15.10. Table 15.3 specifies the changes shown in Figure 15.10.

Once again, the feed rate of 1-butene is the first change to the reactor. Four hours later, the hydrogen feed rate is adjusted to a value 10% lower than its final value. This "overshoot" value is maintained for 18 hours.

Six hours after the change to the 1-butene feed rate, the catalyst feed rate is decreased to 83% of its final value. The catalyst feed rate is maintained at this "overshoot" value for a further sixteen hours before being increased to its final value.

Table 15.3: Characteristics of transition from grade 2 to grade 4

Component	t_{Change} [hr]	Over/ undershoot	Over/ undershoot [%]	Over/undershoot duration [hr]
1-Butene	10	-	-	-
Hydrogen	14	Over	10	18
Catalyst	16	Over	17	16

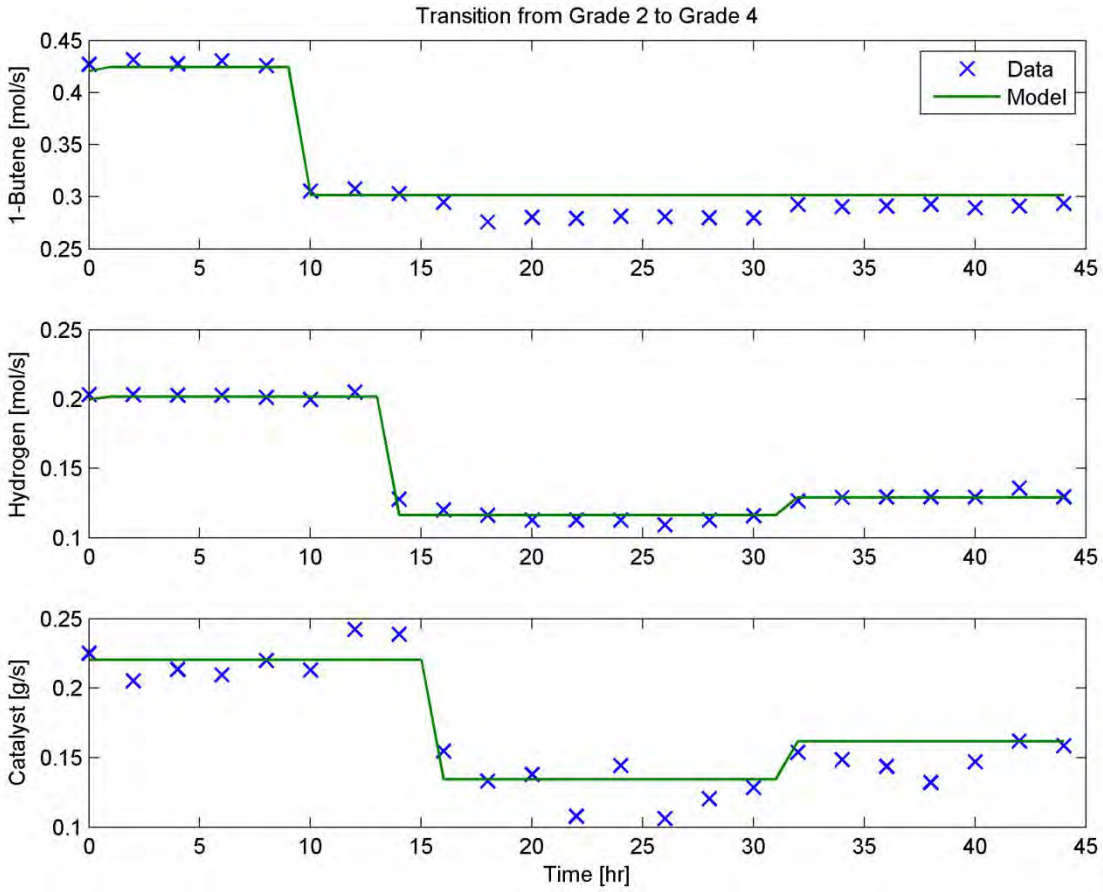

Figure 15.10: Manipulated variables for grade transition from grade 2 to grade 4

The changes to the cap-gas ratio are shown in Figure 15.11. The dynamics of the simulated system match the industrial data fairly closely: there is an initial, relatively stable period before the ratio of hydrogen to ethylene drops rapidly in response to the reduced hydrogen and catalyst flow rates. The simulation lags the

industrial measurements slightly during this period. This lag may be due to the fluctuations in catalyst flow rates during the first few hours in Figure 15.10, which were ignored in the simulation in favour of simpler step-change adjustments to the flow rate. It is also possible that the problem relates to the resolution of the original data; catalyst flow rates are only available at two-hour intervals, which may introduce a slight off-set between the data and the model predictions.

Once the hydrogen and catalyst flow rates reach their final values, the cap-gas ratio increases; the simulation slightly over-predicts the increase in cap-gas ratio, but both curves appear to approach steady-state after 40 hours of simulation time.

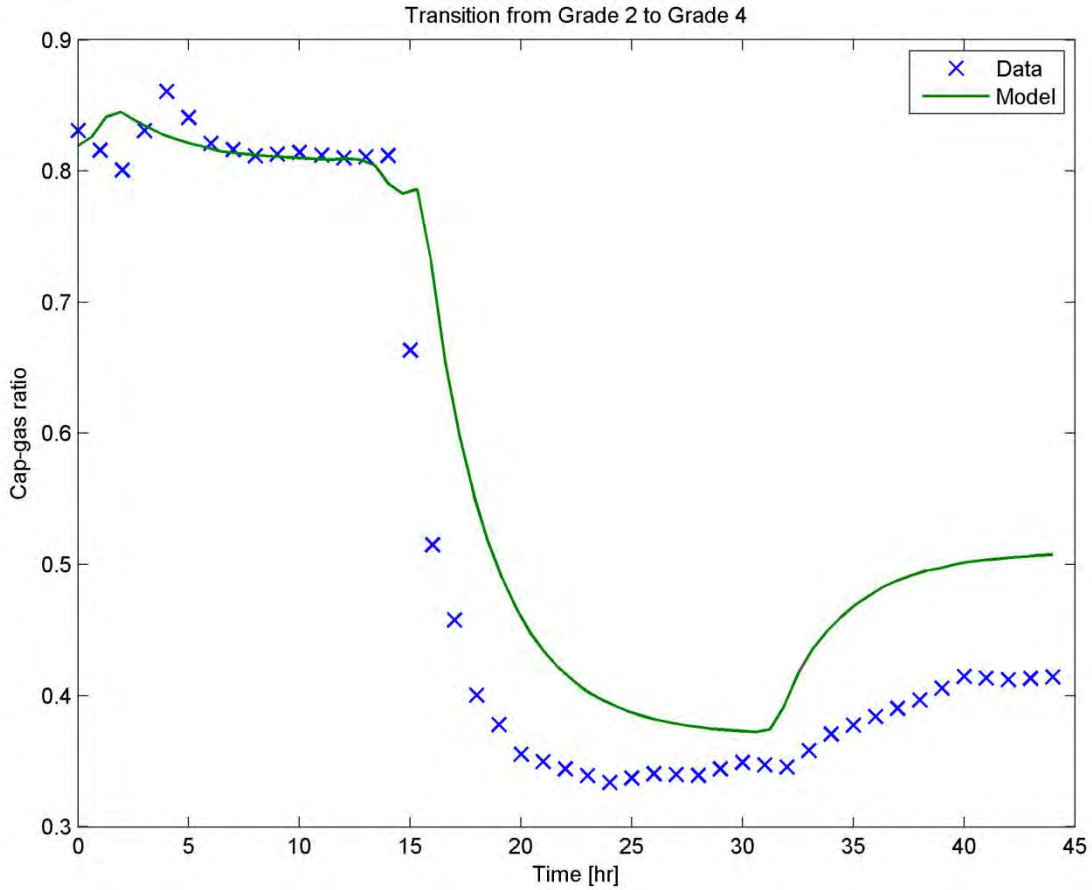

Figure 15.11: Comparison of data and model cap-gas ratios for transition from grade 2 to grade 4

The reaction of the product properties to the feed rate changes is shown in Figure 15.12. Again, the simulation matches the industrial data relatively closely: the simulation slightly lags the decreasing MFI, but then the two curves match closely as the conditions in the reaction begin to steady out. Towards the end of the simulated period, both the industrial data and the simulated MFI are on a slightly upward trend.

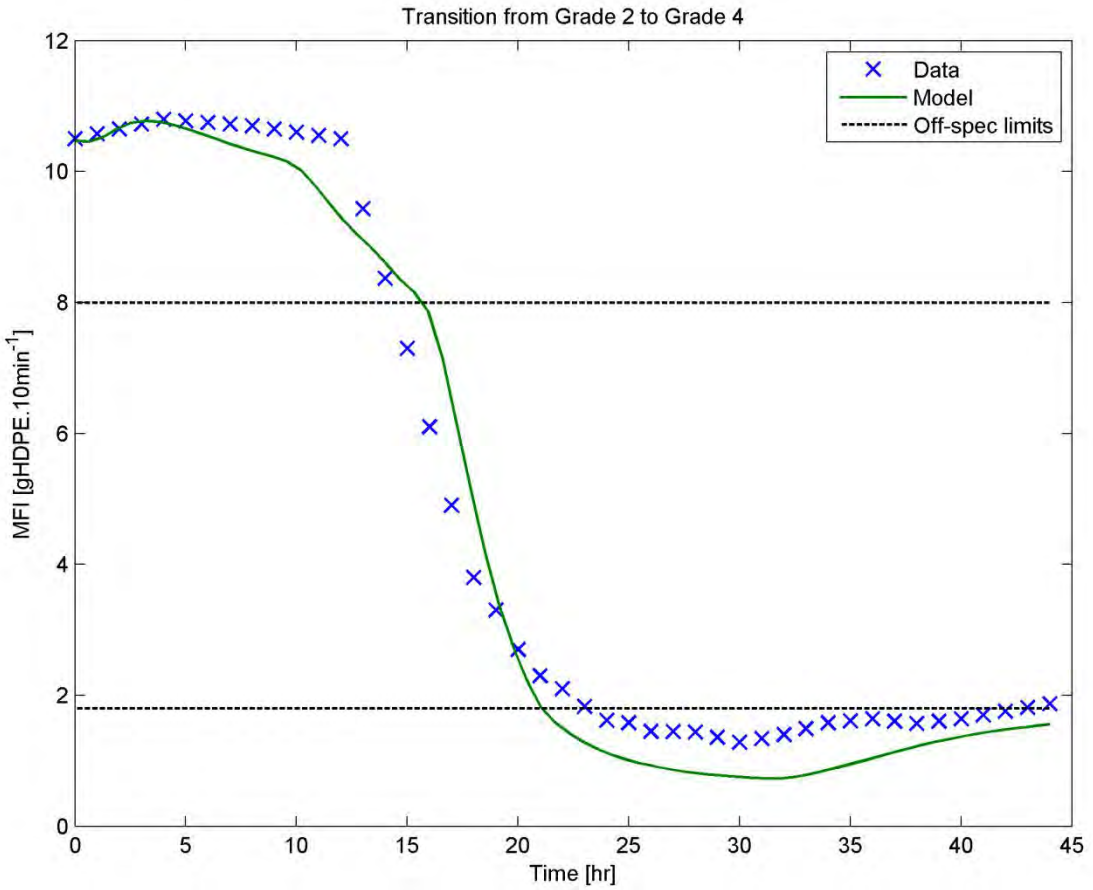

Figure 15.12: Comparison of data and model MFI for transition from grade 2 to grade 4

Table 15.4 shows that this grade transition produces almost 25 tons of off-specification polymer during nearly five hours between specification limits.

The calculation time in Table 15.4 is almost 24s for 44 hours of simulated time; once again, the reactor model is fast enough to be used in optimisation routines.

Table 15.4: Grade transition characteristics for transition from grade 2 to grade 4

Off specification time [hr]	4.98
Off specification mass [ton]	24.38
Calculation time [s]	23.53

15.2.3 Transition from Grade 3 to Grade 2

In the transition from Grade 3 to Grade 2, the reactor product changes from a high MFI to a low MFI. The changes to the manipulated variables are shown in Table 15.5. These simulated changes are compared with the industrial data in Figure 15.13.

The first manipulated variable is again the comonomer feed rate. The feed rate of hydrogen is adjusted two hours after the change to 1-butene. The hydrogen flow rate is maintained at an "overshoot" value of 90% of its final value for nine hours.

The feed rate of catalyst to the reactor is adjusted to an "overshoot" value of 85% of the final value two hours after the 1-butene change, and maintained at that value for a further nine hours, before reaching its final value.

Table 15.5: Characteristics of transition from grade 3 to grade 2

Component	t_{Change} [hr]	Over/ undershoot	Over/ undershoot [%]	Over/undershoot duration [hr]
1-Butene	10	-	-	-
Hydrogen	12	Over	10	9
Catalyst	12	Over	15	9

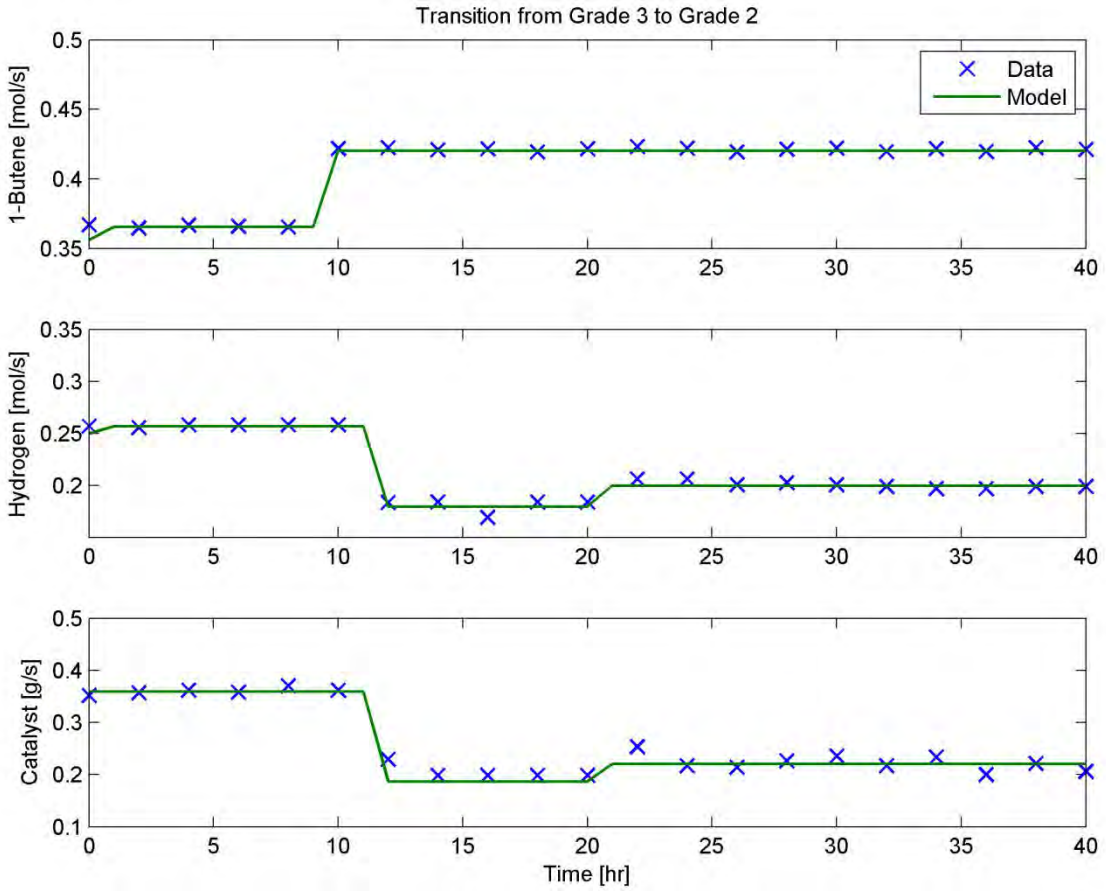

Figure 15.13: Manipulated variables for grade transition from grade 3 to grade 2

The simulated cap-gas ratio response to the grade transition is shown in Figure 15.14. Both the industrially-measured cap-gas ratio and the simulated ratio decrease rapidly from 12 or 13 hours into the simulation until

reaching a minimum approximately 20 hours into the grade transition. In response to the increased feeds of catalyst and hydrogen at this time, the cap-gas ratio increases and reaches a steady value approximately 25 hours after the first changes were made to the feed streams.

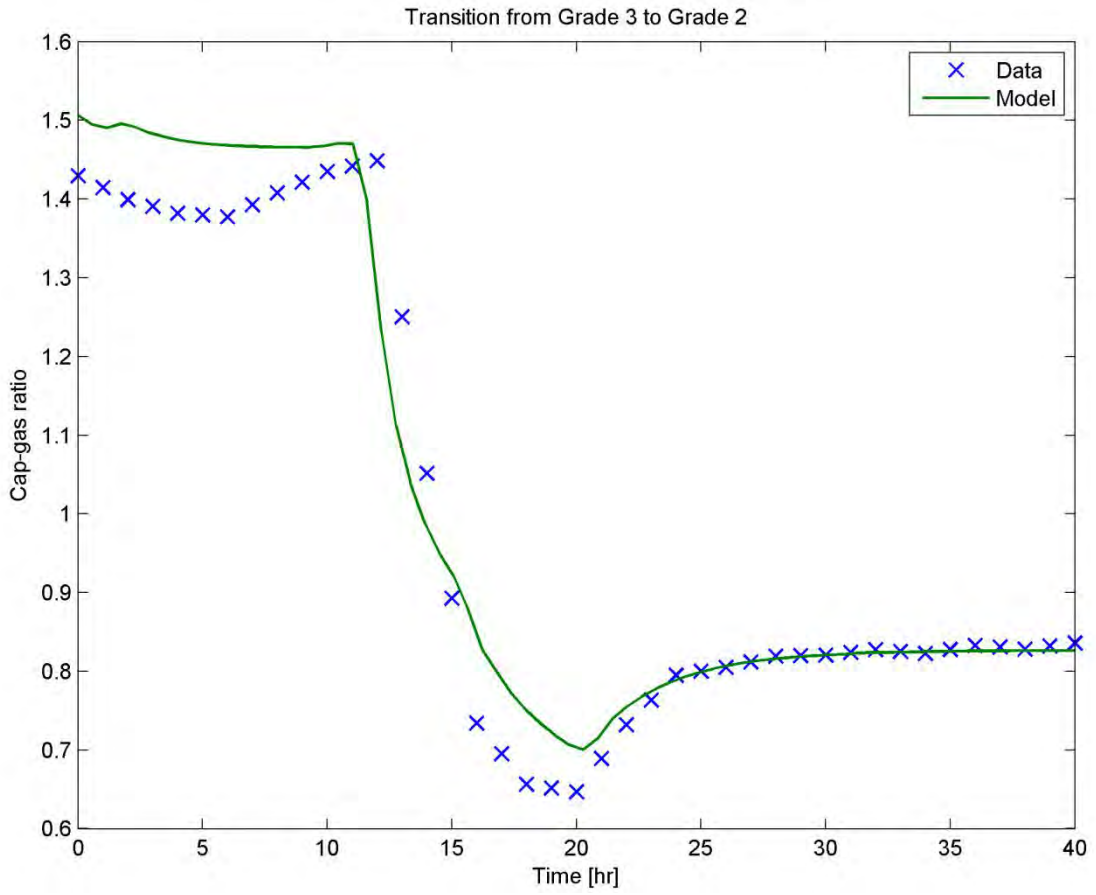

Figure 15.14: Comparison of data and model cap-gas ratios for transition from grade 3 to grade 2

The changes to the MFI of the reactor product are shown in Figure 15.15. Once again, the simulated and measured MFI trends correspond fairly closely. The simulated MFI lags the industrial data slightly during the initial decrease, but the simulation matches the data very well as the MFI approaches a minimum and settles to the final steady value about 35 hours into the simulation.

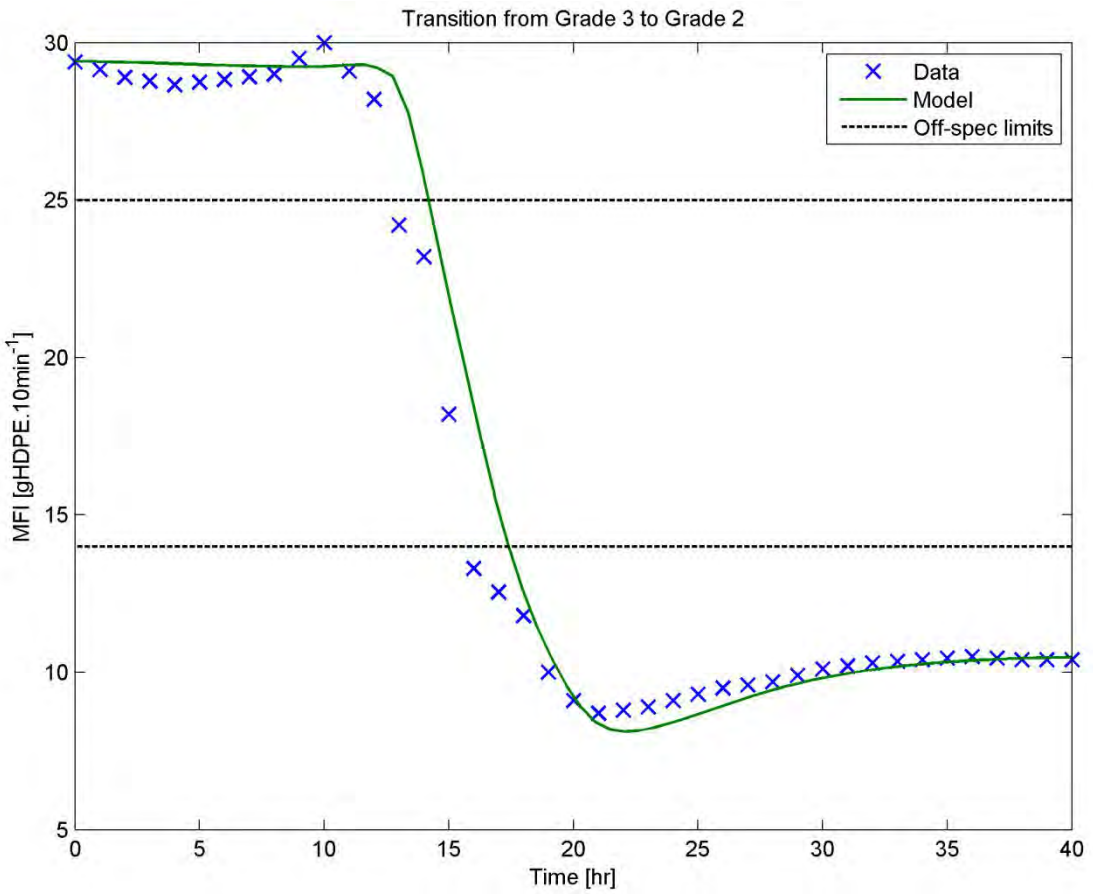

Figure 15.15: Comparison of data and model MFI for transition from grade 3 to grade 2

Table 15.6 shows that for just over three hours, off-specification polymer was produced by the reactor. A total of almost 16 tons of polymer was produced that was outside of the specification boundaries.

Also shown in Table 15.6 is the calculation time required for 40 hours of simulated time, just over 17s. Given the time scales for changes in the industrial reactor, the reactor model is fast enough to be useful for optimisation routines.

Table 15.6: Grade transition characteristics for transition from grade 3 to grade 2

Off specification time [hr]	3.21
Off specification mass [ton]	15.72
Calculation time [s]	17.35

15.3 Summary

The three simulations of grade transitions described above have shown that the reactor model is capable of reproducing the dynamic behaviour of an industrial polymerisation reactor, even under highly unsteady-steady-state conditions. The two most important variables during a grade transition (the Internal Check of the cap-gas ratio and the Output of the Melt Flow Index) were compared with the industrial data; the simulation matched the data closely for all three cases.

This result is also significant, and should be seen as rigorous model validation. In Chapter 14, the parameters in the model were adjusted to reconcile the laboratory and steady-state industrial data sets. The reactor model has not been shown to reproduce an independent set of data.

The simulations were based on inspection of the industrial data for grade transitions, which revealed that the industrial strategy generally consisted of adjustments to the 1-butene, hydrogen and catalyst feed rates. The hydrogen feed rate trajectory always employed an overshoot strategy. The catalyst feed rate trajectories made use of overshoot and undershoot strategies, depending on the specific transition.

Using specifications based on the industrial limits for the Melt Flow Index, each of the grades could be distinguished on the basis of the MFI of the simulated product stream. Thus the duration of each grade transition could be determined from the times at which the product MFI left the first specification range, and entered the target band. In addition, the exact mass of off-specification polymer produced in this period was calculated.

The mass of waste produced, and the time taken for a given transition, represent the two most likely candidates for optimisation of grade transitions.

The calculation time for the reactor model was between 16 and 24s, for simulated times of 32 to 36 hours. This shows that the reactor model solves very quickly compared to the timescales of interest, making it useful within optimisation routines or even process control applications such as those mentioned in the literature review (Chatzidoukas et al., 2003, Wei et al., 2014, Xu & Liu, 2014).

In order to inform the attempts at optimisation, a sensitivity study of the reactor model will be performed.

CHAPTER 16. DEVELOPMENT OF IMPROVED CONTROL STRATEGIES: SENSITIVITY STUDY

A sensitivity study of a system (whether an experimental system or a model formulation) can be performed for a variety of reasons. These can include exploring and testing the operation of the system, giving insight into the responses of the important outputs to the various inputs, or providing information for the pairings of outputs to inputs in a control engineering context.

In the case of the simulation of an industrial reactor producing high density polyethylene, a number of Inputs have been identified (see Figure 11.2 in the discussion of the industrial operational data): the reactor volume, temperature and pressure, and the feed rates of the various reactants. The feed rates of the reactants can in principle be manipulated freely (when compared with the reactor volume, which cannot, and the temperature and pressure, whose influence have not been investigated in this study). Thus the Inputs to the sensitivity study are the feed rates of the reactants.

The outputs from the sensitivity study will include the Outputs and Internal Checks identified in Figure 11.2 from the industrial data, and also some other polymer properties that are predicted by the reactor model.

The purpose of this sensitivity study is to determine which Inputs have the greatest impact on the duration of grade transitions; since the duration of a grade transition is defined by the MFI value and the off-specification limits for each transition, the most important Output is the value of the MFI.

We seek the Inputs to which the MFI is most sensitive in our region of operation, in order to inform attempts to improve the grade transitions simulated previously.

16.1 Inputs

There are six Inputs to the system which can in principle be manipulated freely, and which could be used to control the industrial reactor. These inputs are:

- Catalyst feed rate;
- Co-catalyst feed rate;
- Ethylene feed rate;
- 1-Butene feed rate;
- Hydrogen feed rate and
- n-Nonane feed rate

For the sensitivity study, each of these inputs will be varied over a range of values, determined by the inputs to the four different sets of industrial data, as shown in Table 16.1 below. The inputs to the Base Case for the sensitivity study are defined as the average of the values for each input to each of the four grades; thus the Base Case represents operation of the reactor at an intermediate point that doesn't correspond to a particular industrial grade, but is a "midpoint" of the operating space, which is defined by the various inputs.

The sensitivity study will be performed by one-at-a-time variation of the inputs: each input is set to the Minimum and then the Maximum values in Table 16.1, while the other inputs are maintained at their Base Case values. This allows us to study the influence of each of the inputs on the outputs.

Table 16.1: Range of values of inputs

		Catalyst	TEA	Ethylene	1-Butene	Hydrogen	Solvent
		g/s	mol/s	mol/s	mol/s	mol/s	mol/s
Industrial data	**Grade 1**	0.5166	0.00367	51.567	0.1558	0.2742	25.642
	Grade 2	0.2204	0.00363	49.673	0.4206	0.1998	24.965
	Grade 3	0.3595	0.00354	48.353	0.3559	0.2499	24.310
	Grade 4	0.1619	0.00404	50.159	0.3018	0.1292	25.210
Sensitivity study	**Base Case**	0.3146	0.00372	49.938	0.3085	0.2133	25.032
	Minimum	0.1619	0.00354	48.353	0.1558	0.1292	24.310
	Maximum	0.5166	0.00404	51.567	0.4206	0.2742	25.642

16.2 Outputs

The outputs for the sensitivity consist of the Internal Checks and Outputs from the reactor model, as previously defined, as well as several other parameters relating to polymer properties.

The Outputs from the reactor model are:

- Ethylene conversion [%];
- Melt Flow Index [g-HDPE/10 min] and
- Catalyst efficiency [ton-HDPE/kg-cat]

The Internal Checks in the reactor model are:

- Ethylene to hydrogen ratio in cap-gas [-] and
- Liquid concentration of co-catalyst [mol-TEA/m^3].

The other parameters relating to polymer properties are:

- Number-average molecular weight, M_n [g/mol];
- Weight-average molecular weight, M_w [g/mol] and
- Comonomer content [C_4H_8 mol%].

Sensitivity has been characterised as the partial derivative of each output with respect to the normalised change in each input. The partial derivatives are calculated about the Base Case value. The inputs are normalised with respect to the Base Case values. Normalisation allows comparison between the sensitivity of a given output to the various inputs, which may have very different absolute values.

The partial derivative of each output (represented in the equations below by Y_i) with respect to each input (represented by X_j) is calculated by averaging the derivatives for the Minimum and Maximum cases, as equation 16.1 shows.

$$\frac{\partial Y_i}{\partial X_j} \approx \frac{1}{2}\left(\frac{\partial Y_{i,Min}}{\partial X_{j,Min}} + \frac{\partial Y_{i,Max}}{\partial X_{j,Max}} \right) \qquad 16.1$$

The partial derivatives for the Minimum and Maximum cases are found using the forward difference formula for numerical differentiation, as shown in equation 16.2.

$$\frac{\partial Y_{i,Min}}{\partial X_{j,Min}} \approx \frac{Y_i\left(X_{k\neq j,BaseCase}, X_{j,Min}\right) - Y_i\left(X_{k\neq j,BaseCase}, X_{j,BaseCase}\right)}{X_{j,Min} - X_{j,BaseCase}}$$
$$\frac{\partial Y_{i,Max}}{\partial X_{j,Max}} \approx \frac{Y_i\left(X_{k\neq j,BaseCase}, X_{j,BaseCase}\right) - Y_i\left(X_{k\neq j,BaseCase}, X_{j,Max}\right)}{X_{j,BaseCase} - X_{j,Max}} \qquad 16.2$$

The averaging of the results (in equation 16.1) of the two forward difference derivatives (from equation 16.2) is equivalent to the use of the central difference formula for numerical differentiation, which is more accurate.

16.3 Results

The results from the sensitivity study are shown in Table 16.2. The values of each of the outputs are shown for the Base Case, and for the Minimum and Maximum cases for each of the inputs.

Table 16.2: Results of sensitivity study

Inputs	Case	Outputs						
		MFI	**M_w**	**M_n**	**1-Butene content**	**C_2H_4 conversion**	**Cap-gas ratio**	**C_{TEA}**
		[g/10 min]	[g/mol]	[g/mol]	[mol%]	[%]	[-]	[mol/m^3]
	Base	**14.30**	**13403**	**71771**	**0.131**	**98.58**	**0.725**	**0.712**
Catalyst	Min	1.63	22493	125546	0.108	96.93	0.303	0.717
	Max	24.00	11357	62808	0.154	99.31	0.903	0.705
TEA	Min	14.05	13477	72102	0.130	98.55	0.720	0.677
	Max	14.74	13279	71217	0.132	98.63	0.734	0.774
Ethylene	Min	15.71	13018	70058	0.135	98.60	0.751	0.712
	Max	13.01	13798	73544	0.126	98.57	0.700	0.712
1-Butene	Min	7.19	15418	85685	0.0680	98.63	0.693	0.713
	Max	18.16	12302	67488	0.175	98.55	0.745	0.711
Hydrogen	Min	7.71	15798	84148	0.140	98.95	0.541	0.714
	Max	17.90	12413	67737	0.126	98.34	0.820	0.711
Solvent	Min	14.80	13261	71137	0.132	98.63	0.735	0.733
	Max	13.89	13524	72312	0.130	98.54	0.717	0.695

The values in Table 16.1 and Table 16.2 were used to determine the partial derivatives of the outputs with respect to the normalised inputs, as was described in equation 16.1. The results of these calculations are shown in Table 16.3.

Table 16.3: Partial derivatives of outputs

Output	Inputs					
	Catalyst	**TEA**	**Ethylene**	**1-Butene**	**Hydrogen**	**Solvent**
MFI [g/10 min]	20.608	5.215	-41.966	12.498	14.658	-17.113
M_w [g/mol]	-10958	-1498	12109	-3553	-4769	4955
M_n [g/mol]	-62380	-6719	54167	-19954	-22756	22083
mol% C_4H_8	0.0419	0.0148	-0.144	0.125	-0.0198	-0.0489
C_2H_4 conversion [%]	2.268	0.542	-0.492	-0.0910	-0.880	-1.793
Cap-gas ratio [-]	0.574	0.109	-0.795	0.0591	0.399	-0.337
TEA concentration [mol/m^3]	-0.0106	0.729	-0.00766	-0.00203	-0.00508	-0.708

The values in Table 16.3 give the response of each of the output variables to the changes in the input variables (which were normalised with respect to the Base Case values). Since the MFI has been determined as the most important output during grade transitions, only the sensitivity of the MFI to the inputs is discussed in detail here (see Figure 16.1); the sensitivities of the other outputs are shown in Chapter 29 in the Appendix.

As discussed at length previously (especially Chapter 12 and Chapter 13) the behaviour of the polymerisation reactor, and especially the MFI, is highly dependent on the hold-up of monomer in the reactor relative to the hold-up of hydrogen (the principal terminating agent). The results of the sensitivity study confirm this.

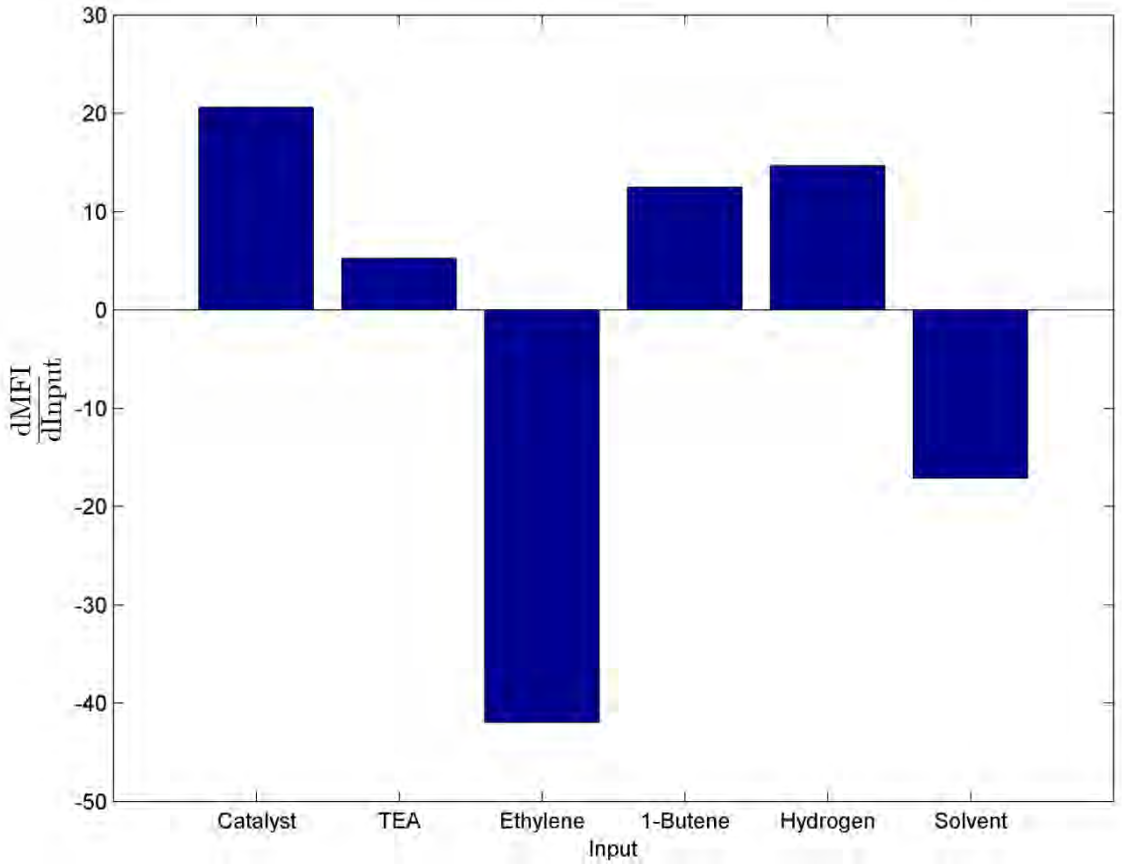

Figure 16.1: Sensitivity of MFI to inputs. MFI in [g-HDPE/10min]

As shown in Table 16.3 and Figure 16.1, the MFI of the reactor product is most sensitive to changes in the feed rate of ethylene. This agrees with the findings of previous studies of similar systems, which found that the feed rate of ethylene had the greatest impact on the performance of an industrial reactor (Neto et al., 2005).

The MFI is inversely correlated with the ethylene feed rate: an increase in the ethylene feed rate causes an increase in the hold-up of ethylene in the reactor. This raises the average propagation rate within the reactor, increasing the average chain length of the product, and thus decreasing the MFI.

The catalyst feed rate is also shown to have a large influence on the MFI. An increase in the catalyst feed rate increases the hold-up of catalyst in the reaction volume, raising the conversion of the monomer. An increase in the conversion of the monomer raises the ratio of terminating to propagating reaction rates, producing shorter polymer chains, and thus a higher MFI value.

The MFI is shown to be almost as sensitive to the solvent feed rate as to the catalyst. Increasing the solvent flow rate reduces the mean residence time of the reactor, decreasing the conversion of the monomer, and thus (by similar arguments to those above) lowering the final MFI value.

However, although the MFI is most sensitive to the ethylene, catalyst and solvent feed rates, these are not necessarily the most appropriate variables to manipulate to improve grade transitions. Although grade transitions are inherently unsteady periods of operation, they should not be periods of unstable operation. Unstable operation can result in decreased equipment efficiency and even unsafe operation.

In order to maintain stability, the solvent rate should not be manipulated, because it has a direct influence on the hold-up of liquid phase in the reactor, where polymerisation occurs. If too little solvent is present, the slurry phase may thicken to the extent that mechanical mixing is limited. If too much solvent is added to the reactor, the reactants will be diluted and the residence time will decrease, both of which will decrease polymerisation efficiency.

Similarly, to maintain reactor stability, limits must be imposed on the changes that are made to the ethylene and catalyst feed rates, which can also have a large impact on the residence time of the reactor, via the hold-up of monomer in the gas phase. As seen in the industrial strategies for grade transitions (see section 15.1), the ethylene flow rate was not adjusted at all, and the catalyst feed rate was only overshot by a maximum of 17%.

Thus, although the MFI is most sensitive to the feed rates of ethylene, catalyst and solvent, attempts to improve the grade transitions shown in Chapter 15 will be limited: the solvent and ethylene feed rates will not be adjusted, and the catalyst flow rate will be adjusted by a maximum of 17% from the target values.

With limitations imposed on the three variables with the greatest impact on the MFI, attempts at improvement will focus on the feed rates of hydrogen and 1-butene. These reactants were identified as the most active terminating agents in the fitting of kinetic parameters to the laboratory data, so it seems sensible to attempt to control MFI by manipulating the feed rates of hydrogen and 1-butene.

An increase in the hydrogen feed will increase the hydrogen hold-up in the reactor, and increase the ratio of terminating to propagating reaction rates, thus raising the MFI.

The actual quantity of hydrogen fed to the reactor, relative to the monomer and solvent, is very small. Thus, large changes to the hydrogen flow rate (as a fraction of its original value) can occur without dramatically affecting the stability of the reactor, but still having a significant impact on the properties of the polymer product. This makes hydrogen very suitable for controlling the MFI of the reactor product, and suggests that more aggressive changes to the hydrogen feed rate could be made to improve grade transitions.

Similar arguments can be made for 1-butene: the total flow rate of 1-butene is low, compared to monomer and solvent, so the MFI can be adjusted (by changing the ratio of propagation to termination reactions) without affecting the stability of the reactor. However, changing the feed rate of 1-butene will not only affect the chain lengths produced, but also the comonomer content of the product, which is often a separate specification for polymer properties.

Because the hydrogen has a more direct impact on chain length (and the sensitivity study revealed MFI is more sensitive to hydrogen than 1-butene), improvement of grade transitions will be focussed on manipulating the hydrogen feed rate to the reactor.

16.4 Summary

A sensitivity study of the reactor model was performed to investigate the relationships between the six inputs (the feed rates of the various components) and the outputs, most importantly the Melt Flow Index (MFI), in the region of reactor operation of interest.

In the control engineering context, such a method could be used to determine, at each point during a given grade transition, which inputs could have the greatest impact on the progress of the grade transition. This approach would determine a trajectory based on the local optimum at each point, which would not necessarily coincide with the global optimum for the transition between two specified grades. However, the question of globally-optimum grade transition strategies is beyond the scope of the current work; in this thesis, we seek only to demonstrate the use of the reactor model in such a context.

With this in mind, the sensitivity study was used to investigate the sensitivity of the outputs to the inputs over a larger operating region, in order to develop a more heuristic approach to improving grade transitions.

As seemed to be the case from the previous studies of the reactor model, the simulated outputs are very sensitive to the conversion of the monomer and the hold-up of ethylene in the reactor.

When considering the MFI as an indicator of grade transition progress, the most likely manipulated variables appeared to be the ethylene and catalyst feed rates, to which the MFI was most sensitive. However, for the purposes of reactor stability, the changes that can be made to these two inputs are limited.

For similar reactor stability considerations, the solvent feed rate, to which the MFI was next most sensitive, was ignored as a potential manipulated variable.

The next most important input, the hydrogen feed rate, was considered an ideal candidate for improving the grade transitions, because its small absolute flow rate means that large adjustments can be made without significantly influencing the reactor stability, while still having an impact on the MFI of the polymer product.

Thus the following heuristics are proposed for improving grade transitions:

When the grade transition involves an increase in MFI:

- Hydrogen flow rate should be increased using an aggressive overshoot strategy and
- When increasing the catalyst flow rate, an undershoot strategy should not be employed, or the undershoot should be minimised.

When the grade transition involves a decrease in MFI:

- Hydrogen flow rate should be decreased using an aggressive overshoot strategy and
- Catalyst flow rate should be decreased using an overshoot strategy, with a maximum overshoot of 17%.

In the following chapter, some strategies to improve the grade transitions shown previously are developed, based on the insights from the sensitivity study and the heuristics proposed.

CHAPTER 17. DEVELOPMENT OF IMPROVED CONTROL STRATEGIES: CASE STUDIES

The sensitivity study of the polymerisation reactor model revealed that although the Melt Flow Index (MFI) is most sensitive to the feed rates of ethylene, catalyst and solvent, the parameter which could influence grade transitions the most without affecting reactor stability was the feed rate of hydrogen.

This chapter shows some attempts to optimise the grade transitions simulated previously, making use of the heuristics proposed following the sensitivity study. Although the reactor model solves rapidly enough to be used for full optimisation and control loop development (for example in models such as those proposed by (Wei et al., 2014) and (Xu & Liu, 2014)), this is not the goal of this work; the intention is to demonstrate the development of a model which could be useful for these purposes.

The grade transitions will therefore be improved through simple modifications to the degree of under- or overshoot, and the time scales at which parameters are manipulated during transitions. These changes will be determined by inspection, informed by the results of the sensitivity study.

Each of the three grade transitions will be improved in this manner, and the results compared with the simulated grade transition time and off-specification mass from Chapter 15, which matched the industrial grade transition data. As before, a grade transition is considered to start when the MFI of the reactor product leaves the specification band for the original grade, and to end when the MFI enters the specification band for the target polymer grade; these boundaries determine the transition time, and any polymer produced during this period contributes to the off-specification mass.

17.1 Case Study: Transition from Grade 4 to Grade 1

The grade transition from Grade 4 to Grade 1 is a change from the lowest MFI (highest molecular weight) of the four grades to the second highest MFI (second lowest molecular weight), representing a significant change in operating conditions and product properties.

The transition is accomplished industrially with a 10% undershoot in catalyst feed rate, and a slight overshoot in the hydrogen feed rate (see Figure 15.7; note that the first six hours of simulation from Figure 15.7 have been excluded from the figures below, to focus on the grade transition). The sensitivity study suggested that undershoot should be minimised when the catalyst flow rate is increased during a transition, and that much more aggressive overshoot strategies could be employed when altering the hydrogen flow rate.

As shown in Table 17.1 and Figure 17.1, in order to improve this transition, the hydrogen feed rate overshoot was increased to 40% (although the duration was reduced from 10 to 8 hours), and the catalyst feed rate was increased without any undershoot. These values were chosen by inspection to improve the grade transition.

The impact of these changes to the feed rates is shown in Figure 17.2 (cap gas ratio) and Figure 17.3 (MFI).

Table 17.1: Characteristics of transition from grade 4 to grade 1 (model-based control)

Component	t_{Change} [hr]	Over/ undershoot	Over/ undershoot [%]	Over/undershoot duration [hr]
1-Butene	1	-	-	-
Hydrogen	4	Over	40	8
Catalyst	4	-	-	-

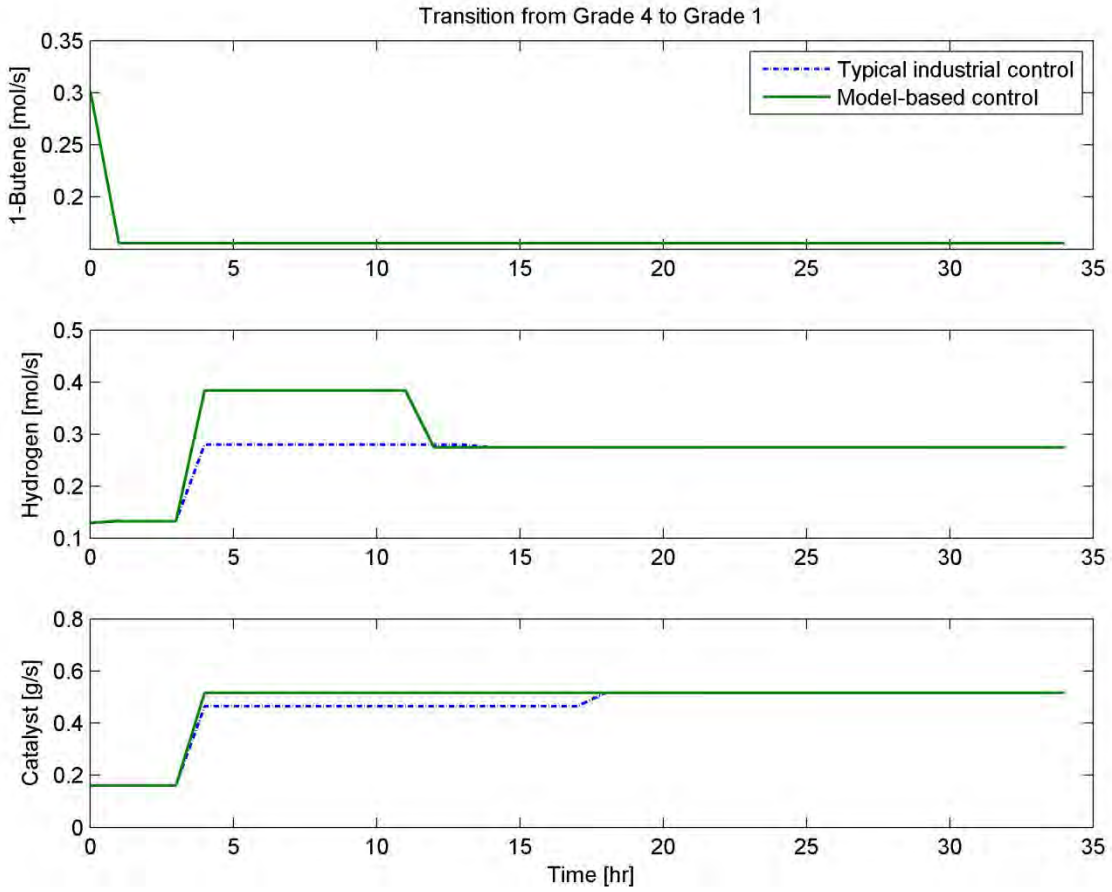

Figure 17.1: Manipulated variables for case study transition from grade 4 to grade 1

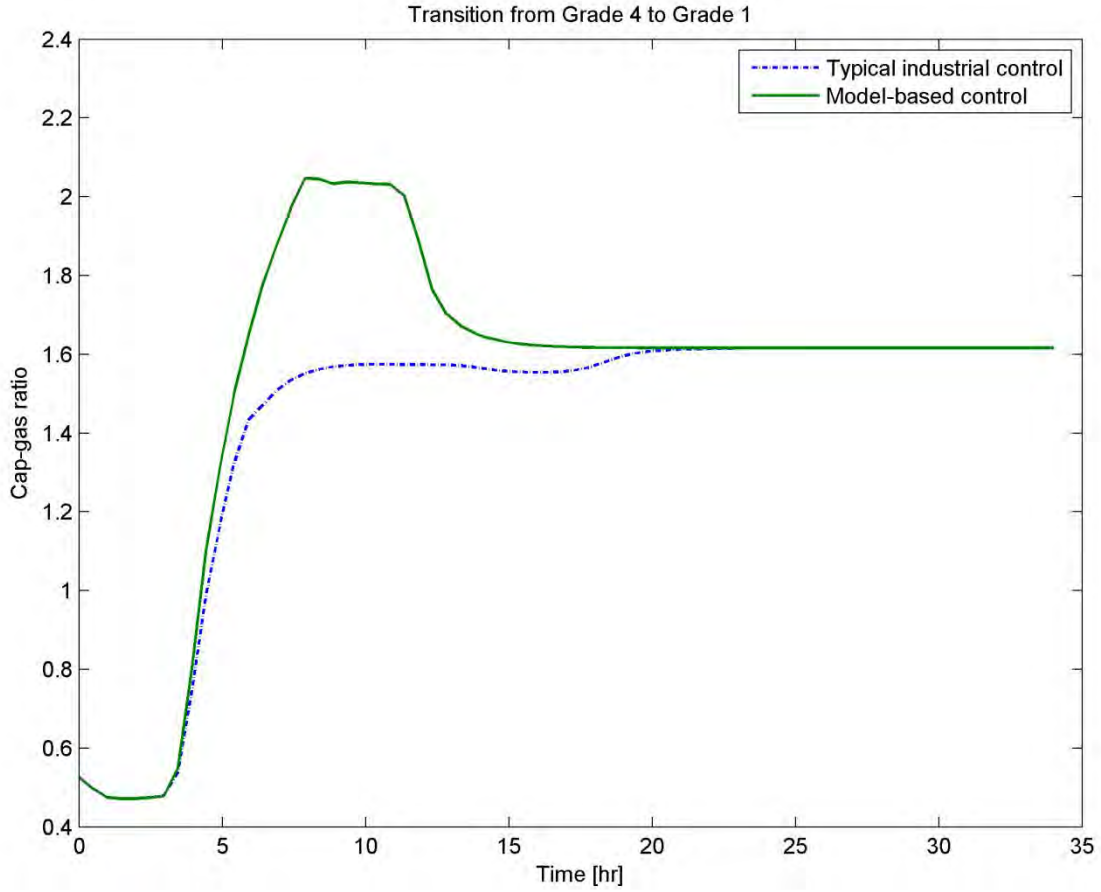

Figure 17.2: Comparison of industrial and case study cap-gas ratio for transition from grade 4 to 1

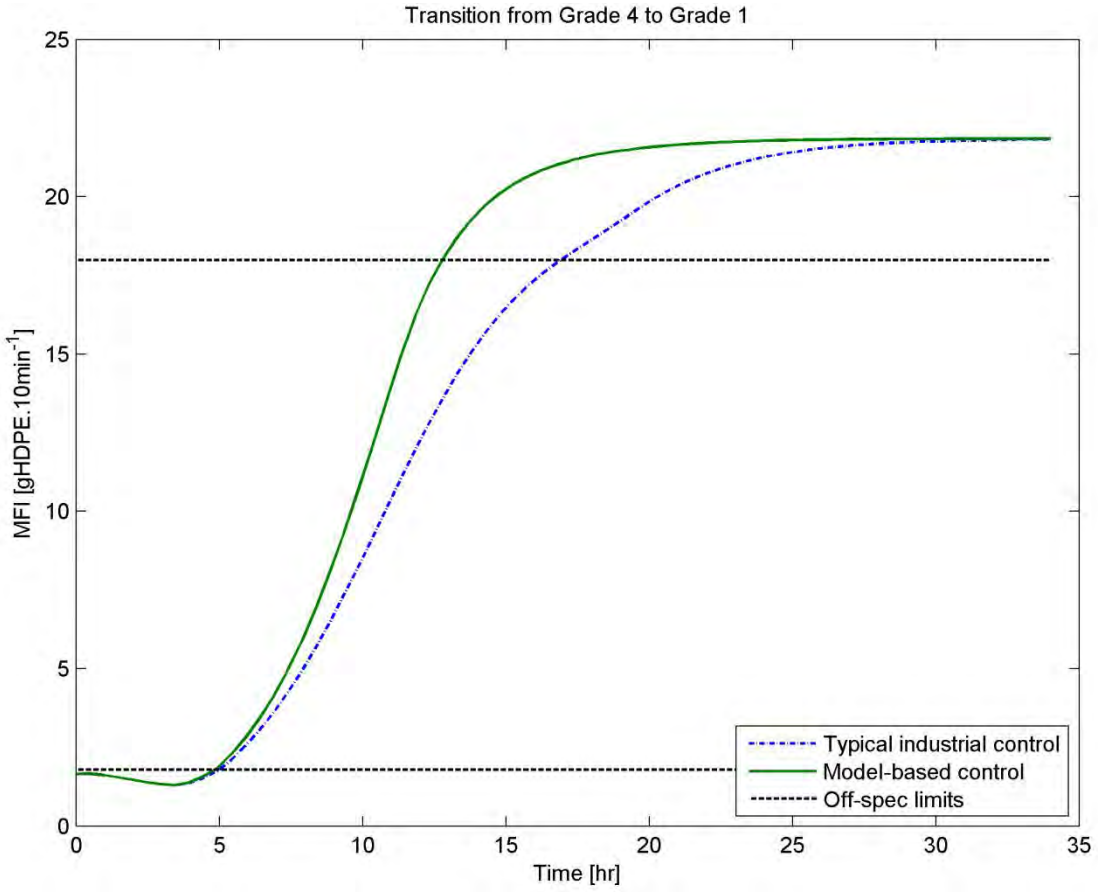

Figure 17.3: Comparison of industrial and case study MFI for transition from grade 4 to 1

The more drastic changes in hydrogen feed rate, and the increased feed of catalyst to the reactor, result in a more rapid transition from grade 4 to grade 1, as seen in Figure 17.3. Table 17.2 compares the time and waste production for this improved transition with the values from simulating the industrial transitions.

Both the mass of waste material produced, and the time period between grades, decreased by ~30% as a result of the simple improvement of the grade transition.

Table 17.2: Case study transition characteristics for transition from grade 4 to grade 1

Case	Typical Industrial Control	Model-based Control
Off specification time [hr]	11.92	7.90
Off specification mass [ton]	62.19	41.60
Calculation time [s]	23.53	24.57

Integrating the total hydrogen fed to the reactor for this improved grade transition allowed a calculation of the increase in hydrogen consumed, when compared to the industrial grade transition strategy. Approximately 9% more hydrogen is consumed, in order to decrease the off-specification product by ~30%.

Similarly, the total quantity of catalyst fed to the reactor was only 4.6% higher in this grade transition than the industrial data.

The increased reactant and catalyst consumption could be further inputs to an objective function to optimise grade transitions; the economics are beyond this study, but the reactor model can be used to determine the optimum operating points.

17.2 Case Study: Transition from Grade 2 to Grade 4

The grade transition between Grade 2 and Grade 4 involves a change between the two polymer grades with the lowest MFI (highest molecular weight) of the four grades, and thus represents a relatively small change in reactor conditions and product properties.

Industrially, the transition from Grade 2 to Grade 4 is achieved with a 17% overshoot in the catalyst feed rate, and 10% overshoot in the hydrogen feed rate, as summarised in Table 15.3 (note that the first 8 hours of simulation time shown in Figure 15.10 and associated figures has been excluded from the simulation below, to focus on the grade transition). Since reactor stability requires that the catalyst flow rate is not adjusted by more than 17% of the final value, the extent of overshoot cannot be modified for this transition.

The hydrogen feed rate can be adjusted with a much more aggressive overshoot strategy, however: as shown in Table 17.3 and Figure 17.4, for this transition an overshoot of 50% was employed. In addition, the changes to the hydrogen and catalyst feeds were made after four hours, rather than six to eight hours (as in Table 15.3), to increase the rate at which the grade transition occurs.

The response of the reactor model to the manipulated variables is shown in Figure 17.5 (cap-gas ratio) and Figure 17.6 (MFI).

Table 17.3: Characteristics of transition from grade 2 to grade 4 (model-based control)

Component	t_{Change} [hr]	Over/ undershoot	Over/ undershoot [%]	Over/undershoot duration [hr]
1-Butene	2	-	-	-
Hydrogen	4	Over	50	6
Catalyst	4	Over	17	16

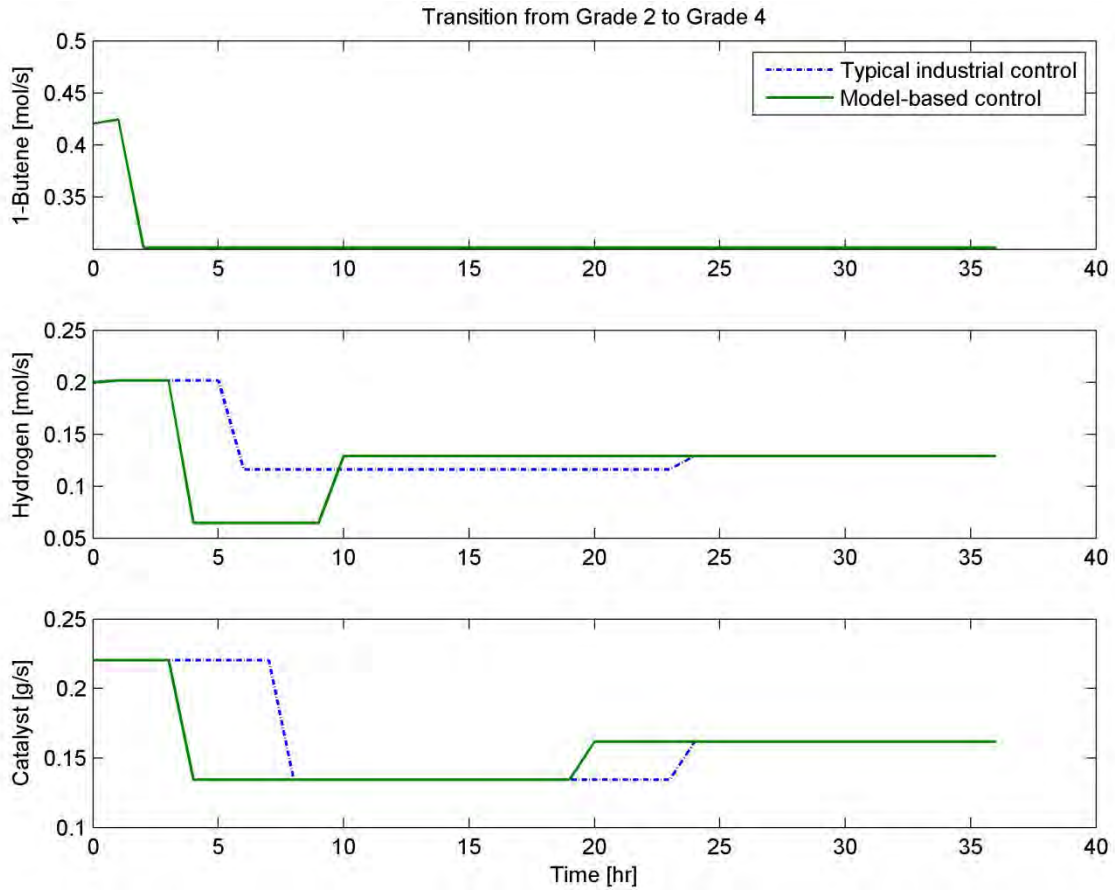

Figure 17.4: Manipulated variables for case study transition from grade 2 to grade 4

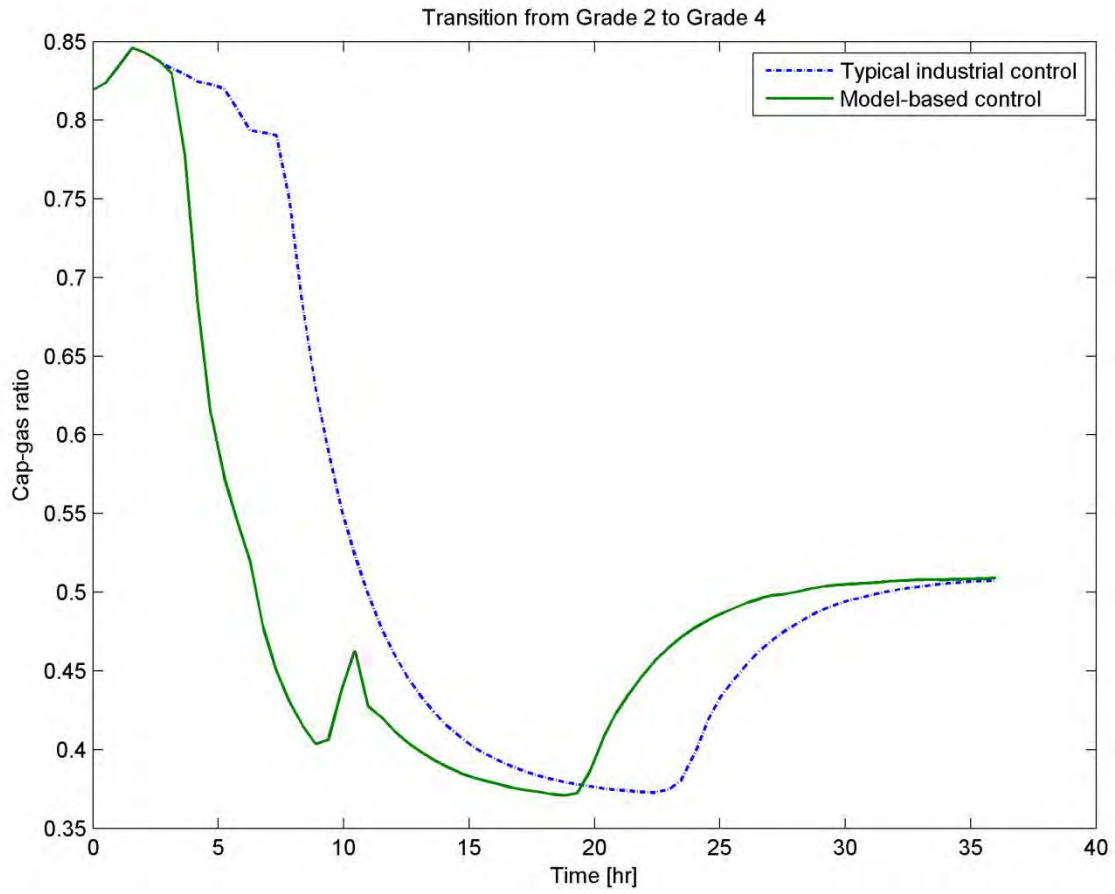

Figure 17.5: Comparison of industrial and case study cap-gas ratio for transition from grade 2 to 4

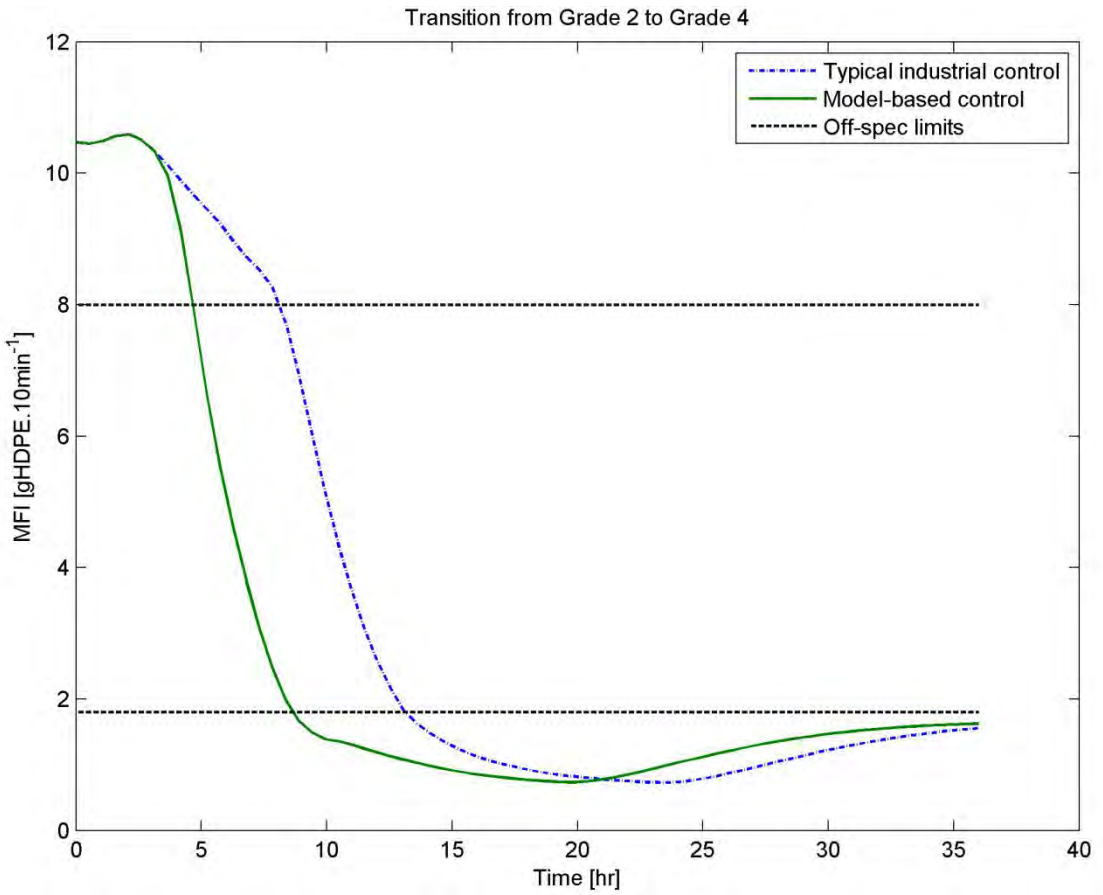

Figure 17.6: Comparison of industrial and case study MFI for transition from grade 2 to grade 4

Employing a more drastic overshoot strategy with the hydrogen feed rate, and making earlier adjustments to the catalyst and hydrogen flow rates, results in a more rapid transition between the two grades (see Figure 17.6, comparing the industrial and case study MFI trajectories), and the production of less waste material (as summarised in Table 17.4). The grade transition (in terms of time period and waste produced) is improved by approximately 20%.

Table 17.4: Case study transition characteristics for transition from grade 2 to grade 4

Case	Typical Industrial Control	Model-based Control
Off specification time [hr]	4.98	3.97
Off specification mass [ton]	24.38	18.79
Calculation time [s]	16.83	18.55

This 20% improvement in the grade transition is achieved without changing the total quantity of catalyst fed to the reactor (only changing when the adjustments are made), and by reducing the total quantity of hydrogen consumed during the period by just over 6%.

This illustrates that grade transitions which involve a decrease in the MFI can be improved by decreasing the quantity of reactant consumed.

17.3 Case Study: Transition from Grade 3 to Grade 2

The grade transition between Grade 3 and Grade 2 is from production of the highest MFI (lowest molecular weight) to the second lowest MFI (second highest molecular weight), representing a relatively large change in reactor operating conditions and product properties.

As shown in Table 15.5 and Figure 15.13, the transition from Grade 3 to Grade 2 is accomplished in the industrial reactor by an overshoot of 15% in the catalyst flow rate change, and by overshooting the hydrogen feed rate by 10%. This transition was improved by increasing the overshoot on the hydrogen feed to 50%, and increasing the overshoot on the catalyst from 15 to 17%, as shown in Table 17.5 and Figure 17.7.

The response of the cap-gas ratio and MFI in the simulated reactor are shown in Figure 17.8 and Figure 17.9, respectively. Note that the first eight hours of simulation shown in Table 15.5 and Figure 15.13 has been excluded from the simulation below, in order to focus on the grade transition itself.

Table 17.5: Characteristics of transition from grade 3 to grade 2 (model-based control)

Component	t_{Change} [hr]	Over/ undershoot	Over/ undershoot [%]	Over/undershoot duration [hr]
1-Butene	2	-	-	-
Hydrogen	4	Over	50	5
Catalyst	4	Over	17	5

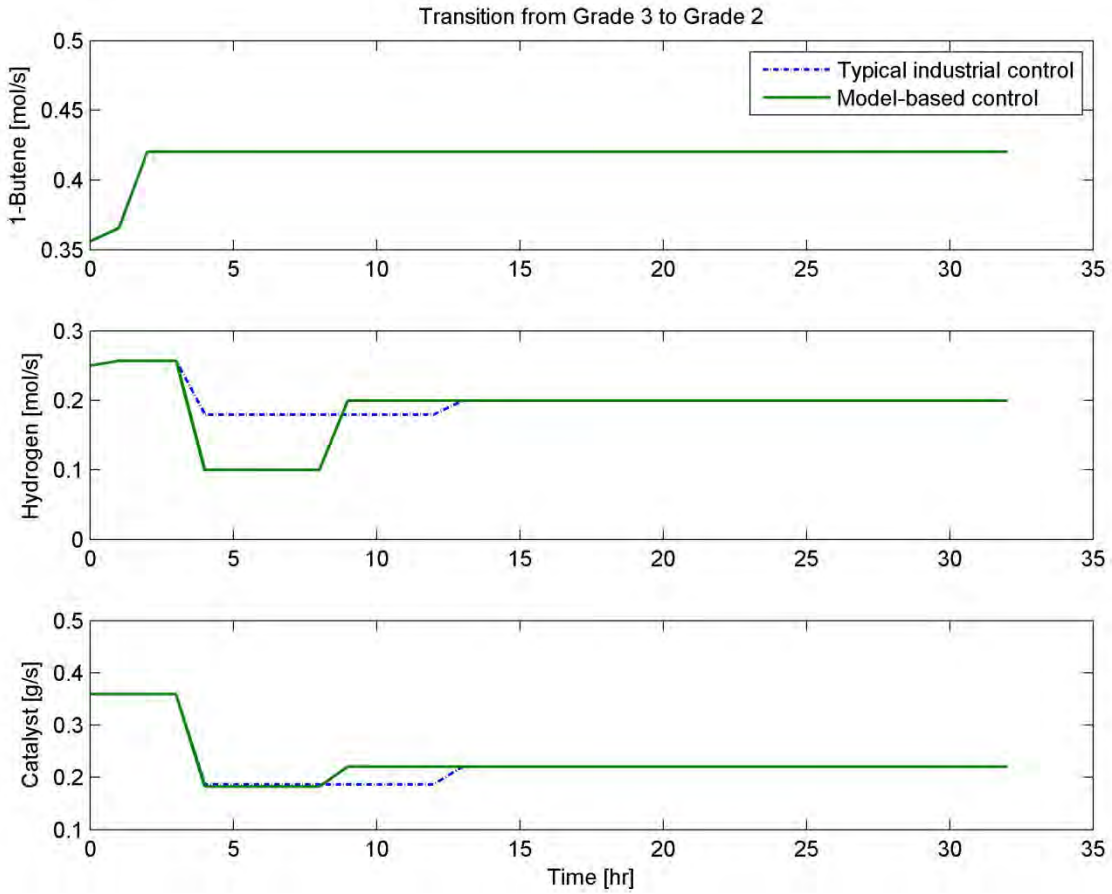

Figure 17.7: Manipulated variables for case study transition from grade 3 to grade 2

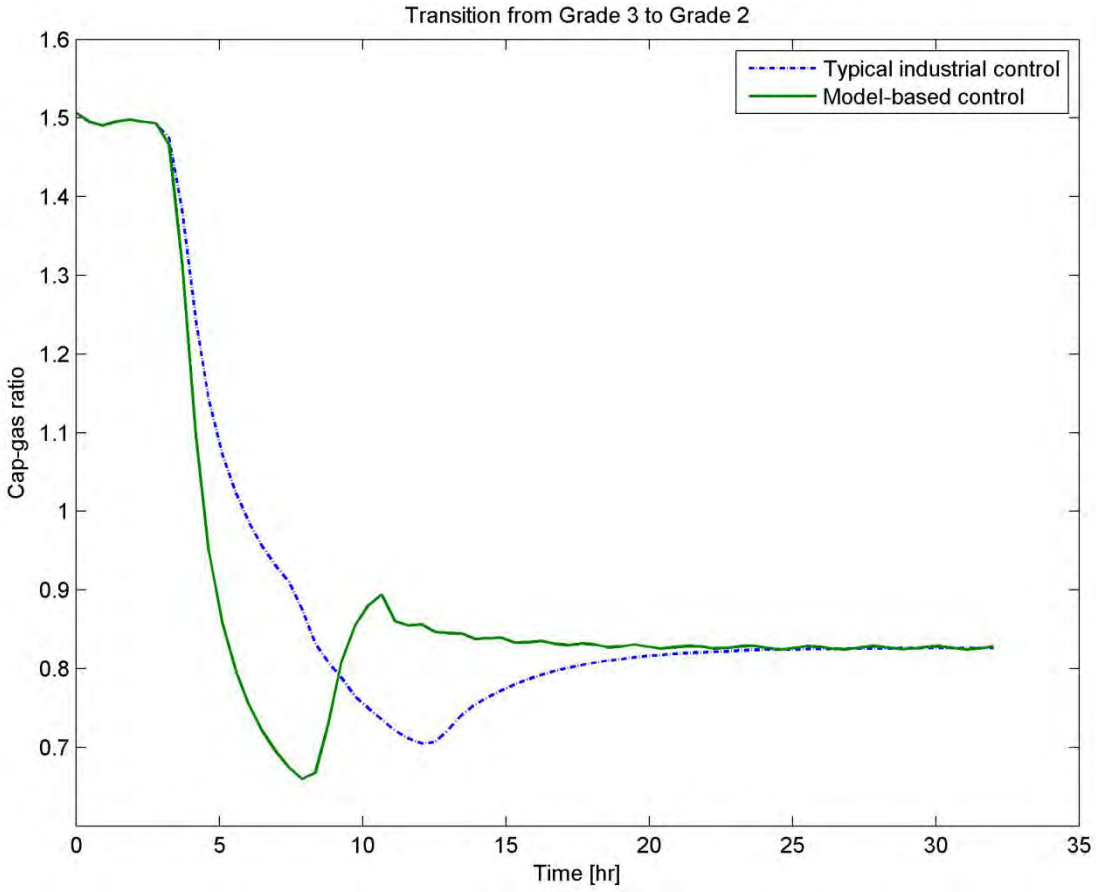

Figure 17.8: Comparison of industrial and case study cap-gas ratio for transition from grade 3 to 2

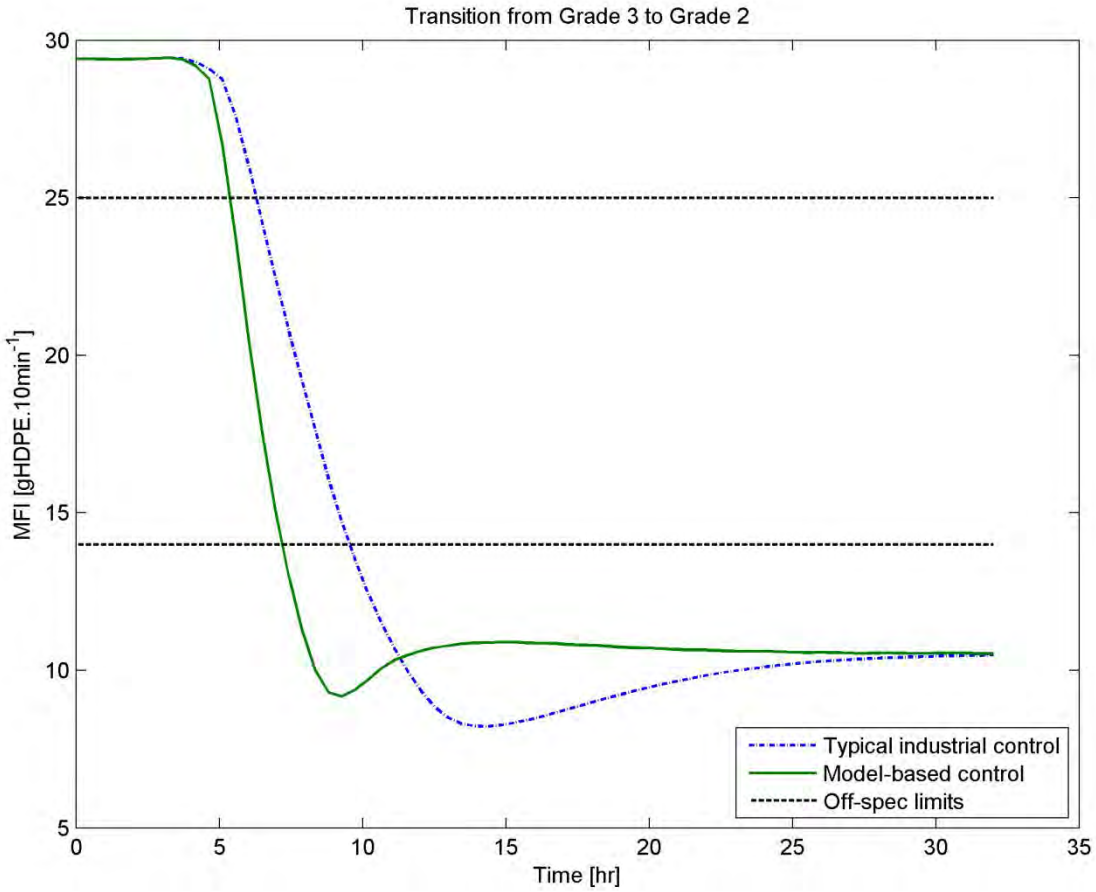

Figure 17.9: Comparison of industrial and case study MFI for transition from grade 3 to 2

As a result of the larger overshoots in the hydrogen and catalyst feed rates, the transition from Grade 3 to Grade 2 is completed in less than two hours, rather than the more than three hours that the industrial transition required (see Table 17.6). A similar reduction of approximately 45% in the mass of waste polymer produced is also achieved.

Table 17.6: Case study transition characteristics for transition from grade 3 to grade 2

Case	Typical Industrial Control	Model-based Control
Off specification time [hr]	3.21	1.80
Off specification mass [ton]	15.72	8.51
Calculation time [s]	16.47	13.45

The 45% improvement in the grade transition is achieved with approximately 5% less total hydrogen feed to the reactor, and only 1.5% additional catalyst feed, when compared to the industrial transition.

As before, a more complete economic assessment would be required to determine the optimum balance between increased reactant or catalyst consumption and the reduction in waste production and transition duration.

17.4 Summary

The three grade transitions which were previously matched to the industrial data have been re-examined in order to improve the transition, by minimising the mass of waste material and time between the polymer grades. In each of the cases, when the reactor model was used to modify the trajectory of the grade transition, significant improvements were achieved (between 20 and 45% reductions) with minimal increases to the total quantities of hydrogen or catalyst consumed during the transition period.

This exercise has illustrated that the reactor model developed during this project is useful as a tool to investigate the operation of an industrial polymerisation reactor, including periods of unsteady-state operation such as grade transitions, where there is a need for optimisation.

In the three case studies above, very simple modifications to the extent and duration of over- and undershoot strategies have been made by inspection to find improved grade transition strategies. Because of the speed with which the reactor model solves (typically 15-25s to simulate up to 36 hours of reactor operation), the model is suitable for application in more complex control engineering applications, which could use more rigorous methods to determine the optimum grade transition strategy.

An objective function for optimising grade transitions would require an economic basis, determined by the costs of the various reactants and products, and including the effects of producing off-specification material, and the impact of waste material on production schedules and storage capacities. Although the detailed economics of such an exercise are beyond the scope of this project, the model which has been developed lends itself to working within just such a structure, with a suitably-defined objective function.

PART E. CONCLUSIONS

CHAPTER 18. CONCLUSIONS

Although Ziegler-Natta catalysts are used to produce a significant fraction of the world's polyolefins, there are very few available models capable of simulating the performance of the industrial reactors; even fewer of these models are based on mathematical methods efficient enough to be used for real-time process control and optimisation.

This thesis focussed on the development of an unsteady-state simulation of an industrial polymerisation reactor, based on experimentally-derived kinetic parameters, that could be used in a real-time process control application for the optimisation of polymer grade transitions.

The work began with the development of a rigorous regression scheme, building on the work in Rawatlal (2004) on the pseudo-sites kinetic model of polymerisation. In particular, improved methods for the regression of polymerisation and copolymerisation propagation rate constants were proposed. Although the model does not predict the chemical composition distribution, the prediction of the CCD is regarded by the author as less important than the accurate reproduction of catalyst activity profiles, molecular weight distributions and the overall comonomer incorporation.

The regression methods were applied to a set of kinetic experimental data, in the first test of the pseudo-sites concept (and associated kinetic scheme) with a comprehensive set of kinetic data. The regression resulted in a set of eleven kinetic constants, which were able to accurately reproduce the activity profiles, comonomer incorporation and Molecular Weight Distribution of the laboratory data

A rigorous comparison between the Population Balance Model (PBM) and the Segregation Approach was conducted in the context of simulation of particle size distribution (PSD) in a polymerisation reactor. Despite giving every advantage to the PBM, the comparison showed that the Segregation Approach is significantly more computationally efficient for solving this type of problem, due to the differences in formulation and the number of calculation steps required for solution. To the author's knowledge, this was the first direct comparison of these two methods, proving the efficiency of the Segregation Approach and suggesting that it could provide the basis for reactor models that are useful for real time control applications.

In light of the ease with which complex reactor mixing patterns can be incorporated into the Segregation Approach, an analytical solution for the Residence Time Distribution (RTD) function of the industrial reactor of interest was developed. The system consisted of a Continuous Stirred Tank Reactor (CSTR) with a Plug Flow Reactor (PFR) recycle. To the author's knowledge, an analytical solution for the RTD of this system has not been presented before.

This complex RTD function was to have a negligible impact on predicted reactor operation, and so was not further applied to simulations of the industrial reactor. However, the RTD function was used to further investigate the operation of reactor systems of this configuration, to suggest guidelines for designing similar systems, such as limits to the residence time of the cooling loops before significant deviations from ideal reactor mixing behaviour occur. The formulation of this RTD function could also be useful in the wider field of reactor design.

A large set of industrial data was examined, and methods proposed for the analysis and classification of industrial data, to aid comparisons between the reactor model and industrial data. The initial comparison revealed significant discrepancies between the model predictions and steady-state industrial data, highlighting the difficulty of scaling up laboratory data.

After re-evaluating some assumptions in the reactor model formulation, the laboratory and industrial data were used to refit some of the parameters of the kinetic model. The refitted kinetic scheme was able to reproduce the steady-state industrial data, and reconcile this data with the laboratory data. The successful

reconciliation of two such disparate data sets demonstrates the utility of detailed analysis of complex systems through modelling analysis.

The reactor model was then validated with unsteady-state data from the industrial reactor, successfully reproducing changes in both the Melt Flow Index and the Cap-Gas ratio during each of three simulated grade transitions.

The computational efficiency of the Segregation Approach was again demonstrated: the reactor model typically simulated between 32 and 44 hours of reactor operation in 16 to 26s of computation time.

Simple adjustments to the grade transition strategies from the industrial data were proposed, based on heuristics developed in a sensitivity study; the simulated grade transitions making use of improved trajectories were between 20 and 45% more rapid (and less wasteful) than the simulated grade transitions based on industrial grade transition strategies.

It is fair to assume that, if applied within more sophisticated process control models, the improvements to unsteady-state reactor operation and control could be much greater.

Through the combination of an experimental study and generalised kinetic parameter regression approach, a number of reactor model formulation steps and extensive comparison and validation with industrial operating data, the development of an efficient steady- and unsteady-state simulation of industrial polymer production has been demonstrated.

PART F. REFERENCES

Ahmadzadeh, A, Arastoopour, H, Teymour, F, & Strumendo, M. 2008. Population balance equations' application in rotating fluidized bed polymerization reactor. *Chemical Engineering Research and Design*, **86**, 329–343.

Alexopoulos, AH, & Kiparissides, C. 2005. Part II: Dynamic evolution of the particle size distribution in particulate processes undergoing simultaneous particle nucleation, growth and aggregation. *Chemical Engineering Science*, **60**, 4157–4169.

Alexopoulos, AH, Roussos, AI, & Kiparissides, C. 2004. Part I: Dynamic evolution of the particle size distribution in particulate processes undergoing combined particle growth and aggregation. *Chemical Engineering Science*, **59**, 5751–5769.

Alexopoulos, AH, Roussos, AI, & Kiparissides, C. 2009. Part V: Dynamic evolution of the multivariate particle size distribution undergoing combined particle growth and aggregation. *Chemical Engineering Science*, **64**, 3260–3269.

Ali, EM, & Ali, MA. 2010. Broadening the polyethylene molecular weight distribution by controlling the hydrogen concentration and catalyst feed rates. *ISA Transactions*, **49**, 177–187.

Ali, MA, & Ali, EM. 2011. Effect of monomer feed and production rate on the control of molecular weight distribution of polyethylene in gas phase reactors. *Computers & Chemical Engineering*, **35**, 2480–2490.

Alizadeh, M, Mostoufi, N, Pourmahdian, S, & Sotudeh-Gharebagh, R. 2004. Modeling of fluidized-bed reactor of ethylene polymerization. *Chemical Engineering Journal*, **97**, 27–35.

Anantawaraskul, S, Soares, JBP, Wood-Adams, PM, & Monrabal, B. 2003. Effect of molecular weight and average comonomer content on the crystallization analysis fractionation (Crystaf) of ethylene alpha-olefin copolymers. *Polymer*, **44**, 2393–2401.

Andoni, A, Chadwick, JC, Niemantsverdriet, HJW, & Thüne, PC. 2008. The role of electron donors on lateral surfaces of MgCl2-supported Ziegler-Natta catalysts: Observation by AFM and SEM. *Journal of Catalysis*, **257**, 81–86.

Ashrafi, O, Mostoufi, N, & Sotudeh-Gharebagh, R. 2012. Two phase Steady-state particle size distribution in a gas-phase fluidized bed ethylene polymerization reactor. *Chemical Engineering Science*, **73**, 1–7.

Assumption, HF, Vermeulen, JP, Jarrett, WL, Mathias, LJ, & van Reenen, AJ. 2006. High resolution solution and solid state NMR characterization of ethylene/1-butene and ethylene/1-hexene copolymers fractionated by preparative temperature rising elution fractionation. *Polymer*, **47**, 67–74.

ASTM:D1238. 2010. *Standard Test Method for Melt Flow Rates of Thermoplastics by Extrusion Plastometer*. ASTM International, West Conshohocken, PA.

Attarakih, MM, Drumm, C, & Bart, HJ. 2009. Solution of the population balance equation using the sectional quadrature method of moments (SQMOM). *Chemical Engineering Science*, **64**, 742–752.

Bahri-Laleh, N, Correa, A, Mehdipour-Ataei, S, Arabi, H, Haghighi, MN, Zohuri, G, & Cavallo, L. 2011. Moving up and down the Titanium Oxidation State in Ziegler-Natta Catalysis. *Macromolecules*, **44**, 778–783.

Barabanov, A.A., Sukulova, V.V., Matsko, M.A., & Zakharov, V.A. 2015. Kinetic features of ethylene polymerization over titanium-magnesium Ziegler-Natta catalysts: Effect of monomer concentration on the number of active centers and propagation rate constant. *Journal of Molecular Catalysis A: Chemical*, **396**, 328–334.

Bhaduri, S, Mukhopadhyay, S, & Kulkarni, SA. 2006. Role of titanium oxidation states in polymerization activity of Ziegler-Natta catalyst: A density functional study. *Journal of Organometallic Chemistry*, **691**, 2810–2820.

Bhagwat, MS, Bhagwat, SS, & Sharma, MM. 1994. Mathematical modeling of the slurry polymerization of ethylene: Gas-Liquid mass transfer limitations. *Industrial & Engineering Chemistry Research*, **33**, 2322–2330.

Boero, M, Terakura, K, & Parrinello, M. 2002. First principles molecular dynamics study of catalysis for polyolefins: the Ziegler-Natta heterogeneous system. *International Journal of Molecular Sciences*, **3**, 395–406.

Brambilla, L, Zerbi, G, Piemontesi, F, Nascetti, S, & Morini, G. 2007. Structure of MgCl2-TiCl4 complex in co-milled Ziegler-Natta catalyst precursors with different TiCl4 content: Experimental and theoretical vibrational spectra. *Journal of Molecular Catalysis A: Chemical*, **263**, 103–111.

Bremner, T, Rudin, A, & Cook, DG. 1990. Melt flow index values and molecular weight distributions of commercial thermoplastics. *Journal of Applied Polymer Science*, **41**, 1617–1627.

Browning, B, Pitault, I, Sheibat-Othman, N, Tioni, E, Monteil, V, & McKenna, TFL. 2012. Dynamic modelling of a stopped flow fixed bed reactor for gas phase olefin polymerisation. *Chemical Engineering Journal*, **207-208**, 635–644.

Chakraborty, J, & Kumar, S. 2007. A new framework for solution of multidimensional population balance equations. *Chemical Engineering Science*, **62**, 4112–4125.

Chatzidoukas, C, Perkins, JD, Pistikopoulos, EN, & Kiparissides, C. 2003. Optimal grade transition and selection of closed-loop controllers in a gas-phase olefin polymerization fluidized-bed reactor. *Chemical Engineering Science*, **58**, 3643–3658.

Che, Y, Tian, Z, Liu, Z, Zhang, R, Gao, Y, Zou, E, Wang, S, & Liu, B. 2015. A CFD-PBM model considering ethylene polymerization for the flow behaviors and particle size distribution of polyethylene in a pilot-plant fluidized bed reactor. *Powder Technology*, **286**, 107–123.

Chen, YP, & Fan, Z. 2006. Ethylene/1-hexene copolymerization with TiCl4/MgCl2/AlCl3 catalyst in the presence of hydrogen. *European Polymer Journal*, **42**, 2441–2449.

Chen, YP, Fan, ZQ, Liao, JH, & Liao, SQ. 2006. Molecular weight distribution of polyethylene catalyzed by Ziegler-Natta catalyst supported on MgCl2 doped with AlCl3. *Journal of Applied Polymer Science*, **102**, 1768–1772.

Choi, KY, Zhao, X, & Tang, S. 1994. Population balance modeling for a continuous gas phase olefin polymerization reactor. *Journal of Applied Polymer Science*, **53**, 1589–1597.

Czaja, K, & Bialek, M. 2001. Effect of hydrogen on the ethylene polymerization process over Ziegler-Natta catalysts supported on MgCl2(THF)2 II Kinetic studies. *Journal of Applied Polymer Science*, **79**, 361–365.

D'Agnillo, L, Soares, JBP, & Penlidis, A. 2002. Round-robin experiment in high-temperature gel permeation chromatography. *Journal of Applied Polymer Science: Part B: Polymer Physics*, **40**, 905–921.

Danckwerts, PV. 1953. Continuous flow systems: distribution of residence times. *Chemical Engineering Science*, **2**(1), 1–13.

de Camargo Forte, MM, da Cunha, FOV, dos Santos, JHZ, & Zacca, JJ. 2003. Ethylene and 1-butene copolymerization catalyzed by a Ziegler-Natta/metallocene hybrid catalyst through a 2^3 factorial experimental design. *Polymer*, **44**, 1377–1384.

de Pooter, M, Smith, PB, Dohrer, KK, Bennett, KF, Meadows, MD, Smith, CG, Schouwenaars, HP, & Geerards, RA. 1991. Determination of the composition of common linear low density polyethylene copolymers by 13C-NMR spectroscopy. *Journal of Applied Polymer Science*, **42**, 399–408.

Dompazis, G, Kanellopoulos, V, & Kiparissides, C. 2005. A multi-scale model approach for the prediction of molecular and morphological properties in multi-site catalyst, olefin polymerization reactors. *Macromolecular Materials and Engineering*, **290**, 525–536.

Dompazis, G, Kanellopoulos, V, & Kiparissides, C. 2006. Assessment of particle agglomeration in catalytic olefin polymerization reactors using rheological measurements. *Industrial & Engineering Chemistry Research*, **45**, 3800–3809.

Dompazis, G, Kanellopoulos, V, Touloupides, V, & Kiparissides, C. 2008. Development of a multi-scale, multi-phase, multi-zone dynamic model for the prediction of particle segregation in catalytic olefin polymerization FBRs. *Chemical Engineering Science*, **63**, 4735–4753.

Dorao, CA, & Jakobsen, HA. 2006. Application of the least-squares method for solving population balance problems in R^(d+1). *Chemical Engineering Science*, **61**, 5070–5081.

Dube, MA, Soares, JBP, Penlidis, A, & Hamielec, AE. 1997. Mathematical modeling of multicomponent chain-growth polymerizations in batch, semibatch and continuous reactors: A Review. *Industrial & Engineering Chemistry*, **36**, 966–1015.

Dyson, F. 2004. A meeting with Enrico Fermi. *Nature*, **427**, 297.

Embirucu, M, & Fontes, C. 2006. Multirate multivariable generalized predictive control and its application to a slurry reactor for ethylene polymerization. *Chemical Engineering Science*, **61**, 5754–5767.

Fazeli, N, Arabi, H, & Bolandi, S. 2006. Effect of branching characteristics of ethylene/1-butene copolymers on melt flow index. *Polymer Testing*, **25**, 28–33.

Fernandes, FAN, & Lona, LMF. 2002. Heterogeneous modeling of fluidized bed polymerization reactors: Influence of mass diffusion into the polymer particle. *Computers & Chemical Engineering*, **26**, 841–848.

Fisch, AG, dos Santos, JHZ, Cardozo, NSM, & Secchi, AR. 2008. Mass transfer in olefin polymerization: estimative of macro- and microscale diffusion coefficients through the swollen polymer. *Chemical Engineering Science*, **63**, 3727–3739.

Flory, PJ. 1953. *Principles of Polymer Chemistry*. Cornell University Press, Ithaca, NY.

Floyd, S, Choi, KY, Taylor, TW, & Ray, WH. 1986a. Polymerization of olefins through heterogeneous catalysis III: Polymer particle modelling with an analysis of intraparticle heat and mass transfer effects. *Journal of Applied Polymer Science*, **32**, 2935–2960.

Floyd, S, Hutchinson, RA, & Ray, WH. 1986b. Polymerization of olefins through heterogeneous catalysis V: Gas-Liquid mass transfer limitations in liquid slurry reactors. *Journal of Applied Polymer Science*, **32**, 5451–5479.

Floyd, S, Heiskanen, T, Taylor, TW, Mann, GE, & Ray, WH. 1987. Polymerization of olefins through heterogeneous catalysis VI: Effect of particle heat and mass transfer on polymerization behavior and polymer properties. *Journal of Applied Polymer Science*, **33**, 1021–1065.

Fogler, HS. 2005. *Elements of Chemical Reaction Engineering*. 4th edn. Prentice Hall, New Jersey.

Fregonese, D, Mortara, S, & Bresadola, S. 2001. Ziegler-Natta MgCl2-supported catalysts: relationship between titanium oxidation states distribution and activity in olefin polymerization. *Journal of Molecular Catalysis A: Chemical*, **172**, 89–95.

Gabriel, C, & Lilge, D. 2001. Comparison of different methods for the investigation of the short-chain branching distribution of LLDPE. *Polymer*, **42**, 297–303.

Garoff, T, Johansson, S, Pesonen, K, Waldvogel, P, & Lindgren, D. 2002. Decrease in activity caused by hydrogen in Ziegler-Natta ethene polymerisation. *European Polymer Journal*, **38**, 121–132.

Garoff, T, Virkkunen, V, Jaaskelainen, P, & Vestberg, T. 2003. A qualitative model for polymerisation of propylene with a MgCl2-supported TiCl4 Ziegler-Natta catalyst. *European Polymer Journal*, **39**, 1679–1685.

Gerdeen, JC, Lord, HW, & Rorrer, RAL. 2006. *Engineering Design with Polymers and Composites*. Taylor & Francis, Boca Raton.

Ghafelebashi Zarand, SM, & Mortazavi, SMM. 2005. Mathematical modeling of ethylene polymerization with Ziegler-Natta catalyst. *In:* Puigianer, L, & Espuna, A (eds), *European Symposium on Computer Aided Process Engineering 15, 29 May-1 June 2005, Barcelona, Spain*.

Groppo, E, Seenivasan, K, Gallo, E, Sommazzi, A, Lamberti, C, & Bordiga, S. 2015. Activation and In Situ Ethylene Polymerization on Silica-Supported Ziegler-Natta Catalysts. *ACS Catalysis*, **5**, 5586–5595.

Ha, KS, & Rhee, HK. 2001. A continuum approach for the active sites in a Ziegler-Natta catalytic system. *Chemical Engineering Science*, **56**, 905–910.

Ha, KS, Yoo, KY, & Rhee, HK. 2001. Modeling and analysis of a slurry reactor system for heterogeneous olefin polymerization: The effects of hydrogen concentration and initial catalyst size. *Journal of Applied Polymer Science*, **79**, 2480–2493.

Hakim, S, & Moballegh, L. 2006. Simulation of a series of industrial slurry reactors for HDPE polymerization process using deconvolution of the GPC graph of only the first reactor. *Iranian Polymer Journal*, **15**(8), 655–666.

Hakim, S, Nekoomanesh, M, & Nieat, MA. 2008. Investigating the behaviour of a bi-supported SiO2/TiCl4/THF/MgCl2 catalyst in slurry ethylene polymerization: activity and molecular weight. *Iranian Polymer Journal*, **17**(3), 209–216.

Hamba, M, Han-Adebekun, GC, & Ray, WH. 1997. Kinetic study of gas phase olefin polymerization with a TiCl4/MgCl2 Catalyst II: Kinetic parameter estimation and model building. *Journal of Applied Polymer Science A: Polymer Chemistry*, **35**, 2075–2096.

Han-Adebekun, GC, & Ray, WH. 1997. Polymerization of olefins through heterogeneous catalysis XVII: Experimental study and model interpretation of some aspects of olefin polymerization over a TiCl4/MgCl2 catalyst. *Journal of Applied Polymer Science*, **65**, 1037–1052.

Han-Adebekun, GC, Hamba, M, & Ray, WH. 1997a. Kinetic study of gas phase olefin polymerization with a TiCl4/MgCl2 catalyst I. Effect of polymerization conditions. *Journal of Applied Polymer Science A: Polymer Chemistry*, **35**, 2063–2074.

Han-Adebekun, GC, Debling, JA, & Ray, WH. 1997b. Polymerization of olefins through heterogeneous catalysis XVI: Design and control of a laboratory stirred bed copolymerization reactor. *Journal of Applied Polymer Science*, **64**, 373–382.

Harshe, YM, Utikar, RP, & Ranade, VV. 2004. A computational model for predicting particle size distribution and performance of fluidized bed polypropylene reactor. *Chemical Engineering Science*, **59**, 5154–5156.

Hatzantonis, H, & Kiparissides, C. 1998. The effect of the mean particle size on the dynamic behaviour of catalyzed olefin polymerization fluidized bed reactors. *Computers & Chemical Engineering*, **22**(Supplement 1), S127–S134. European Symposium on Computer Aided Process Engineering-8.

Hatzantonis, H, Goulas, A, & Kiparissides, C. 1998. A comprehensive model for the prediction of particle-size distribution in catalyzed olefin polymerization fluidized-bed reactors. *Chemical Engineering Science*, **53**(18), 3251–3267.

Hatzantonis, H, Yiannoulakis, H, Yiagopoulous, A, & Kiparissides, C. 2000. Recent developments in modeling gas-phase catalyzed olefin polymerization fluidized-bed reactors: The effect of bubble size variation on the reactor's performance. *Chemical Engineering Science*, **55**, 3237–3259.

Ho, YK, Shamiri, A, Mjalli, FS, & Hussain, MA. 2012. Control of industrial gas phase propylene polymerization in fluidized bed reactors. *Journal of Process Control*, **22**, 947–958.

Hocine, S, Pibouleau, L, Azzaro-Pantel, C, & Domenech, S. 2008. Modelling systems defined by RTD curves. *Computers & Chemical Engineering*, **32**, 3112–3120.

Huang, JCK, Lacombe, Y, Lynch, DT, & Wanke, SE. 1997. Effects of hydrogen and 1-butene concentrations on the molecular properties of polyethylene produced by catalytic gas-phase polymerization. *Industrial & Engineering Chemistry Research*, **36**, 1136–1143.

Hulburt, HM, & Katz, S. 1964. Some problems in particle technology: A statistical mechanical formulation. *Chemical Engineering Science*, **19**, 555–574.

Hutchinson, RA, Chen, CM, & Ray, WH. 1992. Polymerization of olefins through heterogeneous catalysis X: Modeling of particle growth and morphology. *Journal of Applied Polymer Science*, **44**, 1389–1414.

Iserles, A. 1984. Solving linear ordinary differential equations by exponentials of iterated commutators. *Numerische Mathematik*, **45**, 183–199.

Kanellopoulos, V, Dompazis, G, Gustafsson, B, & Kiparissides, C. 2004. Comprehensive analysis of single-particle growth in heterogeneous olefin polymerization: The random-pore polymeric flow model. *Industrial & Engineering Chemistry Research*, **43**, 5166–5180.

Khan, MJH, Hussain, MA, Mansourpour, Z, Mostoufi, N, Ghasem, NM, & Abdullah, EC. 2014. CFD simulation of fluidized bed reactors for polyolefin production – A review. *Journal of Industrial and Engineering Chemistry*, **20**, 3919–3946.

Khang, DY, & Lee, HH. 1996. Particle size distribution in fluidized beds for catalytic polymerization. *Chemical Engineering Science*, **52**, 421–431.

Khare, NP, Seavey, KC, Liu, YA, Ramanathan, S, Lingard, S, & Chen, CC. 2002. Steady-state and dynamic modeling of commercial slurry high-density polyethylene (HDPE) processes. *Industrial & Engineering Chemistry Research*, **41**(23), 5601–5618.

Khare, NP, Lucas, B, Seavey, KC, Liu, YA, Sirohi, A, Ramanathan, S, Lingard, S, Song, Y, & Chen, CC. 2004. Steady-state and dynamic modeling of gas-phase polypropylene processes using strirred-bed reactors. *Industrial & Engineering Chemistry Research*, **43**, 884–900.

Kiashemshaki, A, Mostoufi, N, & Sotudeh-Gharebagh, R. 2006. Two-phase modeling of a gas phase polyethylene fluidized-bed reactor. *Chemical Engineering Science*, **61**, 3997–4006.

Kim, I, & Woo, SI. 1990. Kinetic study for the decay rate of ethylene polymerization catalyzed over silica supported TiCl4/MgCl2 catalysts. *Korean Journal of Chemical Engineering*, **7**(2), 95–99.

Kim, I, Kim, JH, & Woo, SI. 1990. Kinetic study of ethylene polymerization by highly active silica supported TiCl4/MgCl2 catalysts. *Journal of Applied Polymer Science*, **39**, 837–854.

Kim, SH, & Somorjai, GA. 2000a. Polymer growth mode on the heterogeneous Ziegler-Natta catalyst: active sites at the bottom of the growing polymer layer. *Catalysis Letters*, **68**, 7–11.

Kim, SH, & Somorjai, GA. 2000b. TDP characterization of surface adsorption sites of model Ziegler-Natta polymerization catalysts. *Applied Surface Science*, **161**, 333–339.

Kim, TY, & Yeo, YK. 2010. Development of Polyethylene melt index inferential model. *Korean Journal of Chemical Engineering*, **27**, 1669–1674.

Kissin, Y. 2012. Active centers in Ziegler-Natta catalysts: Formation kinetics and structure. *Journal of Catalysis*, **292**, 188–200.

Kissin, YV, Nowlin, TE, & Mink, RI. 1993. Ethylene oligomerization and chain growth mechanisms with Ziegler-Natta catalysts. *Macromolecules*, **26**, 2151–2158.

Kissin, YV, Mink, RI, Nowlin, TE, & Brandolin, AJ. 1999. Kinetics and mechanism of ethylene homopolymerization and copolymerization reactions with heterogeneous Ti-based Ziegler-Natta catalysts. *Topics in Catalysis*, **7**, 69–88.

Kissin, YV, Liu, X, Pollick, DJ, Brungard, NL, & Chang, M. 2008. Ziegler-Natta catalysts for propylene polymerization: Chemistry of reactions leading to the formations of active centres. *Journal of Molecular Catalysis A: Chemical*, **287**, 45–52.

Kittilsen, P, & McKenna, TF. 2001. Study of the kinetics, mass transfer and particle morphology in the production of high-impact polypropylene. *Journal of Applied Polymer Science*, **82**, 1047–1060.

Kittilsen, P, McKenna, TF, Svendsen, H, Jakobsen, HA, & Fredriksen, SW. 2001. The interaction between mass transfer effects and morphology in heterogeneous olefin polymerization. *Chemical Engineering Science*, **56**, 4015–4028.

Koshevoy, EI, Mikenas, TB, Zakharov, VA, Volodin, AM, & Kenzhin, RM. 2014. Formation of isolated titanium(III) ions in superactive titanium–magnesium catalysts with a low titanium content as active sites in ethylene polymerization. *Catalysis Communications*, **48**, 38–40.

Kotoulas, C, & Kiparissides, C. 2006. A generalized population balance model for the prediction of particle size distribution in suspension polymerization reactors. *Chemical Engineering Science*, **61**, 332–346.

Kotsiopoulos, A, Hansford, GS, & Rawatlal, R. 2008. An approach of segregation in modeling continuous flow tank bioleach systems. *AIChE Journal*, **54**(6), 1592–1599.

Kou, B, McAuley, KB, Hsu, CC, Bacon, DW, & Yao, KZ. 2005a. Gas-phase ethylene/hexene copolymerization with metallocene catalyst in a laboratory-scale reactor. *Industrial & Engineering Chemical Research*, **44**, 2443–2450.

Kou, B, McAuley, KB, Hsu, CC, Bacon, DW, & Yao, KZ. 2005b. Mathematical model and parameter estimation for gas-phase ethylene homopolymerization with supported metallocene catalyst. *Industrial & Engineering Chemical Research*, **44**, 2428–2442.

Kou, B, McAuley, KB, Hsu, CC, & Bacon, DW. 2005c. Mathematical model and parameter estimation for gas-phase ethylene/hexene copolymerization with metallocene catalyst. *Macromolecular Materials and Engineering*, **290**, 537–557.

Krallis, A, Kanellopoulos, V, & Ali, MH. 2015. Comprehensive Study of Reactants Depletion in Catalytic Olefin Polymerization Industrial Loop Reactors. *Industrial & Engineering Chemistry Research*, **54**, 8247–8254.

Kumar, J, Peglow, M, Warnecke, G, & Heinrich, S. 2008. The cell average technique for solving multi-dimensional aggregation population balance equations. *Computers & Chemical Engineering*, **32**, 1810–1830.

Laquerbe, C, Laborde, JC, Soares, S, Ricciardi, L, Floquet, P, Pibouleau, L, & Domenech, S. 2001a. Computer aided synthesis of RTD models to simulate the air flow distribution in ventilated rooms. *Chemical Engineering Science*, **56**, 5727–5738.

Laquerbe, C, Laborde, JC, Soares, S, Floquet, P, Pibouleau, L, & Domenech, S. 2001b. Synthesis of RTD models via stochastic procedures: simulated annealing and genetic algorithm. *Computers & Chemical Engineering*, **25**, 1169–1183.

Lee, EH, Kim, TY, & Yeo, YK. 2008. Prediction and quality control of the melt index during production of high-density polyethylene. *Korean Journal of Chemical Engineering*, **25**, 613–622.

Lee, JW, & Jo, WH. 2007. Theoretical investigation on the model active site for isotactic polypropylene in heterogeneous Ziegler-Natta catalyst: A density functional study. *Journal of Organometallic Chemisty*, **692**, 4639–4646.

Lee, MH, Han, C, & Chang, KS. 1999. Dynamic Optimization of a Continuous Polymer Reactor Using a Modified Differential Evolution Algorithm. *Industrial & Engineering Chemistry Research*, **38**, 4825–4831.

Levenspiel, O. 1999. *Chemical reaction engineering*. 3rd edn. Wiley, New York.

Lim, SY, & Choung, SJ. 1997. Studies on the catalytic deactivation in propylene polymerization. *Applied Catalysis A: General*, **153**, 103–118.

Lin, JS, & Catlow, CRA. 1995. Quantum mechanical study of Ti/MgCl2-supported Ziegler-Natta catalysts. *Journal of Catalysis*, **157**, 145–152.

Lo, DP, & Ray, WH. 2005. Kinetic modeling and prediction of polymer properties for ethylene polymerization over nickel diimine catalysts. *Industrial & Engineering Chemistry Research*, **44**, 5932–5949.

Lo, DP, & Ray, WH. 2006. Dynamic modeling of polyethylene grade transitions in fluidized-bed reactors employing nickel-diimine catalysts. *Industrial & Engineering Chemistry Research*, **45**, 993–1008.

Luo, ZH, Wang, W, & Su, PL. 2008. Modeling of the propylene polymerization catalyzed by single-/multi-active site catalyst: A Monte Carlo study. *Journal of Applied Polymer Science*, **110**, 3360–3367.

Luo, ZH, Su, PL, Shi, DP, & Zheng, ZW. 2009. Steady-state and dynamic modeling of commercial bulk polypropylene process of Hypol technology. *Chemical Engineering Journal*, **149**, 370–382.

Martin, C, & McKenna, TF. 2002. Particle morphology and transport phenomena in olefin polymerisation. *Chemical Engineering Journal*, **87**, 89–99.

Matos, V, Neto, AGM, & Pinto, JC. 2001. Method for quantitative evaluation of kinetic constants in olefin polymerizations I Kinetic study of a conventional Ziegler-Natta catalyst used for propylene polymerizations. *Journal of Applied Polymer Science*, **79**, 2076–2108.

Matsko, MA, Echevskaya, LG, Zakharov, VA, Kinolaeva, MI, Mikenas, TB, & Vanina, MP. 2009. Study of multi-site nature of supported Ziegler-Natta catalysts in ethylene-hexene-1 copolymerization. *Macromolecular Symposia*, **282**, 157–166.

McAuley, KB, & MacGregor, JF. 1992. Optimal grade transitions in a gas phase polyethylene reactor. *AIChE Journal*, **38**(10), 1564–1576.

McAuley, KB, MacGregor, JF, & Hamielec, AE. 1990. A kinetic model for industrial gas-phase ethylene copolymerization. *AIChE Journal*, **36**, 837–850.

McCoy, BJ. 2002. A population balance framework for nucleation, growth, and aggregation. *Chemical Engineering Science*, **57**, 2279–2285.

McCoy, BJ, & Madras, G. 2003. Analytical solution for a population balance equation with aggregation and fragmentation. *Chemical Engineering Science*, **58**, 3049–3051.

McKenna, TF, & Soares, JBP. 2001. Single particle modelling for olefin polymerization on supported catalysts: a review and proposals for future developments. *Chemical Engineering Science*, **56**, 3931–3949.

McKenna, TF, Barbotin, F, & Spitz, R. 1996. Modeling of transfer phenomena on heterogeneous Ziegler catalysts II Experimental investigation of intraparticle mass transfer resistance during the polymerization of ethylene in slurry. *Journal of Applied Polymer Science*, **62**, 1835–1841.

McKenna, TF, Dupuy, J, & Spitz, R. 1997. Modeling of transfer phenomena on heterogeneous Ziegler catalysts III Modeling of intraparticle mass transfer resistance. *Journal of Applied Polymer Science*, **63**, 315–322.

McKenna, TF, Cokljat, D, Spitz, R, & Schweich, D. 1999. Modelling of heat and mass transfer during the polymerisation of olefins on heterogeneous Ziegler catalysts. *Catalysis Today*, **48**, 101–108.

McKenna, TF, Soares, JBP, & Simon, LC. 2005. Polyolefin reaction engineering - An overview of recent developments. *Macromolecular Materials and Engineering*, **290**, 507–510.

Meimaroglou, D, Roussos, AI, & Kiparissides, C. 2006. Part IV: Dynamic evolution of the particle size distribution in particulate processes. A comparative study between Monte Carlo and the generalized method of moments. *Chemical Engineering Science*, **61**, 5620–5635.

Meng, W, Li, J, Chen, B, & Li, H. 2013. Modeling and Simulation of Ethylene Polymerization in Industrial Slurry Reactor Series. *Chinese Journal of Chemical Engineering*, **21**, 850–859.

Moudgalya, KM, & Jaguste, S. 2001. A class of discontinuous dynamical systems II. An industrial slurry high density polyethylene reactor. *Chemical Engineering Science*, **56**, 3611–3621.

Nacerodien, MT. 2014. *Investigation of polymer grade blending in Ziegler-Natta catalysed ethylene polymerisation systems*. M.Phil. thesis, University of Cape Town.

Nagel, EJ, Kirillov, VA, & Ray, WH. 1980. Prediction of molecular weight distributions for high-density polyolefins. *Industrial & Engineering Chemistry Product Research and Development*, **19**, 372–379.

Nelder, JA, & Mead, R. 1965. A simplex method for function minimization. *Computer Journal*, **7**, 308–313.

Neto, AGM, Freitas, MF, Nele, M, & Pinto, JC. 2005. Modeling Ethylene/1-butene copolymerizations in industrial slurry reactors. *Industrial & Engineering Chemical Research*, **44**, 2697–2715.

Ostrovskii, NM, & Kenig, F. 2005. About mechanism and model of deactivation of Ziegler-Natta polymerization catalysts. *Chemical Engineering Journal*, **107**, 73–77.

Peng, DY, & Robinson, DB. 1976. A new two-constant equation of state. *Industrial & Engineering Chemistry Fundamentals*, **15**, 59–64.

Perry, RH, & Green, DW (eds). 1997. *Perry's Chemical Engineers' Handbook*. 7 edn. McGraw-Hill.

Philipsen, HJA. 2004. Review: Determination of chemical composition distributions in synthetic polymers. *Journal of Chromatography A*, **1037**, 329–350.

Pinto, MA, Immanuel, CD, & Doyle III, FJ. 2008. A two-level discretisation algorithm for the efficient solution of higher-dimensional population balance models. *Chemical Engineering Science*, **63**, 1304–1314.

Podzimek, S. 2004. Round-robin test on the molecular characterization of epozy resins by liquid chromatography. *International Journal of Polymer Analysis and Characterization*, **9**, 305–316.

Pontes, KV, Maciel, R, & Embirucu, M. 2008. An approach for complete molecular weight distribution calculation: Application in ethylene coordination polymerization. *Journal of Applied Polymer Science*, **109**, 2176–2186.

Qamar, S, Warnecke, G, & Elsner, MP. 2009. On the solution of population balances for nucleation, growth, aggregation and breakage processes. *Chemical Engineering Science*, **64**, 2088–2095.

Rashedi, R, & Sharif, F. 2015. Variation of Comonomer Content in LLDPE Particles with Different Sizes from Industrial Fluidized Bed Reactor. *Industrial & Engineering Chemistry Research*, **In press**.

Rawatlal, R. 2004. *Unsteady-state Modelling of Ziegler-Natta Catalyzed Olefin Polymerization Reactor Systems*. Ph.D. thesis, University of Kwa-Zulu Natal.

Rawatlal, R. 2009. A simpler approach to population balance modelling in predicting the performance of Ziegler-Natta catalysed gas-phase olefin polymerisation reactor systems. *Macromolecular Reaction Engineering*, **3**(2-3), 108–117.

Rawatlal, R, & Starzak, M. 2003. Unsteady-state Residence-Time Distribution in Perfectly Mixed Vessels. *AIChE Journal*, **49**(2), 471–484.

Rawatlal, R, & Tincul, I. 2008. An analysis of the heterogeneous propagation rate assumption in predicting the polydispersity index. *Pages 72–77 of:* Terano, M, & Liu, B (eds), *Current Achievements on Heterogeneous Olefin Polymerization Catalysts*, vol. 2. Sankeisha Co, Ltd.

Ray, WH. 1986. Modeling of polymerization phenomena. *Berichte der Bunsen-Gesellschaft fur Physikalische Chemie*, **90**, 947–955.

Ray, WH. 1988. *Transition Metal Catalyzed Polymerization*. Harwood: New York. Chap. Practical benefits from modelling olefin polymerization reactors.

Roussos, AI, Alexopoulos, AH, & Kiparissides, C. 2005. Part III: Dynamic evolution of the particle size distribution in batch and continuous particulate processes: a Galerkin on finite elements approach. *Chemical Engineering Science*, **60**, 6998–7010.

Sandler, SI. 1998. *Chemical and Engineering Thermodynamics*. 3 edn. Wiley.

Sarzotti, DM, Soares, JBP, Simon, LC, & Britto, LJD. 2004. Analysis of the chemical composition distribution of ethylene/alpha-olefin copolymers by solution differential scanning calorimetry: an alternative technique to Crystaf. *Polymer*, **45**, 4787–4799.

Schiesser, WE. 1991. *The Numerical Method of Lines*. Academic Press, San Diego, CA.

Schiesser, WE, & Griffiths, GW. 2009. *A Compendium of Partial Differential Equation Models: Method of Lines Analysis with Matlab*. 1 edn. Cambridge University Press.

Schneiderbauer, S, Puttinger, S, Pirker, S, Aguayo, P, & Kanellopoulos, V. 2015. CFD modeling and simulation of industrial scale olefin polymerization fluidized bed reactors. *Chemical Engineering Journal*, **264**, 99–112.

Seavey, KC, Liu, YA, Khare, NP, Bremner, T, & Chen, CC. 2003. Quantifying relationships among the molecular weight distribution, non-Newtonian shear viscosity, and melt index for linear polymers. *Industrial & Engineering Chemistry Research*, **42**(21), 5354–5362.

Shamiri, A, Hussain, MA, Mjalli, FS, & Mostoufi, N. 2010. Kinetic modeling of propylene homopolymerization in a gas-phase fluidized-bed reactor. *Chemical Engineering Journal*, **161**, 240–249.

Shamiri, A, Hussain, MA, Mjalli, FS, & Mostoufi, N. 2012. Improved single phase modeling of propylene polymerization in a fluidized bed reactor. *Computers & Chemical Engineering*, **36**, 35–47.

Shamiri, A, Hussain, MA, Mjalli, FS, Mostoufi, N, & Hajimolana, S. 2013. Dynamics and Predictive Control of Gas Phase Propylene Polymerization in Fluidized Bed Reactors. *Chinese Journal of Chemical Engineering*, **21**, 1015–1029.

Shiga, A, Kawamura-Kuribayashi, H, & Sasaki, T. 1995. A theoretical study of Ziegler-Natta olefin polymerization on the TiCl3 crystalline surface. *Journal of Molecular Catalysis A: Chemical*, **98**, 15–24.

Singh, D, & Merrill, RP. 1971. Molecular weight distribution of polyethylene produced by Ziegler-Natta catalysts. *Macromolecules*, **4**(5), 599–604.

Soares, JBP. 2001. Mathematical modelling of the microstructure of polyolefins made by coordination polymerization: a review. *Chemical Engineering Science*, **56**, 4131–4153.

Soares, JBP, & Hamielec, AE. 1995a. Deconvolution of chain-length distributions of linear polymers made by multiple-site-type catalysts. *Polymer*, **36**(11), 2257–2263.

Soares, JBP, & Hamielec, AE. 1995b. Effect of reactor residence time distribution on the size distribution of polymer particles made with heterogeneous Ziegler-Natta and supported metallocene catalysts: A generic mathematical model. *Macromolecular Theory and Simulations*, **4**, 1085–1104.

Soares, JBP, & Hamielec, AE. 1996a. Effect of hydrogen and of catalyst prepolymerization with propylene on the polymerization kinetics of ethylene with a non-supported heterogeneous Ziegler-Natta catalyst. *Polymer*, **37**(20), 4599–4605.

Soares, JBP, & Hamielec, AE. 1996b. Kinetics of propylene polymerization with a non-supported heterogeneous Ziegler-Natta catalyst - effect of hydrogen on rate of polymerization, stereoregularity, and molecular weight distribution. *Polymer*, **37**(20), 4607–4614.

Soga, K, Chen, SI, & Ohnishi, R. 1982. Correlation between the oxidation states of titanium and the polymerization activities for higher alpha-olefins and diene compounds. *Polymer Bulletin*, **8**, 473–478.

Soni, NJ, & Bhagwat, SS. 2008. Simulation of slurry polymerization of ethylene. *International Journal of Chemical Reactor Engineering*, **6**, A107. Available at: http://www.bepress.com/ijcre/vol6/A107.

Stukalov, DV, & Zakharov, VA. 2009. Active Site Formation in MgCl2-Supported Ziegler-Natta Catalysts. A Density Functional Theory Study. *Journal of Physical Chemistry: C*, **113**, 21376–21382.

Takeda, M, & Ray, WH. 1999. Optimal-Grade Transition Strategies for Multistage Polyolefin Reactors. *AIChE Journal*, **45**(8), 1776–1793.

Taniike, T, Chammingkwan, P, & Terano, M. 2012. Structure–performance relationship in Ziegler–Natta olefin polymerization with novel core–shell MgO/MgCl2/TiCl4 catalysts. *Catalysis Communications*, **27**, 13–16.

Thompson, DE, McAuley, KB, & McLellan, PJ. 2010. Design of optimal sequential experiments to improve model predictions from a polyethylene molecular weight distribution model. *Macromolecular Reaction Engineering*, **4**, 73–85.

Touloupides, V, Kanellopoulos, V, Pladis, P, Kiparissides, C, Mignon, D, & Van-Grambezen, P. 2010. Modeling and simulation of an industrial slurry-phase catalytic olefin polymerization reactor series. *Chemical Engineering Science*, **65**, 3208–3222.

Vale, HM, & McKenna, TF. 2005. Modeling particle size distribution in emulsion polymerization reactors. *Progress in Polymer Science*, **30**, 1019–1048.

van Krevelen, DW. 1994. *Properties of Polymers*. 3rd edn. Elsevier Science BV, Amsterdam.

Wei, Y, Jiang, Y, & Huang, D. 2014. A Three-section Algorithm of Dynamic Programming Based on Three-stage Decomposition System Model for Grade Transition Trajectory Optimization Problems. *Chinese Journal of Chemical Engineering*, **22**, 1122–1130.

Weng, J, Shao, Z, Chen, X, Gu, X, Yao, Z, Feng, L, & Biegler, LT. 2014. A Novel Strategy for Dynamic Optimization of Grade Transition Processes Based on Molecular Weight Distribution. *AIChE Journal*, **60**, 2498–2512.

Weng, J, Chen, X, & Biegler, LT. 2015. A multi-thread parallel computation method for dynamic simulation of molecular weight distribution of multisite polymerization. *Computers & Chemical Engineering*, **82**, 55–67.

Wester, TS, & Ystenes, M. 1997. Kinetic studies of the injection of ccomonomer during polymerisation of ethene and propene with MgCl2-supported Ziegler-Natta catalysts. *Macromolecular Chemistry and Physics*, **198**, 1623–1648.

Wu, L, Lynch, DT, & Wanke, SE. 1999. Kinetics of gas-phase ethylene polymerization with morphology-controlled MgCl2-supported TiCl4 catalyst. *Macromolecules*, **32**, 7990–7998.

Xu, S, & Liu, X. 2014. Melt index prediction by fuzzy functions with dynamic fuzzy neural networks. *Neurocomputing*, **142**, 291–298.

Xu, T, Yang, H, Fu, Z, & Fan, Z. 2015. Effects of comonomer on active center distrbution of TiCl4/MgCl2-AlEt3 catalyst in ethylene/1-hexene copolymerization. *Journal of Organometallic Chemistry*, **In press**, 1–7.

Yan, WC, Li, J, & Luo, ZH. 2012. A CFD-PBM coupled model with Polymerization kinetics for multizone circulating polymerization reactors. *Powder Technology*, **231**, 77–87.

Yang, H, Zhang, L, Zang, D, Fu, Z, & Fan, Z. 2015. Effects of alkylaluminum as cocatalyst on the active center distribution of 1-hexene polymerization with MgCl2-supported Ziegler–Natta catalysts. *Catalysis Communications*, **62**, 104–106.

Yao, KZ, Shaw, BM, Kou, B, McAuley, KB, & Bacon, DW. 2003. Modeling Ethylene/Butene Copolymerization with Multi-site Catalysts: Parameter Estimability and Experimental Design. *Polymer Reaction Engineering*, **11**, 563–588.

Yermakov, YI, Mikhalchenko, VG, Beskov, VS, Grabovskii, YP, & Emirova, IV. 1970. *Plasticheskije Massy*, **9**, 7.

Yiagopoulous, A, Yiannoulakis, H, Dimos, V, & Kiparissides, C. 2001. Heat and mass transfer phenomena during the early growth of a catalyst particle in gas-phase olefin polymerization: the effect of prepolymerization temperature and time. *Chemical Engineering Science*, **56**, 3979–3995.

Yiannoulakis, H, Yiagopoulous, A, Pladis, P, & Kiparissides, C. 2000. Comprehensive dynamic model for the calculation of the molecular weight and long chain branching distributions in metallocene-catalyzed ethylene polymerization reactors. *Macromolecules*, **33**, 2757–2766.

Yiannoulakis, H, Yiagopoulous, A, & C;, Kiparissides. 2001. Recent developments in the particle size distribution modeling of fluidized-bed olefin polymerization reactor. *Chemical Engineering Science*, **56**, 917–925.

Zacca, JJ, & Debling, JA. 2001. Particle population overheating phenomena in olefin polymerization reactors. *Chemical Engineering Science*, **56**, 4029–4042.

Zacca, JJ, Debling, JA, & Ray, WH. 1996. Reactor residence time distribution effects on the multistage polymerization of olefins I Basic principles and illustrative examples, polypropylene. *Chemical Engineering Science*, **51**, 4859–4886.

Zacca, JJ, Debling, JA, & Ray, WH. 1997. Reactor residence time distribution effects on the multistage polymerization of olefins II Polymer properties: bimodal polypropylene and linear low-density polyethylene. *Chemical Engineering Science*, **52**, 1941–1967.

Zakharov, VA, Matsko, MA, Echevskaya, LG, & Mikenas, TB. 2007. Ethylene polymerization over supported titanium-magnesium catalysts: Heterogeneity of active centers and effect of catalyst composition on the molecular mass distribution of polymer. *Macromolecular Symposia*, **260**, 184–188.

Zhu, YP, Luo, ZH, & Xiao, J. 2014. Multi-scale product property model of polypropylene produced in a FBR: From chemical process engineering to product engineering. *Computers & Chemical Engineering*, **71**, 39–51.

PART G. APPENDIX

CHAPTER 19. NOMENCLATURE

The symbols used in this thesis are summarised in the tables below.

B	Birth function in the Population Balance Equation
$\underline{\underline{C}}$	Matrix of reactant concentrations for each experiment
C_d	Concentration of deactivated catalyst sites
C_p	Concentration of potential catalyst sites
D	Death function in the Population Balance Equation
D_l	Macroparticle diffusivity (Multigrain Model)
$D_{n,i}^{q}$	Concentration of chains of length n with monomer i most recently added, at site q
D_s	Microparticle diffusivity (Multigrain Model)
$E(t)$	External residence time distribution function
$E(\Theta)$	Normalised external residence time distribution function
f_{cat}	Catalyst poison factor
$f_{co\text{-}cat}$	Co-catalyst poison factor
f_f	Flow fraction, defining recycle ratio
f_m	Pseudo-site fraction for pseudo-site *m*
f_{M_i}	Fraction of a polymer which was monomer i
$f_m(l)$	Mass-based PSD
$f_n(l)$	Number-based PSD
f_v	Volume fraction, defining PFR to CSTR volumes
G	Particle growth function
H	Holdup
h_{in}	Inlet flow rate
h_{out}	Outlet flow rate
$I(\theta)$	Internal residence time distribution function
$I(t,\theta)$	Unsteady-state internal residence time distribution function
$k_{0,i}^{q}$	Rate constant for chain initiation by monomer i at empty site of type q
$k_{a,X}^{q}$	Rate constant for catalyst site activation of site q by reactant X

$k_{d,X}^{q}$	Rate constant for catalyst site deactivation of site q by reactant X
$k_{p,ij}^{q}$	Rate constant for chain propagation of monomer j onto a chain with monomer i most recently added, at site q
$k_{st,X}^{q,r}$	Rate constant for site transformation of site q to site r by agent X
$k_{t,X}^{q}$	Rate constant for chain termination at site q by agent X
l	Particle diameter
l_0	Initial particle diameter
$m_{cat,e}$	Catalyst holdup for experiment *e*
$MM_{ethylene}$	Molar mass of ethylene
m_p	Particle mass
m_{pol}	Mass of polymer in reactor
$m_{polymer,e}$	Mass of polymer recovered in experiment *e*
$[M]_b$	Bulk fluid concentration of monomer (Multigrain Model)
$[M]_l$	Macroparticle concentration of monomer (Multigrain Model)
$[M]_s$	Microparticle concentration of monomer (Multigrain Model)
P_0^q	Concentration of vacant catalyst sites of type q
P_*^q	Concentration of potential sites of type q
$P_{n,i}^{q}$	Concentration of chains of length n at site q, with monomer i most recently added
t	Time
r_l	Macroparticle radial position (Multigrain Model)
R_l	Macroparticle radius (Multigrain Model)
r_{M_1}	Consumption of monomer 1 due to polymerisation
r_p	Polymerisation rate
r_s	Microparticle radial position (Multigrain Model)
R_s	Microparticle radius (Multigrain Model)
V_C	Volume of CSTR
V_P	Volume of PFR
X_M	Conversion of reactant *M*

Greek symbols

α_i	Property i, in the Population Balance Equation
α_X	Stoichiometric coefficient for site transformation agent X
$\beta_{st}^{q,r}$	Lumped site transformation parameter for transformation from site q to site r
β_t	Lumped termination rate parameter
γ^m	Chain Length Characteristic Parameter for pseudo-site *m*
ε	Particle voidage fraction
η_{crys}	Adsorption onto microparticle (Multigrain Model)
θ	Age, in reactor residence time distribution
Θ	Normalised age, in reactor residence time distribution
λ_k	k-th moment of a distribution
λ_k^m	k-th live polymer moment at pseudo-site *m*
μ_k	k-th bulk polymer moment
ν_F	Volumetric flow
ξ_i	Fraction of chains ending in monomer i
ρ	Polymer density (Multigrain Model)
ρ_{cat}	Catalyst density (Multigrain Model)
τ	Mean residence time
$\tau_{rxn,e}$	Reaction time for experiment *e*
Ψ	Population balance distribution function

Subscripts

A	Aluminium co-catalyst (triethyl aluminium in this work)
e	Experiment number
et	Experimental time
H_2	Hydrogen (chain transfer agent)
ind	Industrial grade number
M_i	Monomer i (ethylene or 1-butene in this work)
n	Chain length
sp	Spontaneous reaction
st	Site transformation reaction
t	Termination reaction

CHAPTER 20. EXPERIMENTAL DATA

20.1 Activity profiles

The polymerisation activity profiles from the laboratory experiments are shown in the figures below.

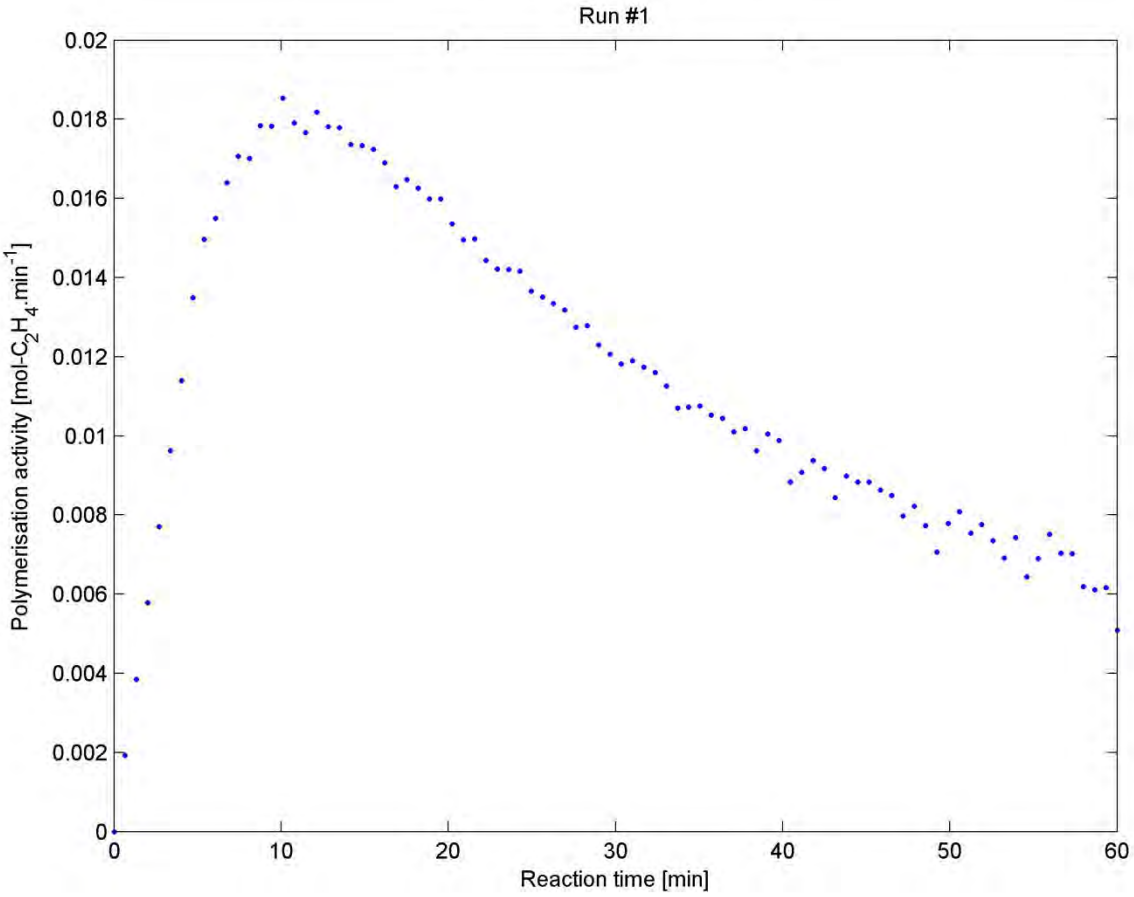

Figure 20.1: Polymerisation activity profile for Experimental Run #1

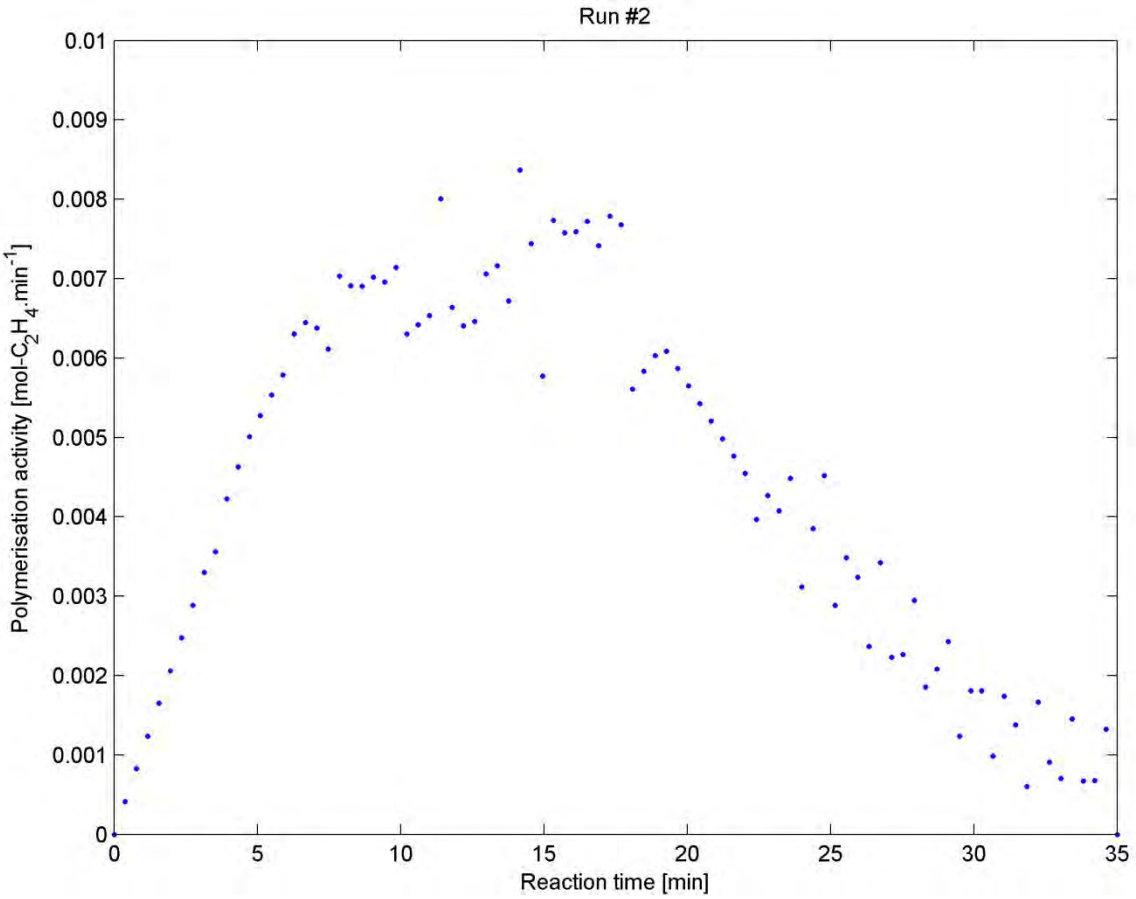

Figure 20.2: Polymerisation activity profile for Experimental Run #2

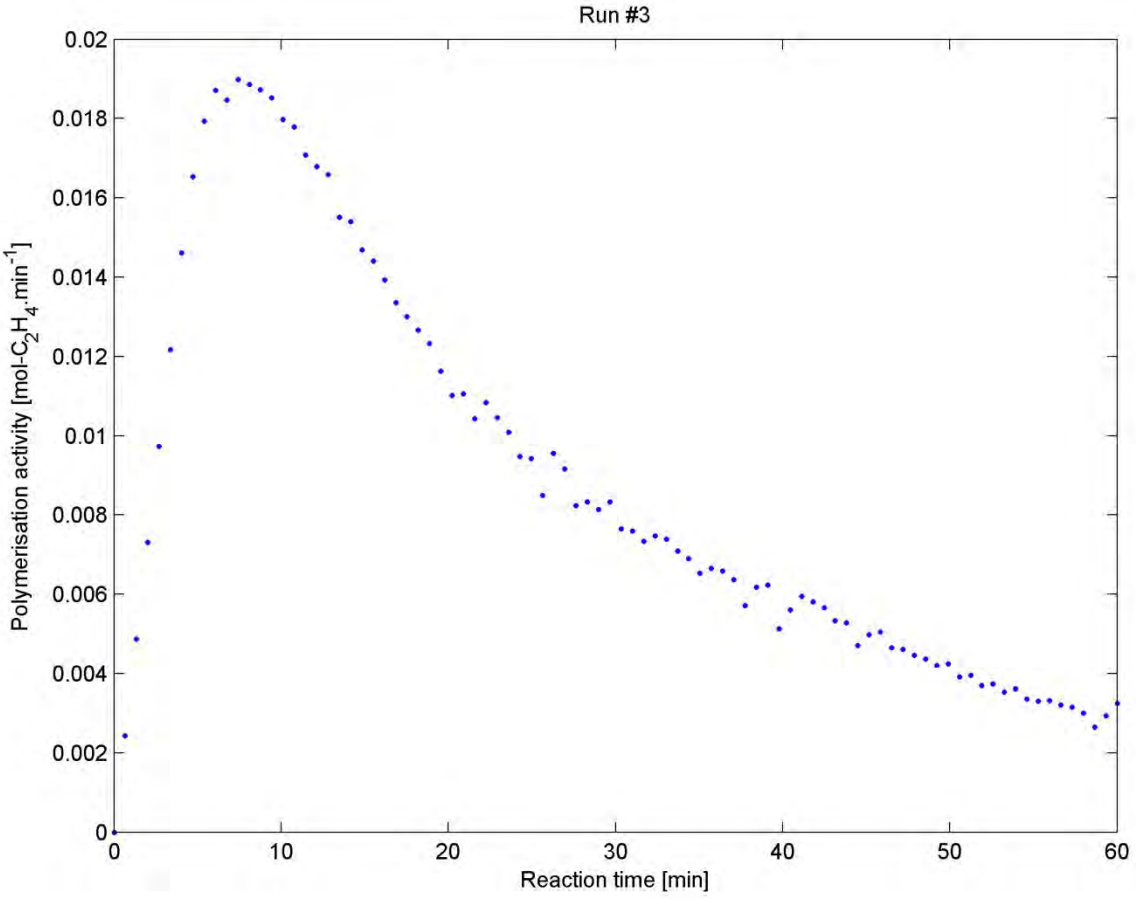

Figure 20.3: Polymerisation activity profile for Experimental Run #3

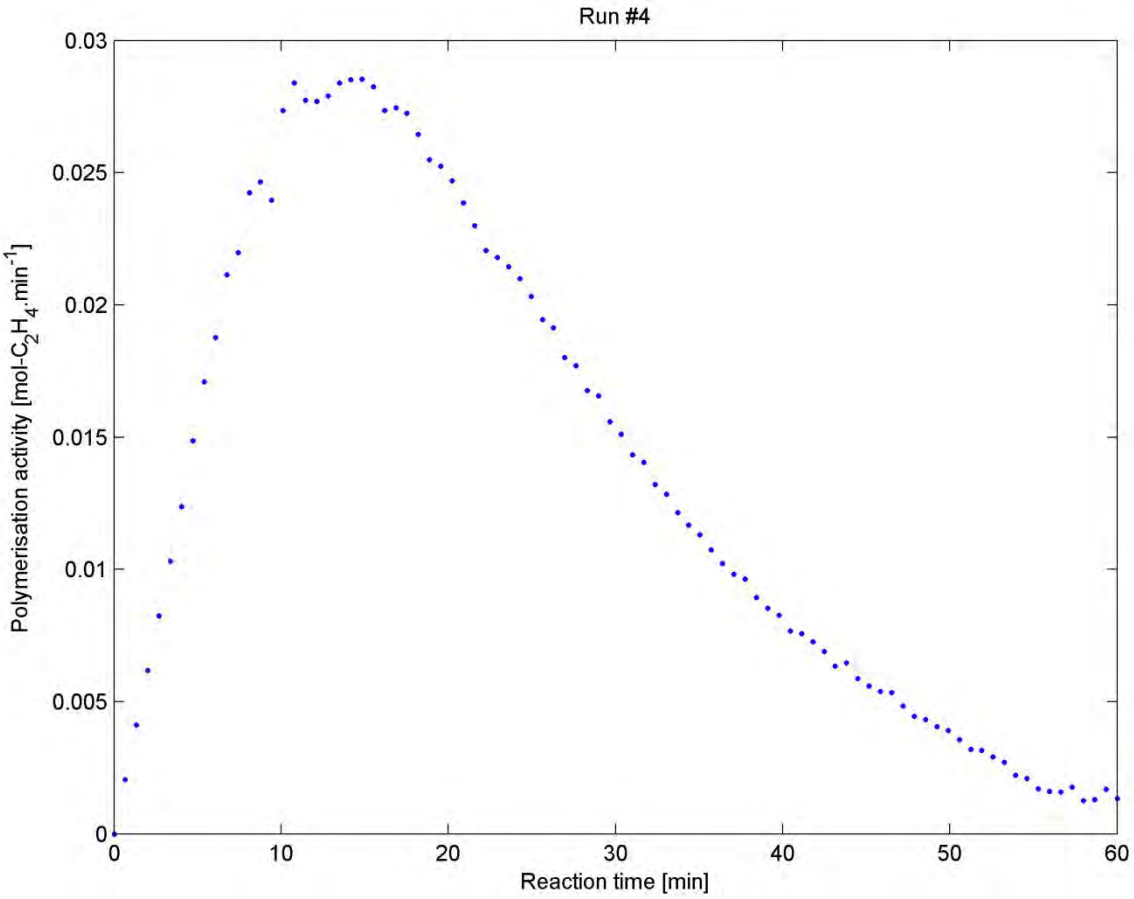

Figure 20.4: Polymerisation activity profile for Experimental Run #4

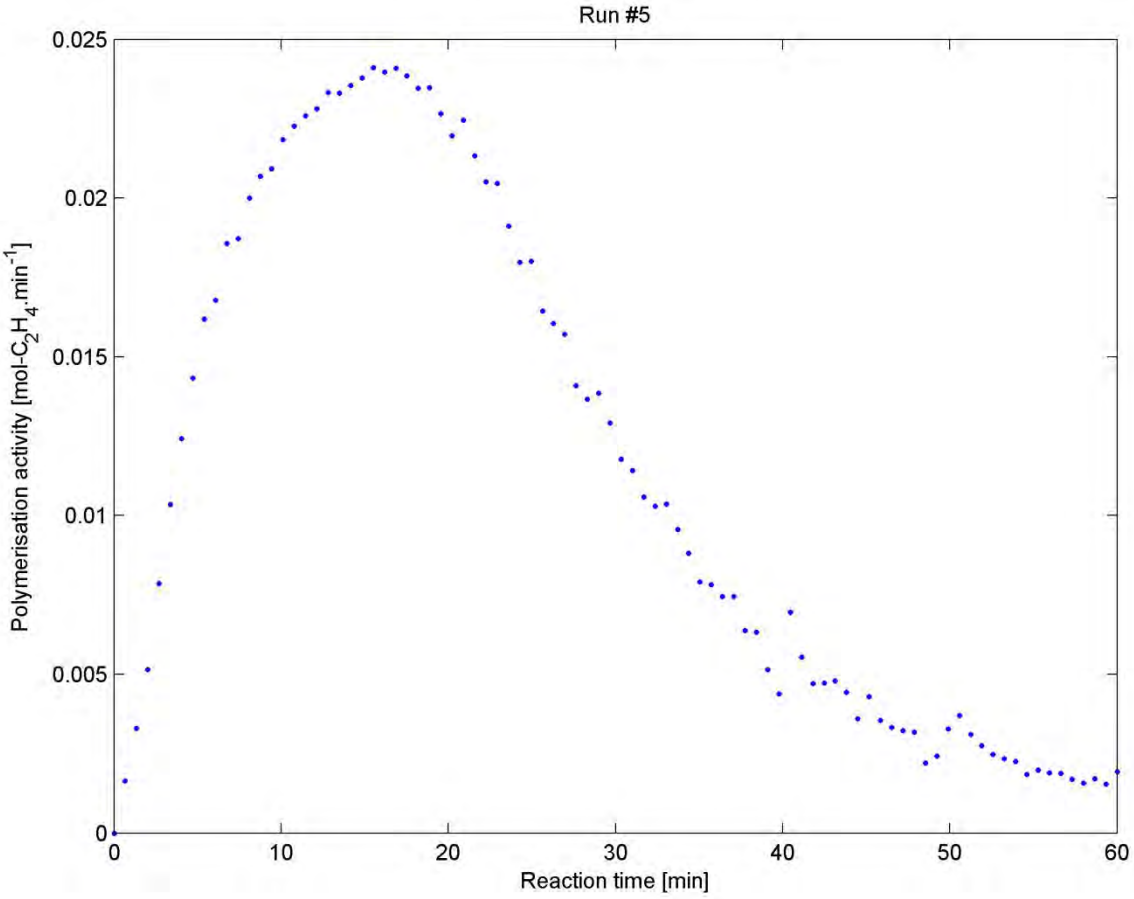

Figure 20.5: Polymerisation activity profile for Experimental Run #5

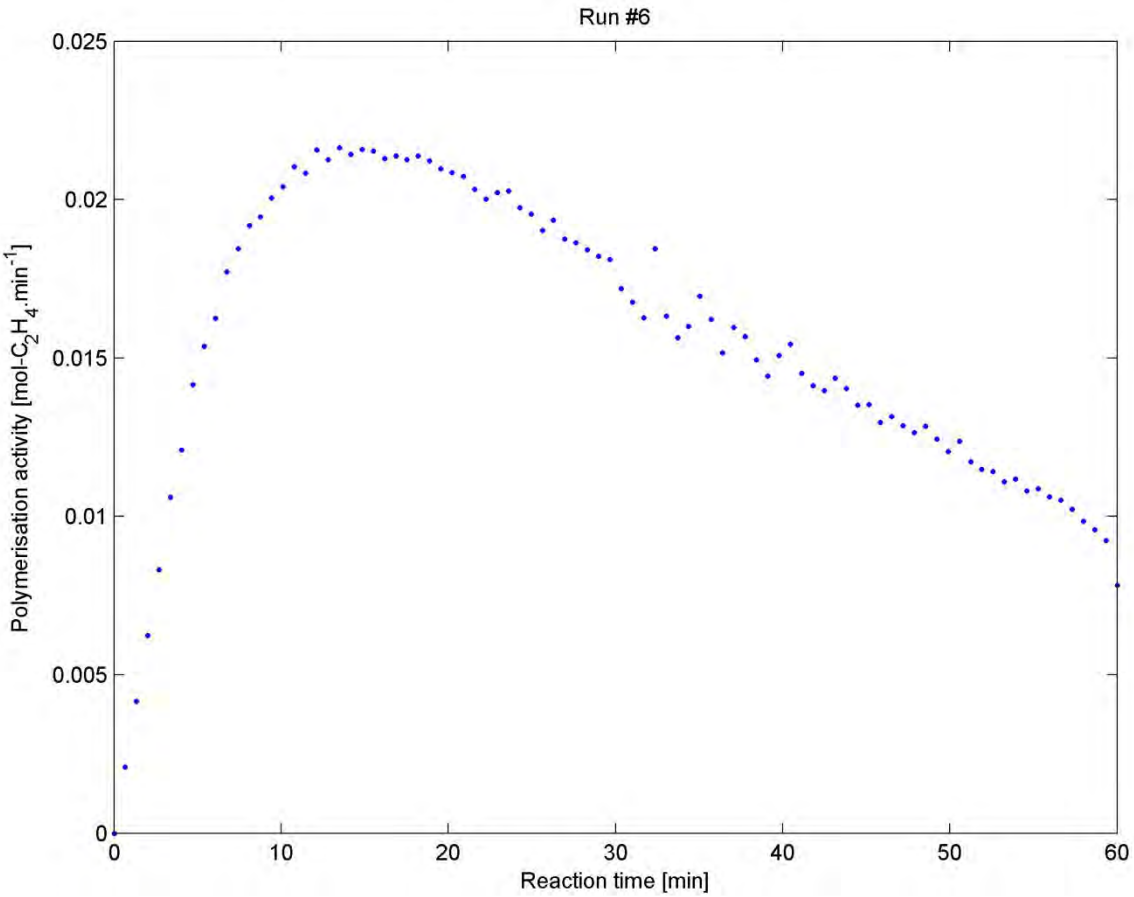

Figure 20.6: Polymerisation activity profile for Experimental Run #6

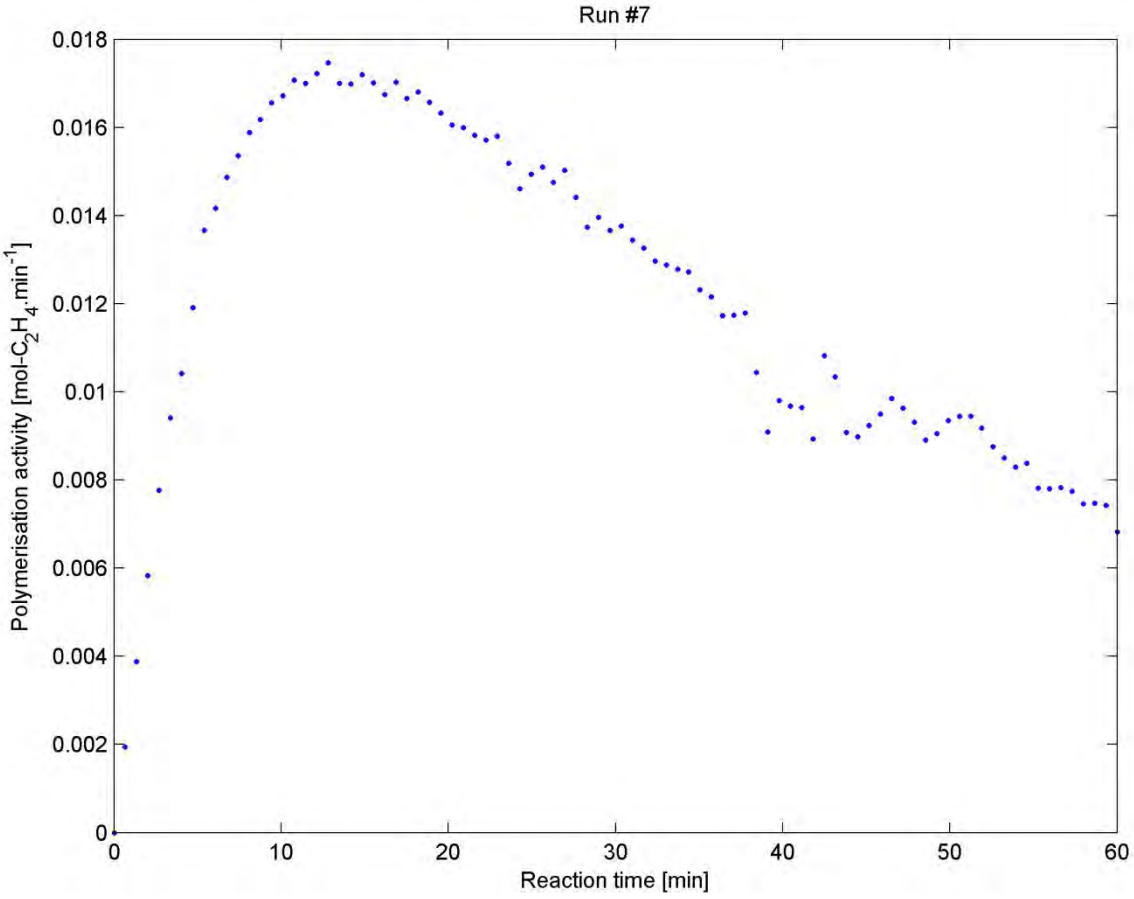

Figure 20.7: Polymerisation activity profile for Experimental Run #7

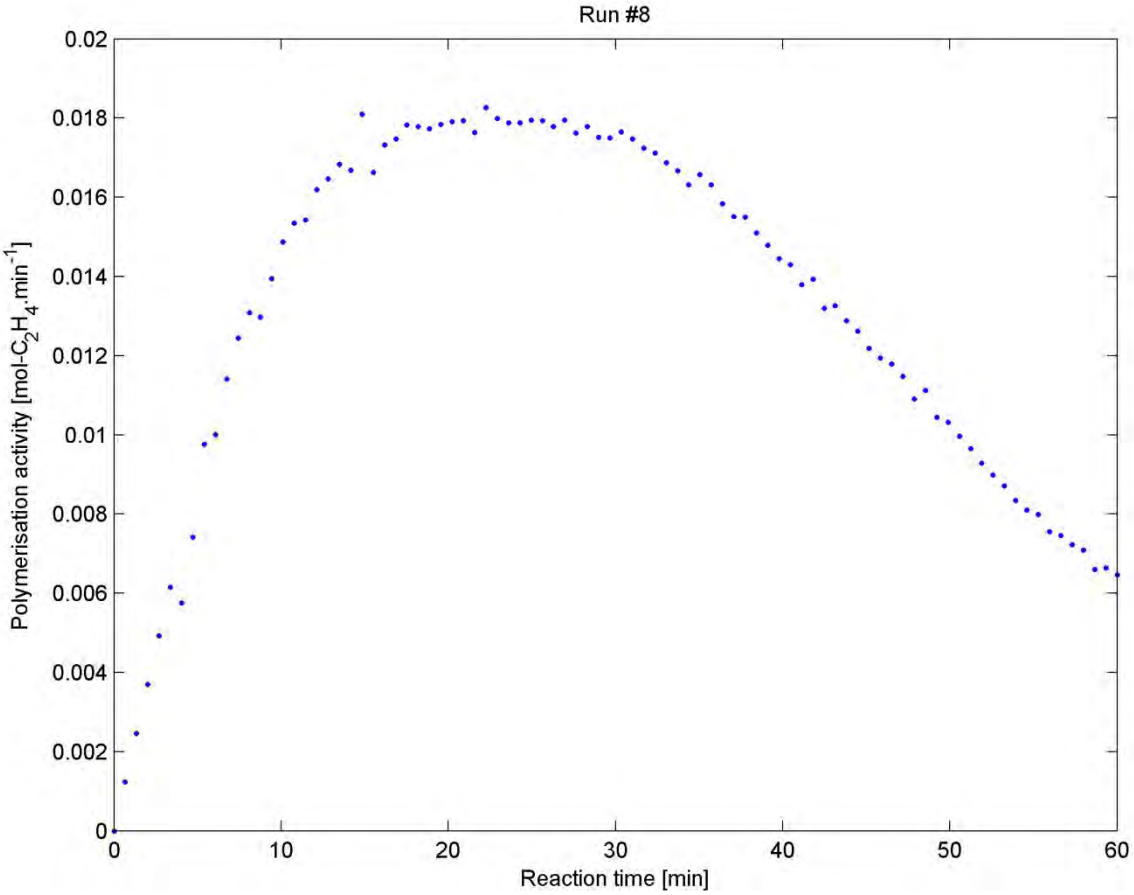

Figure 20.8: Polymerisation activity profile for Experimental Run #8

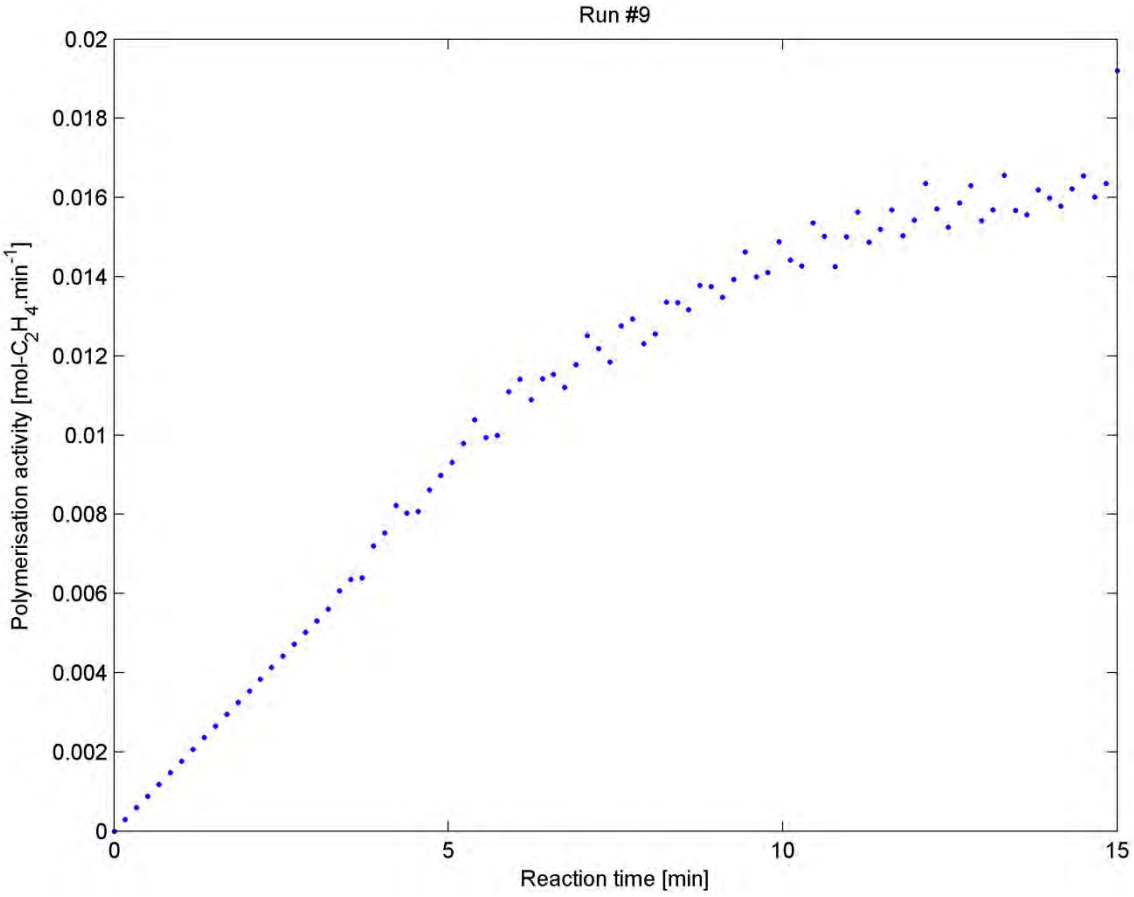

Figure 20.9: Polymerisation activity profile for Experimental Run #9

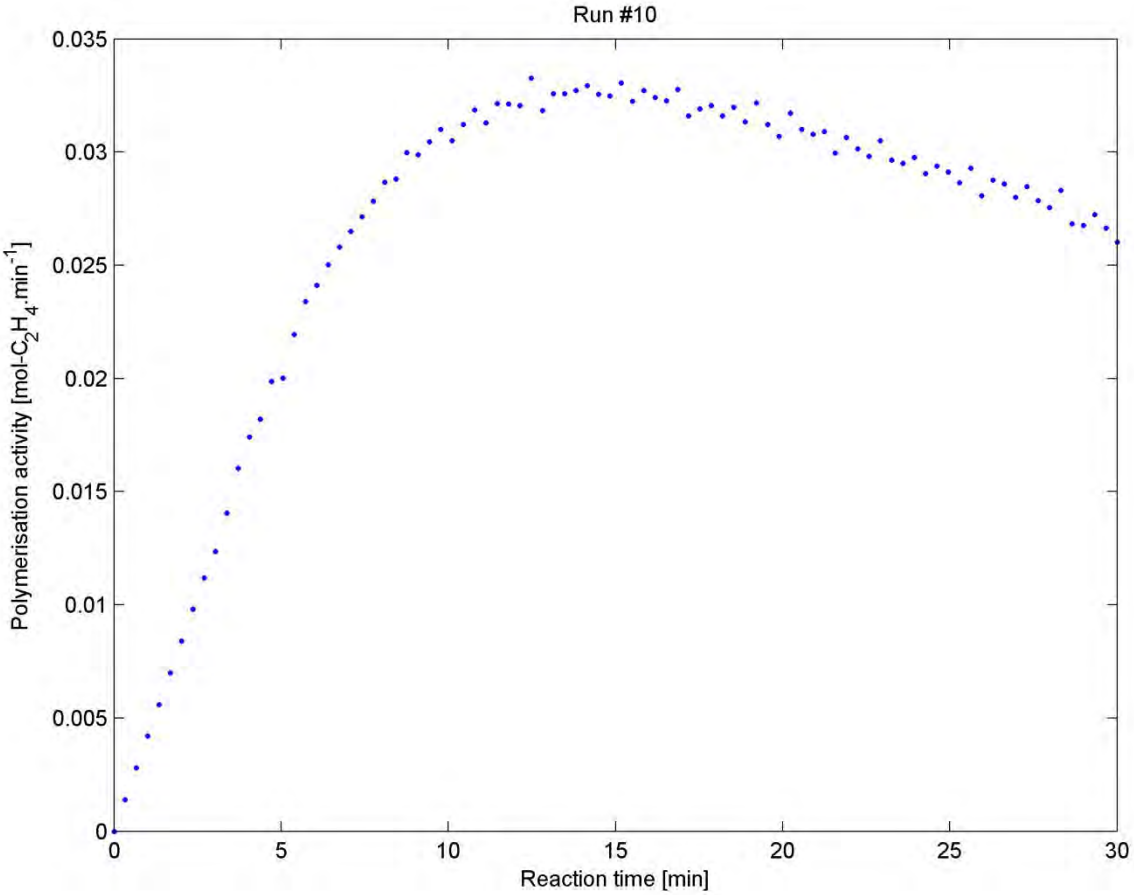

Figure 20.10: Polymerisation activity profile for Experimental Run #10

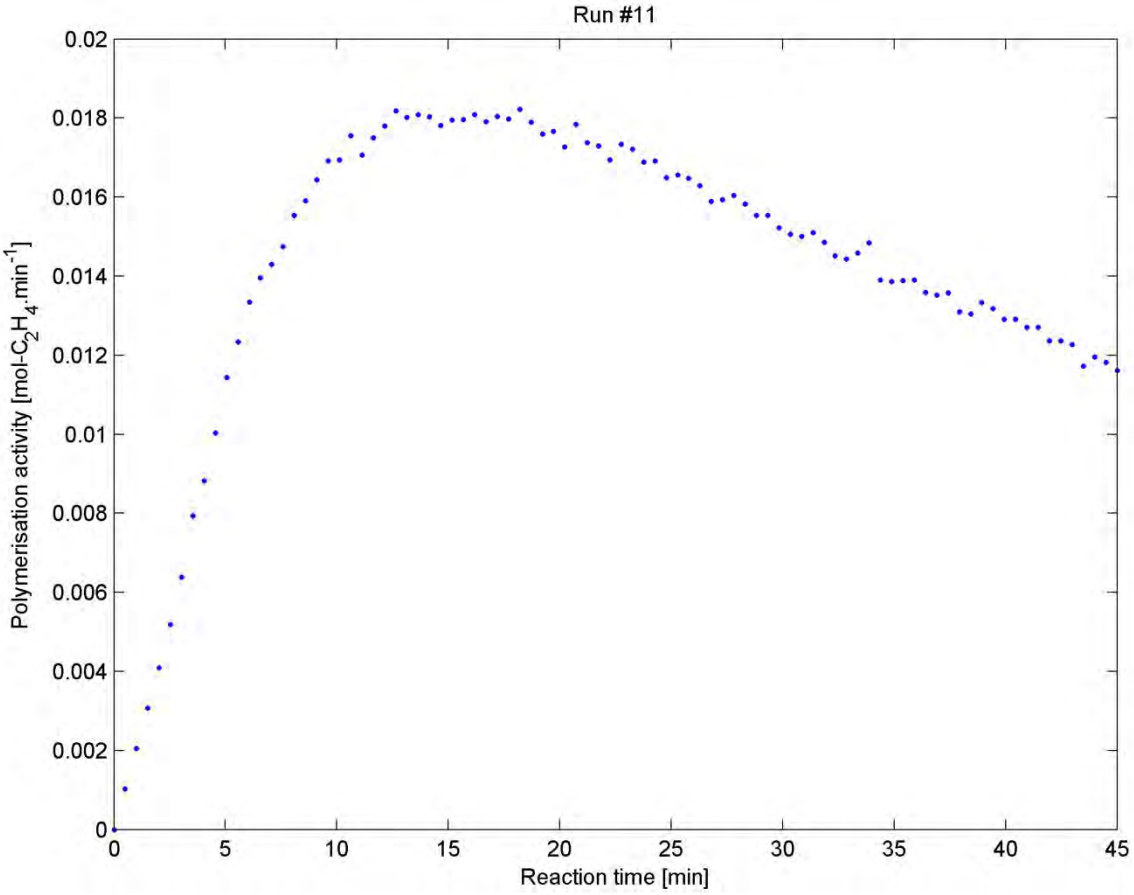

Figure 20.11: Polymerisation activity profile for Experimental Run #11

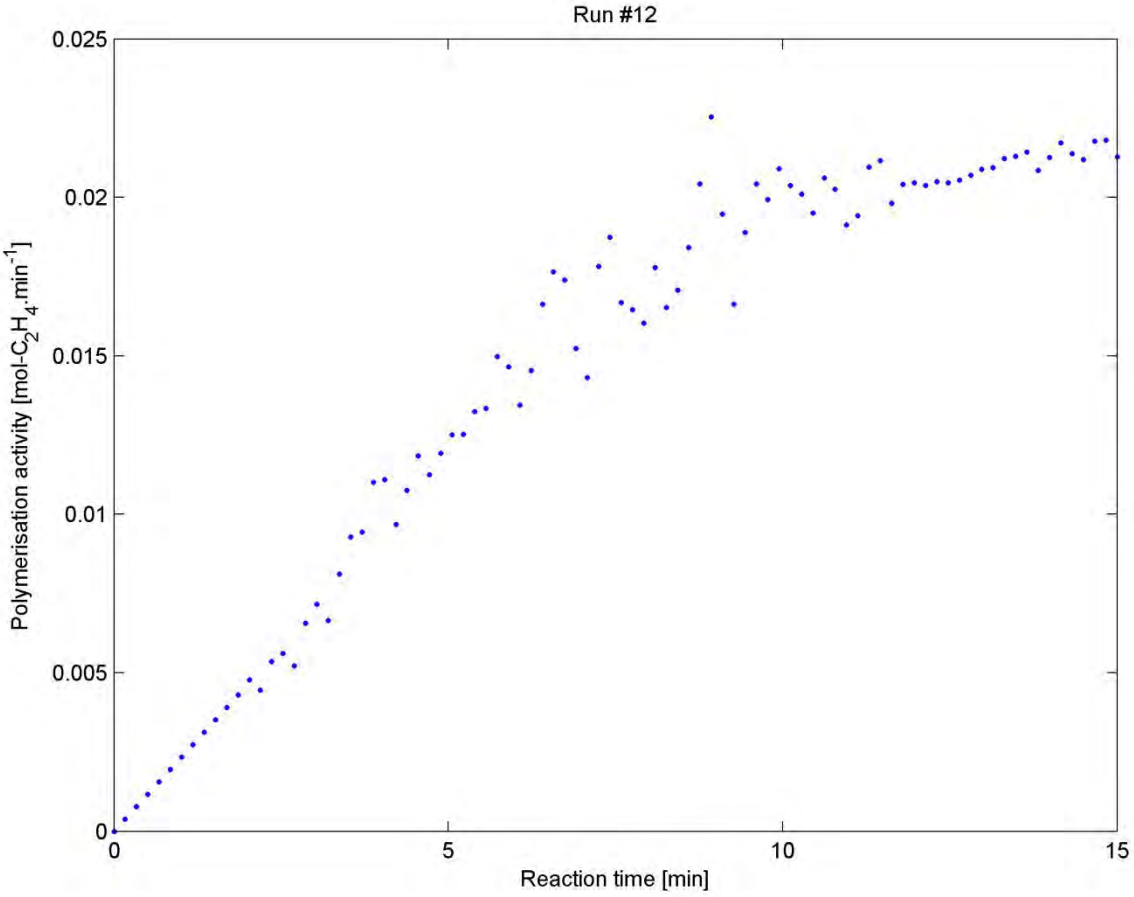

Figure 20.12: Polymerisation activity profile for Experimental Run #12

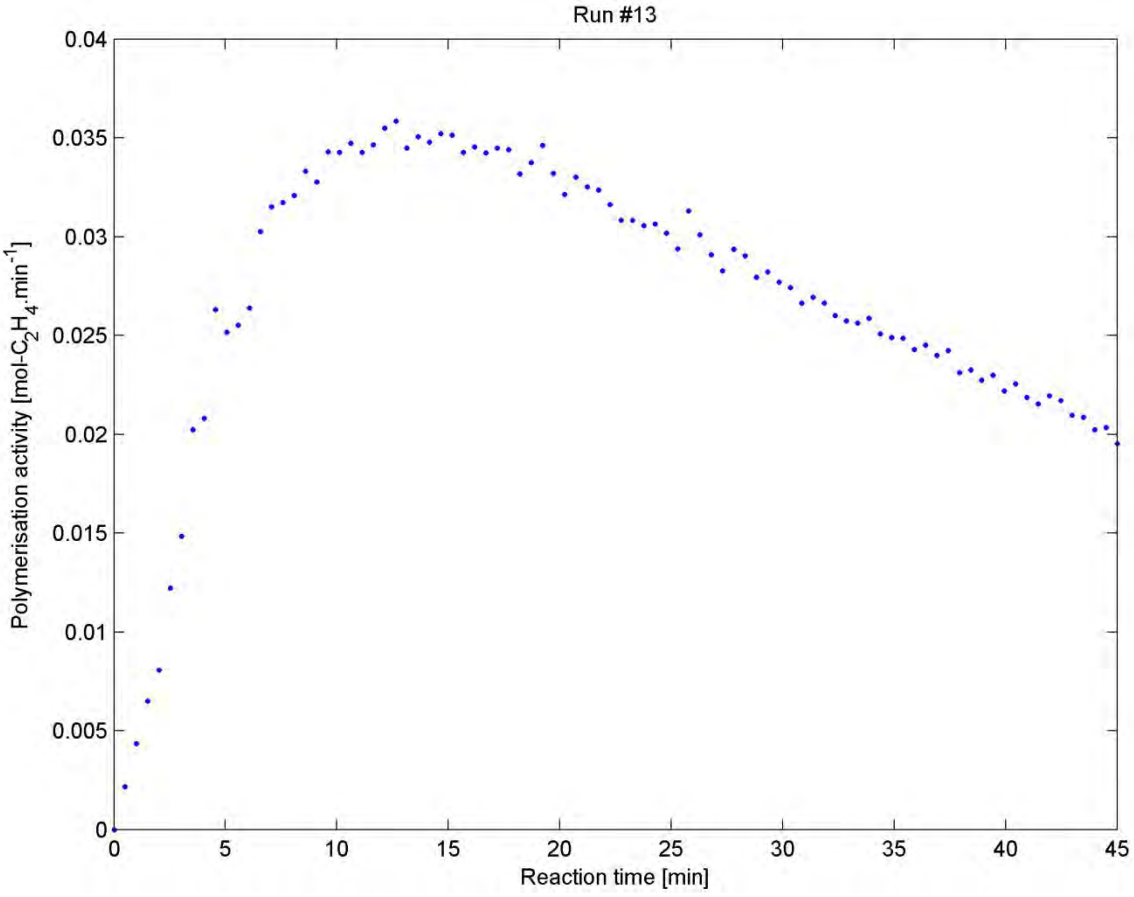

Figure 20.13: Polymerisation activity profile for Experimental Run #13

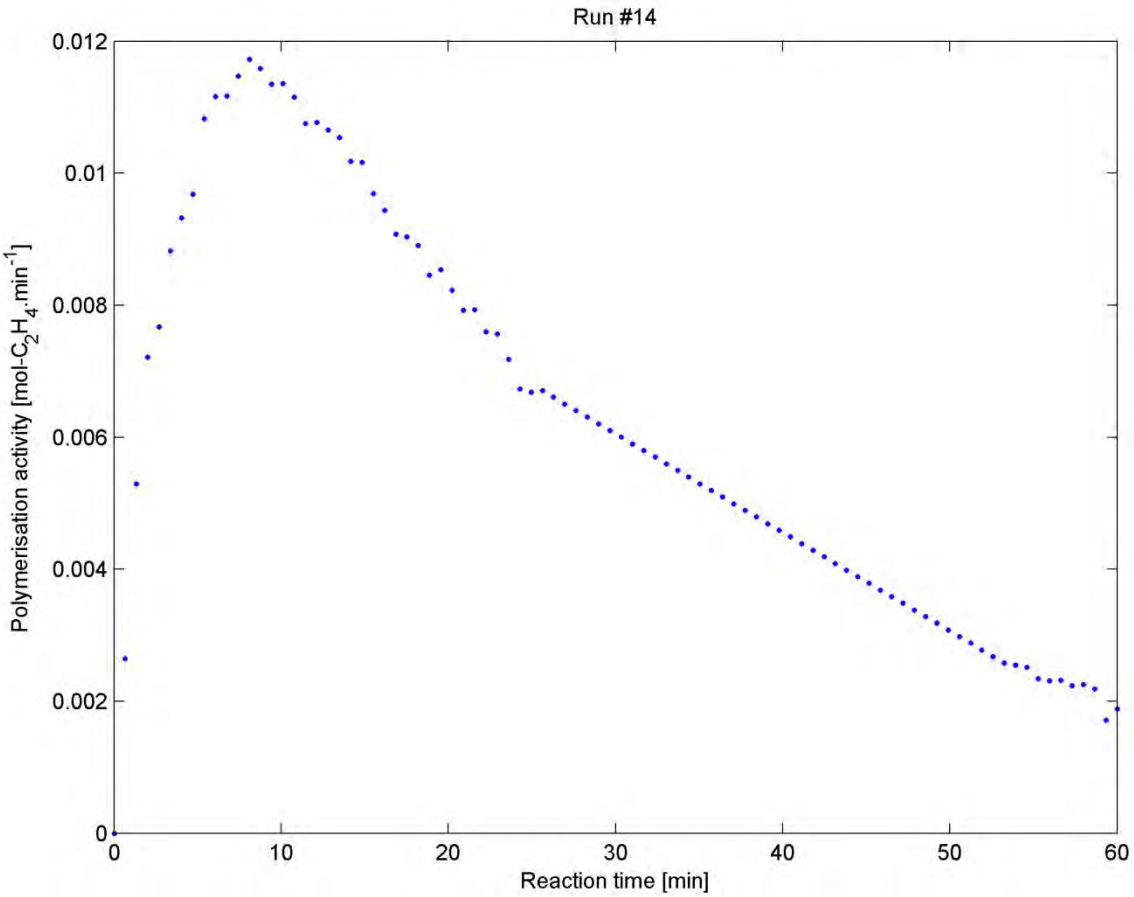

Figure 20.14: Polymerisation activity profile for Experimental Run #14

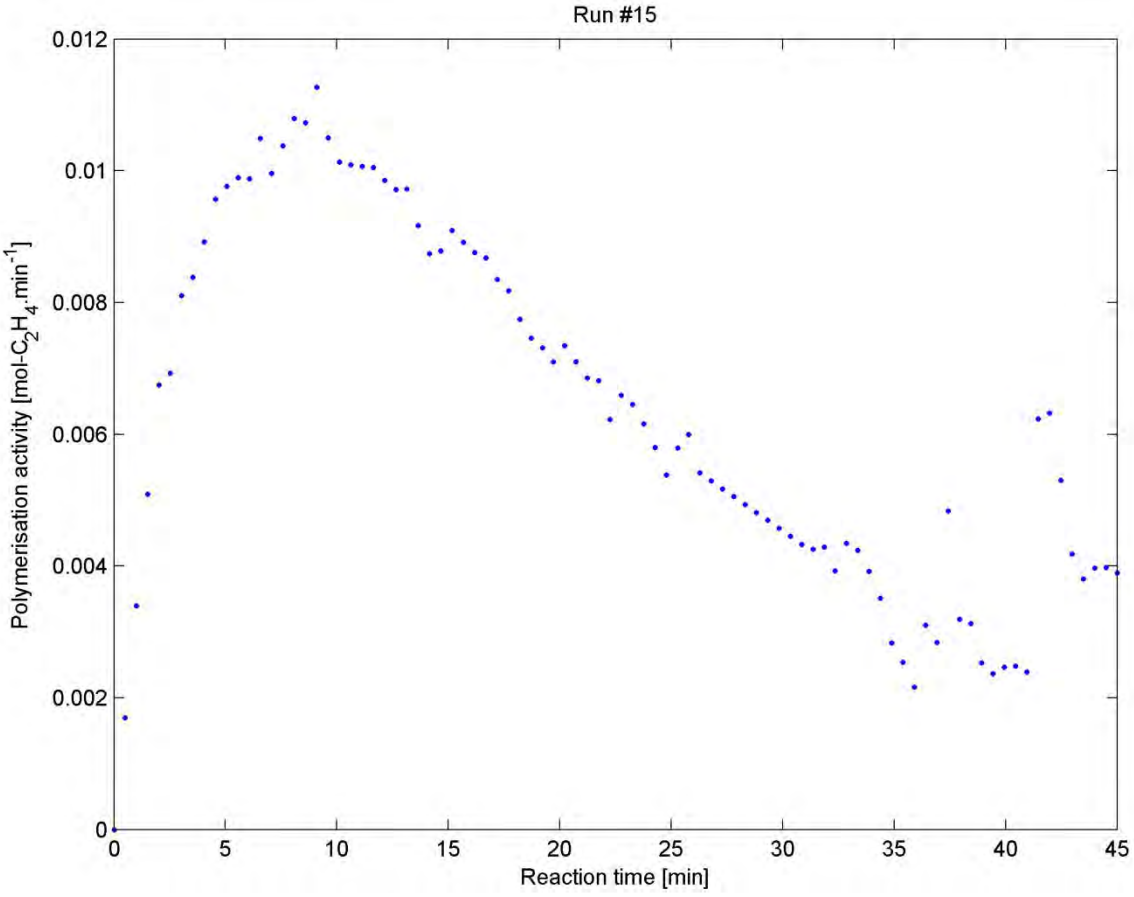

Figure 20.15: Polymerisation activity profile for Experimental Run #15

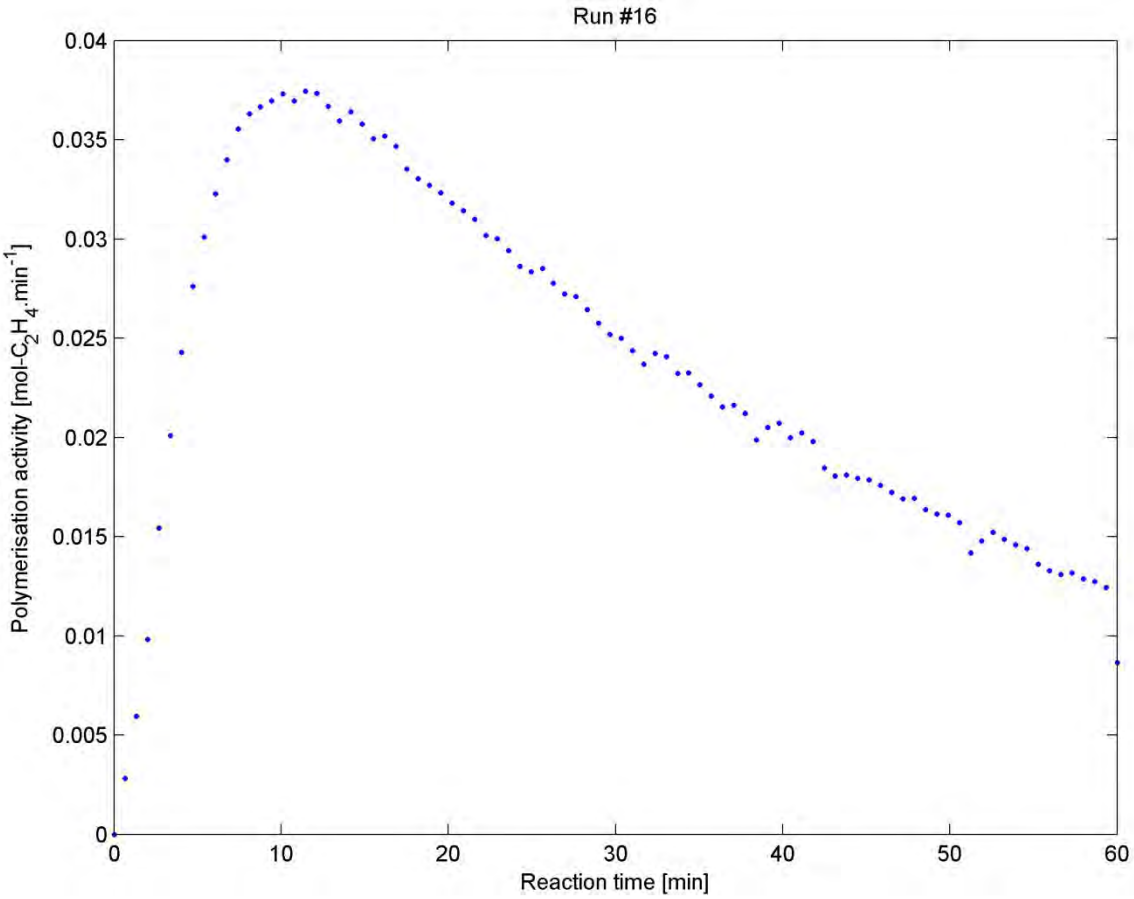

Figure 20.16: Polymerisation activity profile for Experimental Run #16

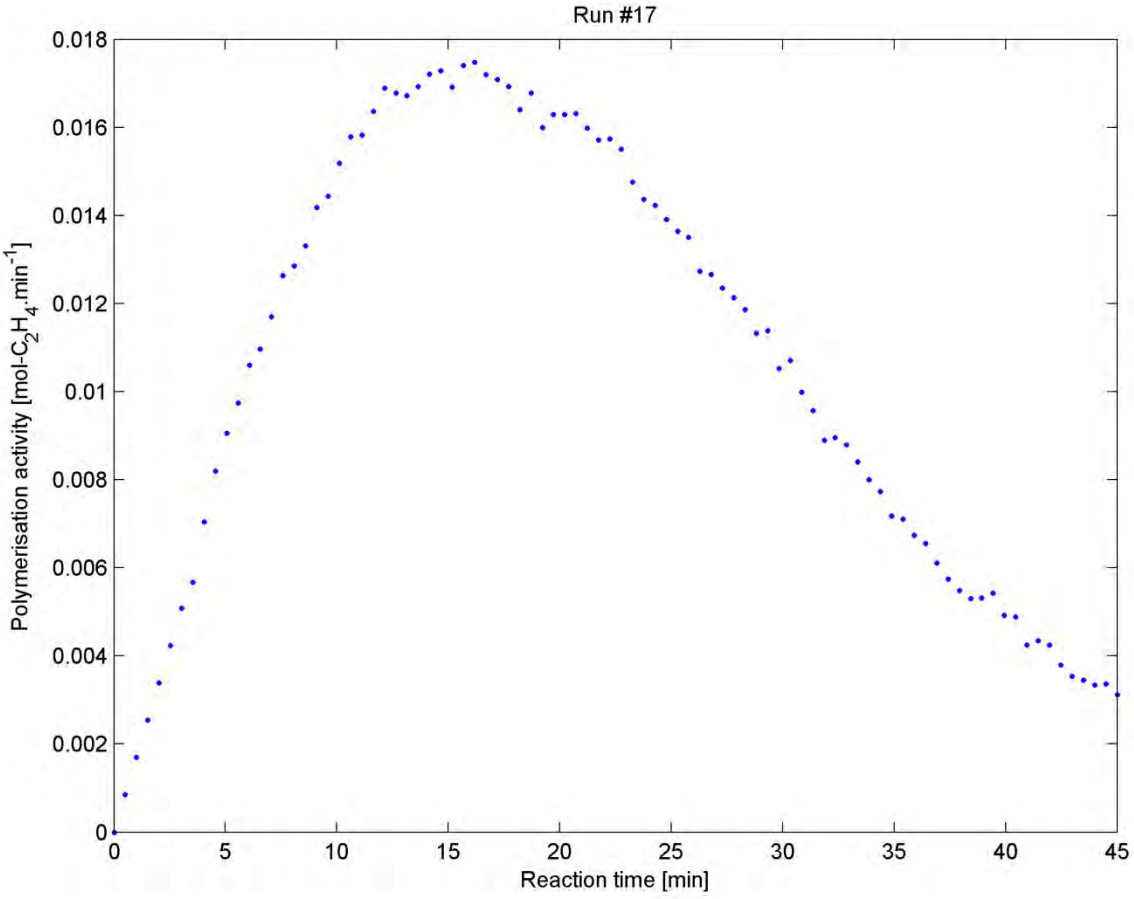

Figure 20.17: Polymerisation activity profile for Experimental Run #17

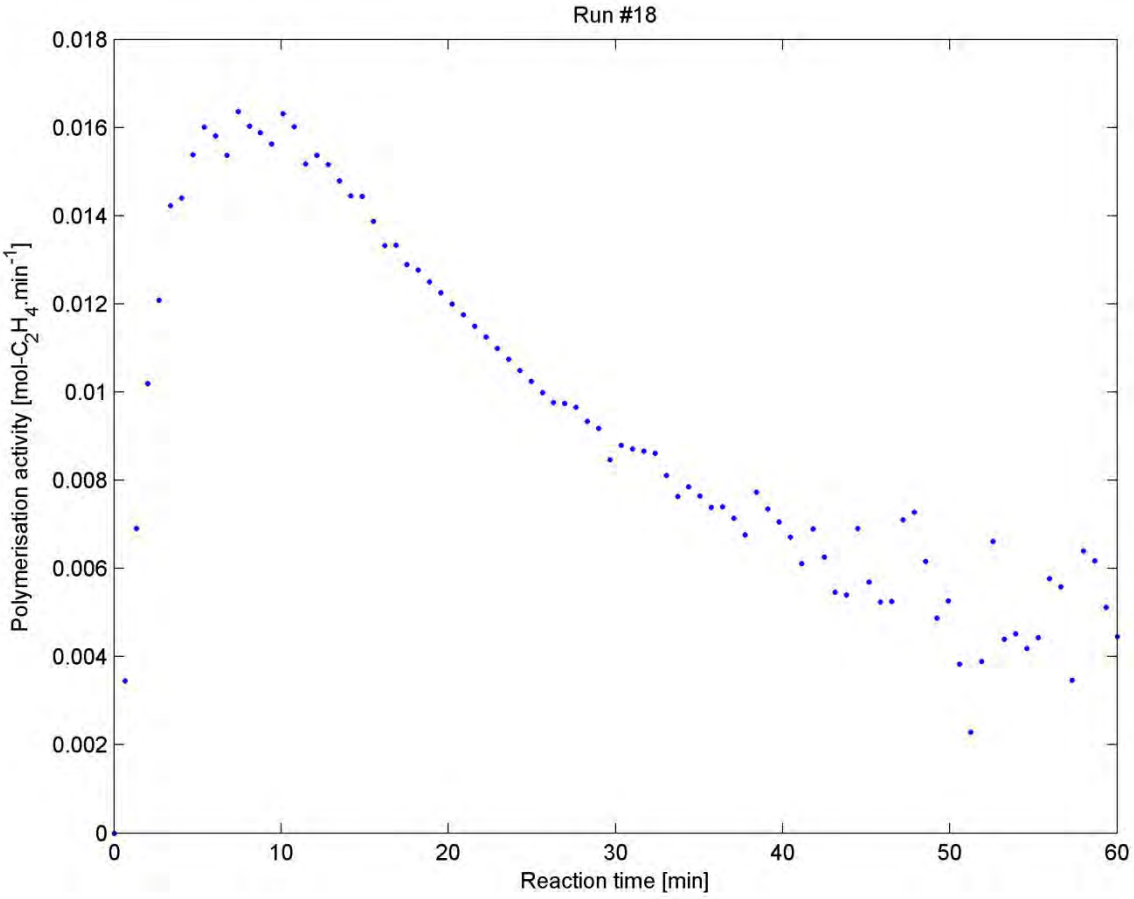

Figure 20.18: Polymerisation activity profile for Experimental Run #18

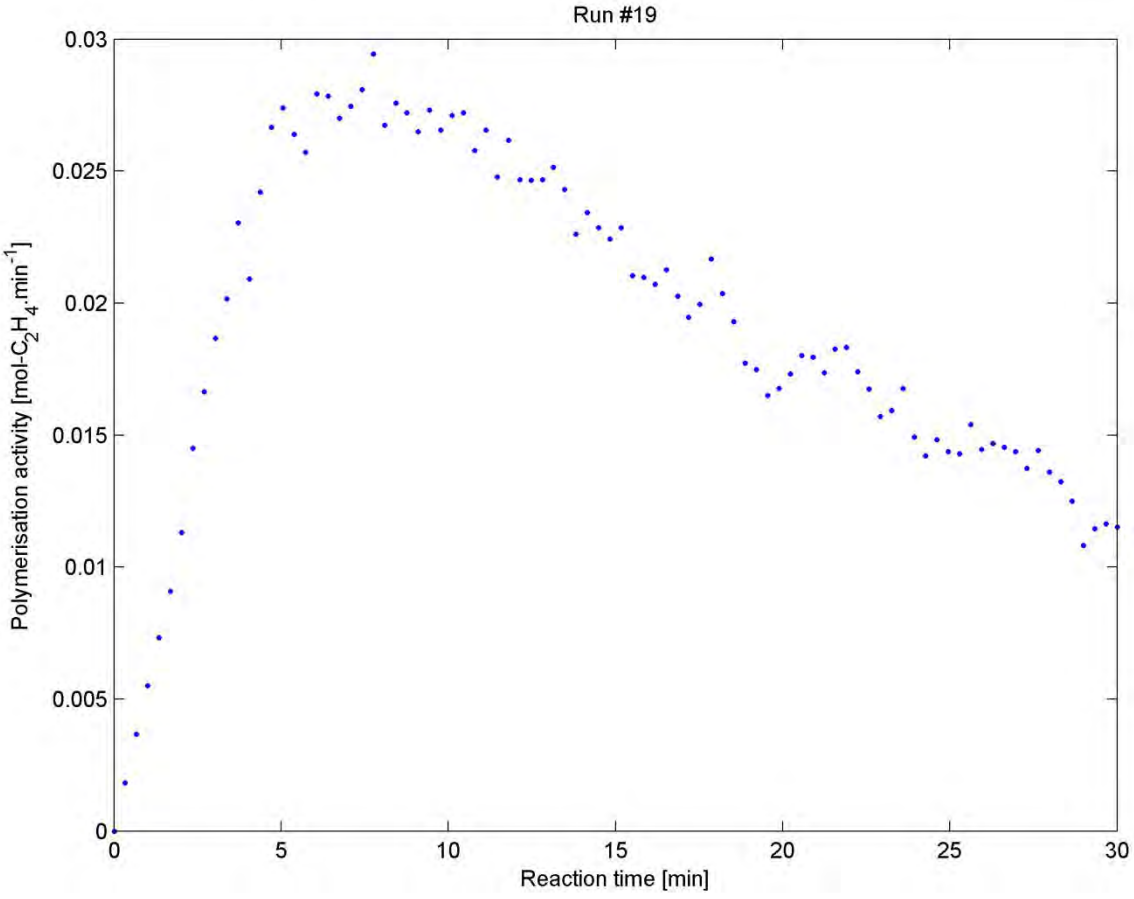

Figure 20.19: Polymerisation activity profile for Experimental Run #19

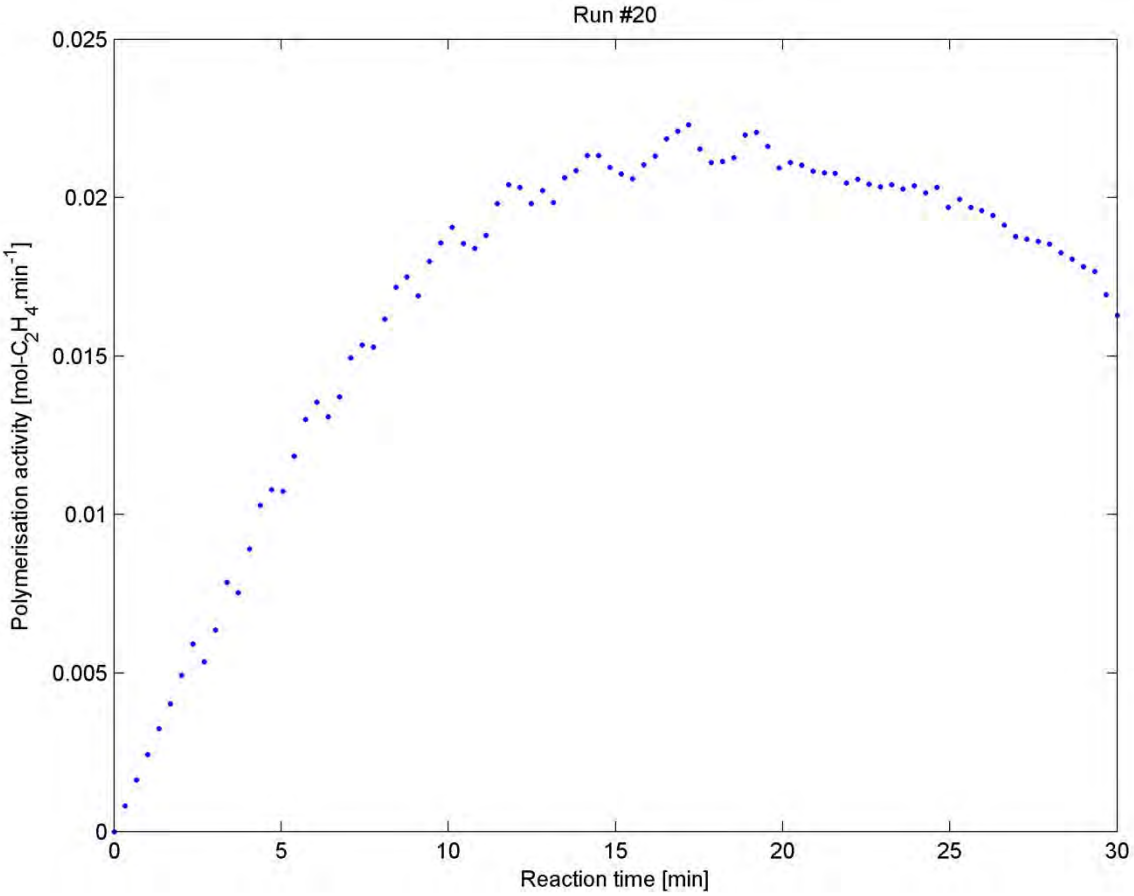

Figure 20.20: Polymerisation activity profile for Experimental Run #20

20.2 NMR Spectra

The Nuclear Magnetic Resonance spectra for Experimental Runs 6, 7, 10, 12-15, 17 and 19 are shown in the figures below.

This data was used to determine the comonomer content of the ethylene/1-butene co-polymer produced in the experimental reactor, using the methods of de Pooter et al (1991).

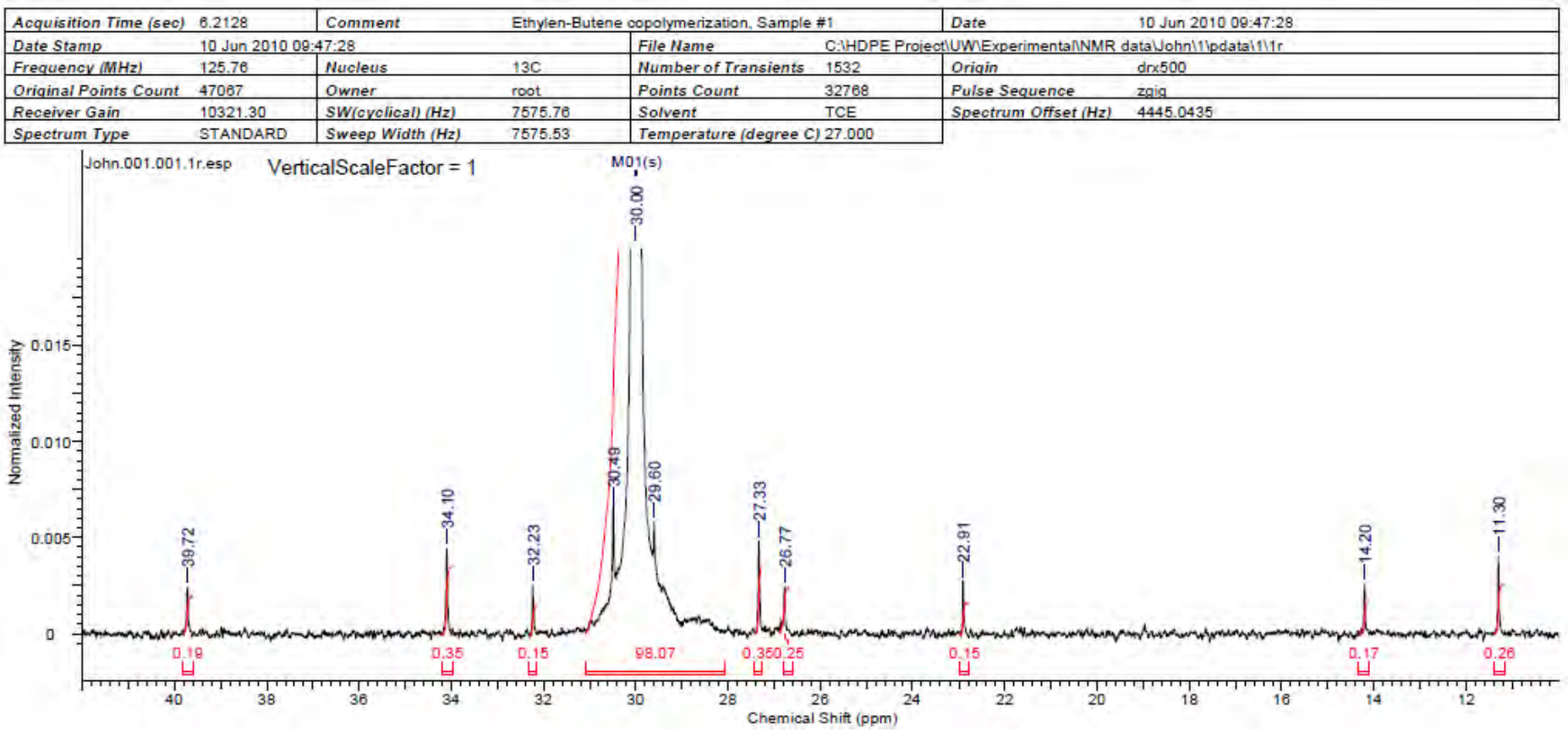

Figure 20.21: NMR spectrum for Experimental Run #6

Acquisition Time (sec)	6.2128	*Comment*	Ethylene-Butene Copolymerization, sample#2			*Date*	10 Jun 2010 17:00:32
Date Stamp	10 Jun 2010 17:00:32			*File Name*	C:\HDPE Project\UW\Experimental\NMR data\John\2\pdata\1\1r		
Frequency (MHz)	125.76	*Nucleus*	13C	*Number of Transients*	1662	*Origin*	drx500
Original Points Count	47067	*Owner*	root	*Points Count*	32768	*Pulse Sequence*	zgig
Receiver Gain	9195.20	*SW(cyclical) (Hz)*	7575.76	*Solvent*	TCE	*Spectrum Offset (Hz)*	4444.8120
Spectrum Type	STANDARD	*Sweep Width (Hz)*	7575.53	*Temperature (degree C)*	27.000		

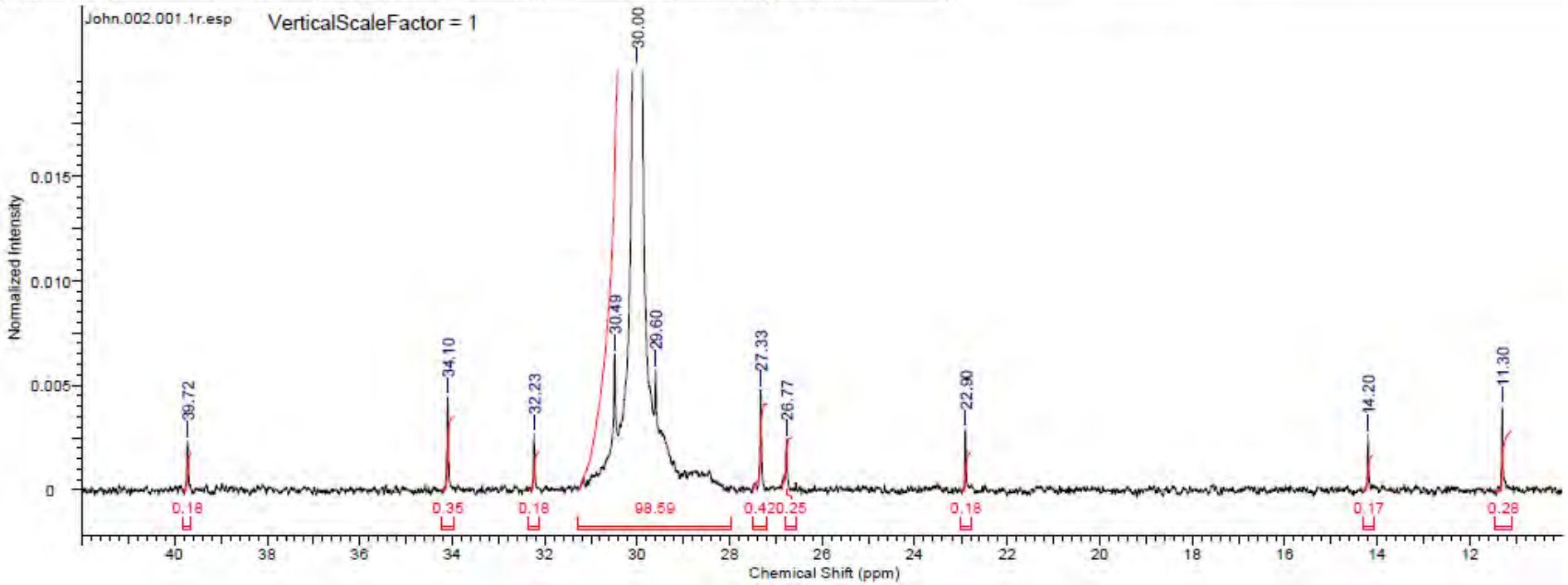

Figure 20.22: NMR spectrum for Experimental Run #7

Acquisition Time (sec)	6.2128	*Comment*	Ethylene-Butene Copolymerization, Sample #3			*Date*	11 Jun 2010 00:37:04
Date Stamp	11 Jun 2010 00:37:04			*File Name*	C:\HDPE Project\UW\Experimental\NMR data\John\3\pdata\1\1r		
Frequency (MHz)	125.76	*Nucleus*	13C	*Number of Transients*	2102	*Origin*	drx500
Original Points Count	47067	*Owner*	root	*Points Count*	32768	*Pulse Sequence*	zgig
Receiver Gain	9195.20	*SW(cyclical) (Hz)*	7575.76	*Solvent*	TCE	*Spectrum Offset (Hz)*	4444.8120
Spectrum Type	STANDARD	*Sweep Width (Hz)*	7575.53	*Temperature (degree C)*	27.000		

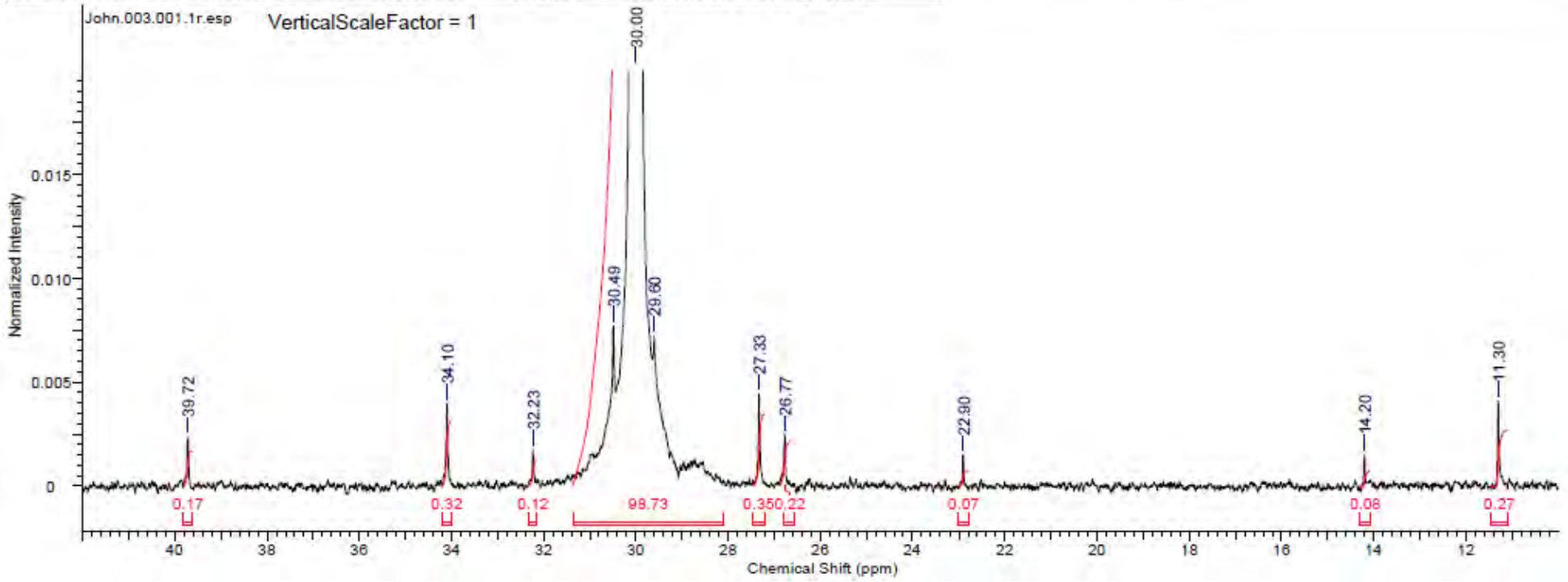

Figure 20.23: NMR spectrum for Experimental Run #10

Acquisition Time (sec)	6.2128	*Comment*	Ethylene-Butene Copolymerization, Sample #4			*Date*	12 Jun 2010 01:19:44
Date Stamp	12 Jun 2010 01:19:44			*File Name*	C:\HDPE Project\UW\Experimental\NMR data\John\4\pdata\1\1r		
Frequency (MHz)	125.76	*Nucleus*	13C	*Number of Transients*	1966	*Origin*	drx500
Original Points Count	47067	*Owner*	root	*Points Count*	32768	*Pulse Sequence*	zgig
Receiver Gain	9195.20	*SW(cyclical) (Hz)*	7575.76	*Solvent*	TCE	*Spectrum Offset (Hz)*	4445.2744
Spectrum Type	STANDARD	*Sweep Width (Hz)*	7575.53	*Temperature (degree C)*	27.000		

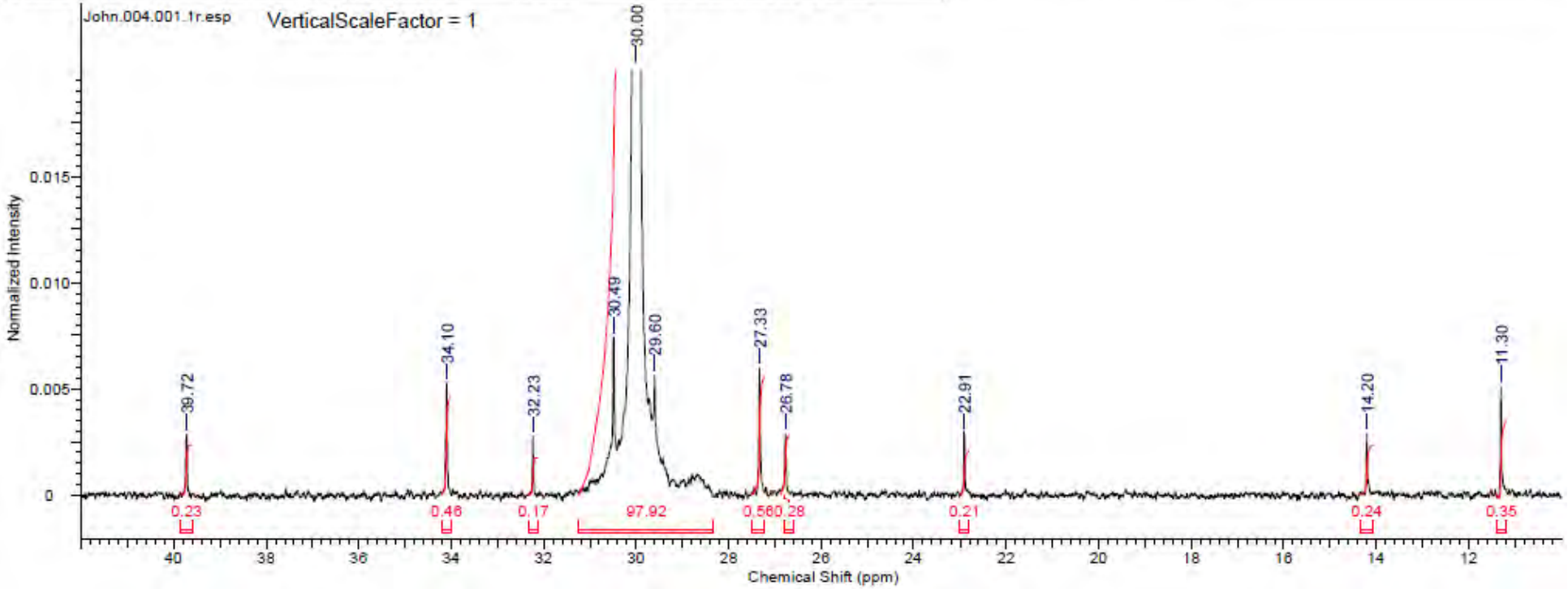

Figure 20.24: NMR spectrum for Experimental Run #12

Acquisition Time (sec)	6.2128	*Comment*	Ethylene-Butene Copolymerization, sample #5			*Date*	11 Jun 2010 10:17:20
Date Stamp	11 Jun 2010 10:17:20			*File Name*	C:\HDPE Project\UW\Experimental\NMR data\John\5\pdata\1\1r		
Frequency (MHz)	125.76	*Nucleus*	13C	*Number of Transients*	1766	*Origin*	drx500
Original Points Count	47067	*Owner*	root	*Points Count*	32768	*Pulse Sequence*	zgig
Receiver Gain	9195.20	*SW(cyclical) (Hz)*	7575.76	*Solvent*	TCE	*Spectrum Offset (Hz)*	4444.8120
Spectrum Type	STANDARD	*Sweep Width (Hz)*	7575.53	*Temperature (degree C)*	27.000		

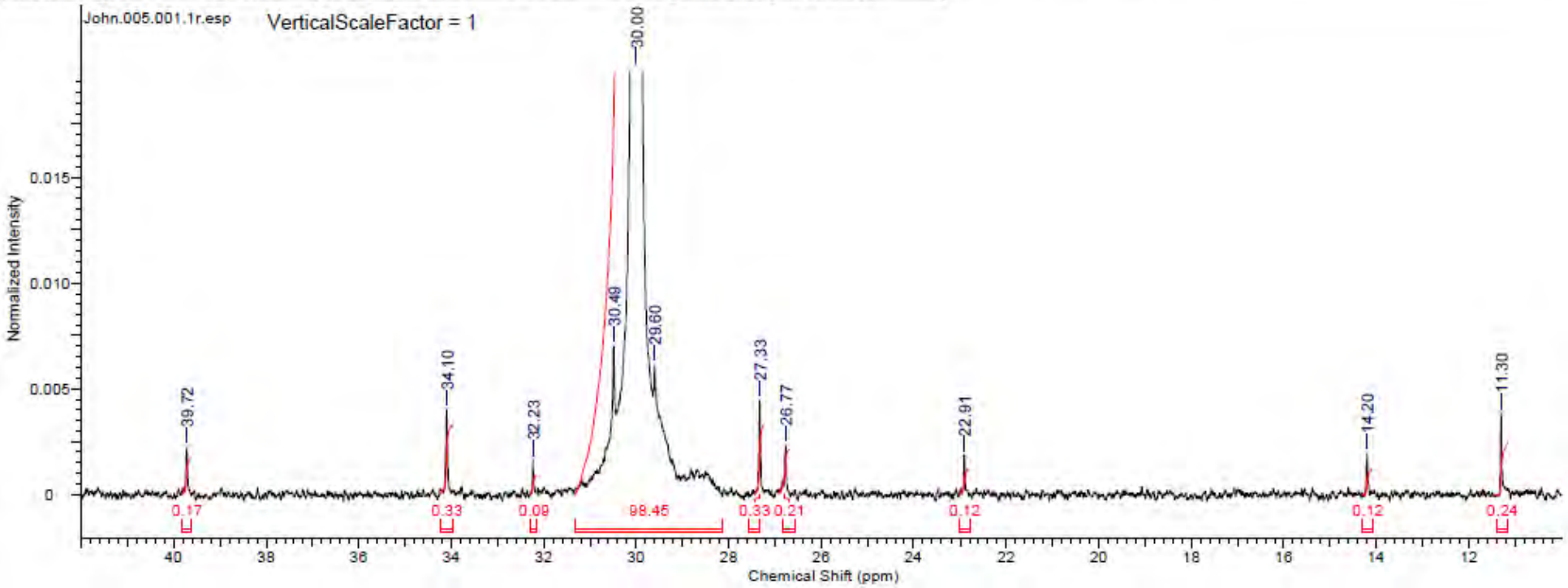

Figure 20.25: NMR spectrum for Experimental Run #13

Acquisition Time (sec)	6.2128	*Comment*	Ethylene-Butene Copolymerization, Sample #6			*Date*	13 Jun 2010 10:32:16
Date Stamp	13 Jun 2010 10:32:16			*File Name*	C:\HDPE Project\UW\Experimental\NMR data\John\6\pdata\1\1r		
Frequency (MHz)	125.76	*Nucleus*	13C	*Number of Transients*	1621	*Origin*	drx500
Original Points Count	47067	*Owner*	root	*Points Count*	32768	*Pulse Sequence*	zgig
Receiver Gain	9195.20	*SW(cyclical) (Hz)*	7575.76	*Solvent*	TCE	*Spectrum Offset (Hz)*	4446.2002
Spectrum Type	STANDARD	*Sweep Width (Hz)*	7575.53	*Temperature (degree C)*	27.000		

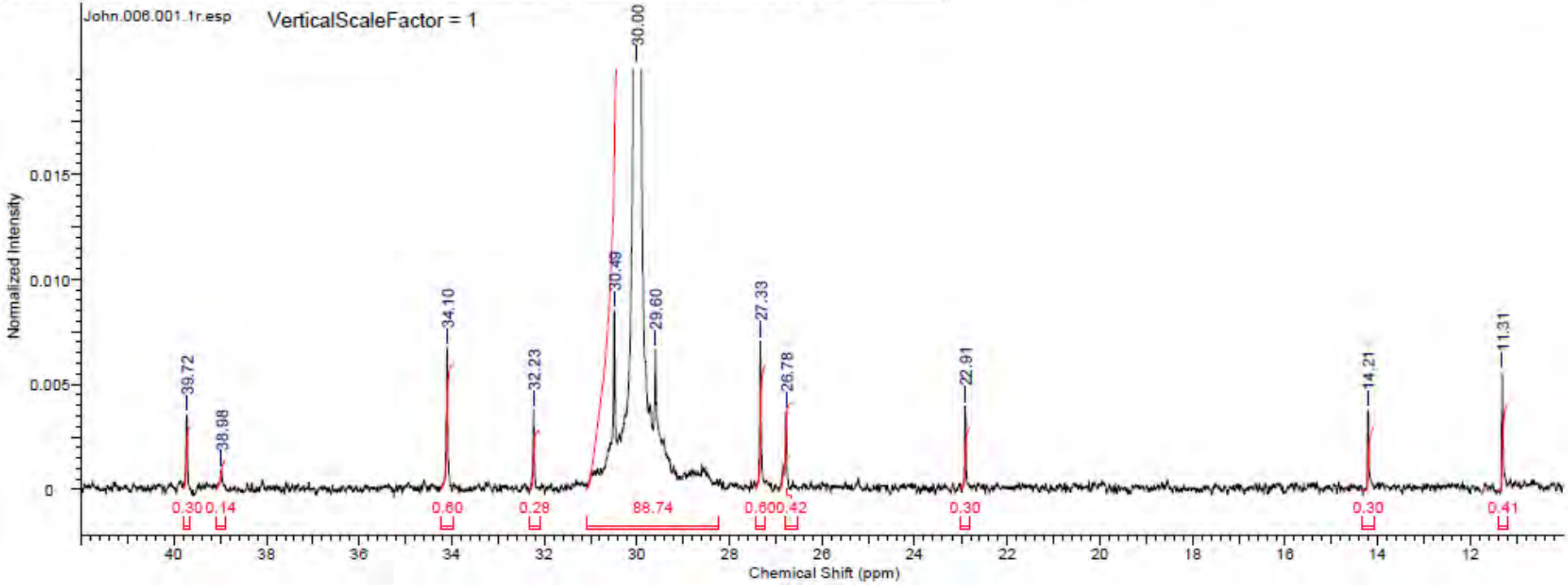

Figure 20.26: NMR spectrum for Experimental Run #14

Acquisition Time (sec)	6.2128	*Comment*	ethylene-butene copolymerization, sample #7			*Date*	12 Jun 2010 01:04:48
Date Stamp	12 Jun 2010 01:04:48			*File Name*	C:\HDPE Project\UW\Experimental\NMR data\John\7\pdata\1\1r		
Frequency (MHz)	125.76	*Nucleus*	13C	*Number of Transients*	1481	*Origin*	drx500
Original Points Count	47067	*Owner*	root	*Points Count*	32768	*Pulse Sequence*	zgig
Receiver Gain	9195.20	*SW(cyclical) (Hz)*	7575.76	*Solvent*	TCE	*Spectrum Offset (Hz)*	4446.4297
Spectrum Type	STANDARD	*Sweep Width (Hz)*	7575.53	*Temperature (degree C)*	27.000		

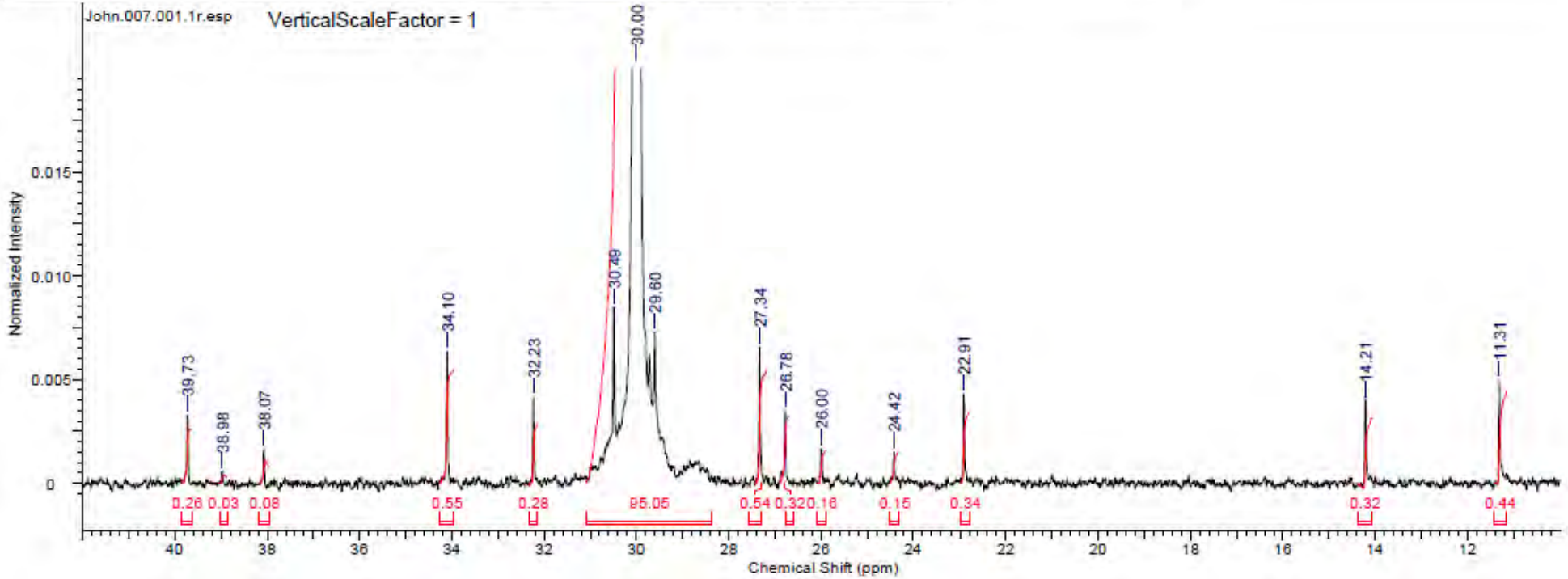

Figure 20.27: NMR spectrum for Experimental Run #15

Acquisition Time (sec)	6.2128	*Comment*	ethylene-Butene Copolymerization, sample #8			*Date*	12 Jun 2010 10:23:44
Date Stamp	12 Jun 2010 10:23:44			*File Name*	C:\HDPE Project\UW\Experimental\NMR data\John\8\pdata\1\1r		
Frequency (MHz)	125.76	*Nucleus*	13C	*Number of Transients*	1695	*Origin*	drx500
Original Points Count	47067	*Owner*	root	*Points Count*	32768	*Pulse Sequence*	zgig
Receiver Gain	9195.20	*SW(cyclical) (Hz)*	7575.76	*Solvent*	TCE	*Spectrum Offset (Hz)*	4445.2744
Spectrum Type	STANDARD	*Sweep Width (Hz)*	7575.53	*Temperature (degree C)*	27.000		

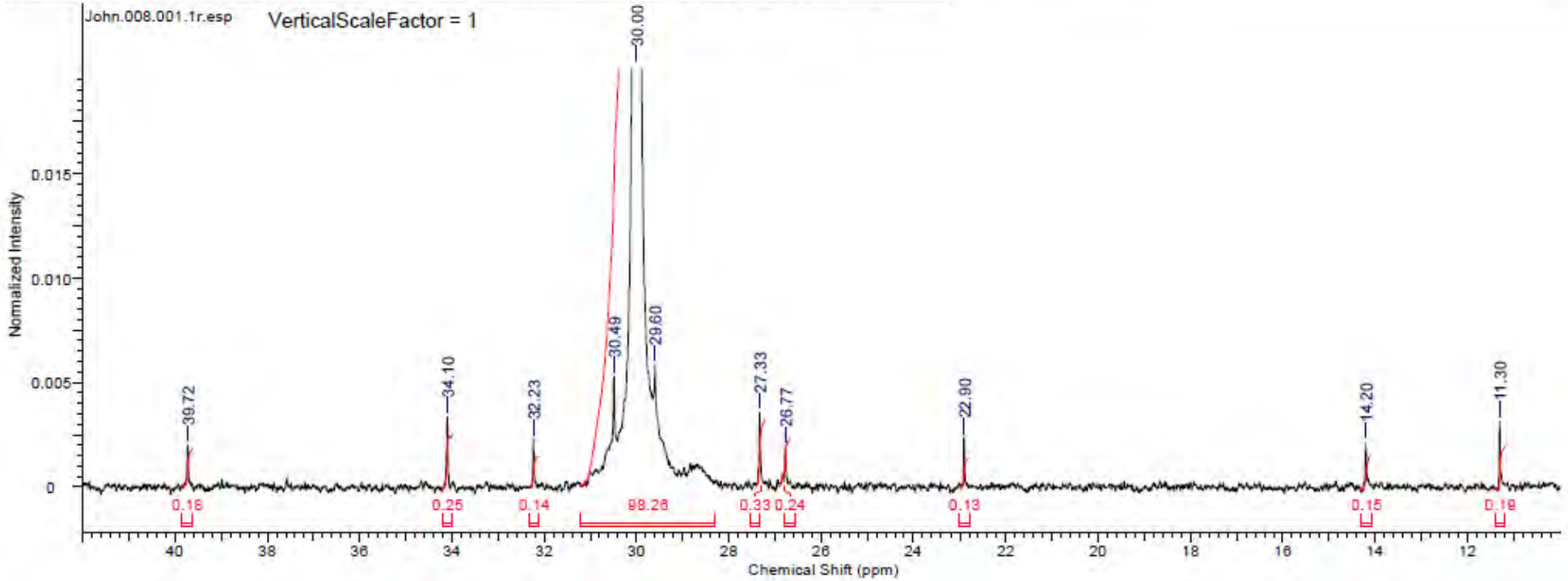

Figure 20.28: NMR spectrum for Experimental Run #17

Acquisition Time (sec)	6.2128	*Comment*	Ethylene-Butene Copolymerization Sample #9			*Date*	12 Jun 2010 18:08:48
Date Stamp	12 Jun 2010 18:08:48			*File Name*	C:\HDPE Project\UW\Experimental\NMR data\John\9\pdata\1\1r		
Frequency (MHz)	125.76	*Nucleus*	13C	*Number of Transients*	1465	*Origin*	drx500
Original Points Count	47067	*Owner*	root	*Points Count*	32768	*Pulse Sequence*	zgig
Receiver Gain	9195.20	*SW(cyclical) (Hz)*	7575.76	*Solvent*	TCE	*Spectrum Offset (Hz)*	4451.2861
Spectrum Type	STANDARD	*Sweep Width (Hz)*	7575.53	*Temperature (degree C)*	27.000		

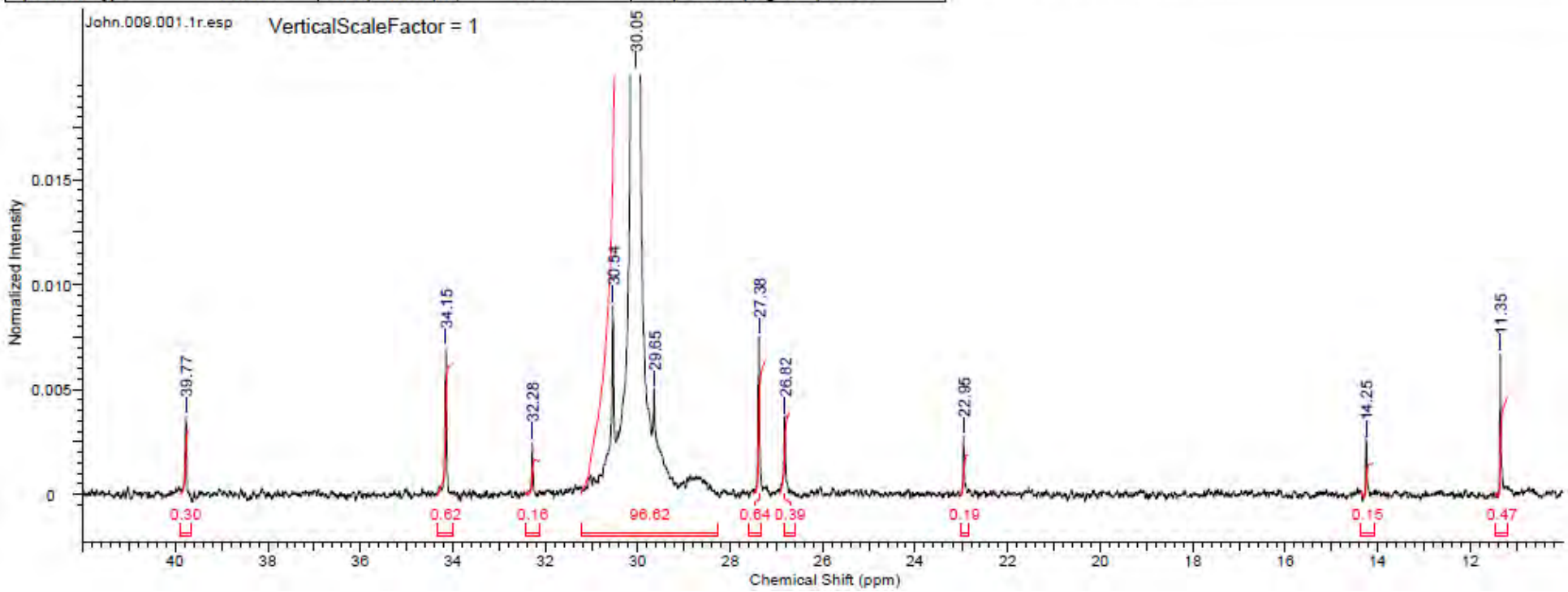

Figure 20.29: NMR spectrum for Experimental Run #19

20.3 CEF profiles

The figures below show the crystallisation elution fractionation curves for each of the polymer samples that was analysed. This data was correlated with the NMR data to determine comonomer content of the polymer. This correlated data is shown in Table 20.1.

Table 20.1: Comonomer content based on correlation

	NMR	CEF	CEF correlated data
Run #	C_4H_8 (mol%)	$T_{crys,mean}$ (deg C)	C_4H_8 (mol%)
1		93.41	0.432
2		95.73	0.269
3		92.31	0.509
4		96.36	0.224
5		92.77	0.477
6	0.371	93.74	0.409
7	0.356	93.89	0.398
8		93.66	0.414
9		92.91	0.467
10	0.326		
11		93.72	0.410
12	0.470	92.49	0.497
13	0.340	95.39	0.293
14	0.808	89.30	0.721
15	0.574	89.85	0.682
16		96.60	0.208
17	0.307	95.25	0.302
18		93.53	0.423
19	0.622	91.80	0.545
20		94.47	0.357

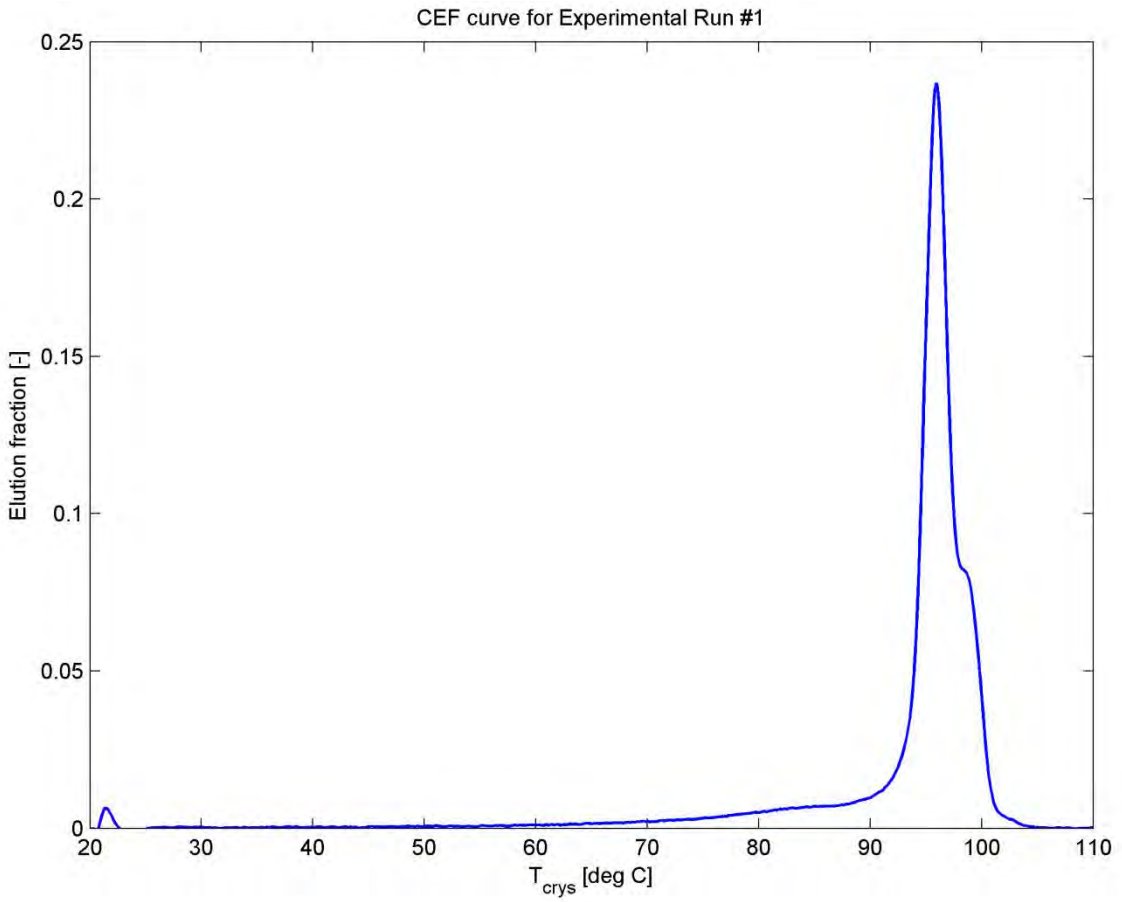

Figure 20.30: CEF curve for Experimental Run #1

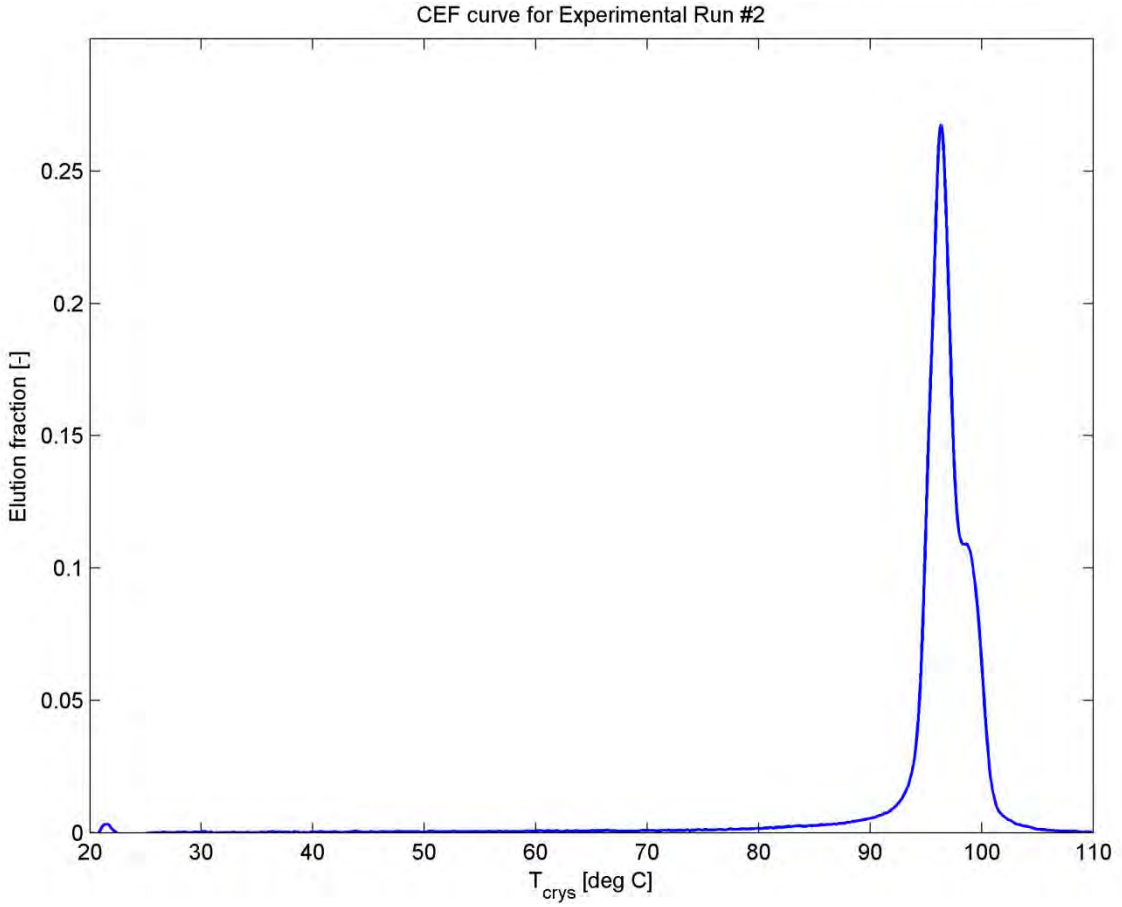

Figure 20.31: CEF curve for Experimental Run #2

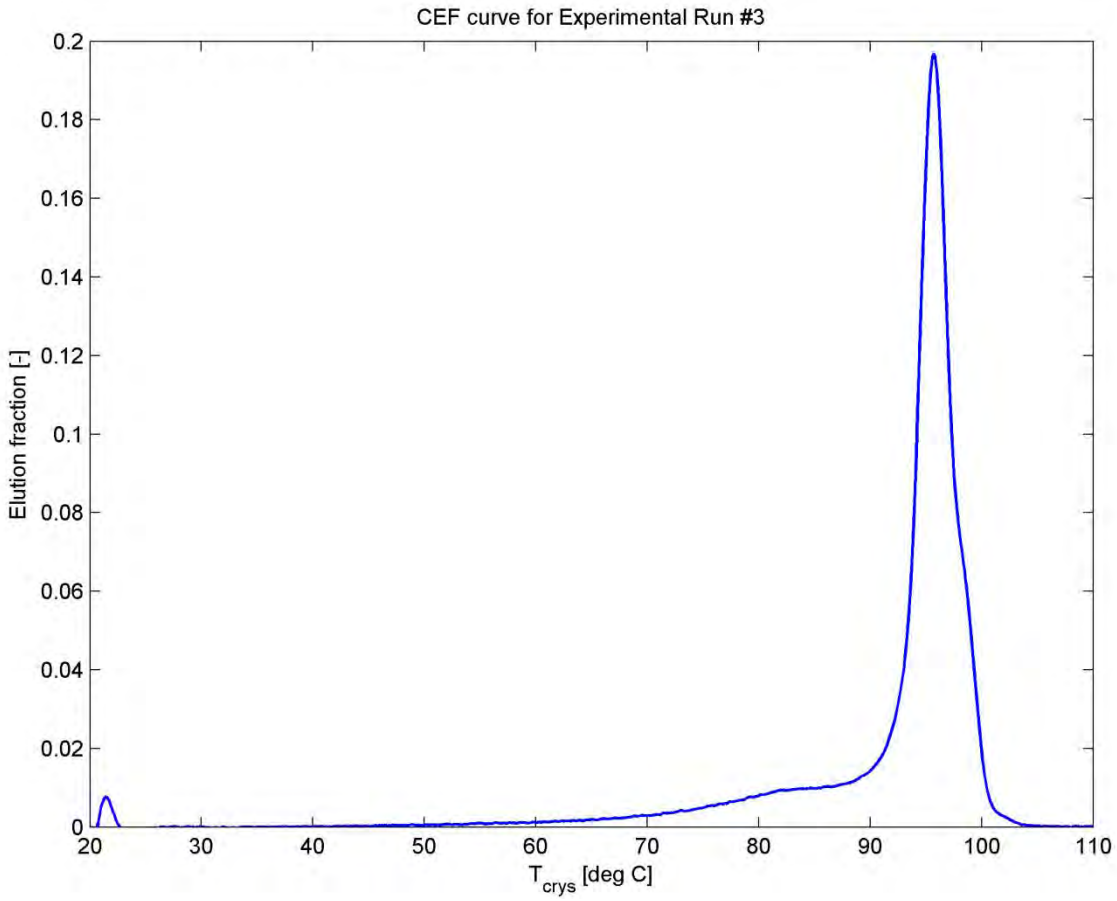

Figure 20.32: CEF curve for Experimental Run #3

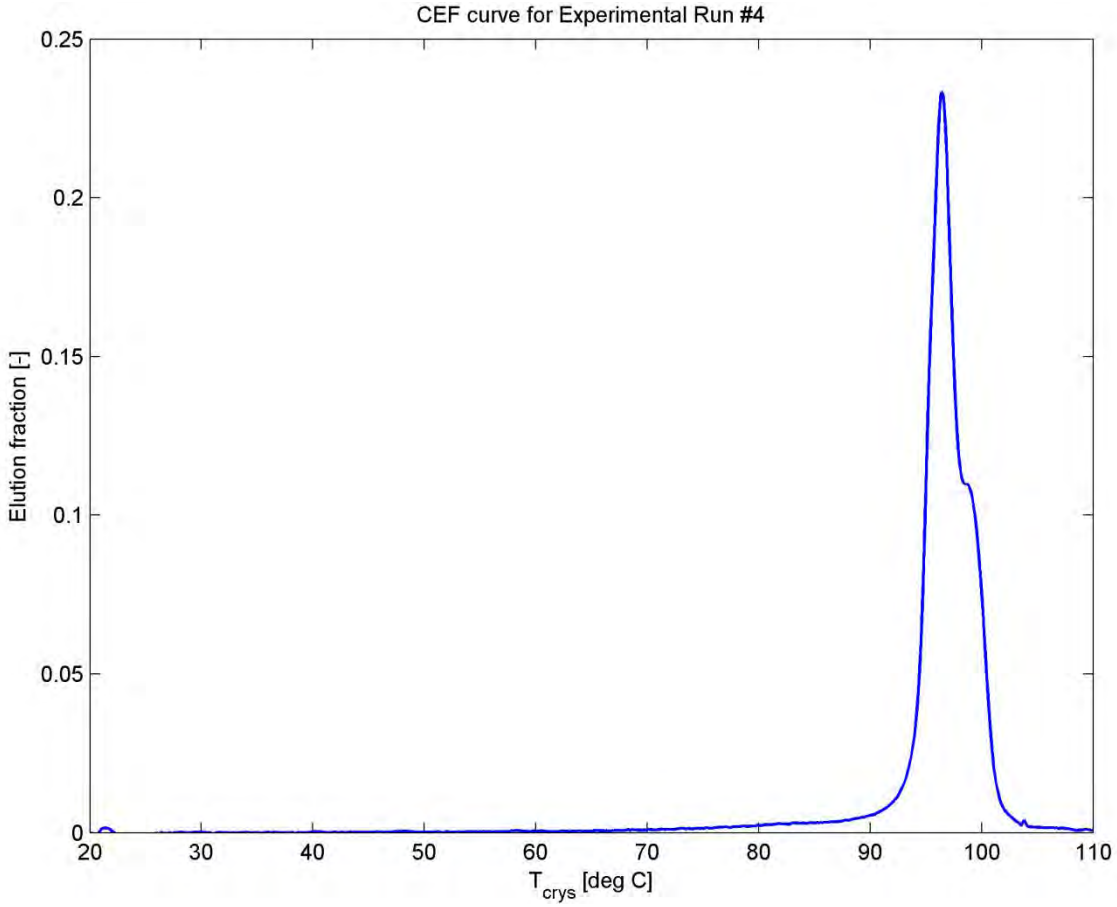

Figure 20.33 CEF curve for Experimental Run #4

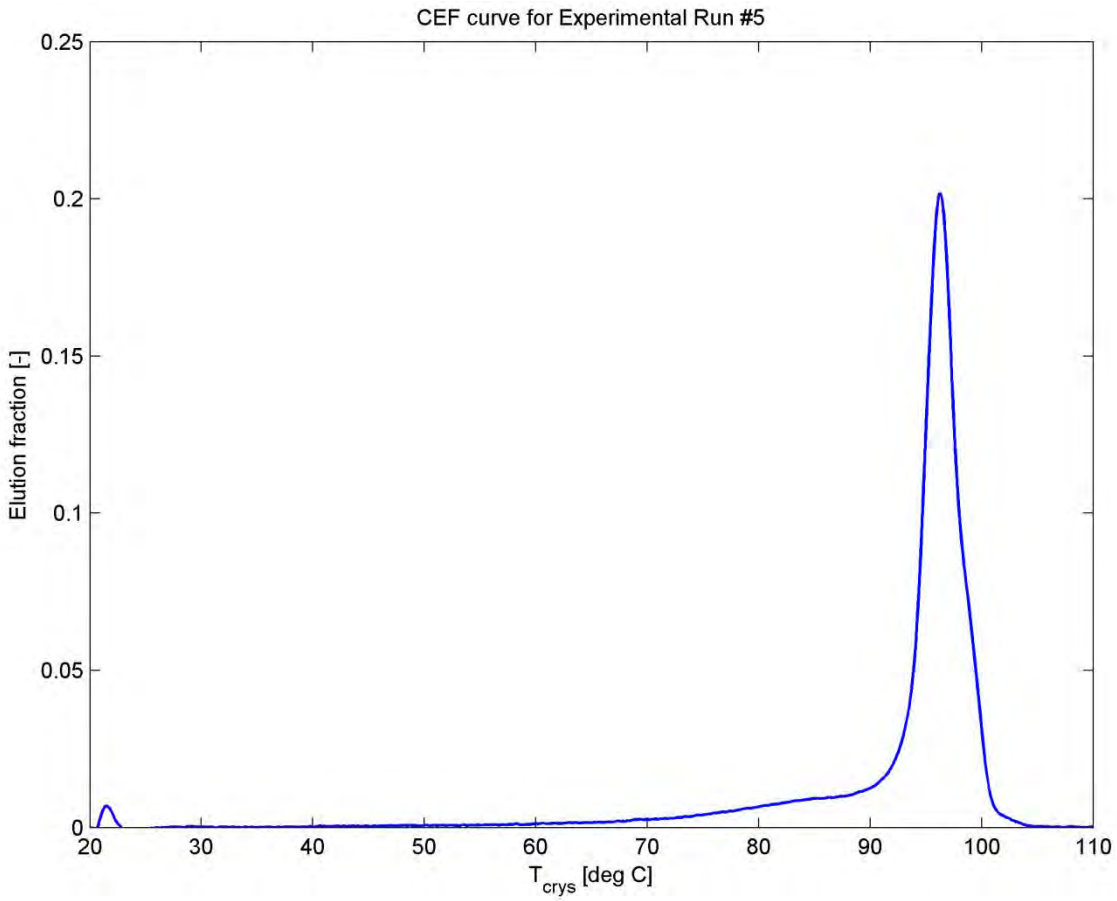

Figure 20.34: CEF curve for Experimental Run #5

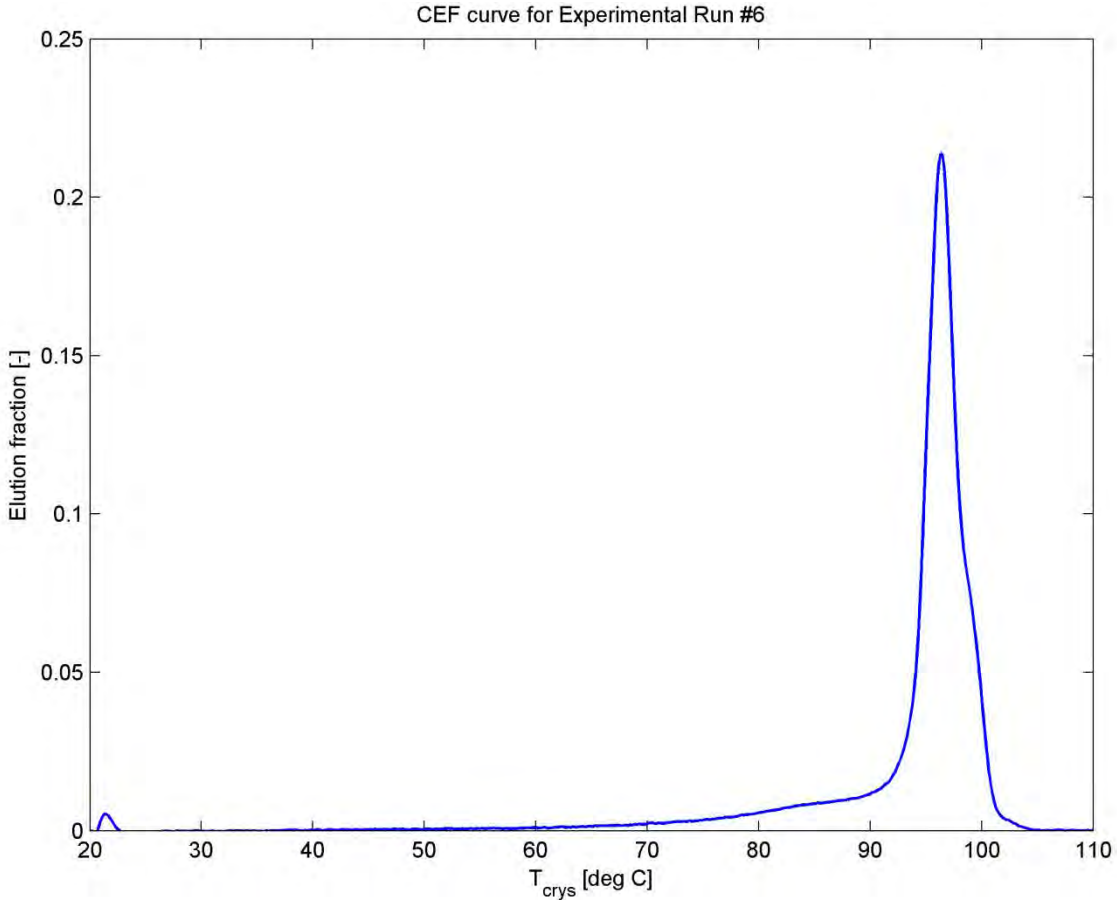

Figure 20.35: CEF curve for Experimental Run #6

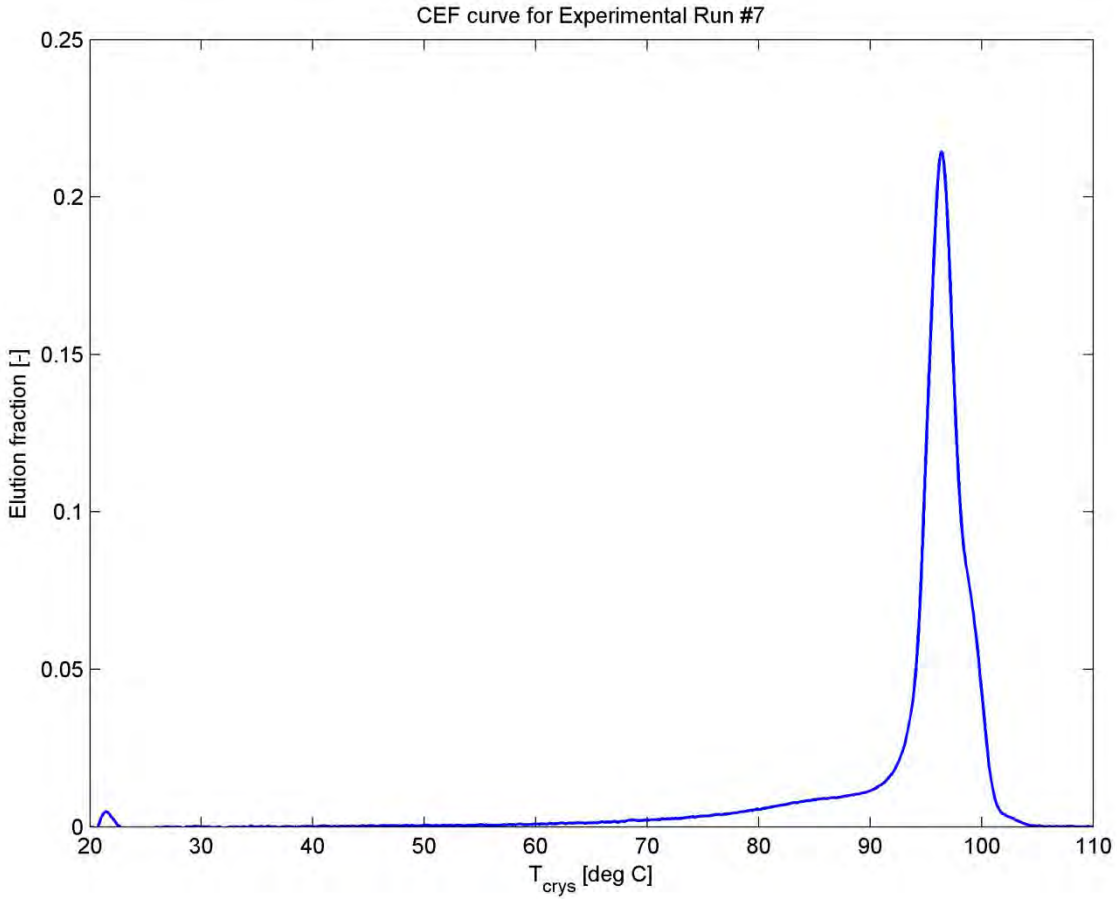

Figure 20.36: CEF curve for Experimental Run #7

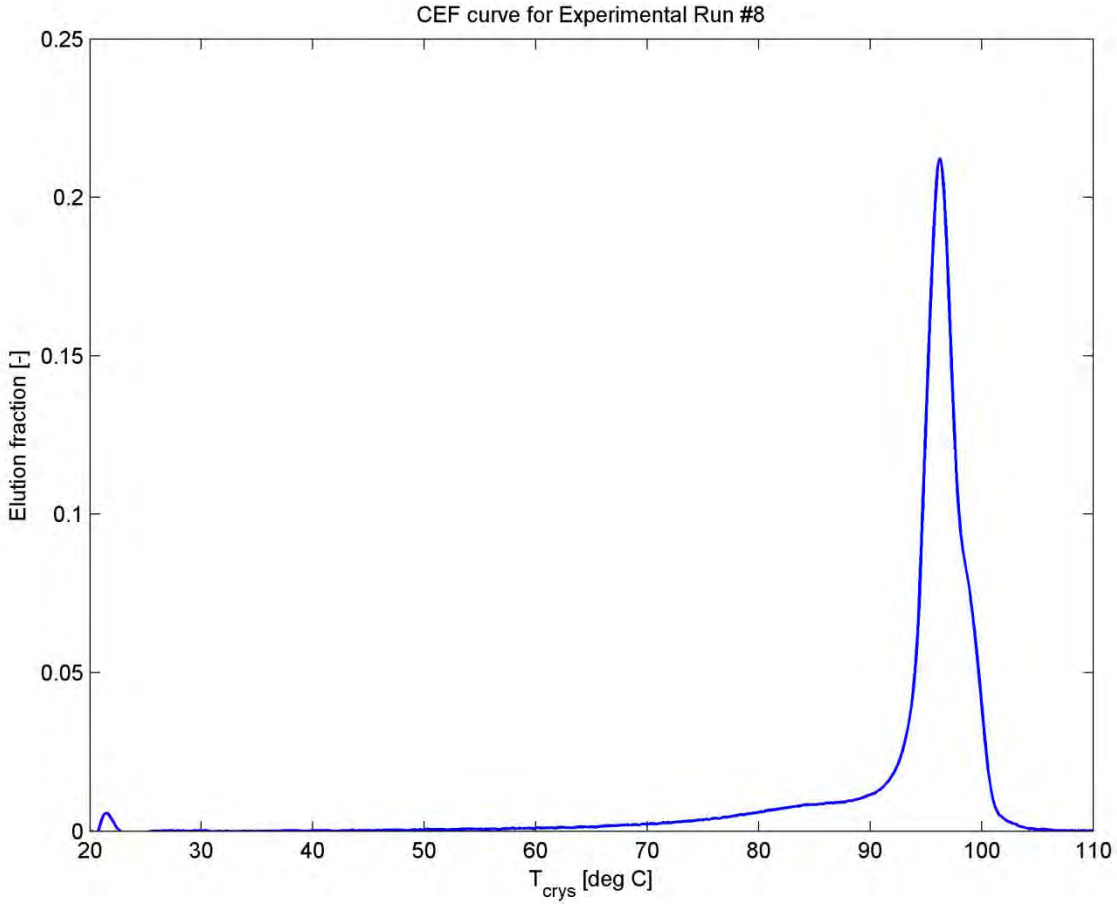

Figure 20.37: CEF curve for Experimental Run #8

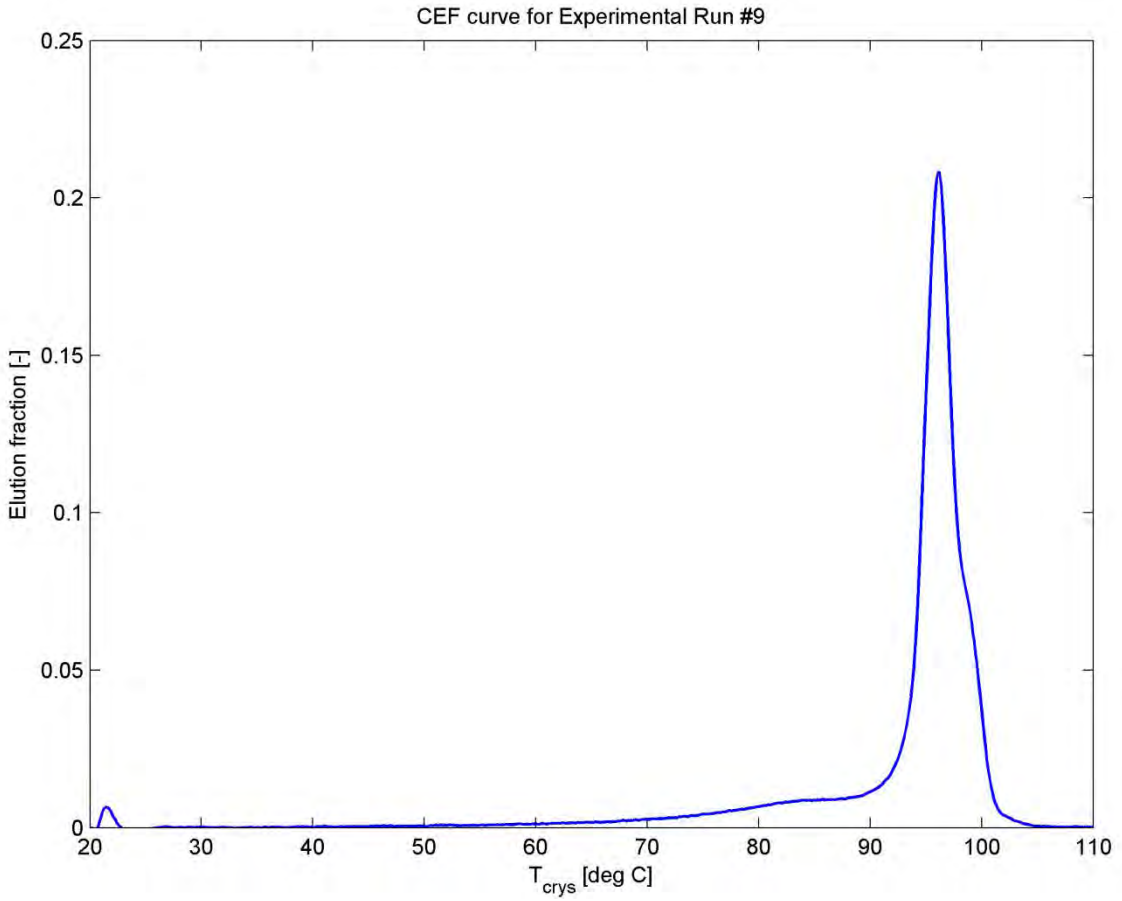

Figure 20.38: CEF curve for Experimental Run #9

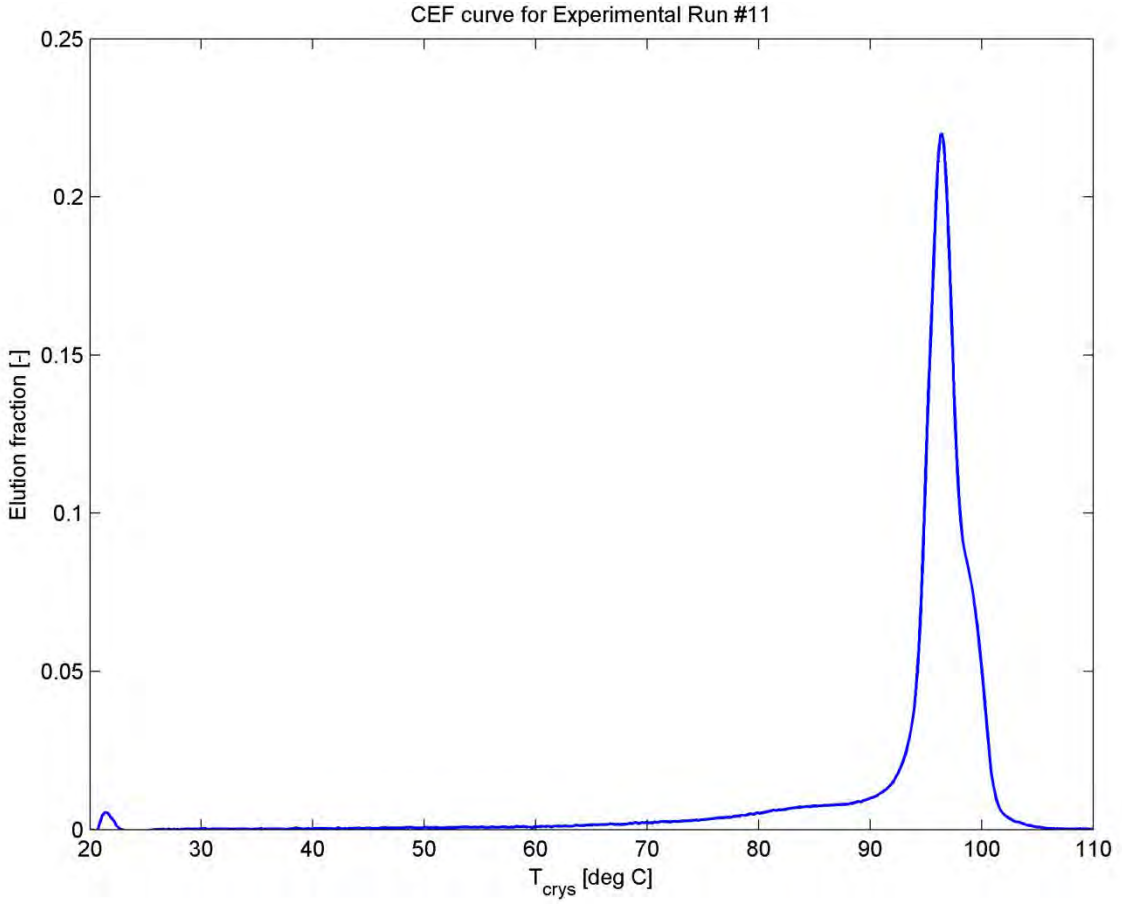

Figure 20.39: CEF curve for Experimental Run #11

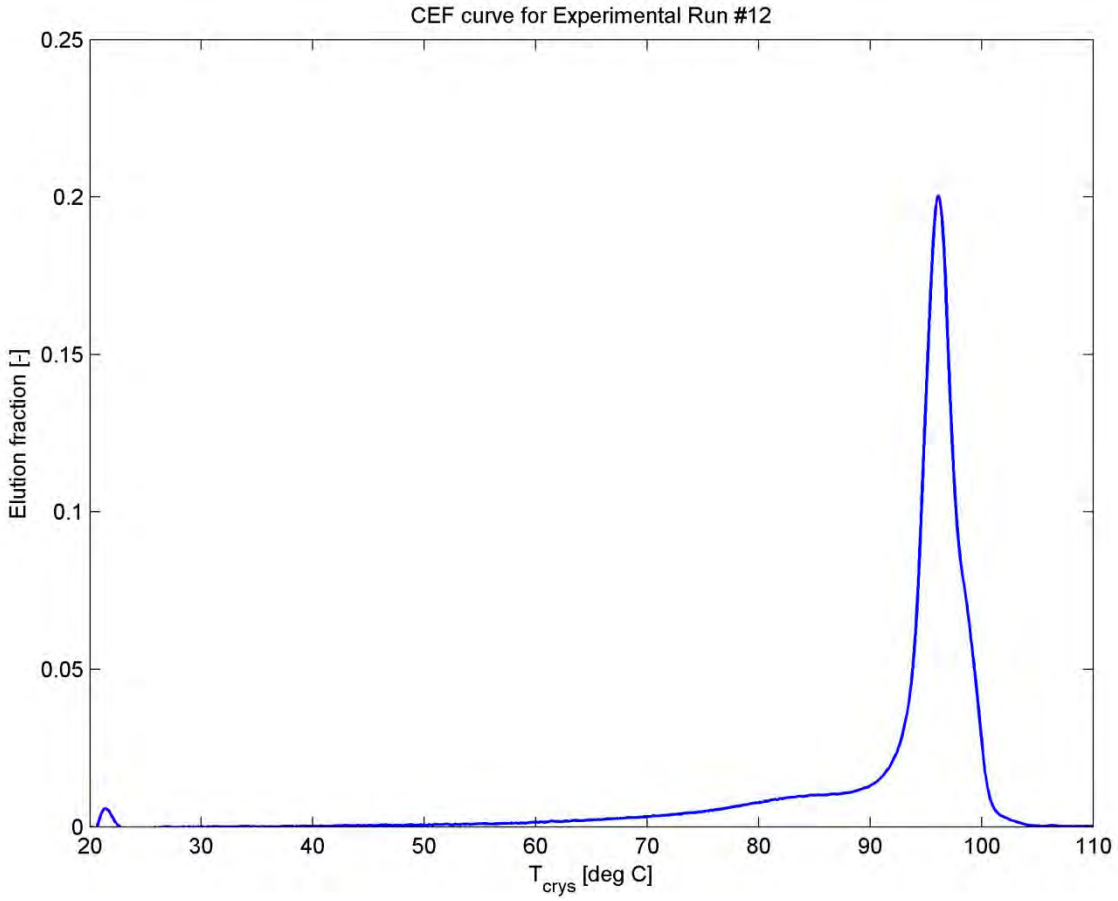

Figure 20.40: CEF curve for Experimental Run #12

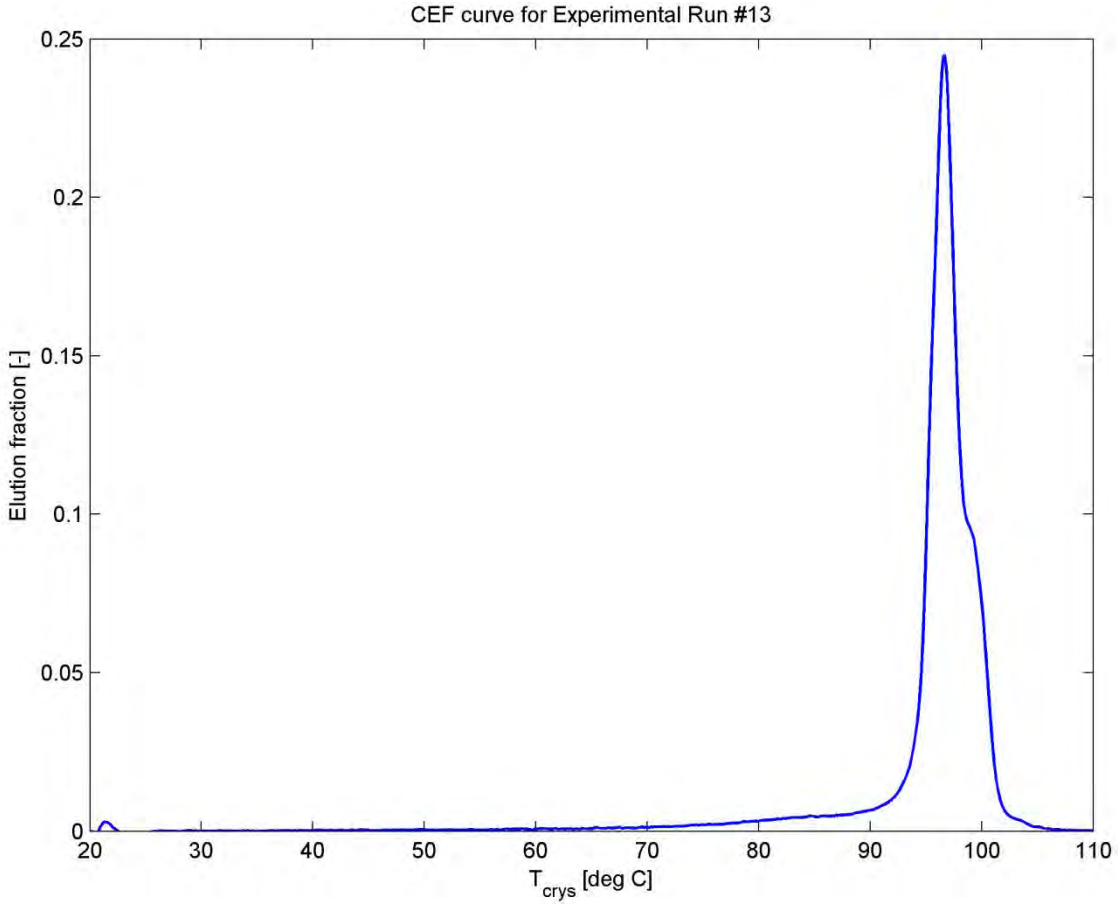

Figure 20.41: CEF curve for Experimental Run #13

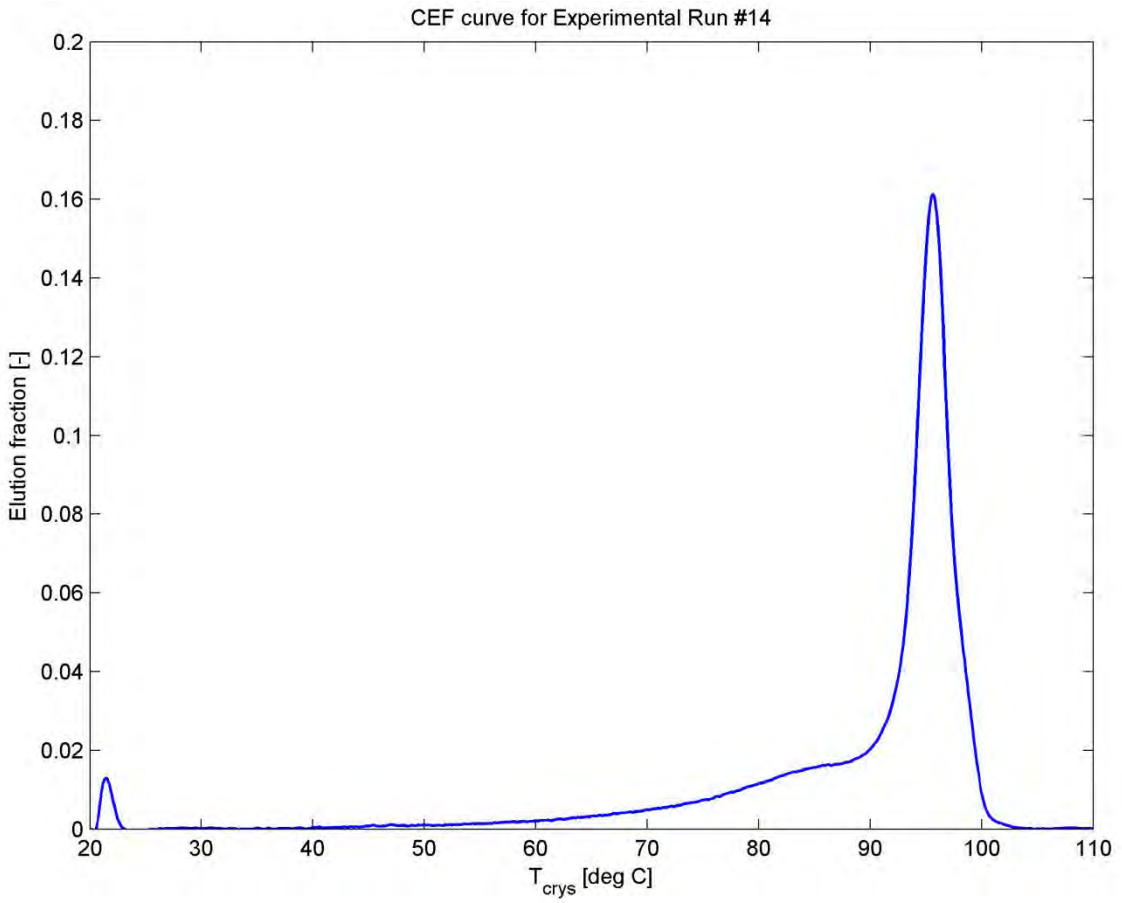

Figure 20.42: CEF curve for Experimental Run #14

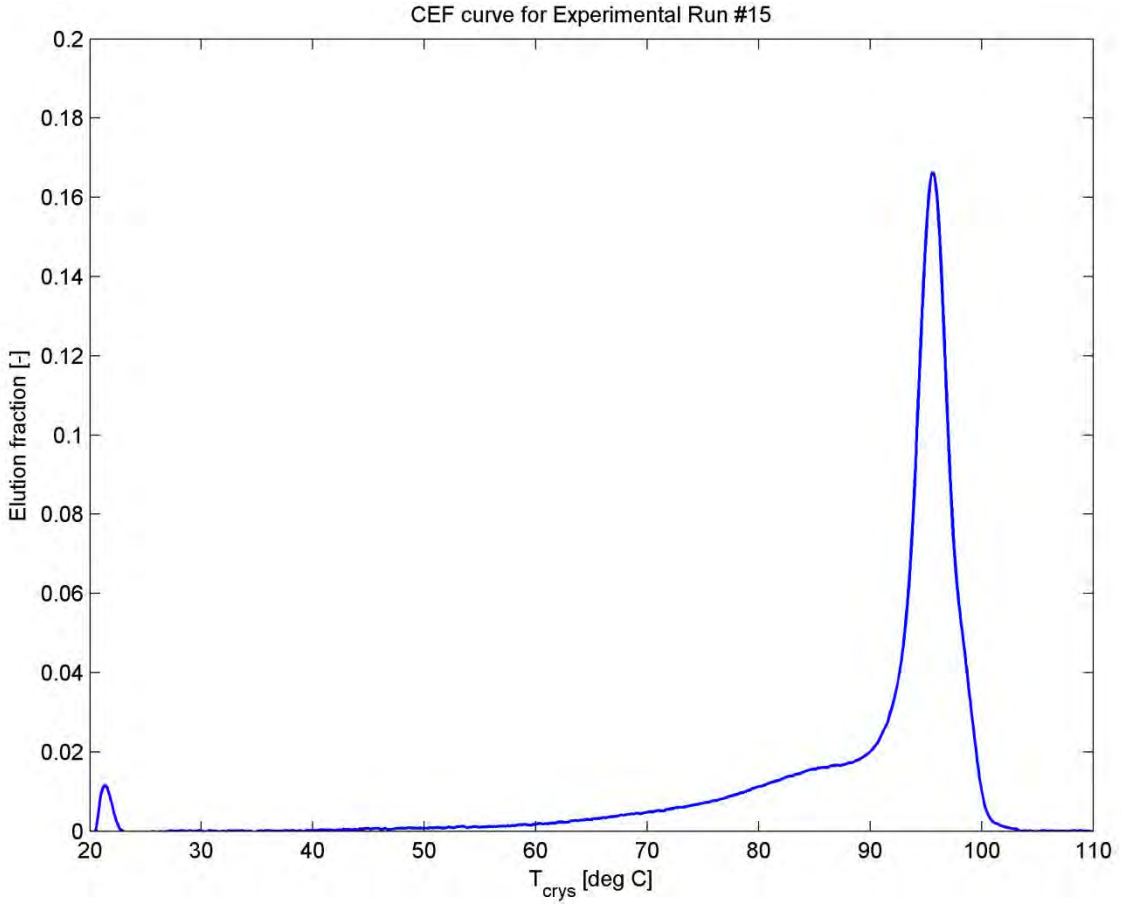

Figure 20.43: CEF curve for Experimental Run #15

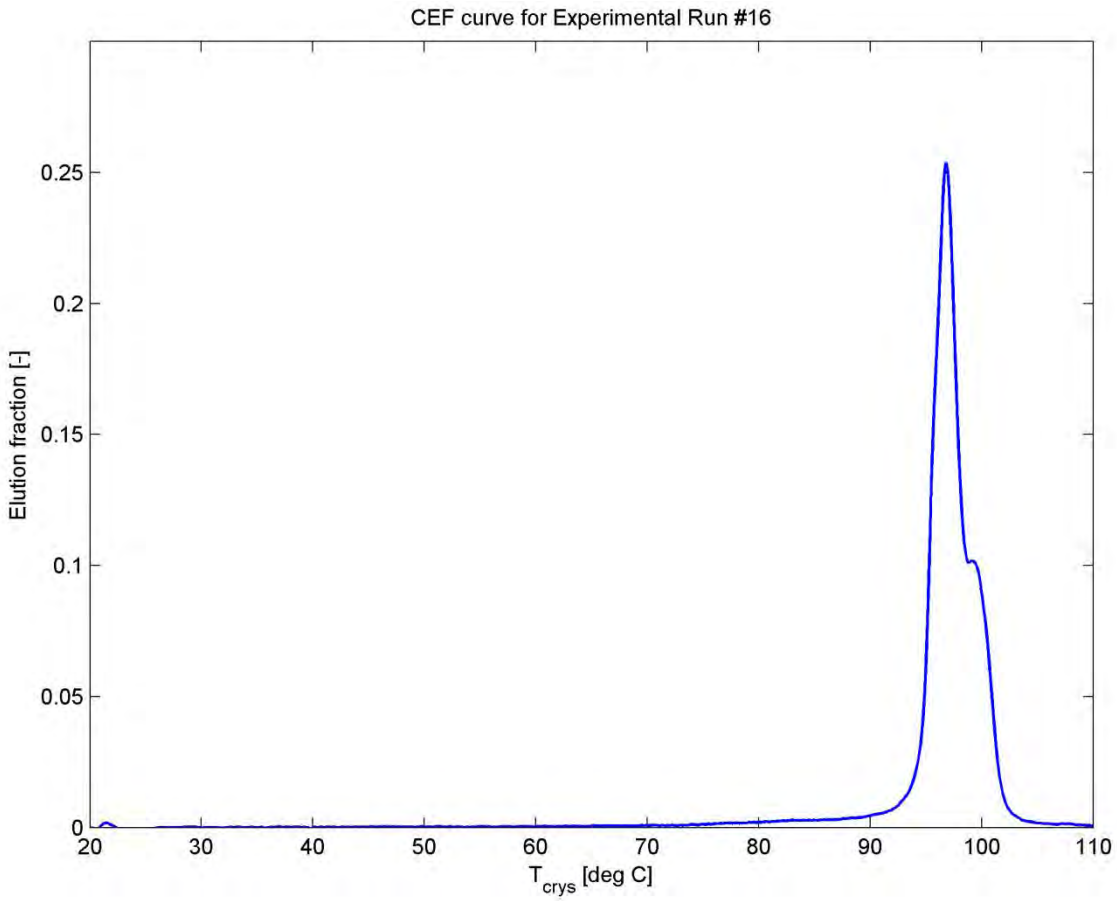

Figure 20.44: CEF curve for Experimental Run #16

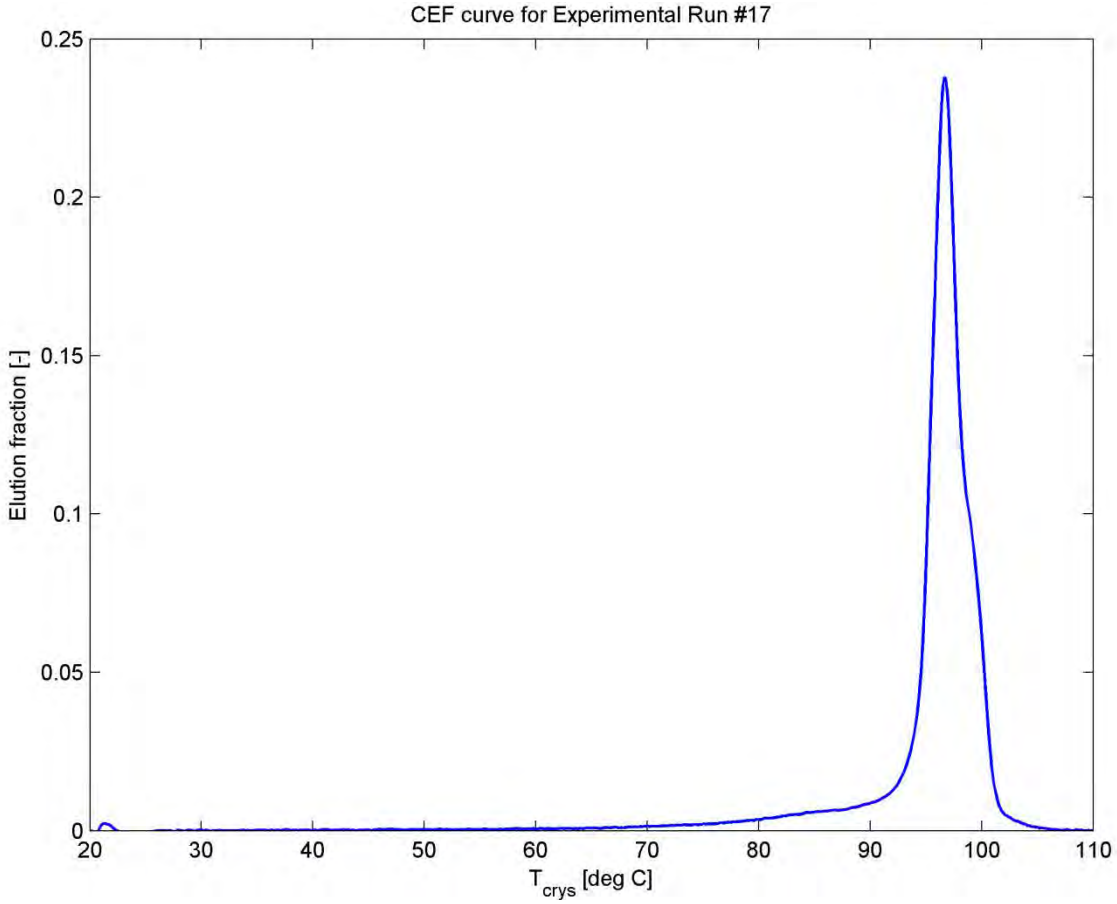

Figure 20.45: CEF curve for Experimental Run #17

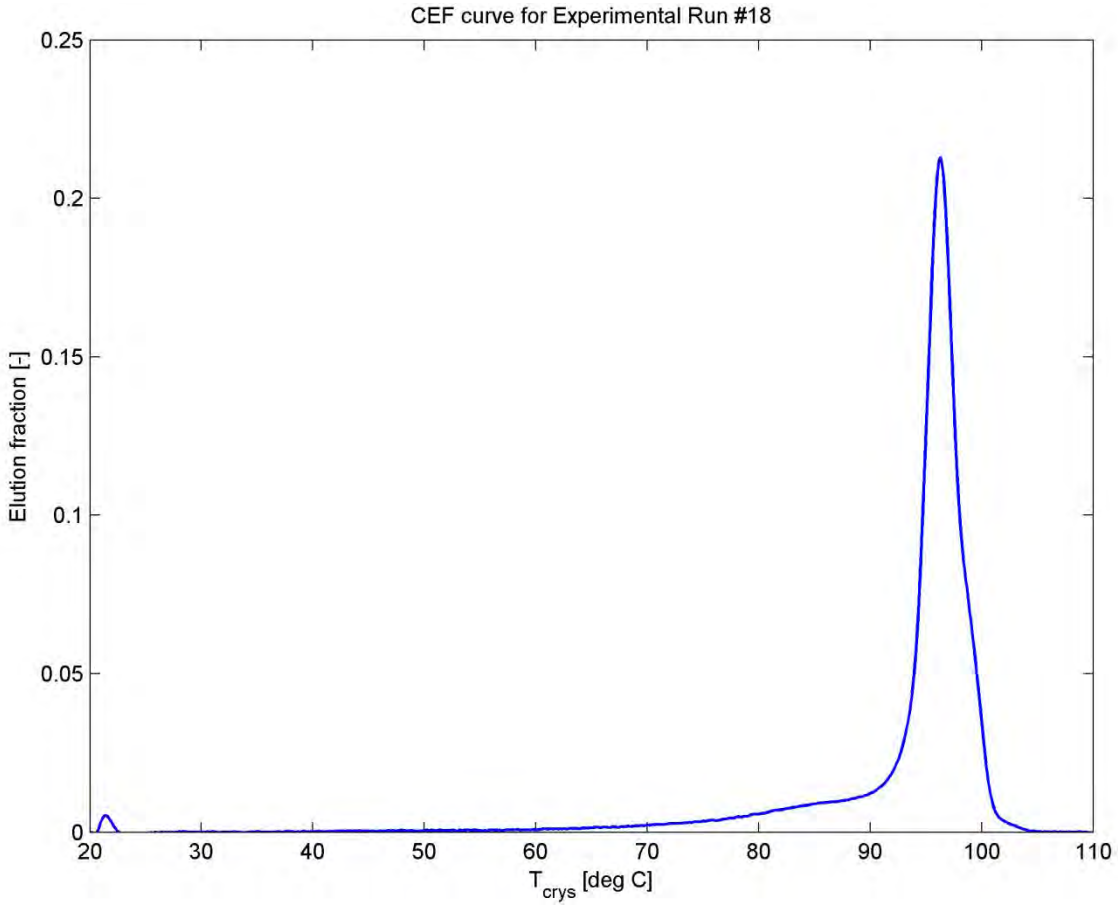

Figure 20.46: CEF curve for Experimental Run #18

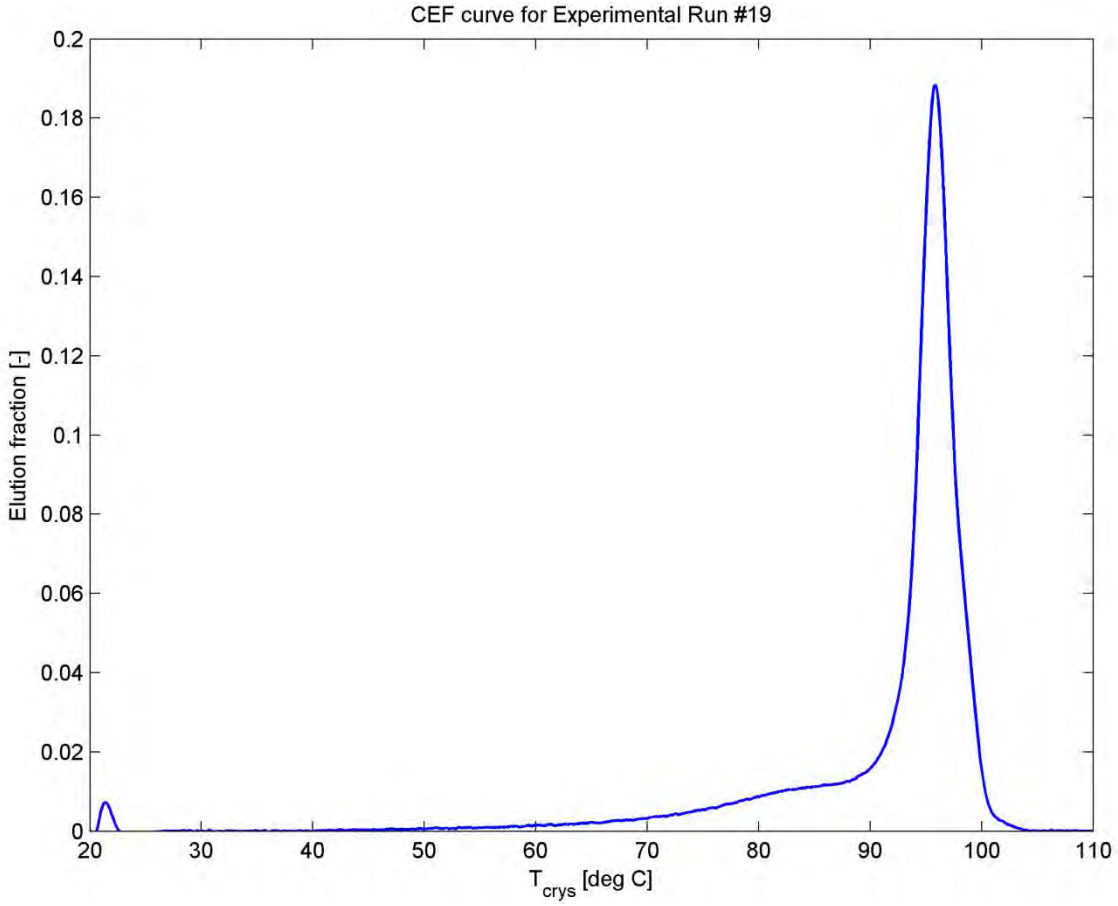

Figure 20.47: CEF curve for Experimental Run #19

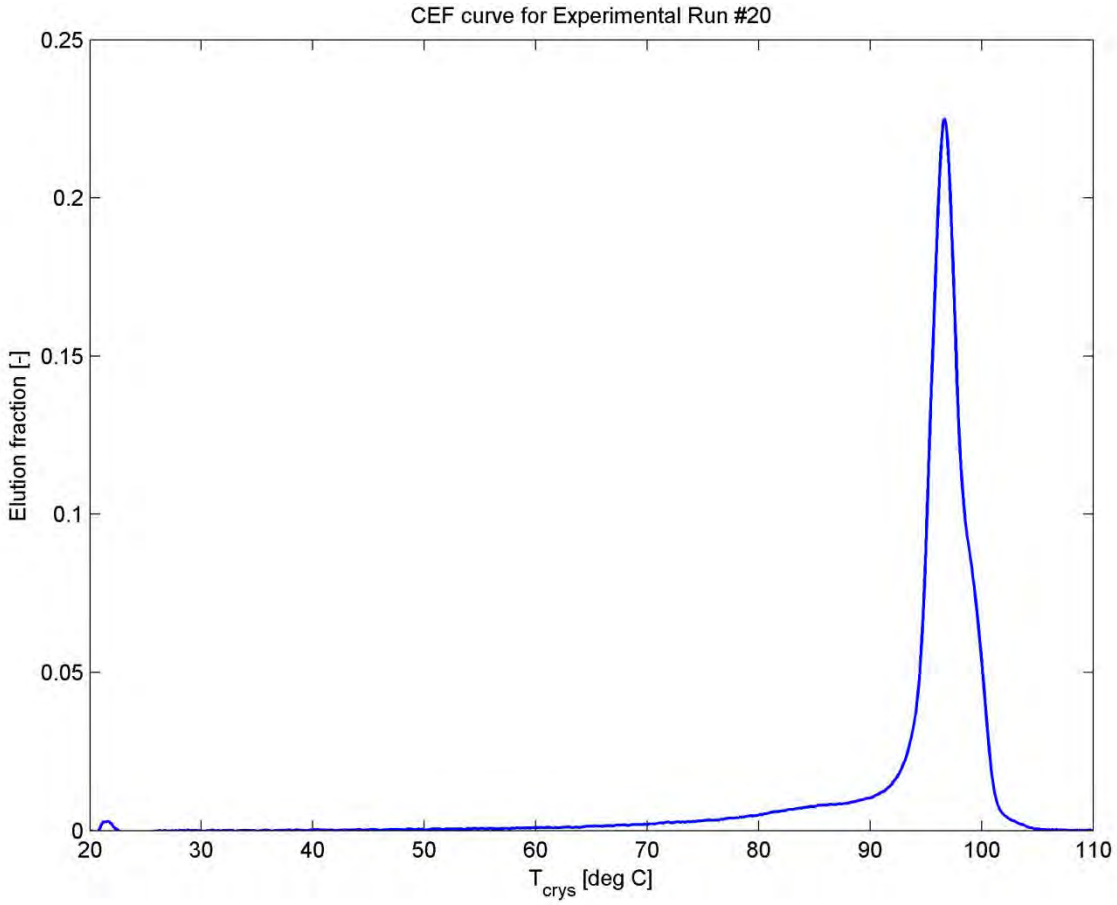

Figure 20.48: CEF curve for Experimental Run #20

20.4 Particle size distribution data

The particle size distribution data for the polymer samples from the laboratory experiments are shown in the figures below.

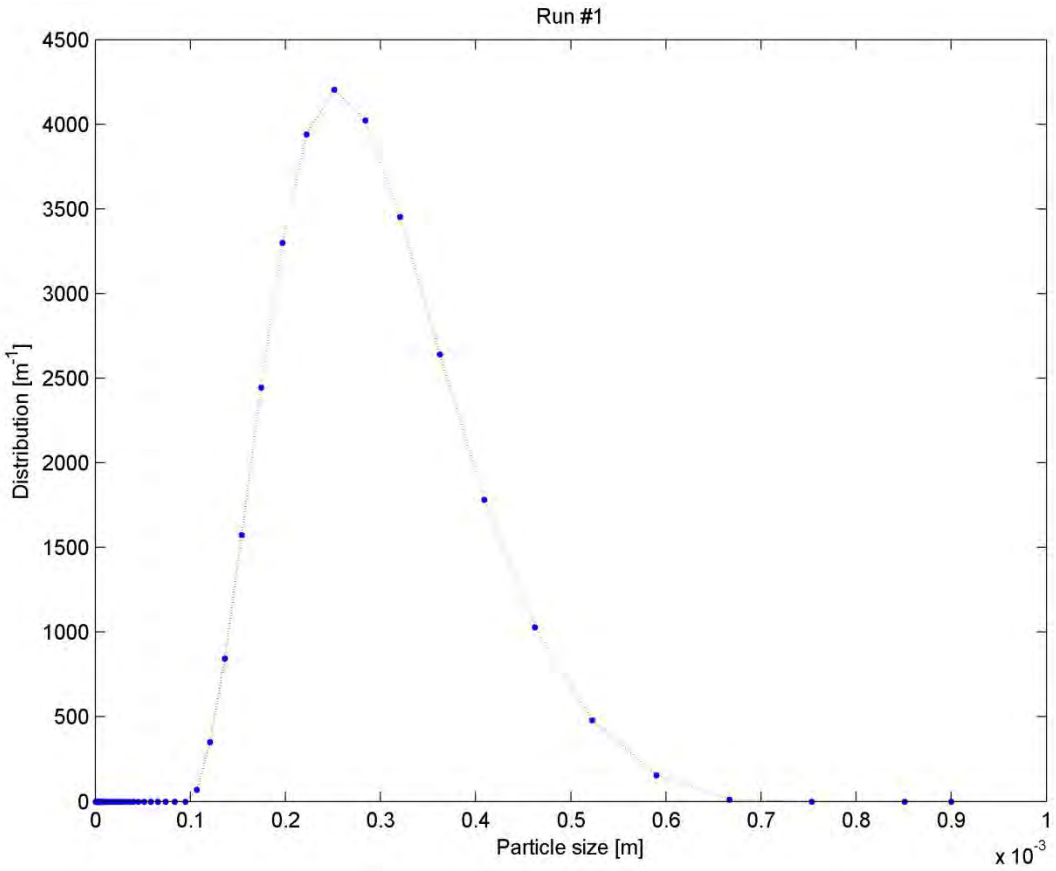

Figure 20.49: Particle size distribution for Experimental Run #1

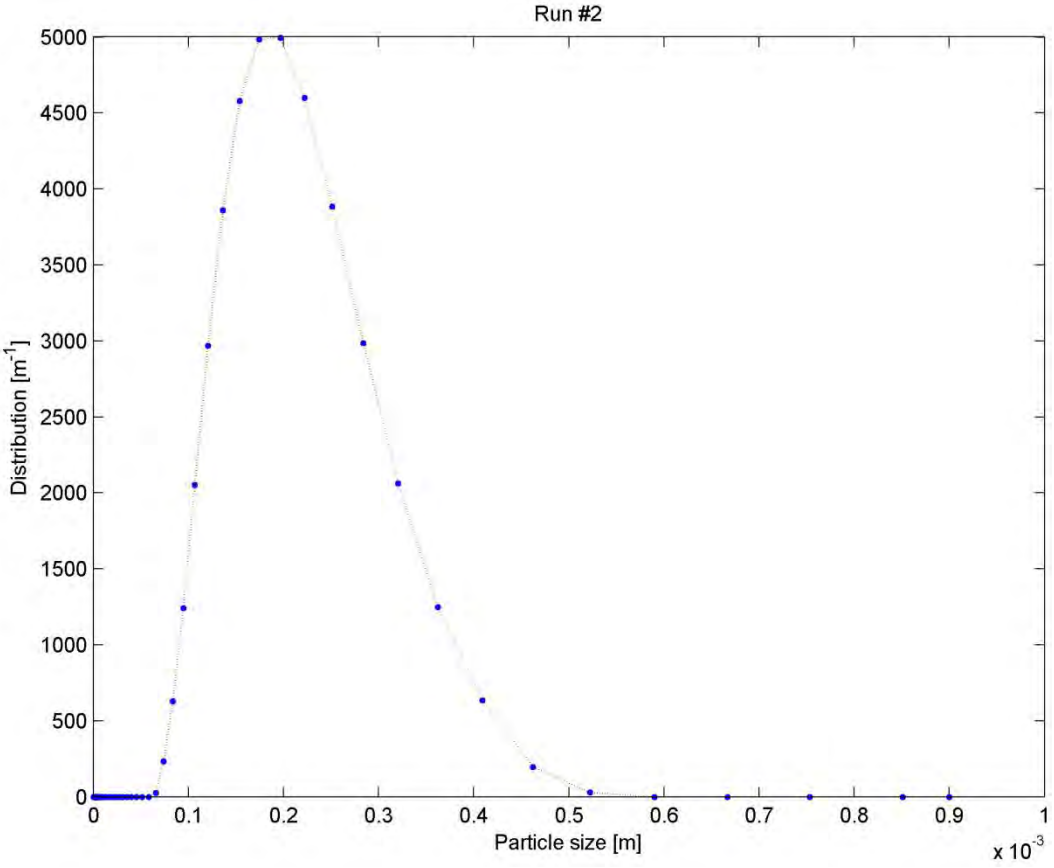

Figure 20.50: Particle size distribution for Experimental Run #2

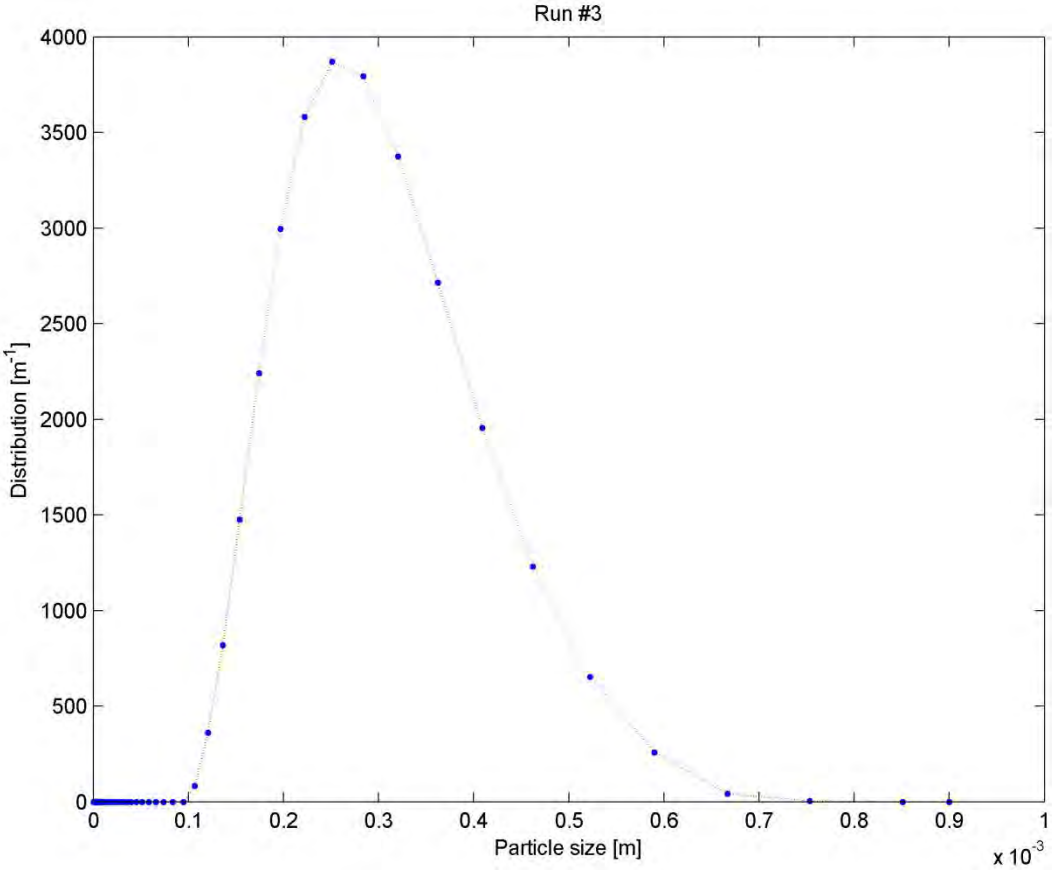

Figure 20.51: Particle size distribution for Experimental Run #3

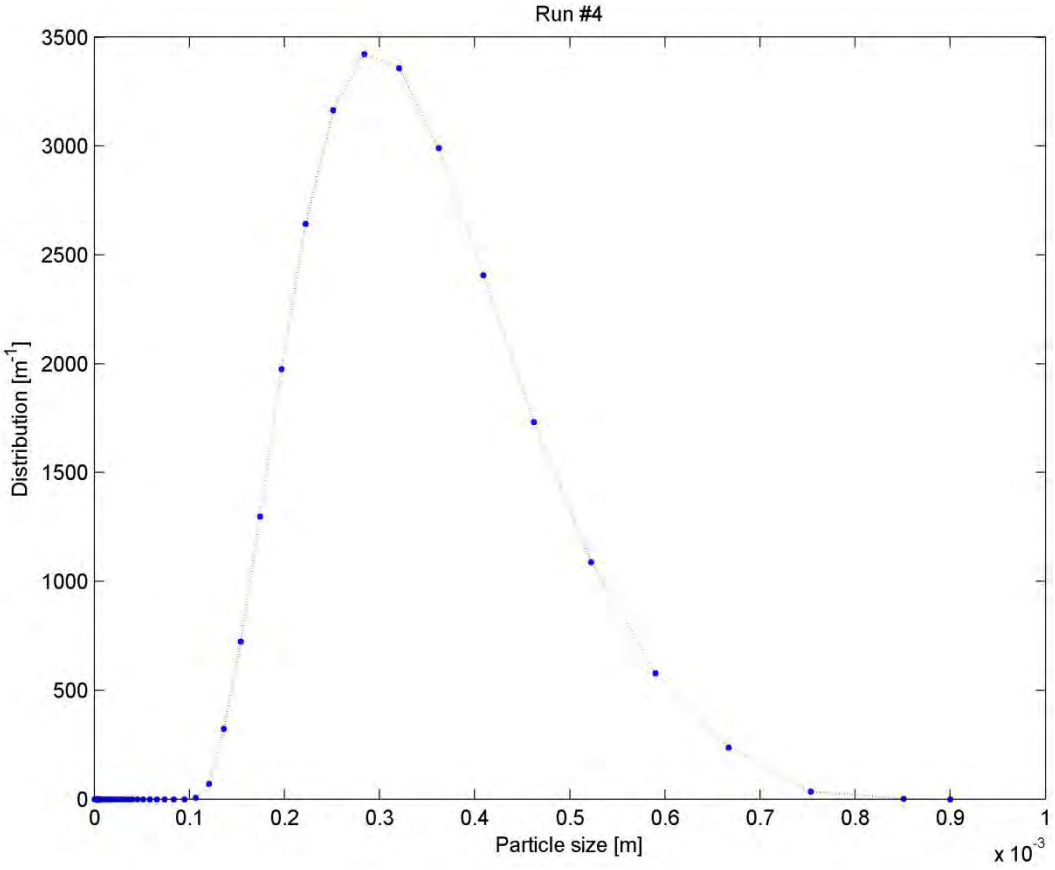

Figure 20.52: Particle size distribution for Experimental Run #4

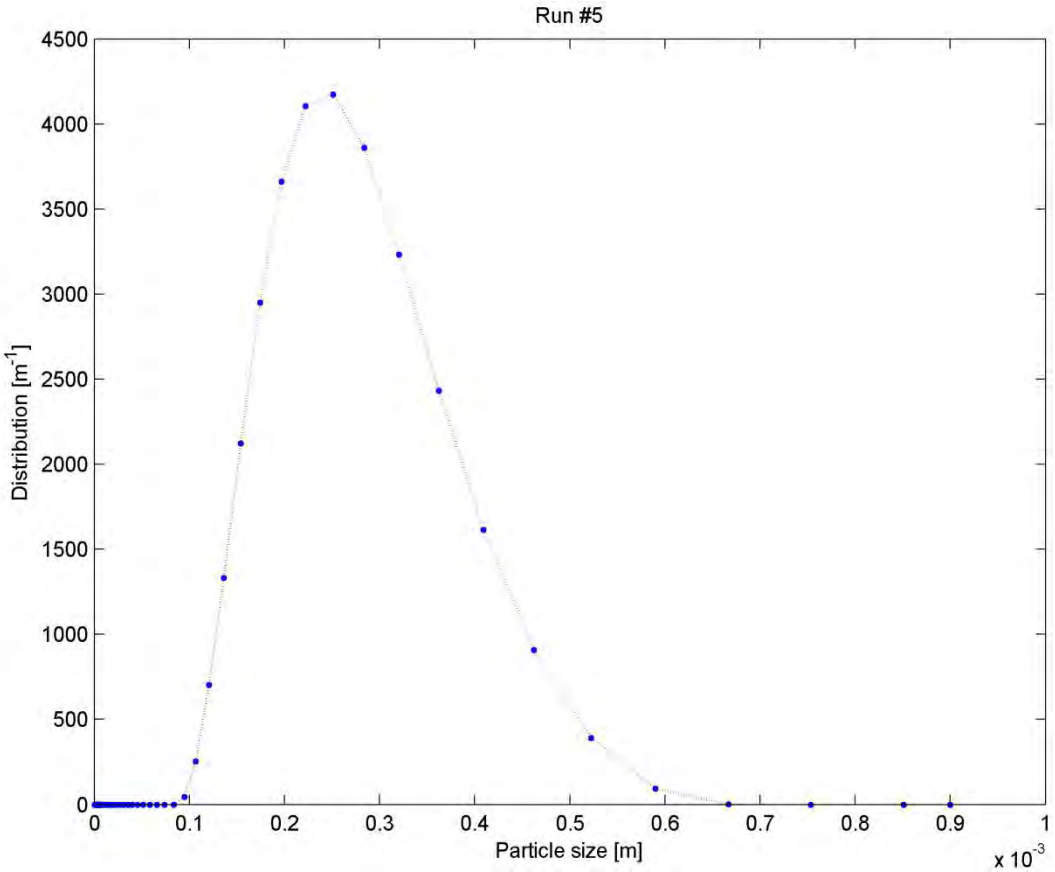

Figure 20.53: Particle size distribution for Experimental Run #5

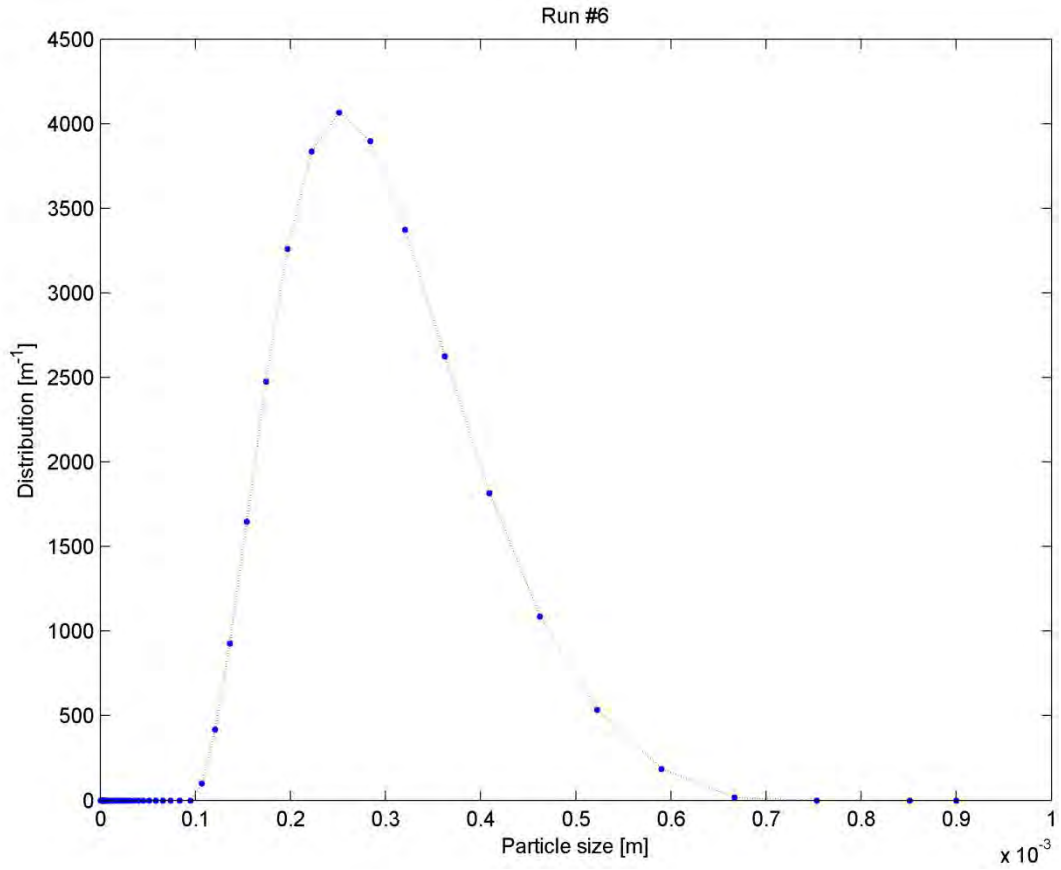

Figure 20.54: Particle size distribution for Experimental Run #6

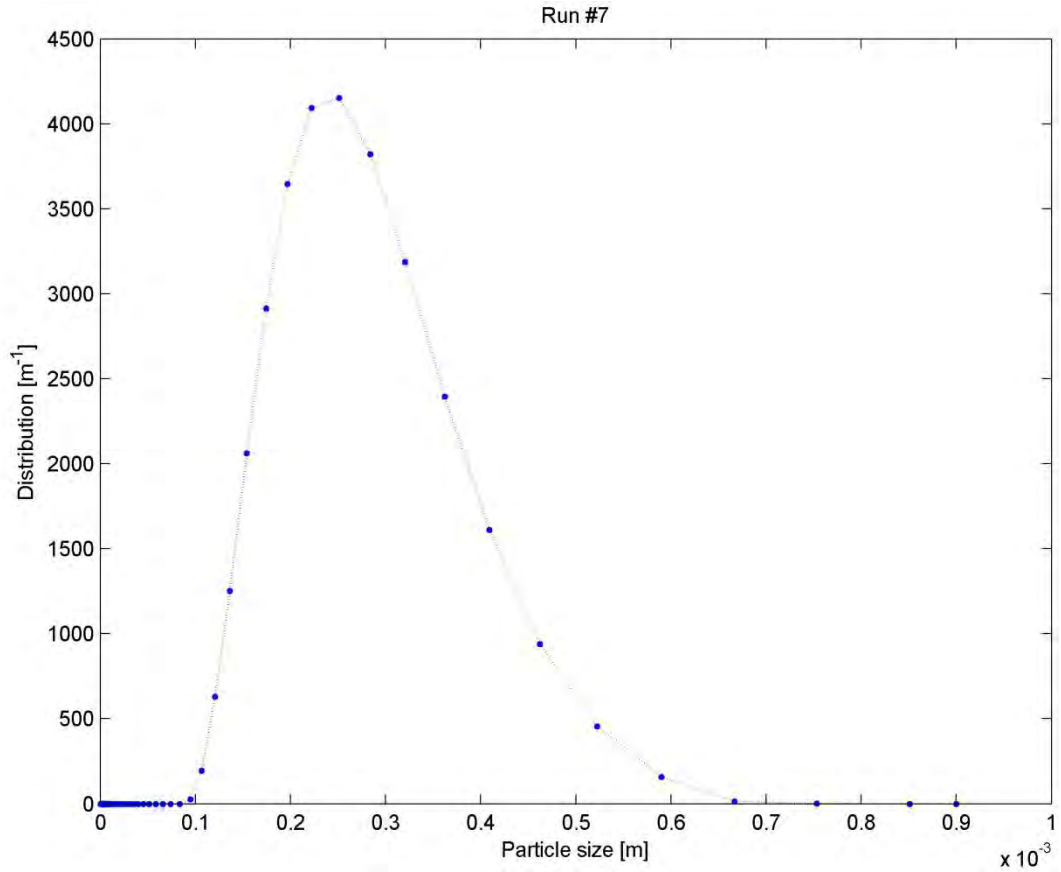

Figure 20.55: Particle size distribution for Experimental Run #7

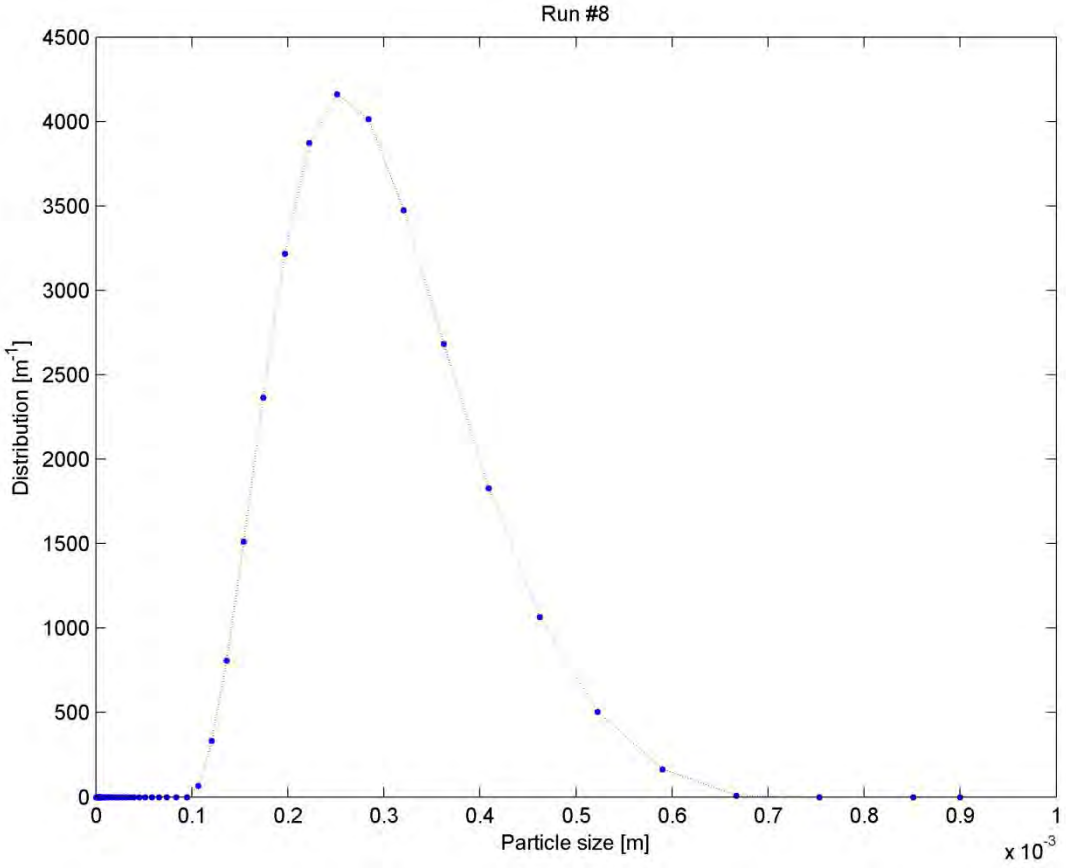

Figure 20.56: Particle size distribution for Experimental Run #8

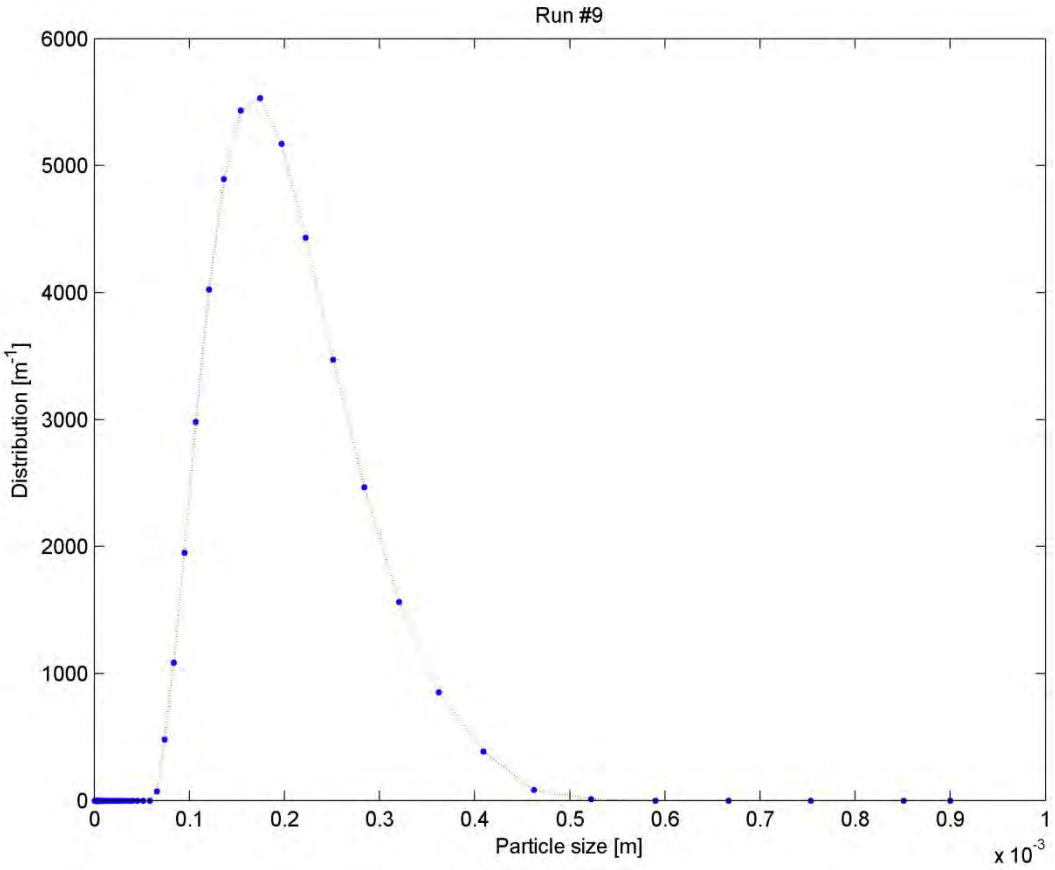

Figure 20.57: Particle size distribution for Experimental Run #9

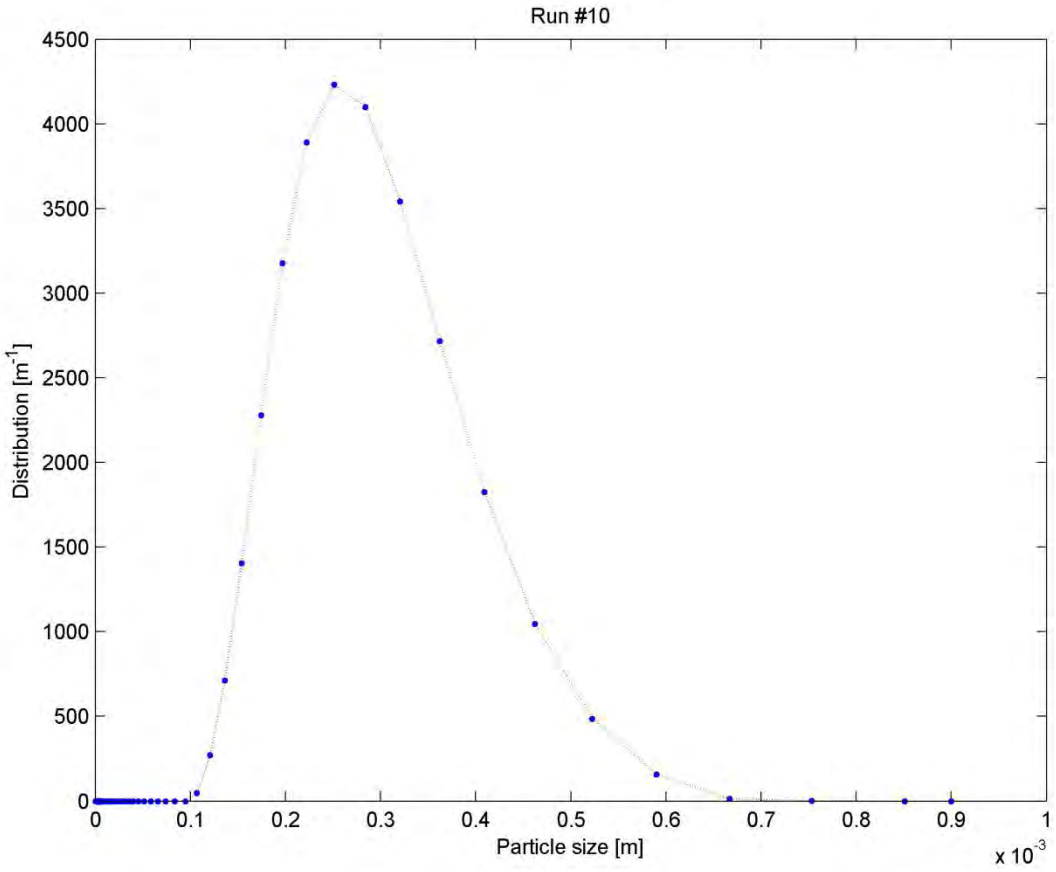

Figure 20.58: Particle size distribution for Experimental Run #10

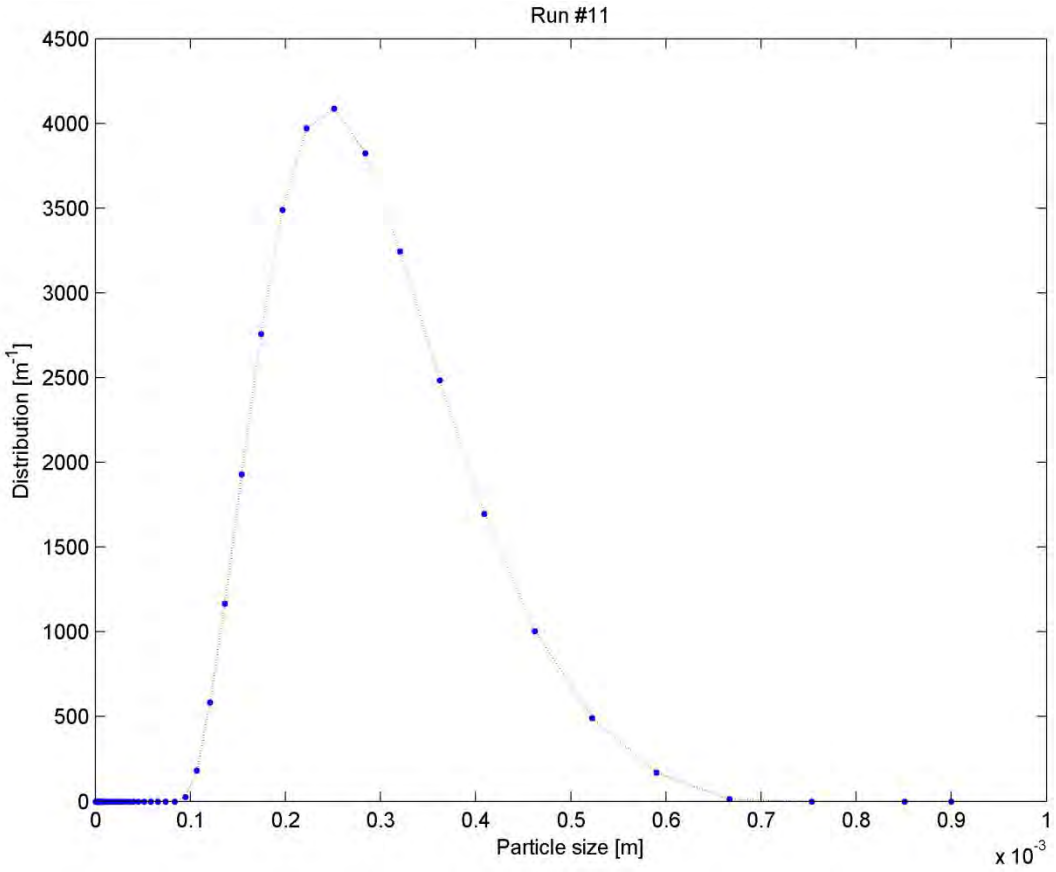

Figure 20.59: Particle size distribution for Experimental Run #11

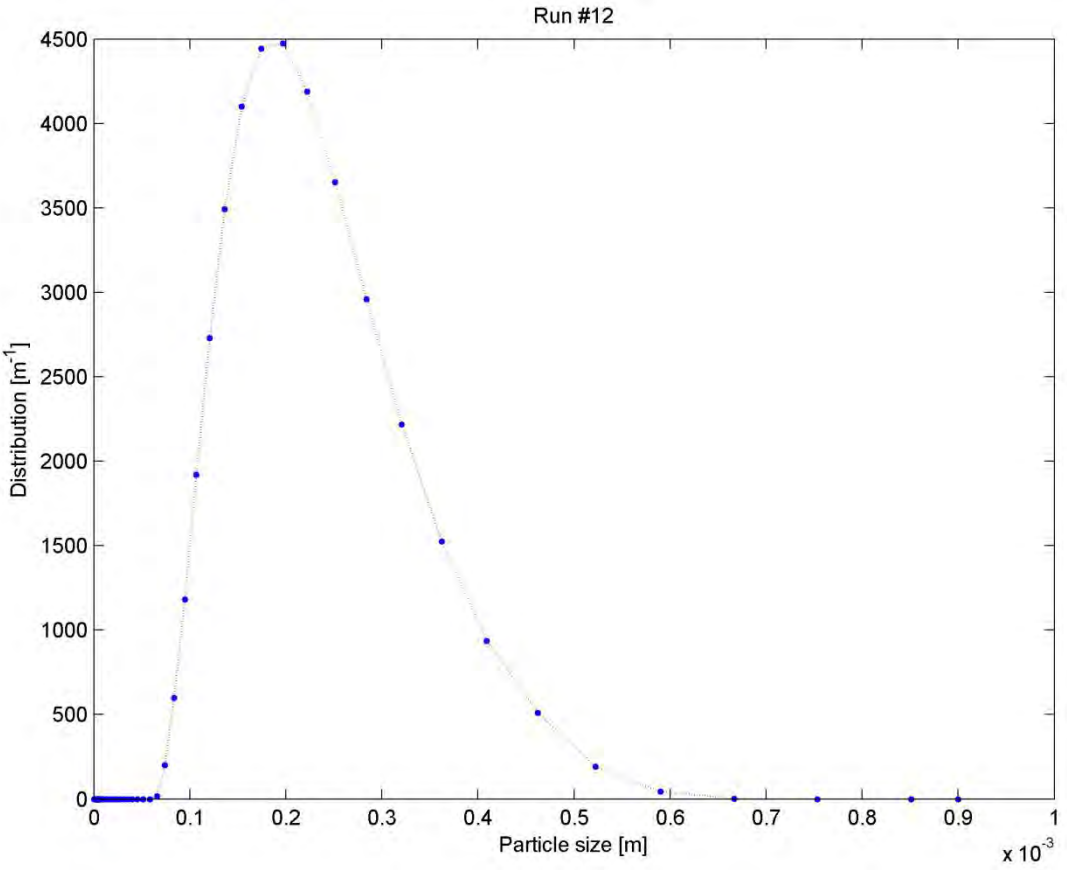

Figure 20.60: Particle size distribution for Experimental Run #12

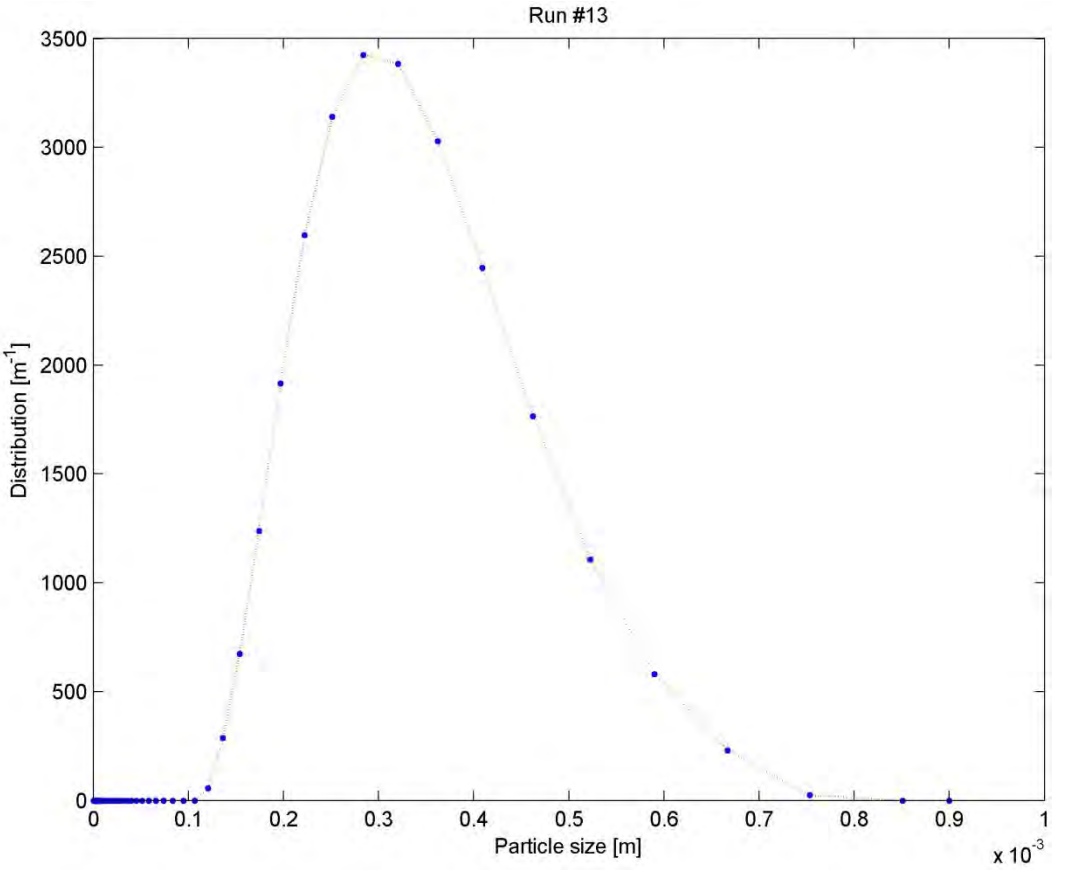

Figure 20.61: Particle size distribution for Experimental Run #13

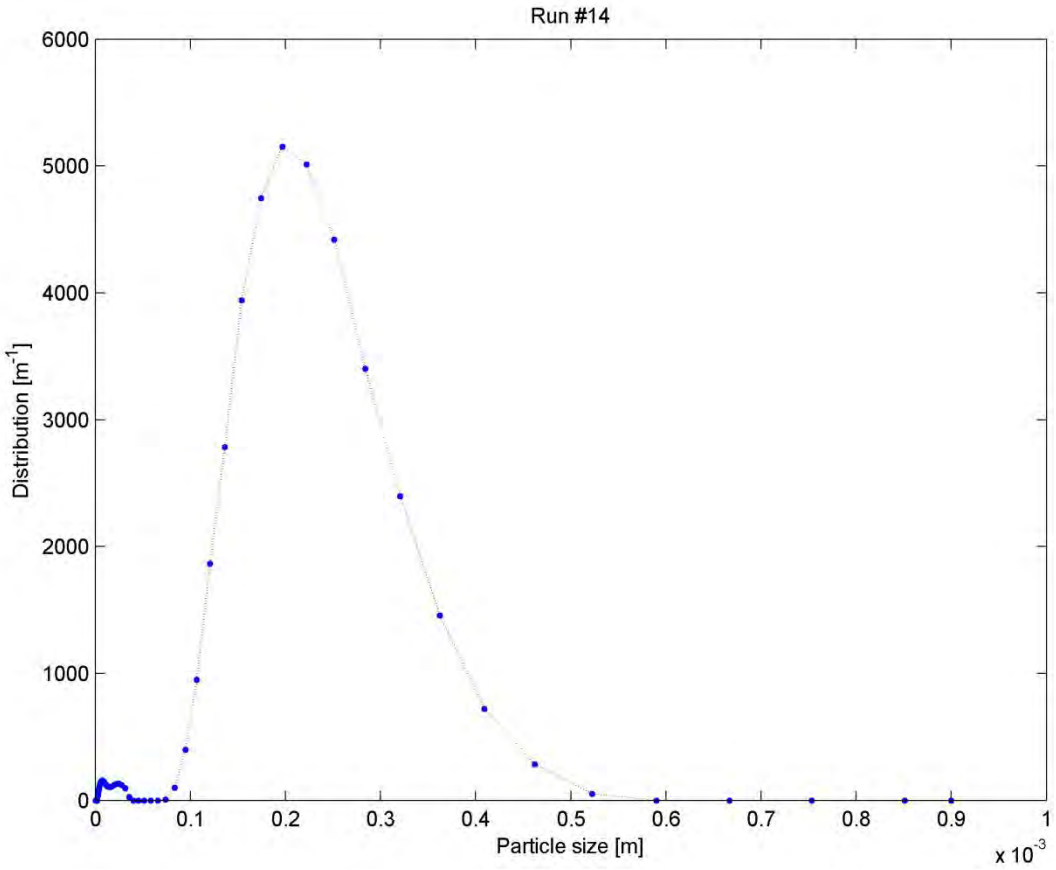

Figure 20.62: Particle size distribution for Experimental Run #14

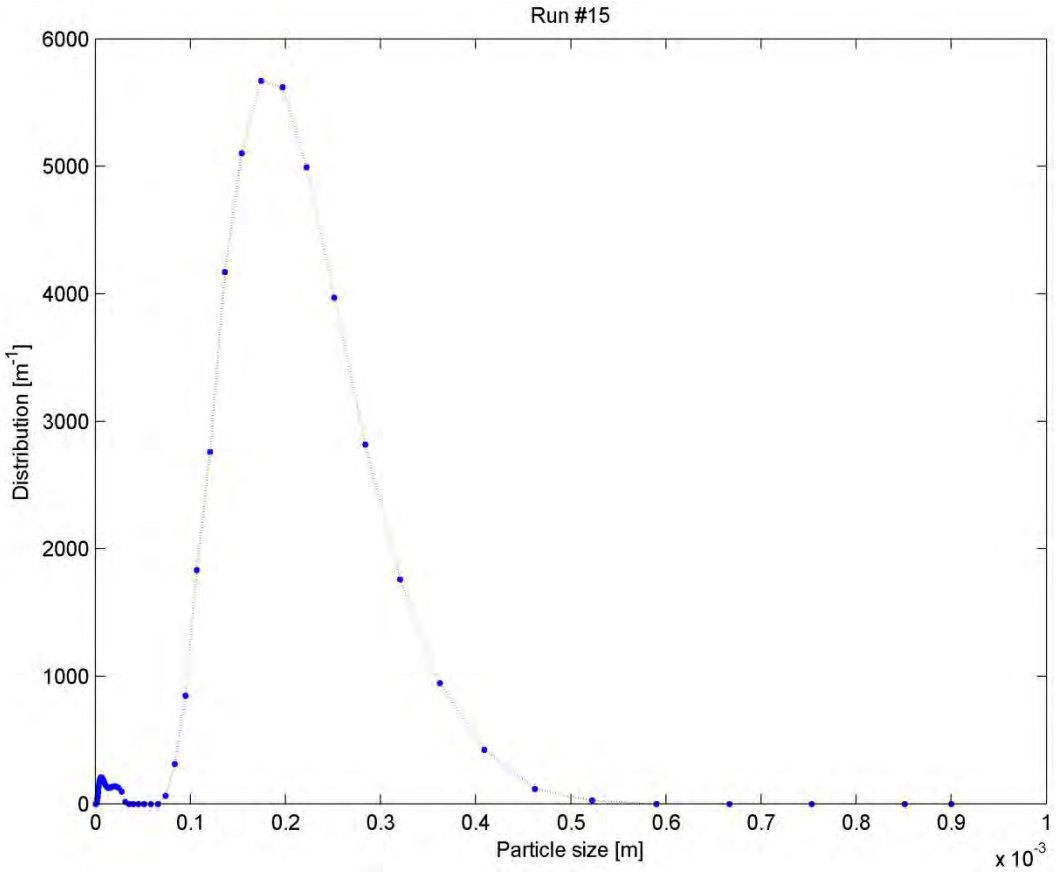

Figure 20.63: Particle size distribution for Experimental Run #15

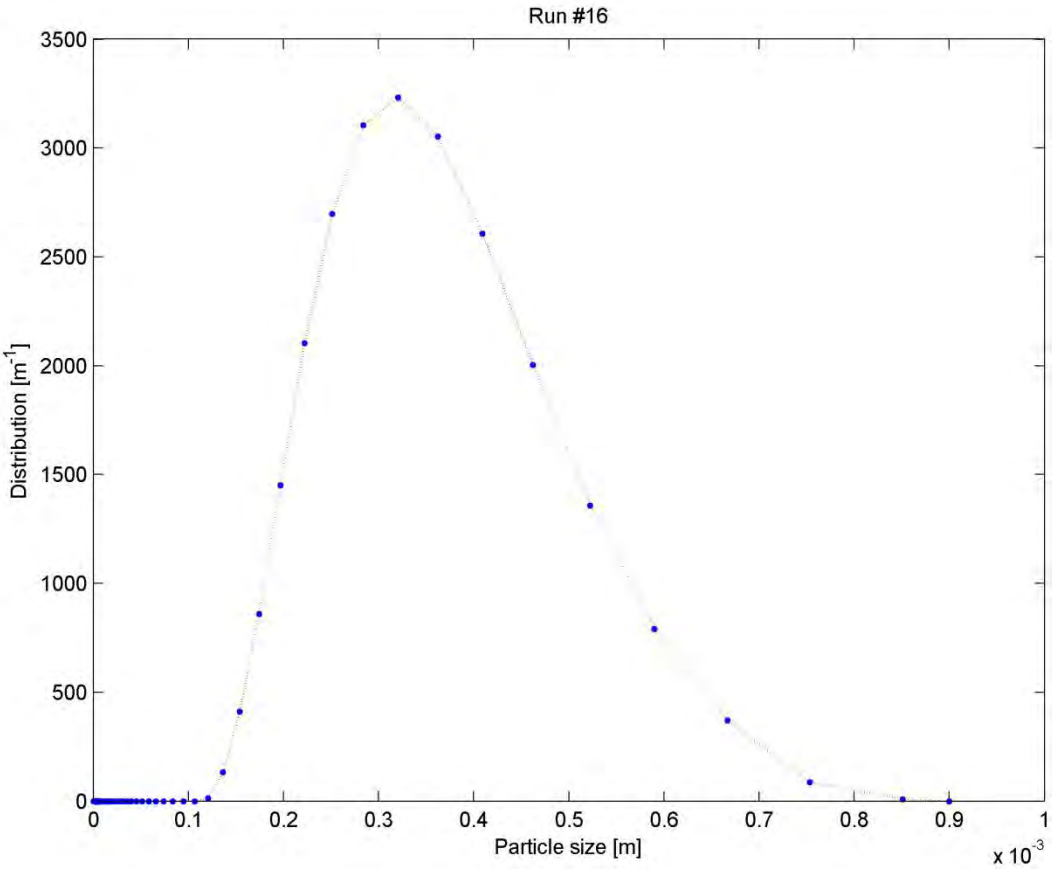

Figure 20.64: Particle size distribution for Experimental Run #16

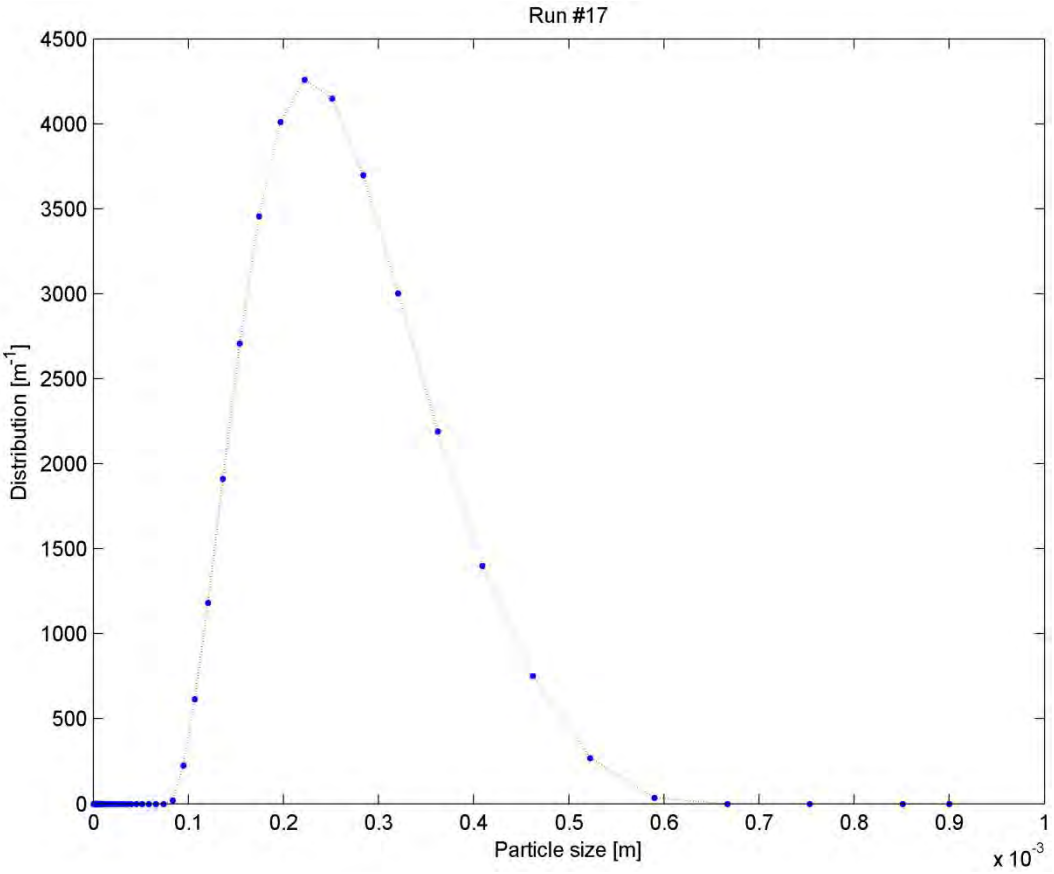

Figure 20.65: Particle size distribution for Experimental Run #17

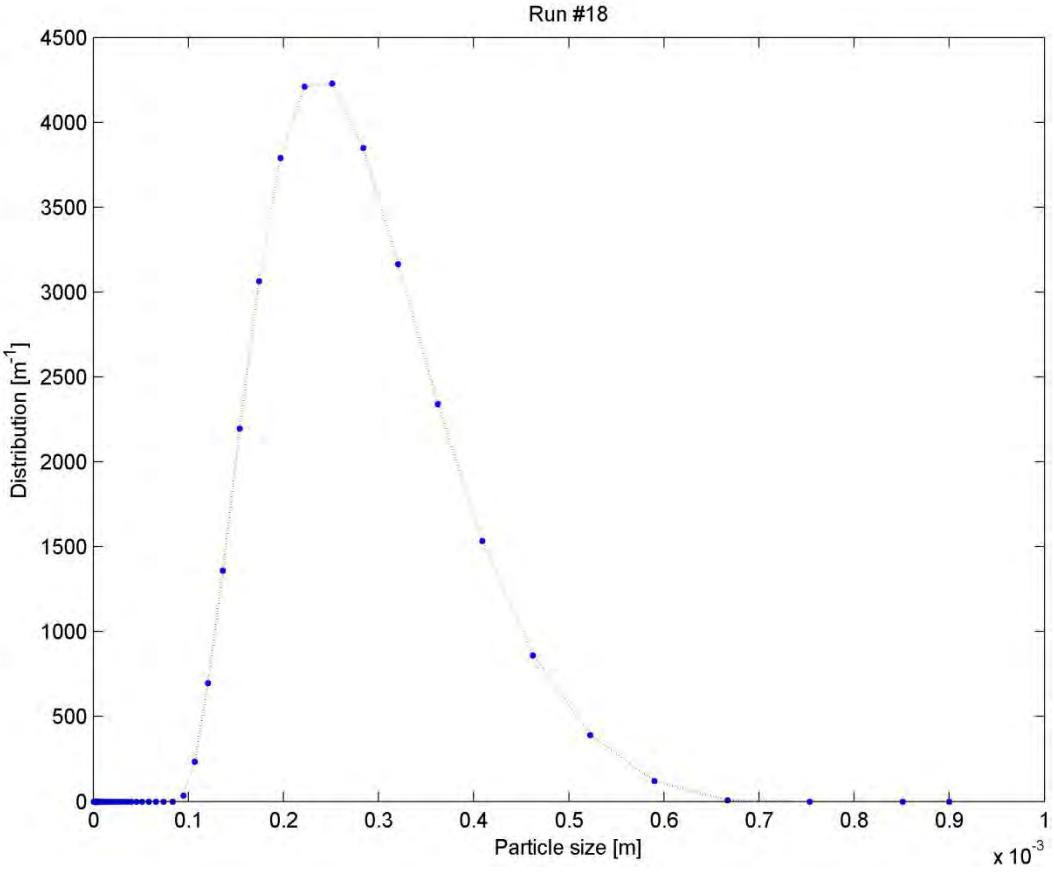

Figure 20.66: Particle size distribution for Experimental Run #18

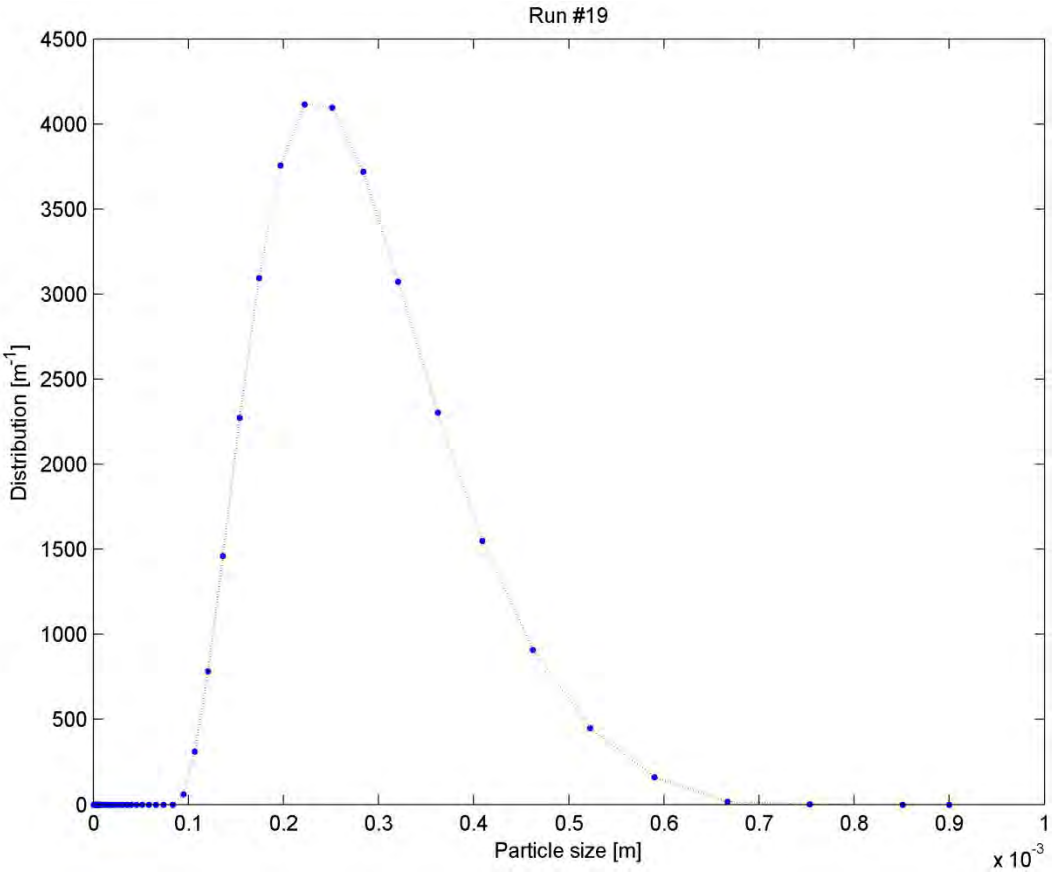

Figure 20.67: Particle size distribution for Experimental Run #19

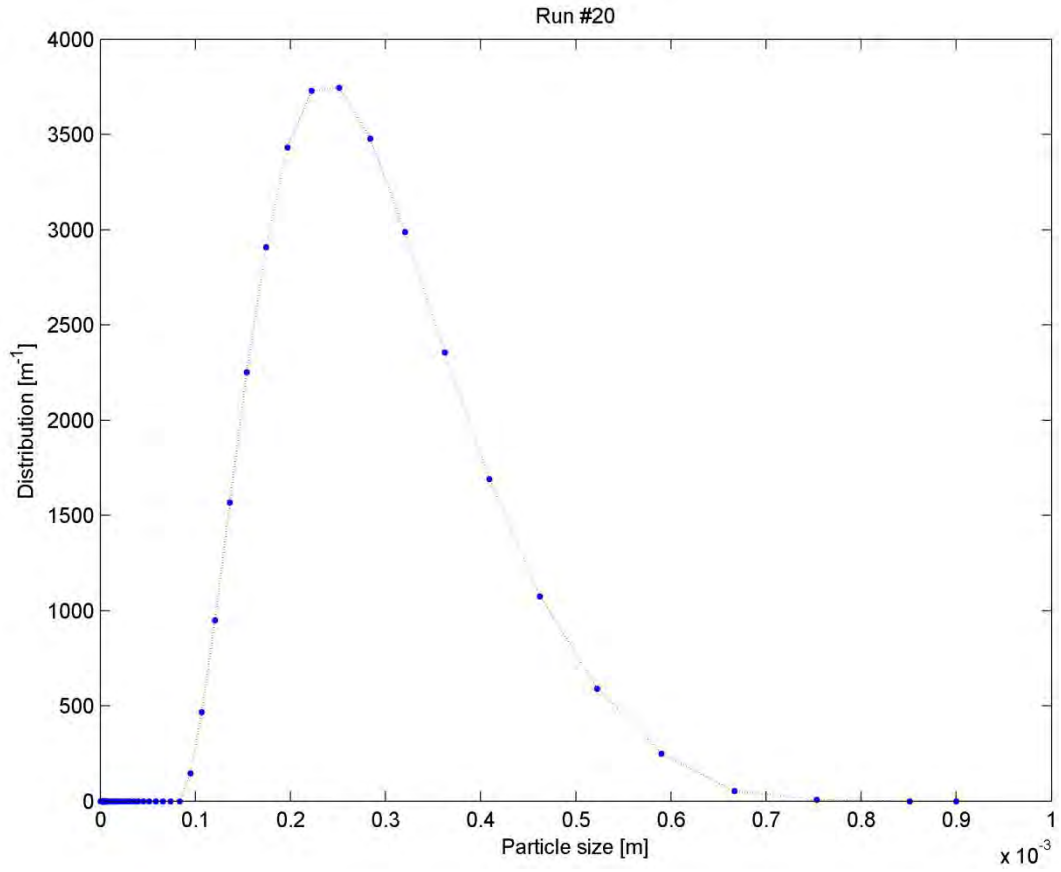

Figure 20.68: Particle size distribution for Experimental Run #20

20.5 SEM figures

The scanning electron microscopy images of two of the experimental runs are shown below.

20.5.1 Run #8

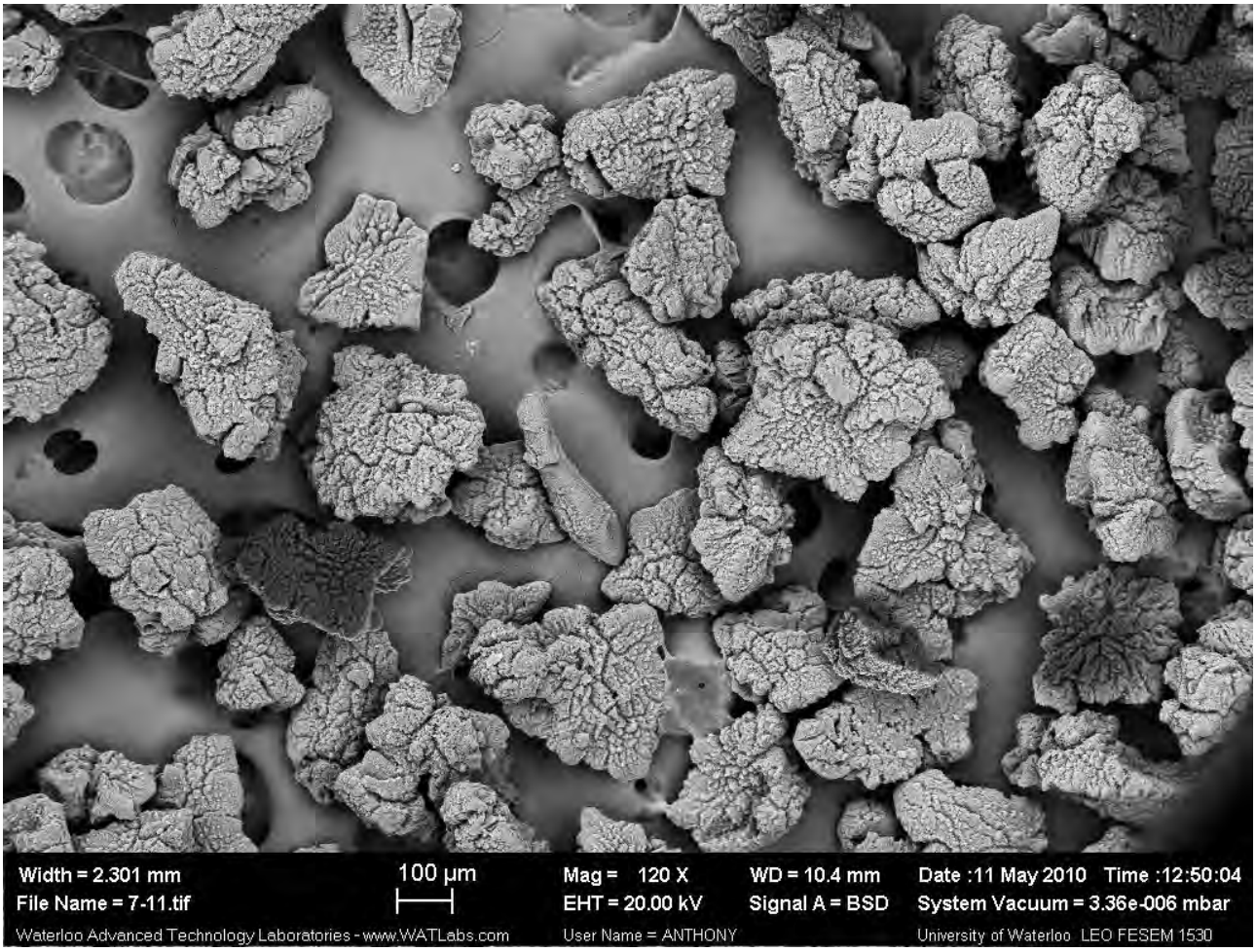

Figure 20.69: SEM of polymer sample from Run #8

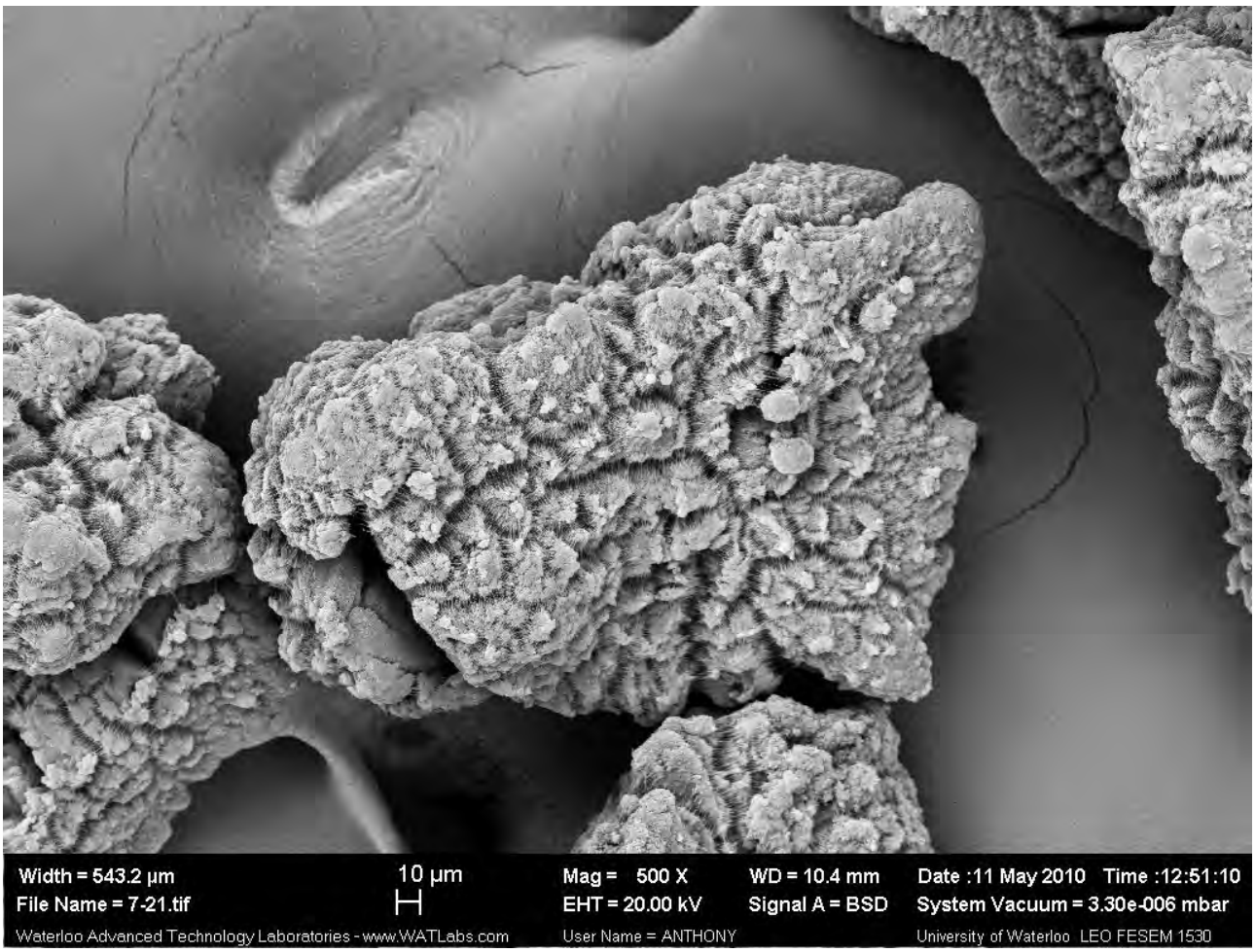

Figure 20.70: SEM of polymer sample from Run #8

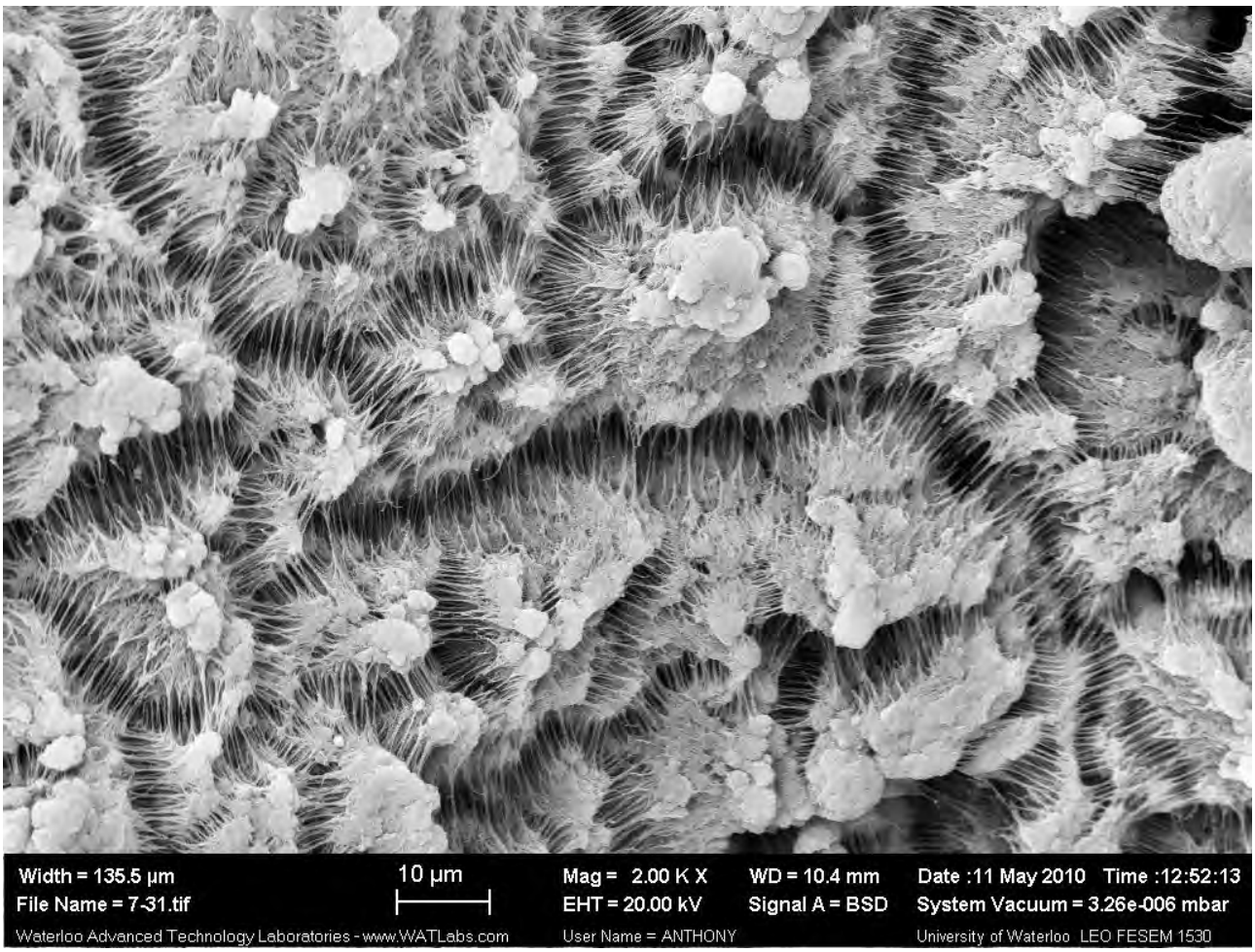

Figure 20.71: SEM of polymer sample from Run #8

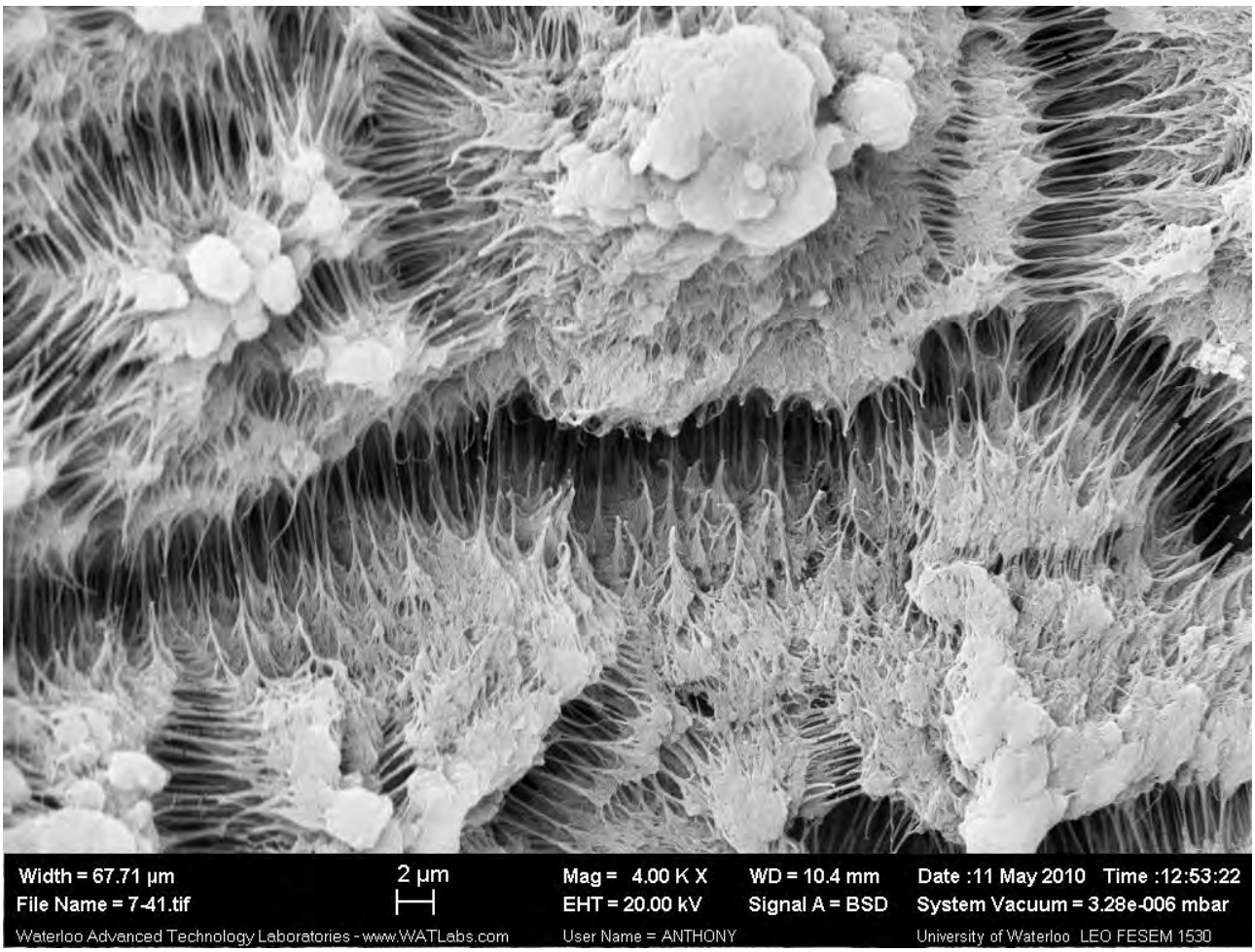

Figure 20.72: SEM of polymer sample from Run #8

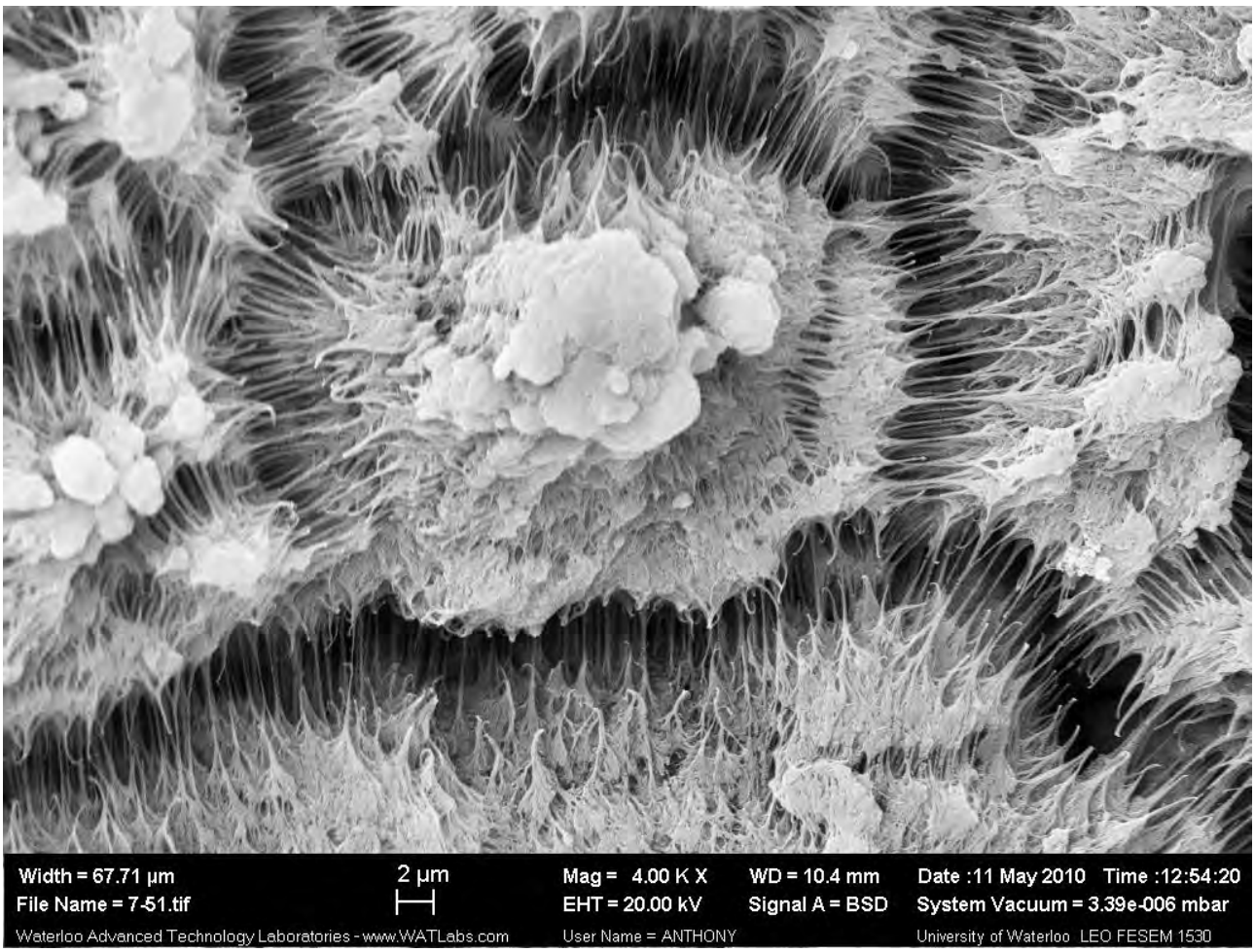

Figure 20.73: SEM of polymer sample from Run #8

20.5.2 Run #9

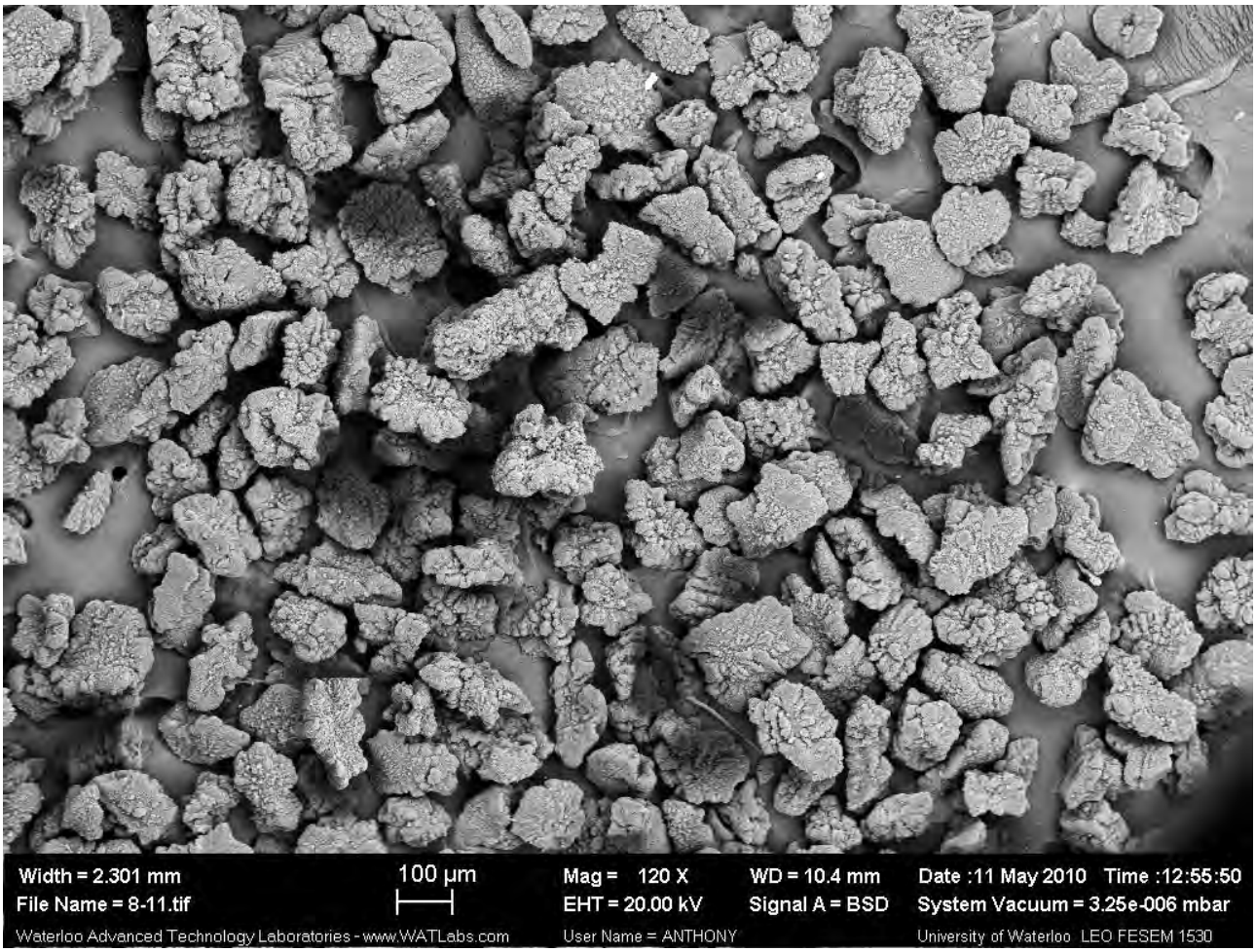

Figure 20.74: SEM of polymer sample from Run #9

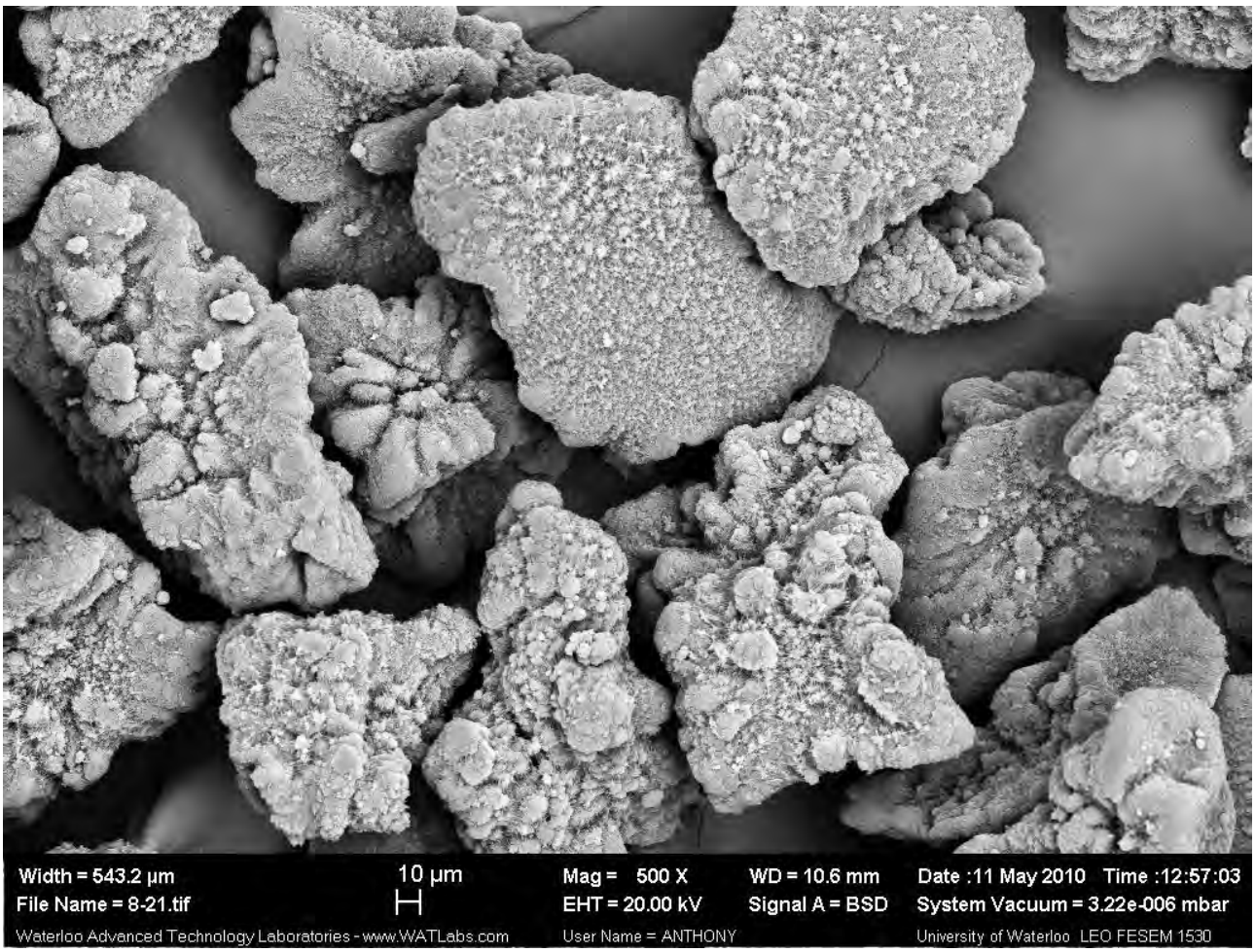

Figure 20.75: SEM of polymer sample from Run #9

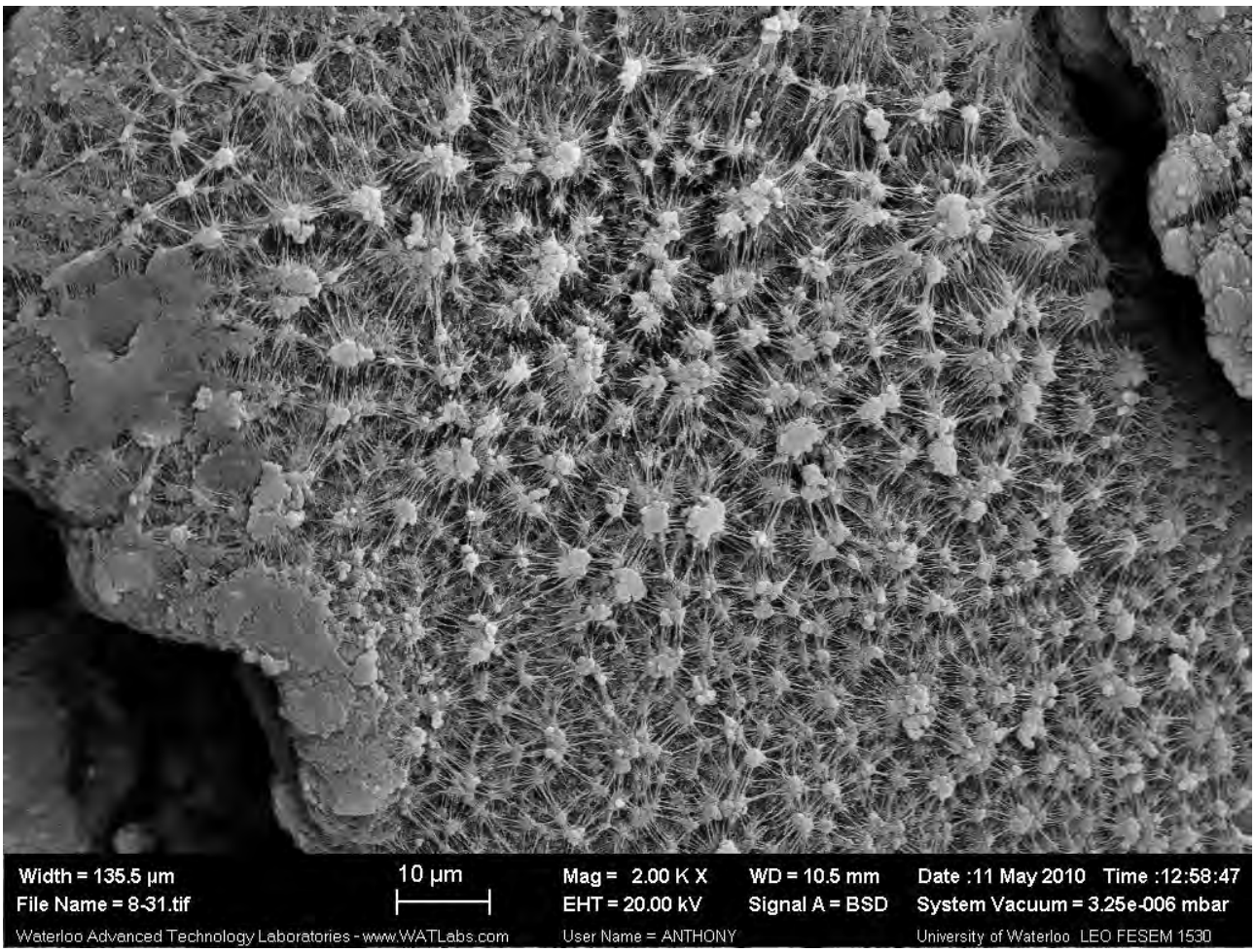

Figure 20.76: SEM of polymer sample from Run #9

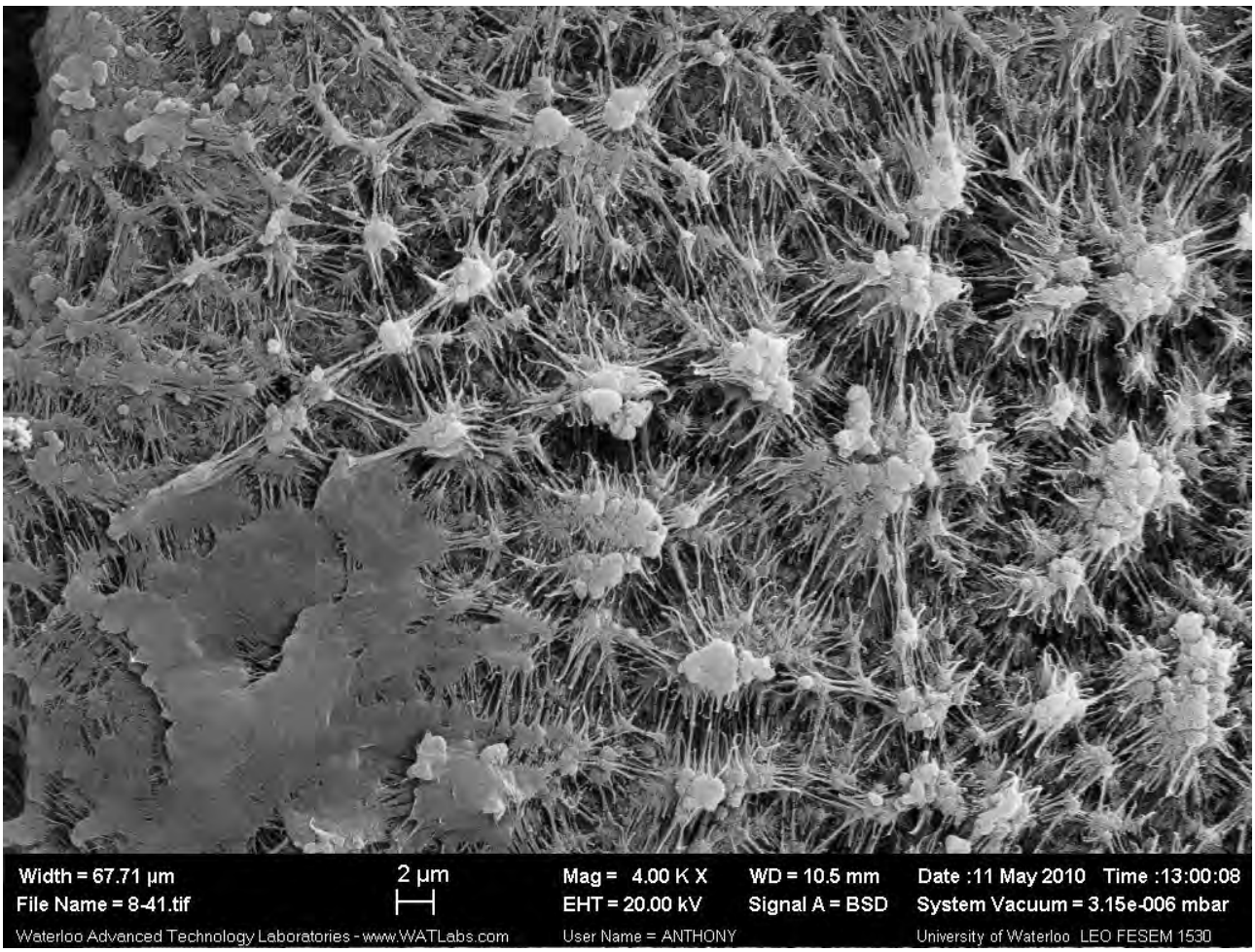

Figure 20.77: SEM of polymer sample from Run #9

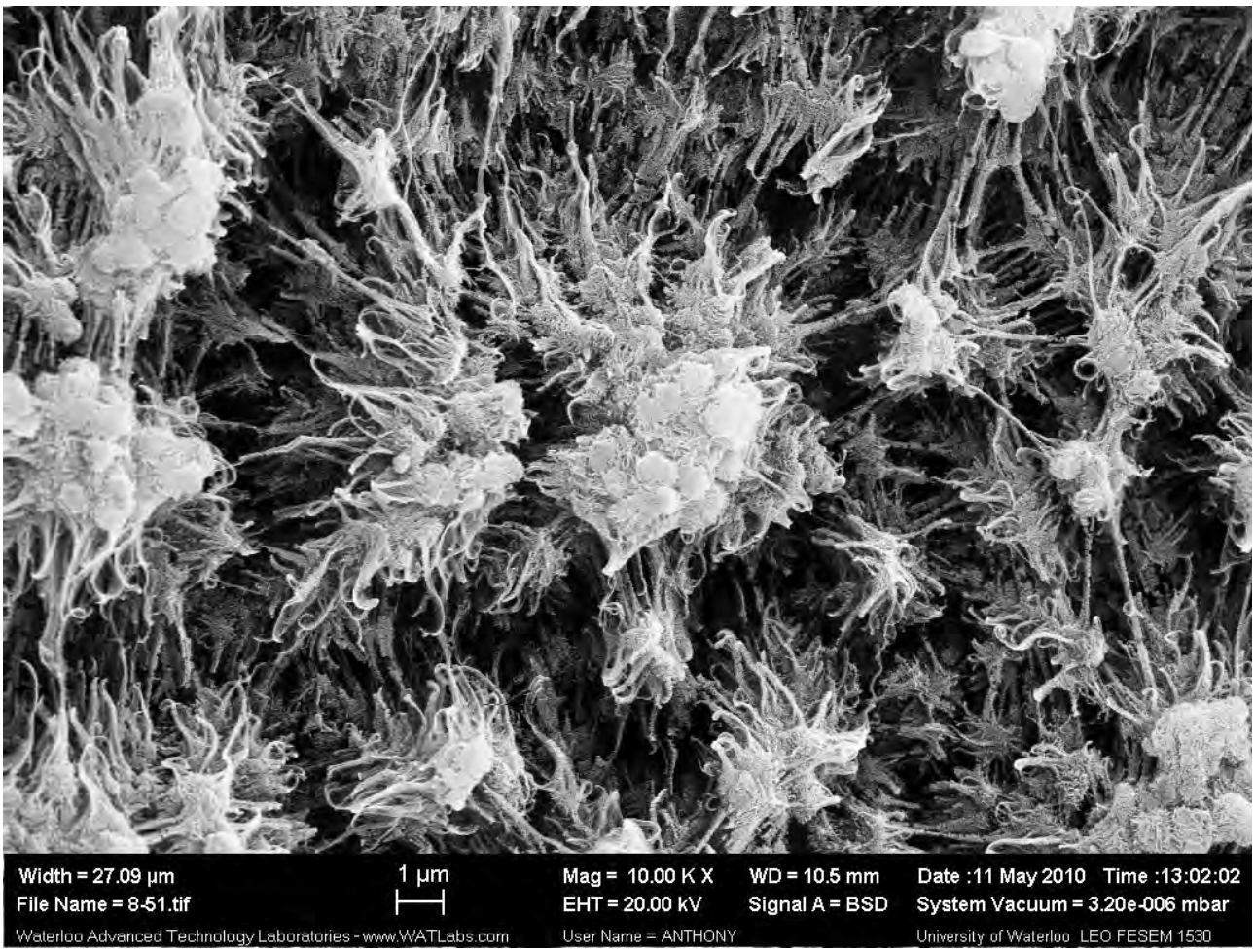

Figure 20.78: SEM of polymer sample from Run #9

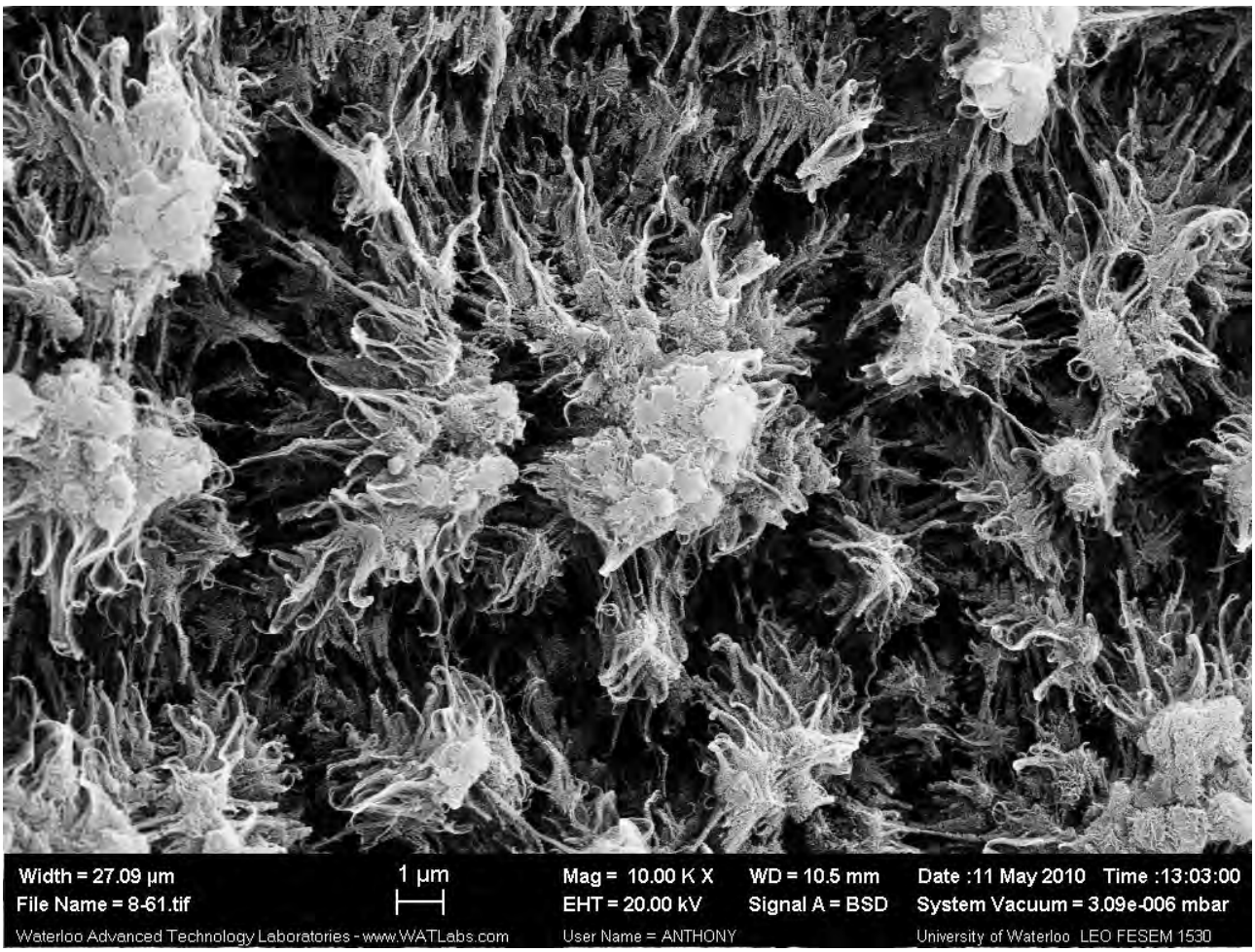

Figure 20.79: SEM of polymer sample from Run #9

CHAPTER 21. ISOTHERMAL FLASH CALCULATIONS

The Peng-Robinson Equation of State was used to determine the result isothermal flash of a multicomponent mixture. In this project, the calculation was set up for a flash of ethylene, 1-butene, hydrogen, and n-nonane or n-hexane. This set of components caters for the components present in both the laboratory and industrial reactors of interest.

Data for these components' critical constants (critical pressure and temperature, and compressibility factor), vapour pressure and binary interaction parameters were sourced from (Perry & Green, 1997) and (Sandler, 1998).

The output is the mole fractions of liquid and gas phases (x,y), the fraction of the feed which is in the liquid phase (L) and the liquid and vapour compressibility factors (ZL,ZV).

The isothermal flash calculation is based on algorithms presented in Sandler (1998); similar to the algorithm in Figure 21.1.

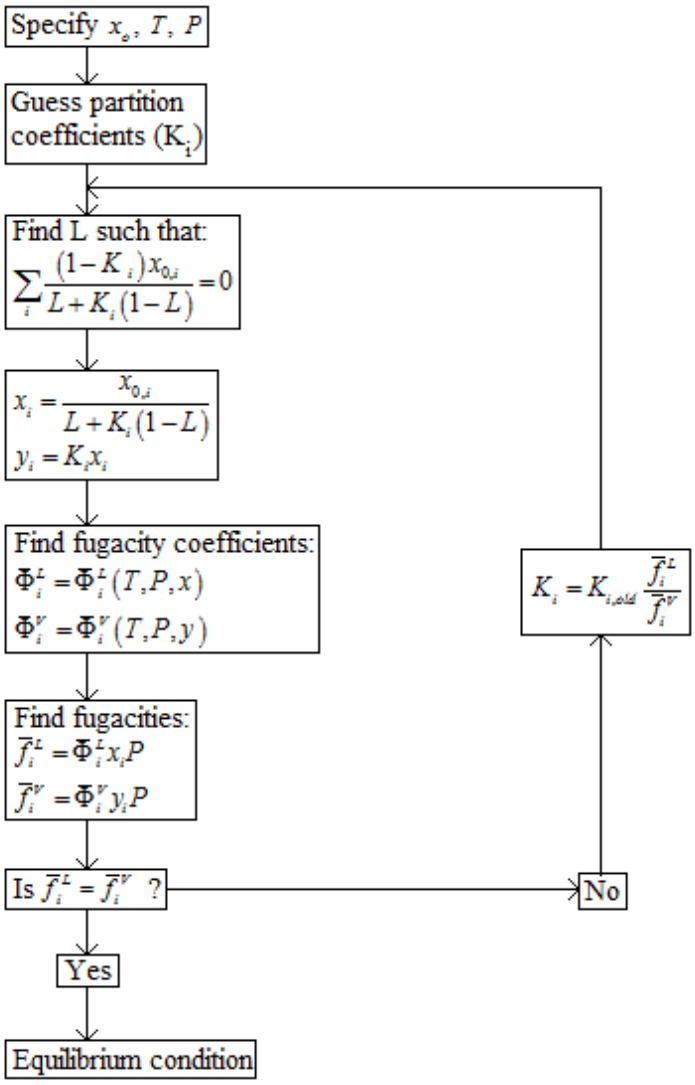

Figure 21.1: Algorithm for isothermal flash calculation

21.1 Peng-Robinson Equation of State (PR EoS)

The Equation of State used in this model was proposed by Peng & Robinson (1976), specifically to deal with systems involving hydrocarbons and non-polar gases.

For a single component, the PR EoS is expressed as:

$$P = \frac{RT}{V_m - b} - \frac{a(T)}{V_m(V_m + b) + b(V_m - b)}$$

Where

$$a(T) = 0.45724\ \alpha(T)\frac{(RT_c)^2}{P_c}$$

$$b = 0.0778\frac{RT_c}{P_c}$$

$$\alpha(T) = \left(1 + \kappa\sqrt{1 - T/T_c}\right)^2$$

$$\kappa = 0.37464 + 1.54226\ \omega - 0.26992\ \omega^2$$

The PR EoS can also be expressed in cubic form:

$$Z^3 - (1 - B)Z^2 + (\mathrm{A} - 3\mathrm{B}^2 - 2B)Z - (AB - B^2 - B^3) = 0$$

Where

$$A = \frac{aP}{(RT)^2}$$

$$B = \frac{bP}{RT}$$

$$Z = \frac{V_m P}{RT}$$

For the case of multicomponent systems, the van der Waals mixing rules are used to find the values of the parameters for the mixture:

$$a = \sum_i \sum_j y_i y_j a_{ij}$$

$$b = \sum_i y_i b_i$$

$$a_{ij} = a_{ji} = \sqrt{a_i a_j}\left(1 - k_{ij}\right)$$

where k_{ij} is a binary interaction parameter, which will be close to zero for similar components, and increasingly large (either negative OR positive) as components become more dissimilar (Peng &Robinson, 1976). Values for some interaction parameters are available in Sandler (1998), and others were found in the databases of the Aspen process simulator.

In order to use the PR EoS for vapour-liquid equilibrium calculations, we need to find the fugacity coefficients for each component in each phase. From these we can find the fugacity of each component, and determine equilibrium, which is when:

$$\bar{f}_i^L = \bar{f}_i^V$$

for all components i.

Fugacity coefficients (and the relationship between fugacity and fugacity coefficient) are found using the following equations:

$$\ln \Phi_i^L\left(T,P,x_i\right) = \ln \frac{\bar{f}_i^L\left(T,P,x_i\right)}{x_i P}$$

$$= \frac{B_i}{B}\left(Z^L - 1\right) - \ln\left(Z^L - B\right) - \frac{A}{2\sqrt{2}B}\left(\frac{2\sum_j x_i A_{ij}}{A} - \frac{B_i}{B}\right)\ln\left(\frac{Z^L + \left(\sqrt{2}+1\right)B}{Z^L - \left(\sqrt{2}-1\right)B}\right)$$

$$\ln \Phi_i^V\left(T,P,y_i\right) = \ln \frac{\bar{f}_i^V\left(T,P,y_i\right)}{y_i P}$$

$$= \frac{B_i}{B}\left(Z^V - 1\right) - \ln\left(Z^V - B\right) - \frac{A}{2\sqrt{2}B}\left(\frac{2\sum_j y_i A_{ij}}{A} - \frac{B_i}{B}\right)\ln\left(\frac{Z^V + \left(\sqrt{2}+1\right)B}{Z^V - \left(\sqrt{2}-1\right)B}\right)$$

where Z^L and Z^V are the roots of the cubic form the equation of state, corresponding to the compressibility factors for the liquid and vapour phases, respectively.

CHAPTER 22. REGRESSION OF EXPERIMENTAL DATA

Non-linear least-squares regression – lumped parameters to rate curves

The figures below show the results of the first non-linear regression step, in which the initial guesses for the propagation rate parameter and three lumped site transformation rate parameters are used to fit an activity curve to each experimental activity profile.

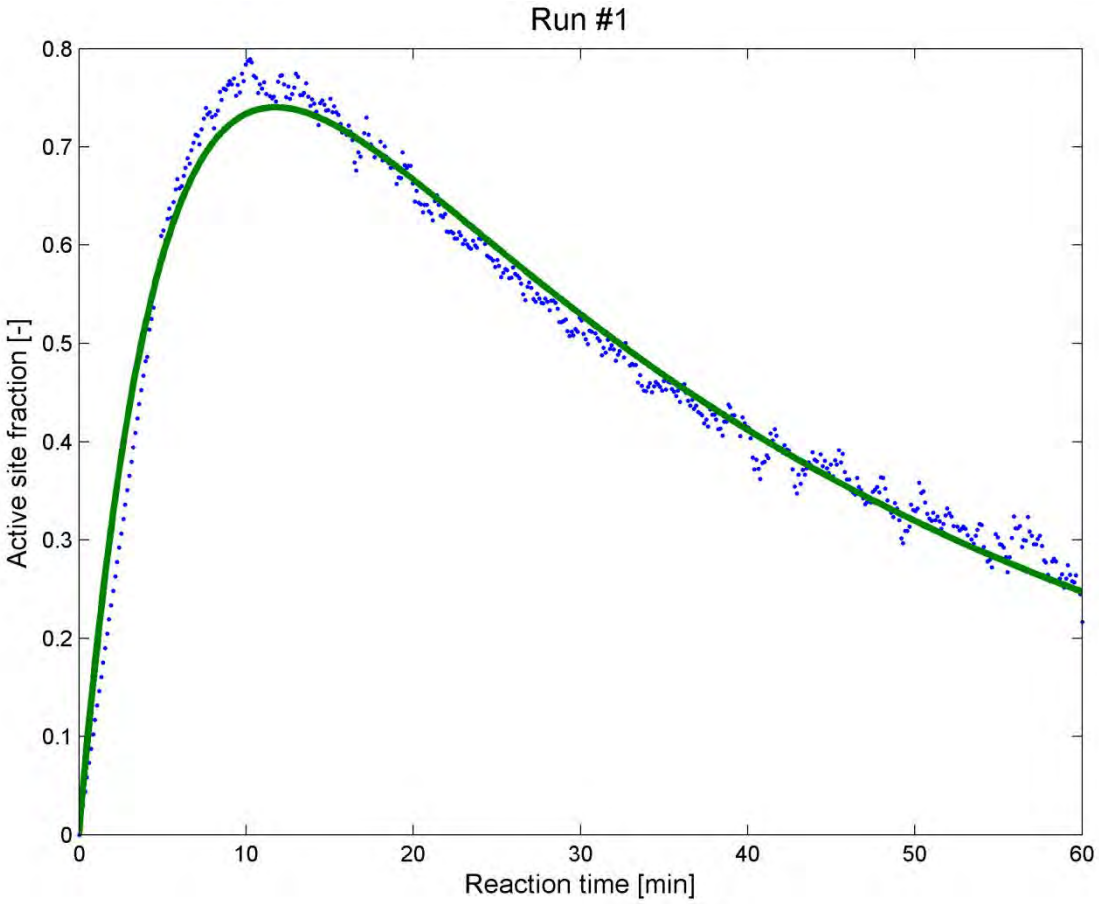

Figure 22.1: Fitting lumped parameters to activity profiles, Experimental Run #1

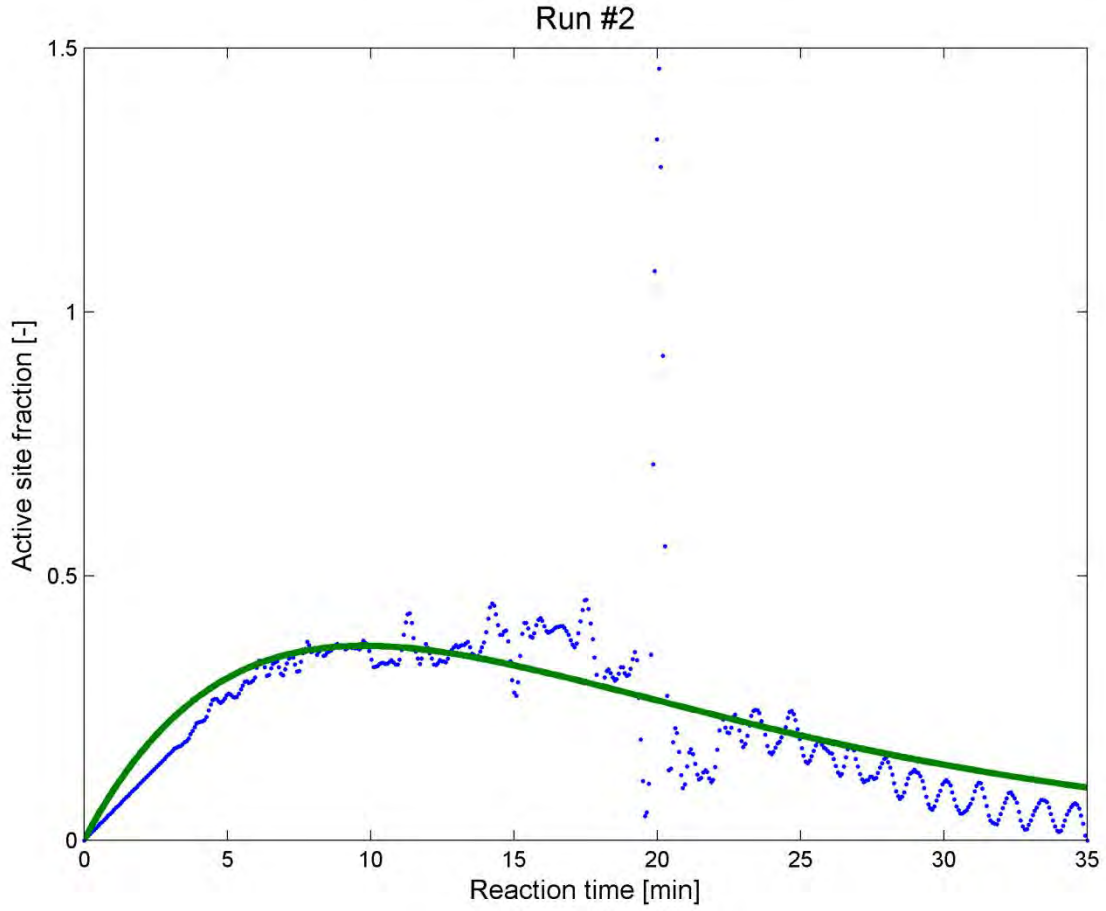

Figure 22.2: Fitting lumped parameters to activity profiles, Experimental Run #2

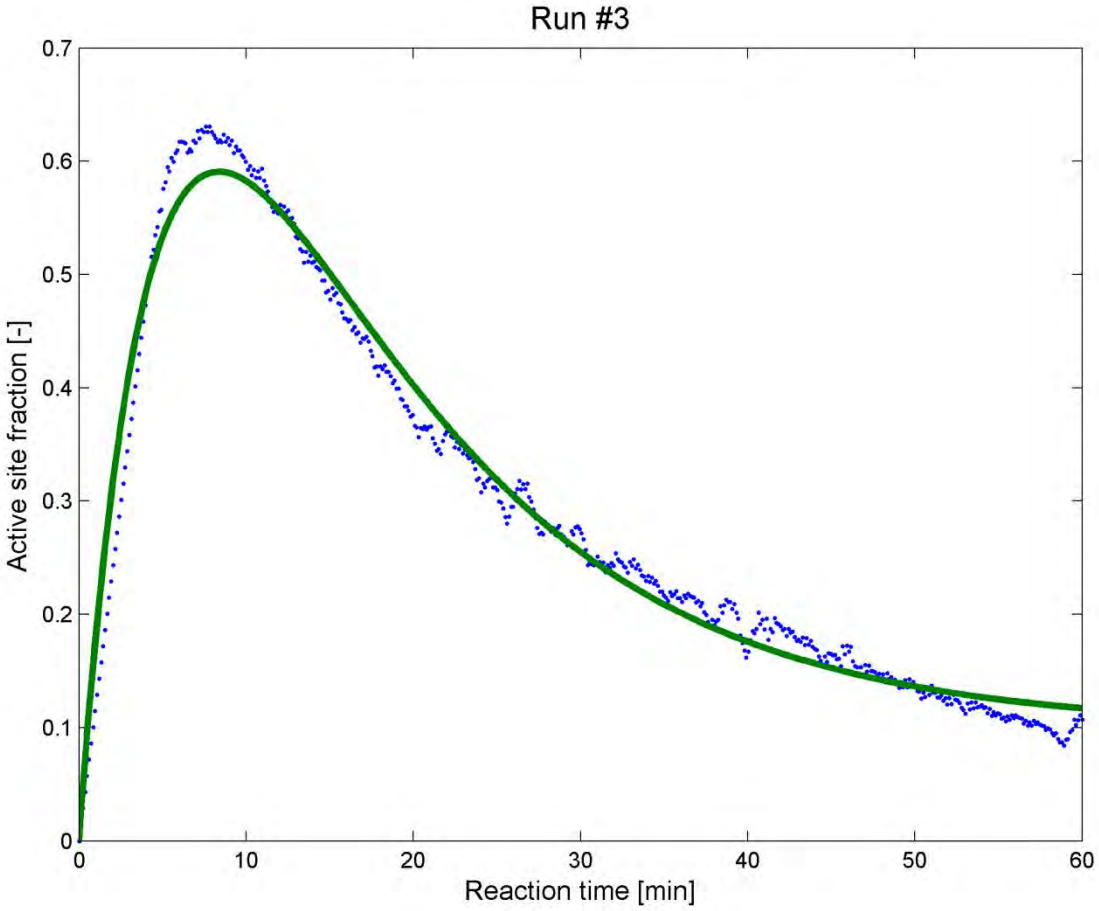

Figure 22.3: Fitting lumped parameters to activity profiles, Experimental Run #3

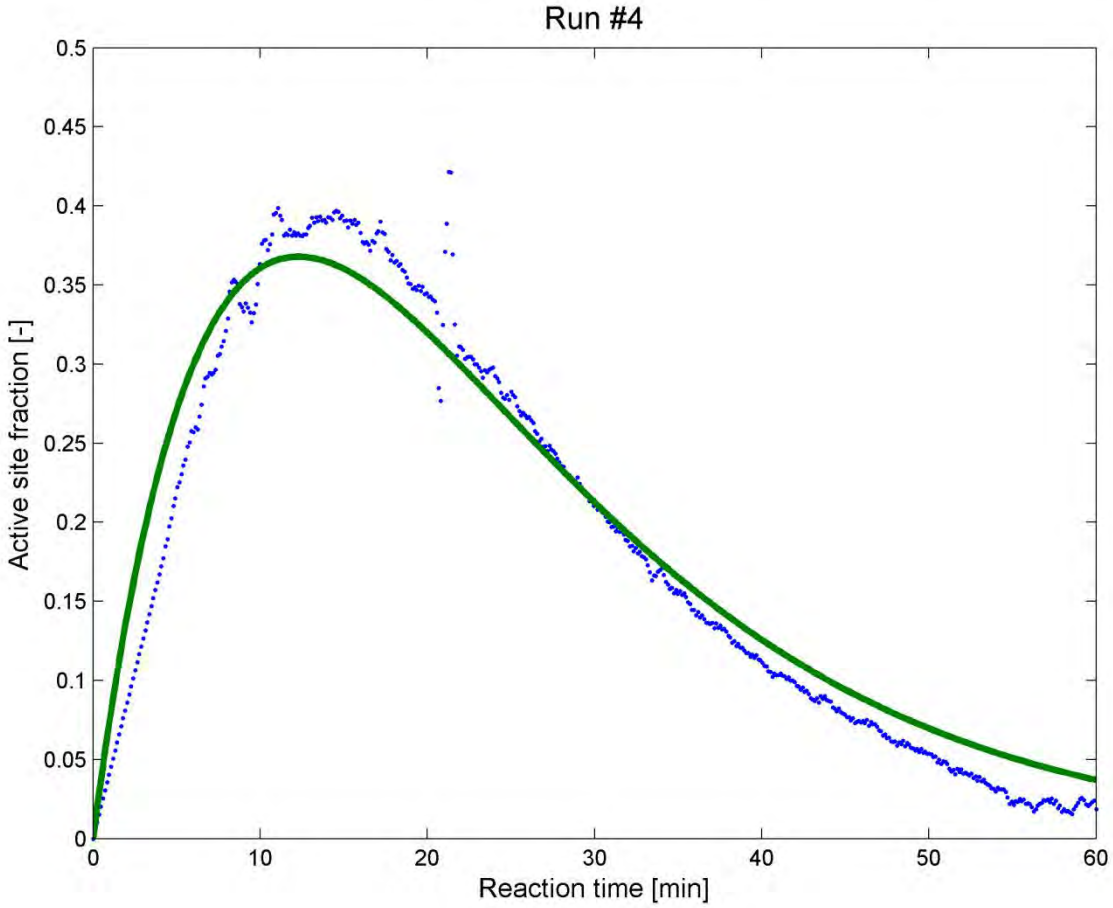

Figure 22.4: Fitting lumped parameters to activity profiles, Experimental Run #4

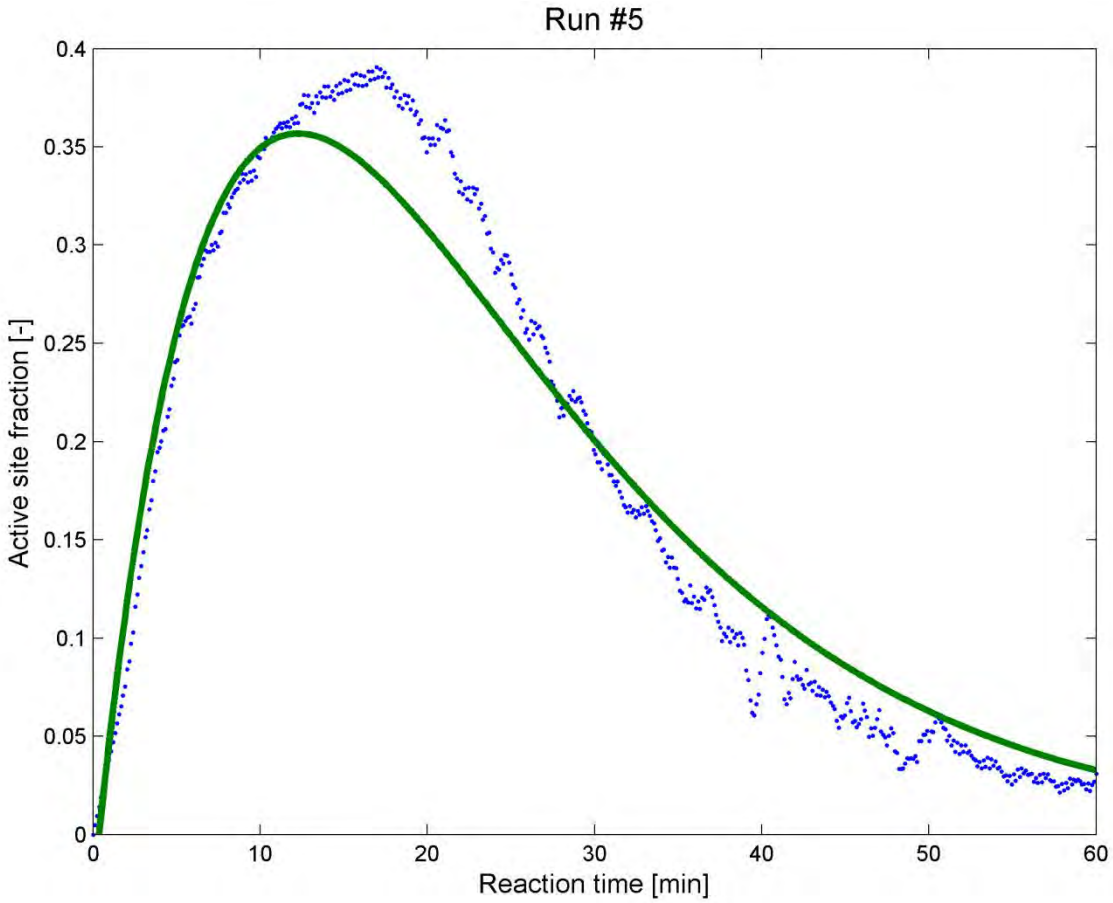

Figure 22.5: Fitting lumped parameters to activity profiles, Experimental Run #5

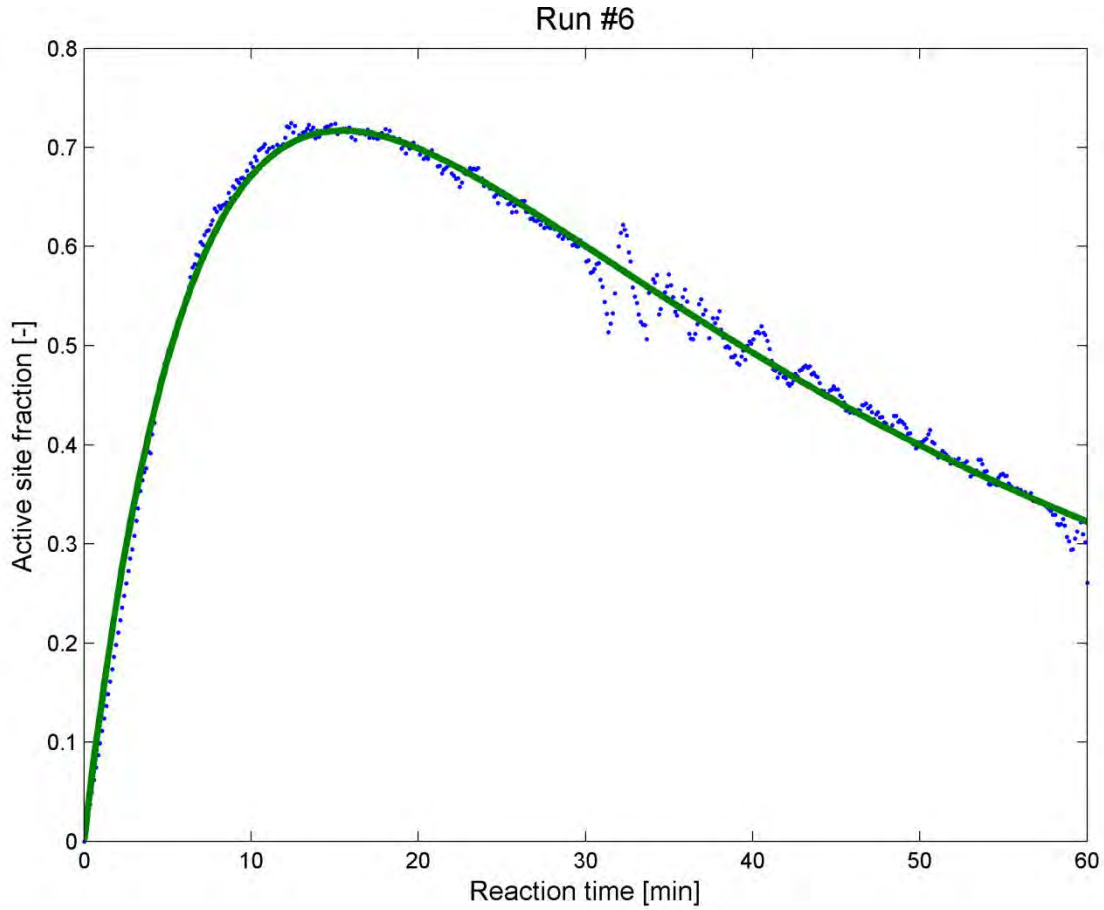

Figure 22.6: Fitting lumped parameters to activity profiles, Experimental Run #6

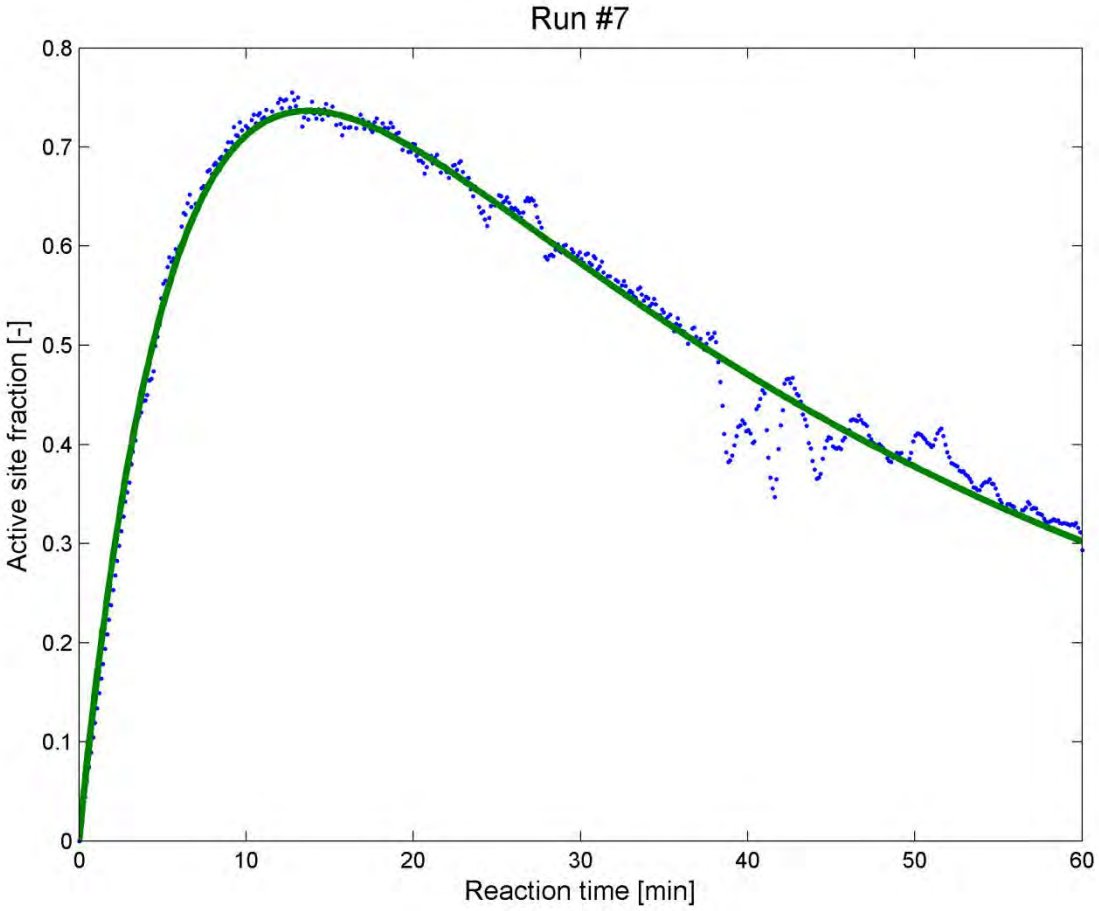

Figure 22.7: Fitting lumped parameters to activity profiles, Experimental Run #7

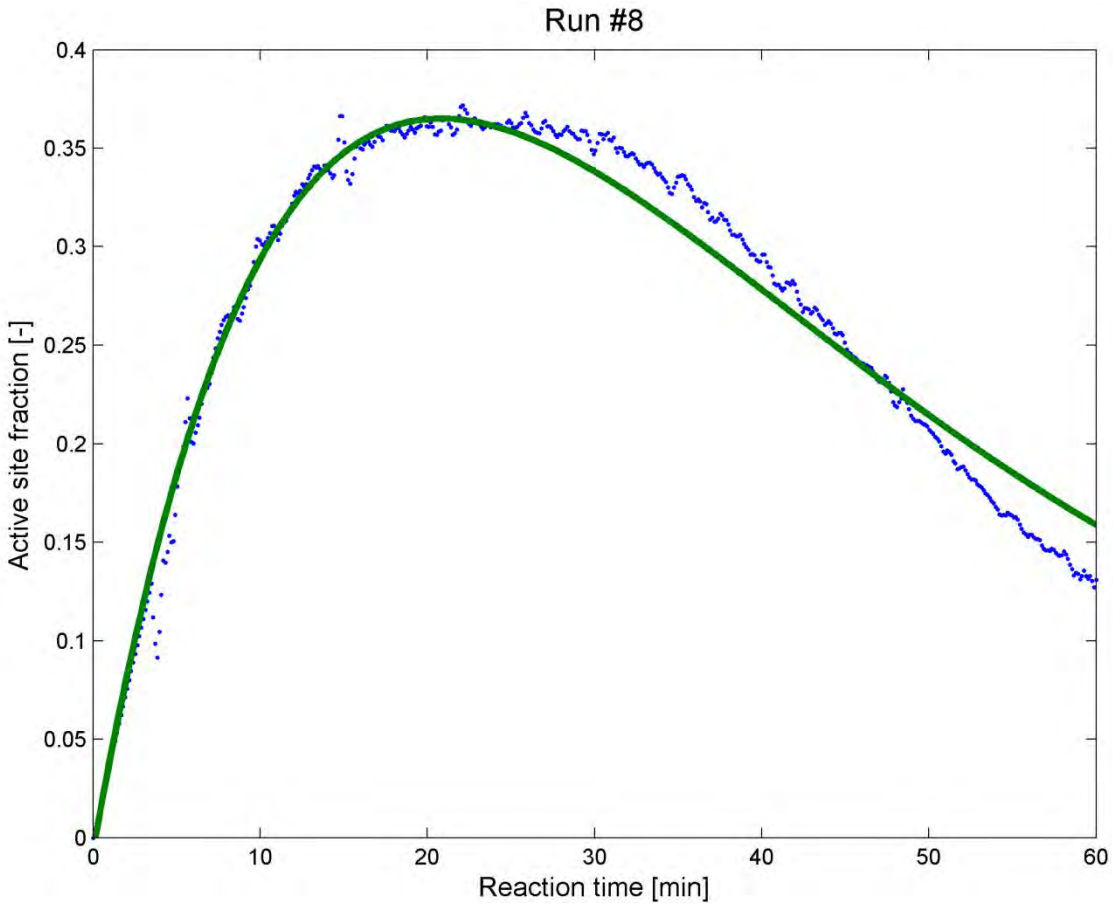

Figure 22.8: Fitting lumped parameters to activity profiles, Experimental Run #8

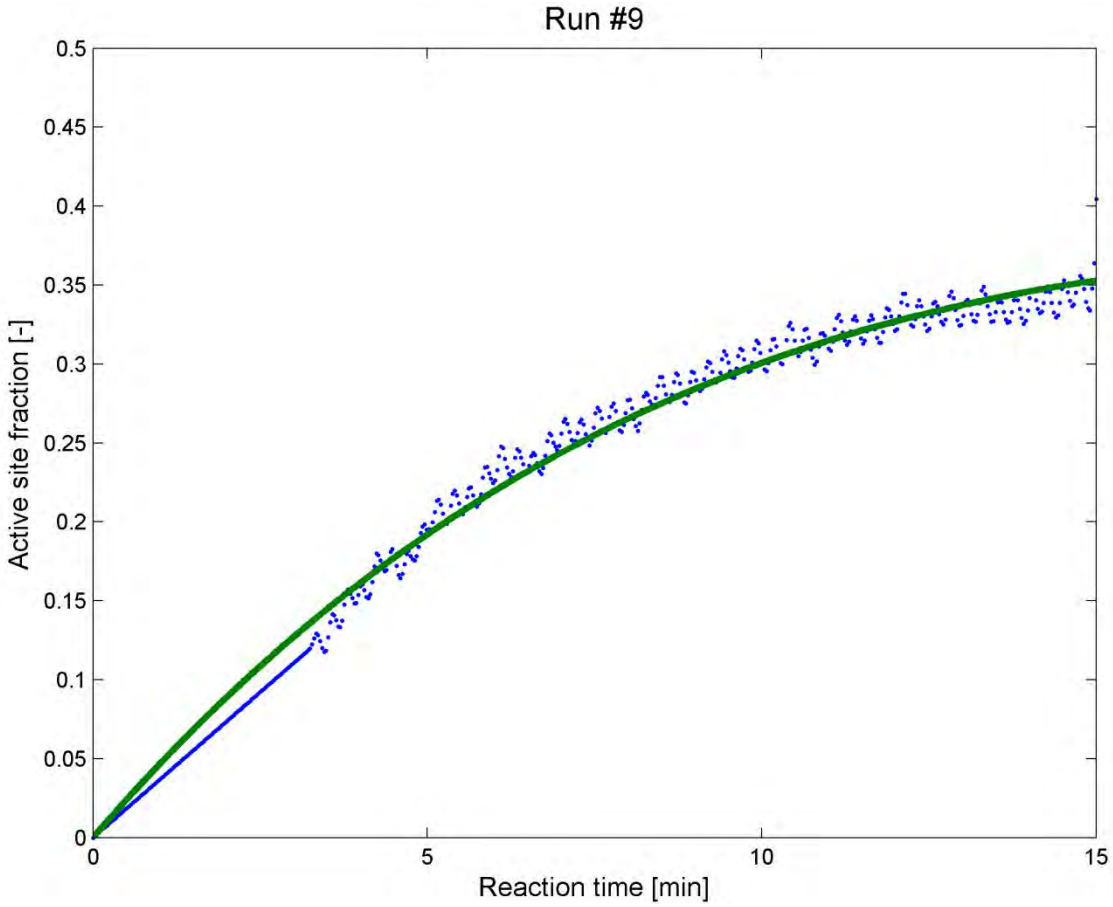

Figure 22.9: Fitting lumped parameters to activity profiles, Experimental Run #9

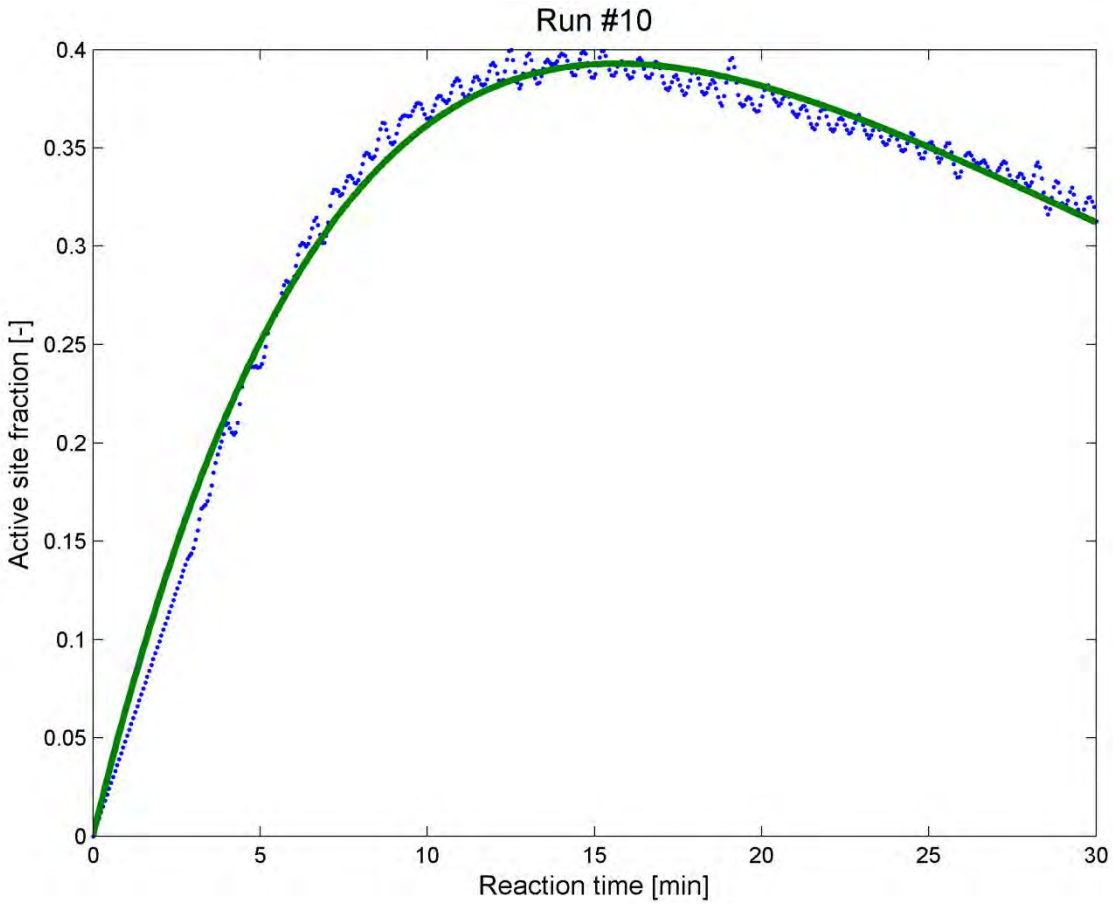

Figure 22.10: Fitting lumped parameters to activity profiles, Experimental Run #10

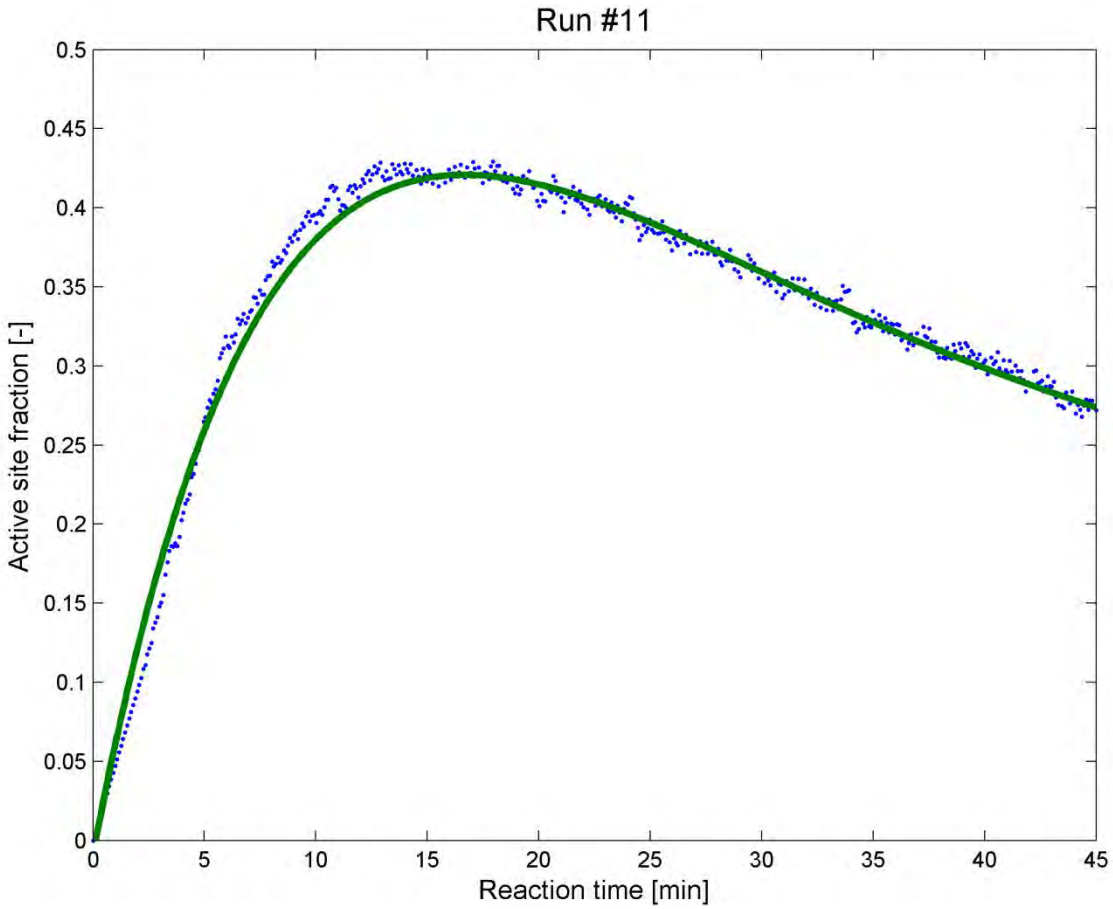

Figure 22.11: Fitting lumped parameters to activity profiles, Experimental Run #11

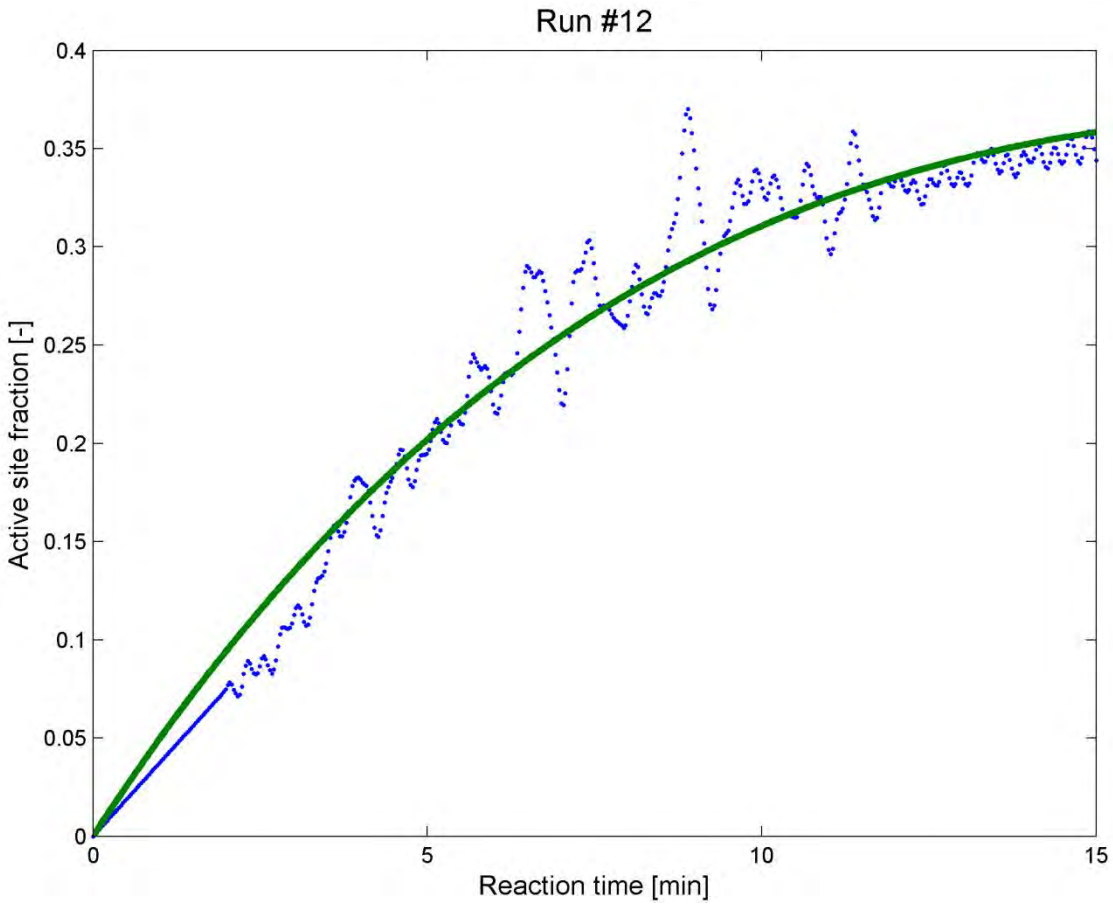

Figure 22.12: Fitting lumped parameters to activity profiles, Experimental Run #12

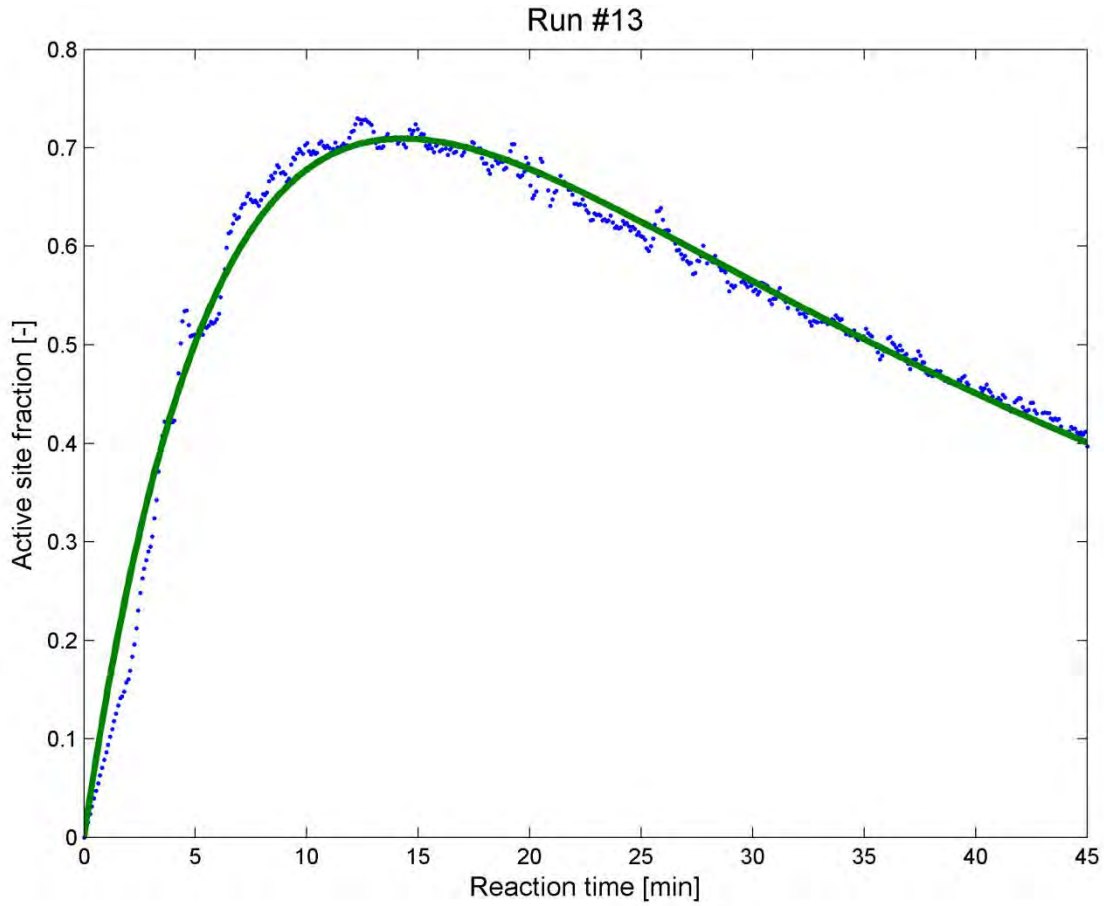

Figure 22.13: Fitting lumped parameters to activity profiles, Experimental Run #13

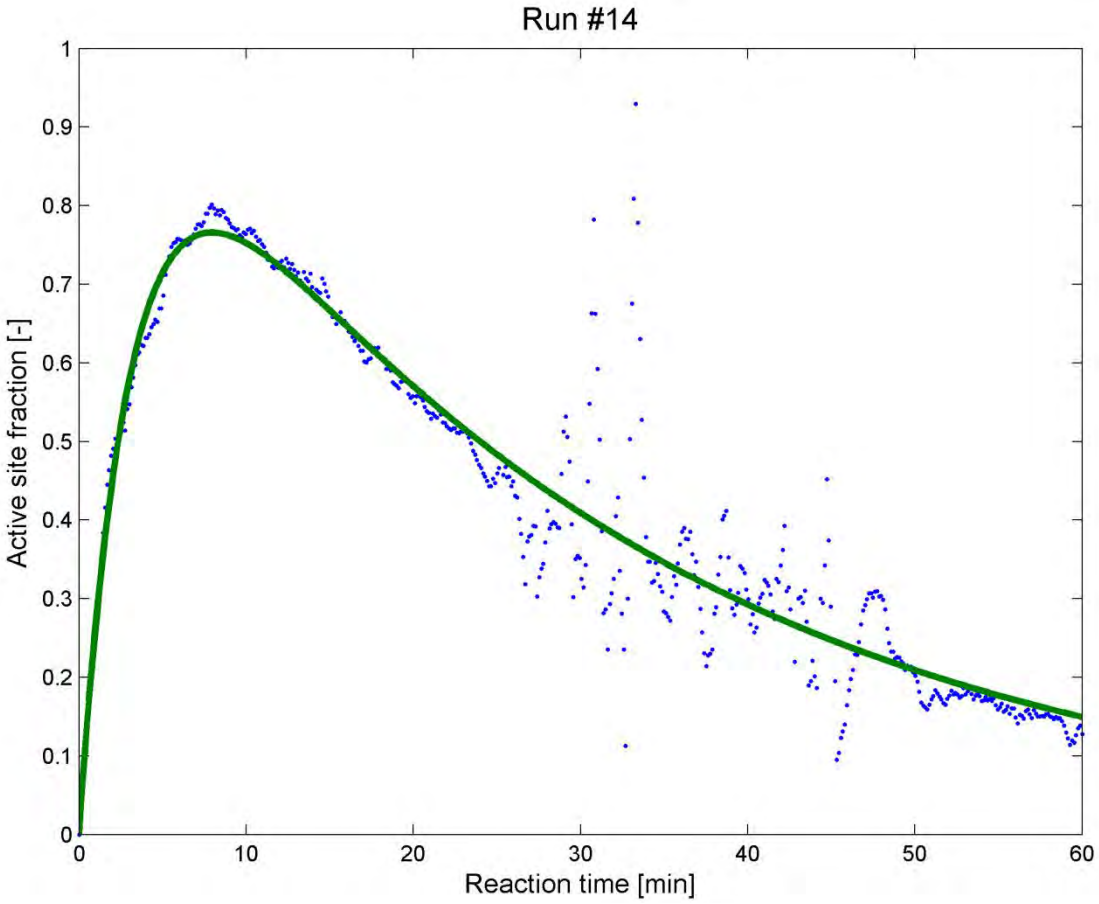

Figure 22.14: Fitting lumped parameters to activity profiles, Experimental Run #14

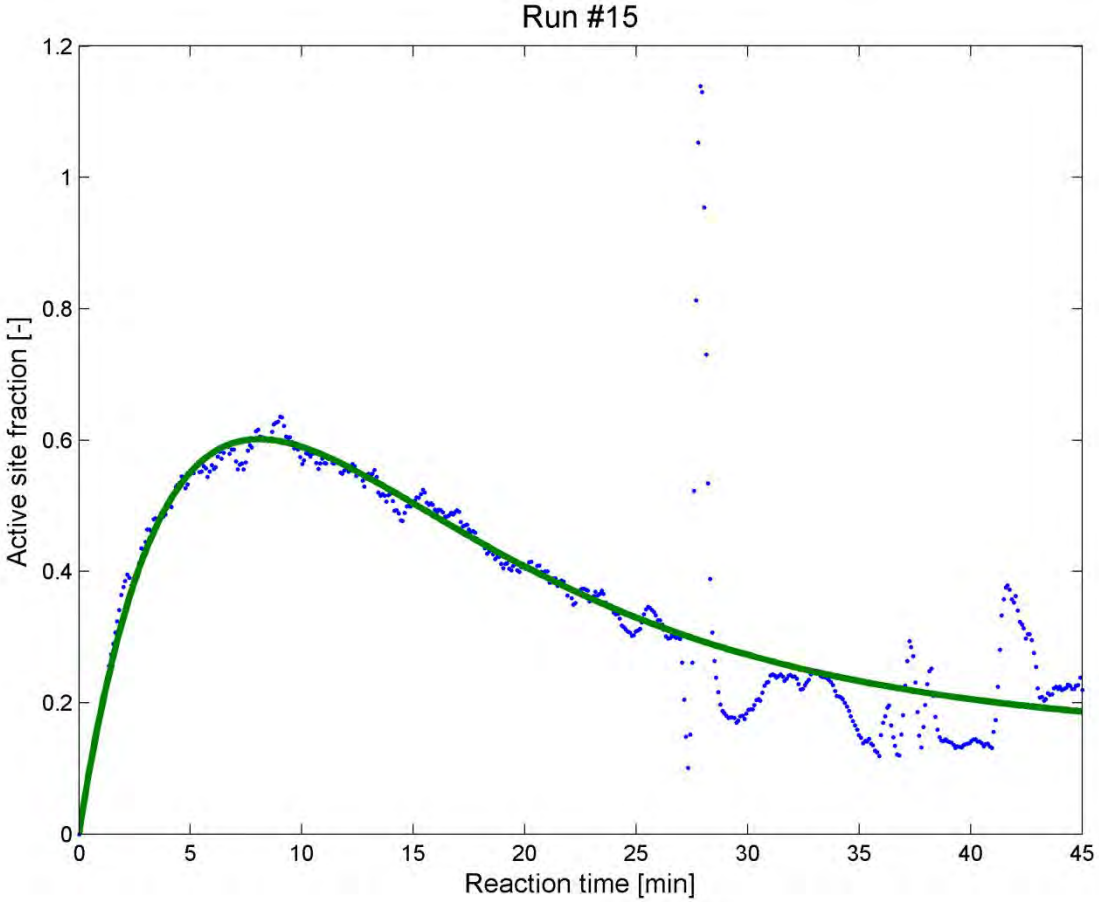

Figure 22.15: Fitting lumped parameters to activity profiles, Experimental Run #15

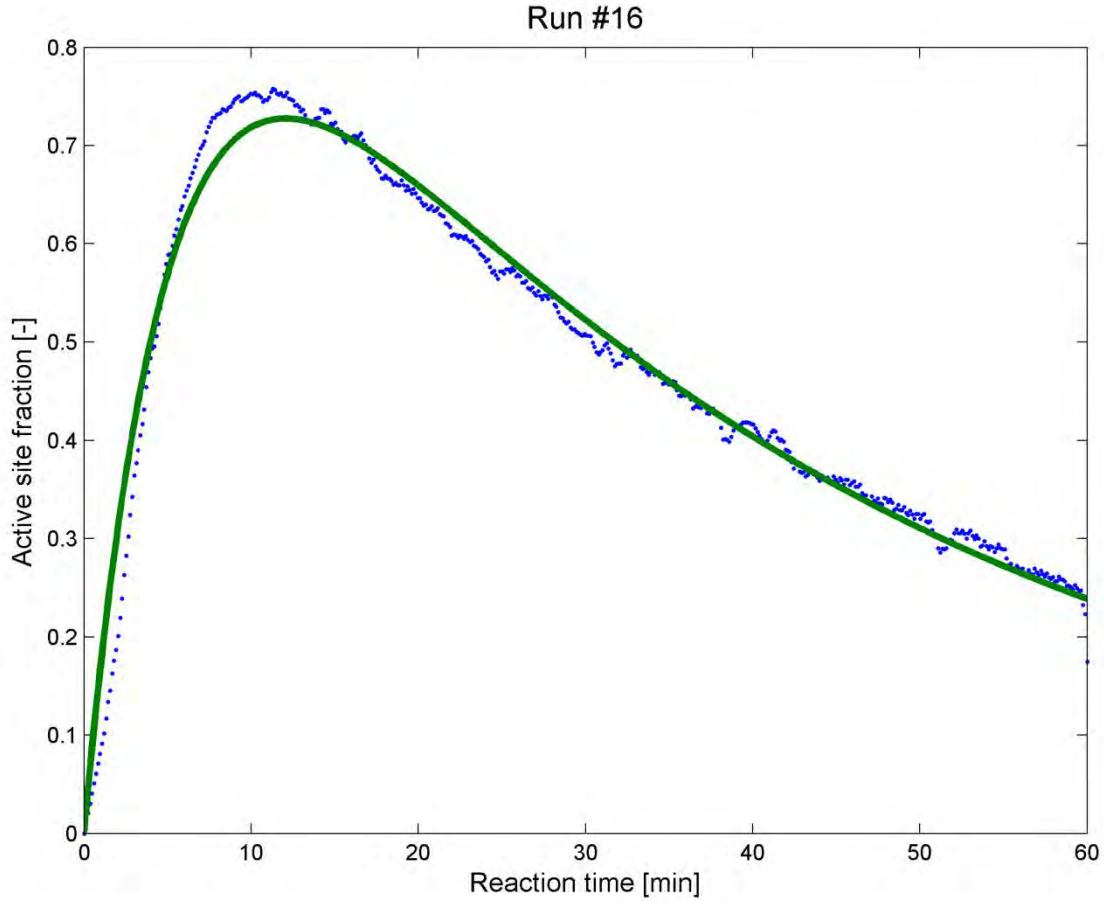

Figure 22.16: Fitting lumped parameters to activity profiles, Experimental Run #16

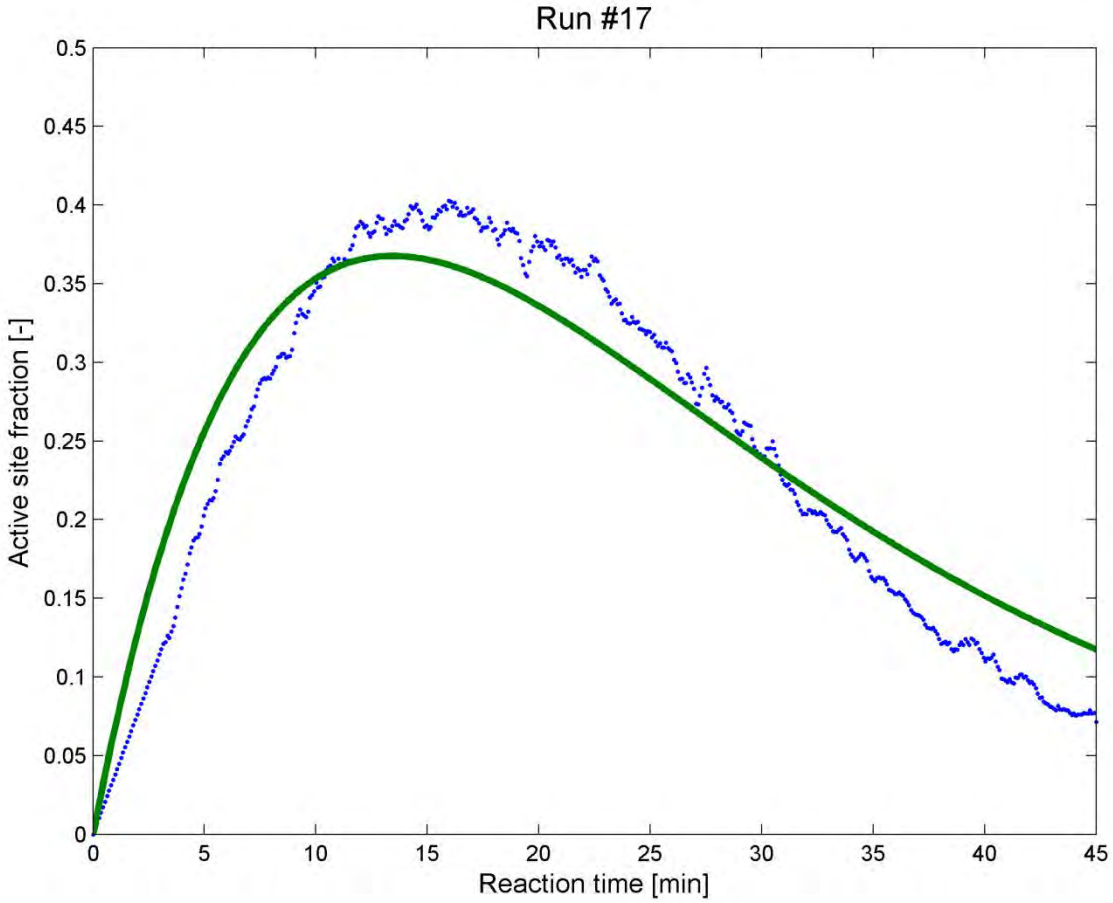

Figure 22.17: Fitting lumped parameters to activity profiles, Experimental Run #17

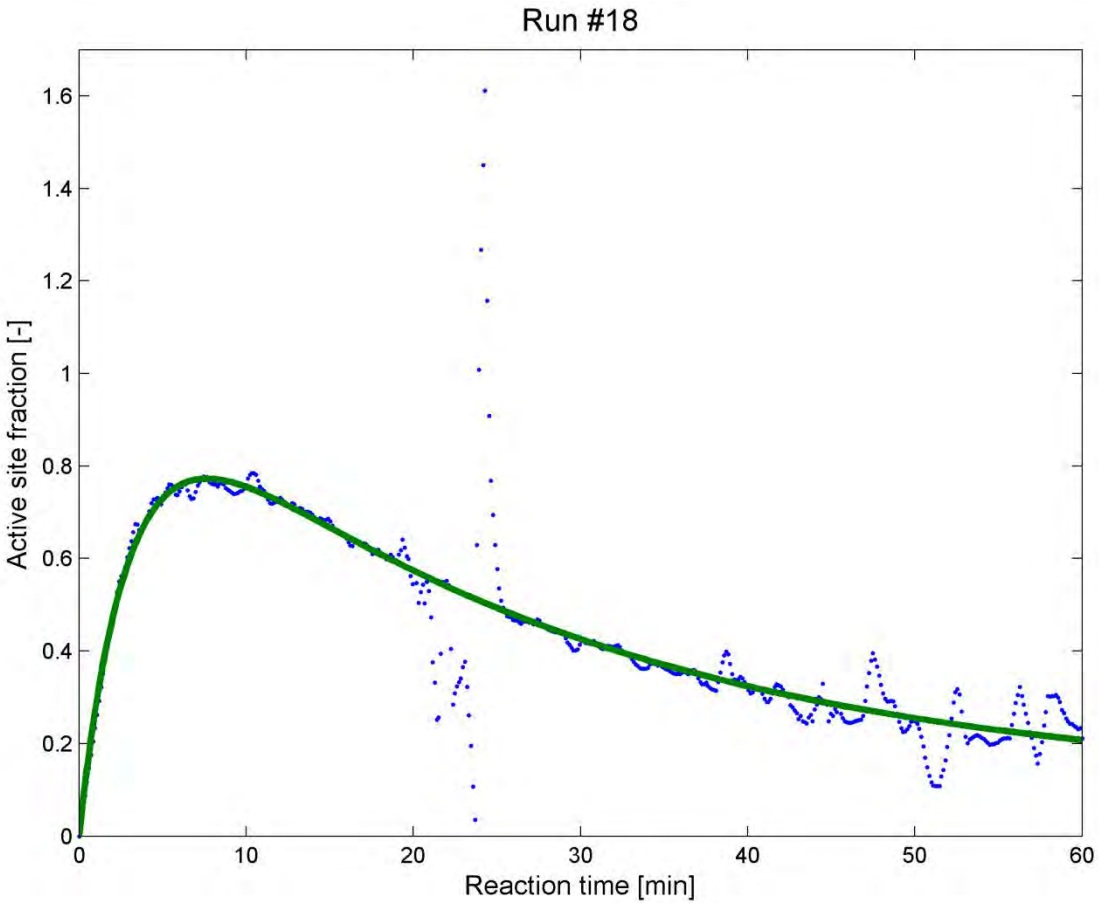

Figure 22.18: Fitting lumped parameters to activity profiles, Experimental Run #18

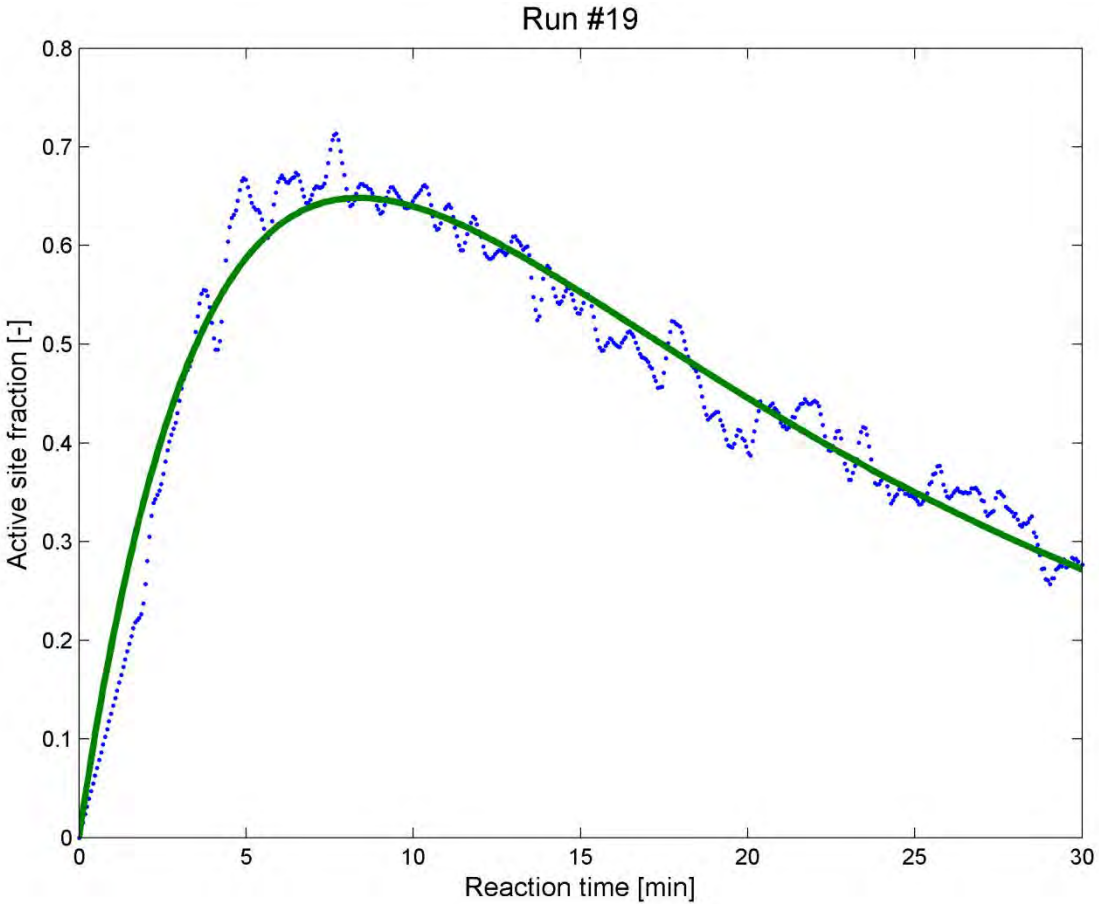

Figure 22.19: Fitting lumped parameters to activity profiles, Experimental Run #19

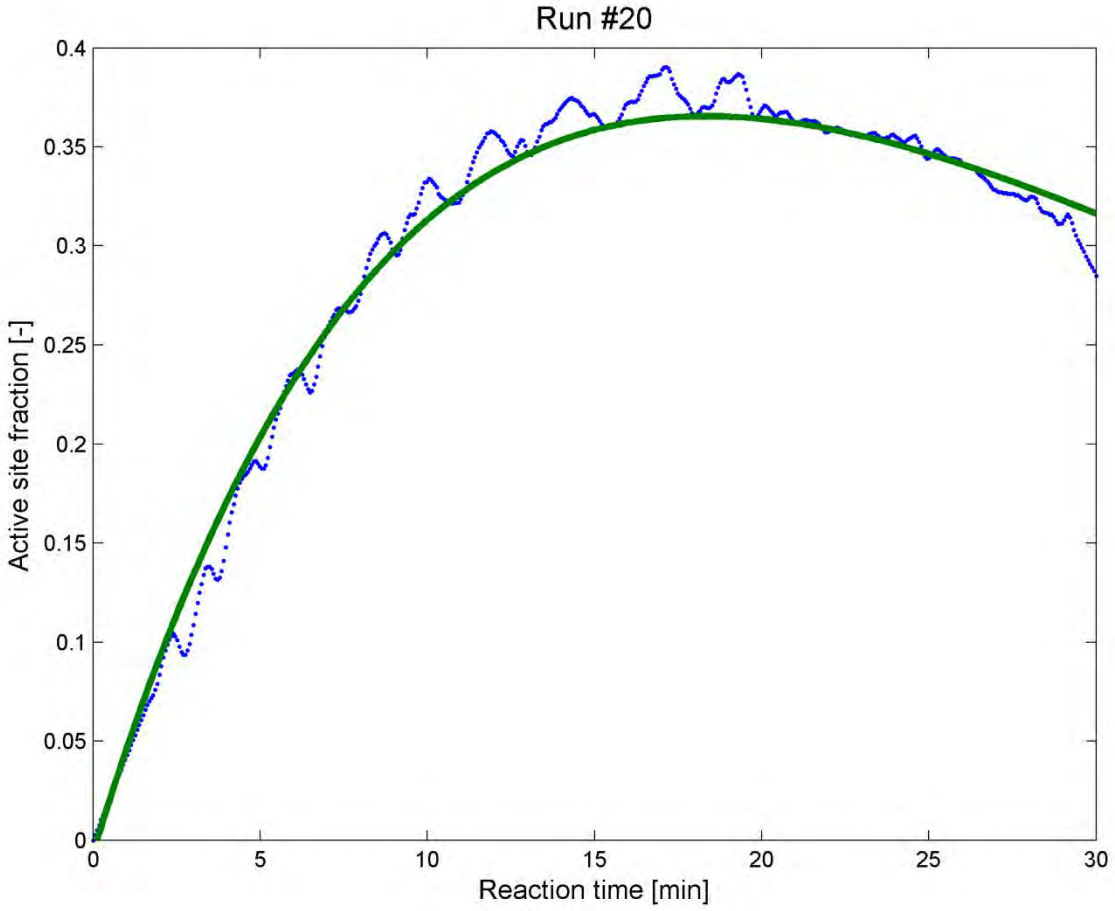

Figure 22.20: Fitting lumped parameters to activity profiles, Experimental Run #20

Non-linear least-squares regression – consolidating propagation rates

The figures below show the results of the regression step which iteratesthe values for the propagation rate parameter and lumped site transformation rate parameters until a consistent set of values is found.

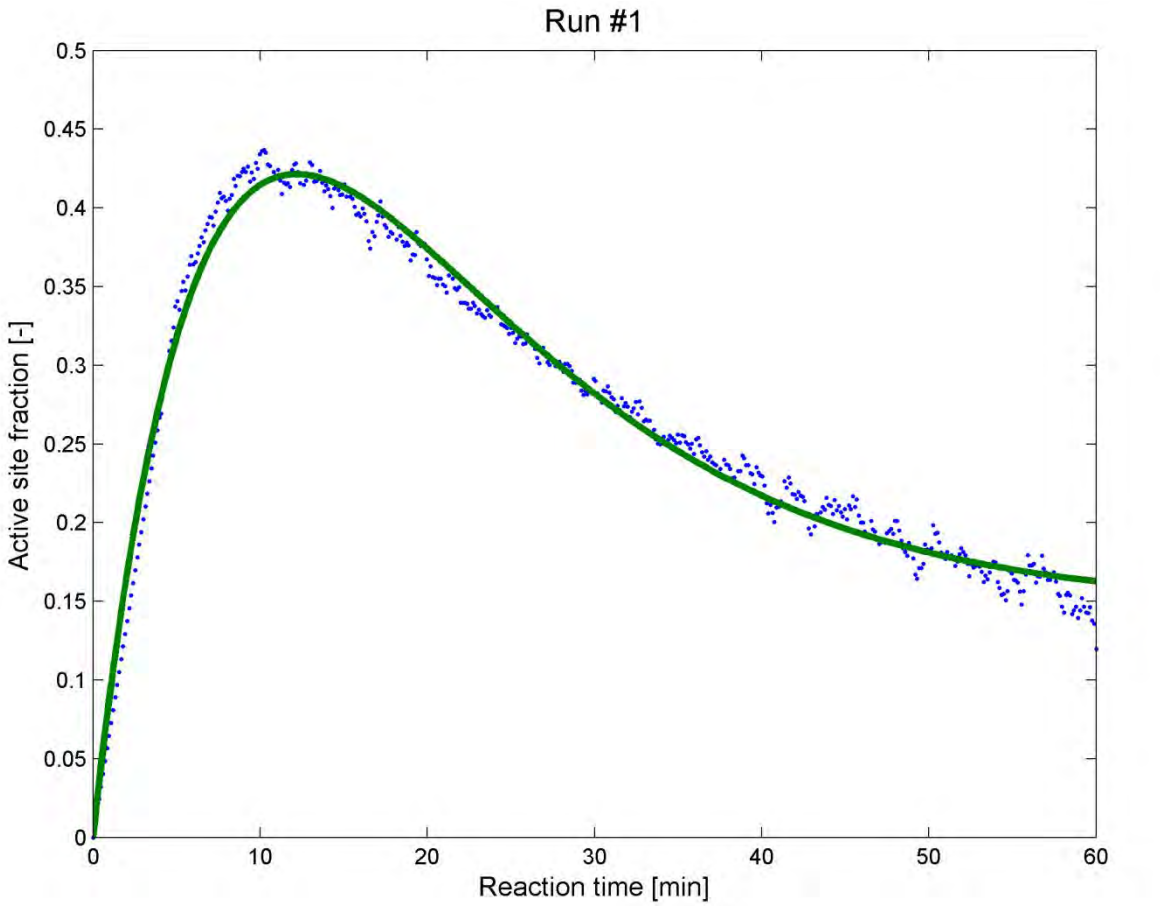

Figure 22.21: Consolidating propagation rates, Experimental Run #1

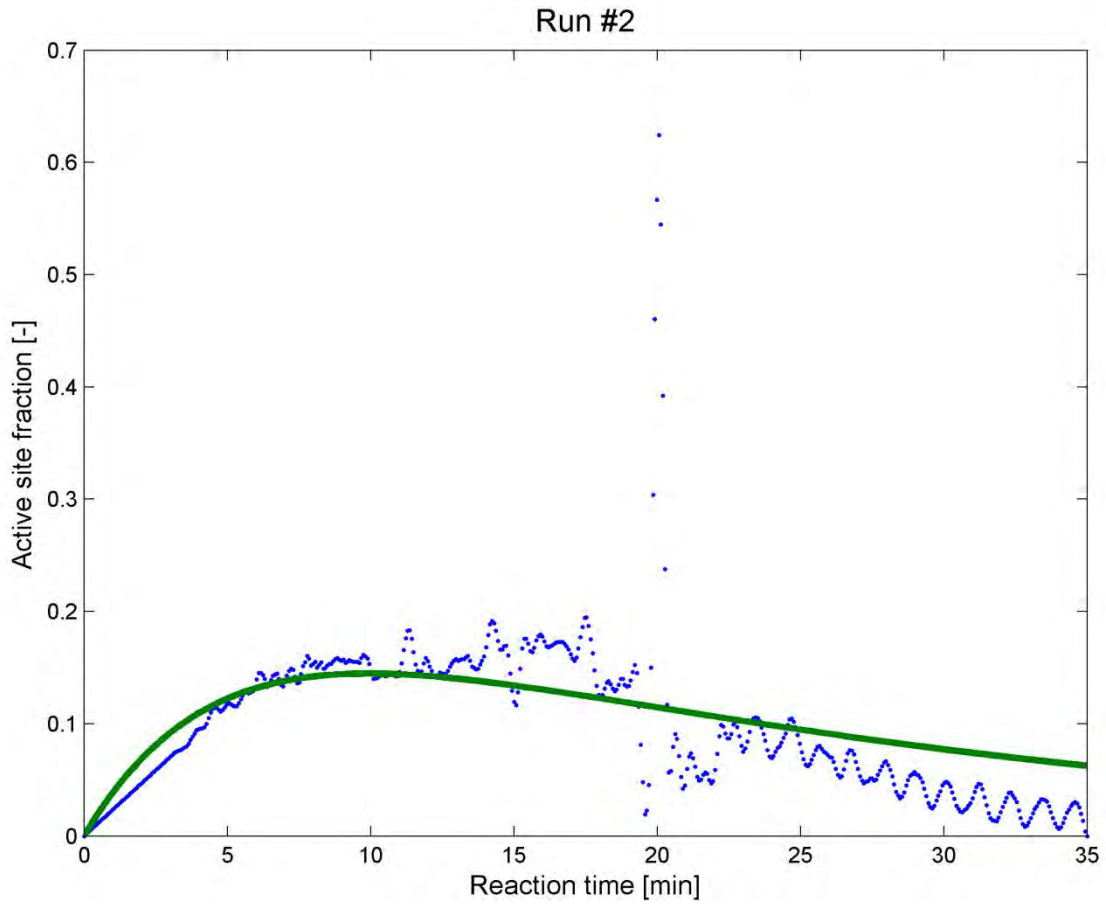

Figure 22.22: Consolidating propagation rates, Experimental Run #2

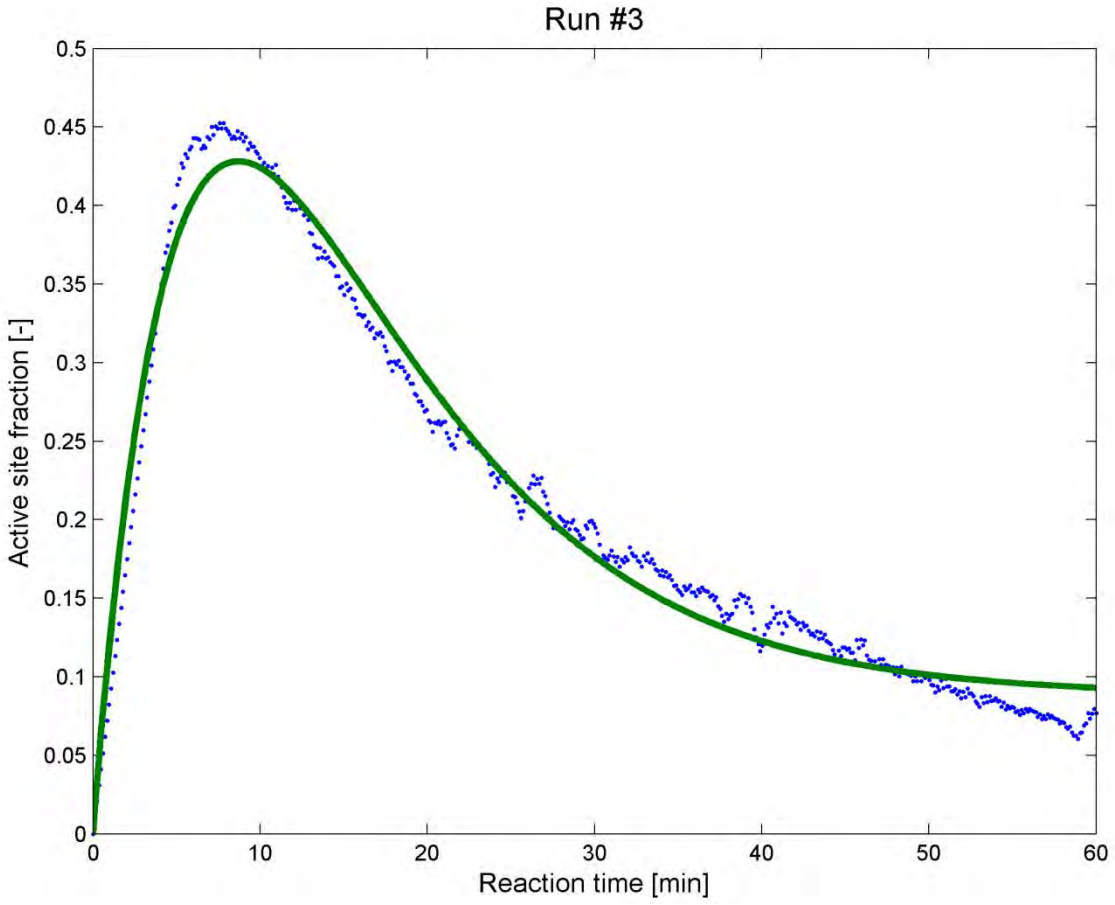

Figure 22.23: Consolidating propagation rates, Experimental Run #3

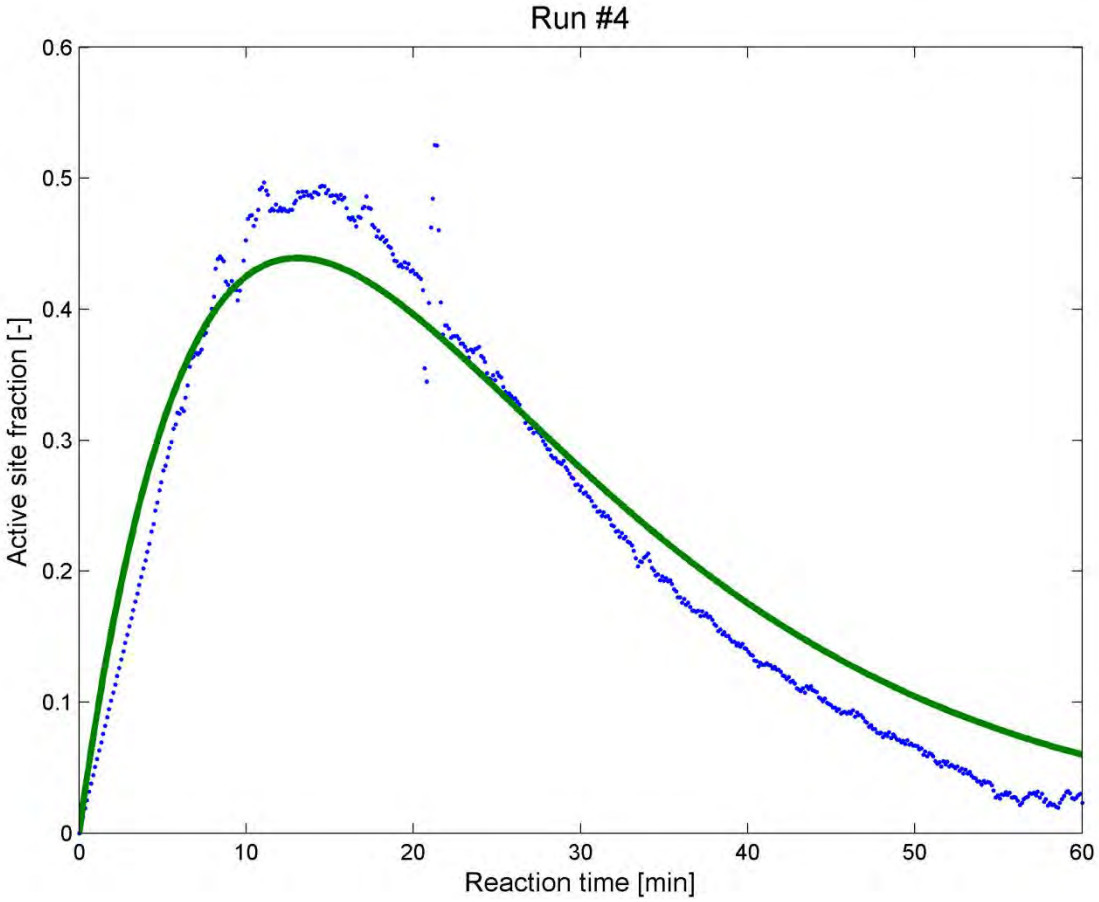

Figure 22.24: Consolidating propagation rates, Experimental Run #4

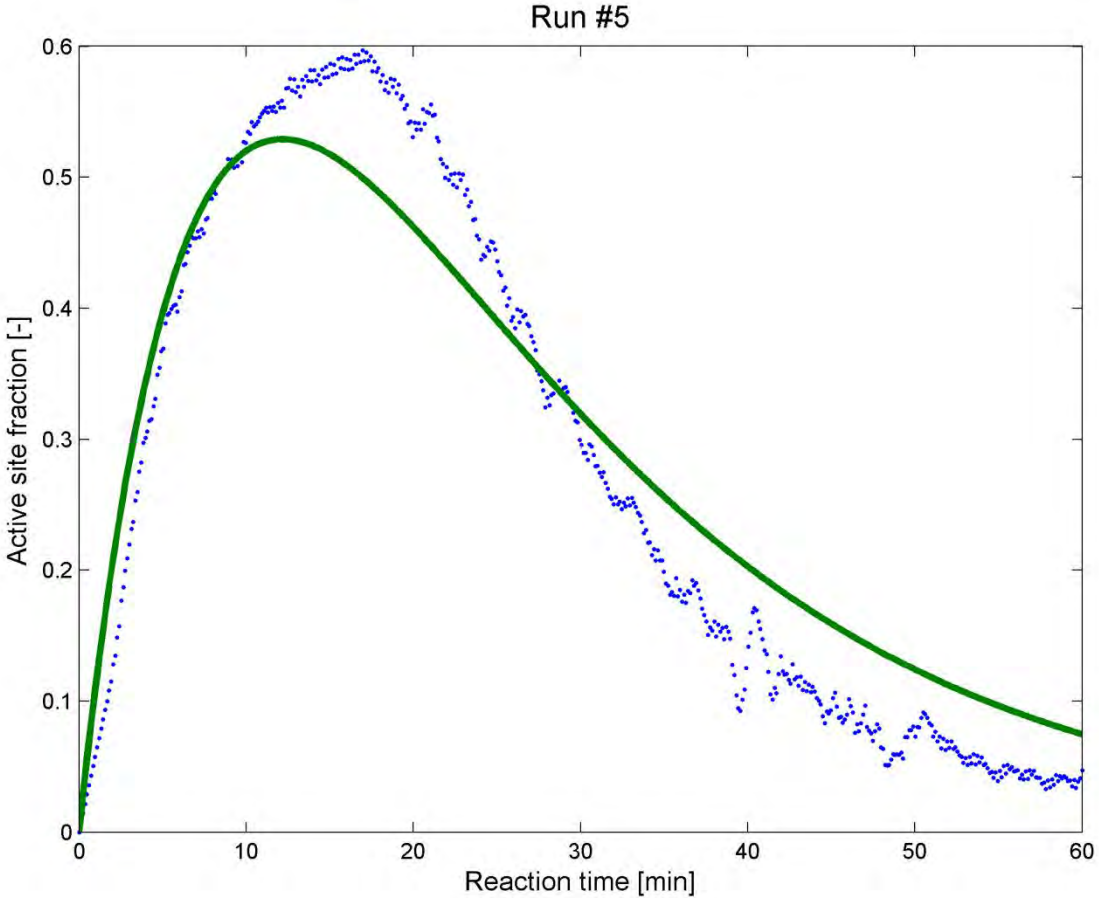

Figure 22.25: Consolidating propagation rates, Experimental Run #5

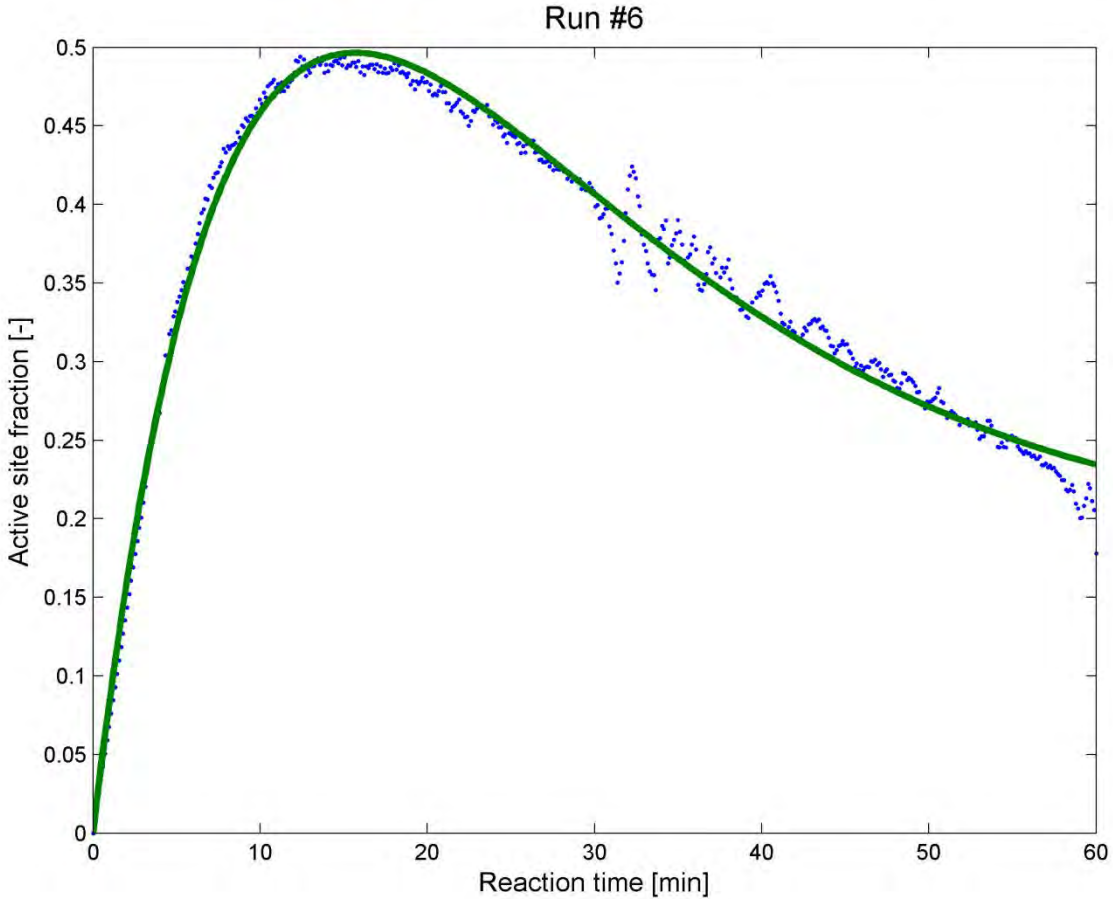

Figure 22.26: Consolidating propagation rates, Experimental Run #6

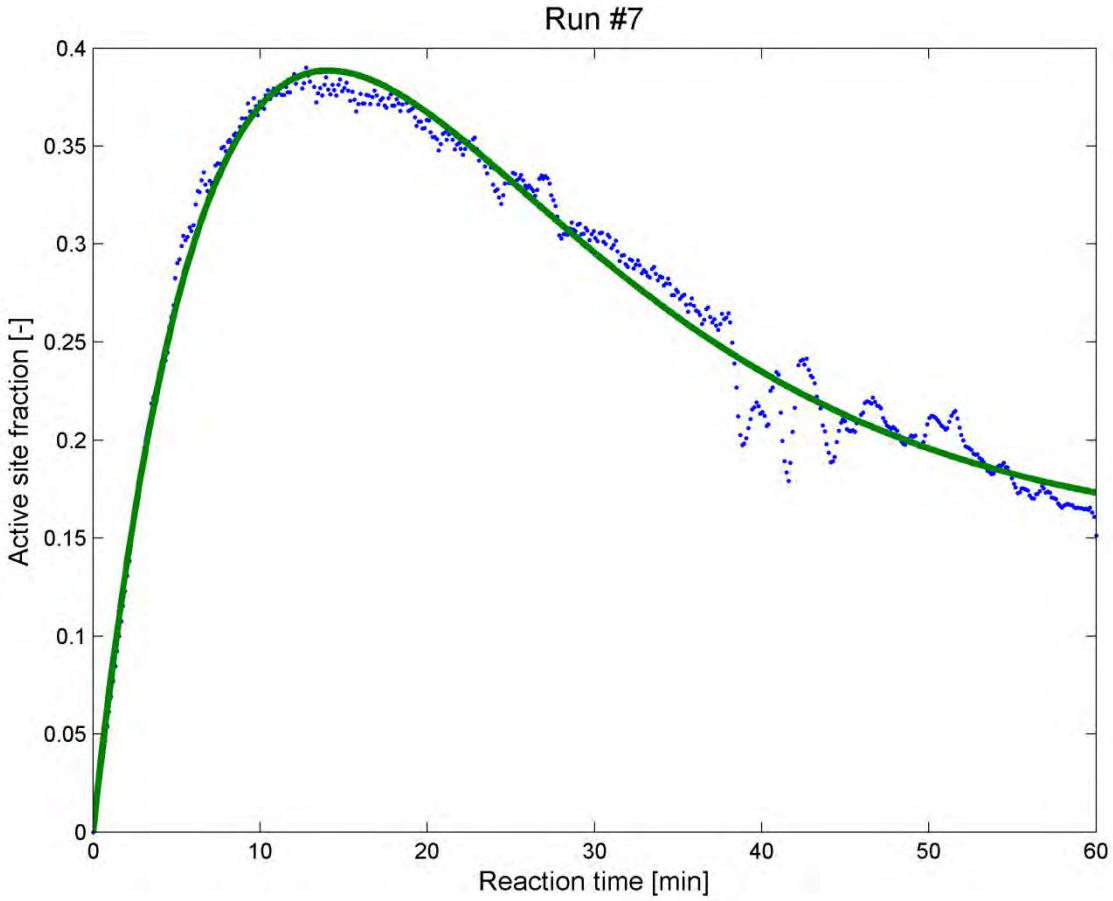

Figure 22.27: Consolidating propagation rates, Experimental Run #7

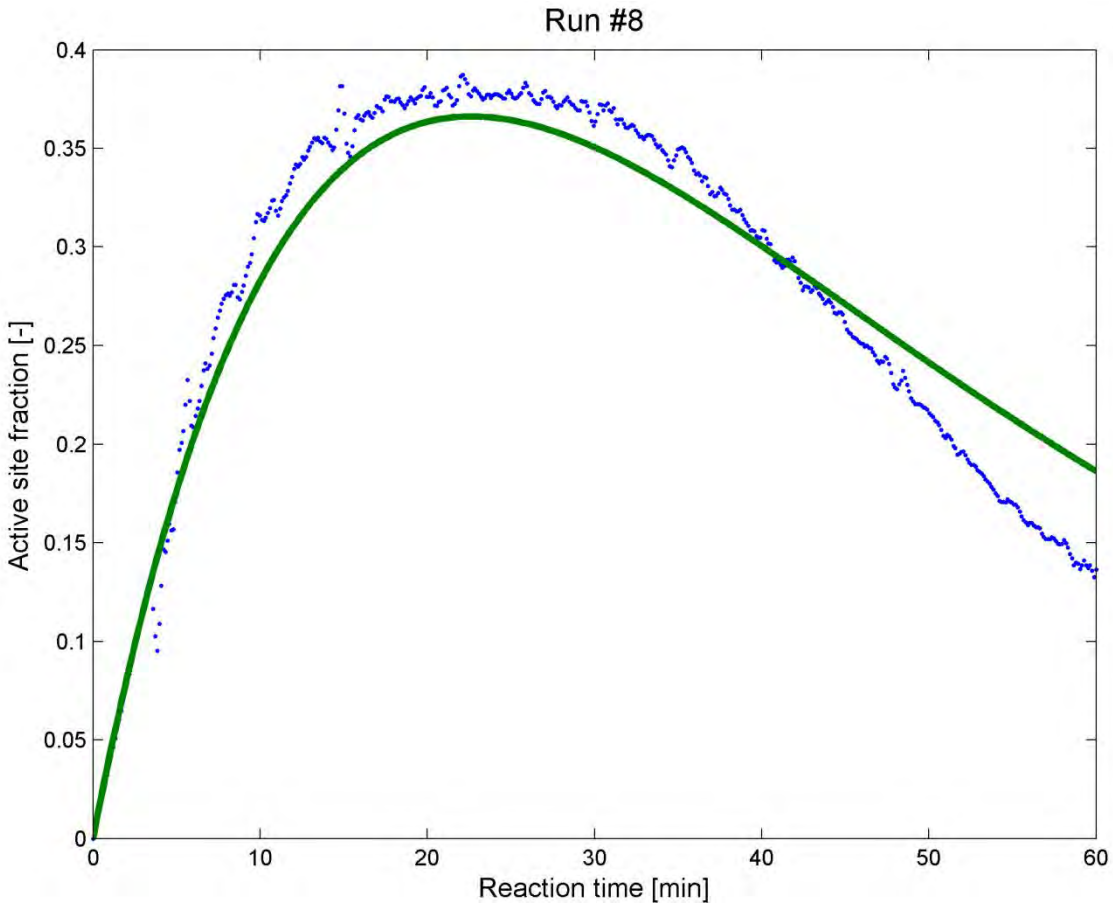

Figure 22.28: Consolidating propagation rates, Experimental Run #8

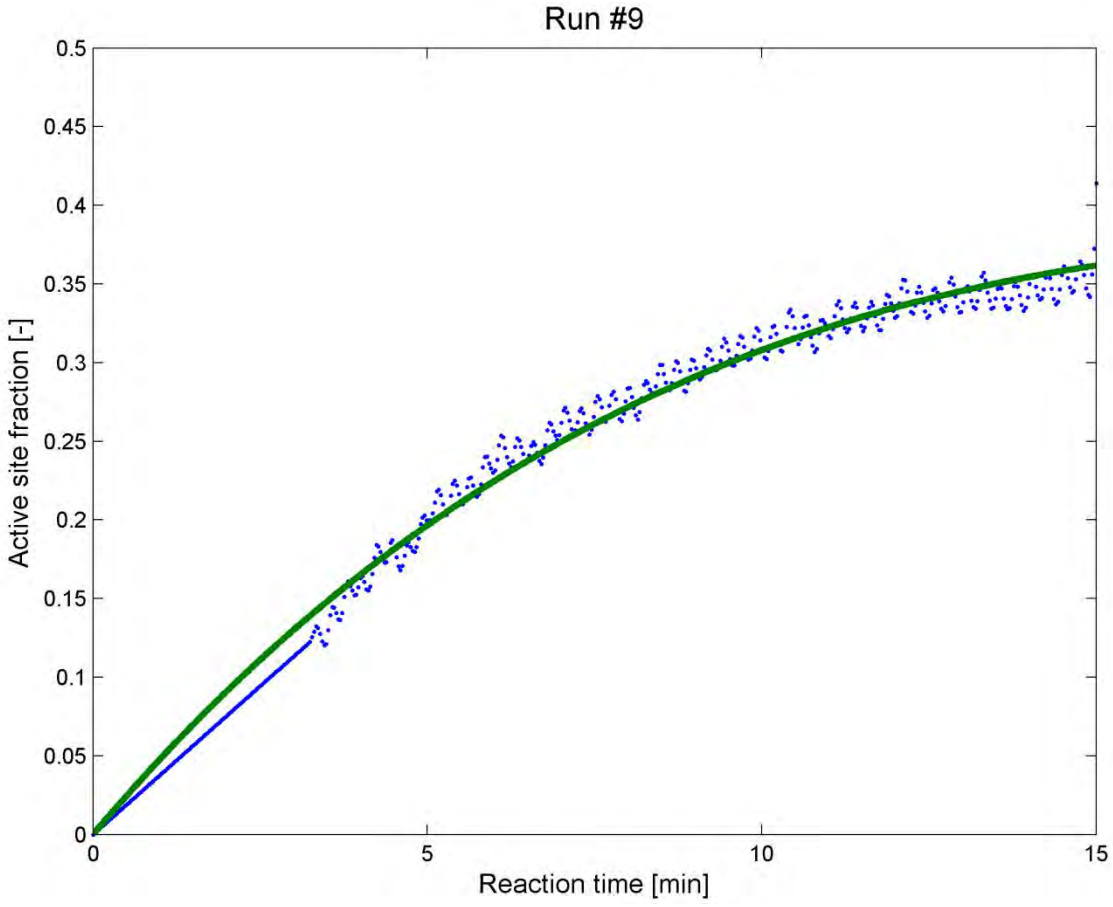

Figure 22.29: Consolidating propagation rates, Experimental Run #9

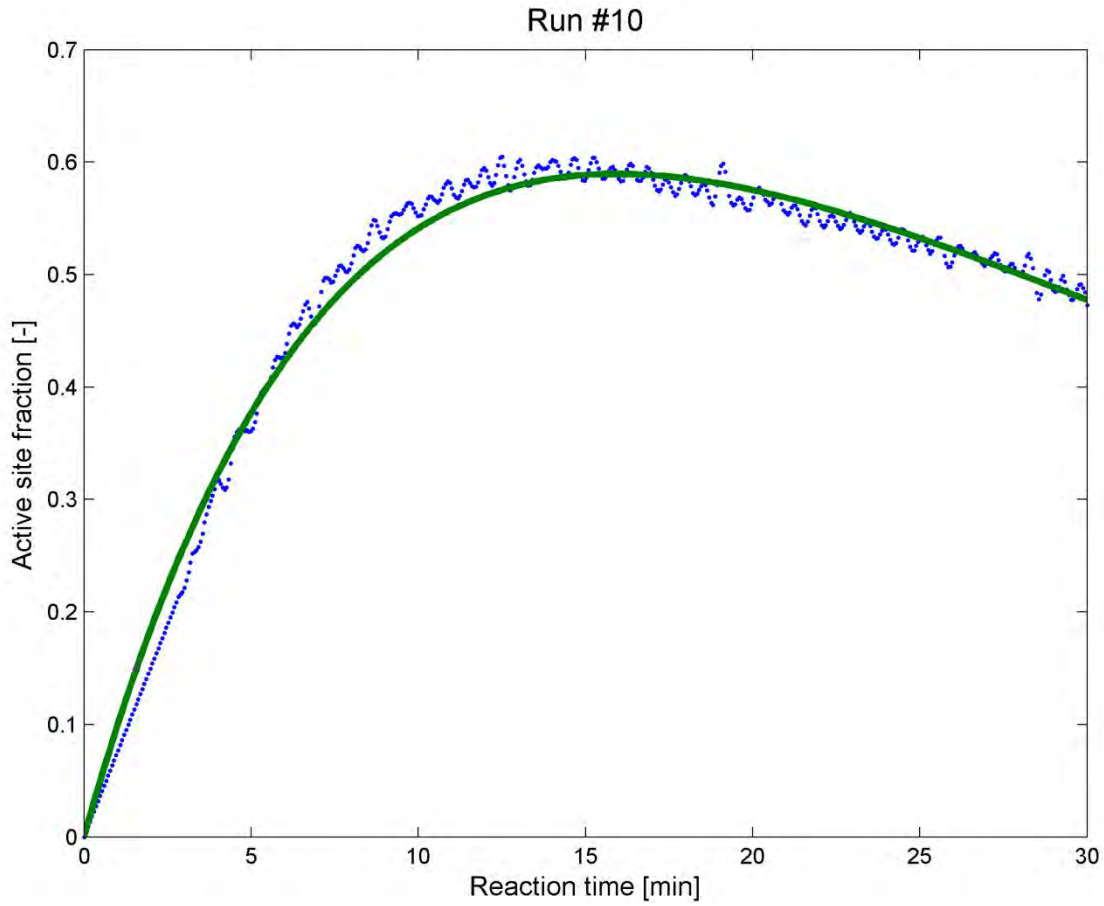

Figure 22.30: Consolidating propagation rates, Experimental Run #10

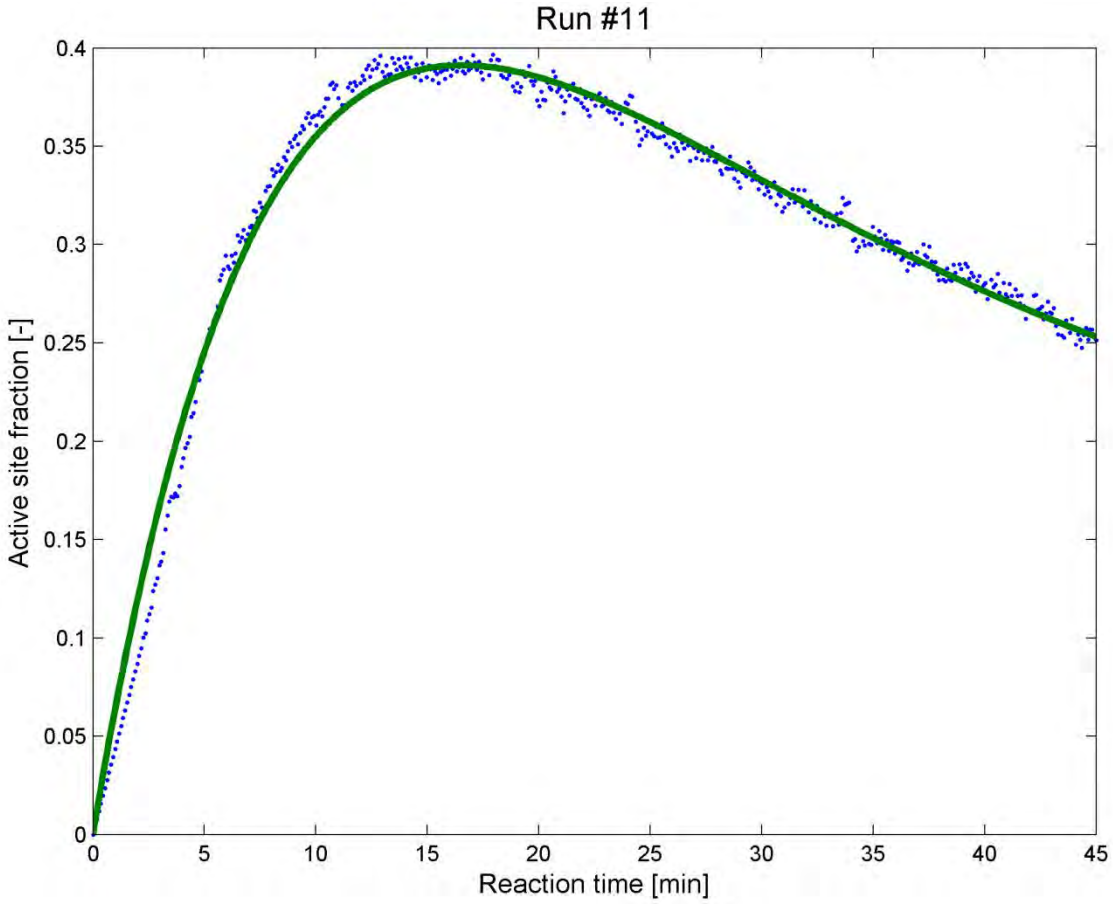

Figure 22.31: Consolidating propagation rates, Experimental Run #11

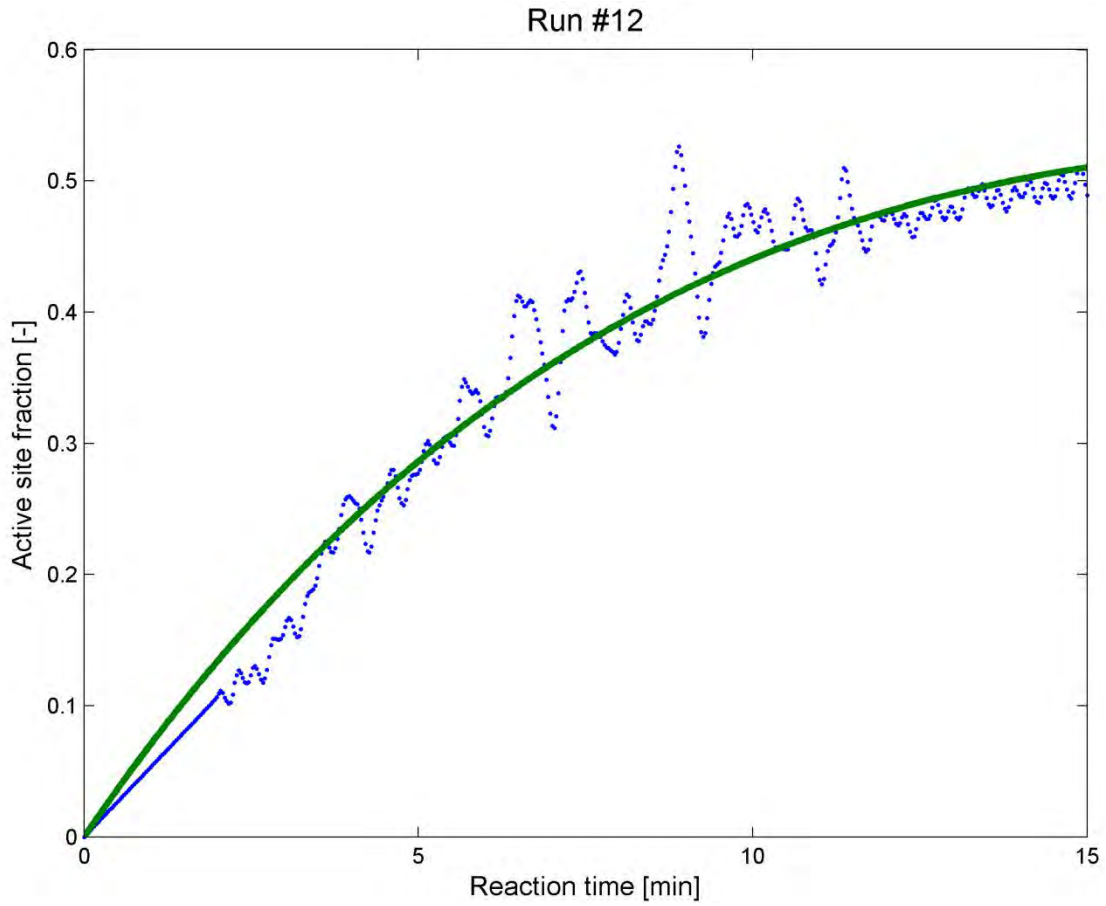

Figure 22.32: Consolidating propagation rates, Experimental Run #12

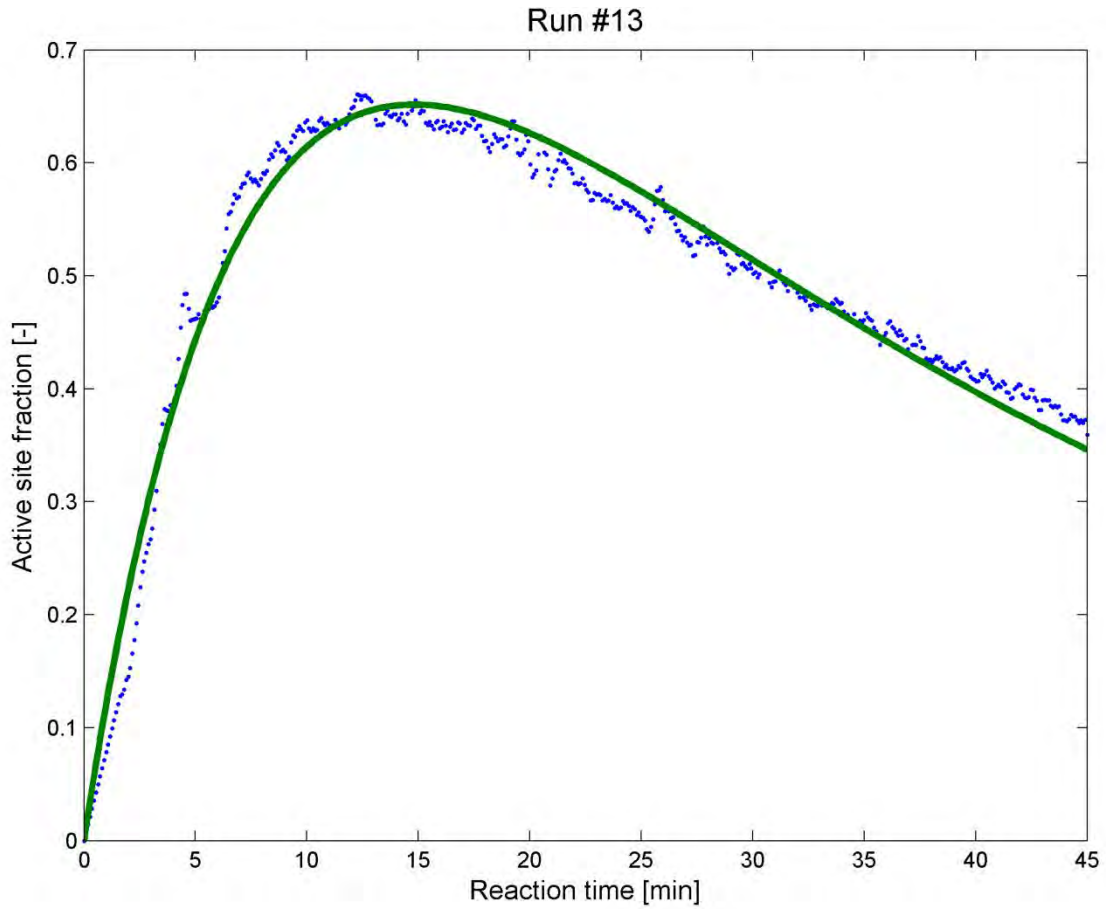

Figure 22.33: Consolidating propagation rates, Experimental Run #13

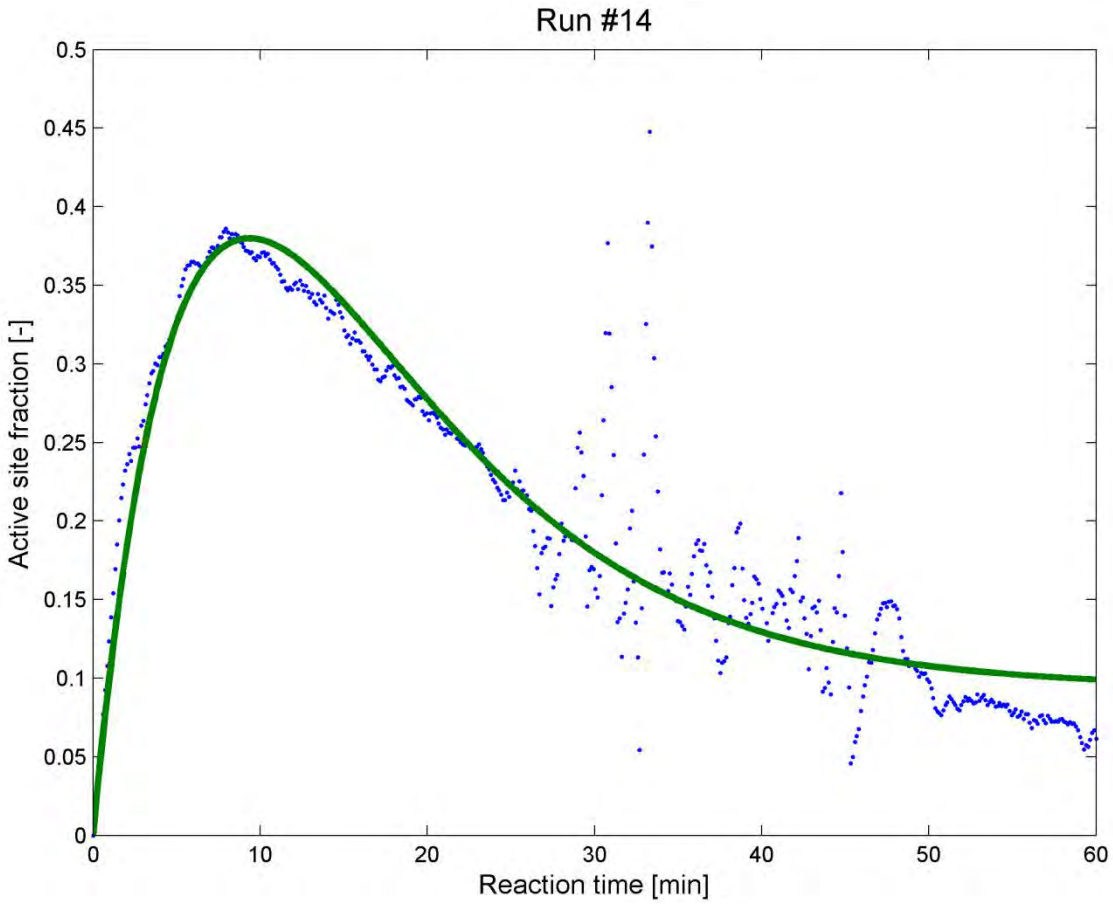

Figure 22.34: Consolidating propagation rates, Experimental Run #14

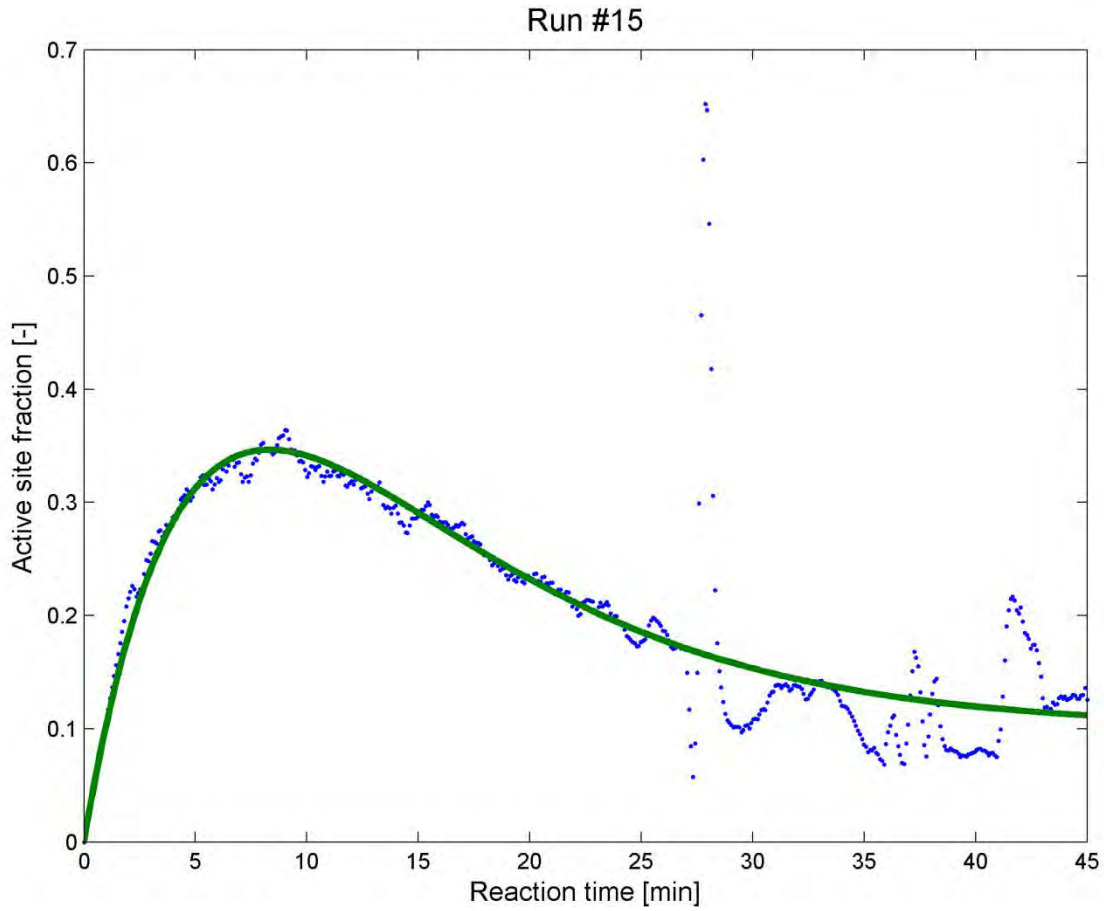

Figure 22.35: Consolidating propagation rates, Experimental Run #15

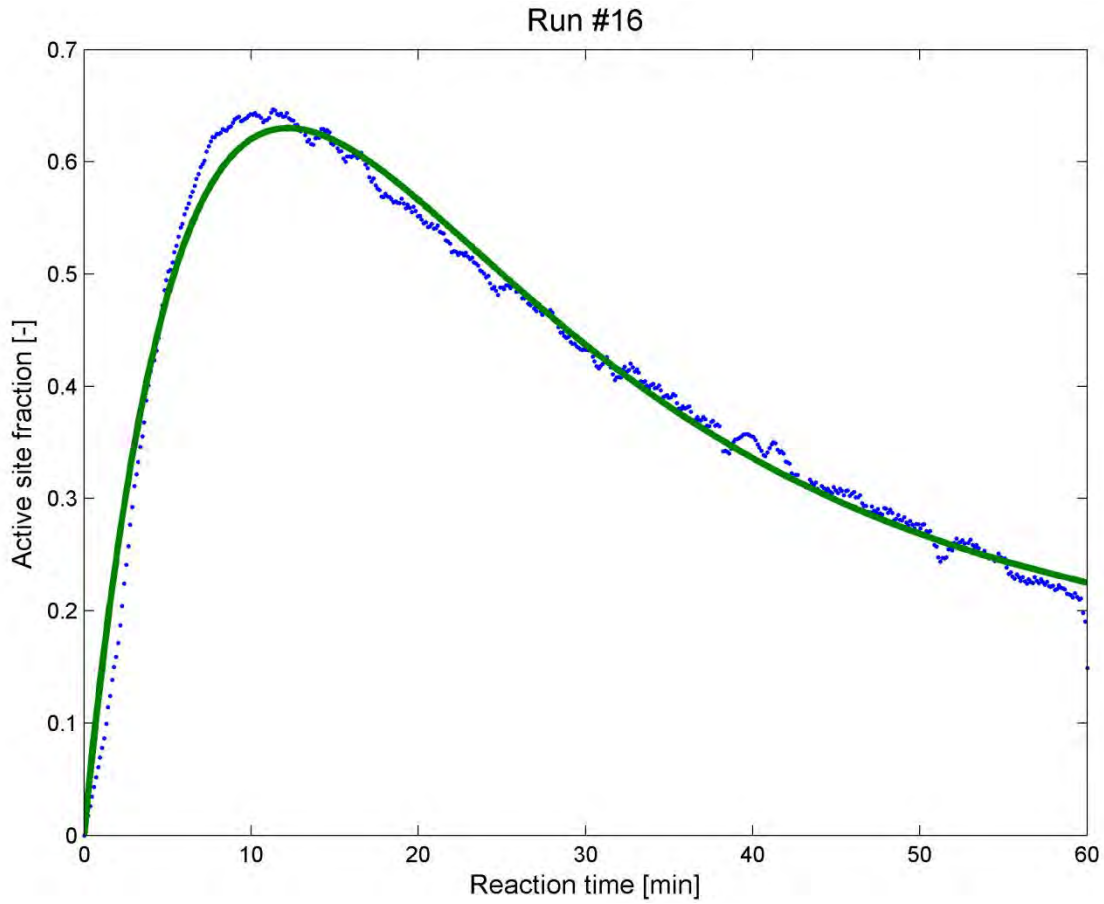

Figure 22.36: Consolidating propagation rates, Experimental Run #16

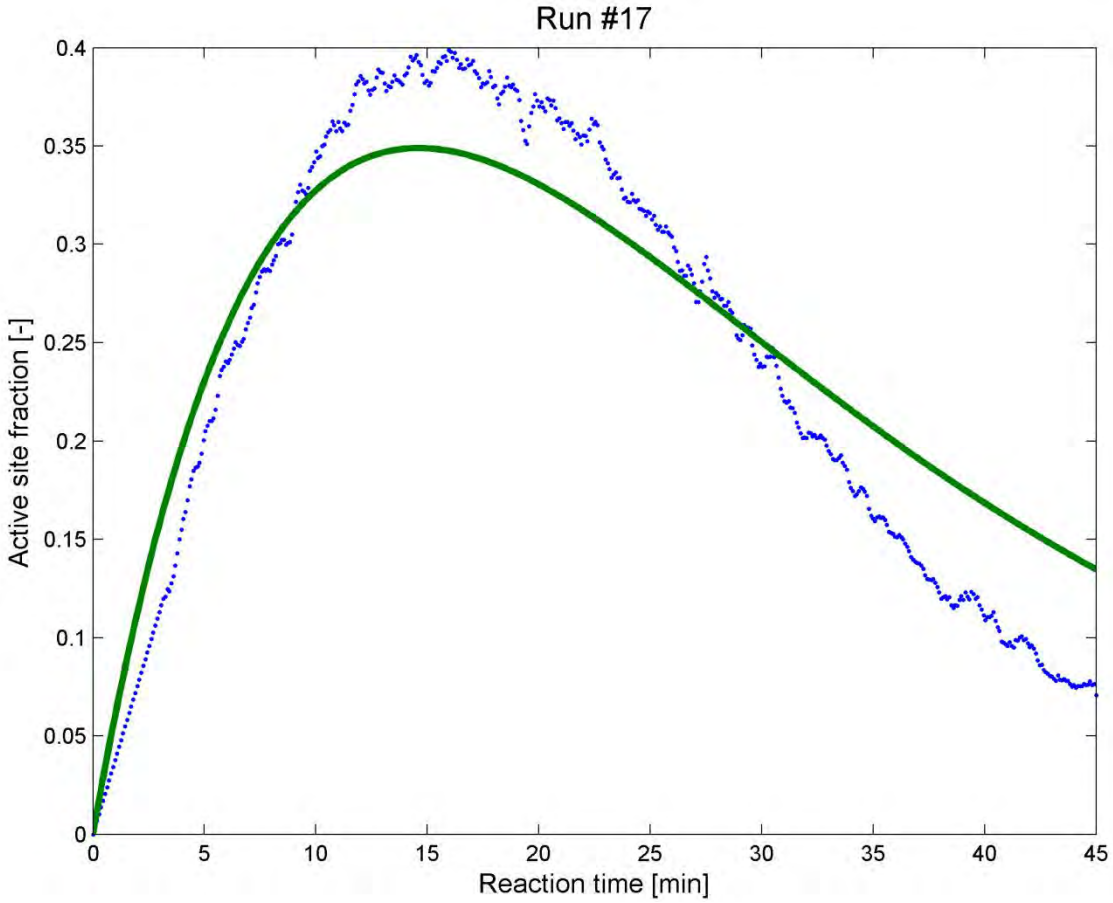

Figure 22.37: Consolidating propagation rates, Experimental Run #17

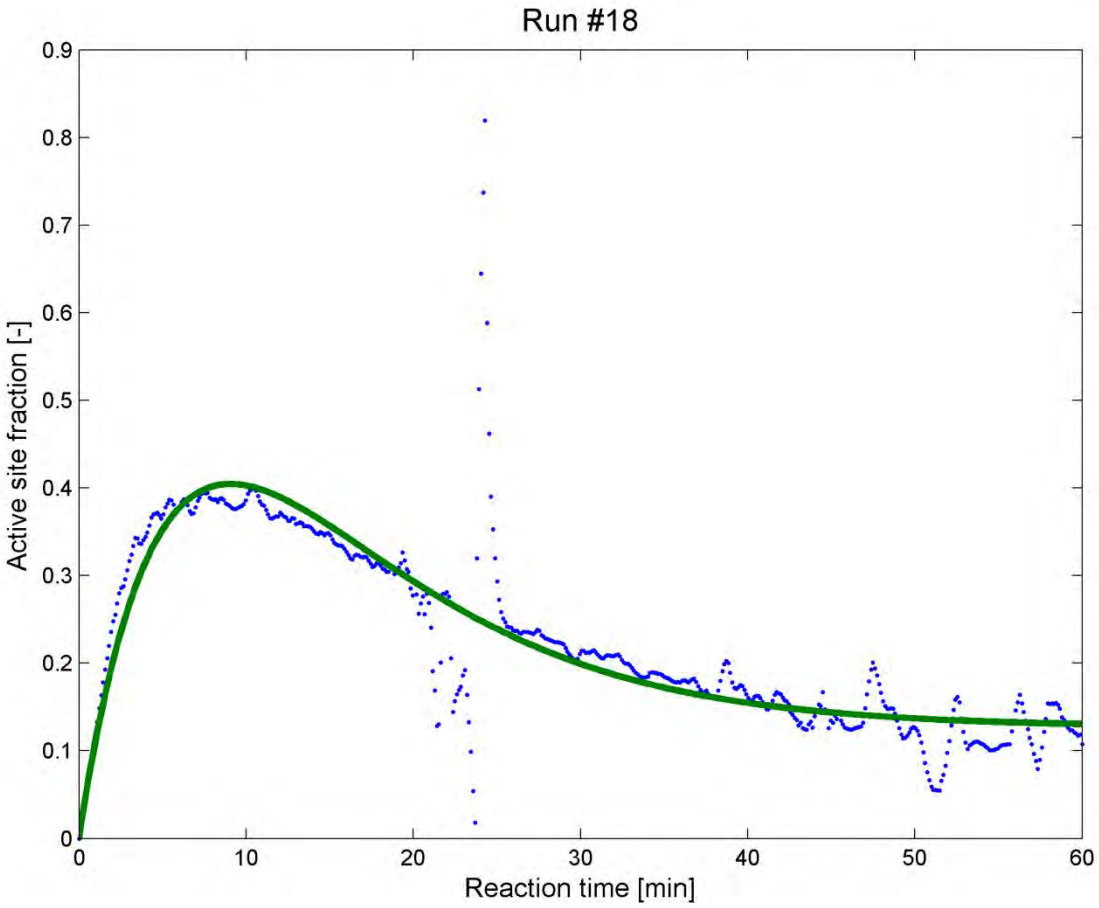

Figure 22.38: Consolidating propagation rates, Experimental Run #18

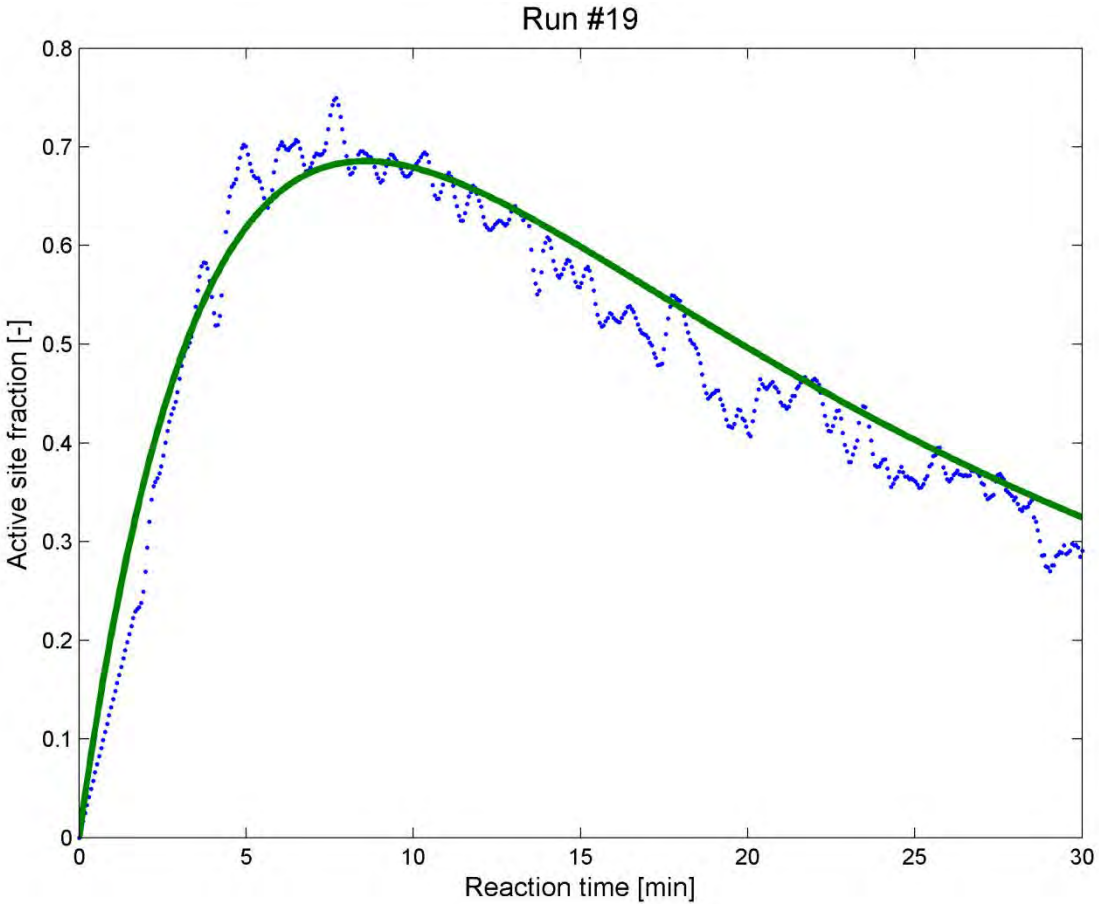

Figure 22.39: Consolidating propagation rates, Experimental Run #19

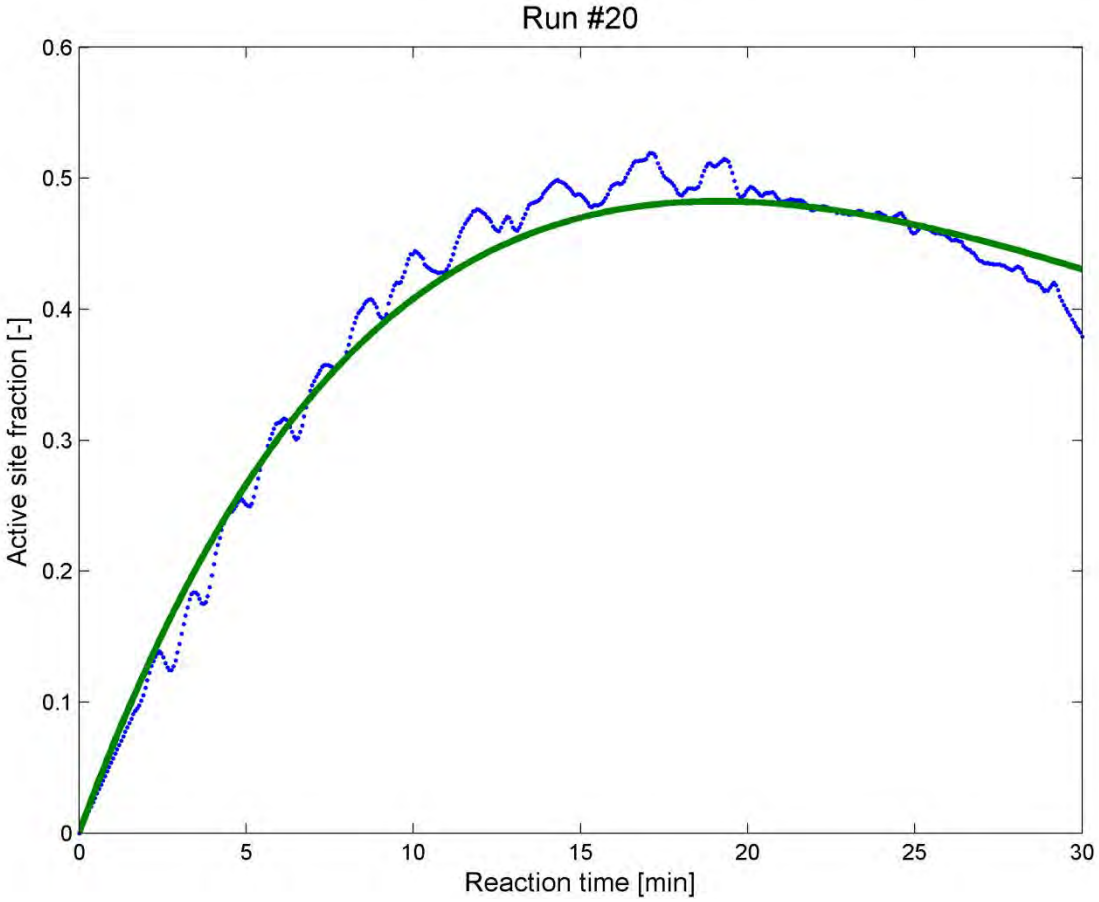

Figure 22.40: Consolidating propagation rates, Experimental Run #20

CHAPTER 23. DISTRIBUTION TYPES

Since the Population Balance Model (PBM) predicts the number-based Particle Size Distribution (PSD), and the Segregation model predicts the mass-based PSD, a method to convert the basis of the distribution is required.

The starting point is to define the total mass and number flows in the stream of interest, $\dot{M}_{in}$ and $\dot{N}_{in}$, such that $\dot{M}_{in} f_m(l)\Delta l$ is the mass of particles in the size range $[l, l+\Delta l]$; and $\dot{N}_{in} f_n(l)\Delta l$ is the number of particles in the size range $[l, l+\Delta l]$. The mass- and number-based size distribution functions, $f_m(l)$ and $f_n(l)$, have the following property:

$$\int_0^\infty f_m(l)dl = \int_0^\infty f_n(l)dl = 1 \qquad 23.1$$

Using the relation between particle mass and size (equation 8.6) the mass of particles in size range $[l, l+\Delta l]$, using either of the distributions, can be expressed with equation 23.2:

$$\dot{M}_{in} f_m(l)\Delta l = \tfrac{\pi}{6} l^3 \rho \varepsilon \dot{N}_{in} f_n(l)\Delta l \qquad 23.2$$

The mass of particles up to size l can then be found by integrating the expression above, to give equation 23.3.

$$\int_0^l \dot{M}_{in} f_m(l)dl = \int_0^l \tfrac{\pi}{6} l^3 \rho \varepsilon \dot{N}_{in} f_n(l)dl \qquad 23.3$$

The mass fraction of particles up to size l can be found by dividing the mass of particles up to size l by the total mass of particles of all sizes. This gives equation 23.4.

$$\frac{\int_0^l f_m(l)dl}{\int_0^\infty f_m(l)dl} = \frac{\int_0^l l^3 f_n(l)dl}{\int_0^\infty l^3 f_n(l)dl} \qquad 23.4$$

Differentiating with respect to l allows the conversion of a cumulative distribution into a size distribution function, and gives the conversion from number-based size distribution to mass-based size distribution, equation 23.5.

$$f_m(l) = \frac{l^3 f_n(l)}{\int_0^\infty l^3 f_n(l)dl} \qquad 23.5$$

Similar reasoning can be applied to find the conversion from mass-based size distribution to number-based size distribution, equation 23.6.

$$f_n(l) = \frac{\frac{f_m(l)}{l^3}}{\int_0^\infty \frac{f_m(l)}{l^3} dl} \qquad 23.6$$

CHAPTER 24. MODIFIED PARTICLE GROWTH FUNCTION

The modification of the particle growth function (equation 8.7) to account for catalyst activity profiles is shown below, and the impact of this modification on the efficiency of the models discussed.

If activation and deactivation are assumed to be first order and governed by rate constants k_a and k_d respectively, then it can be shown that the fraction of active sites will be given by equation 24.1.

$$a(t) = \frac{k_a}{k_a - k_d}\left[\exp\left(-k_d t\right) - \exp\left(-k_a t\right)\right] \qquad 24.1$$

Substituting equation 24.1 into equation 8.7 will result in the form shown in equation 24.2.

$$l\left(l_0, t\right) = l_0 \sqrt[3]{1 + Gf(k_a, k_d, t)} \qquad 24.2$$

The function *f* is defined in equation 24.3.

$$f(k_a, k_d, t) = \frac{k_a}{k_a - k_d}\left[\frac{1}{k_a}\exp\left(-k_a t\right) - \frac{1}{k_d}\exp\left(-k_d t\right) - \left(\frac{1}{k_a} - \frac{1}{k_d}\right)\right] \qquad 24.3$$

This re-formulation will not affect the solution time for the Segregation Model, since the kernel is calculated once, before the integration is performed.

However, the inclusion of activation and deactivation in the PBM formulation will complicate the form of the solution with the inclusion of the function $f(k_a, k_d, t)$. Although the formulation will not change, and the method of characteristics can still be applied, reducing the PDE's to a set of ODE's, the evaluation of the integration limits and interpolation steps in the model solution will require more computation time.

Thus, including deactivation will negatively affect the performance of the PBM, without affecting the performance of the Segregation approach; this counteracts our attempts to compare the best-case performance of the PBM to the worst case performance of the Segregation approach.

CHAPTER 25. DEVELOPMENT OF RTD FUNCTION FOR INDUSTRIAL REACTOR

25.1 Defining the system

The industrial reactor of interest is an 80m^3 stirred tank, with jacketing and an external cooling loop to remove heat from the reactor. This model, of a CSTR with PFR recycle, is chosen as the system for analysis in this section, and is defined and outlined in Figure 25.1.

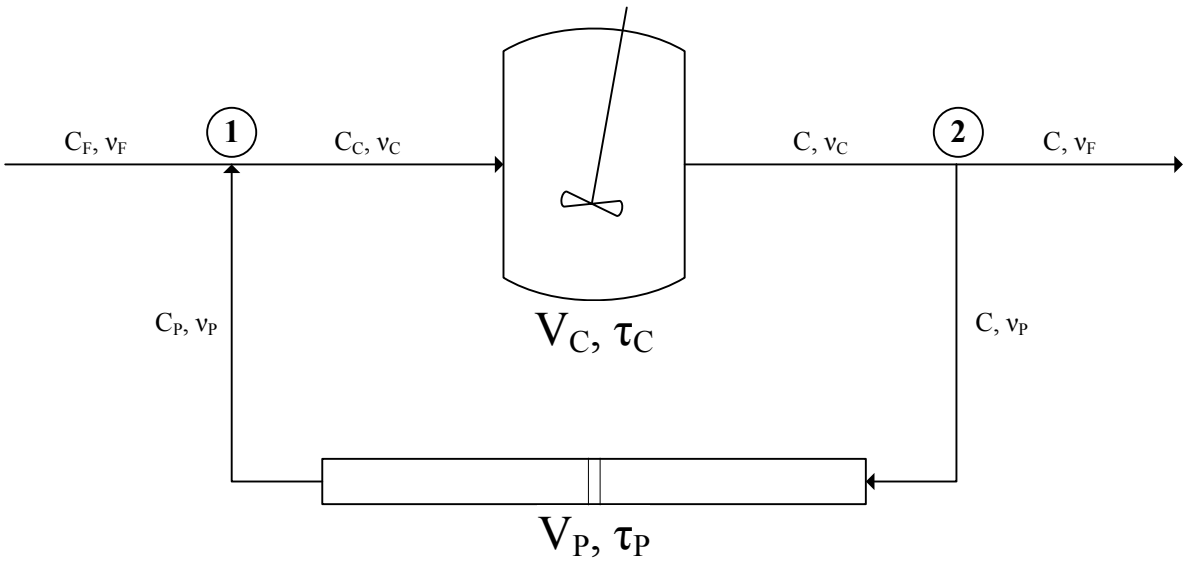

Figure 25.1: System for RTD development

For the development of the RTD function to describe the system illustrated in Figure 25.1, we will simulate the response of this system to a pulse tracer input, of concentration C_t, as shown in equation 25.1.

$$C_F(t) = C_t\delta(t) \qquad 25.1$$

The mass balance around node 1, to find the concentration in the feed to the CSTR, results in equation 25.2.

$$C_C = \frac{\nu_F C_F + \nu_P C_P}{\nu_C} \qquad 25.2$$

The mass balance around the CSTR, using the design equation for a CSTR, predicts the outlet concentration of tracer, as a function of time, in terms of the feed concentration and mean residence time (equation 25.3).

$$\frac{dC}{dt} = \frac{1}{\tau_C}(C_C - C) \qquad 25.3$$

The balance around the PFR recycle is shown in equation 25.4, and represents the delay in the recycle stream: the concentration at the exit of the PFR at time t is the same as the concentration at the entry to the PFR at time $t - \tau_P$.

$$C_P(t) = C(t - \tau_P) \qquad 25.4$$

Combining the equation above results in the delay differential equation (DDE) shown in equation 25.5. This equation defines the time-dependent tracer concentration in the exit stream, in response to a tracer impulse in the feed stream.

$$\frac{dC}{dt} = \frac{1}{\tau_C}\left(\frac{\nu_F C_t \delta(t) + \nu_P C(t-\tau_P)}{\nu_C} - C\right) \qquad C(0) = C_0; \quad C(-\tau_P : 0) = 0 \qquad 25.5$$

A DDE is a differential equation in which the rate of change of a variable depends on a combination of current and previous values of that variable, as shown in equation 25.6. The previous value-dependence is included in the "delay term", represented in equation 25.6 by $y(t-\tau)$.

$$\frac{dy}{dt} = f(y, y(t-\tau)) \qquad \mathrm{y}(-\tau : 0) = y_0(t) \qquad 25.6$$

The DDE must be solved in successive intervals of τ_P, as an initial value problem. The solution to the previous interval replaces the delay term of the differential equation, $C(t-\tau_P)$, and the initial condition for each interval is the value of the function at the end of the previous interval.

25.2 Solving the DDE

For the first time interval ($0 \le \mathrm{t} \le \tau_P$), the delay term is zero, which results in the ordinary differential equation shown in equation 25.7.

$$\frac{dC}{dt} = \frac{1}{\tau_C}\left(\frac{\nu_F C_t \delta(t)}{\nu_C} - C\right) \qquad C(0) = C_0 \qquad 25.7$$

We make use of the Integrating Factor method for solving ODEs, as shown in equations 25.8.

$$\frac{dC}{dt} + \frac{1}{\tau_C} C = \frac{1}{\tau_C}\frac{\nu_F}{\nu_C} C_t \delta(t)$$

$$IF = \exp\left(\int_0^t \frac{1}{\tau_C} dt\right) = \exp\left(\frac{t}{\tau_C}\right)$$

$$C = \frac{\left(\frac{1}{\tau_C}\frac{\nu_F}{\nu_C}\right)\int \exp\left(\frac{t}{\tau_C}\right) C_t \delta(t) dt + K}{\exp\left(\frac{t}{\tau_C}\right)} \qquad 25.8$$

$$C = \frac{C_t\left(\frac{1}{\tau_C}\frac{\nu_F}{\nu_C}\right) + K}{\exp\left(\frac{t}{\tau_C}\right)}$$

Applying initial condition to the result of the IF method gives the tracer concentration in the exit stream for the first interval.

$$C(\mathrm{t}) = \mathrm{C}_0 \exp\left(-\frac{\mathrm{t}}{\tau_C}\right) \qquad 0 \le \mathrm{t} \le \tau_P \qquad 25.9$$

In the second interval ($\tau_P \le t \le 2\tau_P$), the delay term assumes the value of the solution to the first interval (equation 25.9), and the initial condition is the value of equation 25.9, evaluated at $t = \tau_P$. This ODE is shown in equation 25.10.

$$\frac{dC}{dt} = \frac{1}{\tau_C}\left(\frac{\nu_P}{\nu_C}C(t-\tau_P) - C\right) \qquad C(\tau_P) = C_0 \exp\left(-\frac{\tau_P}{\tau_C}\right); \quad C(t-\tau_P) = C_0 \exp\left(-\frac{t-\tau_P}{\tau_C}\right) \tag{25.10}$$

Making use of the same method as before to solve the ODE results in the integrating factor shown in equation 25.11.

$$IF = \exp\left(\int_{\tau_P}^{t} \frac{1}{\tau_C}\,dt\right) = \exp\left(\frac{t-\tau_P}{\tau_C}\right) \tag{25.11}$$

The solution to equation 25.10 is given in equation 25.12.

$$C(t) = C_0\left[\exp\left(-\frac{t}{\tau_C}\right) + \left(\frac{1}{\tau_C}\frac{\nu_P}{\nu_C}\right)(t-\tau_P)\exp\left(-\frac{t-\tau_P}{\tau_C}\right)\right] \qquad \tau_P \le t \le 2\tau_P \tag{25.12}$$

The solutions to the DDE for the next two intervals ($2\tau_P \le t \le 3\tau_P$ and $3\tau_P \le t \le 4\tau_P$) are given in equations 25.13 and 25.14.

For $2\tau_P \le t \le 3\tau_P$:

$$C(t) = C_0\left[\exp\left(-\frac{t}{\tau_C}\right) + \left(\frac{1}{\tau_C}\frac{\nu_P}{\nu_C}\right)(t-\tau_P)\exp\left(-\frac{t-\tau_P}{\tau_C}\right) + \frac{1}{2}\left(\frac{1}{\tau_C}\frac{\nu_P}{\nu_C}\right)^2 (t-2\tau_P)^2 \exp\left(-\frac{t-2\tau_P}{\tau_C}\right)\right] \tag{25.13}$$

For $3\tau_P \le t \le 4\tau_P$:

$$C(t) = C_0\left[\begin{array}{l}\exp\left(-\frac{t}{\tau_C}\right) + \left(\frac{1}{\tau_C}\frac{\nu_P}{\nu_C}\right)(t-\tau_P)\exp\left(-\frac{t-\tau_P}{\tau_C}\right) + \ldots \\ \frac{1}{2}\left(\frac{1}{\tau_C}\frac{\nu_P}{\nu_C}\right)^2 (t-2\tau_P)^2 \exp\left(-\frac{t-2\tau_P}{\tau_C}\right) + \frac{1}{2}\frac{1}{3}\left(\frac{1}{\tau_C}\frac{\nu_P}{\nu_C}\right)^3 (t-3\tau_P)^3 \exp\left(-\frac{t-3\tau_P}{\tau_C}\right)\end{array}\right] \tag{25.14}$$

By inspection of the equations above, the solution to the DDE in equation 25.5 is an infinite series of terms, defined by the ratio of the time to the mean residence time of the PFR recycle: a new term is added when the time increases into a new integer multiple of τ_P. The concentration of tracer exiting the system is defined by equation 25.15.

$$C(t) = C_0 \sum_{X=0}^{n}\left[\frac{1}{X!}\left(\frac{1}{\tau_C}\frac{\nu_P}{\nu_C}\right)^X (t-X\tau_P)^X \exp\left(-\frac{t-X\tau_P}{\tau_C}\right)\right] \tag{25.15}$$

$$n = \left\lfloor t/\tau_P \right\rfloor$$

25.3 Residence time distribution function

Having found the time-dependant tracer concentration (equation 25.15), we seek the external residence time distribution function. By definition, the external RTD function can be found by equation 25.16.

$$E(t)=\frac{C(t)}{\int_o^\infty C(t)dt} \tag{25.16}$$

The denominator in equation 25.16 can be expanded into the form shown in equation 25.17, in which each term is integrated from some multiple of τ_P up to infinity.

$$\begin{aligned}\int_o^\infty C(t)dt = {} & C_0\int_o^\infty \exp\left(-\frac{t}{\tau_C}\right)dt + C_0\int_{\tau_P}^\infty \left(\frac{1}{\tau_C}\frac{\nu_P}{\nu_C}\right)(t-\tau_P)\exp\left(-\frac{t-\tau_P}{\tau_C}\right)dt + \\ & C_0\int_{2\tau_P}^\infty \frac{1}{2!}\left(\frac{1}{\tau_C}\frac{\nu_P}{\nu_C}\right)^2(t-2\tau_P)^2\exp\left(-\frac{t-2\tau_P}{\tau_C}\right)dt + \ldots \\ & + C_0\int_{X\tau_P}^\infty \frac{1}{X!}\left(\frac{1}{\tau_C}\frac{\nu_P}{\nu_C}\right)^X(t-X\tau_P)^X\exp\left(-\frac{t-X\tau_P}{\tau_C}\right)dt + \ldots\end{aligned} \tag{25.17}$$

Using limits to evaluate the last term in equation 25.17 gives equation 25.18, defining the integrals in terms of the Gamma ($\Gamma(x)$) and incomplete Gamma ($\Gamma(x,a)$) functions.

$$\begin{aligned}&\lim_{B\to\infty}\int_{X\tau_P}^B \frac{1}{X!}\left(\frac{1}{\tau_C}\frac{\nu_P}{\nu_C}\right)^X(t-X\tau_P)^X\exp\left(-\frac{t-X\tau_P}{\tau_C}\right)dt \\ &= \lim_{B\to\infty}\frac{1}{X!}\left(\frac{1}{\tau_C}\frac{\nu_P}{\nu_C}\right)^X \tau_C{}^{X+1}\left[\Gamma(X+1)-\Gamma\left(X+1,\frac{B-X\tau_P}{\tau_C}\right)\right]\end{aligned} \tag{25.18}$$

By definition of the Gamma function, if x is a positive integer then equation 25.19 holds.

$$\Gamma(x)=(x-1)! \tag{25.19}$$

The first step to solving equation 25.18 is to evaluate the Incomplete Gamma function term. By definition of the Incomplete Gamma Function, equation 25.20 represents this term.

$$\lim_{B\to\infty}\Gamma\left(X+1,\frac{B-X\tau_P}{\tau_C}\right)=\lim_{B\to\infty}\int_{\frac{B-X\tau_P}{\tau_C}}^B \exp(-t)t^X dt \tag{25.20}$$

The integral of the product of $\exp(-t)$ and t^n will be the product of $\exp(-t)$ and some linear combination of powers of t, designated $f(t^n,t^{n-1},\ldots,t,t^0)$, as shown in equation 25.21.

$$\int_A^B \exp(-t)t^n dt = \exp(-B)f(B^n,B^{n-1},\ldots,B,B^0)-\exp(-A)f(A^n,A^{n-1},\ldots,A,A^0) \tag{25.21}$$

Thus (and by successive application of L'Hospital's rule to terms of the form $\exp(-B)/B^X$), it can be shown (in equation 25.22) that the Incomplete Gamma term of equation 25.18 is equal to zero.

$$\lim_{B\to\infty}\int_{\frac{B-X\tau_P}{\tau_C}}^{B}\exp(-t)t^X dt = \lim_{B\to\infty}\exp(-B)f\left(B^X, B^{X-1},\ldots,B,B^0\right) - \exp\left(-\frac{B-X\tau_P}{\tau_C}\right)f\left(\frac{B-X\tau_P}{\tau_C}^X, \frac{B-X\tau_P}{\tau_C}^{X-1},\ldots,\frac{B-X\tau_P}{\tau_C},\frac{B-X\tau_P}{\tau_C}^0\right) = 0 \quad 25.22$$

Substituting the results of equations 25.19 and 25.22 into equation 25.18 results in equation 25.23.

$$\lim_{B\to\infty}\int_{X\tau_P}^{\infty}\frac{1}{X!}\left(\frac{1}{\tau_C}\frac{\nu_P}{\nu_C}\right)^X(t-X\tau_P)^X\exp\left(-\frac{t-X\tau_P}{\tau_C}\right)dt = \frac{1}{X!}\left(\frac{1}{\tau_C}\frac{\nu_P}{\nu_C}\right)^X {\tau_C}^{X+1}(X!+0) = \tau_C\left(\frac{\nu_P}{\nu_C}\right)^X \quad 25.23$$

Thus each term in equation 25.17 can be represented by the solution in equation 25.23, and the denominator in equation 25.16 is given by equation 25.24.

$$\int_o^\infty C(t)dt = C_0\sum_{X=0}^{\infty}\tau_C\left(\frac{\nu_P}{\nu_C}\right)^X \quad 25.24$$

Since the flow rate through the PFR recycle is a fraction of the flow rate through the CSTR, $\frac{\nu_P}{\nu_C}<1$, and thus equation 25.24 is a convergent series, with solution given in equation 25.25.

$$\int_o^\infty C(t)dt = C_0\tau_C\frac{1}{1-\frac{\nu_P}{\nu_C}} = C_0\tau_C\frac{\nu_C}{\nu_C-\nu_P} \quad 25.25$$

Substituting equation 25.25 into equation 25.16 results in a final expression for the external RTD function for the system of interest (equation 25.26).

$$E(t) = \frac{\sum_{X=0}^{n}\frac{1}{X!}\left(\frac{1}{\tau_C}\frac{\nu_P}{\nu_C}\right)^X(t-X\tau_P)^X\exp\left(-\frac{t-X\tau_P}{\tau_C}\right)}{\tau_C\frac{\nu_C}{\nu_C-\nu_P}} \quad 25.26$$

$$n = \left\lfloor t/\tau_P \right\rfloor$$

It is expected that the mean residence time of the system is given by the sum of the reactor volumes, divided by the feed flow rate. It is rigorously shown in the following section that the mean residence time of equation 25.26 does indeed take the form shown in equation 25.27.

$$\tau = \frac{V_C+V_P}{\nu_F} \quad 25.27$$

25.4 Mean residence time

To confirm that the mean residence time of equation 25.26 is equal to the predicted value in equation 25.27, the definition of the mean of a distribution is required. The mean value of the residence time distribution function, $E(t)$, which represents the mean residence time, τ , can be found with equation 25.28.

$$\tau = \int_0^\infty tE(t)dt \qquad 25.28$$

Because of the periodic nature of the function $E(t)$, the mean residence time can be found by the evaluation of a set of integrals, as shown in equation 25.29.

$$\begin{aligned}\tau = &\frac{1}{\tau_C \dfrac{\nu_C}{\nu_C - \nu_P}} \int_0^\infty t \exp\left(-\frac{t}{\tau_C}\right) dt + \frac{1}{\tau_C \dfrac{\nu_C}{\nu_C - \nu_P}} \int_{\tau_P}^\infty t \left(\frac{1}{\tau_C}\frac{\nu_P}{\nu_C}\right)(t-\tau_P)\exp\left(-\frac{t-\tau_P}{\tau_C}\right) dt + \ldots \\ &\ldots + \frac{1}{\tau_C \dfrac{\nu_C}{\nu_C - \nu_P}} \int_{n\tau_P}^\infty t \frac{1}{n!}\left(\frac{1}{\tau_C}\frac{\nu_P}{\nu_C}\right)^n (t-n\tau_P)^n \exp\left(-\frac{t-n\tau_P}{\tau_C}\right) dt + \ldots\end{aligned} \qquad 25.29$$

It can be shown (with some algebra) that equation 25.29 reduces to the infinite sum shown in equation 25.30.

$$\tau = \sum_{n=0}^{\infty} \frac{\nu_P^n \nu_C - \nu_P^{n+1}}{\nu_C^{n+1}} \left((n+1)\tau_C + n\tau_P\right) \qquad 25.30$$

Equation 25.30 can be rewritten in terms of the reactor volumes, V_C and V_P, the feed flow rate, ν_F, and a new factor, f , which defines the relationship between the CSTR product stream and the recycle stream flow rates. This recycle ratio is defined in equation 25.31.

$$f = \frac{\nu_P}{\nu_C} \qquad 25.31$$

Equation 25.32 shows the substitution of this new factor into equation 25.30, and the simplification of the expression into two infinite sums.

$$\begin{aligned}\tau &= \sum_{n=0}^{\infty} \frac{\left(\dfrac{\nu_F f}{1-f}\right)^n \dfrac{\nu_F}{1-f} - \left(\dfrac{\nu_F f}{1-f}\right)^{n+1}}{\left(\dfrac{\nu_F}{1-f}\right)^{n+1}} \left((n+1)\frac{V_C(1-f)}{\nu_F} + n\frac{V_P(1-f)}{\nu_F f}\right) \\ &= \frac{V_C}{\nu_F}(1-f)^2 \sum_{n=0}^{\infty} f^n (n+1) + \frac{V_P}{\nu_F}\frac{(1-f)^2}{f}\sum_{n=0}^{\infty} f^n n\end{aligned} \qquad 25.32$$

Since the factor f is always less than one (based on the physical definition of a recycle ratio), both of the infinite sums in the second line of equation 25.32 will be convergent; the values to which they converge are shown in equations 25.33.

$$\sum_{n=0}^{\infty} f^n(n+1) = \frac{1}{(1-f)^2}$$
$$\sum_{n=0}^{\infty} f^n n = \frac{f}{(1-f)^2} \qquad 25.33$$

Thus, substitution of these converged infinite series into equation 25.32 proves that the mean residence time of a CSTR with a PFR recycle, derived from the definition in equation 25.28, is the same as the predicted value in equation 25.27.

$$\tau = \frac{V_C + V_P}{\nu_F} \qquad 25.27$$

CHAPTER 26. MASS BALANCE FOR INDUSTRIAL REACTOR

In Chapter 11, the industrial process of interest was described, and a schematic diagram of the process shown in Figure 11.1, which is reproduced below. Ideally, a mass balance analysis of the system would allow the extraction of all parameters of interest, and allow for simple comparison between the industrial data and the predictions of the reactor model. However, the available industrial data makes this analysis somewhat difficult.

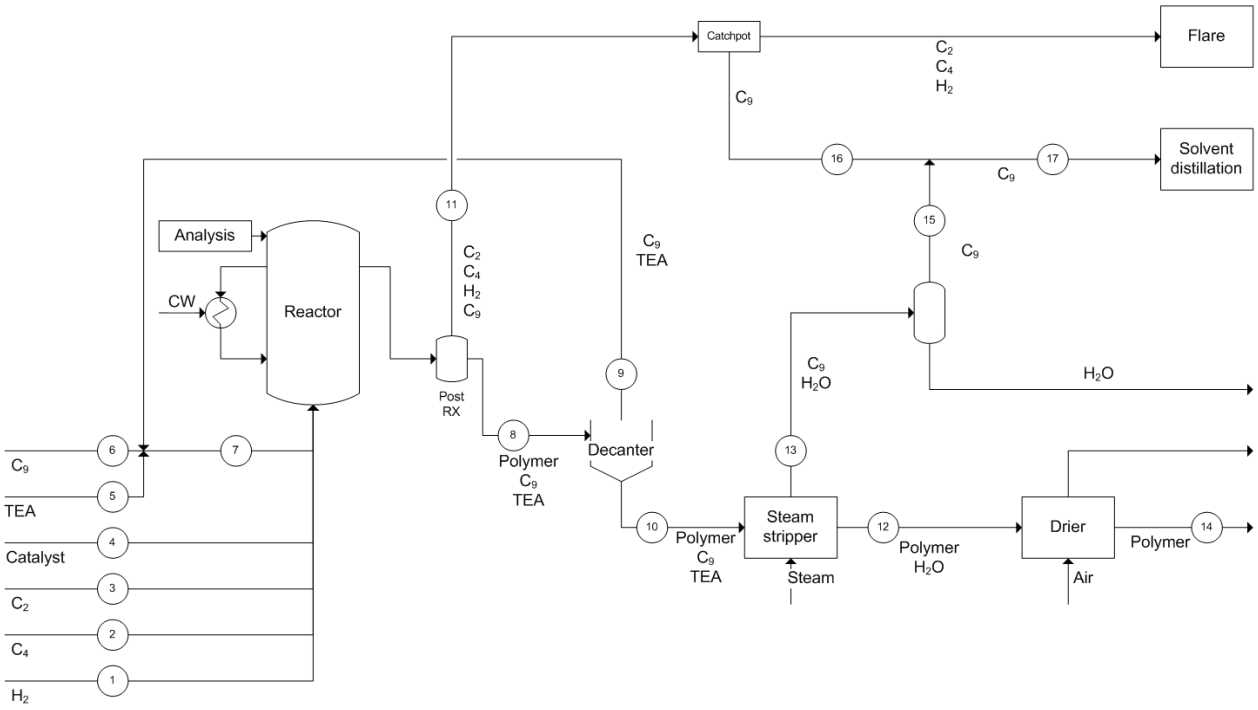

Figure 11.1: Schematic diagram of slurry-phase HDPE production

The most important part of the mass balance is that around the reactor itself. To close the balance around the reactor, post-reactor and decanter, all component flows in streams 1-6, 10 and 11 must be quantified. The component flows in these streams represent 13 unknown values. If it is assumed that the component flows in all feed streams are known, there are seven unknowns.

The component balances can be expressed as shown in Table 26.1. Note that $m_{A,B}$ refers to the mass flow rate of component A in stream B, and X_A refers to the fractional conversion of component A in the polymerisation reaction.

Table 26.1: Component mass balances

Component	Balance equations
Ethylene	$m_{C_2,3} - m_{C_2,11} - X_{C_2} m_{C_2,3} = 0$
1-Butene	$m_{C_4,2} - m_{C_4,11} - X_{C_4} m_{C_4,2} = 0$
Hydrogen	$m_{H_2,1} - m_{H_2,11} - X_{H_2} m_{H_2,1} = 0$
Solvent	$m_{C_9,6} - m_{C_9,10} - m_{C_9,11} = 0$
TEA	$m_{TEA,5} - X_{TEA} m_{TEA,7} - m_{TEA,10} = 0$ $m_{TEA,5} + m_{TEA,9} - m_{TEA,7} = 0$
Polymer	$m_{Pol,10} - X_{C_2} m_{C_2,3} - X_{C_4} m_{C_4,2} - X_{H_2} m_{H_2,1} - m_{cat,4} - X_{TEA} m_{TEA,7} = 0$

Although there are seven independent balance equations, there are also six new variables: the four component conversions and the flow rate of co-catalyst in streams 7 and 9, leaving six degrees of freedom. The actual performance of the reactor cannot be rigorously determined without identifying six additional measurements or known values.

Possible sources of information include:

- Assumed ethylene conversion (X_{C_2});
- Mother liquor analysis for co-catalyst content;
- Flow rate measurement of off-gas (stream 11);
- Analysis of composition of off-gas (stream 11);
- Assumed mother liquor entrainment with polymer powder at the decanter and
- Measured polymer production rate (stream 14).

Unfortunately, these additional plant measurements are not available; even with some reasonable assumptions, it is not possible to determine, from the plant data alone, every aspect of the performance of the industrial reactor, such as component conversions or the actual reactor hold-up.

Thus, in the absence of a complete mass balance around the reaction system of interest, we must look for other methods to compare the industrial data with the predictions of the reactor model. This development is shown in section 11.3 in Chapter 11.

CHAPTER 27. CATALYST AND CO-CATALYST POISONS

This chapter provides the kinetic parameter values and reactor model outputs in response to the presence of a hypothetical impurity in the experimental study. This poison affects either the catalyst or the co-catalyst.

27.1 Effect on co-catalyst

27.1.1 Kinetic parameters

As shown in Table 13.1 (reproduced below), the only kinetic parameters that were affected by accounting for effects of co-catalyst poisoning were those for site transformation and chain termination by the co-catalyst. All other parameters remained unchanged.

Table 13.1: Summary of parameters in kinetic model (co-catalyst poison factor)

$k_{p,ij}$			***j*=C_2H_4**	***j*=C_4H_8**	
		***i*=C_2H_4**	16.93	0.524	[L.min^{-1}.g-cat^{-1}]
		***i*=C_4H_8**	265.5	0	
	sp	**TEA**	**C_2H_4**	**C_4H_8**	**H_2**
	[min^{-1}]	[L.mol^{-1}.min^{-1}]	-	-	[min^{-1}.{mol-H_2.L^{-1}}$^{-0.5}$]
$k_{st,i}^{4+,3+}$	-	$31.7 / f_{co-cat}$	-	-	-
$k_{st,i}^{3+,2+}$	-	-	-	-	0.325
$k_{st,i}^{2+,3+}$	-	$0.924 / f_{co-cat}$	-	-	-
	[min^{-1}]	[L.mol^{-1}.min^{-1}]	[L.mol^{-1}.min^{-1}]	[L.mol^{-1}.min^{-1}]	[L.mol^{-1}.min^{-1}]
k_t^m	7.04x10^{-4}	$3701.2 / f_{co-cat}$	51.74	353.8	2311.4

27.1.2 Reactor model outputs

The tables below show the reactor model outputs for various values of the co-catalyst poison factor.

Table 27.1: Reactor model outputs (co-catalyst poison factor = 0.75)

Grade		**1**	**2**	**3**	**4**
Residence time [min]		179.5	186.2	191.0	186.7
Conversion [%]	TEA	19.7	17.8	18.0	20.3
	C_2H_4	96.1	89.4	94.5	86.6
	C_4H_8	54.0	44.9	51.0	41.7
	H_2	14.7	1.1	6.1	0.5
Catalyst efficiency	ton HDPE/kg-cat	2.69	5.69	3.59	7.55
Polymer properties	MFI (5 kg / 190^{o}C)	7.02×10^{-2}	1.25×10^{-3}	3.11×10^{-2}	1.13×10^{-4}
	M_n [g/mol]	3.963×10^{4}	5.576×10^{4}	4.280×10^{4}	6.883×10^{4}
	M_w [g/mol]	2.824×10^{5}	7.970×10^{5}	3.484×10^{5}	1.480×10^{6}
	mol% C_4H_8	0.0532	0.128	0.121	0.0877
Cap-gas ratio	H_2:C_2H_4	0.2370	0.04861	0.14634	0.02330
Liquid concentration [mol/m^3]	TEA	0.562	0.583	0.583	0.624
	C_2H_4	240.1	279.2	258.3	286.2
	C_4H_8	12.9	36.1	31.7	25.4
	H_2	9.81	2.35	6.54	1.157
Hold-up [m^3]	Liquid	56.5	57.2	57.1	57.8
	Gas	38.3	169.7	68.0	228.5
	Polymer	15.8	14.8	15.6	14.4
Chain length characteristic parameter $\left(1-\gamma^m\right)$	sp	2.19×10^{-6}	9.38×10^{-7}	1.66×10^{-6}	6.55×10^{-7}
	TEA	1.87×10^{-4}	1.65×10^{-4}	1.79×10^{-4}	1.72×10^{-4}
	C_2H_4	8.28×10^{-4}	8.23×10^{-4}	8.24×10^{-4}	8.25×10^{-4}
	C_4H_8	3.07×10^{-4}	7.28×10^{-4}	6.93×10^{-4}	5.02×10^{-4}
	H_2	1.51×10^{-3}	3.11×10^{-4}	9.32×10^{-4}	1.50×10^{-4}
Pseudo-sites fraction $\left(f^m\right)$	sp	1.659×10^{-5}	1.982×10^{-5}	1.654×10^{-5}	2.383×10^{-5}
	TEA	0.065	0.081	0.068	0.104
	C_2H_4	0.293	0.406	0.314	0.501
	C_4H_8	0.108	0.359	0.264	0.305
	H_2	0.534	0.153	0.355	0.090

Table 27.2: Reactor model outputs (co-catalyst poison factor = 0.5)

Grade		**1**	**2**	**3**	**4**
Residence time [min]		179.5	186.2	191.0	186.7
Conversion [%]	TEA	30.4	28.6	28.5	31.9
	C_2H_4	96.4	90.5	95.0	87.9
	C_4H_8	54.9	46.0	51.9	42.9
	H_2	17.2	1.4	7.4	0.6
Catalyst efficiency	ton HDPE/kg-cat	2.70	5.76	3.61	7.67
Polymer properties	MFI (5 kg / 190°C)	$1.19\text{x}10^{-1}$	$2.15\text{x}10^{-3}$	$5.51\text{x}10^{-2}$	$1.83\text{x}10^{-4}$
	M_n [g/mol]	$3.622\text{x}10^{4}$	$5.293\text{x}10^{4}$	$3.976\text{x}10^{4}$	$6.574\text{x}10^{4}$
	M_w [g/mol]	$2.464\text{x}10^{5}$	$6.929\text{x}10^{5}$	$3.005\text{x}10^{5}$	$1.308\text{x}10^{6}$
	mol% C_4H_8	0.0540	0.129	0.123	0.0890
Cap-gas ratio	H_2:C_2H_4	0.2687	0.05582	0.16716	0.02648
Liquid concentration [mol/m^3]	TEA	0.487	0.507	0.509	0.533
	C_2H_4	233.9	277.3	253.5	285.2
	C_4H_8	12.8	36.4	31.6	25.7
	H_2	10.82	2.68	7.32	1.310
Hold-up [m^3]	Liquid	56.4	57.2	57.1	57.8
	Gas	32.3	147.0	58.5	200.2
	Polymer	15.8	14.9	15.6	14.6
Chain length characteristic parameter $\left(1-\gamma^m\right)$	sp	$2.36\text{x}10^{-6}$	$1.01\text{x}10^{-6}$	$1.79\text{x}10^{-6}$	$6.97\text{x}10^{-7}$
	TEA	$2.49\text{x}10^{-4}$	$2.16\text{x}10^{-4}$	$2.38\text{x}10^{-4}$	$2.21\text{x}10^{-4}$
	C_2H_4	$8.28\text{x}10^{-4}$	$8.23\text{x}10^{-4}$	$8.24\text{x}10^{-4}$	$8.25\text{x}10^{-4}$
	C_4H_8	$3.11\text{x}10^{-4}$	$7.39\text{x}10^{-4}$	$7.03\text{x}10^{-4}$	$5.10\text{x}10^{-4}$
	H_2	$1.71\text{x}10^{-3}$	$3.57\text{x}10^{-4}$	$1.06\text{x}10^{-3}$	$1.70\text{x}10^{-4}$
Pseudo-sites fraction $\left(f^m\right)$	sp	$1.557\text{x}10^{-5}$	$1.896\text{x}10^{-5}$	$1.566\text{x}10^{-5}$	$2.285\text{x}10^{-5}$
	TEA	0.080	0.101	0.084	0.128
	C_2H_4	0.267	0.386	0.291	0.478
	C_4H_8	0.100	0.346	0.249	0.295
	H_2	0.553	0.167	0.376	0.098

Table 27.3: Reactor model outputs (co-catalyst poison factor = 0.25)

Grade		**1**	**2**	**3**	**4**
Residence time [min]		179.5	186.2	191.0	186.7
Conversion [%]	TEA	52.2	50.9	50.4	54.4
	C_2H_4	96.7	91.6	95.5	89.3
	C_4H_8	56.0	47.1	52.9	44.1
	H_2	20.5	1.8	9.2	0.7
Catalyst efficiency	ton HDPE/kg-cat	2.71	5.83	3.63	7.79
Polymer properties	MFI (5 kg / 190°C)	$2.12\text{x}10^{-1}$	$4.04\text{x}10^{-3}$	$1.06\text{x}10^{-1}$	$3.19\text{x}10^{-4}$
	M_n [g/mol]	$3.236\text{x}10^{4}$	$4.925\text{x}10^{4}$	$3.605\text{x}10^{4}$	$6.170\text{x}10^{4}$
	M_w [g/mol]	$2.123\text{x}10^{5}$	$5.890\text{x}10^{5}$	$2.538\text{x}10^{5}$	$1.133\text{x}10^{6}$
	mol% C_4H_8	0.0550	0.132	0.125	0.0904
Cap-gas ratio	H_2:C_2H_4	0.3100	0.06567	0.19557	0.03077
Liquid concentration [mol/m^3]	TEA	0.335	0.348	0.353	0.357
	C_2H_4	226.3	274.5	247.3	283.9
	C_4H_8	12.6	36.6	31.4	26.0
	H_2	12.07	3.12	8.35	1.515
Hold-up [m^3]	Liquid	56.4	57.2	57.1	57.8
	Gas	26.3	124.1	48.7	171.3
	Polymer	15.9	15.1	15.7	14.9
Chain length characteristic parameter $\left(1-\gamma^m\right)$	sp	$2.57\text{x}10^{-6}$	$1.09\text{x}10^{-6}$	$1.95\text{x}10^{-6}$	$7.50\text{x}10^{-7}$
	TEA	$3.52\text{x}10^{-4}$	$3.00\text{x}10^{-4}$	$3.38\text{x}10^{-4}$	$2.97\text{x}10^{-4}$
	C_2H_4	$8.28\text{x}10^{-4}$	$8.23\text{x}10^{-4}$	$8.24\text{x}10^{-4}$	$8.25\text{x}10^{-4}$
	C_4H_8	$3.17\text{x}10^{-4}$	$7.51\text{x}10^{-4}$	$7.16\text{x}10^{-4}$	$5.18\text{x}10^{-4}$
	H_2	$1.97\text{x}10^{-3}$	$4.19\text{x}10^{-4}$	$1.24\text{x}10^{-3}$	$1.97\text{x}10^{-4}$
Pseudo-sites fraction $\left(f^m\right)$	sp	$1.437\text{x}10^{-5}$	$1.782\text{x}10^{-5}$	$1.455\text{x}10^{-5}$	$2.156\text{x}10^{-5}$
	TEA	0.101	0.131	0.108	0.162
	C_2H_4	0.239	0.359	0.264	0.449
	C_4H_8	0.091	0.328	0.229	0.282
	H_2	0.569	0.183	0.399	0.107

Table 27.4: Reactor model outputs (co-catalyst poison factor = 0.1)

Grade		**1**	**2**	**3**	**4**
Residence time [min]		179.5	186.2	191.0	186.7
Conversion [%]	TEA	76.3	75.5	75.2	77.8
	C_2H_4	96.9	92.3	95.8	90.1
	C_4H_8	56.7	47.9	53.6	44.9
	H_2	23.0	2.1	10.7	0.9
Catalyst efficiency	ton HDPE/kg-cat	2.72	5.88	3.64	7.86
Polymer properties	MFI (5 kg / 190^{o}C)	$3.06\text{x}10^{-1}$	$6.25\text{x}10^{-3}$	$1.64\text{x}10^{-1}$	$4.69\text{x}10^{-4}$
	M_n [g/mol]	$2.980\text{x}10^{4}$	$4.649\text{x}10^{4}$	$3.342\text{x}10^{4}$	$5.870\text{x}10^{4}$
	M_w [g/mol]	$1.932\text{x}10^{5}$	$5.265\text{x}10^{5}$	$2.269\text{x}10^{5}$	$1.026\text{x}10^{6}$
	mol% C_4H_8	0.0557	0.133	0.127	0.0914
Cap-gas ratio	H_2:C_2H_4	0.3415	0.07363	0.21813	0.03415
Liquid concentration [mol/m^3]	TEA	0.166	0.174	0.177	0.174
	C_2H_4	220.8	272.4	242.5	282.9
	C_4H_8	12.4	36.7	31.2	26.2
	H_2	12.96	3.47	9.12	1.676
Hold-up [m^3]	Liquid	56.4	57.2	57.1	57.9
	Gas	22.7	110.0	42.8	153.6
	Polymer	15.9	15.2	15.8	15.0
Chain length characteristic parameter $\left(1-\gamma^m\right)$	sp	$2.73\text{x}10^{-6}$	$1.16\text{x}10^{-6}$	$2.08\text{x}10^{-6}$	$7.89\text{x}10^{-7}$
	TEA	$4.48\text{x}10^{-4}$	$3.76\text{x}10^{-4}$	$4.31\text{x}10^{-4}$	$3.63\text{x}10^{-4}$
	C_2H_4	$8.28\text{x}10^{-4}$	$8.23\text{x}10^{-4}$	$8.24\text{x}10^{-4}$	$8.25\text{x}10^{-4}$
	C_4H_8	$3.21\text{x}10^{-4}$	$7.59\text{x}10^{-4}$	$7.25\text{x}10^{-4}$	$5.23\text{x}10^{-4}$
	H_2	$2.17\text{x}10^{-3}$	$4.70\text{x}10^{-4}$	$1.38\text{x}10^{-3}$	$2.19\text{x}10^{-4}$
Pseudo-sites fraction $\left(f^m\right)$	sp	$1.356\text{x}10^{-5}$	$1.696\text{x}10^{-5}$	$1.376\text{x}10^{-5}$	$2.059\text{x}10^{-5}$
	TEA	0.118	0.155	0.128	0.188
	C_2H_4	0.220	0.339	0.245	0.428
	C_4H_8	0.085	0.313	0.215	0.271
	H_2	0.577	0.193	0.412	0.113

27.2 Effect on catalyst

27.2.1 Kinetic parameters

The "catalyst poison factor" defines the fraction of catalyst in the experimental study that was not deactivated by the hypothetical impurity.

The kinetic parameter values determined for each value of the catalyst poison factor are shown in the tables below.

Table 27.5: Summary of parameters in kinetic model (catalyst poison factor = 0.75)

$k_{p,ij}$			***j*=C_2H_4**	***j*=C_4H_8**	
		***i*=C_2H_4**	22.63	0.699	[L.min^{-1}.g-cat^{-1}]
		***i*=C_4H_8**	353.5	0	
	sp	**TEA**	**C_2H_4**	**C_4H_8**	**H_2**
	[min^{-1}]	[L.mol^{-1}.min^{-1}]	-	-	[min^{-1}.{mol-H_2.L^{-1}}$^{-0.5}$]
$k_{st,i}^{4+,3+}$	-	30.6	-	-	-
$k_{st,i}^{3+,2+}$	-	-	-	-	0.407
$k_{st,i}^{2+,3+}$	-	1.06	-	-	-
	[min^{-1}]	[L.mol^{-1}.min^{-1}]	[L.mol^{-1}.min^{-1}]	[L.mol^{-1}.min^{-1}]	[L.mol^{-1}.min^{-1}]
k_t^m	8.0x10^{-4}	4949.3	69.2	472.1	3091.6

Table 27.6: Summary of parameters in kinetic model (catalyst poison factor = 0.6)

$k_{p,ij}$			***j*=C_2H_4**	***j*=C_4H_8**	
		***i*=C_2H_4**	26.87	0.830	[L.min^{-1}.g-cat^{-1}]
		***i*=C_4H_8**	419.6	0	
	sp	**TEA**	**C_2H_4**	**C_4H_8**	**H_2**
	[min^{-1}]	[L.mol^{-1}.min^{-1}]	-	-	[min^{-1}.{mol-H_2.L^{-1}}$^{-0.5}$]
$k_{st,i}^{4+,3+}$	-	32.4	-	-	-
$k_{st,i}^{3+,2+}$	-	-	-	-	0.378
$k_{st,i}^{2+,3+}$	-	0.909	-	-	-
	[min^{-1}]	[L.mol^{-1}.min^{-1}]	[L.mol^{-1}.min^{-1}]	[L.mol^{-1}.min^{-1}]	[L.mol^{-1}.min^{-1}]
k_t^m	6.0x10^{-4}	5874.4	82.2	556.9	3674.1

Table 27.7: Summary of parameters in kinetic model (catalyst poison factor = 0.5)

$k_{p,ij}$			***j*=C_2H_4**	***j*=C_4H_8**	
		***i*=C_2H_4**	34.41	1.063	[L.min^{-1}.g-cat^{-1}]
		***i*=C_4H_8**	537.5	0	
	sp	**TEA**	**C_2H_4**	**C_4H_8**	**H_2**
	[min^{-1}]	[L.mol^{-1}.min^{-1}]	-	-	[min^{-1}.{mol-H_2.L^{-1}}$^{-0.5}$]
$k_{st,i}^{4+,3+}$	-	30.2	-	-	-
$k_{st,i}^{3+,2+}$	-	-	-	-	0.415
$k_{st,i}^{2+,3+}$	-	1.10	-	-	-
	[min^{-1}]	[L.mol^{-1}.min^{-1}]	[L.mol^{-1}.min^{-1}]	[L.mol^{-1}.min^{-1}]	[L.mol^{-1}.min^{-1}]
k_t^m	6.0x10^{-4}	7523.8	105.3	710.8	4709.0

Table 27.8: Summary of parameters in kinetic model (catalyst poison factor = 0.3)

$k_{p,ij}$			***j*=C_2H_4**	***j*=C_4H_8**	
		***i*=C_2H_4**	53.43	1.65	[L.min^{-1}.g-cat^{-1}]
		***i*=C_4H_8**	834.7	0	
	sp	**TEA**	**C_2H_4**	**C_4H_8**	**H_2**
	[min^{-1}]	[L.mol^{-1}.min^{-1}]	-	-	[min^{-1}.{mol-H_2.L^{-1}}$^{-0.5}$]
$k_{st,i}^{4+,3+}$	-	32.6	-	-	-
$k_{st,i}^{3+,2+}$	-	-	-	-	0.375
$k_{st,i}^{2+,3+}$	-	0.889	-	-	-
	[min^{-1}]	[L.mol^{-1}.min^{-1}]	[L.mol^{-1}.min^{-1}]	[L.mol^{-1}.min^{-1}]	[L.mol^{-1}.min^{-1}]
k_t^m	3.0x10^{-4}	11683	163.7	1095.1	7322.4

Table 27.9: Summary of parameters in kinetic model (catalyst poison factor = 0.2)

$k_{p,ij}$			***j*=C_2H_4**	***j*=C_4H_8**	
		***i*=C_2H_4**	78.89	2.44	[L.min^{-1}.g-cat^{-1}]
		***i*=C_4H_8**	1232.2	0	
	sp	**TEA**	**C_2H_4**	**C_4H_8**	**H_2**
	[min^{-1}]	[L.mol^{-1}.min^{-1}]	-	-	[min^{-1}.{mol-H_2.L^{-1}}$^{-0.5}$]
$k_{st,i}^{4+,3+}$	-	33.1	-	-	-
$k_{st,i}^{3+,2+}$	-	-	-	-	0.366
$k_{st,i}^{2+,3+}$	-	0.832	-	-	-
	[min^{-1}]	[L.mol^{-1}.min^{-1}]	[L.mol^{-1}.min^{-1}]	[L.mol^{-1}.min^{-1}]	[L.mol^{-1}.min^{-1}]
k_t^m	2.0x10^{-4}	17245	241.8	1610.7	10818

Table 27.10: Summary of parameters in kinetic model (catalyst poison factor = 0.15)

$k_{p,ij}$			***j*=C_2H_4**	***j*=C_4H_8**	
		***i*=C_2H_4**	112.2	3.465	[L.min^{-1}.g-cat^{-1}]
		***i*=C_4H_8**	1752.6	0	
	sp	**TEA**	**C_2H_4**	**C_4H_8**	**H_2**
	[min^{-1}]	[L.mol^{-1}.min^{-1}]	-	-	[min^{-1}.{mol-H_2.L^{-1}}$^{-0.5}$]
$k_{st,i}^{4+,3+}$	-	30.9	-	-	-
$k_{st,i}^{3+,2+}$	-	-	-	-	0.402
$k_{st,i}^{2+,3+}$	-	1.04	-	-	-
	[min^{-1}]	[L.mol^{-1}.min^{-1}]	[L.mol^{-1}.min^{-1}]	[L.mol^{-1}.min^{-1}]	[L.mol^{-1}.min^{-1}]
k_t^m	2.0x10^{-4}	24527	343.9	2287.1	15391

27.2.2 Reactor model outputs

The outputs from the reactor model for each value of the catalyst poison factor are shown in the tables below.

Table 27.11: Reactor model outputs (catalyst poison factor = 0.75)

Grade		**1**	**2**	**3**	**4**
Residence time [min]		179.5	186.2	191.0	186.7
Conversion [%]	TEA	13.9	12.1	12.4	13.9
	C_2H_4	96.3	90.5	94.8	88.4
	C_4H_8	54.4	45.9	51.5	43.3
	H_2	16.3	1.4	7.1	0.7
Catalyst efficiency	ton HDPE/kg-cat	2.70	5.76	3.60	7.71
Polymer properties	MFI (5 kg / 190°C)	$6.70\text{x}10^{-2}$	$1.81\text{x}10^{-3}$	$3.32\text{x}10^{-2}$	$2.09\text{x}10^{-4}$
	M_n [g/mol]	$3.861\text{x}10^{4}$	$5.512\text{x}10^{4}$	$4.191\text{x}10^{4}$	$6.837\text{x}10^{4}$
	M_w [g/mol]	$2.857\text{x}10^{5}$	$7.246\text{x}10^{5}$	$3.424\text{x}10^{5}$	$1.264\text{x}10^{6}$
	mol% C_4H_8	0.0538	0.130	0.123	0.0897
Cap-gas ratio	H_2:C_2H_4	0.2533	0.05528	0.15896	0.02789
Liquid concentration [mol/m^3]	TEA	0.603	0.624	0.623	0.674
	C_2H_4	236.9	277.4	255.4	284.8
	C_4H_8	12.9	36.3	31.7	25.8
	H_2	10.33	2.66	7.02	1.378
Hold-up [m^3]	Liquid	56.5	57.2	57.1	57.8
	Gas	34.9	148.5	61.8	189.6
	Polymer	15.8	14.9	15.6	14.7
Chain length characteristic parameter $\left(1-\gamma^m\right)$	sp	$2.13\text{x}10^{-6}$	$9.34\text{x}10^{-7}$	$1.63\text{x}10^{-6}$	$6.66\text{x}10^{-7}$
	TEA	$1.53\text{x}10^{-4}$	$1.33\text{x}10^{-4}$	$1.45\text{x}10^{-4}$	$1.40\text{x}10^{-4}$
	C_2H_4	$8.29\text{x}10^{-4}$	$8.24\text{x}10^{-4}$	$8.25\text{x}10^{-4}$	$8.25\text{x}10^{-4}$
	C_4H_8	$3.09\text{x}10^{-4}$	$7.36\text{x}10^{-4}$	$6.98\text{x}10^{-4}$	$5.11\text{x}10^{-4}$
	H_2	$1.61\text{x}10^{-3}$	$3.53\text{x}10^{-4}$	$1.01\text{x}10^{-3}$	$1.79\text{x}10^{-4}$
Pseudo-sites fraction $\left(f^m\right)$	sp	$1.394\text{x}10^{-5}$	$1.679\text{x}10^{-5}$	$1.393\text{x}10^{-5}$	$2.026\text{x}10^{-5}$
	TEA	0.052	0.065	0.054	0.084
	C_2H_4	0.286	0.403	0.308	0.499
	C_4H_8	0.106	0.360	0.261	0.309
	H_2	0.557	0.172	0.378	0.108

Table 27.12: Reactor model outputs (catalyst poison factor = 0.6)

Grade		**1**	**2**	**3**	**4**
Residence time [min]		179.5	186.2	191.0	186.7
Conversion [%]	TEA	13.5	11.9	12.2	13.9
	C_2H_4	97.2	93.2	96.1	92.0
	C_4H_8	57.6	49.1	54.3	46.9
	H_2	28.4	3.2	13.6	1.7
Catalyst efficiency	ton HDPE/kg-cat	2.73	5.94	3.65	8.03
Polymer properties	MFI (5 kg / 190°C)	$1.41\text{x}10^{-1}$	$6.14\text{x}10^{-3}$	$8.35\text{x}10^{-2}$	$8.23\text{x}10^{-4}$
	M_n [g/mol]	$3.014\text{x}10^{4}$	$4.930\text{x}10^{4}$	$3.460\text{x}10^{4}$	$6.315\text{x}10^{4}$
	M_w [g/mol]	$2.358\text{x}10^{5}$	$5.288\text{x}10^{5}$	$2.700\text{x}10^{5}$	$8.876\text{x}10^{5}$
	mol% C_4H_8	0.0566	0.135	0.129	0.0935
Cap-gas ratio	H_2:C_2H_4	0.3767	0.08720	0.24138	0.04481
Liquid concentration [mol/m^3]	TEA	0.606	0.625	0.625	0.673
	C_2H_4	215.0	268.8	237.9	279.9
	C_4H_8	12.3	36.8	30.9	26.5
	H_2	13.91	4.06	9.90	2.174
Hold-up [m^3]	Liquid	56.4	57.2	57.1	57.9
	Gas	18.2	91.4	36.9	114.8
	Polymer	16.0	15.4	15.8	15.3
Chain length characteristic parameter $\left(1-\gamma^m\right)$	sp	$2.12\text{x}10^{-6}$	$9.20\text{x}10^{-7}$	$1.61\text{x}10^{-6}$	$6.54\text{x}10^{-7}$
	TEA	$1.69\text{x}10^{-4}$	$1.38\text{x}10^{-4}$	$1.56\text{x}10^{-4}$	$1.43\text{x}10^{-4}$
	C_2H_4	$8.29\text{x}10^{-4}$	$8.24\text{x}10^{-4}$	$8.25\text{x}10^{-4}$	$8.26\text{x}10^{-4}$
	C_4H_8	$3.23\text{x}10^{-4}$	$7.63\text{x}10^{-4}$	$7.27\text{x}10^{-4}$	$5.30\text{x}10^{-4}$
	H_2	$2.39\text{x}10^{-3}$	$5.56\text{x}10^{-4}$	$1.53\text{x}10^{-3}$	$2.87\text{x}10^{-4}$
Pseudo-sites fraction $\left(f^m\right)$	sp	$7.577\text{x}10^{-6}$	$9.813\text{x}10^{-6}$	$7.812\text{x}10^{-6}$	$1.207\text{x}10^{-5}$
	TEA	0.045	0.060	0.048	0.080
	C_2H_4	0.223	0.361	0.255	0.463
	C_4H_8	0.086	0.335	0.224	0.297
	H_2	0.645	0.244	0.473	0.161

Table 27.13: Reactor model outputs (catalyst poison factor = 0.5)

Grade		**1**	**2**	**3**	**4**
Residence time [min]		179.5	186.2	191.0	186.7
Conversion [%]	TEA	13.4	11.7	12.0	13.7
	C_2H_4	97.7	94.7	96.8	93.9
	C_4H_8	59.9	51.2	56.5	49.1
	H_2	40.1	5.7	20.8	3.3
Catalyst efficiency	ton HDPE/kg-cat	2.74	6.03	3.68	8.19
Polymer properties	MFI (5 kg / 190°C)	$2.17\text{x}10^{-1}$	$1.34\text{x}10^{-2}$	$1.43\text{x}10^{-1}$	$2.18\text{x}10^{-3}$
	M_n [g/mol]	$2.513\text{x}10^{4}$	$4.441\text{x}10^{4}$	$2.962\text{x}10^{4}$	$5.821\text{x}10^{4}$
	M_w [g/mol]	$2.111\text{x}10^{5}$	$4.330\text{x}10^{5}$	$2.349\text{x}10^{5}$	$6.902\text{x}10^{5}$
	mol% C_4H_8	0.0588	0.139	0.133	0.0963
Cap-gas ratio	H_2:C_2H_4	0.4900	0.12230	0.32214	0.06539
Liquid concentration [mol/m^3]	TEA	0.608	0.626	0.627	0.674
	C_2H_4	198.3	260.1	222.9	274.2
	C_4H_8	11.8	36.7	30.0	26.7
	H_2	16.64	5.50	12.35	3.106
Hold-up [m^3]	Liquid	56.3	57.2	57.0	57.9
	Gas	9.5	62.5	24.2	75.4
	Polymer	16.1	15.6	16.0	15.6
Chain length characteristic parameter $\left(1-\gamma^m\right)$	sp	$2.14\text{x}10^{-6}$	$9.43\text{x}10^{-7}$	$1.64\text{x}10^{-6}$	$6.78\text{x}10^{-7}$
	TEA	$1.83\text{x}10^{-4}$	$1.43\text{x}10^{-4}$	$1.67\text{x}10^{-4}$	$1.46\text{x}10^{-4}$
	C_2H_4	$8.29\text{x}10^{-4}$	$8.24\text{x}10^{-4}$	$8.25\text{x}10^{-4}$	$8.26\text{x}10^{-4}$
	C_4H_8	$3.34\text{x}10^{-4}$	$7.84\text{x}10^{-4}$	$7.51\text{x}10^{-4}$	$5.43\text{x}10^{-4}$
	H_2	$3.10\text{x}10^{-3}$	$7.79\text{x}10^{-4}$	$2.04\text{x}10^{-3}$	$4.19\text{x}10^{-4}$
Pseudo-sites fraction $\left(f^m\right)$	sp	$5.349\text{x}10^{-6}$	$7.139\text{x}10^{-6}$	$5.572\text{x}10^{-6}$	$8.882\text{x}10^{-6}$
	TEA	0.041	0.056	0.044	0.075
	C_2H_4	0.186	0.326	0.218	0.427
	C_4H_8	0.075	0.310	0.198	0.281
	H_2	0.699	0.308	0.540	0.217

Table 27.14: Reactor model outputs (catalyst poison factor = 0.3)

Grade		**1**	**2**	**3**	**4**
Residence time [min]		179.5	186.2	191.0	186.7
Conversion [%]	TEA	20.5	11.2	12.7	12.7
	C_2H_4	98.8	97.2	98.3	96.8
	C_4H_8	72.2	57.2	64.4	54.4
	H_2	70.3	25.3	59.8	19.1
Catalyst efficiency	ton HDPE/kg-cat	2.78	6.20	3.74	8.45
Polymer properties	MFI (5 kg / 190°C)	8.6645×10^{-1}	1.561×10^{-1}	8.664×10^{-1}	4.362×10^{-2}
	M_n [g/mol]	1.742×10^{4}	2.904×10^{4}	1.765×10^{4}	4.070×10^{4}
	M_w [g/mol]	1.478×10^{5}	2.298×10^{5}	1.478×10^{5}	3.192×10^{5}
	mol% C_4H_8	0.0703	0.154	0.152	0.1047
Cap-gas ratio	H_2:C_2H_4	0.7885	0.31645	0.70897	0.18473
Liquid concentration [mol/m^3]	TEA	0.562	0.631	0.624	0.682
	C_2H_4	117.5	220.5	166.8	245.4
	C_4H_8	8.3	34.4	25.6	26.0
	H_2	15.61	11.99	20.16	7.821
Hold-up [m^3]	Liquid	55.9	57.1	56.8	57.9
	Gas	0.1	15.6	0.1	17.6
	Polymer	16.3	16.1	16.2	16.1
Chain length characteristic parameter $\left(1-\gamma^m\right)$	sp	2.03×10^{-6}	9.44×10^{-7}	1.62×10^{-6}	6.88×10^{-7}
	TEA	2.84×10^{-4}	1.69×10^{-4}	2.22×10^{-4}	1.65×10^{-4}
	C_2H_4	8.29×10^{-4}	8.24×10^{-4}	8.25×10^{-4}	8.26×10^{-4}
	C_4H_8	3.95×10^{-4}	8.60×10^{-4}	8.46×10^{-4}	5.85×10^{-4}
	H_2	4.90×10^{-3}	2.00×10^{-3}	4.44×10^{-3}	1.18×10^{-3}
Pseudo-sites fraction $\left(f^m\right)$	sp	2.010×10^{-6}	1.776×10^{-6}	1.427×10^{-6}	2.241×10^{-6}
	TEA	0.044	0.044	0.035	0.060
	C_2H_4	0.129	0.214	0.130	0.300
	C_4H_8	0.061	0.223	0.133	0.213
	H_2	0.766	0.520	0.702	0.428

Table 27.15: Reactor model outputs (catalyst poison factor = 0.2)

Grade		**1**	**2**	**3**	**4**
Residence time [min]		179.5	186.2	191.0	186.7
Conversion [%]	TEA	33.9	12.4	22.8	13.2
	C_2H_4	99.3	98.2	99.0	97.9
	C_4H_8	81.7	63.7	75.8	59.9
	H_2	80.3	56.9	72.3	50.2
Catalyst efficiency	ton HDPE/kg-cat	2.79	6.27	3.77	8.56
Polymer properties	MFI (5 kg / 190^{o}C)	1.62	$5.92\text{x}10^{-1}$	2.09	$2.10\text{x}10^{-1}$
	M_n [g/mol]	$1.548\text{x}10^4$	$2.007\text{x}10^4$	$1.512\text{x}10^4$	$2.843\text{x}10^4$
	M_w [g/mol]	$1.257\text{x}10^5$	$1.630\text{x}10^5$	$1.177\text{x}10^5$	$2.130\text{x}10^5$
	mol% C_4H_8	0.0791	0.172	0.178	0.1151
Cap-gas ratio	H_2:C_2H_4	0.9022	0.57238	0.85339	0.35946
Liquid concentration [mol/m^3]	TEA	0.469	0.625	0.556	0.681
	C_2H_4	69.3	172.6	97.8	202.0
	C_4H_8	5.5	30.0	17.5	23.5
	H_2	10.41	16.84	14.00	12.435
Hold-up [m^3]	Liquid	55.7	56.9	56.4	57.7
	Gas	0.1	0.1	0.1	0.1
	Polymer	16.3	16.2	16.4	16.3
Chain length characteristic parameter $\left(1-\gamma^m\right)$	sp	$1.86\text{x}10^{-6}$	$9.41\text{x}10^{-7}$	$1.51\text{x}10^{-6}$	$6.94\text{x}10^{-7}$
	TEA	$4.01\text{x}10^{-4}$	$2.14\text{x}10^{-4}$	$3.35\text{x}10^{-4}$	$1.99\text{x}10^{-4}$
	C_2H_4	$8.29\text{x}10^{-4}$	$8.24\text{x}10^{-4}$	$8.24\text{x}10^{-4}$	$8.26\text{x}10^{-4}$
	C_4H_8	$4.42\text{x}10^{-4}$	$9.52\text{x}10^{-4}$	$9.83\text{x}10^{-4}$	$6.40\text{x}10^{-4}$
	H_2	$5.54\text{x}10^{-3}$	$3.58\text{x}10^{-3}$	$5.24\text{x}10^{-3}$	$2.27\text{x}10^{-3}$
Pseudo-sites fraction $\left(f^m\right)$	sp	$1.366\text{x}10^{-6}$	$7.069\text{x}10^{-7}$	$9.394\text{x}10^{-7}$	$8.585\text{x}10^{-7}$
	TEA	0.055	0.038	0.045	0.050
	C_2H_4	0.114	0.148	0.111	0.210
	C_4H_8	0.061	0.171	0.133	0.162
	H_2	0.769	0.644	0.711	0.577

Table 27.16: Reactor model outputs (catalyst poison factor = 0.15)

Grade		**1**	**2**	**3**	**4**
Residence time [min]		179.5	186.2	191.0	186.7
Conversion [%]	TEA	43.7	18.6	31.9	19.6
	C_2H_4	99.5	98.8	99.3	98.5
	C_4H_8	86.1	71.5	81.6	67.9
	H_2	85.0	65.6	78.8	59.4
Catalyst efficiency	ton HDPE/kg-cat	2.80	6.31	3.79	8.62
Polymer properties	MFI (5 kg / 190°C)	1.74	$8.63\text{x}10^{-1}$	2.54	$2.88\text{x}10^{-1}$
	M_n [g/mol]	$1.466\text{x}10^{4}$	$1.799\text{x}10^{4}$	$1.400\text{x}10^{4}$	$2.538\text{x}10^{4}$
	M_w [g/mol]	$1.234\text{x}10^{5}$	$1.479\text{x}10^{5}$	$1.120\text{x}10^{5}$	$1.963\text{x}10^{5}$
	mol% C_4H_8	0.0833	0.192	0.191	0.1297
Cap-gas ratio	H_2:C_2H_4	0.9576	0.65572	0.93161	0.41795
Liquid concentration [mol/m^3]	TEA	0.400	0.584	0.492	0.634
	C_2H_4	50.1	122.1	69.1	144.2
	C_4H_8	4.2	23.7	13.3	18.9
	H_2	7.95	13.48	10.73	10.194
Hold-up [m^3]	Liquid	55.6	56.6	56.2	57.4
	Gas	0.1	0.1	0.1	0.1
	Polymer	16.4	16.4	16.4	16.5
Chain length characteristic parameter $\left(1-\gamma^m\right)$	sp	$1.73\text{x}10^{-6}$	$9.19\text{x}10^{-7}$	$1.45\text{x}10^{-6}$	$6.79\text{x}10^{-7}$
	TEA	$4.74\text{x}10^{-4}$	$2.81\text{x}10^{-4}$	$4.19\text{x}10^{-4}$	$2.59\text{x}10^{-4}$
	C_2H_4	$8.29\text{x}10^{-4}$	$8.23\text{x}10^{-4}$	$8.23\text{x}10^{-4}$	$8.25\text{x}10^{-4}$
	C_4H_8	$4.64\text{x}10^{-4}$	$1.06\text{x}10^{-3}$	$1.05\text{x}10^{-3}$	$7.20\text{x}10^{-4}$
	H_2	$5.85\text{x}10^{-3}$	$4.05\text{x}10^{-3}$	$5.68\text{x}10^{-3}$	$2.60\text{x}10^{-3}$
Pseudo-sites fraction $\left(f^m\right)$	sp	$1.258\text{x}10^{-6}$	$6.291\text{x}10^{-7}$	$8.643\text{x}10^{-7}$	$7.539\text{x}10^{-7}$
	TEA	0.062	0.045	0.052	0.059
	C_2H_4	0.108	0.132	0.103	0.187
	C_4H_8	0.060	0.170	0.132	0.163
	H_2	0.769	0.653	0.714	0.591

CHAPTER 28. VALIDATION OF STEADY-STATE MODEL

28.1 Laboratory reactor model output

The figures below show the liquid-phase concentrations of the various reactants in the laboratory reactor, as predicted by the dynamic reactor model formulation described in Section 14.1.

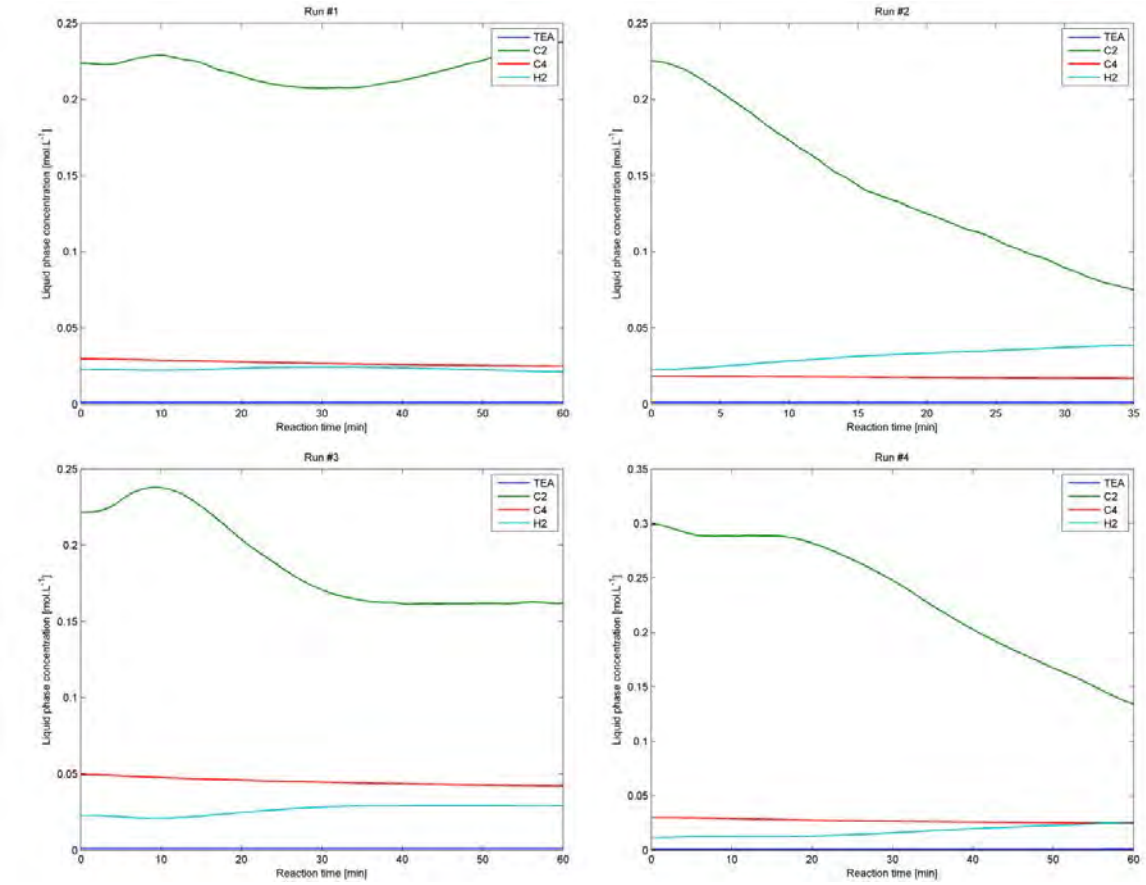

Figure 28.1: Simulated liquid-phase concentrations in the laboratory reactor, Runs 1-4

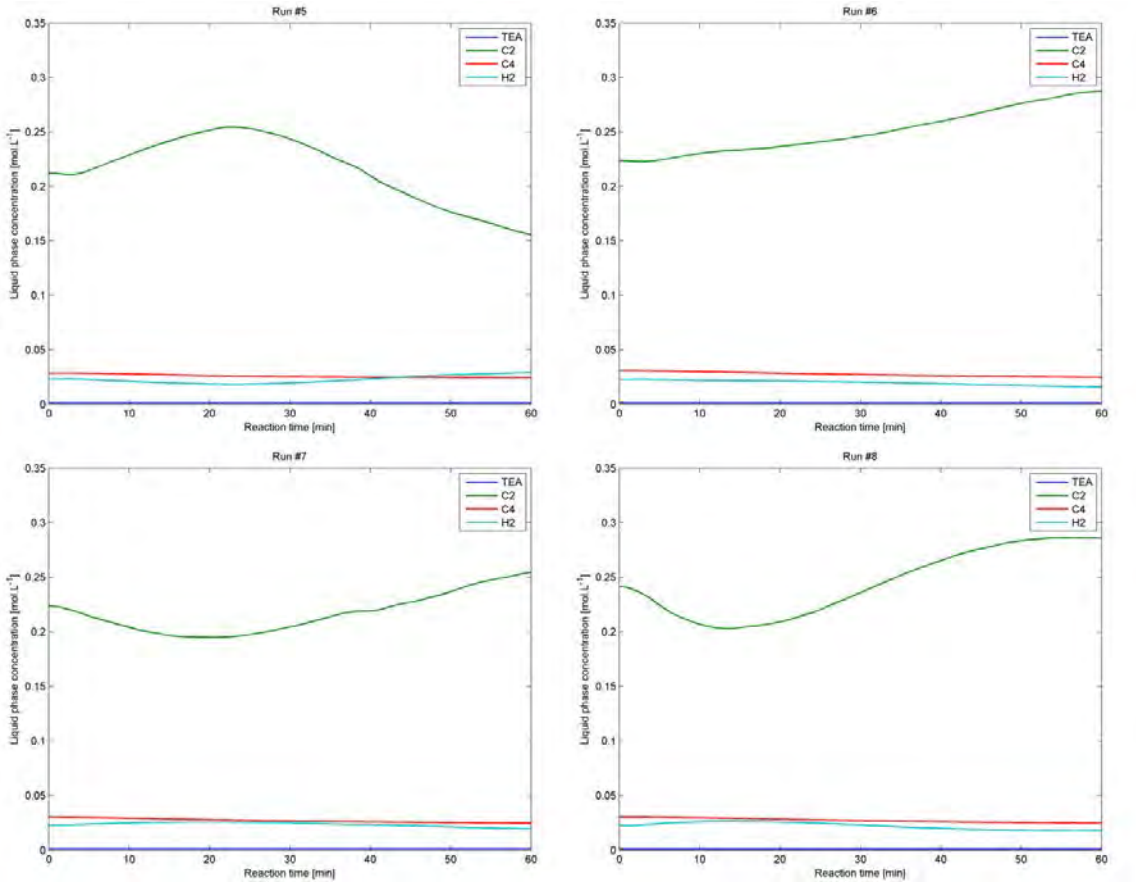

Figure 28.2: Simulated liquid-phase concentrations in the laboratory reactor, Runs 5-8

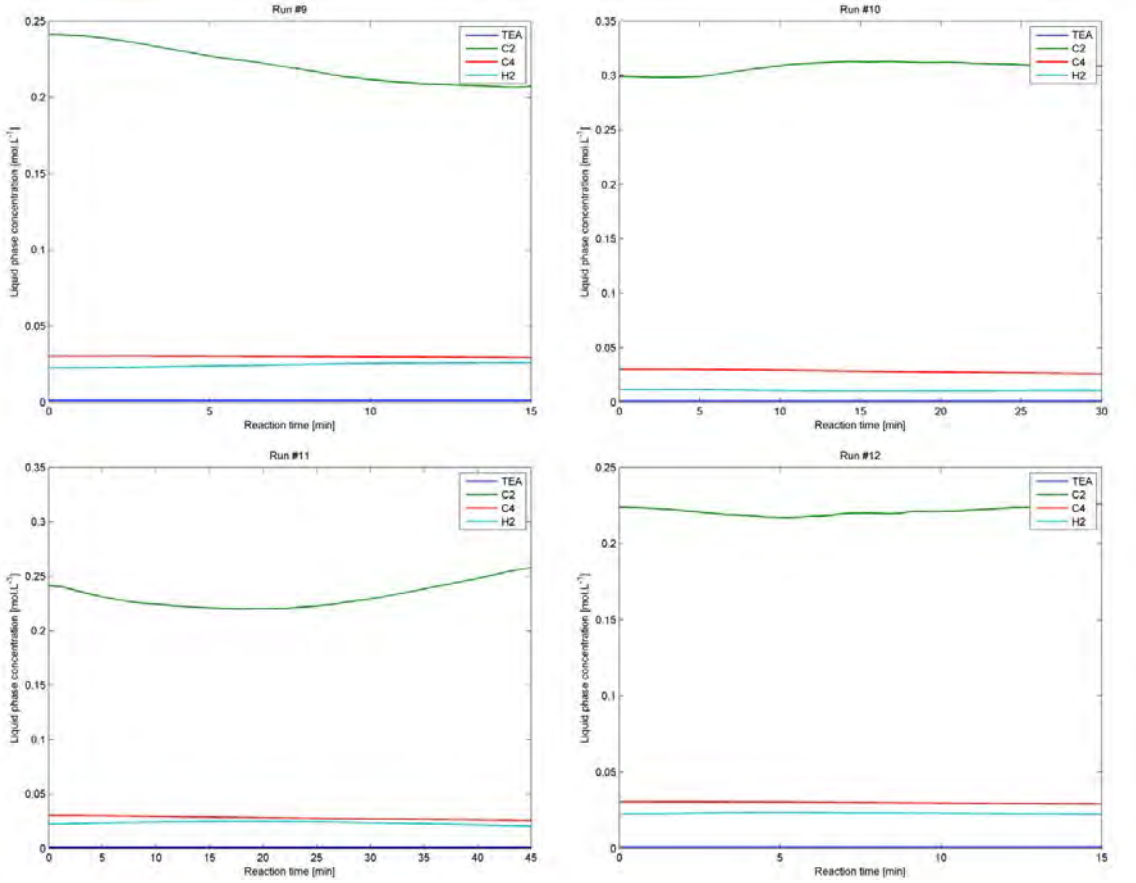

Figure 28.3: Simulated liquid-phase concentrations in the laboratory reactor, Runs 9-12

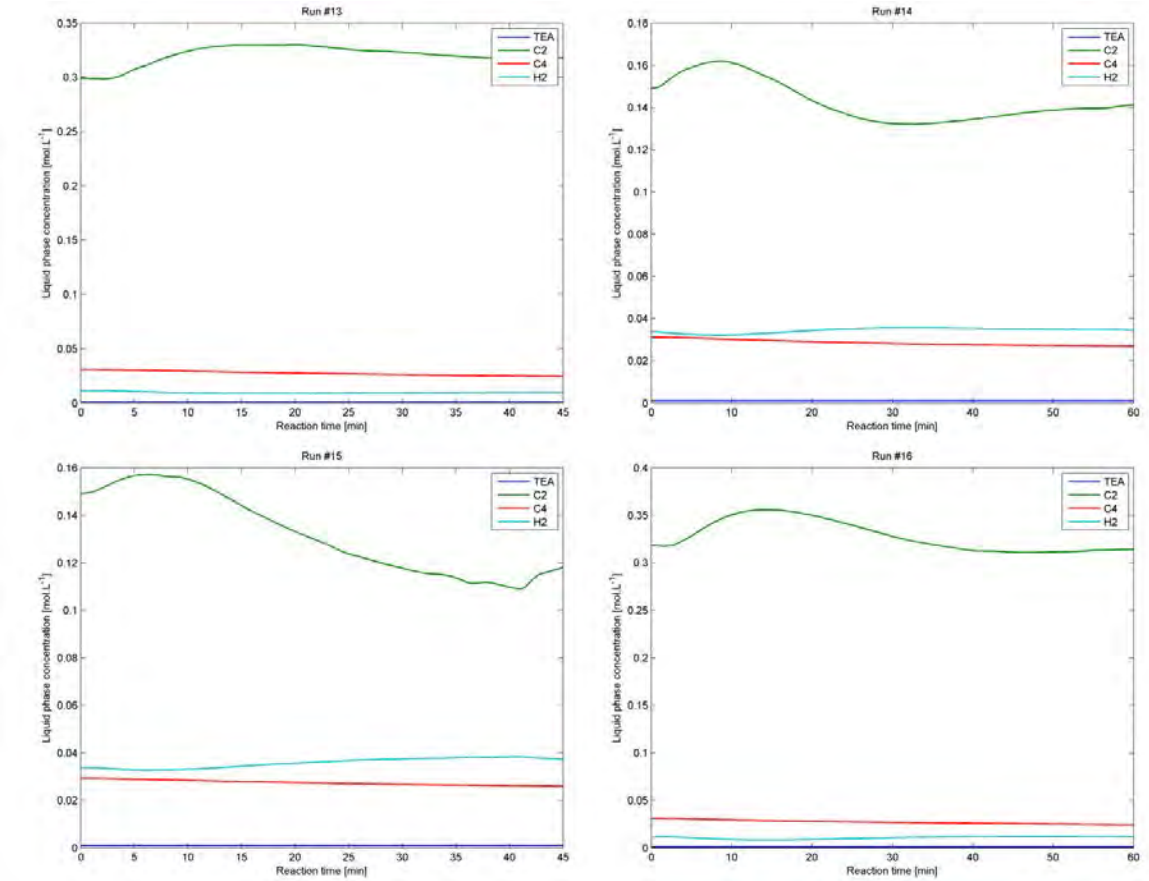

Figure 28.4: Simulated liquid-phase concentrations in the laboratory reactor, Runs 13-16

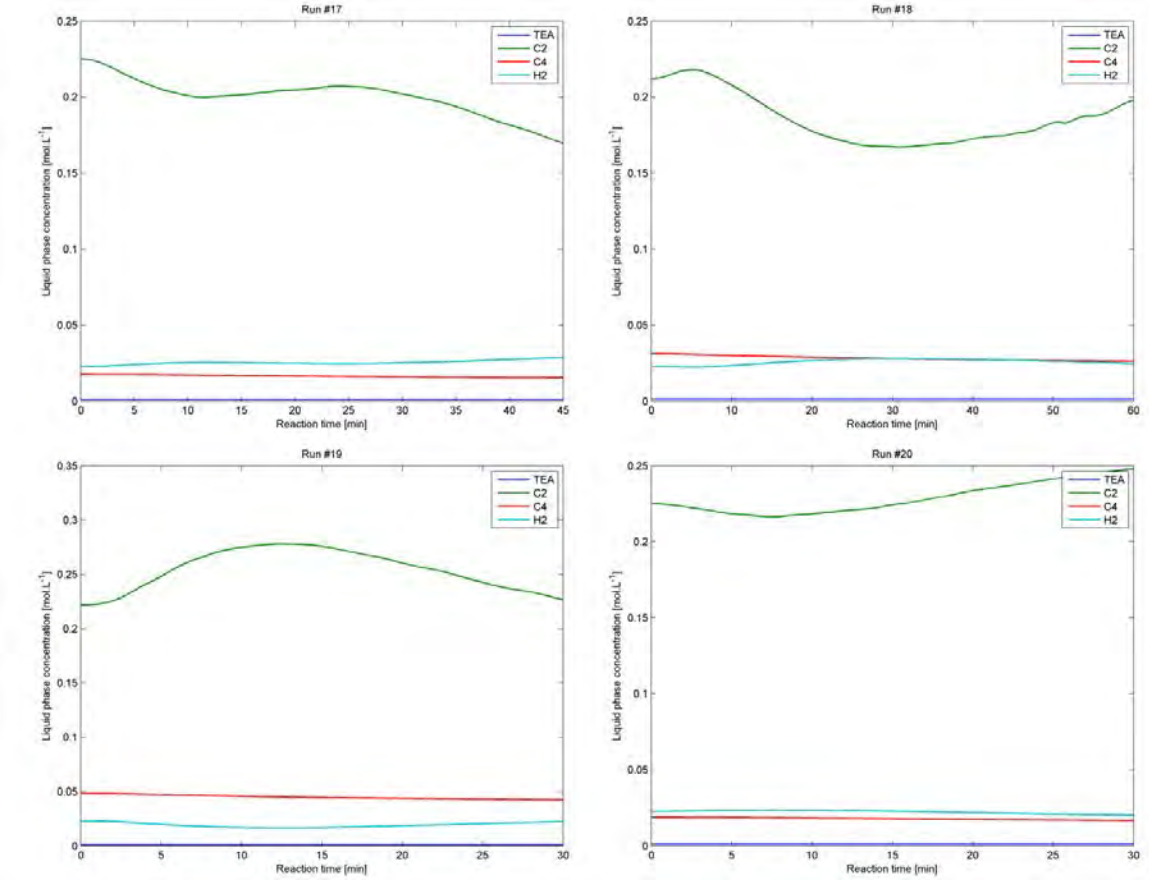

Figure 28.5: Simulated liquid-phase concentrations in the laboratory reactor, Runs 17-20

28.2 Industrial reactor model output

The reactor model outputs from the simultaneous fitting of laboratory and industrial data are shown in Table 28.1.

Table 28.1: Output from reactor model

Grade		**1**	**2**	**3**	**4**
Residence time [min]		179.5	186.2	191.0	186.7
Conversion [%]	TEA	4.35	1.92	3.24	1.30
	C_2H_4	99.2	97.8	98.7	97.5
	C_4H_8	79.6	62.3	72.2	58.9
	H_2	75.1	35.1	62.7	29.8
Catalyst efficiency	ton HDPE/kg-cat	2.79	6.24	3.76	8.52
Polymer properties	MFI (5 kg / 190^{o}C)	13.95	6.935	25.41	1.655
	M_n [g/mol]	1.201×10^4	1.583×10^4	1.112×10^4	2.252×10^4
	M_w [g/mol]	7.224×10^4	8.648×10^4	6.189×10^4	1.251×10^5
	mol% C_4H_8	0.0751	0.157	0.161	0.1060
Cap-gas ratio	H_2:C_2H_4	0.971	0.495	0.906	0.305
Liquid concentration [mol/m^3]	TEA	0.678	0.699	0.695	0.773
	C_2H_4	80.7	193.7	122.8	222.2
	C_4H_8	6.14	30.8	20.0	23.9
	H_2	13.10	16.42	18.78	11.66
Hold-up [m^3]	Liquid	55.8	57.0	56.5	57.8
	Gas	0.058	5.96	0.058	5.60
	Polymer	16.320	16.18	16.307	16.27
Chain length characteristic parameter $\left(1-\gamma^m\right)$	sp	2.68×10^{-6}	1.24×10^{-6}	2.09×10^{-6}	9.16×10^{-7}
	TEA	0	0	0	0
	C_2H_4	9.07×10^{-4}	9.02×10^{-4}	9.02×10^{-4}	9.04×10^{-4}
	C_4H_8	7.96×10^{-4}	1.65×10^{-3}	1.69×10^{-3}	1.12×10^{-3}
	H_2	5.27×10^{-3}	2.75×10^{-3}	4.94×10^{-3}	1.71×10^{-3}
Pseudo-sites fraction $\left(f^m\right)$	sp	1.37×10^{-6}	7.47×10^{-7}	8.27×10^{-7}	9.29×10^{-7}
	TEA	0.000	0.000	0.000	0.000
	C_2H_4	0.129	0.170	0.119	0.242
	C_4H_8	0.113	0.311	0.224	0.300
	H_2	0.757	0.519	0.657	0.458

CHAPTER 29. SENSITIVITY STUDY – FURTHER RESULTS

The figures below show the sensitivity of reactor model outputs to the various inputs, as determined in Chapter 16. The figures are arranged to show first the Outputs and Internal Checks, for comparison between industrial data and reactor model predictions, and then other polymer properties, which do not directly relate to the industrial data, but are important parameters.

29.1 Outputs

The main Output from the reactor model (when optimising grade transitions) is the Melt Flow Index; the sensitivity of this parameter was discussed in Chapter 16. The other two Outputs are the monomer conversion and catalyst efficiency; the sensitivity of these two Outputs is shown in Figure 29.1 and Figure 29.2, respectively.

As expected, monomer conversion (in Figure 29.1) is most sensitive to the feed rate of catalyst: increases in catalyst feed rate have a large impact on the conversion of monomer, due to the very high activity of the Ziegler-Natta catalyst.

The monomer conversion is also relatively sensitive to the feed rate of solvent, since the solvent affects residence time, and will have the effect of diluting reactants, reducing the overall reaction rate.

The influence of hydrogen on monomer conversion is also apparent; hydrogen is involved in catalyst deactivation reactions (through site transformation reactions), and so an increase in hydrogen feed results in a decrease in overall catalyst activity, and thus conversion.

Catalyst efficiency (Figure 29.2) is directly related to monomer conversion, and so the sensitivity of this Output is very similar to the sensitivity of the monomer conversion.

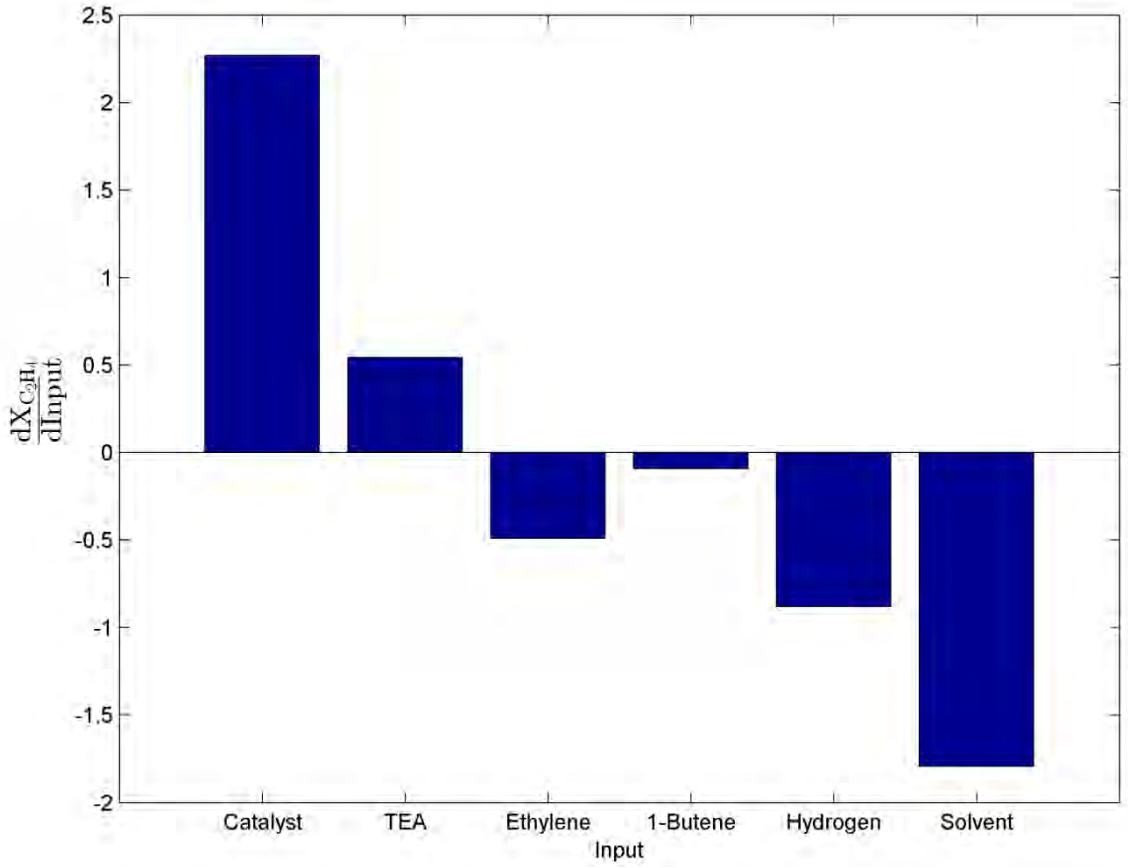

Figure 29.1: Sensitivity of C_2H_4 conversion to inputs. C_2H_4 conversion in [%]

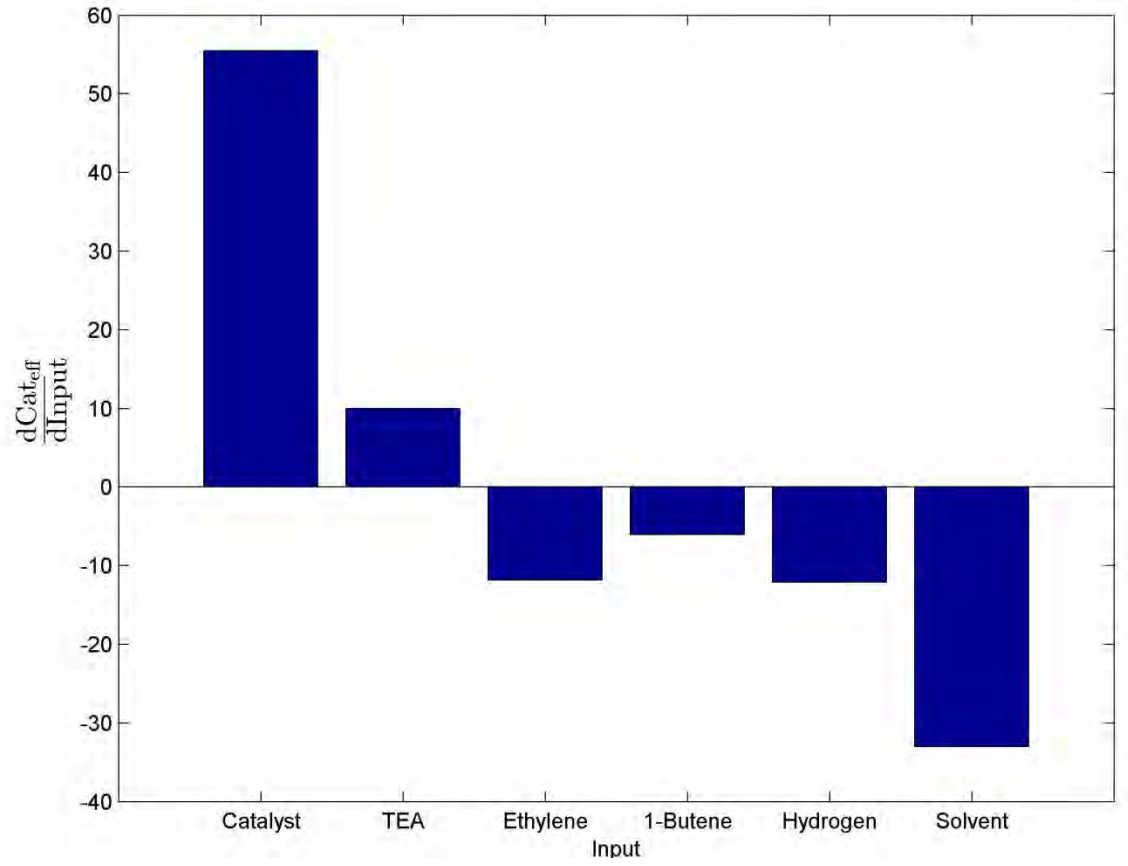

Figure 29.2: Sensitivity of catalyst efficiency to inputs. Catalyst efficiency in [ton-HDPE/kg-cat]

29.2 Internal Checks

The first Internal Check, the cap-gas ratio of hydrogen to ethylene (shown in Figure 29.3), is very sensitive to the feed rates of ethylene and hydrogen, as expected. The cap-gas ratio is also sensitive to feeds which influence monomer conversion (shown in Figure 29.1), since the total quantity of ethylene present in the reactor will affect the ratio of hydrogen to ethylene. Thus, the catalyst and solvent feed rates have a relatively large influence the cap-gas ratio.

Figure 29.4 shows the sensitivity of the co-catalyst content of the reaction medium to the inputs. As expected, the TEA concentration is most sensitive to the feed rates of co-catalyst and solvent; because the conversion of co-catalyst is relatively low in the reactor, the actual concentration is largely determined by the concentration in the feed stream.

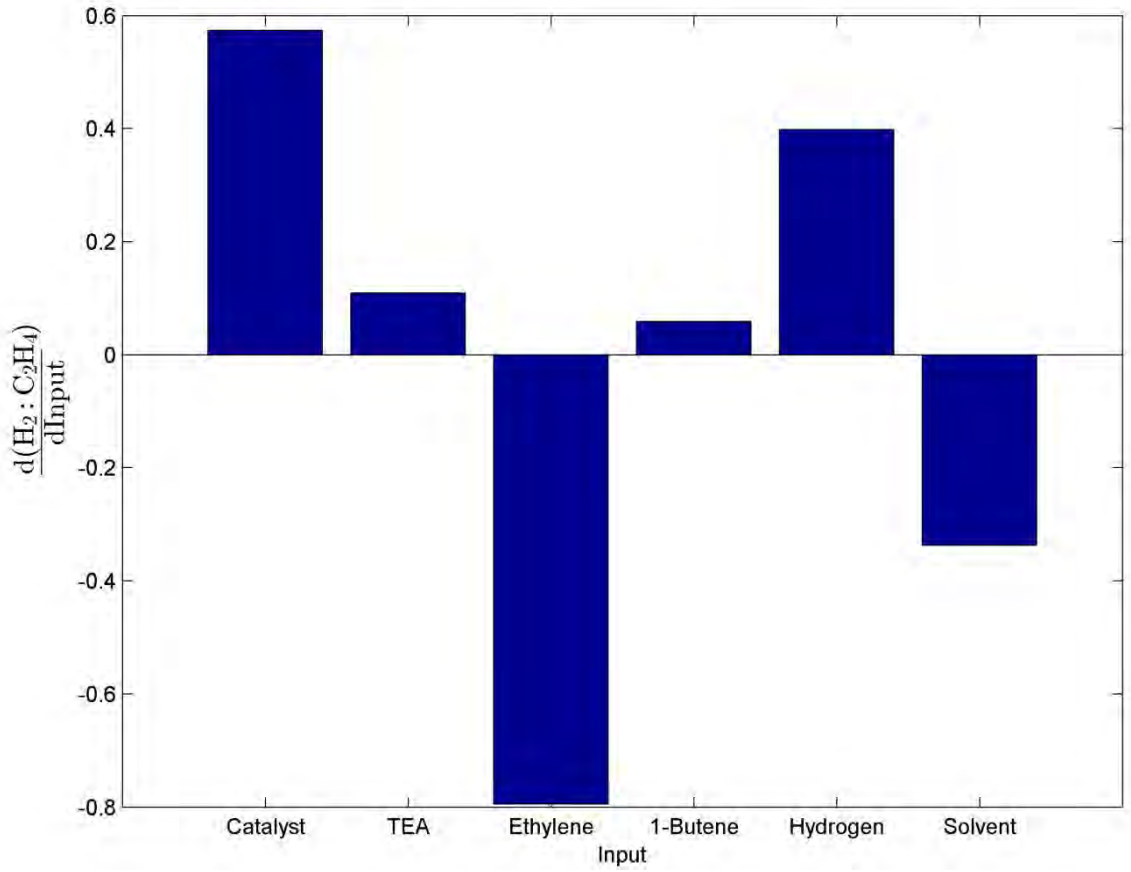

Figure 29.3: Sensitivity of cap-gas ratio to inputs.

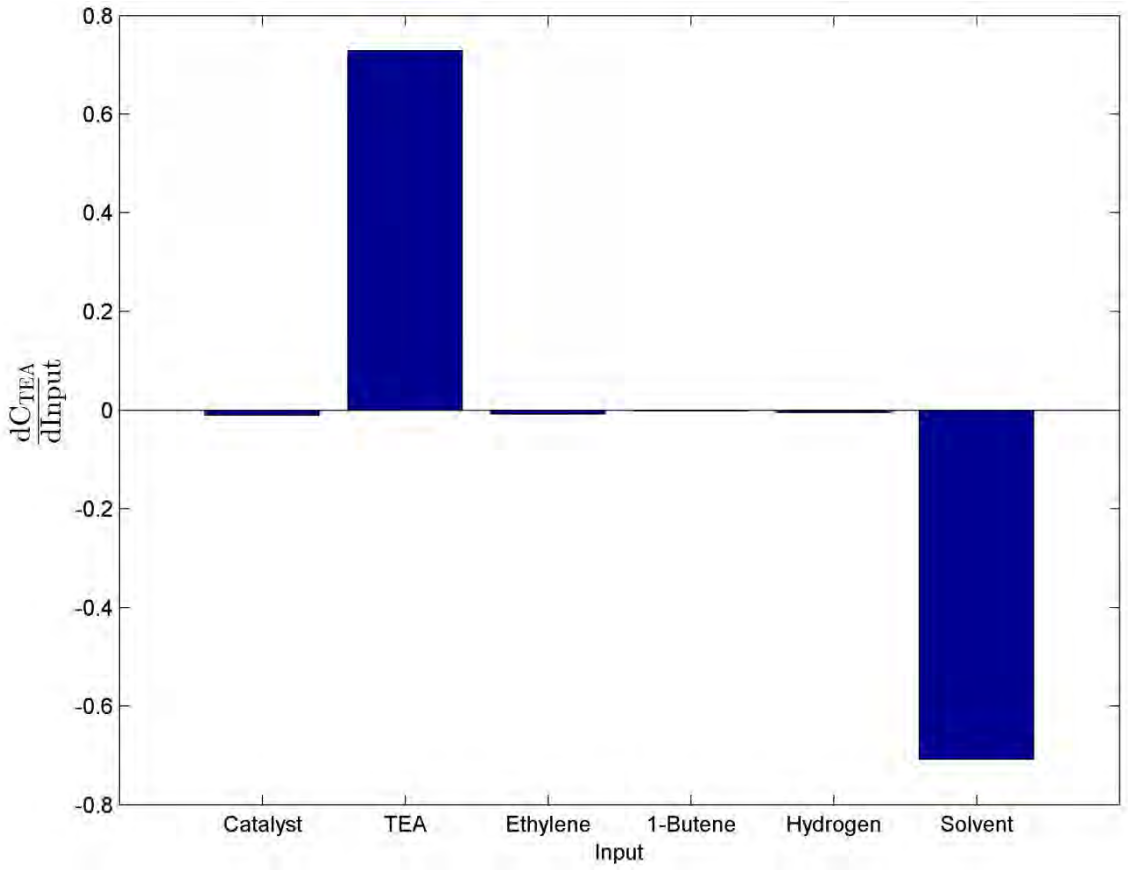

Figure 29.4: Sensitivity of TEA concentration to inputs. TEA concentration in [mol/m^3]

29.3 Polymer properties

Although the sensitivity of the Melt Flow Index (MFI) has been discussed, and is the main point of comparison between the industrial data and the reactor model, other polymer properties are of interest; these include the number- and weight-average molecular weights (M_n and M_w) and the comonomer content of the polymer.

Figure 29.5 and Figure 29.6 show the sensitivity of the number- and weight-average molecular weights to the various inputs. Figure 29.7 shows the sensitivity of comonomer content to the inputs.

The number- and weight-average molecular weights show similar sensitivity to the MFI, since all of these parameters are indications of the distribution of chain lengths present in the final polymer product. Both M_n and M_w decrease significantly in response to increases in catalyst feed rate, since additional catalyst will increase the monomer conversion (as seen in Figure 29.1), increasing the ratio of hydrogen to monomer in the reactor (see Figure 29.3), and increasing the rate of chain termination reactions relative to propagation reactions.

Similarly, increasing the feed rate of ethylene will increase the length of polymer chains produced: the ratio of hydrogen to ethylene will decrease, and the rate of termination reactions will decrease, relative to propagation reactions.

As discussed in Chapter 16, for reactor stability reasons it is unwise to use catalyst, monomer or solvent feed rates to control the trajectory of a grade transition, and so the sensitivity of chain length to hydrogen was used as the manipulated variable for transition optimisation.

The incorporation of comonomer into the ethylene polymer chains has not received significant attention in this work, but can be of great importance to the final properties of the polymer product: comonomer fractions will influence the crystallinity of the polymer, and can affect the end-use to which a product can be put.

As shown in Figure 29.7, the comonomer fraction is most sensitive to the feed rates of ethylene and 1-butene. This result was expected, since the incorporation of comonomer is directly related to the relative rates of propagation for the monomer and comonomer, which depends on the relative reaction-phase concentrations of the two monomers.

Since the other reactor inputs do not significantly impact the comonomer fraction, it is possible to manipulate this property of the polymer product simply by varying the ratio of 1-butene to ethylene in the feed to the reactor.

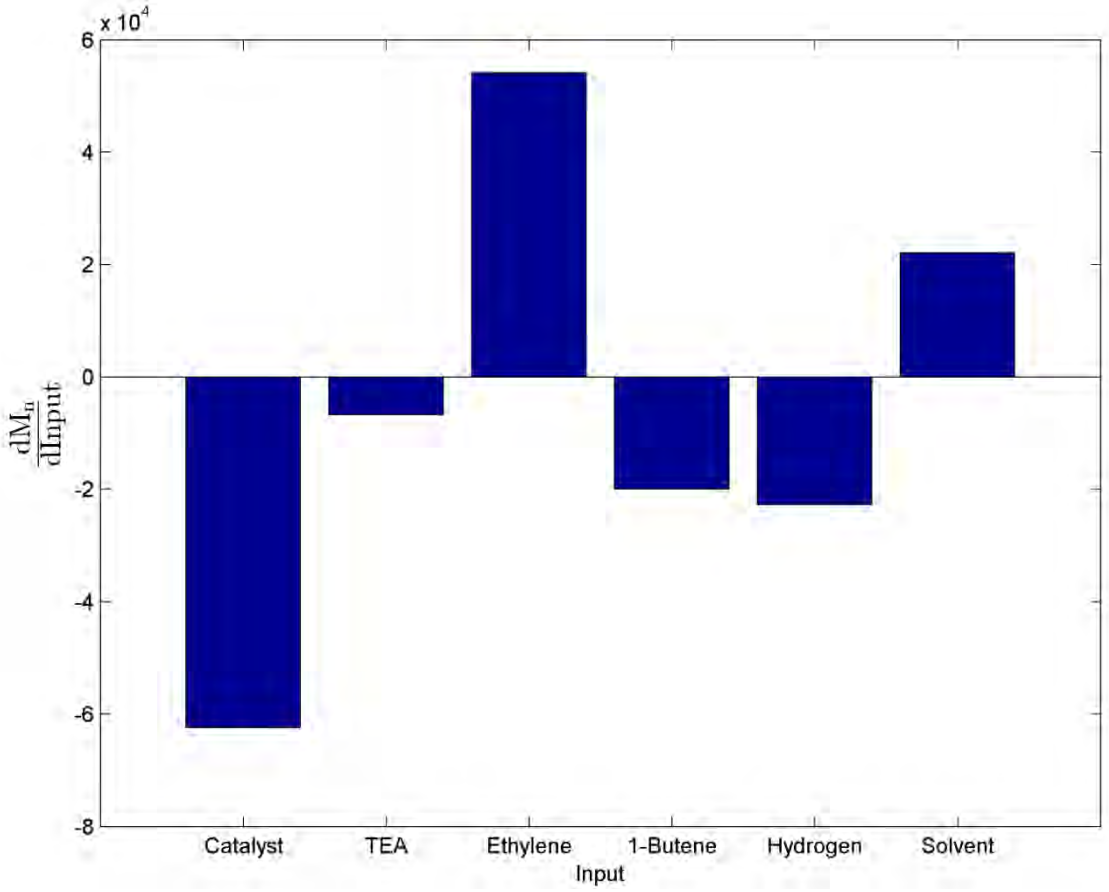

Figure 29.5: Sensitivity of M_n to inputs. M_n in [g/mol]

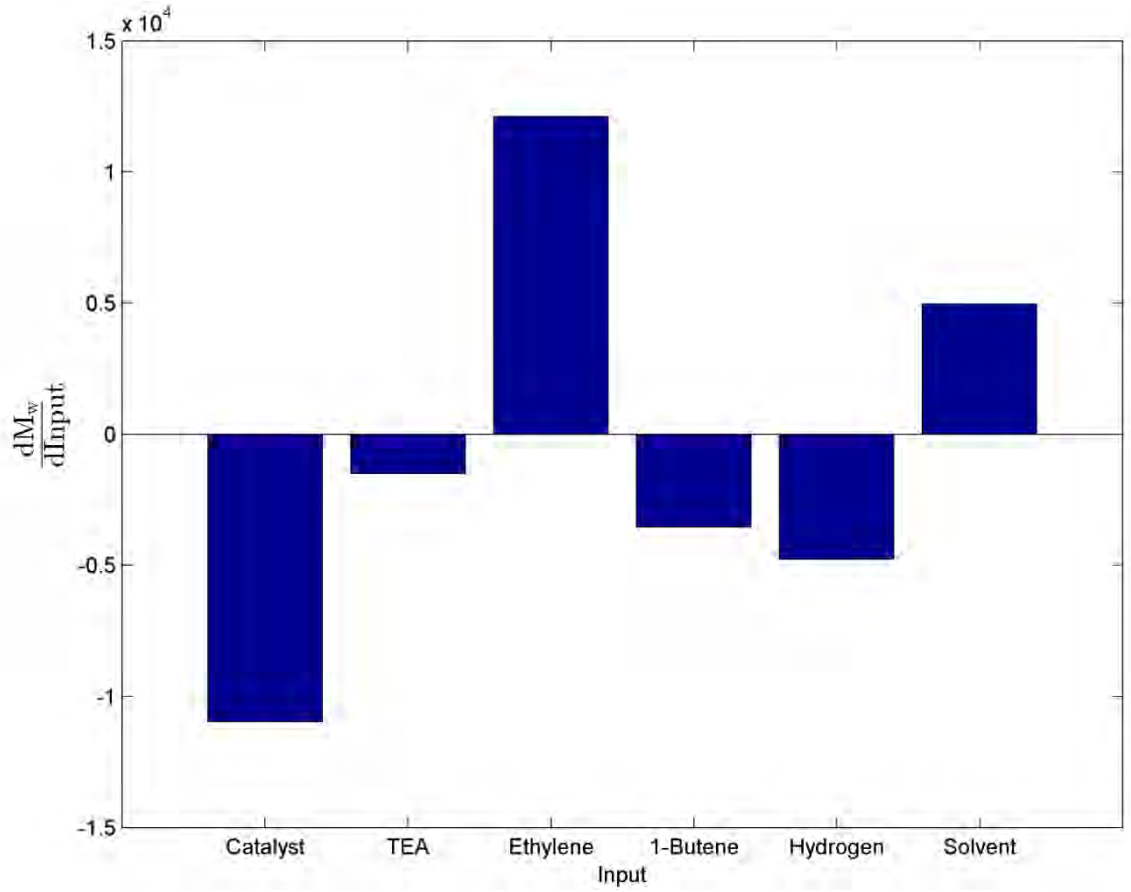

Figure 29.6: Sensitivity of M_w to inputs. M_w in [g/mol]

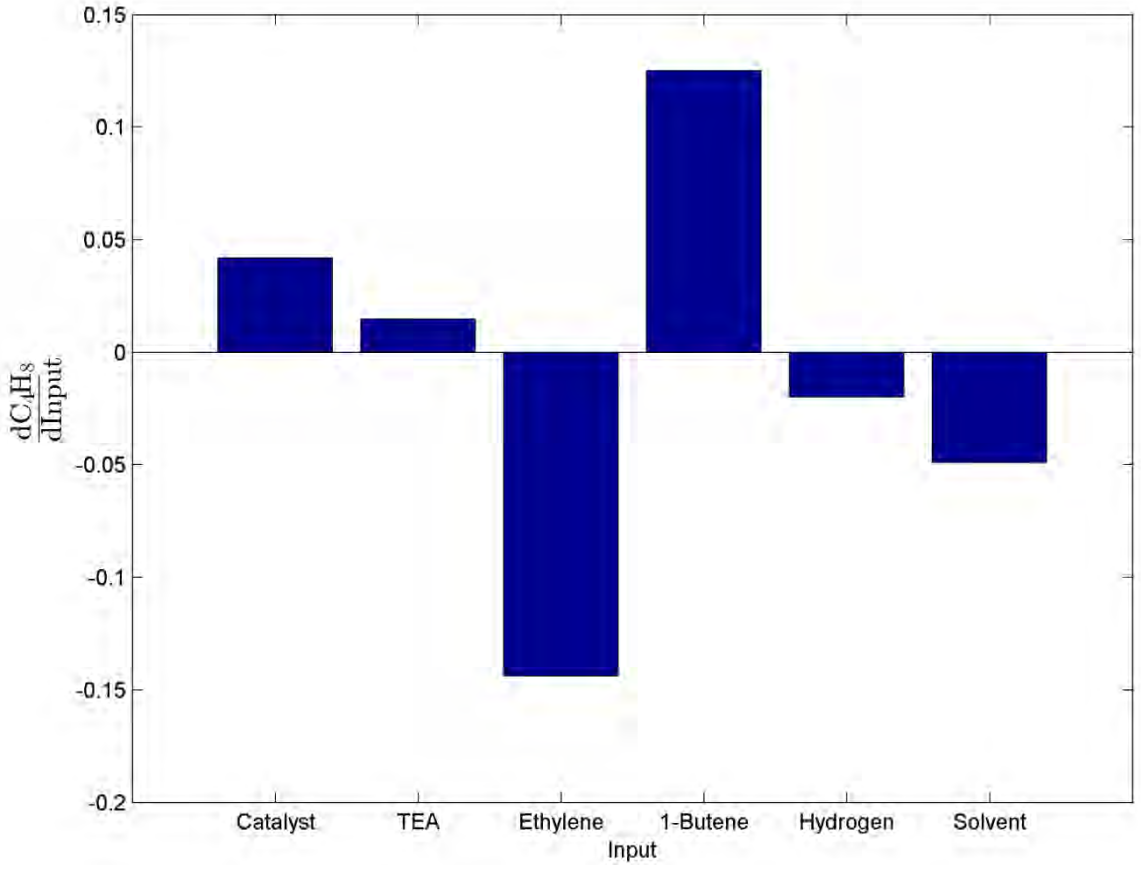

Figure 29.7: Sensitivity of C_4H_8 content to inputs. C_4H_8 content in [mol%]